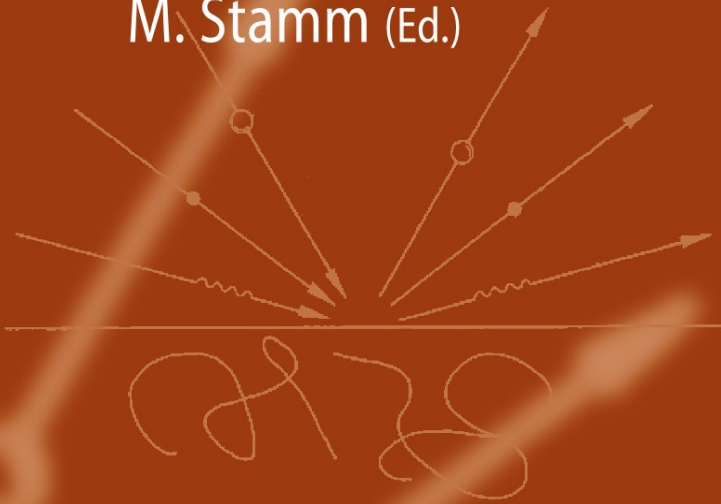


M. Stamm (Ed.)



Polymer Surfaces and Interfaces

Characterization, Modification
and Applications

 Springer

Polymer Surfaces and Interfaces

First edition

Manfred Stamm
Editor

Polymer Surfaces and Interfaces

Characterization, Modification
and Applications

First edition

With 181 Figures and 18 Tables

 Springer

Prof. Dr. Manfred Stamm
Leibniz Institute of Polymer Research Dresden
Hohe Straße 6
01069 Dresden
Germany
stamm@ipfdd.de

ISBN 978-3-540-73864-0

e-ISBN 978-3-540-73865-7

DOI 10.1007/978-3-540-73865-7

Library of Congress Control Number: 2007931850

© 2008 Springer-Verlag Berlin Heidelberg

This work is subject to copyright. All rights are reserved, whether the whole or part of the material is concerned, specifically the rights of translation, reprinting, reuse of illustrations, recitation, broadcasting, reproduction on microfilm or in any other way, and storage in data banks. Duplication of this publication or parts thereof is permitted only under the provisions of the German Copyright Law of September 9, 1965, in its current version, and permissions for use must always be obtained from Springer. Violations are liable to prosecution under the German Copyright Law.

The use of general descriptive names, registered names, trademarks, etc. in this publication does not imply, even in the absence of a specific statement, that such names are exempt from the relevant protective laws and regulations and therefore free for general use.

Typesetting: LE-T_EX Jelonek, Schmidt & Vöckler GbR, Leipzig

Production: LE-T_EX Jelonek, Schmidt & Vöckler GbR, Leipzig

Cover design: KünkelLopka, Heidelberg

Printed on acid-free paper

9 8 7 6 5 4 3 2 1

springer.com

Preface

On the Surface

I do not know what I may appear to the world, but to myself I seem to have been only like a boy playing on the sea-shore, and diverting myself in now and then finding a smoother pebble or a prettier shell than ordinary, whilst the great ocean of truth lay all undiscovered before me.

(Sir Isaac Newton, 1642–1727)

When we look at the advancement of science and scientific knowledge, it is in many cases coupled with the advancement of experimental techniques. This is true for instance in astronomy, where the introduction of telescopes allowed the exploration of space, but it is similarly true at small scales, where for instance the introduction of optical microscopes revolutionized biomedicine and made the discovery of bacteria possible with impacts on diagnostics and medical treatments. Today's modern technologies and in particular nanotechnology would not be possible without all the nice instruments and tools, which even allow the imaging of single molecules and atoms at nanoscale. Therefore it is essential for the researcher to keep track of new developments and to know the possibilities – and limitations – of modern analytical techniques.

Surfaces and interfaces of polymers play an important role, both for basic materials science as well as for the design and development of applications. If one reflects more closely about it, nearly all aspects of polymer research and application are directly or indirectly connected with surface and interface phenomena. So polymers are in large quantities applied as coatings and thin films, where of course the appearance, durability and stability depends on the surface and interface properties. But similarly bulk applications require smooth, coloured or scratch resistant surfaces, to name only some of the surface properties, and also the properties in the bulk like toughness or impact resistance of polymers are connected with defect, void or crack formation, which involves internal interfaces. Many polymer

applications involve blends, copolymers and additives, where again morphologies and interfacial aspects strongly influence materials properties. The detailed analysis of surfaces and interfaces therefore turns out to be essential for materials development and optimization, while on the other hand in most cases this analysis is not easy to perform and involves dedicated techniques. It is the purpose of this book to introduce surface and interface analysis techniques including recent developments and to provide a first help in the choice of the technique – or in most cases in the choice of the combination of techniques – which may serve for the solution of a particular problem. It is on the other hand not possible to cover the techniques in great detail and references for further reading are given. Similarly it is not possible to cover all techniques available, and we therefore have chosen a survey of techniques which we believe are the most important and commonly used ones. We also have chosen some examples and application areas, where surfaces and interfaces play an important role and which illustrate their importance.

The book is based on a course for students, researchers and technicians, which we have been offering regularly at our institute in Dresden since 2003. The course contains also experimental and lab presentations, which are very helpful for a better understanding of the possibilities of the techniques. It also is modified and improved every time with a changing team of experts. The book contains a more detailed presentation of surface and interface analysis techniques and provides in particular also useful hints for further reading. We hope that it will help many researchers in solving their problems in this challenging field.

Dresden, 16 July, 2007

Manfred Stamm

Contents

1	Polymer Surface and Interface Characterization Techniques	1
	<i>Manfred Stamm</i>	
1.1	Surface and Interfacial Tension (ST, IT).....	6
1.2	X-Ray Photoelectron Spectroscopy (XPS).....	7
1.3	Scanning Force Microscopy (SFM)	8
1.4	Ellipsometry (ELLI) and Surface Plasmon Spectroscopy (SP).....	9
1.5	Infrared Spectroscopy (ATR-FTIR).....	9
1.6	X-Ray and Neutron Reflectometry (XR, NR).....	10
1.7	Scanning and Transmission Electron Microscopy (SEM, TEM) ...	11
1.8	Electrokinetic Methods (Zeta Potential).....	12
1.9	Optical Microscopy Techniques (OM).....	12
1.10	Secondary Ion Mass Spectrometry (SIMS).....	13
1.11	Indentation, Adhesion, Mechanical Properties.....	13
1.12	Inverse Gas Chromatography (IGC)	15
1.13	Ion Techniques (FIB, RBS, ERD, NRA)	15
	References	16
2	Structure Determination in Thin Film Geometry Using	
	Grazing Incidence Small-Angle Scattering	17
	<i>Peter Müller-Buschbaum</i>	
2.1	Introduction.....	17
2.2	Real Space Analysis.....	20
2.3	Reciprocal Space Analysis – Scattering.....	21
	2.3.1 Conventional Diffuse Scattering.....	23
	2.3.2 Grazing Incidence Small-Angle Scattering	24
2.4	Experimental Set-Ups for GISAS	27
	2.4.1 GISAXS.....	28
	2.4.2 GISANS.....	29

2.5	Selected Cuts from 2D Data.....	30
2.5.1	Out-of Plane Scans	30
2.5.2	Detector and Off-Detector Scans	31
2.6	Selected Examples	33
2.6.1	Spin-Coated Thin Polymer Films	33
2.6.2	Dewetted Polymer Blend Films.....	35
2.6.3	Dewetted Diblock Copolymer Films	36
2.7	Summary	38
	Acknowledgments	39
	References	39
3	Vibrational Spectroscopic and Optical Methods	47
	<i>Martin Müller</i>	
3.1	Introduction.....	47
3.2	Vibrational Spectroscopic Methods	48
3.2.1	Principles	48
3.2.2	Transmission Infrared (TRANS-IR).....	51
3.2.3	Attenuated Total Reflexion Infrared (ATR-IR).....	52
3.2.4	Grazing Incidence Infrared (GIR).....	58
3.2.5	Diffuse Reflexion Infrared (FT) (DRIFT)	59
3.2.6	Raman Spectroscopy	61
3.3	Optical Methods.....	62
3.3.1	Ellipsometry	62
3.3.2	Surface Plasmon Resonance (SPR)	65
3.4	Summary	69
	Acknowledgments	69
	References	69
4	X-Ray Photoelectron Spectroscopy	71
	<i>Dieter Pleul and Frank Simon</i>	
4.1	Introduction, History and Physical Principle	71
4.2	Instrumentation	73
4.3	Information Depth.....	74
4.4	Polymer and Other Non-Conducting Samples	75
4.5	Wide-Scan Spectra – Quantification and Interpretation.....	76
4.6	High-Resolution Element Spectra – Peak Deconvolution and Interpretation	80
4.7	Labelling – The Derivatization of Functional Groups for its Identification.....	82
4.8	Angle-Resolved XPS	84
4.9	Special XPS Techniques	85
4.9.1	Kryo-XPS	86
4.9.2	Small-Spot XPS.....	86
4.9.3	Imaging-XPS	87

References	88
Monographs and Reviews	89
5 Time-of-Flight Secondary Ion Mass Spectrometry	91
<i>Dieter Pleul and Frank Simon</i>	
5.1 Introduction, History and Physical Principle	91
5.2 Instrumentation	93
5.3 Samples	95
5.4 Time-of-Flight Secondary Ion Mass Spectra and Their Interpretation.....	95
5.5 Imaging Time-of-Flight Secondary Ion Mass Spectroscopy.....	99
References	101
Monographs and Reviews	101
6 Characterization of Polymer Surfaces by Wetting and Electrokinetic Measurements – Contact Angle, Interfacial Tension, Zeta Potential .	103
<i>Karina Grundke</i>	
6.1 Introduction.....	103
6.2 Theoretical Background of Wetting and Electrokinetic Phenomena	106
6.2.1 Contact Angle, Interfacial Tension, Laplace and Young Equations.....	106
6.2.2 Wettability of Solid Surfaces.....	113
6.2.3 Origin of Surface Charge, Electrical Double Layer, Zeta Potential.....	119
6.3 Experimental Techniques.....	124
6.3.1 Contact Angle Measurements: Sessile Drop or Adhering Bubbles, Wilhelmy Balance Technique, Capillary Penetration	124
6.3.2 Zeta Potential Measurements: Particle Electrophoresis, Electro-Osmosis, Streaming Potential, Sedimentation Potential	134
References	136
7 Mechanical Properties of Polymers at Surfaces and Interfaces	139
<i>Konrad Schneider</i>	
7.1 Introduction.....	139
7.2 Overview of Mechanical Bulk Behaviour.....	140
7.3 Fracture Mechanical Characterization of Polymers and Composites.....	144
7.3.1 Stress Intensity-(K-)Factor	144
7.3.2 Energy Release Rate	145
7.3.3 The Concept of Crack Resistance-(R-)Curve	146
7.3.4 Stress–Strain Situation and Failure in Heterogeneous Systems.....	147

7.3.5	Characterization of Interlaminar Strength in Composites	147
7.3.6	Some Remarks on Shear Tests	149
7.4	Characterization of Surface Forces and Adhesion	150
7.4.1	Peel Test	150
7.4.2	Blister Tests	151
7.4.3	Blade Cutting Test (Hesiometer)	152
7.4.4	The Adhesion Scratch Test (Diamond Scratch Test, Stylometer), Nanoscratch Test.....	153
7.4.5	Nanoindentation Test.....	154
7.4.6	Surface Force Measurement: Surface Force Apparatus/MASIF	156
7.4.7	Force Measurement by AFM/SFM.....	158
7.4.8	Colloidal Probe Techniques with the SFM.....	159
	References	160
8	Interfaces Between Incompatible Polymers	161
	<i>Peter Busch and Roland Weidisch</i>	
8.1	Introduction	161
8.2	Theory	163
8.3	Neutron Reflectometry	165
8.4	Applications	168
8.4.1	Homopolymers	168
8.4.2	Polymer Blends	171
8.4.3	Block Copolymers	172
8.4.4	Organic Films and Polymer Brushes	177
8.4.5	Comparison with Real Space Techniques.....	179
8.5	Conclusion	181
	References	182
9	Liquid–Liquid and Liquid–Vapor Interfaces in Polymeric Systems	183
	<i>Marcus Müller</i>	
9.1	Introduction	183
9.2	Interfaces in Binary Polymer Blends	184
9.3	Self-Consistent Field (SCF) Theory.....	186
9.4	Excess Quantities	188
9.5	Interface Fluctuations.....	189
9.6	Kinetics of Phase Separation.....	190
9.7	Liquid–Vapor Interfaces	193
9.7.1	Phase Behavior, Packing Effects and Density Functional Theory.....	193
9.7.2	Wetting and Stability of Thin Films	197
9.7.3	Explicit Solvent	198
9.8	Outlook	199

Acknowledgements	200
References	200
10 Plasma Modification of Polymer Surfaces and Plasma Polymerization	203
<i>Mirko Nitschke</i>	
10.1 Plasma Modification of Polymer Surfaces	203
10.1.1 Why Use Low Pressure Plasma?	203
10.1.2 How to Apply Low Pressure Plasma	205
10.1.3 Examples	207
10.2 Plasma Polymerization	211
10.2.1 Why Use Plasma Polymerization?	211
10.2.2 How to Apply Plasma Polymerization	212
10.2.3 Example	213
10.3 Recommended Literature	213
References	214
11 Grafting on Solid Surfaces: “Grafting to” and “Grafting from” Methods	215
<i>Sergiy Minko</i>	
11.1 Introduction	215
11.2 Behavior of Polymer Brushes	217
11.2.1 Homopolymer Brushes	217
11.2.2 Bidisperse Polymer Brushes	219
11.2.3 Mixed Polymer Brushes	220
11.2.4 Block-Copolymer Brushes	224
11.3 Synthesis of Polymer Brushes	225
11.3.1 Modification of Solid Substrate	225
11.3.2 “Grafting to” Method	227
11.3.3 “Grafting from” Method	228
11.3.4 Synthesis of Mixed Brushes	229
11.3.5 Controlled Synthesis of Polymer Brushes by “Living” Free Radical Polymerization	230
References	231
12 Surface Modification by Adsorption of Polymers and Surfactants	235
<i>Cornelia Bellmann</i>	
12.1 Introduction	235
12.2 Fundamentals	236
12.2.1 The Role of the Solid Surface	240
12.2.2 The Role of the Solvent	240
12.2.3 Influence of the Third Substance	241
12.2.4 Adsorption of Uncharged Macromolecules	241
12.2.5 Adsorption of Polyelectrolytes and Polyampholytes	243
12.2.6 Adsorption of Surfactants	244

12.3	Selected Methods for Investigation of Adsorption Processes	246
12.4	Applications	249
12.4.1	Adsorption of Surfactants	250
12.4.2	Adsorption of Polyelectrolytes	254
12.4.3	Adsorption of Coupling Agents	255
	References	257
13	Nanostructures in Thin Films from Nanostructured Polymeric Templates: Self-Assembly	261
	<i>Alexander Sydorenko</i>	
13.1	Introduction	261
13.2	Self-Assembly for Nanostructuring	261
13.2.1	Self-Assembly in Block Copolymers	262
13.2.2	Supramolecular Assemblies Based on Block Copolymers	265
13.2.3	Self-Assembly in SMA	265
13.3	Ordering and Orientation in SMA	268
13.4	Nanoreactors for Nanoparticles	271
13.5	Conclusions	271
	References	272
14	Influencing the Interface in Polymer Blends by Compatibilization with Block Copolymers	275
	<i>Doris Pospiech</i>	
14.1	Introduction: Why Block Copolymers and Polymer Blends?	275
14.2	Miscibility of Polymers: Thermodynamic Basics	278
14.3	Compatibilization of Immiscible Polymer Blends: General Options	281
14.3.1	Introduction of Specific Interactions	282
14.3.2	Reactions Between the Polymer Phases in the Blend	283
14.3.3	Block Copolymers as Compatibilizers	286
14.4	Compatibilization in Polymer Blends: Examples	287
14.4.1	Compatibilization by Using Reactions Between the Polymers	287
14.4.2	Compatibilization with Block Copolymers	292
14.4.3	Conclusions	295
	References	296
15	Interfacial Phenomena of Biomaterials	299
	<i>Carsten Werner</i>	
15.1	Introduction	299
15.2	The Hierarchy of Bio-Interfacial Phenomena	301
15.2.1	Surfaces of Biomaterials in Pre-Application Settings	302
15.2.2	Biopolymers at Interfaces	303
15.2.3	Biomaterials in Contact with Cells and Tissues	305

15.3	Surface Modification of Polymeric Biomaterials.....	308
15.3.1	Minimizing Non-Specific Interactions	308
15.3.2	Implementing Bioactive Elements – Modulating Molecular Signals	310
15.3.3	Supramolecular Biopolymer Assemblies Providing Morphogenetic Cues	313
15.4	Conclusion	315
	Acknowledgements	316
	References	316
Index	319

Contributors

Cornelia Bellmann

Leibniz Institute of Polymer Research Dresden, Hohe Str. 6, 01069 Dresden, Germany, bellmann@ipfdd.de

Peter Busch

JCNS-FRMII, TU-München, Lichtenbergstr. 1, 85747 Garching, Germany, p.busch@fz-juelich.de

Karina Grundke

Leibniz Institute of Polymer Research Dresden, Hohe Str. 6, 01069 Dresden, Germany, grundke@ipfdd.de

Sergiy Minko

Department of Chemistry and Biomolecular Science #5810, Clarkson University, 8 Clarkson Ave., Potsdam, NY 13699, USA, sminko@clarkson.edu

Marcus Müller

Institut für Theoretische Physik, Georg-August Universität, Friedrich-Hund-Platz 1, 37077 Göttingen, Germany, mmueller@theorie.physik.uni-goettingen.de

Martin Müller

Leibniz Institute of Polymer Research Dresden, Hohe Str. 6, 01069 Dresden, Germany, mamuller@ipfdd.de

Peter Müller-Buschbaum

Technical University München, Physik Department LS E13, James-Franck-Str. 1, 85747 Garching, Germany, peter.mueller-buschbaum@ph.tum.de

Mirko Nitschke

Leibniz Institute of Polymer Research Dresden & Max Bergmann Center of Biomaterials Dresden, Hohe Str. 6, 01069 Dresden, Germany, nitschke@ipfdd.de

Dieter Pleul

Leibniz Institute of Polymer Research Dresden, Hohe Str. 6, 01069 Dresden, Germany

Doris Pospiech

Leibniz Institute of Polymer Research Dresden, Hohe Str. 6, 01069 Dresden, Germany, pospiech@ipfdd.de

Konrad Schneider

Leibniz Institute of Polymer Research Dresden, Hohe Str. 6, 01069 Dresden, Germany, schneider@ipfdd.de

Frank Simon

Leibniz Institute of Polymer Research Dresden, Hohe Str. 6, 01069 Dresden, Germany, frsimon@ipfdd.de

Manfred Stamm

Leibniz Institute of Polymer Research Dresden, Hohe Str. 6, 01069 Dresden, Germany, stamm@ipfdd.de

Alexander Sydorenko

University of the Sciences in Philadelphia, Department of Chemistry and Biochemistry, Philadelphia, Pennsylvania, 19104, a.sidorenko@usip.edu

Roland Weidisch

Friedrich-Schiller-Universität Jena, Institut für Materialwissenschaft und Werkstofftechnologie, Lößdergraben 32, 07743 Jena, Germany, roland.weidisch@uni-jena.de

Carsten Werner

Leibniz Institute of Polymer Research Dresden & Max Bergmann Center of Biomaterials Dresden, Hohe Str. 6, 01069 Dresden, Germany, werner@ipfdd.de

Chapter 1

Polymer Surface and Interface Characterization Techniques

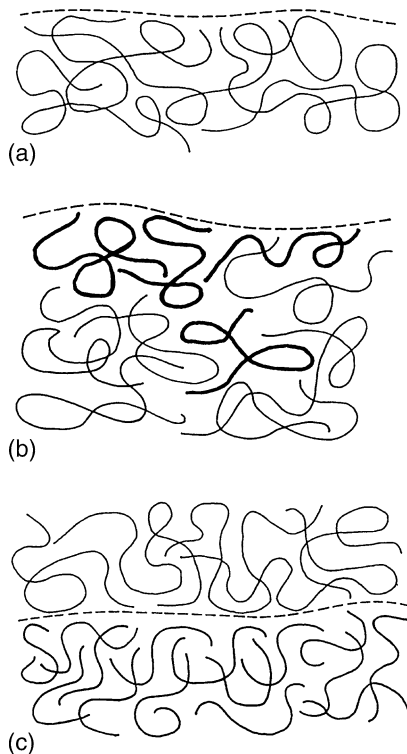
Manfred Stamm

Leibniz Institute of Polymer Research Dresden, Hohe Str. 6, 01069 Dresden, Germany,
stamm@ipfdd.de

Abstract The surfaces and hidden interfaces of polymers play an important role in the properties and applications of polymers. The most important characterization techniques are briefly discussed and compared with each other with respect to the information that can be gained, but also with respect to applicability to polymer surface and interface analysis. This survey should help in the choice of the techniques for a particular problem and provides an introduction to the more detailed descriptions of individual techniques of the book.

Surfaces and interfaces are important for many properties and applications of polymers, although one often may not recognize their importance at first glance. This is for instance true for inhomogeneous polymer blends, where the interface between different phases plays a crucial role for mechanical properties, or for the application of ultra-strength composite materials in airplanes, where adhesion between material layers is essential. But also for everyday polymeric parts, for instance in toys or automotives, one may ask questions like “how do they feel” or “how do they look” which might critically influence the decision for the purchase of the product. Those properties also depend on “the surface”, where the optical or mechanical appearance for the user, and also corrosion or scratch resistance, are determined by surface composition and structure. The analysis of polymer surfaces and interfaces in many cases requires quite special techniques, and often only a combination of different techniques can help. It is however the prerequisite for the understanding and finally the dedicated design of the properties. This is in particular the case, when functional or smart surfaces or interfaces are desired, which for instance provide biocompatibility, switching or adaptive properties.

Fig. 1.1 Schematical picture of polymer surfaces and interfaces. (a) amorphous homopolymer surface; (b) polymer blend with surface segregation of one component; (c) interface between polymers



The situation does not become easier by the fact that different people may understand quite different things when talking about surfaces and interfaces. So the surface or interfacial region may range from sub-nanometres to micro- or even millimetres depending on the properties under consideration, thus covering a range of more than 6 orders of magnitude. Looking at the individual polymer chains (Fig. 1.1), the surface and interfacial region ranges typically over one chain, where the radius of gyration is of the order of 3–30 nm. Similarly quite different microscopic surface properties or in general a combination of them might be important to achieve a particular macroscopic property or appearance. When the wetting of a smooth surface by a liquid is concerned, it is basically the composition of the outermost surface layer which is important for the wetting behaviour and one would have to learn about the composition of the first atomic layers at a sub-nanometre scale. When on the other hand the optical appearance of a surface is on demand, one is dealing with optical properties of a surface layer of typically micrometre thickness, while for the adhesion between two sheets of polymeric materials a region in the vicinity of the interface of up to more than a millimetre may be important where most of the deformation energy is dissipated in the plastic zone. Thus different applications and questions require different approaches with respect to analytical techniques and one should first carefully define the problem before one can look for the suitable surface or interface analysis technique.

A compilation of some common surface and interface analysis techniques is given in tables 1.1 and 1.2 indicating the typical information which can be obtained utilizing a particular technique as well as its typical minimal information depth. In some cases the parameters indicated depend very much on the mode used, the sample system and available contrast, and some quantities cannot be obtained independent from each other. Thus for instance there are many different optical microscopy techniques ranging from simple dark and bright field to differential interference, fluorescent or phase measurement interference techniques. The possibilities and the information obtained are quite different for the different techniques.

There are several reviews and general books available which cover surface and interfacial analysis (see, e. g. [1–6]) or provide information on particular aspects [7–10]. In the following we will cover briefly the different techniques from Tables 1.1 and 1.2. Some of most important techniques then will be discussed in more detail in the following contributions, where also examples of applications will be given. Very schematically some techniques for surface analysis are shown in Fig. 1.2 where different types of radiation are utilized for the incident and outgoing beams.

We will distinguish in Tables 1.1 and 1.2 between surface and interface analysis techniques, although this distinction is not rigorously possible. Some techniques (Figs. 1.2 and 1.3) can be used both for surface and interface analysis (e. g. X-Ray reflectometry, SIMS, optical techniques, etc.), but they are used in different modes of application. The optimal sample requirements are also different from one technique to the next, and the surface might be facing vacuum, air, liquid or even a polymer solution. The choice and the information content of a particular technique depends of course very much on this environment and one has to be careful, to really analyse the true materials behaviour and not artefacts. One might on the other hand also just be interested in a contamination layer at the surface, which can change surface properties of materials quite significantly. Also the resolution will very much depend on many parameters and in particular on the sample condition and preparation, and therefore only “typical” values for favourable conditions are given in the tables. Again it should be emphasized that in this short introductory review not all of those aspects can be discussed, and many techniques have elegant ways to focus on particular aspects or to overcome some of the shortages. Those aspects will be discussed in more detail in the following contributions.

Table 1.1 Most common techniques for surface characterization

Technique	Probe In / out	Smallest information depth / width (nm)	Information	Comments
Surface tension / Contact angle ST	Liquid drop	0.1 / 1000	Surface energy	Easy to use, molecu- lar information difficult
X-Ray photoelectron spectroscopy XPS	X-Rays / electrons	5 / 3000	Chemical composi- tion, binding state	Quantitative, vacu- um technique, later- al imaging possible
Scanning force micros- copy SFM	Canti- lever	0.05 / 1	Surface topography, composition, tough- ness	Atomic resolution, many different modes
Ellipsometry ELLI	Polar- ized light	0.1 / 500	Thin surface layer	Molecular interpre- tation difficult
Infrared attenuated total reflection ATR-FTIR	Infrared light	2000 / 2000	Surface composi- tion, binding state	Specific ATR- crystal needed
X-Ray reflectometry XR Grazing incidence X-Ray small angle scattering GISAXS	X-Rays	0.5 / 0.1	Surface roughness, thin surface layers, lateral structure	Flat surfaces required
Scanning electron mi- croscopy SEM	Elec- trons	2 / 1	Surface topography	Vacuum technique
Focused ion beam FIB	Ions (elec- trons)	2/10 (1 for SEM)	Imaging, cutting, deposition	Nanomaniplation possible, often in combination with SEM, vacuum
Scanning tunnelling microscopy STM	Cantile- ver	0.05 / 1	Tunnelling current	Surface conductivity required
Electrokinetic meas- urements/ zeta potential	Voltage	0.1 / -	Surface charge	Measurement in aqueous medium
Optical microscopy OM	Light	0.1 / 300	Surface roughness, structure	Many possibilities, good height resolu- tion with interfer- ence techniques
Surface plasmon spec- troscopy SP	Light / plas- mons	0.1 / 300	Thin surface layers	Metallic layer on prism necessary
Secondary ion mass spectroscopy SIMS	Ions	0.1 / 1000	Surface composi- tion, contaminations	« Static » mode, vacuum technique
Micro-indentation MI	Canti- lever	100 / 200	Surface hardness, module	Quantitative inter- pretation difficult
Neutron reflectometry NR	Neutrons	0.5 / -	Surface roughness, enrichment layer	Deuterated com- pounds needed

Table 1.1 (continued)

Technique	Probe In / out	Smallest information depth / width (nm)	Information	Comments
Auger spectroscopy AS High-resolution electron energy loss spectroscopy HREELS	Electrons	0.2 / 100 1	Electronic excitation, surface composition Vibration spectrum	Surface conductivity needed, vacuum technique
Scanning near field optical microscopy SNOM	Light	1 / 50	Vibrational modes, fluorescence, orientation	Local optical spectroscopy possible
Inverse gas chromatography IGC	Gas	0.1 / –	Gas adsorption, surface functionality, energetics	Measurement on powder
Resonance enhanced Raman spectroscopy RS	Light	0.5 / 500	Surface composition, binding state	Resonance enhancement with metal clusters

Table 1.2 Most common techniques for interface characterization

Technique	Probe In / out	Smallest information depth (at 100 nm depth) (nm)	Information	Comments
Pendent drop	Liquid	0.2	Interface tension	Indirect technique
Elastic recoil detection ERD Forward recoil spectroscopy FRD	^4He / ^1H , ^2H (H, D)	20	H/D distribution, interface width	Contrast by deuteration
Nuclear reaction analysis NRA	15 N / γ (4.4 MeV) ^3He / ^4He	12	H/D distribution, interface width	Contrast by deuteration
Rutherford backscattering RBS	^4He / ^4He	30	Backscattering from heavy atoms, interface width	Contrast from heavy atoms
Secondary ion mass spectrometry SIMS	Ions	20	Element distribution, interface width	Dynamic (destructive) technique
Neutron reflectometry NR	Neutrons	0.2	Interference fringes, interface width/ roughness	Contrast by deuteration
Focused ion beam FIB	Ions (electrons)	10 (1 for SEM)	Concentration profile, element distribution, interface width	Cut perpendicular to interface with ions, imaging with SEM

Table 1.2 (continued)

Technique	Probe In / out	Smallest information depth (at 100 nm depth) (nm)	Information	Comments
Transmission electron microscopy TEM	Electrons	0.5	Absorption/ reflection of electrons, interface width	Cut perpendicular to interface, staining
X-Ray reflectometry XR	X-Rays	0.2	Interference fringes, interface width/roughness	Contrast of heavy elements
Scanning force microscopy SFM	Cantilever	0.2	Interface width/ roughness/ topography	Cut perpendicular to interface/ etching, dissolution/hard tapping
Small angle X-Ray scattering SAXS	X-Rays	1	Porod analysis, electron density variation, interface width	Bulk sample possible
Nuclear magnetic resonance NMR	Magnetic field	1	Spin diffusion from species, interface width	Bulk sample possible
Fluorescence quenching	Light	0.3	Quenching of donor/ acceptor molecules	Fluorescence tagging of molecules necessary

1.1 Surface and Interfacial Tension (ST, IT)

The most common way to obtain a picture of the surface properties and to measure the surface energetic state is the determination of the *surface tension*. It is mostly determined by the outermost layers of atoms and therefore by a surface region of typically 0.2 nm. It depends, on the other hand, on surface roughness and is very sensitive to surface segregation of components and in particular to contaminations. It thus in many practical cases may not reflect the properties of the bulk material but of a thin surface contamination layer. Information on surface composition and structure is only provided in a quite indirect way, while it is relatively easy to measure in the lab and often provides helpful practical information for the application.

The surface tension is a very fundamental property of solids and liquids. It reflects in principle directly the strength of bonding within the bulk material. Due to very different binding forces, hard solids (covalent, ionic, metallic) typically reveal “high-energy” surfaces (surface tension $\sim 500\text{--}5000 \text{ mJ/m}^2$) in contrast to weak molecular solids and liquids (soft matter) with “low-energy” surfaces (surface tension $< 100 \text{ mJ/m}^2$). Most polymers belong to the second class of materials where interactions between chains are dominated by van der Waals forces and hydrogen bonds.

Surface and interfacial tensions of polymers play a key role in wetting and coating processes, in biocompatibility or polymer blending, and in corrosion and adsorption processes. The behaviour of colloidal dispersions, adhesion, and friction is influenced by surface and interface tension. Despite their importance, interrelationships between interfacial aspects and materials properties are still poorly understood. The surface tension of polymers is in most cases determined from the *contact angle*, when a liquid drop is positioned on the sample surface. Besides measuring directly the contact angle between drop and sample surface at the drop edge, drop profile analysis techniques are used to enhance sensitivity. Measurements are in many cases performed in a dynamic way, where the drop volume is continuously enlarged (advancing contact angle) or decreased (receding contact angle). In particular for inhomogeneous and rough surfaces the advancing and receding contact angles can be significantly different.

The *interfacial tension* between different polymers and between a polymer and a substrate on the other hand is in general much more difficult to determine than the surface tension and has been measured only for specific examples. High viscosities of materials, long time scales for achievement of equilibrium and sample decomposition make the measurement for high molecular weight polymer compounds very difficult. It provides, however, a way to determine the interface width and compatibility of polymer materials on the basis of model assumptions (mean field theory). In most cases either the pendant or rotating drop technique are used.

1.2 X-Ray Photoelectron Spectroscopy (XPS)

XPS is a powerful technique to characterize the chemical composition of polymer surfaces, where with polymers a depth of typically 7 nm is probed. For XPS also the acronym *ESCA* for *electron spectroscopy for chemical analysis* is used to demonstrate the aim of the method (chemical analysis) as well as the combination of photoelectron and Auger electron peaks in the observed spectra (electron spectroscopy). Soft X-Rays excite electrons from the inner shells or valence bands, which are ejected. The photoelectron spectrometer measures quantitatively the number of photoelectrons as a function of incident energy which are leaving the sample surface. The energy spectrum is characteristic of the elemental composition and binding state of atoms at the sample surface. Therefore it can be used to quantitatively determine the surface composition of different species. It has to be applied under vacuum and with non-conducting surfaces special care has to be taken to avoid surface charging.

While the lateral resolution with conventional scanning XPS instruments is typically not better than several micrometres, the lateral resolution is significantly improved with X-Ray photo-electron emission microscopy XPEEM, where electron microscopy optics is used to image the outgoing electrons. The lateral resolution can be of the order of 30 nm, when soft X-Rays from a synchrotron source are used. Transmission X-Ray microscopy TXM utilizes the absorption of soft X-Rays

from a synchrotron source in a thin sample film for lateral imaging of chemical composition at a similarly good resolution.

1.3 Scanning Force Microscopy (SFM)

Scanning force microscopy (anonym: atomic force microscopy AFM) provides high resolution both in width and height at the surface of a film or substrate, and single polymer molecules adsorbed on a smooth solid substrate have been resolved. Its development has advanced significantly over the last years. With many features including contact, non-contact, hard/soft tapping, materials, adhesion, phase, friction or chemical contrast, indentation, soft mode, measurement of force in different directions, use of tunnelling current or magnetic interactions and its ability to measure in vacuum, air, inert atmosphere or liquid, to list only the most common features of commercial instruments, it offers fascinating and versatile possibilities. Different aspects of a surface can be used to obtain a microscopic picture at nanoscopic resolution. One can measure and image the surface with respect to topography, surface hardness, roughness, adhesion, friction, conductivity, charge or magnetism. Since the strength of interaction of the tip with the substrate can be controlled (e. g. from non-contact to hard tapping) and the surface can be carefully removed by slow etching or dissolution techniques, it can also be used for the investigation of structures inside the sample and at interfaces.

In addition it allows manipulation of molecules and atoms at the surface and for example single atoms have been positioned on the surface in a regular way by the tip. It therefore is not only an analytical but also a nano-manipulation tool. The tip can also be functionalised (chemical recognition) or modified by attachment of colloidal particles (measurement of interaction forces, adhesion, friction) or carbon nanotubes (improved resolution). Its strength comes from the fact that one can get relatively easily a lateral image in different modes at nanoscopic resolution, while it is not trivial to obtain surface properties at quantitative level with this technique.

A similar technique is scanning tunnelling microscopy where the tunnelling current between tip and surface is measured and used for tip control. It is however mostly applied with conductive samples like metals or semiconductors. Spectroscopic information can be obtained with scanning near-field optical microscopy, SNOM, where a tiny light guiding tip illuminates the sample. The emitted or absorbed light is then analysed.

1.4 Ellipsometry (ELLI) and Surface Plasmon Spectroscopy (SP)

With ellipsometry the change of the polarization state of reflected light from a surface is determined (Fig. 1.3). It can be used to measure the thickness and index of refraction of a thin film on a reflecting substrate at high precision (resolution better than 1 nm depending on optical contrast) and as a function of time. For very thin films the two quantities cannot be measured independently and only the optical thickness is determined. For thicker films the technique can provide however the thickness and index of refraction of the layer independent of each other, as well as information on its anisotropy and roughness. Also lateral information on the variation of thickness or index of refraction on a micrometre scale can be resolved either by direct ellipsometric imaging (microscopy) or by scanning techniques. Problems and limitations often arise from the correlation of thickness and index of refraction, insufficient optical contrast in multilayer samples, but also from ambiguities in the interpretation of data in more complex situations, where detailed information is difficult to extract from the limited experimental data. In those cases spectroscopic or variable angle ellipsometry may help to some extent. Measurements are possible under various environmental conditions and for instance the adsorption kinetics of molecules from solution at a solid substrate may be measured in situ with a liquid cell. By use of a synchrotron source also IR ellipsometry can be performed, which can provide information on binding states in monolayer polymer films or elemental composition.

A very similar technique is surface plasmon spectroscopy (Fig. 1.3) where surface plasmons in a thin metal layer are excited by the incident light. The interaction with the adjacent polymer layer influences the plasmon resonance, which can be analysed with respect to polymer film thickness and index of refraction. Information is thus comparable to ellipsometry.

1.5 Infrared Spectroscopy (ATR-FTIR)

Infrared spectroscopy can be used in reflection or attenuated total reflection mode (ATR-FTIR) for surface and thin film investigations. As a spectroscopic technique it also allows quantitative determination of composition or binding states via vibrational modes and is a powerful analytical tool for the molecular detection of dynamics at the solid/liquid or solid/air interface. With ATR-FTIR multiple reflections from a smooth crystal are applied, and the interface between this crystal and the surrounding medium is investigated. At the interface the IR beam is totally reflected, but still penetrates into the surrounding medium (evanescent wave). Different materials can be distinguished by their IR spectrum and deuteration is sometimes used to enhance contrast between components. The penetration depth of the evanescent wave is of the order of the wavelength and the technique therefore probes a depth of several micrometres. With an IR microscope a sample can

be scanned or directly imaged, but lateral resolution is typically determined by the wavelength of the radiation. Scan speed and imaging is highly facilitated by use of an IR array detector where spectroscopic information is obtained at high spatial resolution. In addition high intensity IR synchrotron radiation may be used which enhances time resolution, but also allows us to utilize IR ellipsometric imaging techniques for the measurement of composition, orientation, thickness and index of refraction of thin films and surfaces.

1.6 X-Ray and Neutron Reflectometry (XR, NR)

Reflectometry techniques use the fact that X-Rays and neutrons are reflected at the interface (Fig. 1.3) when a suitable contrast is present. This contrast is given by the difference in electron density between materials for X-Rays, which means that X-Rays are sensitive in particular for the surface of thin films to air or vacuum. Only in special cases they can resolve the interface between two polymer films, where the electron densities are in most practical cases not very different. The contrast for neutrons on the other hand can very generally be generated by deuteration of one component, and the interfaces between polymers then can be resolved at nanometre resolution. Both techniques cannot easily distinguish between the “true” interface (generated, e. g. by interdiffusion between components) and the lateral fluctuations of the interface (generated by, e. g. thermal fluctuations, surface roughness or capillary waves). Both quantities are sometimes in the range of several nanometres. The quantitative interpretation of reflectometry data in terms of nanoscopic interface width therefore turns out to be difficult, but a separation between interdiffusion and lateral fluctuations may not be necessary in all cases. Both techniques can however provide valuable information on other aspects of thin films and interfaces at nanometre resolution including film thickness, surface segregation and profile of components in a blend, surface and interface roughness, capillary waves, interface width and asymmetry, interdiffusion, etc. They generally need highly smooth and flat samples, which extend laterally typically over several centimetres. They are then capable to provide information at sub-nanometre resolution largely depending also on quality of sample preparation (smoothness).

To obtain information on lateral structure at the surface or in a thin film, surface sensitive scattering of X-Rays and neutrons is performed at grazing incidence. The incident radiation should illuminate the sample at a small angle in the vicinity of the critical angle of total reflection to obtain best resolution. With high brilliant sources (synchrotron or high flux neutron reactor) the small (GISAXS) or wide (GIWAXS) angle scattering in the plane of the surface can be detected and provides information on lateral structure at nanometre level.

A careful analysis of small angle X-Ray or neutron scattering (SAXS, SANS) data also allows for a determination of the interface width in a two phase system (Porod law). This measurement is again only possible with high scattering contrast

between components. For scanning X-Ray microscopy a X-Ray microbeam (0.5–20 μm in diameter) from a hard X-Ray synchrotron source is scanned over the sample, and at each spot a full X-Ray small or wide angle scattering pattern is recorded with an area detector. This provides structural information at nanometre level spatially resolved at different locations of the sample.

1.7 Scanning and Transmission Electron Microscopy (SEM, TEM)

For surface investigations electron microscopy is used in scanning and reflection mode (SEM). SEM reveals an image of the surface at nanometre lateral resolution where contrast is obtained by electron absorption or emission. With several additional features for contrast generation for instance by electron energy loss or X-Ray fluorescence spectroscopy it can be used to image the element distribution. Sample degradation by the electron beam has to be considered (but also can be used for electron lithography). To improve contrast and resolution, the surface may be covered by a thin conducting film, which typically is sputtered at an angle with respect to the surface normal to obtain shading effects.

Interfaces may be investigated by transmission electron microscopy (TEM), when a typically 50 nm thick cut perpendicular to the interfacial plane (Fig. 1.3) is achieved. This cut can be produced with a microtome (cut with diamond knife) or with a focused ion beam (FIB, see below). With staining and other contrasting techniques the interface then may be envisaged. Resolution is limited by the average over the sample depth, but also by the preparation technique, which can cause artefacts and smearing of the interface width.

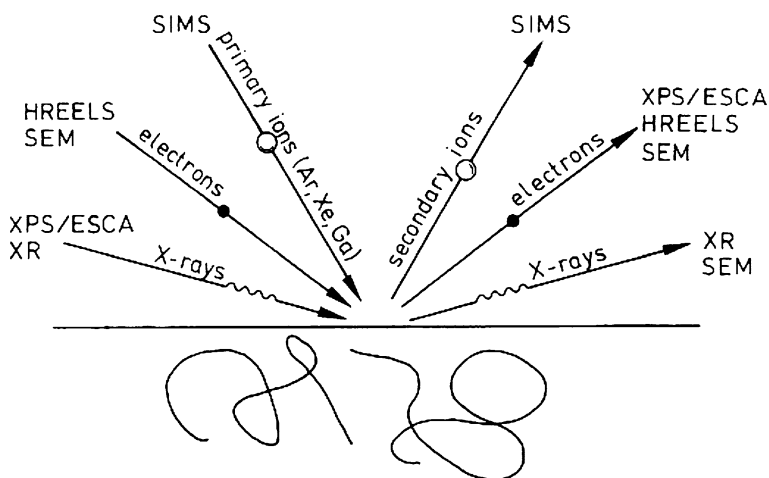


Fig. 1.2 Schematics of some surface characterization techniques where different types of radiation are used for incident and outgoing beam

1.8 Electrokinetic Methods (Zeta Potential)

The electrokinetic potential on the surface of a solid in contact with a polar medium is governed by the dissociation of surface groups, the preferential adsorption of cations or anions, the adsorption of polyelectrolytes, the isomorphic substitution of cations and anions, and the accumulation or depletion of electrons. Generally, descriptions of the charge distribution at an interface assume the presence of an electric double layer consisting of two regions: a fixed layer and a diffuse layer. Between these two parts lies a “surface of shear” or “slipping plane”. Externally applied electrical or mechanical forces cause a relative movement between the fixed part and the diffuse part. The potential at this surface is called the electrokinetic or zeta (ζ) potential. The electrokinetic potential can be determined by an externally applied electrical field, which causes a relative movement of the solid and liquid phases (electrophoresis, electro-osmosis), or a relative movement of the solid and liquid phases, which generates an electrical potential or produces an electrical current (streaming potential/streaming current, sedimentation potential). Several experimental techniques can be used, but with planar surfaces often the streaming potential is measured.

1.9 Optical Microscopy Techniques (OM)

The advantage of optical microscopy techniques is the easy possibility of lateral imaging of the surface and in some cases also of an interface in the sample. Lateral resolution is limited by the wavelength of light and ranges from typically 300 nm to micrometres. By the use of a tiny waveguide the lateral resolution can be enhanced to some nanometres (SNOM). With the use of interference techniques the sampling depth can be much better than that, and it enhanced with phase measurement interference microscopy to 0.5 nm. There are several microscopic techniques available at different level of sophistication which can be used for surface and interface characterization:

1. Light microscopy in reflection or transmission with, e. g. dark field or differential interference contrast for lateral inhomogeneities;
2. Phase measurement interference microscopy for surface topography with sub-nanometre; Height resolution;
3. Brewster angle, ellipsometric or surface plasmon microscopy for lateral thickness variation;
4. Fluorescence microscopy with labeled molecules for distribution and movement of molecules;
5. IR or Raman microscopy for lateral distribution of specific molecules;
6. Confocal laser scanning microscopy for lateral and depth sensitivity in sub-micrometre range.

1.10 Secondary Ion Mass Spectrometry (SIMS)

SIMS is a very versatile tool to investigate the chemical composition of surfaces and interfaces at high resolution. By the bombardment with an ion beam secondary ions are generated, which are analysed in a mass spectrometer. With organic materials one obtains characteristic fragments, which allow identification of the composition (fingerprint technique). This technique is often used for surface investigations in the “static” mode of operation, where only a monolayer is removed from the surface (static SIMS). In this way it allows very sensitive investigations of surface contaminations for instance.

In the “dynamic” mode (Fig. 1.3) the material is continuously sputtered away at higher incident ion flux and one can obtain a depth profile of elements and fragments (dynamic SIMS). In this way interfaces between polymers may be investigated and depth resolution can be as small as 12 nm depending on the sputter rate.

1.11 Indentation, Adhesion, Mechanical Properties

A classical mechanical surface characterization is the hardness measurement. A hardness estimate is done by indenting a well defined diamond stylus with a certain load into a surface measuring the permanent depth of the indent. For the investigation of thin layers and anisotropic material the test was miniaturized (micro-hardness test). If a diamond stylus of well defined geometry is used, both indentation depth and indentation load as a function of time are simultaneously recorded. From the load–displacement data, hardness and Young’s modulus can be calculated. If a surface is scanned by indentation experiments it is possible to create a hardness as well as a stiffness image. Nano-indentation experiments can also be performed with a scanning force microscope. With scanning force microscopy it is also possible to deform the surface elastically, and knowing the cantilever stiffness a stiffness image of the specimen is obtained. Quantitative stiffness values are difficult to obtain and the technique is usually used in a qualitative way to obtain a stiffness contrast between components for lateral imaging.

The mechanical stability of an interface is usually described by its adhesion. Tests of adhesion are essentially fracture tests and the adhesion energy is largely determined by the deformation at the crack tip. Adhesion of thin films deposited on bulk materials is most commonly measured by peel tests. Alternatively adhesion of thin polymer films may be determined from blister or the double cantilever beam tests. Adhesion values however depend in most cases on the measurement technique and tests should be performed in view of the desired application. Similarly the friction between two solid samples can be measured at macroscopic and microscopic level utilizing different techniques and local probes. The mechanical properties at the surface can be very different from the bulk, but a detailed understanding is still missing.

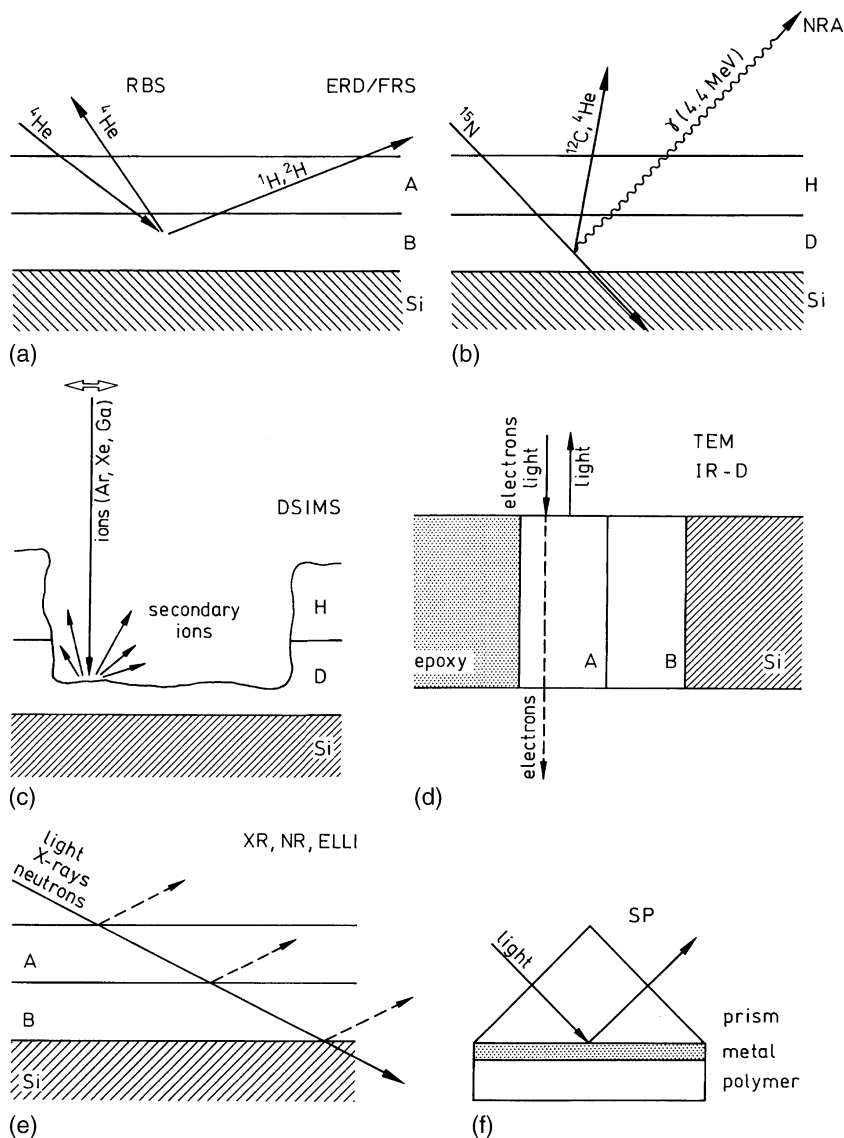


Fig. 1.3 Schematics of several surface and interface analysis techniques described in the text. **(a)** Rutherford backscattering (RBS), elastic recoil detection (ERD), forward recoil scattering (FRS); **(b)** nuclear reaction analysis (NRA); **(c)** dynamic secondary ion mass spectrometry (DSIMS); **(d)** transmission electron microscopy (TEM); **(e)** X-Ray (XR) and neutron reflectometry (NR) as well as ellipsometry (ELLI); and **(f)** surface plasmon spectroscopy (SP)

1.12 Inverse Gas Chromatography (IGC)

The adsorption of test gases (and vapours of liquids) at the surface of the material under investigation can provide interesting information on surface activity, composition and phase transitions. While gas chromatography is aiming at the characterization of the gas, inverse gas chromatography is aiming at the characterization of the filler material, i.e. the polymer powder or fibre surface. Specific solutes (“probes”) of known properties are used to elucidate the interaction behaviour, and hence the surface characteristics and functionality of the packing material. Since a commercial gas chromatographic apparatus can be used, the method is relatively cheap and easy to apply.

1.13 Ion Techniques (FIB, RBS, ERD, NRA)

Besides SIMS several techniques utilize ions as probes for interface analysis (RBS, ERD/FRS, NRA Figs. 1.2 and 1.3). They require dedicated equipment and usually an ion accelerator in the appropriate energy range as well as the corresponding ion source and detectors are necessary. Contrast between polymers is typically generated by deuteration of one component (ERD/FRS, NRA). Ion techniques are nevertheless very helpful for interface width determination of polymers because the resolution is quite good. Some of the well developed techniques are Elastic Recoil Detection/Forward Recoil Detection (ERD/FRS) and Nuclear Reaction Analysis (NRA). Rutherford backscattering (RBS) can be used when heavy atoms are present in the sample. For a description several reviews exist [3.13].

A focused ion beam (FIB) can also be used for imaging, but in many cases is utilized in combination with a SEM (cross-beam) for micro-/nano-machining at the surface (cutting, milling, etching, ion deposition) [11]. For instance the ion beam can be used for the etching of deep cuts into the sample, which then for instance are used for SEM or TEM imaging. This allows the visualization of hidden interfaces where the ion beam can also cut soft/hard interfaces. FIB offers many possibilities for nano-machining, ion-beam lithography and nano-pattern generation, but one should keep in mind that there will be always a thin surface layer, which has been modified by the ion beam treatment. Structures can be generated in the range from 10 nm to many micrometres. The combination of FIB and SEM offers the possibility to simultaneously image the treated region with the SEM at high resolution, while the ion beam is machining the surface. Of course also nano-manipulators can be included (for instance for conductivity measurements) and the FIB can also be utilized for ion-beam activated deposition of various materials (Pt, W, SiO₂, etc.) by local decomposition of molecules from a directed gas flow. In this way the FIB may be used as a nano-lab. Because of the wealth of the surface and interface characterization techniques, we cannot cover details here but refer to the individual chapters on those topics. Some of the main

aspects for surface and interface characterizations are given in Tables 1.1 and 1.2, but one has to keep in mind that there is fast technical development in some areas, see, e. g. [12–14], and that resolution also depends on experimental conditions and samples, which have to be prepared in a dedicated way to achieve optimal resolution or contrast. The comparison therefore is very difficult and has to be read with care. The choice of the suitable and optimal technique for a particular problem is of crucial importance and should take into account aspects like sample preparation, contrast generation, necessary spatial and depth resolution as well as environmental conditions needed.

References

1. H.M. Tong, S.P. Kowalczyk, R. Saraf, N.J. Chou, *Characterization of Polymers* (Butterworth Heinemann, Boston, 1994)
2. I.C. Sanchez (ed.), *Physics of Polymer Surfaces and Interfaces* (Butterworth Heinemann, Boston, 1992)
3. M. Stamm, Polymer interfaces on a molecular scale: comparison of techniques and some examples. *Adv. Polymer Sci.* 100, 357 (1992)
4. F. Garbassi, M. Morra, E. Occhiello, *Polymer Surfaces* (Wiley, New York, 1997)
5. H. Bubert, H. Jenett, *Surface and Thin Film Analysis* (Wiley-VCH, Weinheim, 2002)
6. A. Karim, S. Kumar, *Polymer Surfaces Interfaces and Thin Films* (World Scientific, Singapore, 2000)
7. A.W. Adamson, A.P. Gast, *Physical Chemistry of Surfaces* (Wiley, New York, 1997)
8. S. Wu, *Polymer Interface and Adhesion* (Marcel Dekker, New York, 1982)
9. J.N. Israelachvili, *Intermolecular and Surface Forces* (Academic, London, 1991)
10. M. Stamm, *Polymer Surfaces, Interfaces and Thin Films Studied by X-Ray and Neutron Reflectometry*, in *Scattering in Polymeric and Colloidal Systems*, ed. by W. Brown, K. Mortensen (Gordon and Breach, Amsterdam, 2000), p. 495
11. L.A. Giannouzzi, F.A. Stevie, *Introduction to Focused Ion Beams: Instrumentation, Theory Techniques and Practice* (Springer, New York, 2005)
12. M. Kappl, K. Graf, H.J. Butt, *Physics and Chemistry of Interfaces* (Wiley-VCH, Berlin, 2006)
13. D.J. O'Connor, B.A. Sexton, R.S.C. Smart, *Surface Analysis Methods in Materials Science*, vol. 23 (Springer, Berlin, Heidelberg, New York 2003)
14. P. Somasundaran, *Encyclopedia of Surface and Colloid Science* (Taylor & Francis, CRC Press, New York, 2006)

Chapter 2

Structure Determination in Thin Film Geometry Using Grazing Incidence Small-Angle Scattering

Peter Müller-Buschbaum

Technical University München, Physik Department LS E13, James-Franck-Str.1,
85747 Garching, Germany, peter.mueller-buschbaum@ph.tum.de

Abstract In the thin film geometry reflectivity measurements are a widespread technique to determine the density profile perpendicular to the sample surface. From off-specular scattering additional information about the surface roughness, lateral correlations, sizes and shapes of objects (particles, nanostructures) positioned on top of the surface or in a surface near region are accessible. The use of a grazing incidence geometry enhances the surface sensitivity. Grazing incidence small-angle scattering (GISAS) overcomes the limitations of conventional small-angle scattering with respect to extremely small sample volumes in the thin film geometry. Although real space analysis techniques such as scanning force microscopy (SFM) enable an easy access to surface structures, reciprocal space analysis techniques such as GISAS with X-Rays and neutrons include several advantages:

1. scattering yields averaged statistical information over the whole illuminated sample surface;
2. scattering is applicable in numerous environments such as ultra-high vacuum, different gas atmospheres and in liquids;
3. scattering can be performed in real time accessing kinetics phenomena; and
4. using the variable probed depth as function of the incidence angle, scattering offers the opportunity to characterize buried lateral structures destruction-free as well. By the use of either X-Rays or neutrons the scattering contrast in a system can be reversed. To demonstrate the possibilities of GISAS several different examples of thin polymer films are presented.

2.1 Introduction

The investigation of surfaces, interfaces and thin films requires dedicated analytical techniques, which provide molecular resolution for the location and analysis of individual atoms or molecules at the surface or at buried interfaces of thin films or

multilayer systems. One can distinguish between techniques providing depth information (e. g. the enrichment of one surface component) and techniques providing lateral resolution (e. g. the two-dimensional phase separation of components in a thin blend film).

For many years, due to the large penetration depth of X-Rays and neutrons and due to the small signal to noise ratio of low intensity sources, scattering techniques were limited to three dimensional samples only [1]. For the investigation of *bulk samples* usually a transmission geometry is applied. The beam passes through the sample volume and the surrounding container, which defines the environmental conditions. The well established techniques of wide angle X-Ray/neutron scattering (WAXS/WANS), small-angle X-Ray/neutron scattering (SAXS/SANS) and ultra-small-angle X-Ray/neutron scattering (USAXS/USANS) cover a broad range of length scales accessible [2–5]. Information about the sample structure from an intermolecular level up to the optical resolution limit are addressable. Special sample environments like high pressure cells or mechanical testing machines can be introduced into the beam [6]. However, the surface contribution in a transmission geometry is nearly zero and thin film samples are not accessible. To address *thin film samples* the common transmission geometry had to be replaced by a reflection geometry [7, 8]. In the grazing incidence regime the surface sensitivity is maximized, which enables the investigation of surfaces and thin films with thicknesses down to the submono-molecular range. Following the same principles as in the transmission geometry larger length scales are addressable by an increase in the sample detector distance [9].

In widespread use are reflectivity experiments [10–15] which detect the specular scattering and yield the density profile perpendicular to the sample surface. In the absence of surface or interface roughness as well as of lateral structures thin film samples are well characterized by the density profile. It displays the possible layer sequence perpendicular to the sample surface in terms of thickness, root-mean square roughness and mass density.

To detect a lateral surface or interface roughness, lateral correlations, sizes and shapes of objects such as particles positioned on top of the surface or in a surface near region off-specular scattering is required. Usually information about in-plane structures are investigated with conventional diffuse (or off-specular) X-Ray scattering [16–24]. Due to a relaxed resolution in one of the three components of the scattering wavevector, these experiments are possible in laboratory based experimental set-ups. Compared to reflectivity measurements the demand for a high primary intensity is increased already. As a consequence of the quite complex data fitting procedure required to extract the desired information from conventional diffuse scattering data, grazing incidence small-angle scattering (GISAS) experiments receive an increasing attention within the last years [25–72]. In case of many sample systems GISAS enables an easy access to the desired structural information, because the Fresnel transmission functions enter only as scaling factors [12, 32]. GISAS involves a combination of two techniques, GID (grazing incidence diffraction), which uses a reflection geometry to obtain surface and near surface sensitive scattering, and SAS (small-angle scattering), which meas-

ures structures of 1–100 nm length in normal transmission mode. It is a non-destructive structural probe and does not require a special sample preparation. GISAS yields an excellent sampling statistics (averages over macroscopic regions to provide information on nanometer scale) and provides information on particle geometry, size distributions and spatial correlations. In GISAS experiments however, the high demand on collimation makes the use of high flux sources of large scale facilities such as synchrotron radiation advantageous [28–67]. In addition, experiments were successfully performed with neutrons [40, 41, 47, 52, 56, 68] at high flux neutron reactors. Thus comparable to reflectivity measurements and conventional diffuse scattering, two probes namely X-Rays and neutrons are available. Recently, micro-beam GISAXS experiments enabling a local resolution become possible [73, 74] and picture the ongoing experimental developments in the field of GISAS.

Published GISAS investigations focus on metallic [26, 27, 45, 48, 63, 70, 72], semiconductor [36, 37, 39, 44, 49, 54, 59, 60, 62, 65, 66], ceramic [34, 46, 48, 50, 71], polymeric [33, 35, 40, 41, 47, 51, 52, 55–58, 67, 69] or biological [43] thin film samples, including multilayer samples [28–32]. Thus there are no limitations in principle of the technique with respect to the types of samples addressable. In addition as compared to the transmission set-up the resolution is even increased [33], which makes GISAS interesting alternatively to the common transmission geometry. Basic origin is the absence of the extremely intense primary beam in the reflection geometry.

Despite its big success in many different types of sample systems and the increasing interest in GISAS, it is still an advanced scattering technique and basic articles are very limited in number. Within this article the basic ideas and possibilities of the technique GISAS are presented. This includes a theoretical introduction as well as the principles of the experimental set-up required. Selected examples are included to picture this in detail. Within these examples we restrict to polymeric thin films, which enable to demonstrate all these ideas and mark a type of samples which are difficult to access with X-Rays due to the weak scattering. The structure of polymers and thin polymeric films at the mesoscopic scale is of interest both for application and basic research. As the size of many technical devices decreases, the natural length scales of many typical polymers such as radius of gyration, persistence length, or the domain size in block copolymers, match the feature size and the materials are expected to display anomalous behaviour. On the other hand, the tendency towards spontaneous structure formation may stabilize or even generate morphological features of interest. Surface structures of thin polymer films on solid surfaces depend on the nature of interactions between polymer and solid.

2.2 Real Space Analysis

Perhaps it is most natural to investigate the surface of thin film samples with scanning force microscopy (SFM) [75–80]. As a real space analysis technique a direct picture of the surface results from the three-dimensional imaging which makes its interpretation much easier as compared to any scattering experiment. SFM provides a high lateral resolution of the surface topography in the nanometre range and may be applied in several modes (contact, non-contact, tapping, force, friction, phase, or others). In addition SFM measurements are performed in the laboratory and do not need large scale facility visits.

Figure 2.1(a) shows the example of a surface topography as measured with SFM in non-contact mode. The non-contact mode was chosen to minimize tip induced sample damages. The tip does not touch the sample [83] and the cantilever is oscillated at a frequency which is slightly above the cantilever’s resonance frequency typically with an amplitude of a few nanometres (<10 nm) only. The selected example pictures a thin polymer blend film [81]. The phase separation of the two immiscible polymers forces a very pronounced surface structure, which is shown by the topography data. Already by the unguided eye a dominant lateral surface structure is visible in Fig. 2.1(a). To obtain a statistical information the topography data are further processed.

Within most commercially delivered SFM software a root-mean-square (rms) surface roughness is calculated from the three-dimensional topography data. This rms-roughness displays the deviation of the individual heights from the mean surface and statistically describes the sample perpendicular to the surface [84]. Its value can be well compared with rms-roughness resulting from reflectivity measurements.

To determine a statistical description parallel to the sample surface, the power spectral density (PSD) function needs to be calculated [85]. From a two-dimensional Fourier transformation an intensity distribution in reciprocal space is

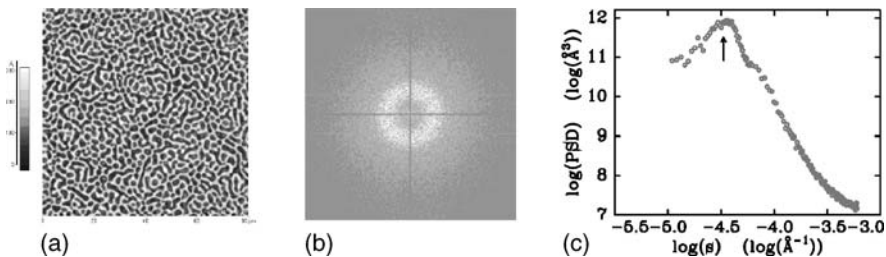


Fig. 2.1 Statistical analysis of SFM data. (a) Example of topography data measured in non-contact mode in a scan range of $80 \times 80 \mu\text{m}^2$ picturing the surface of a binary polymer blend film [81]. (b) Calculated two-dimensional Fourier transformed displaying a ring of intensity in the Fourier space as signature of an isotropic structure [82]. (c) After radial averaging a power spectral density (PSD) function results. PSD functions of different scan ranges can be combined into one master curve. In the double logarithmic presentation the master curve is shown as a function of the inverse lengths

obtained as shown in Fig. 2.1(b). In case a ring of intensity appears (as demonstrated within the particular example chosen here), after a radial averaging the PSD results. Repeating these steps with SFM data collected for different scan ranges yields a set of PSD functions covering different ranges in reciprocal space (given by the resolution and the maximal scan range of the individual SFM data). To enlarge the total accessible range in reciprocal space in a final step these PSD functions are merged into one (so called) master curve [81,82] as shown in Fig. 2.1(c). The position s^* of the intensity peak (shown by the arrow in Fig. 2.1(c)) corresponds to the most prominent in-plane length $\xi = 2\pi s^*$ statistically describing the surface structure parallel to the sample surface.

It should be noted, that previously unfiltered height data are required for the Fourier transformation, which might be difficult to access depending on the type of SFM apparatus operated. Any filtering of the data corrupts the shape of the intensity curve in reciprocal space. This might even affect peak positions and will prevent a correct merging of individual PSD functions into one master curve.

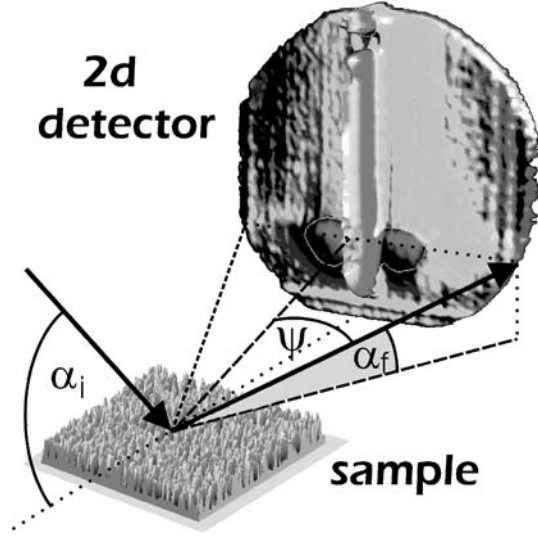
Of course only isotropic surface structures yield an intensity ring in Fourier space. In case of an anisotropic surface structure in Fourier space the ring is replaced by an ellipse. The orientation of the ellipse is perpendicular to the real space anisotropy of the surface structure. The above described radial averaging is no longer appropriate and the two major axes a^* and b^* of the ellipse need to be measured. As a consequence, line or pie-shaped cuts from the two-dimensional Fourier data are required. These cuts commonly have a significantly reduced statistics as compared to the PSD resulting after radial averaging. Accordingly one most prominent in-plane length is no longer sufficient for a statistical description and replaced by two most prominent in-plane lengths $\xi_a = 2\pi a^*$ and $\xi_b = 2\pi b^*$. Of course there is no need for the existence of any dominant in-plane structure at all. A well known example is a statistically rough surface, e. g. resulting from a non-specific surface etching. In Fourier space the intensity exhibits no maximum at all and simply decays as a function of the inverse length s . The power law of this decay is a measure for the kind of statistical roughness [86].

However, the statistical relevance of these statistical quantities, rms-roughness and most prominent in-plane length, is rather limited due to the very small surface area probed. Even a drastic increase in the number of sampled surface positions is not helpful to overcome this problem.

2.3 Reciprocal Space Analysis – Scattering

In the region of total external reflection, the incident and exit angle α_i and α_f are so small, that the influence of the periodic crystal structure can be neglected and a description based on one mean refractive index is appropriate. The scattering originates essentially from strong variations of the mean electronic density for X-Rays or the mean scattering lengths for neutrons as an homogeneous medium

Fig. 2.2 Schematic picture of the experimental set-up for the detection of diffuse scattering with a two-dimensional detector. The sample surface is placed horizontally. A typical phase separation structure as measured with SFM is shown representing the sample surface. The incident angle is denoted α_i , the exit angle α_f and the out-of plane angle ψ . The colour coding visualizes differences in the scattered intensity. In the particular chosen example the diffusely scattered intensity in the scattering plane, the detector scan, exhibits a split-up Yoneda peak and a specular peak as common features



does not scatter. Because the phase velocity in the medium j is larger than in vacuum, the refractive index n_j of the medium j is slightly smaller than 1 and can be written as [11]

$$n_j = 1 - \delta_j + i\beta_j \quad (2.1)$$

with in case of X-Rays the dispersion

$$\delta_j(\vec{q}, \lambda) = \frac{e^2 \lambda^2}{8\pi^2 m_e c^2 \epsilon_0} \rho_j \frac{\sum_k [f_k^0(\vec{q}, \lambda) + f'(\lambda)]}{\sum_k M_k} \quad (2.2)$$

and absorption contribution

$$\beta_j(\lambda) = \frac{e^2 \lambda^2}{8\pi^2 m_e c^2 \epsilon_0} \rho_j \frac{\sum_k f''(\lambda)}{\sum_k M_k} \quad (2.3)$$

depending on the speed of light c , the elementary charge e , the electron rest mass m_e , the permittivity constant ϵ_0 , the mass density ρ_j , the wavelength λ , the atomic weight M_k and the dispersion corrections f' and f'' . f_k^0 can be approximated by the number of electrons Z_k and the summation is performed over all atoms k of a monomer subunit in the case of polymers under investigation.

The scattering plane is defined by the incident and exit angle α_i and α_f and scattering outside this plane is probed under an out-of plane angle ψ (see Fig. 2.2).

Specular scattering fulfils the condition $\alpha_i = \alpha_f$ whereas off-specular or diffuse scattering satisfies $\alpha_i \neq \alpha_f$. Usually the coordinate system is chosen that way, defining the (x,y) -plane by the sample surface with the x -axis oriented in the direction of the X-Ray or neutron beam. As a consequence the z -axis is perpendicular to the sample surface. In this case $q_x = 2\pi(\cos\psi\cos\alpha_f - \cos\alpha_i)/\lambda$, $q_y = 2\pi(\sin\psi\cos\alpha_f)/\lambda$ and $q_z = 2\pi(\sin\alpha_i + \sin\alpha_f)/\lambda$ denote the components of the wavevector \mathbf{q} . For specular scattering the wavevector components are $q_x = q_y = 0$ and $q_z \neq 0$, sampling a depth sensitive information only. With off-specular scattering the lateral component is $q_{\parallel} = (q_x, q_y) \neq 0$ probing the in-plane structure of the sample surface.

In the past for a theoretical description of the diffuse scattering different concepts have been developed, depending on the value of wavevector \mathbf{q} and the value of the rms-surface roughness. Including dynamical effects the intensity distribution in the region of total external reflection can be described in the framework of the distorted wave Born approximation (DWBA) [17–23, 87–91].

The DWBA is the application of a first order perturbation theory induced by the roughness at the substrate surface or the contrast variation to the correct unperturbed wave, i. e. the trio of incident–reflected–refracted waves.

2.3.1 Conventional Diffuse Scattering

Measurements which satisfy $\alpha_i \neq \alpha_f$ and $\psi = 0$ are denoted conventional diffuse scattering [92], because they are restricted to the scattering plane. Due to the missing q_y -resolution the experimental realization is easier as compared to GISAS and can be performed with a point detector already.

Figure 2.3 shows schematically the most common scans fulfilling the above condition of conventional diffuse scattering. The corresponding paths through the reciprocal space are all located in the (q_x, q_z) -plane only. A part of this plane is not accessible because it is shadowed by the sample, as seen from the source or from the detector (principle of optical reversibility).

Within the DWBA the diffuse scattering cross-section of an m -layer system has a rather complicated appearance [19]

$$\left(\frac{d\sigma}{d\Omega}\right)_{diff} = \frac{C\pi^2}{\lambda^4} \sum_{j,k=1}^m (n_j^2 - n_{j+1}^2)(n_k^2 - n_{k+1}^2) \sum_{h,l=0}^3 W_{h,j} W_{l,k} F_{j,k}^{h,l} \quad (2.4)$$

with the Fresnel transmission functions $T_{i,f}$ entering directly by $W_{0,j} = T_{i,j}T_{f,j}$; $W_{1,j} = T_{i,j}R_{f,j}$; $W_{2,j} = R_{i,j}T_{f,j}$ and $W_{3,j} = R_{i,j}R_{f,j}$. C denotes the illuminated surface area, λ the wavelength used, n the refractive index. Due to the q_z -dependence of the diffuse scattering factor $F_{j,k}^{h,l}$ no easy data fitting is possible. A detailed description can be found for example in the references [19] or [92].

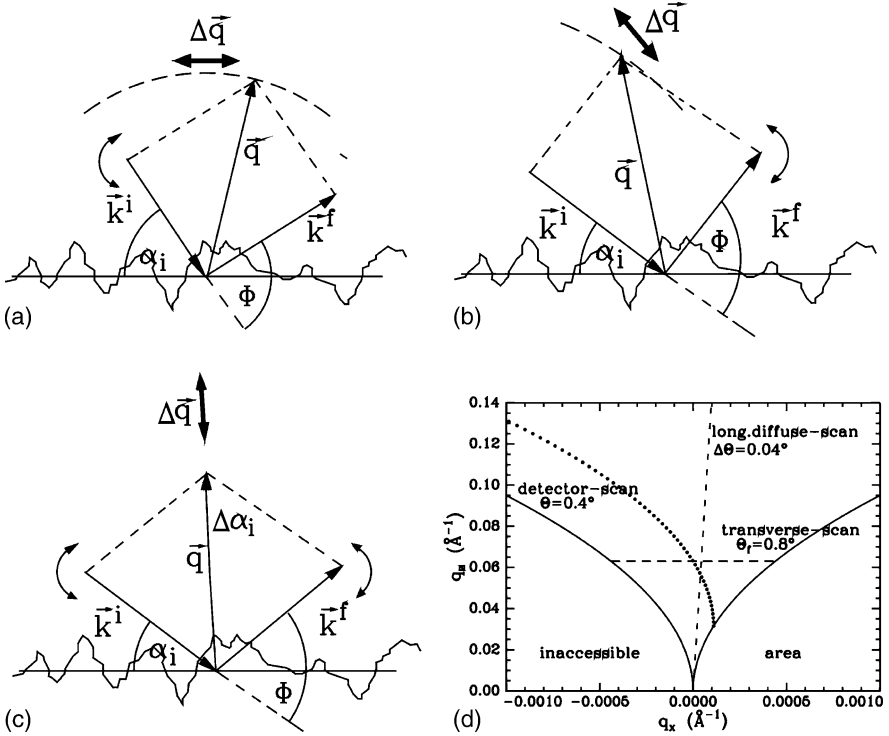


Fig. 2.3 Schematic visualization of a (a) transverse scan, (b) detector scan and (c) longitudinal diffuse scan. The incident angle is denoted α_i and the detector angle $\Phi = \alpha_i + \alpha_f$. (d) The corresponding paths of these scans are all located in the $(q_x q_z)$ -plane of the reciprocal space

2.3.2 Grazing Incidence Small-Angle Scattering

Grazing incidence small-angle scattering experiments require a q_y -resolution which increases the complexity in the experimental realisation. However, the theoretical description simplifies. In the framework of the distorted-wave Born approximation (DWBA) the differential cross-section can be approximated by [31]

$$\frac{d\sigma}{d\Omega} = \frac{C\pi^2}{\lambda^4} (1-n^2)^2 |T_i|^2 |T_f|^2 F(\vec{q}) \propto F(\vec{q}) \quad (2.5)$$

where C denotes the illuminated surface area, λ the wavelength used, n the refractive index, $T_{i,f}$ the Fresnel transmission functions and $F(q)$ the diffuse scattering factor. Because the incident and exit angle are fixed, the Fresnel transmission functions act only as overall scaling factors and the diffuse scattering factor is directly probed. The intensity is dominated by the Fourier transform of the height–height correlation function of one “effective surface” [32]. In case either the incident or exit angle is equal to the critical angle of the material, e. g. PS, the transmission

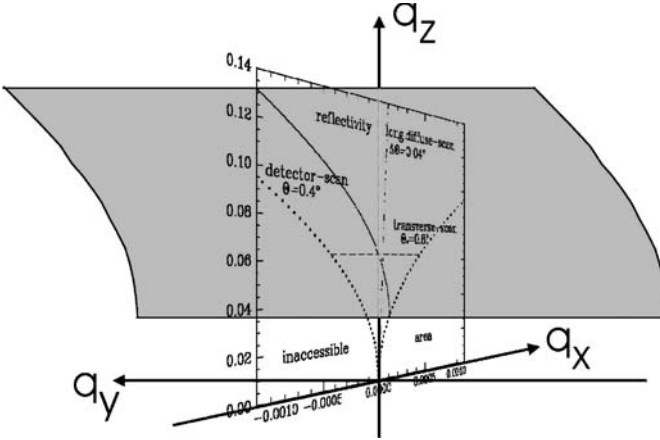


Fig. 2.4 Schematic visualization of the accessible area in reciprocal space within a GISAS experiment. The shaded, parabolic curved plane corresponds to the active area of a two-dimensional detector

functions have a maximum, which is called Yoneda peak [16]. Therefore out-of plane cuts at these positions increase the scattering contribution of the material (e. g. PS).

The probed part of reciprocal space in a GISAS experiment utilizing a two-dimensional detector is shown in Fig. 2.4.

For N identical and centro-symmetrical objects with a random orientation, the diffuse scattering factor can be approximated [48]

$$F(\vec{q}) \propto NP(\vec{q})S(\vec{q}) \tag{2.6}$$

to depend on the form factor $P(q)$ of the individual objects and to depend on the structure factor $S(q)$.

If the objects are having a well defined nearest neighbor distance, irrespective of the monodispersity of the individual objects, the structure factor $S(q)$ yields directly the most prominent in-plane length ξ via a simple Bragg law.

The form factor $P(q)$ is only the Fourier transform of the shape of the particle. A mathematical description of the form factor depends on the type of object like cylinder, sphere or slab. Only in case of highly monodisperse objects the form factor becomes visible in the GISAS data. In polymeric systems prominent examples of common shapes of surface structures are cylinders of a volume $V = \pi R^2 H$

$$P_{cy}(\vec{q}, R, H) = 2\pi R^2 H \frac{J_1(p_{\parallel} R)}{p_{\parallel} R} \frac{\sin(q_z H/2)}{q_z H/2} \exp(-iq_z H/2) \tag{2.7}$$

or a cut-off sphere with height H of a volume

$$V = \pi R^3 \left(\frac{2}{3} + \frac{H-R}{R} - \frac{1}{3} \left(\frac{H-R}{R} \right)^3 \right) \quad (2.8)$$

$$P_{sp}(\vec{q}, R, H) = \exp(i q_z (H-R)) \int_0^H 2\pi R_z^2 \frac{J_1(q_{\parallel} R_z)}{q_{\parallel} R_z} \exp(i q_z z) dz \quad (2.9)$$

with $q_{\parallel} = \sqrt{q_x^2 + q_y^2}$ and $R_z = \sqrt{R^2 - z^2}$. Surface structures resulting from a dewetting process are pictured by SFM to look like pancakes and consequently they can be described as a special type of cut-off sphere with $R \gg H$. Island structures frequently detected in the case of thin diblock copolymer films are well described by cylinders fulfilling $R \gg H$. In contrast non-polymeric systems commonly exhibit other form factors, such as parallelepipeds with a height H and a squared surface with one edge of $2R$ length

$$P_{pa}(\vec{q}, R, H) = 4R^2 H \frac{\sin(q_x R)}{q_x R} \frac{\sin(q_y R)}{q_y R} \frac{\sin\left(q_z \frac{H}{2}\right)}{q_z \frac{H}{2}} \exp\left(-i q_z \frac{H}{2}\right) \quad (2.10)$$

or pyramids with a height H , a tilt angle β and a squared surface with one edge of $2R$ length

$$P_{py}(\vec{q}, R, H, \beta) = \int_0^H 4R_z^2 \frac{\sin(q_x R_z)}{q_x R_z} \frac{\sin(q_y R_z)}{q_y R_z} \exp(-i q_z z) dz \quad (2.11)$$

with $R_z = R - z/\tan(\beta)$.

In many sample systems the up to now described easy GISAS data analysis is sufficient. In a more general description not only N identical and centrosymmetrical objects with a random orientation are present. As a consequence, the objects have to be sorted out in classes Θ of sizes and shapes of occurrence probability P_{Θ} . The probability per unit of surface to find an object of class Θ , knowing that there is an object of class Ω is called the partial pair correlation function.

In case the interplay between interference function and form factor or the particle size distributions can no longer be neglected, only a direct modelling of the data is appropriate [93]. For instance, most of the time for particles, the interparticle spacing is directly extracted from the Bragg-law method which could induce up to 30% of error in case of complex systems. Moreover, concerning particle size, the coupling between the interference function and form factor greatly increases the complexity of the analysis and prevents the use of classical Guinier or Porod approaches. Modelling of the GISAS data is possible with the program IsGISAXS by R. Lazzari, it is freely available for non-commercial use [94].

2.4 Experimental Set-Ups for GISAS

In Fig. 2.2 an experimental set-up for the detection of diffuse scattering is schematically shown. Due to necessary of the detection of scattered intensity in the out-of plane direction $\psi \neq 0$ the use of a two-dimensional detector is most appropriate in a GISAS experiment. The beam quality is optimized by using a set-up of two high quality entrance cross-slits, separated by the collimation distance D , and a completely or mostly evacuated pathway. The slit width is adapted to the required resolution in q_y and q_z , so that basically the detector imposes the resolution limit. By avoiding any additional windows the background is minimized. The direct beam is not recorded with the detector to avoid detector saturation as several orders of magnitude in intensity separate the incoming intensity from the reflected one. In addition the specular reflected peak (condition $\alpha_f = \alpha_i$) is shielded with a beam stop to use the full available flux of the source because specular and diffuse scattering are as well separated by orders of magnitude in intensity.

Because GISAS can be understood as a replacement of the transmission geometry in the common SAS experiment by a reflection geometry, the sample is mounted on a stage with a two-circle goniometer and a z -translation table. With the two-cycle goniometer the incident angle α_i is controlled as well as the perpendicular angular alignment is adapted to the positioning of the two-dimensional detector. With the z -translation table the sample height is aligned. GISAS measurements are performed at one fixed angle of incidence α_i .

The distance between the sample and the detector determines the accessible q_y -range as in any common SAS experiment. Of course the resolution needs to be adapted as well. In accordance to the transmission geometry three different distances between the sample and the detector can be separated. For very short distances a grazing incidence diffraction (GID) set-up results [7]. At larger distances typically on the order of 1–2 m the grazing incidence small-angle scattering (GISAS) set-up is realized [26], which already requires a significantly higher q_y -resolution as compared to GID. A very high resolution set-up is possible at very larger distances (larger than 10 m) and enables grazing incidence ultra-small-angle scattering (GIUSAS) [35]. The requirements with respect to beam purity and q_y -resolution are significantly higher as compared to GISAS. As a consequence, typical accumulation times in a GIUSAS set-up are significantly longer as compared to the GISAS or GID geometry.

Due to the required q_y -resolution GISAS experiments are most likely successful at small-angle scattering beamlines at large scale facilities. GISAS can be performed with both probes, with X-Rays at synchrotron sources and with neutrons at high flux reactors. With the increasing number of research groups interested in GISAS, the number of beamlines offering proper conditions for GISAS experiments increases as well.

Figure 2.5 shows an example of a GISAXS set-up as routinely used at the BW4 beamline at HASYLAB (Hamburg).

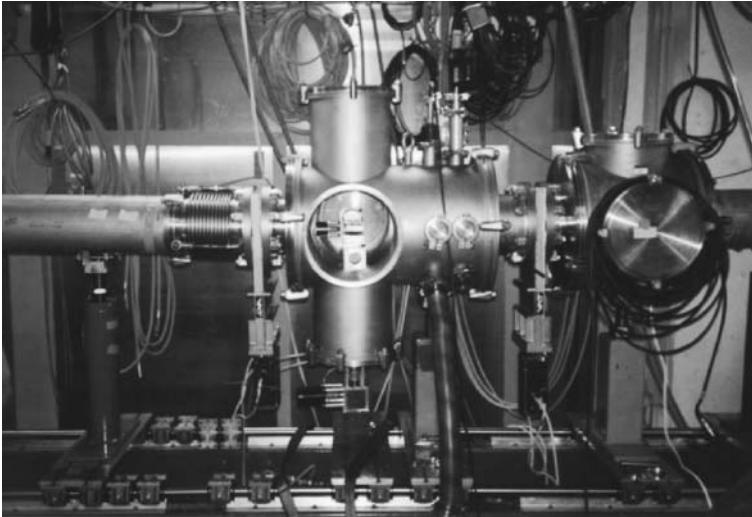


Fig. 2.5 Photograph of the experimental set-up for GISAXS used at BW4 at HASYLAB. The sample is placed inside the chamber shown in the centre of the picture. The detector is located to the left at a distance of 12 m and the synchrotron ring is located to the right

2.4.1 GISAXS

GISAS measurements using synchrotron radiation are most likely denoted with grazing incidence small-angle X-Ray scattering (GISAXS). The term GIUSAXS is only rarely applied. In early publications alternatively GISAXS was called “diffuse X-Ray scattering under the conditions of small-angle scattering” [33], “reflection USAX” [35] or “Glancing incidence small-angle X-Ray scattering” [95].

For example, published GISAXS/GIUSAXS experiments were performed at LURE (Orsay) at the beamline D22 [34, 40, 46, 48, 50], at the ESRF (Grenoble) at the beamline ID01 [48, 96, 97], ID3 [42, 49], ID10a [54, 98], ID10b [51, 99–101], ID32 [72] and BM32 [63], at HASYLAB (Hamburg) at the beamline A2 [67, 102, 103], B1 [31, 32] and BW4 [9, 33, 35, 40, 41, 47, 55, 104–108], at ELETTRA (Trieste) at the SAXS beamline [59, 60, 62, 65, 66], CHESS (Cornell) at the D-line [57, 58], at NSLS (Brookhaven) at the beamline X22B [53] and X21 [64], and at APS (Argonne) at the beamline 1-BM-C [61, 71] and 12-ID-C [70]. Recently, GISAXS experiments using micro-focused X-Ray beams with diameters of only 10 μm or smaller were possible at the ID13 beamline at the ESRF (Grenoble) [73, 74]. The X-Ray beam was monochromatized and typical X-Ray wavelengths of $\lambda \approx 0.1 \text{ nm}$ were used.

Figure 2.6(a) shows a typical example of a two-dimensional intensity distribution measured with a high resolution set-up at the beamline BW4 at the HASYLAB (Hamburg). A 512×512 wire detector is operated at a sample detector distance larger than 12 m, which enables a resolution of lateral structures up to

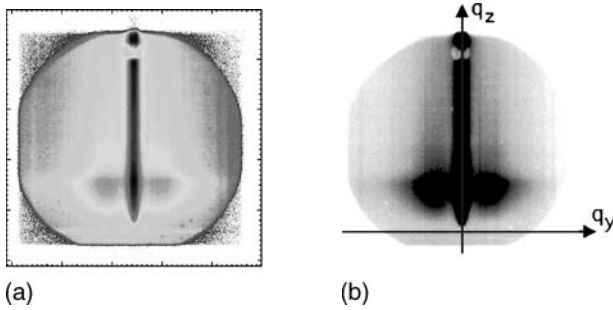


Fig. 2.6 (a) Typical examples of two-dimensional detector data as measured with a high resolution set-up at the beamline BW4 at HASYLAB. High intensity is marked in black, low intensity in blue. The beamstop is shadowing the specular peak. The shown raw data are not corrected for the detector efficiency resulting in a slight stripy appearance. (b) Two-dimensional intensity distribution transformed into reciprocal space. The q_z is the wavevector component perpendicular to the surface and q_y the component parallel to the surface and perpendicular to the scattering plane

2500 nm. Shown is a logarithmic colour coding of the intensity, because the off-specular scattering in a GISAS geometry covers several orders of magnitude as well. In Fig. 2.6(b) the as before coloured intensity distribution in real space is transferred into a grey scale and reciprocal space as explained in Sect. 2.5.

2.4.2 GISANS

As compared to GISAS measurements with synchrotron radiation, experiments using neutron are still rather rare. Up to now, the largest body of work was performed at the beamline D22 at the ILL (Grenoble) [40, 41, 47, 52, 56, 108–113]. Experiments at the SANSII beamline at the GKSS (Geesthacht) were restricted to selected samples [112, personal communication, R. Kampmann] and required significantly longer accumulation times. Recently, experiments at the PAPOL beamline at the LLB (Saclay) [68] and at the ADAM beamline at the ILL (Grenoble) were reported (personal communication, M. Wolf).

The instruments, such as D22 were most likely operated in the region of highest neutron flux available at wavelengths of typically $\lambda \approx 0.6$ nm (wavelength selector $\Delta\lambda/\lambda = 10\%$). At a distance of 17.7 m between sample and detector at the D22 a comparable high resolution such as with synchrotron radiation at the BW4 beamline is accessible. However, due to the reduced flux of neutrons as compared to X-Ray photons at a synchrotron beamline, the accumulation times are significantly longer (in the order of hours).

2.5 Selected Cuts from 2D Data

Figure 2.6(a) pictures the anisotropy of the observed scattering pattern. Different main features are already determined right from the two-dimensional images. The specular reflected peak [11] in the upper part of the detector and the Yoneda peak [16] in the middle of the detector are well separated. The shown example was measured in the GIUSAX set-up [9]. Transferred into reciprocal space the two-dimensional (ψ, α_f) -map becomes a (q_y, q_z) -map. The weak q_x dependence ($q_x \ll q_z$) is neglected in Fig. 2.6(b).

In the selected example an ultra-thin diblock copolymer film was measured. The diblock copolymer P(A-b-B) consists of two blocks of the homopolymers “A” and “B”. A nanostructured surface pattern results. On top of the oxide layer of the silicon substrate polymeric droplets have formed. The well ordered arrangement of the droplets on the surface, resulting in the presence of a nearest neighbour distance causes a structure factor peak. It is visible in the splitting of the Yoneda peak into two isolated off-centered peaks.

Instead of a full treatment of the two-dimensional intensity distribution from selected cuts a valuable information is obtained already. Basically two different types of cuts are advantageous: Horizontal slices at constant q_z and vertical slices at constant q_y (the naming of horizontal and vertical refers to the sample surface) [29]. For an improvement of the statistics the intensity is usually integrated along a slice consisting of a few detector lines only [9]. At optimized conditions the width of this slice is adapted to the resolution of the experimental set-up.

2.5.1 Out-of Plane Scans

As Fig. 2.6(b) pictures, a horizontal slice depends on the wavevector component q_y only [29]. As a consequence only structures parallel to the sample surface are probed.

With the sample surface within the (x,y) -plane and the scattering plane defined by the (x,z) -plane, these horizontal slices are frequently called “out-of plane scan”, as it would be measured with a point detector moving out of the scattering plane along the y -direction. The chosen geometry allows a high parallel momentum transfer q_y without the usual limitations of conventional diffuse X-Ray scattering imposed by the sample surface.

To become sensitive to one component of the diblock copolymer P(A-b-B) we performed the slice at the exit angle equal to the critical angle α_c of one component, such as the homopolymer “A” (red line in Fig. 2.7) and the homopolymer “B” (orange line Fig. 2.7). The critical angle is easily calculated from the dispersion part of the refractive index [7]

$$\alpha_c(A, B) = \sqrt{2\delta(A, B)} \quad (2.12)$$

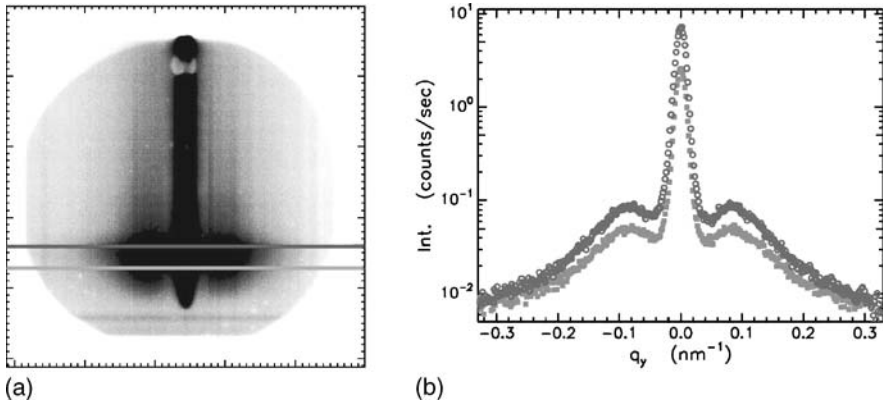


Fig. 2.7 (a) Grey scale reciprocal space presentation of the two-dimensional intensity distribution indicating two selected horizontal cuts. (b) Intensity of the corresponding cuts displayed as a function of the lateral wavevector component q_y

Thus, depending on the sample system under investigation, a material sensitivity is achievable. Figure 2.7(b) shows the corresponding intensity as a function of the lateral wavevector component q_y . The scattered intensity is symmetric with respect to the centre. For the chosen example of the nanostructured diblock copolymer surface (thin film) two pronounced peaks are visible in both cuts. The strong peaks correspond to a highly ordered surface structure as installed in thin diblock copolymer films. Its presence in both cuts is typical for a pure lateral structure of a diblock copolymer, because both blocks are chemically linked via a covalent bond and cannot be separated.

Most likely instead of the presentation shown in Fig. 2.7(b), a double logarithmic one is chosen (see examples in Sect. 2.6) [9].

2.5.2 Detector and Off-Detector Scans

From vertical slices an information depending on the q_z component of the wavevector is resulting (see Fig. 2.6(b)) [29]. At $\psi=0$ (corresponding to $q_y=0$) this scan is called detector scan as it would be measurable with a point detector moving in the reflection plane behind the sample [17–20]. Neglecting the small q_x component in this scan which yields the parabolic path of the detector scan in the (q_x, q_y) -plane (see Fig. 2.3(d)), basically a structure perpendicular to the sample surface is probed. Figure 2.8 shows this cut as a blue line.

Figure 2.8(b) shows data measured at the diblock copolymer films in the commonly used detector scan plot showing the logarithmic intensity as a function of the perpendicular wavevector component. Like in the two-dimensional maps the Yoneda and the specular peak, shadowed with a beam stop, are visible [9]. In the present example no further intensity modulation is present.

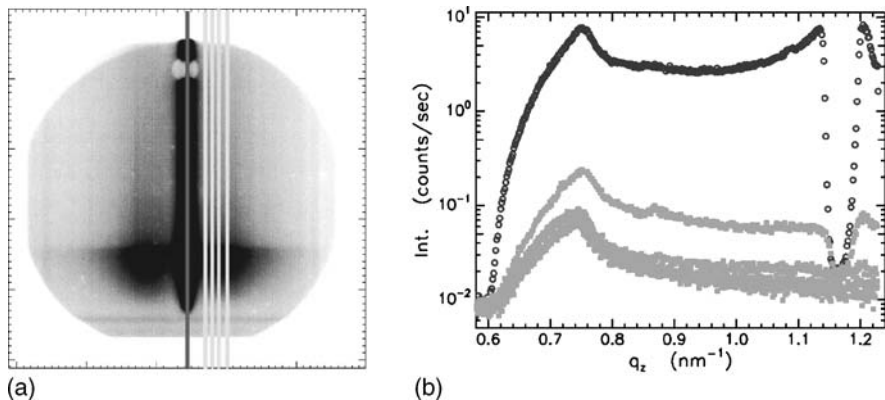


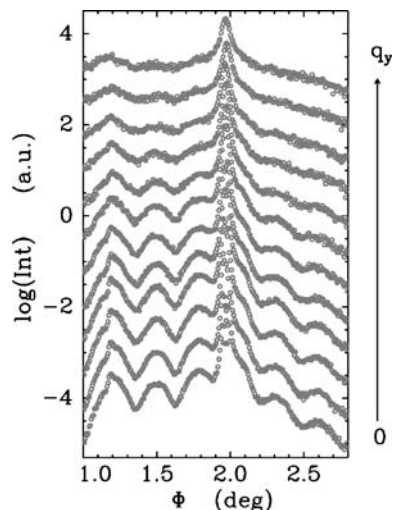
Fig. 2.8 (a) Grey scale reciprocal space presentation of the two-dimensional intensity distribution indicating several selected vertical cuts. The cuts are visualized by the dark and the light grey vertical lines. (b) Intensity of the corresponding cuts displayed as a function of the perpendicular wavevector component q_z .

However, in addition to a Yoneda peak and a specular peak in a detector scan an additional feature originated from resonant diffuse scattering can occur (see Fig. 2.9) [19, 23, 104–107]. As the detector scan probes the in-plane wavevector dependence of long-wavelength fluctuations, a determination of the displacement–displacement correlation function without assumptions about the local layer structure is possible. The correlation between separated interfaces yields a coupling of the correlation functions of the individual interfaces. In case of the example of a thick P(A-b-B) film these interfaces are the air–polymer and the polymer–substrate interface [104]. From the detector scan a direct information about such interface correlation is obtained. In the case of uncorrelated interfaces all interfaces scatter independently and the diffuse intensities of all individual interfaces superpose. Partially or fully correlated roughness gives rise to scattering with partial coherence and resonant diffuse scattering (RDS) is observed [19]. The partial phase coherence of the waves diffusely scattered from different interfaces concentrates the intensity in narrow sheets. These sheets of resonant diffuse scattering are oriented parallel to the q_x -axis with the centre fulfilling the one dimensional Bragg condition $\Delta q_z = 2\pi d_{\text{corr}}$. The modulations of the resonant diffuse scattering (RDS) are in phase with the fringes of the reflectivity and enable a direct determination of the distance d_{corr} of the correlated interfaces.

While the detector scan is cut from the two-dimensional intensity distribution at $q_y = 0$ along the vertical direction, off-detector scans are vertical cuts with $q_y \neq 0$ [106, 107]. In Fig. 2.8 these cuts are displayed as cyan lines. Figure 2.9 shows 11 of these cuts in the relaxed resolution set-up displaying the decay of the RDS with increasing q_y as a function of the detector angle $\Phi = \alpha_i + \alpha_f$.

Due to the relaxed resolution as compared to Figs. 2.6–2.8, the specular peak, the Yoneda peak as well as the modulations of the RDS are resolved. From the bottom to the top q_y increases in small steps of Δq_y . The decreasing amplitude of

Fig. 2.9 Detector scan and off-detector scans cut from the two-dimensional intensity distribution with increasing value of q_y . The increase in q_y from the bottom to the top is pictured with the arrow. For clarity the curves are shifted against each other. The cuts from the two-dimensional intensity distribution exhibit the Yoneda, the specular peak and resonant diffuse scattering originated intensity modulations as most prominent features



the fringes resulting from resonant diffuse scattering with increasing q_y indicates the loss of correlation at smaller in-plane length scales. At long in-plane length scales the substrate and the polymer–vacuum interface are highly correlated. Understanding the surface roughness of the substrate as a wavelength spectrum, the thick diblock copolymer film acts as a band pass filter and only a part of this spectrum is transferred through the film. The substrate morphology is replicated by the thin polymer film for in-plane length scales larger than a characteristic cut-off length R_c .

2.6 Selected Examples

As pointed out, GISAS receives an increasingly attention and the number of investigated sample systems increases as well. The few selected examples are restricted to thin polymer films which enable a demonstration of the possibilities of GISAS.

2.6.1 Spin-Coated Thin Polymer Films

Polymer films on top of rigid substrates have received significant attention within the last years. Concerning thickness and density a defect-free and smooth coating is desired. With spin-coating thin homogeneous polymer films may also be prepared on non-wetting surfaces [105]. The surface morphology of thin polystyrene (PS) films on top of silicon substrates as prepared by spin-coating was probed with GISAXS at the BW4 beamline at HASYLAB.

Films of different film thickness, molecular weight of the spin-coated PS, annealing temperature applied after the spin-coating and solvent used for the spin-coating were examined [104–107]. Measurements were performed at an angle of incidence $\alpha_i > \alpha_c$ above the critical angle of total reflection of the polymer film. Therefore the typical characteristics of the scattered intensity (Yoneda peak, specular peak, modulations due to resonant diffuse scattering) can be easily separated. As an example Fig. 2.10 displays this for (a) different film thicknesses and (b) different molecular weights. Displayed are detector scans resulting from a vertical cut of the two-dimensional intensity distribution at $q_y = 0$.

In Fig. 2.10(a) for one molecular weight of $M_w = 28000$ g/mol the thickness of the PS film is varied between 15 nm and 500 nm. A comparison to the bare substrate (abbreviated with 0 nm) is shown, too. With the exception of the thick film all samples show correlated roughness. However a roughness correlation over 500 nm would lead to a spacing of the Bragg sheets which cannot be resolved in the chosen GISAXS set-up [105]. The molecular weight dependence at a fixed film thickness of (22 ± 2) nm is presented in Fig. 2.10(b). Above the entanglement molecular weight M_E resonant diffuse scattering is detected, whereas below M_E the scattering curve exhibits no fringes. This behaviour was proven over a big film thickness range with additional samples series [105].

A correlation between two interfaces yields a dependence of the in-plane morphology of the upper layer from the underlying one. In a one layer system such as PS on top of Si the film follows the curvature of the substrate like a thin layer of snow, if both are fully correlated (a hill is on top of a hill and a valley on top of a valley). As a consequence, not only the mean averaged film thickness is constant,

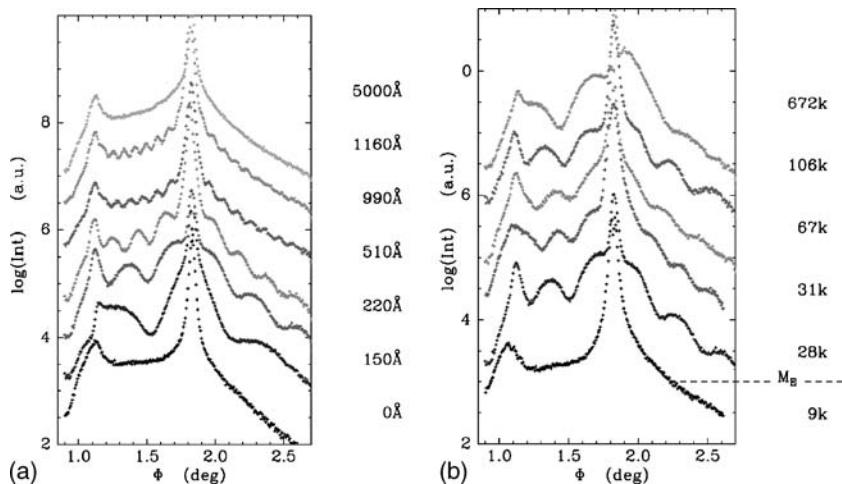


Fig. 2.10 (a) Detector scans measured at the angle of incidence $\alpha_i = 0.91^\circ$ of the PS28k films as prepared for different film thicknesses. (b) Detector scans measured at the angle of incidence $\alpha_i = 0.91^\circ$ of films with a film thicknesses $l = (22 \pm 2)$ nm at different molecular weights. For clarity the curves are shifted by one order of magnitude against each other. Reproduced with permission from *Macromolecules* 1998, 31, 3686–3692. Copyright 1998 Am. Chem. Soc [105]

but the local film thickness at each lateral position of the sample is constant (which is rather desirable for many coatings).

2.6.2 Dewetted Polymer Blend Films

Resulting from an annealing above the glass transition temperature of both components, a confined thin polymer blend film of deuterated polystyrene (dPS) and poly-paramethylstyrene (PpMS) is destabilized into an assembly of isolated droplets [41]. The created surface topography is visualized with SFM (see Fig. 2.11(a)). It consists of rather irregularly shaped droplets which deviate significantly from a pancake shape (see line-scan in Fig. 2.11(b)). Since dPS and PpMS are weakly incompatible and phase separate in a thin film geometry [114–118], in addition to the dewetting structure as displayed with SFM a phase separation structure is expectable. However, from the SFM topography pictures as for example presented in Fig. 2.11(a) no information about the internal distribution of the blend components can be obtained.

Because both blend components dPS and PpMS differ only by one methyl group, despite the deuteration, their chemical and mechanical properties are very

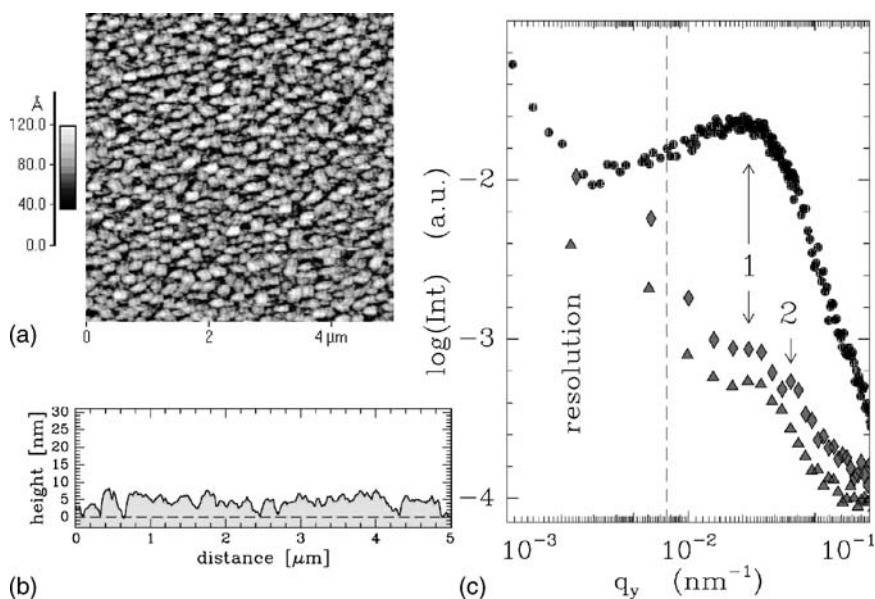


Fig. 2.11 Example of a dewetted dPS:PpMS = 40:60 blend film of $1/3 R_g$ original film thickness as probed after 8 h of annealing above the glass transition temperature. (a) Non-contact SFM measurement of the surface topography displaying irregularly shaped droplets. (b) Line-scan taken from the SFM data. (c) Comparison of the statistical information calculated from the SFM data (black dots) via the master curve construction and GISANS data of blend (rhombi) and a homopolymer dPS (triangles) film. Two most prominent in-plane structures are marked with the arrows and "1" and "2". See [41]

similar. Therefore surface characterization methods like friction and stiffness measurements [119] yield not enough contrast to distinguish between the components and a selective dissolution [120] of one component is not possible. However, due to the contrast generated by the deuteration, possible super- or sub-structures are detectable with GISANS [47].

In Fig. 2.11(c) data measured at the D22 beamline at the ILL are shown. Both measurements, dPS (blue triangles) and dPS:PpMS (rhombi), exhibit one peak in the intensity at a q_y -position corresponding to an in-plane length scale of $\xi_1 = (293 \pm 5)$ nm (marked “1”). Additionally, the dPS:PpMS sample shows a second peak in the intensity, resulting from a smaller length scale of $\xi_2 = (171 \pm 2)$ nm (marked “2”), which appears to have a smaller FWHM due to the logarithmic x -axis. The intensity of the second peak is weak as compared to the peak originated by ξ_1 but well above the noise level. The used symbol size gives an impression for the uncertainty of the data in y -range of the second peak. It should be noted that, in the master curve from the SFM data (black dots) this peak at ξ_2 is not present, whereas the peak at ξ_1 is even more pronounced. Thus ξ_1 corresponds to a topographical and ξ_2 to a chemical composition length scale.

To detect this sub-structure with increased statistics both scans were measured at $\lambda = 0.7$ nm which enlarges the resolvable length scale regime towards smaller in-plane lengths. Due to the rather irregular surface topography a peak in the PSD from GISANS as compared to the one in the master curve from the SFM is not that well pronounced. The present larger length scales are not measured with SFM due to the small scan range as compared to the coherently illuminated surface area in GISANS. In the scattering data they yield an increase of intensity towards smaller q_y -values. The observed composition sub-structure pictures an internal structure with regular distances. In a thick film system the minimization of the surface free energy yields a segregation of the polymer with the lower surface tension at the surface. In a two dimensional system the surface is replaced by the contact line and segregation at the contact line reduces the free energy. Additionally the isolation of polymer chains in the perpendicular direction forces a local phase separation process [121]. Due to the strong confinement the investigated system can be regarded as two dimensional. Each irregular shaped droplet consists of several dPS and PpMS molecules which internally arrange to the different interaction with the substrate. PpMS has a smaller surface tension as compared to dPS [122] and surrounds dPS inside each droplet.

GISANS is well suited to probe the roughness spectrum from a molecular to mesoscopic in-plane length scale and provides information about the internal chemical composition of the examined samples.

2.6.3 Dewetted Diblock Copolymer Films

Instead of blending the two homopolymers deuterated polystyrene dPS and polyparamethylstyrene PpMS in a diblock copolymer P(dS-b-pMS) both are chemically

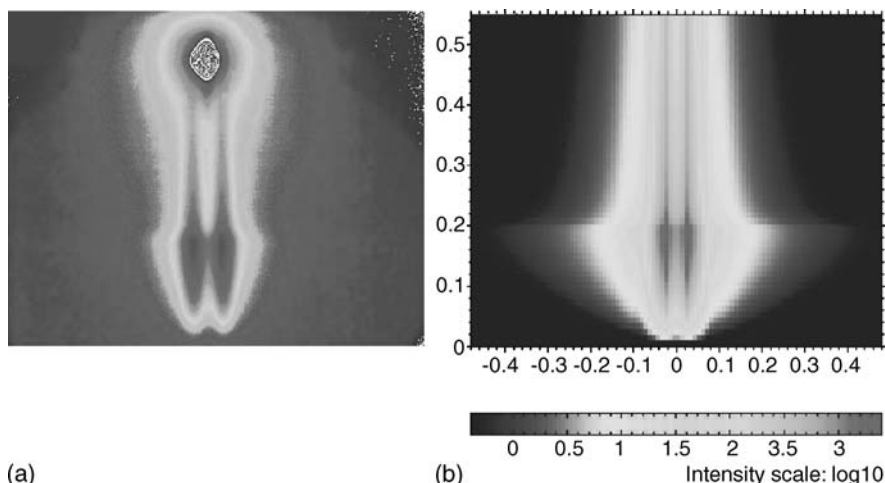


Fig. 2.12 (a) Typical two-dimensional GIUSAXS scattering pattern measured at a large distance between the sample and the detector, covering a range of $-0.48^\circ < \psi < 0.48^\circ$ in horizontal direction and $0.0^\circ < \alpha_f < 0.55^\circ$ in vertical direction. The intensity is shown on a logarithmic scale. The colour coding was chosen to emphasize on the features in the diffuse scattering (blue = low and red = high intensity). As a consequence, the specular peak in the top region of each two-dimensional intensity mapping appears with a staggered intensity. (b) Calculated two-dimensional GISAXS scattering pattern using the program IsGISAXS as described in the text. The colour coding was chosen to be comparable to the measured data. See [124]

linked together via a covalent bond. The weak incompatibility causes a micro-phase separation [123] yielding well pronounced surface structures in the case of confined thin films [52, 55, 91, 104]. Again the arrangement of the molecules inside the polymeric droplets is well resolvable by GISAXS [52] as explained in the section above. Due to the small contrast for X-Rays between both blocks dPS and PpMS, GISAXS is most sensitive to the host structure resulting from the dewetting process. To resolve the evolving structures a very high resolution GIUSAXS set-up was realized at the BW4 beamline at HASYLAB [124].

Figure 2.12 compares the measured two-dimensional intensity distribution with a modelled one using the program IsGISAXS by R. Lazzari [93, 94]. On the first sight, Fig. 2.12(a) is rather similar to the intensity distribution shown in Figs. 2.6–2.8. The Yoneda peak is split up in two side maxima. But in contrast to the previous example (Figs. 2.6–2.8) no central peak at $q_y = 0$ is present. The absence of a central Yoneda peak in the two-dimensional intensity mapping is related to the absence of large lateral lengths outside the resolvable length scale regime. It is typically observed in case of supported dominant isolated objects such as cylinders, pancakes or spherical caps.

The type of data analysis presented in the previous section (about dewetted polymer blend films) was restricted to a comparison of GISAXS data with other experimentally determined data, based on a statistical interpretation of SFM data. For the modelling of the full two-dimensional intensity distribution basically the

form and structure factor have to be chosen. Because the polymeric material probed is placed on top of the solid support the model of supported particles is well suited. In a first approximation the form factor of the host structure is chosen to obey a cylinder type and the structure factor to behave like a one-dimensional paracrystal [125].

Figure 2.12(b) displays the best fits obtained with these assumptions, yielding the parameters: cylinder radius $R=50$ nm (with a Gaussian distribution with $\sigma R/R=0.25$), cylinder height $H=3.5$ nm and peak position of the interference function $D=290$ nm (Ω -parameter used in the pair correlation function of the paracrystal $\Omega=100$ nm) [124].

The fitted two-dimensional intensity mapping in Fig. 2.12(b) covers exactly the same angular range as compared to the measured GIUSAXS data displayed in Fig. 2.12(a). The colour coding was adapted to match the one chosen in the presentation of the data. Because only the diffuse scattering is modelled, no specular peak is present in Fig. 2.12(b). As a consequence the comparison mainly can focus to the region around the Yoneda peaks. The basic features of the measured two-dimensional intensity mapping, the split-up Yoneda peaks in its positions and shape, are captured by the modelling. Most deviations are originated from a missing background in the modelled data and effect the outer parts at large ψ (or q_y) values. In general, the agreement for the presented example is very good.

2.7 Summary

The investigation of surfaces, interfaces and thin films requires dedicated analytical techniques, which provide atomic/molecular resolution for the location and analysis of individual atoms/molecules at the surface or at buried interfaces of thin films or multilayer systems. Techniques providing depth information (e. g. the enrichment of one surface component) and techniques providing lateral resolution (e. g. the two-dimensional phase separation of components in a thin blend film) can be distinguished.

GISAS (grazing incidence small-angle scattering) involves a combination of two techniques; GID (grazing incidence diffraction), which uses reflection geometry to obtain surface and near surface sensitive scattering, and SAS (small-angle scattering), which measures structures in a range of 1–100 nm in normal transmission mode. It is a non-destructive structural probe, does not require a special sample preparation (in situ characterization possible), yields excellent sampling statistics (averages over macroscopic regions to provide information on nanometre scale) and provides information on particle geometry, size distributions, spatial correlations. From a direct comparison with other experimental data e. g. from SFM or from detailed modelling the relevant sample structures are deduced. By choosing the probe, either X-Rays or neutrons, the contrast of the system under investigation can be altered. In the field of polymeric samples due to deuteration a combination of both gives a direct access to a chemical structural information not

accessible with other techniques. GISAS however demands high collimation and thus requires high flux sources, typically provided at large scale facilities such as synchrotrons or neutron reactors. The typical accumulation times strongly depend on the type of sample systems. In case of very weakly scattering sub-monomolecular polymeric layers easily accumulation times on the order of hours are necessary whereas metallic nanoparticles samples enable real time investigations.

Resulting from its high versatility GISAS will receive a further increasing attention in the structural investigation of thin film samples. At present the number of beamlines offering GISAXS and GISANS increases, as well as more and more different systems are under investigation with this advanced scattering technique [126–148].

Acknowledgments

This work has benefited strongly from fruitful and enjoyable collaborations with J.S. Gutmann, N. Hermsdorf, W. Petry, S.V. Roth and M. Stamm. Cooperation of E. Bauer, M. Casagrande, A. Götzendorfer, T. Ittner, J. Kraus, V. Körstgens, T. Kuhlmann, V. Lauter-Pasyuk, S. Loi, C. Lorenz-Haas, B. Mahltig, E. Maurer, P. Panagiotou, G. Pfütze, T. Titz, I. Tokarev, A. Vix, P. Volodin, H. Walter, M. Wolkenhauer and O. Wunnicke in many beamtimes at large scale facilities and stimulating discussions with G.T. Baumbach, H. Dosch, M.D. Foster, A. Gibaud, V. Holý, R. Kampmann, R. Lazzari, T.H. Metzger, H. Okuda, C.M. Papadakis, J. Peisl, U. Pietsch, M. Rauscher, F. Rieutord, T. Salditt, M. Schmidbauer and S.K. Sinha is gratefully acknowledged. Support at HASYLAB was provided by S. Cunis, M. Dommach, W. Fenzl, S.S. Funari, R. Gehrke, G. von Krosigk and A. Meyer, at ILL by R. Cubitt and at ESRF by M. Burghammer, C. Riekell and D. Smilgies. The used silicon substrates were kindly made available by Wacker Siltronic, Burghausen (Germany). Financial support was provided by the BMBF (Förderkennzeichen 03DU03MU) and by DFG in the framework of the priority program SPP 1164 “Nano- and Microfluidics” (Mu1487/2).

References

1. S. Steeb, P. Lamparter, Röntgenbeugung an nichtkristallinen Metallen und Legierungen, in *Forschung mit Röntgenstrahlen Bilanz eines Jahrhunderts (1895–1995)*, ed. by F.H.W. Heuck, E. Macherauch (Springer, Berlin Heidelberg New York, 1995), p. 447–461
2. A. Guinier, G. Fournet, *Small-Angle Scattering of X-Rays* (Wiley, New York, 1955)
3. A. Guinier, *X-Ray Diffraction in Crystals, Imperfect Crystals and Amorphous Bodies* (Dover, New York, 1963)
4. G. Glatter, O. Kratky, *Small Angle X-Ray Scattering* (Academic, London, 1982)
5. J.S. Higgins, H.C. Benoît, *Polymers and Neutron Scattering* (Clarendon, Oxford, 1994)
6. W. Bras, SAXS/WAXS experiments using extreme sample environments. *Nucl. Instr. Meth. Phys Res. B*, 199, 90 (2003)

7. H. Dosch, Critical phenomena at surfaces and interfaces: Evanescent X-Ray and neutron scattering (Springer, Berlin Heidelberg New York, 1992)
8. S. Dietrich, A. Haase, Scattering of X-Rays and neutrons at interfaces. Phys. Rep. 260, 1 (1995)
9. P. Müller-Buschbaum, Grazing incidence small-angle X-Ray scattering – an advanced scattering technique for the investigation of nanostructured polymer films. Anal. Bioanal. Chem. 376, 3 (2003)
10. L.G. Parrat, Surface studies of solids by total reflection of X-Rays. Phys. Rev. 55, 359 (1954)
11. R.W. James, *The Optical Principles of the Diffraction of X-Rays* (OxBow Press, Woodbridge, CT, 1962)
12. M. Born, E. Wolf, *Principles of Optics*, 2nd edn. (Pergamon, Oxford, 1964)
13. B.E. Warren, *X-Ray Diffraction* (Addison-Wesley, Reading, MA, 1969)
14. M. Stamm, D.W. Schubert, Interfaces between incompatible interfaces. Annu. Rev. Mater. Sci. 25, 325 (1995)
15. D.W. Schubert, V. Abetz, M. Stamm, T. Hack, W. Siol, Composition and temperature dependence of the segmental interaction parameter in statistical copolymer/homopolymer blends. Macromolecules 28, 2519 (1995)
16. Y. Yoneda, Anomalous surface reflection of X-Rays. Phys. Rev. 131, 2010 (1963)
17. S.K. Sinha, E.B. Sirota, S. Garoff, H.B. Stanley, X-Ray and neutron scattering from rough surfaces. Phys. Rev. B 38, 2297 (1988)
18. V. Holý, J. Kubuena, I. Ohlídal, K. Lischka, W. Plotz, X-Ray reflection from rough layered systems. Phys. Rev. B 47, 15896 (1993)
19. V. Holý, T. Baumbach, Non specular X-Ray reflection from rough multilayers. Phys. Rev. B 49, 10668 (1994)
20. G.T. Baumbach, V. Holý, U. Pietsch, M. Gailhanou, The influence of specular interface reflection on grazing-incidence X-Ray diffraction and diffuse-scattering from superlattices. Physica B 198, 249 (1994)
21. M. Rauscher, T. Salditt, H. Spohn, Small-angle X-Ray scattering under grazing incidence: the cross section in the distorted-wave Born approximation. Phys. Rev. B 52, 16855 (1995)
22. J. Stettner, L. Schwalowsky, O.H. Seeck, M. Tolan, W. Press, C. Schwarz, H.v. Känel, Interface structure of MBE-grown $\text{CoSi}_2/\text{Si}/\text{CoSi}_2$ layers on $\text{Si}(111)$: Partially correlated roughness and diffuse X-Ray scattering. Phys. Rev. B 53, 1398 (1996)
23. J. Daillant, K. Quinn, C. Gourier, F. Rieutord, Grazing incidence surface scattering of X-Rays. J. Chem. Soc. Faraday Transactions 92, 505 (1996)
24. M. Tolan, W. Press, X-Ray and neutron reflectivity. Z. Kristallog 213, 319 (1998)
25. M. Tolan, *X-Ray Scattering from Soft-matter Thin Films* (Springer, Berlin Heidelberg New York, 1999).
26. J.R. Levine, J.B. Cohen, Y.W. Chung, P. Georgopoulos, Grazing-incidence small-angle X-Ray scattering: new tool for studying thin film growth. J. Appl. Cryst. 22, 528 (1989)
27. J.R. Levine, J.B. Cohen, Y.W. Chung, Thin film island growth kinetics: a grazing incidence small angle X-Ray scattering study of gold on glass. Surf. Sci. 248, 215 (1991)
28. T. Salditt, T.H. Metzger, J. Peisl, X. Jiang, Diffuse X-Ray scattering of amorphous multilayers. J.Phys. III 4, 1573 (1994)
29. T. Salditt, T.H. Metzger, J. Peisl, Kinetic roughness of amorphous multilayers studied by diffuse X-Ray scattering. Phys. Rev. Lett. 73, 2228 (1994)
30. T. Salditt, T.H. Metzger, C. Brandt, U. Klemradt, J. Peisl, Determination of the static scaling exponent of self-affine interfaces by nonspecular X-Ray scattering. Phys. Rev. B 51, 5617 (1995)
31. T. Salditt, T.H. Metzger, J. Peisl, B. Reinker, M. Moske, K. Samwer, Determination of the height–height correlation function of rough surfaces from diffuse X-Ray scattering. Europhys. Lett 32, 331 (1995)

32. T. Salditt, T.H. Metzger, J. Peisl, G. Goerigk, Non-specular X-Ray scattering from thin films and multilayers with small-angle scattering equipment. *J. Phys. D Appl. Phys.* 28, A236 (1995)
33. P. Müller-Buschbaum, P. Vanhoorne, V. Scheumann, M. Stamm, Observation of nano-dewetting structures. *Europhys. Lett.* 40, 655 (1997)
34. A. Naudon, D. Thiaudiere, Grazing-incidence small-angle scattering. Morphology of deposited clusters and nanostructure of thin films. *J. Appl. Cryst.* 30, 822 (1997)
35. P. Müller-Buschbaum, M. Casagrande, J. Gutmann, T. Kuhlmann, M. Stamm, S. Cunis, G. von Krosigk, U. Lode, R. Gehrke, Determination of micrometer length scales with an X-Ray reflection ultra small-angle scattering set-up. *Europhys. Lett.* 42, 517 (1998)
36. T. H. Metzger, I. Kegel, R. Paniago, A. Lorke, J. Peisl, J. Schulze, I. Eisele, P. Schittenhelm, G. Abstreiter, Shape, size, strain and correlations in quantum dot systems studied by grazing incidence X-Ray scattering methods. *Thin Solid Films* 336, 1 (1998)
37. M. Schmidbauer, T. Wiebach, H. Raidt, M. Hanke, R. Köhler, H. Wawra, Ordering of self-assembled $\text{Si}_{1-x}\text{Ge}_x$ islands studied by grazing incidence small-angle X-Ray scattering and atomic force microscopy. *Phys. Rev B* 58, 10523 (1998)
38. M. Maaza, A. Gibaud, C. Sella, B. Pardo, F. Dunsteter, J. Corno, F. Bridou, G. Vignaud, A. Desert, A. Menelle, X-Ray scattering by nano-particles within granular thin films, investigation by grazing angle X-Ray reflectometry. *Euro. Phys. J. B* 7, 339 (1999)
39. T.H. Metzger, I. Kegel, R. Paniago, J. Peisl, Grazing incidence X-Ray scattering: an ideal tool to study the structure of quantum dots. *J. Phys. D Appl. Phys.* 32, A202 (1999)
40. P. Müller-Buschbaum, J.S. Gutmann, M. Stamm, Dewetting of confined polymer films: An X-Ray and neutron scattering study. *Phys. Chem. Chem. Phys.* 1, 3857 (1999)
41. P. Müller-Buschbaum, J.S. Gutmann, R. Cubitt, M. Stamm, Probing the in-plane composition of thin polymer films with grazing-incidence small angle scattering and atomic force microscopy. *Colloid. Polym. Sci.* 277, 1193 (1999)
42. M. Rauscher, R. Paniago, H. Metzger, Z. Kovats, J. Domke, H. D. Pfannes, J. Schulze, I. Eisele, Grazing incidence small angle X-Ray scattering from free-standing nanostructures. *J. Appl. Phys.* 86, 6763 (1999)
43. T. Salditt, C. Münster, Y. Lu, , M. Vogel, W. Fenzl, A. Souvorov, Specular and diffuse scattering of highly aligned phospholipid membranes. *Phys. Rev. E* 60, 7285 (1999)
44. J. Stangl, V. Holý, P. Mikulik, G. Bauer, I. Kegel, T.H. Metzger, O.G. Schmidt, C. Lange, K. Eberl, Self-assembled carbon-induced germanium quantum dots studied by grazing-incidence small-angle scattering. *Appl. Phys. Lett.* 74, 3785 (1999)
45. D. Babonneau, A. Naudon, T. Cabioch, O. Lyon, Morphology of encapsulated iron nanoparticles obtained by co-sputtering and implantation: a GISAXS study. *J. Appl. Crystallogr.* 33, 437 (2000)
46. S. Hazara, A. Gibaud, A. Desert, C. Sella, A. Naudon, Morphology of nanocermet in thin films: X-Ray scattering study. *Physica B* 283, 97 (2000)
47. P. Müller-Buschbaum, J.S. Gutmann, M. Stamm, R. Cubitt, S. Cunis, G. von Krosigk, R. Gehrke, W. Petry, Dewetting of thin polymer blend films: Examined with GISAS. *Physica B* 283, 53 (2000)
48. A. Naudon, D. Babonneau, D. Thiaudiere, S. Lequien, Grazing-incidence small-angle X-Ray scattering applied to the characterization of aggregates in surface regions. *Physica B* 283, 69 (2000)
49. R. Paniago, H. Metzger, M. Rauscher, Z. Kovats, J. Peisl, J. Schulze, I. Eisele, S. Ferrer, Grazing incidence small-angle X-Ray scattering from laterally ordered triangular pyramidal Ge islands on Si(111). *J. Appl. Cryst.* 33, 433 (2000)
50. A. Gibaud, S. Hazra, C. Sella, P. Laffez, A. Desert, A. Naudon, G. Van Tendeloo, Particle layering in the ceramic-metal thin Pt- Al_2O_3 . *Phys. Rev. B* 63, 193407 (2001)
51. P. Müller-Buschbaum, J.S. Gutmann, M. Wolkenhauer, J. Kraus, M. Stamm, D. Smilgies, W. Petry, Solvent induced surface morphology of thin polymer films. *Macromolecules* 34, 1369 (2001)

52. P. Müller-Buschbaum, M. Wolkenhauer, O. Wunnicke, M. Stamm, R. Cubitt, W. Petry, Structure formation in two-dimensionally confined diblock copolymer films. *Langmuir* 17, 5567 (2001)
53. A. Gibaud, D. Grosso, B. Smarsly, A. Baptiste, J.F. Bardeau, F. Babonneau, D.A. Doshi, Z. Chen, C.J. Brinker, C. Sanchez, Evaporation-controlled self-assembly of silica surfactant mesophases. *J. Phys. Chem. B* 107, 6114 (2003)
54. J.H. Li, V. Holy, M. Meduna, S.C. Moss, A.G. Norman, A. Mascarenhas, J.L. Reno, Lateral composition modulation in $(\text{InAs})_n/(\text{AlAs})_m$ short-period superlattices investigated by high-resolution X-Ray scattering. *Phys. Rev. B* 66, 115312 (2002)
55. P. Müller-Buschbaum, J.S. Gutmann, C. Lorenz-Haas, O. Wunnicke, M. Stamm, W. Petry, Dewetting of thin diblock copolymer films. *Macromolecules* 35, 2017 (2002)
56. P. Müller-Buschbaum, R. Cubitt, W. Petry, Phase separation of weakly incompatible polymer blends confined into isolated droplets. *Appl. Phys. A* 74, S342 (2002)
57. D.M. Smilgies, P. Busch, C.M. Papadakis, D. Posselt, Characterization of polymer thin films with small-angle X-Ray scattering under grazing incidence (GISAXS). *Synchrotron Rad. News* 5, 35 (2002)
58. P. Busch, D. Posselt, D.M. Smilgies, B. Rheinländer, F. Kremer, C.M. Papadakis, Lamellar diblock copolymer thin films investigated by tapping mode atomic force microscopy: Molar-mass dependence of surface ordering. *Macromolecules* 36, 8717 (2003)
59. M. Buljan, K. Salamon, P. Dubcek, S. Bernstorff, I.D. Desnica-Frankovic, O. Milat, U.V. Desnica, Analysis of 2D GISAXS patterns obtained on semiconductor nanocrystals. *Vacuum* 71, 65 (2003)
60. U.V. Desnica, P. Dubcek, I.D. Desnica-Frankovic, M. Buljan, K. Salamon, O. Milat, S. Bernstorff, C.W. White, GISAXS studies of morphology and size distribution of CdS nanocrystals formed in SiO_2 by ion implantation. *Nucl. Instr. Meth. B* 200, 191 (2003)
61. D.A. Doshi, A. Gibaud, N. Liu, D. Sturmayer, A.P. Malanoski, D.R. Dunphy, H. Chen, S. Narayanan, A. MacPhee, J. Wang, S.T. Reed, A.J. Hurd, F. van Swol, C.J. Brinker, In-situ scattering study of continuous silica-surfactant self-assembly during steady-state dip coating. *J. Phys. Chem. B* 107, 7683 (2003)
62. P. Dubcek, U.V. Desnica, I.D. Desnica-Frankovic, S. Bernstorff, A. Meldrum, GISAXS study of shape and size of CDS nanocrystals formed in monocrystalline silicon by ion implantation. *Nucl. Instr. Meth. B* 200, 138 (2003)
63. O. Fruchart, G. Renaud, A. Barbier, M. Noblet, O. Ulrich, J.P. Deville, F. Scheurer, J. Mane-Mane, V. Repain, G. Baudot, S. Rousset, X-Ray supercell crystallography of self-organized Co/Au(111) deposits. *Europhys. Lett.* 63, 275 (2003)
64. A. Gibaud, A. Baptiste, D.A. Doshi, C.J. Brinker, L. Yang, B.Ocko, Wall thickness and core radius determination in surfactant templated silica thin films using GISAXS and X-Ray reflectivity. *Europhys. Lett.* 63, 833 (2003)
65. D. Garcin, P. Dubcek, M. Jaksic, Z. Medunic, Nanostructural properties of amorphous silicon carbide by GISAXS and optical spectroscopy. *Thin Solid Films* 433, 88 (2003)
66. D. Garcin, M. Jaksic, P. Dubcek, Z. Medunic, Investigation of the nano-structured properties of amorphous silicon carbon alloys by IBA technique, optical spectroscopy and GISAXS. *Vacuum* 71, 47 (2003)
67. P. Müller-Buschbaum, Dewetting and pattern formation in thin polymer films as investigated in real and reciprocal space. *J. Phys. Condens. Matter* 15, R1549 (2003)
68. M. Pannetier, F. Ott, C. Fermon, Y. Samson, Surface diffraction on magnetic nanostructures in thin films using grazing incidence SANS. *Physica B* 335, 54 (2003)
69. B. Smarsly, G. Xomeritakis, K. Yu, N. Liu, H. Fan, R.A. Assink, C.A. Drewien, W. Ruland, C.J. Brinker, Microstructural characterisation of polystyrene-block-poly(ethyleneoxide)-templated silica films with cubic-ordered spherical mesopores. *Langmuir* 19, 7295 (2003)
70. S. Stemmer, Y. Li, B. Foran, P.S. Lysaght, S.K. Streiffer, P. Fuoss, S. Seifert, Grazing-incidence small angle X-Ray scattering studies of phase separation in hafnium silicate films. *Appl. Phys. Lett.* 83, 3141 (2003)

71. G. Xomeritakis, C.M. Braunbarth, B. Smarsly, N. Liu, R. Köhn, Z. Klipowicz, C.J. Brinker, Aerosol-assisted deposition of surfactant-templated mesoporous silica membranes on porous ceramic supports. *Micropor. Mesopor. Mater.* 66, 91 (2003)
72. G. Renaud, C. Revenant-Brizard, R. Lazzari, A. Barbier, M. Noblet, O. Ulrich, Y. Borenstein, J. Jupille, C. R. Henry, J. P. Deville, F. Scheurer, O. Fruchart, Real time monitoring of growing nanoparticles. *Science* 300, 1416 (2003)
73. P. Müller-Buschbaum, S.V. Roth, M. Burghammer, A. Diethert, P. Panagiotou, C. Riekel, Multiple-scaled polymer surfaces investigated with micro-focus grazing incidence small-angle X-Ray scattering. *Europhys. Lett.* 61, 639 (2003)
74. S.V. Roth, M. Burghammer, C. Riekel, P. Müller-Buschbaum, A. Diethert, P. Panagiotou, H. Walter, Self-assembled gradient nanoparticle-polymer multilayers investigated by an advanced characterisation method: Microbeam grazing incidence X-Ray scattering. *Appl. Phys. Lett.* 82, 1935 (2003)
75. G. Binnig, H. Rohrer, Scanning tunneling microscopy. *Helv. Phys. Acta* 55, 726 (1982)
76. G. Binnig, C.F. Quate, C. Gerber, Atomic force microscope. *Phys. Rev. Lett.* 56, 930 (1986)
77. R.J. Behm, N. García, H. Rohrer (eds), *Scanning Tunneling Microscopy and Related Methods*, vol. 184 of Nato ASI Series E (Kluwer, Dordrecht, 1990)
78. D. Rugar, P.K. Hansma, Atomic force microscopy. *Phys. Today* 43, 23 (1990)
79. D. Sarid, *Scanning Force Microscopy* (Oxford University Press, New York, 1991)
80. O. Marti, M. Amrein (eds), *STM and SFM in Biology* (Academic, San Diego, 1993)
81. P. Müller-Buschbaum, J.S. Gutmann, M. Stamm, Influence of blend composition on phase separation and dewetting of thin blend films. *Macromolecules* 33, 4886 (2000)
82. J.S. Gutmann, P. Müller-Buschbaum, M. Stamm, Complex pattern formation by phase separation of polymer blends in thin films. *Faraday Disc.* 112, 285 (1999)
83. M.D. Kirk, T.R. Albrecht, C.F. Quate, Low-temperature atomic force microscope. *Rev. Sci. Instrum.* 59, 833 (1988)
84. J. C. Russ, *Fractal Surfaces*. (Plenum, New York, 1994)
85. J.S. Bendat, A.G. Piersol, *Random Data: Analysis and Measurement Procedures* (Wiley Interscience, New York, 1971)
86. A.M. Yaglom, *Correlation Theory of Stationary and Related Random Functions*. Springer Series in Statistics (Springer, Berlin Heidelberg, New York, 1987)
87. D. Bahr, W. Press, R. Jevasinski, S. Mantl, X-Ray reflectivity and diffuse scattering study on CoSi₂ layers in Si produced by ion beam synthesis. *Phys. Rev. B* 47, 4385 (1993)
88. G.T. Baumbach, D. Lubbert, M. Gailhanou, X-Ray structure investigation of lateral surface nanostructures – a full quantitative analysis of non-uniform lattice strain. *J. Phys. D Appl. Phys.* 32, A208 (1999)
89. B. Toperverg, V. Lauter-Pasyuk, H.J. Lauter, O. Nikonov, D. Ausserre, Y. Gallot, Off-specular neutron scattering from islands on a lamellar film. *Physica B* 276–278, 355 (2000)
90. B. Toperverg, V. Lauter-Pasyuk, H.J. Lauter, O. Nikonov, D. Ausserre, Y. Gallot, Morphology of off-specular neutron scattering pattern from islands on a lamellar film. *Physica B* 283, 60 (2000)
91. V. Lauer-Pasyuk, H.J. Lauter, G.P. Gordeev, P. Müller-Buschbaum, B.P. Toperverg, M. Jernenkou, W. Petry, Nanoparticles in diblock copolymer films investigated by off-specular neutron scattering. *Langmuir* 19, 7783 (2003)
92. V. Holy, U. Pietsch, T. Baumbach, *High Resolution X-Ray Scattering from Crystalline Thin Films* (Springer, Berlin, Heidelberg, New York, 1998)
93. R. Lazzari, IsGISAXS: a program for grazing incidence small-angle X-Ray scattering analysis for supported islands. *J. Appl. Cryst.* 35, 406 (2002)
94. R. Lazzari, IsGISAXS with instructions, <http://www.esrf.fr>. Accessed 2007
95. J.R.L. Parrill, P. Georgopoulos, Y.W. Chung, J.B. Cohen. GISAXS – glancing incidence small-angle X-Ray scattering. *J. Phys. IV* 3, 411 (1993)
96. E. Cattaruzza, F. d'Acapito, F. Gonella, A. Longo, A. Martorana, G. Mattei, C. Maurizio, D. Thiaudiere, GISAXS study of Cu-Ni alloy clusters obtained by double ion implantation in silicate glasses. *J. Appl. Cryst.* 33, 740 (2000)

97. V. Chamard, P. Bastie, D. Le Bolloch, G. Dolino, E. Elkaim, C. Ferrero, J.P. Lauriat, F. Rieutord, D. Thiaudiere, Evidence of pore correlation in porous silicon: A grazing-incidence study. *Phys. Rev. B* 64, 245416 (2001)
98. I. Kegel, T.H. Metzger, J. Peisl, Lateral ordering of coherent Ge islands on Si(001) studied by triple-crystal grazing incidence diffraction. *Appl. Phys. Lett.* 74, 2978 (1999)
99. I. Kegel, T.H. Metzger, J. Peisl, J. Stangl, G. Bauer, D. Smilgies, Vertical alignment of multilayered quantum dots studied by X-Ray grazing-incidence diffraction. *Phys. Rev. B* 60, 2516 (1999)
100. J.S. Gutmann, P. Müller-Buschbaum, D.W. Schubert, N. Stribeck, D. Smilgies, M. Stamm, Roughness correlations in ultra-thin polymer blend films. *Physica B* 283, 40 (2000)
101. D.M. Smilgies, High-resolution grazing-incidence scattering using a combination of analyzer crystal and linear detector. *Rev. Sci. Instr.* 74, 4041 (2003)
102. P. Panagiotou, E. Bauer, S. Loi, T. Titz, E. Maurer, P. Müller-Buschbaum, Polymeric structures at interfaces: An X-Ray scattering study. *Z. Kristallogr.* 219, 210 (2004)
103. N. Hermsdorf, K. Sahre, P. Volodin, M. Stamm, K.J. Eichhorn, S. Cunis, R. Gehrke, P. Panagiotou, T. Titz, P. Müller-Buschbaum, Supported particle track etched polyimide membranes: A grazing incidence small-angle X-Ray scattering study. *Langmuir* 20, 10303 (2004)
104. P. Müller-Buschbaum, J.S. Gutmann, C. Lorenz-Haas, B. Mahltig, M. Stamm, W. Petry, Early stages of film creation in thin diblock copolymer films. *Macromolecules* 34, 7463 (2001)
105. P. Müller-Buschbaum, M. Stamm, Correlated roughness, long-range correlations, and dewetting of thin polymer films. *Macromolecules* 31, 3686 (1998)
106. P. Müller-Buschbaum, J.S. Gutmann, C. Lorenz, T. Schmitt, M. Stamm, Decay of interface correlation in thin polymer films. *Macromolecules* 31, 9265 (1998)
107. P. Müller-Buschbaum, J.S. Gutmann, J. Kraus, H. Walter, M. Stamm, Suppression of roughness replication in bilayer films prepared by spin coating. *Macromolecules* 33, 569 (2000)
108. M. Wolkenhauer, P. Müller-Buschbaum, O. Wunnicke, M. Stamm, J. Roovers, G. von Krosigk, R. Cubitt, Structure analysis of adsorbed starlike polymers with GISAS and SFM. *Appl. Phys. A* 74, S433 (2002)
109. J.S. Gutmann, P. Müller-Buschbaum, M. Stamm, Film thickness dependence of structure formation in ultra-thin polymer blend films. *Appl. Phys. A* 74, S463 (2002)
110. P. Müller-Buschbaum, R. Cubitt, W. Petry, Nano-structured diblock copolymer films: A grazing incidence small-angle neutron scattering study. *Langmuir* 19, 7778 (2003)
111. O. Wunnicke, P. Müller-Buschbaum, M. Wolkenhauer, C. Lorenz-Haas, R. Cubitt, M. Stamm, Enhanced thermal stability of thin polymer bilayer films due to the addition of functional copolymers. *Langmuir* 19, 8511 (2003)
112. J. Kraus, P. Müller-Buschbaum, T. Kuhlmann, D.W. Schubert, M. Stamm, Confinement effects on the chain conformation in thin polymer films. *Europhys. Lett.* 49, 210 (2000)
113. J. Kraus, P. Müller-Buschbaum, D.G. Bucknall, M. Stamm, Roughness correlation and interdiffusion in thin films of polymer chains. *J. Polym. Sci. Phys.* 37, 2862 (1999)
114. P. Müller-Buschbaum, S.A. O'Neil, S. Affrossman, M. Stamm, Phase separation and dewetting of weakly incompatible polymer blend films. *Macromolecules* 31, 5003 (1998)
115. P. Müller-Buschbaum, J.S. Gutmann, M. Stamm, Control of surface morphology by an interplay between phase separation and dewetting. *J. Macromol. Sci. B38*, 577 (1999)
116. P. Müller-Buschbaum, M. Stamm, Film thickness dependence of the domain size in weakly incompatible thin polymer blend films. *Colloid. Polym. Sci.* 279, 376 (2001)
117. M. Geoghegan, H. Ermer, G. Jüngst, G. Krausch, R. Brenn, Wetting in a phase separation polymer blend film: quench depth dependence. *Phys. Rev. E* 62, 940 (2000)
118. M. Geoghegan, G. Krausch, Wetting at polymer surfaces and interfaces. *Prog. Polym. Sci.* 28, 261 (2003)
119. G. Krausch, M. Hipp, M. Böltau, J. Mlynek, High resolution imaging of polymer surfaces with chemical sensitivity. *Macromolecules* 28, 260 (1995)

120. S. Walheim, M. Böltau, J. Mlynek, G. Krausch, U. Steiner, Structure formation via polymer demixing in spin-cast films. *Macromolecules* 30, 4995 (1997)
121. P.G. de Gennes, in *Scaling Concepts in Polymer Physics* (Cornell University Press, Ithaca, NY, 1979)
122. R. Schnell, Dissertation, University of Mainz (1997)
123. I.W. Hamley, *The Physics of Block Copolymers* (Oxford University Press, New York, 1998)
124. P. Müller-Buschbaum, N. Hermsdorf, J.S. Gutmann, M. Stamm, S. Cunis, R. Gehrke, W. Petry, Dewetting of confined diblock copolymer films. *J. Macromol. Sci.* 43, 29 (2004)
125. R. Hosemann, W. Vogel, D. Weick, Novel aspects of the real paracrystal. *Acta. Cryst. A* 37, 85 (1981)
126. P. Müller-Buschbaum, N. Hermsdorf, S.V. Roth, J. Wiedersich, S. Cunis, R. Gehrke, Comparative analysis of nanostructured diblock copolymer films. *Spectrochimica Acta Part B Atomic Spectr.* 59, 1789 (2004)
127. S.V. Roth, P. Müller-Buschbaum, M. Burghammer, H. Walter, P. Panagiotou, A. Diethert, C. Riekel, Microbeam grazing incidence small angle X-Ray scattering – a new method to investigate nanostructured heterogeneous thin films and multilayers. *Spectrochimica Acta Part B Atomic Spectr.* 59, 1765 (2004)
128. R. Steitz, P. Müller-Buschbaum, S. Schemmel, R. Cubitt, G.H. Findenegg, Lateral structure of a surfactant adsorbed layer at the hydrophilic solid/liquid interface. *Europhys. Lett.* 67, 962 (2004)
129. B. Lee, S. Seifert, S.J. Riley, G. Tikhonov, N.A. Tomczyk, S. Vajda, R.E. Winans, Anomalous grazing incidence small-angle X-Ray scattering studies of platinum nanoparticles formed by cluster deposition. *J. Phys. Chem.* 123, 074701 (2005)
130. N. Jedrecy, G. Renaud, R. Lazzari, J. Jupille, Flat-top silver nanocrystals on the two polar faces of ZnO: An all angle X-Ray scattering investigation. *Phys. Rev. B* 72, 045430 (2005)
131. B. Lee, I. Park, J. Yoon, S. Park, J. Kim, K.W. Kim, T. Chang, M. Ree, Structural analysis of block copolymer thin films with grazing incidence small-angle X-Ray scattering. *Macromolecules* 38, 4311 (2005)
132. B. Lee, J. Yoon, W. Oh, Y. Hwang, K. Heo, K.S. Jin, J. Kim, K.W. Kim, M. Ree, In-situ grazing incidence small-angle X-Ray scattering studies on nanopore evolution in low-k organosilicate dielectric thin films. *Macromolecules* 38, 3395 (2005)
133. B. Smarsly, A. Gibaud, W. Ruland, D. Sturmayer, C.J. Brinker, Quantitative SAXS analysis of oriented 2D hexagonal cylindrical silica mesostructures in thin films obtained from non-ionic surfactants. *Langmuir* 21, 3858 (2005)
134. S. Dourdain, J.F. Bardeau, M. Colas, B. Smarsly, A. Mehdi, B.M. Ocko, A. Gibaud, Determination by X-Ray reflectivity and small angle X-Ray scattering of the porous properties of mesoporous silica thin films. *Appl. Phys. Lett.* 86, 113108 (2005)
135. S. Forster, A. Timmann, M. Konrad, C. Schellbach, A. Meyer, S.S. Funari, P. Mulvaney, R. Knott, Scattering curves of ordered mesoscopic materials, *J. Phys. Chem.* 109, 1347 (2005)
136. P. Müller-Buschbaum, S.V. Roth, M. Burghammer, E. Bauer, S. Pfister, C. David, C. Riekel, Local defects in thin polymer films: A scanning sub-microbeam grazing incidence small angle scattering investigation. *Physica B* 357, 148 (2005)
137. S.V. Roth, M. Rankl, G.R.J. Artus, S. Seeger, M. Burghammer, C. Riekel, P. Müller-Buschbaum, Domain nano-structure of thin cellulose layers investigated by microbeam grazing incidence small-angle X-Ray scattering. *Physica B* 357, 190 (2005)
138. W.A. Hamilton, Conformation, directed self-assembly and engineered modification: some recent near surface structure determinations by grazing incidence small angle X-Ray and neutron scattering. *Curr. Opin. Coll. Int. Sci.* 9, 390 (2005)
139. U. Pietsch, T. Panzner, F. Pfeiffer, I.K. Robinson, Substrate morphology repetition in “thick” polymer films. *Physica B* 357, 136 (2005)
140. Z. Sun, M. Wolkenhauer, G.G. Bumbu, D.H. Kim, J.S. Gutmann, GISAXS investigation of TiO₂ nanoparticles in PS-b-PEO block-copolymer films. *Physica B* 357, 141 (2005)

141. D. Babonneau, F. Pailloux, J.P. Eymery, M.-F. Denanot, Ph. Guérin, E. Fonda, O. Lyon, Spontaneous organization of columnar nanoparticles in Fe-BN nanocomposite films. *Phys. Rev. B* 71, 035430 (2005)
142. B.D. Vogt, H.J. Lee, W.L. Wu, Y. Liu, Specular X-Ray reflectivity and small angle neutron scattering for structure determination of ordered mesoporous dielectric films. *J. Phys. Chem. B* 109, 18445 (2005)
143. I. Tokarev, R. Krenek, Y. Burkov, D. Schmeisser, A. Sidorenko, S. Minko, M. Stamm, Microphase separation in thin films of poly(styrene-block-4-vinylpyridine) copolymer-2-(4'-hydroxybenzeneazo)benzoic acid assembly. *Macromolecules* 38, 507 (2005)
144. Y. Lin, A. Böker, H. Skaff, D. Cookson, A.D. Dinsmore, T. Emrick, T.P. Russell, Nanoparticle assembly at fluid interfaces: structure and dynamics. *Langmuir* 21, 191 (2005)
145. R.E. Winans, S. Vajda, B. Lee, S.J. Riley, S. Seifert, G.Y. Tikhonov, N.A. Tomczyk, Thermal stability of supported platinum clusters studied by in situ GISAXS. *J. Phys. Chem. B* 108, 18105 (2004)
146. C. Tang, A. Tracz, M. Kruk, R. Zhang, D.M. Smilgies, K. Matyjaszewski, T. Kowalewski, Long-range ordered thin films of block copolymers prepared by zone-casting and their thermal conversion into ordered nanostructured carbon. *J. Am. Chem. Soc.* 127, 6918 (2005)
147. M. Li, K. Douki, K. Goto, X. Li, C. Coenjarts, D.M. Smilgies, C.K. Ober, Spatially controlled fabrication of nanoporous block copolymers. *Chem. Mater* 16, 3800 (2004)
148. T. Xu, A.V. Zvelindovsky, G.J.A. Sevink, O. Gang, B. Ocko, Y. Zhu, S.P. Gido, T.P. Russell, Electric field induced sphere-to-cylinder transition in diblock copolymer thin films. *Macromolecules* 37, 6980 (2004)

Chapter 3

Vibrational Spectroscopic and Optical Methods

Martin Müller

Leibniz Institute of Polymer Research Dresden, Hohe Str. 6, 01069 Dresden, Germany,
mamuller@ipfdd.de

Abstract Vibrational spectroscopic and optical techniques can be used in different ways to characterize polymer surfaces and interfaces with respect to structure, orientation, composition and dynamics. This contribution focuses on vibrational spectroscopy such as infrared and Raman spectroscopy, but also discusses other optical techniques like ellipsometry and surface plasma resonance. Some applications of infrared surface and interface analysis are discussed in detail.

3.1 Introduction

Substrates and Polymer Interfaces This contribution gives an overview predominantly of vibrational spectroscopic and furthermore of optical methods, which can be used to characterize polymer interfaces. The relevant interfaces are given in Fig. 3.1(a), which are polymer or inorganic colloid particles (e. g. lattices, silica, dye pigments), fibres (e. g. cellulose or thermoplasts), membranes (e. g. polypropylene, polysulfone) and planar substrates (e. g. silicon wafer) or thereupon deposited polymer films. Surface vibrational spectroscopy and optical methods can be applied on both these bare inorganic or polymer substrates and on those modified by polymer interaction like adsorption or coating. In that contribution the planar model substrates and the deposited polymer layer is focussed on, which is generally schemed in Fig. 3.1(b). Especially the optical methods (introduced later) and most of the spectroscopic ones are limited to that experimental setup, since they need a well defined material with known refractive indices, geometry and ray tracing. Nevertheless the planar system itself is of high practical relevance like silicon wafers as standard support, e. g. for (bio) sensor arrays. Furthermore, planar inorganic substrates (i) as well as polymer films (ii) are often usable model systems for the surface of the inorganic colloid particles (i) or for the bulk polymer material (ii), respectively.

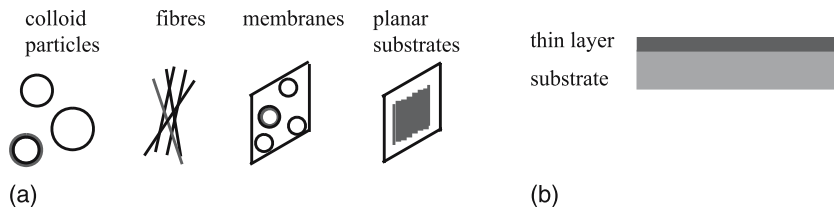


Fig. 3.1 (a) Bare and modified inorganic and polymer substrates (S) to be studied. (b) General experimental setup for the application of the introduced vibrational spectroscopic and optical methods

3.2 Vibrational Spectroscopic Methods

3.2.1 Principles

Basic principles of vibrational spectroscopic methods can be found e.g. therein [1]. Polymer or organic samples can be probed on the molecular level by vibrational spectroscopy, i. e. the excitation of vibrating modes of bonded atom groups (chromophors of polymer functional groups) by light energy. Beside the vibrational contribution the total energy E_{TOT} of a molecule is given by $E_{\text{TOT}} = E_{\text{ELEC}} + E_{\text{VIB}} + E_{\text{ROT}} + E_{\text{TRANS}}$. The E_{VIB} (E_{ROT}) contribution ranges from about $10,000 \text{ cm}^{-1}$ (near IR) to about 10 cm^{-1} (far IR) including the predominantly used mid IR from 4000 to 400 cm^{-1} . The analogous energy units are given in Table 3.1.

The basic principle is, that upon absorption of light transitions – commonly from the ground (E_0) to the first excited vibration state (E_1) – are performed ($\Delta n = 1$) according to (3.1):

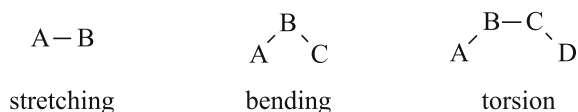
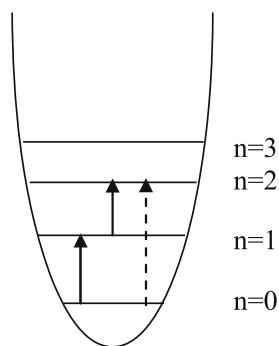
$$E_{\text{VIB}} = E_{n+1} - E_n = h\nu = hc\tilde{\nu} \quad (3.1)$$

However, also overtones with $\Delta n > 1$ are possible and furthermore also rotation transitions (E_{ROT}) take place with special selection rules. Different vibrations modes are possible such as stretching modes ν between two bonded atoms (A-B), bending modes δ of two atoms (A, C) around B (A-B-C) or torsion modes τ rotating around the B-C-axis (A-B-C-D) (Fig. 3.2). A simple model for stretching vibrations is the harmonic oscillator (Fig. 3.3), by which frequencies (wavenumbers) can be estimated (k : force constant, μ : reduced atomic mass) according to:

$$\nu = 1/2 \pi (k/\mu)^{1/2} \quad (3.2)$$

Table 3.1 Wavenumber, wavelength, frequency, energy conversion of IR light

	Wavenumber / $\tilde{\nu}$	Wavelength / λ	Frequency / $\nu = c\tilde{\nu}$	Energy / E
Value [unit]	1000 [cm^{-1}]	10 [μm]	3×10^{13} [s^{-1}]	1.88×10^{-20} [J]

**Fig. 3.2** Basic vibration modes of molecules**Fig. 3.3** Harmonic oscillator model for vibration transitions

These modes need different energies and thus appear at different frequencies. In total for a molecule consisting of N atoms, $3N - 6$ *normal modes* appear theoretically. However, since some modes may occur at identical frequencies, since modes may couple and in reality bands appear with non-zero bandwidths, a certain overlapping is observed especially in the condensed phase (liquid, solid samples). Therefore the concept of group frequencies was established, meaning that e. g. the C=O group of molecule X has an IR band between $1600-1800\text{ cm}^{-1}$.

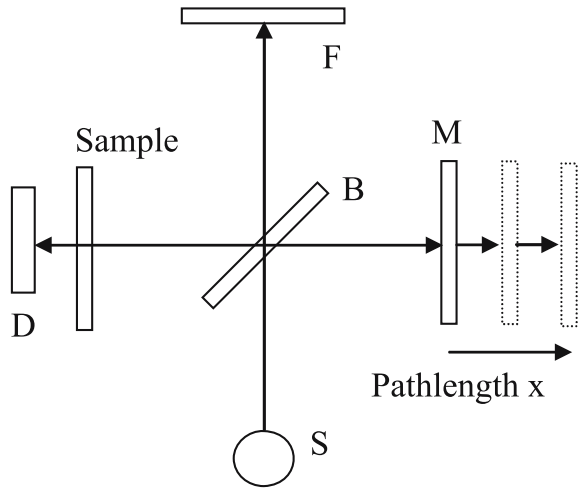
Important vibration spectroscopic techniques are Infrared (IR) and Raman Spectroscopy. Whereas in principle IR is sensitive for changes of dipole moment, Raman is sensitive for changes in polarizability of atom bonds/groups, respectively (see 3.2.6 Raman).

3.2.1.1 Fourier Transform (FT) Concept

In the last 20 years the FT technique has displaced the dispersive spectrometers, which were based on prisms or grids to “produce” different wavelengths from a polychromatic light source by their different optical refractions. The FT technique is based on the Michelson interferometer consisting of a movable semipermeable and fixed mirrors (Fig. 3.4), where from a polychromatic light source different wavelengths (wavenumbers) are “produced” by their different constructive/deconstructive interference behaviour, if two half separated beams after reflection are again guided together (Fig. 3.4) in dependence of the path length x according to eq. (3.3):

$$I(x) = \sum_i A_i \sin(2\pi\nu_i x) \quad (3.3)$$

Fig. 3.4 Michelson Interferometer FT-principle.
 S: Source, B: Beamsplitter,
 F: Fixed mirror, M: Movable
 mirror, D: Detector



Three advantages are commonly cited, which is the high throughput (no aperture, Jaquinot), the multiplexing (Connes: all wavenumbers with one scan) and the fast processing (Fellgett). For a detailed description of Fourier transform infrared spectroscopy the book of Griffith and de Haseth [2] is recommended.

3.2.1.2 Vibrational Spectroscopic Surface Analysis

Infrared (IR) spectroscopy can be used in combination to several surface sensitive methods (Trans, ATR, GIR, DRIFT), where principally the surface bound sample

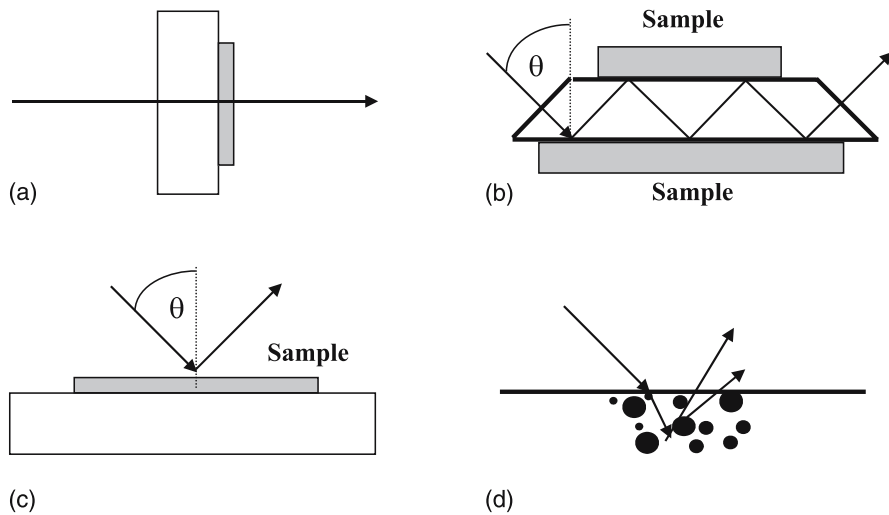


Fig. 3.5 (a) Transmission IR (TRANS-IR). (b) Attenuated total reflection IR (ATR-IR). (c) Grazing incidence IR (GIR). (d) Diffuse reflection IR (DRIR, DRIFT)

absorbs IR light, which is generated by different optical geometries. They are introduced in Fig. 3.5(a)–(d) and shall be described in the following sections.

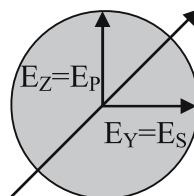
3.2.2 Transmission Infrared (TRANS-IR)

3.2.2.1 Trans-IR Concept

The sample is transmitted by IR light, which is commonly used for solutions in cuvettes, but also layers on silicon wafers may be probed (Fig. 3.5a, 3.6). Quantification of adsorbed amount is performed by the Lambert–Beer law (3.4):

$$-\log(I/I_0) = A = \epsilon c d \quad (3.4)$$

Fig. 3.6 Experimental setup of the TRANS-IR experiment



3.2.2.2 Trans-IR Information

Surface Concentration In general TRANS-IR gives the direct access to concentrations c via the Lambert–Beer law (3.4), from which c knowing d and ϵ can be calculated. From that the adsorbed amount $\Gamma = cd$ can be calculated. However, since TRANS-IR is lacking in sensitivity it is commonly not used for that purpose.

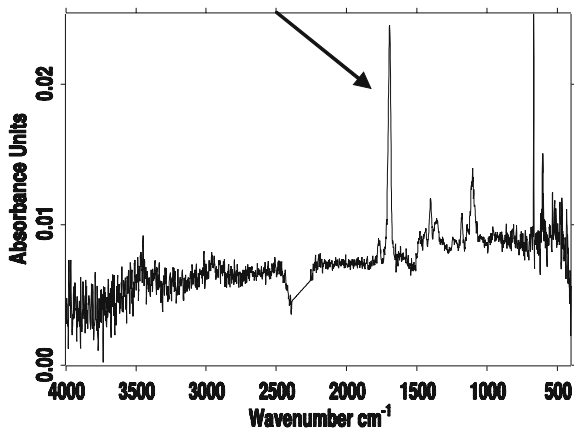
Detection Limit In Fig. 3.7 TRANS-IR spectrum is shown for a solution cast PMI-P film. The detection limit (DL) of TRANS-IR is lower than $0.063 \times 6 \mu\text{g}/\text{cm}^2 \approx 0.375 \mu\text{g}/\text{cm}^2$. This value is related to a yet observable peak intensity of 1 mA (milliabsorbance) of the $\nu(\text{C}=\text{O})$ in Fig. 3.7.

Polymer Orientation Using TRANS-IR orientation can be determined in polymer foils (stretching effect) or in thin films cast on transparent supports (silicon wafer). The orientation theory based on TRANS-IR dichroism may be briefly reviewed. Dichroism of IR bands is related to the different absorption of parallel (p) and vertical (s) polarized IR light E_p , E_s , respectively, as it is shown in Fig. 3.6. The experimental parameter is the so called dichroic ratio R^T of the integrated absorbances A_p and A_s , which generally differs from unity for oriented samples:

$$R^T = A_p/A_s \quad (3.5)$$

IR dichroism ($R^T \neq 1$) occurs, if the polymer (organic compound) sample shows a certain anisotropy due to intermolecular interactions in the bulk phase or in con-

Fig. 3.7 TRANS-IR of solution cast PMI-P (1 mg/ml) (25 μg as a $42 \times 10 \text{ mm}^2$ stripe on an IRE)



finer space such as surfaces, which is generally due to the presence of a molecular axis originating, e. g. from chain stiffness of the polymer. A straightforward derivation of TRANS-IR dichroism is given by Zbinden [3] introducing an orientation parameter S' , which accounts for more or less perfect axial orientation described by the cone model with larger or smaller opening angle γ , respectively. From S' an order parameter S ranging from $S = -1/2$ to 1, comparable to that used in NMR (IR averages ensembles due to space and NMR due to time fluctuations) can be obtained (second Legendre polynomial). Using (3.6) below, the order parameter S can be calculated from the experimental R^T value, if the angle Θ between the transition dipole moment of a considered IR vibration and the molecular main axis is known [4, 5].

$$S = 2(1 - R^T) / [(2R^T + 1)(3 \cos^2 \Theta - 1)] \quad (3.6)$$

perfect parallel axial orientation: $S = 1$, no order: $S = 0$, perfect vertical orientation: $S = -1/2$

3.2.3 Attenuated Total Reflexion Infrared (ATR-IR)

ATR-FTIR spectroscopy, whose surface analytical potential was initially explored by Harrick [6] and further developed by Fringeli [7] to address biological membrane and liquid crystalline systems quantitatively and in situ, is a powerful analytical tool for the molecular detection of processes at the solid/liquid or solid/air interface. Further groups engaged in the application and development of quantitative in situ ATR-FTIR spectroscopy have been Jacobsen and co-workers [8] and Chittur [9], aiming at bioadhesion processes at polymer films on Ge, Sukenik, characterizing acid/base properties of carboxylate terminating SAMs on Ge [10], Granick, analysing polycation (poly(4-vinylpyridine)) adsorption on Si ATR plates [11, 12] and Müller monitoring protein/peptide adsorption [13] as well as

consecutive deposition and protein affinity of polyelectrolyte multilayers at Si substrates [14].

3.2.3.1 ATR-IR Concept

A scheme of the ATR-IR principle is given in Fig. 3.8. If IR light is incident from the optically denser medium 1 (e.g. Si) at a certain angle θ , which exceeds the angle of total reflectance, an evanescent wave penetrating in and interacting with the rarer medium 2, which is material deposited on the internal reflection element (IRE), is established.

Two properties (1, 2) of the evanescent wave, formed in the rarer medium (compare to GIR) are important:

1. Exponential decay of the electrical field amplitude E with distance z , normal to the surface plane (3.7) defining a depth of penetration d_p (3.8), where E_0 has decreased to E_0/e .
2. According to Fresnel's equations the splitting into three space fixed electrical field components E_{0x} , E_{0y} , given in (3.9), and E_{0z} in the rarer medium 2 relative to the surface (at $z=0$) having all unequal amplitudes (2).

$$E_{x,y,z} = E_{0,x,y,z} (e^{-z/d_p}) \quad (3.7)$$

$$d_p = \lambda / (2 \pi n_1 [\sin^2 \theta - n_{21}^2]^{1/2}) \quad (3.8)$$

$$E_{02y}^x = E_{02y} / E_{01\perp} = 2 \cos \theta / (1 - n_{31}^2)^{1/2} \quad (3.9)$$

$$A_S = -\log(I_S/I_{0,S}) = N \epsilon c d_{e,S} \quad (3.10)$$

$$\Gamma = cd \quad (3.11)$$

3.2.3.2 ATR-IR Information

Generally, ATR-FTIR spectroscopy enables in situ detection of surface sorbed species of different molecular sizes (gases, water, ions, surfactants, drugs, reactive polymers, polyelectrolytes, lattices, proteins, cells), whereby the sorbates can be

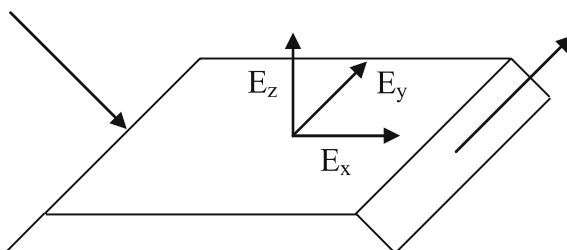
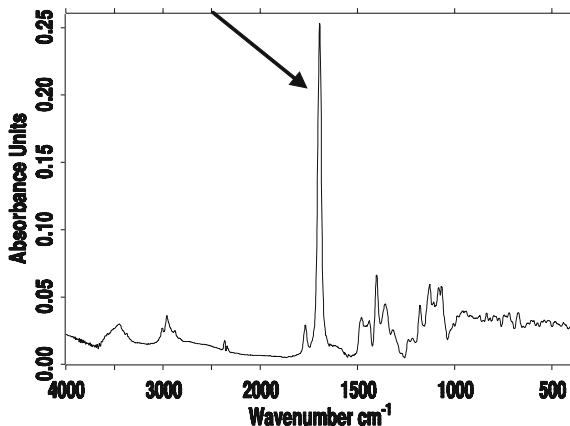


Fig. 3.8 Scheme of the ATR principle. The evanescent wave splits into 3 space fixed E -field components ($E_{x,y,z}$)

Fig. 3.9 ATR-FTIR spectrum of PMI-P sample casted onto Si-IRE (compare to other techniques)



molecularly identified by their diagnostic IR bands. Conveniently, trapezoidal IREs are used, which are incorporated in in situ cells dividing the ATR plate in an O-ring sealed upper (sample) and lower half (reference), which are alternately and repeatedly shuttled in a fixed IR beam (Single Beam Sample Reference (SBSR) concept [7]). Thereby, the reproducibility of the ATR technique, the spectral compensation of the strong water absorptions ($\nu(\text{OH})$, $\delta(\text{OH})$) and the spectral baseline could be significantly improved.

Detection Limit In Fig. 3.9 the ATR-FTIR spectrum of our standard PMI-P cast film sample is given. The $\nu(\text{C}=\text{O})$ shows an absorbance of $A_{\text{PEAK}}=0.25$, which is higher than that measured by TRANS-IR. Thereupon a detection limit $\text{DL} \approx 0.025 \mu\text{g}/\text{cm}^2$ can be estimated for $N=11$ active reflections of this specific IRE.

Surface Concentration Using the eq. 3.10 and 3.11 it is possible to quantify the surface Concentration Γ based on the integrated band area A_S (measured by s-polarized light) according to the concept of effective thickness d_e [6–7] by eq. 3.12:

$$d_{e,s} = n_{21} d_p E_{02y}^r / (2 \cos \theta) [\exp(-2 z_1/d_p) - \exp(-2 z_2/d_p)] \quad (3.12)$$

For that the thickness $d = z_2 - z_1$ has to be approximately known and the absorption coefficient ϵ of a diagnostic IR band has been determined by IR transmission spectroscopy.

3.2.3.3 Examples of ATR-IR studies

In the following some examples for the application of in-situ ATR-FTIR on relevant polymer/surface systems are given.

Surfactant Adsorption In Fig. 3.10(a) ATR-FTIR spectra are shown monitoring the time dependent adsorption of a cationic surfactant (DEEDMAC) from aqueous solution at thin cellulose films cast on Ge, which is accompanied by the desorption

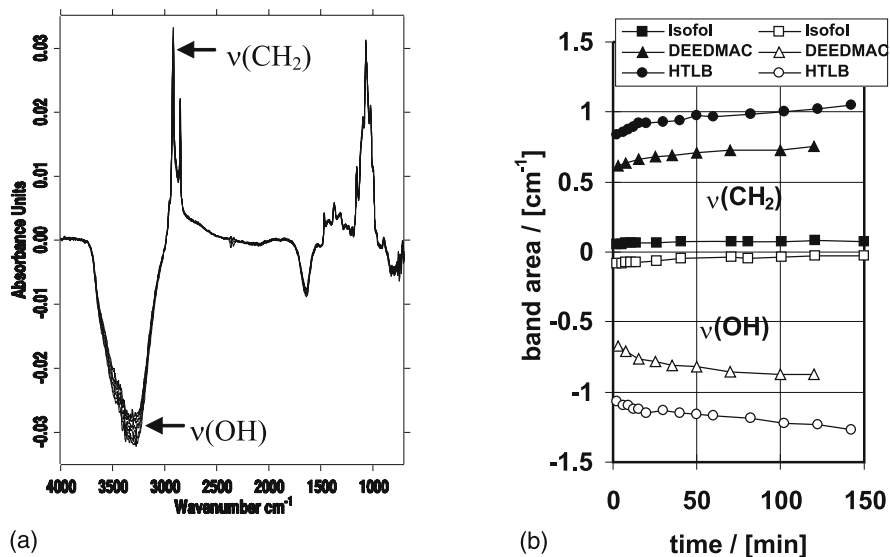


Fig. 3.10 (a) Time dependant *in-situ*-ATR-FTIR spectra recorded during the adsorption of DEEDMAC at a cellulose film (30 nm) casted on a Ge-IRE ($n_1=4$, $n_2=1.5$, $\theta=45^\circ$) [15]. (b) Integrated band areas of the $\nu(\text{CH}_2)$ and the $\nu(\text{OH})$ monitoring adsorption and water desorption of the three surfactants Isofol, DEEDMAC and HTLB [15].

of water. In Fig. 3.10(b) the integrated areas of $\nu(\text{CH}_2)$ due to surfactant deposition and of $\nu(\text{OH})$ due to water desorption, respectively, are shown. From the integrated band areas A_S of the $\nu(\text{CH}_2)$ it was possible to calculate the adsorbed amount $\Gamma = 7.2 \times 10^{-6}$ mol/m² according the eqs. 3.10–3.12, which corresponds to about 2 monolayers. This adsorbed amount was compared to the nonionic Isofol ($\Gamma = 0.3 \times 10^{-6}$ mol/m²) and the sugar derivative HTLBB ($\Gamma = 2.0 \times 10^{-7}$ mol/m²) (all commercial softeners) therein [15].

Consecutive Polyelectrolyte Deposition A novel and versatile surface modification technique is based on the consecutive adsorption of oppositely charged polyelectrolytes (PEL), which was initiated by Decher [16] to produce coatings with defined thickness and surface properties like charge, hydrophilicity, adhesiveness, inertness among others. In the IPF working group polyelectrolytes this polyelectrolyte multilayer (PEM) process is followed by ATR-IR spectroscopy *in-situ* to optimize this modification concept for certain applications. In Fig. 3.11(a) spectra of a typical PEM system of poly(ethyleneimine) PEI and poly(acrylic acid) PAC are shown recorded during the alternate layer deposition. Spectral signal increases reflecting the layer growth and modulating courses reflecting changes the dissociation and charge state of the PEM can be obtained from that technique [17] and are shown in the Fig. 3.11(b). Using ATR-FTIR spectroscopy consecutive growth data of polymer layer systems (absorbance A versus adsorption step z) can be represented by functions of the type $A = A_{\max} (1 - \exp(-Lz))$, since the evanescent wave

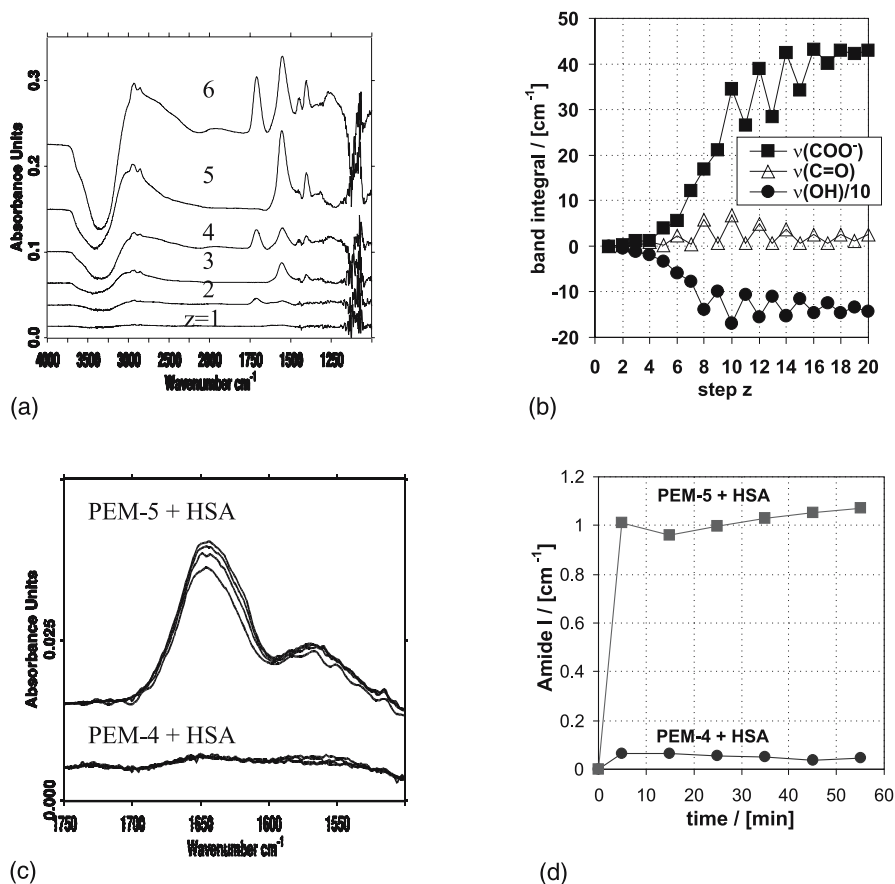


Fig. 3.11 (a) ATR-FTIR spectra on the consecutive PEI/PAC adsorption at the Si-IRE. (b) Integrated band areas of occurring PEL bands visible in (a). (c) Adsorption of HSA (1 mg/ml, D_2O , $\text{pD}=7.4$) at the surface of PEM-4 and PEM-5 of PEI/PAC. (d) Adsorption kinetics and relative adsorbed amounts of HSA at PEM-4 and PEM-5 of PEI/PAC

is exponentially damping with increasing distance from the reflecting interface, which is further described therein [17].

Protein Adsorption PEM are used as a surface modification concept to prevent or enhance protein adsorption at materials of choice. For example in Fig. 3.11(c) (protein Amide I band at various adsorption times) and Fig. 3.11(d) (Amide I integral vs. adsorption time) it is shown that a PEI terminated PEM binds the acidic protein HSA to a high extent whereas PAC terminated PEM shows a significant HSA repulsion, which can be used to create non-fouling surfaces [14, 18]. Generally, ATR-FTIR can be used to compare adsorbed protein amounts on various further polymer films [e. g. 19].

Polypeptide Conformation Generally, FTIR is sensitive to the conformation of proteins and peptides, since especially the Amide I band of the peptide units (CONH) backbone varies in position and lineshape dependent on the local environment, coupling and selection rules of the characteristic amide vibrations due to conformations α -helix, β -sheet, turn and random coil [20]. Hence, ATR-FTIR provides determination of the conformation of adsorbed proteins and peptides, which is highly relevant in pharmaceuticals and biomedicine. In Fig. 3.12 an example is given for a hydrated poly(L-lysine) (PLL) film, which is subjected to a temperature change from 25° to 27° causing a significant amide lineshape variation, which can be assigned to a conformation transition from α -helix (25°C) to β -sheet (27°C) [21].

Polypeptide Orientation ATR-FTIR is also applied for the determination of molecular orientation using the dichroism of diagnostic IR bands. An illustrative example for that is the orientation of α -helical poly(γ -methylglutamate-co- γ -octadecylglutamate) (PMOLG) [22] on texturized substrates [23] in the initial state and after swelling in CHCl_3 . The corresponding ATR-FTIR spectra recorded by p- and s-polarized light are given in Fig. 3.13. From the ATR dichroic ratios $R_y^{\text{ATR}} = A_p/A_s$

Fig. 3.12 Amide region of poly(L-lysine) cast onto a CdTe IRE and hydrated by a saturated $\text{D}_2\text{O}/\text{N}_2$ stream (r.H. = 90%) at the temperatures $T = 25^\circ$ and 27°C [21]

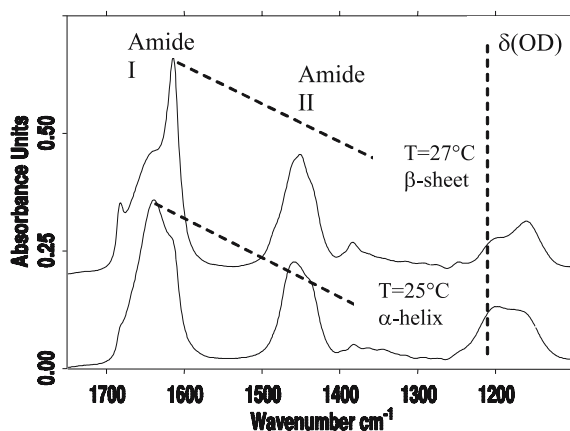
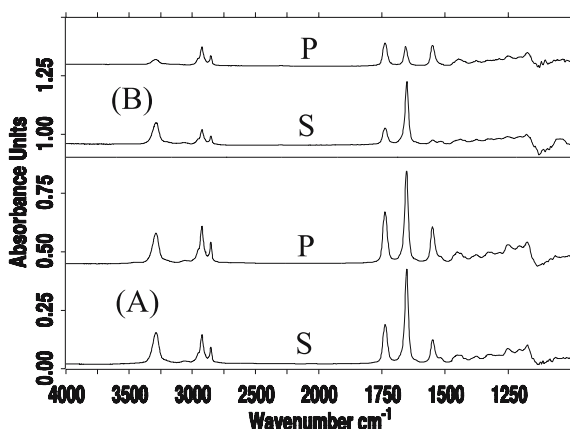


Fig. 3.13 p- and s-polarized ATR-FTIR spectra of solution cast PMOLG on a texturized Si-IRE in the initial state (A, bottom) and after swelling in CHCl_3 (B, top) [23]



of the Amide I and Amide II band, respectively, the transmission dichroic ratios R^T can be calculated knowing the values of the relative electrical field components ($E'_{02x}, E'_{02y}, E'_{02z}$), given exemplarily for E'_{02y} in eq. 3.9, according to (3.13):

$$R_y^{\text{ATR}} = (E_{02x}^{\prime 2} + E_{02z}^{\prime 2}) / E_{02y}^{\prime 2} \times R^T \quad (3.13)$$

From these R^T values the order parameters S can be calculated using (3.6) (see Trans-IR). High order parameters of $S=0.8$ could be obtained proving a high degree of unidirectional alignment of the in-plane assembled polypeptides [23]. A similar in-plane orientation has been shown for water soluble charged polypeptides in polyelectrolyte multilayers [5].

3.2.4 Grazing Incidence Infrared (GIR)

3.2.4.1 GIR Concept

According to Fig. 3.14 IR light is reflected on the surface (gold, silicon) coated with sample (thin film) with an angle near the grazing incidence. Under these conditions a standing wave is formed by the superposition of the incoming and reflected IR light. This electric strong field is only established for incident light, which is parallel polarized to the surface normal. Incident light, which is vertically polarized to the surface normal undergoes a 180° phase shift at the point of reflection at all incident angles and therefore does not contribute to the electric field of the standing wave. So, GIR spectroscopy works only with the E_z component of the electric field and only p-polarized light can be used. From this it follows additionally that only transition dipole moments lying more or less in the z -axis can be excited by IR light (surface selection rule). Using distinct substrates like gold GIR is the most sensitive IR surface technique allowing detection of ultrathin (smaller or equal the polymer radius of gyration R_g) due to the established strong E_z field.

3.2.4.2 GIR Information

Detection Limit GIR has potential in two aspects. On the one hand it is the most sensitive IR method for qualitative detection of ultrathin films. However this is limited to gold substrates. Unfortunately on SiO_x supports reflectivity is lacking. In the Fig. 3.15 the GIR spectrum of the PMI-P film on the Si-IRE is shown. Only a poor $\nu(\text{C}=\text{O})$ is visible, from which a detection limit of $\text{DL}=2 \mu\text{g}/\text{cm}^2$ can be estimated. No direct correlation between the measured absorbance A and the surface concentration as in TRANS-IR and ATR-IR can be derived.

Polymer Orientation On the other hand it allows the quantitative determination of orientation within thin films, whose (macro)molecules have preferential order in the z -axis due to the only active E_z field component. It is frequently used [24] to characterize z -axial order of especially α -helical polypeptides for certain appli-

Fig. 3.14 Principle of GIR

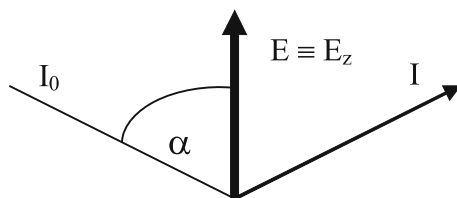
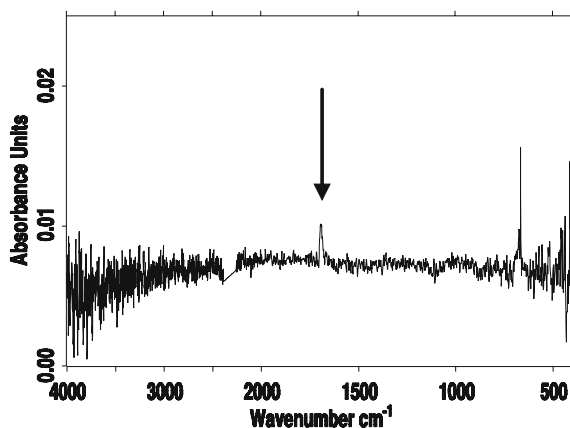


Fig. 3.15 GIR spectrum of the PMI-P film on the Si-IRE



cations. The following formula (3.14) is helpful to calculate the tilt angle γ of α -helical polypeptides with respect to the surface.

$$A_{\text{AMIDE I}}/A_{\text{AMIDE II}} = \epsilon_1 / \epsilon_2 [1/2 (\sin\gamma \sin\theta_1)^2 + (\cos\theta_1 \cos\gamma)^2] / [1/2 \sin\gamma \sin\theta_2)^2 + (\cos\theta_2 \cos\gamma)^2] \quad (3.14)$$

It is based on an orientation theory, in which the orientations, i. e. angles of two transition dipole moments (θ_1, θ_2) of two different IR vibrations (μ_1, μ_2) with two different absorption coefficients (ϵ_1, ϵ_2) are used. Based on this equation the tilt angle of α -helical polypeptides transferred from Langmuir troughs onto gold supports was found to be $\gamma = 33 - 45^\circ$. It could principally be transferred to non-polypeptidic systems, if the exact positions of the transition dipole moments of selected IR bands are known.

3.2.5 Diffuse Reflexion Infrared (FT) (DRIFT)

3.2.5.1 Drift Concept

The experimental setup of DRIFT is given in the Fig. 3.5(d). IR Light is directed on a powdered sample (powder cell, ca. 5 mm diameter), where it can be partly specularly reflected at the particle solid/air interface. The other part enters the par-

ticle and can be nondirectionally, i. e. diffusely, reflected and collected with a special detection optics. Quantification access may be obtained by the Kubelka–Munk function. Instead of the transmittance ($A = -\log T$) the relative reflectance R (for infinitely thick sample) is measured ratioing the reflexion intensity of the sample RI and that of the reference RI_0 according to (3.15):

$$R = RI / RI_0 \quad (3.15)$$

Furthermore, from R the Kubelka–Munk function KM , which is an approximation for the absorbance of the scattered light, may be calculated according to (3.16):

$$KM = (1 - R)^2 / 2R \quad (3.16)$$

3.2.5.2 Drift Information

Detection Limit In Fig. 3.16(a) DRIFT spectrum of silica is shown, which had been suspended in 10 ml water and was modified by PMI-P (polymer/silica ratio: 1/50 w/w). The $\nu(C=O)$ peak is clearly visible and from the peak height a detection limit of $DL = 0.031 \times 1/50 \approx 1/1600$ (w/w: polymer/silica) can be estimated.

Surface Concentration Generally DRIFT is lacking quantitative determination of surface concentrations. In single cases the calibration of determined KM values by gravimetric measurements might lead to reproducible and reliable DRIFT data.

3.2.5.3 Examples of DRIFT Data

An interesting qualitative study on the interaction of flocculants based on poly(acrylic acid) with iron oxide particles has been published by Jones [25]. Using DRIFT measurements on dried PAC treated iron oxide particles, it was possible to characterize the coordination type of the carboxylate iron interaction. By comparing the shift of the asymmetric ($\nu_a(\text{COO}^-)$) and symmetric ($\nu_s(\text{COO}^-)$) carboxylate stretch band of PAC in the unbound state with the shift obtained for

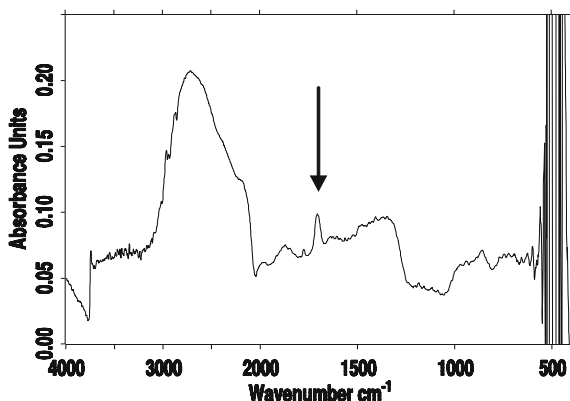


Fig. 3.16 DRIFT spectrum of dried silica (50 mg, Silmicron, Degussa), on which 1 mg of PMI-P was adsorbed from 10 ml solution

the bound state, samples with unidentate coordination could be distinguished from samples with bidentate (bridging, chelating) coordination type.

3.2.6 Raman Spectroscopy

3.2.6.1 Raman Concept

Generally in Raman spectroscopy [26] the sample is excited by a strong monochromatic laser source (usually in the VIS region) and light is reemitted or inelastically scattered from the excited molecules. The resulting energy difference and the obtained frequencies (Stokes and Anti-Stokes lines) are due to transitions between vibrational and rotational energy levels in the electronic ground state and are in the same range as IR frequencies. (Raman: Change in polarizability during vibration, complementary to IR: change of dipole moment).

3.2.6.2 Raman Information

Raman spectroscopy is very useful for the characterization of polymer fibres, since the scattering geometry is uniquely suited for that particular problem. An experimental problem with Raman is fluorescence background excited by the Raman laser frequency. To suppress this FT-Raman is applied using near IR excitation (Nd/YAG: 1064 nm, Power: 50–1000 mW). The FT technique offers additionally higher throughput, speed and wavelength accuracy. Furthermore Resonance Raman Spectroscopy (RRS) is used to amplify (several orders of magnitude) the signal when the sample has an electronic absorption (but not fluorescent) in the frequency region (edge) of the laser and a certain resonance may occur.

Surface Concentration and Detection Limit Still a direct (without using another calibration method) quantitative relation between Raman intensity and surface concentration is lacking. No useful Raman spectrum of the standard PMI-P film deposited onto Si-IRE could be recorded.

3.2.6.3 Examples of Raman Data

Raman is particularly suited for fibres and fibre surfaces and has been frequently applied for carbon nanotubes, since Raman unlike IR is sensitive to C-C-bonds exhibiting no dipole moments. A related comprehensive review can be found therein [27].

SERS A surface sensitive Raman method has been shown to be SERS (Surface Enhanced Raman Spectroscopy) using small metal particles distributed by evapo-

ration or sputtering onto the sample of choice [28]. The SERS effect is still not understood quantitatively. It is commonly stated, that by this technique the scattering in the sample is enhanced, so that more light paths are taken by the sampling beam. As an example SERS is applied for the detection of analyte spots in thin layer chromatography [29], where the Kieselgel 60 thin layers were coated with evaporated silver. A detection limit of $20 \mu\text{g}/\text{cm}^2$ was obtained. Benzo[a]pyrene (PAH, polyaromatic hydrocarbon) amounts, which were deposited from a nmol solution onto a polished silver electrode (bar) surface could be also detected by SERS [30]. Not much Raman work has been done on samples at planar substrates.

TERS Recently, TERS (Tip (i.e. AFM) Enhanced Raman Spectroscopy) has been shown to provide for signal amplification and prospectively for extraordinary high lateral resolution [31]. TERS claims to combine the sensitivity of the Raman with the lateral resolution of the AFM technique. Thereby, very sharp tips are generated/modified by silver or gold deposition/nanoparticles. Using an inverted microscope configuration the excitation laser is guided on a macroscopic sample like a thin film of a dye or carbon nanotubes and the scattered light might be measured classically. If now the modified AFM tip is brought into direct contact to the sample a dramatic enhancement of Raman scattered light is obtained at that very position. This can be used for imaging purposes. However, similar to SERS the enhancement effect is still far from being fully understood and the technique can not yet be used in a routine way.

3.3 Optical Methods

3.3.1 Ellipsometry

Ellipsometry [32] is a non-destructive method for characterizing thin layers at solid substrates due to thickness d and refractive index n .

3.3.1.1 Experimental Setup (Null Ellipsometry)

Ellipsometry is based on the principle that upon reflection of monochromatic linear polarized light on a substrate under the angle θ the relative phases of its electrical components are changed and an ellipse is formed (and vice versa) (Fig. 3.17). According to Fig. 3.17 circular polarized light is linear polarized by a polarizer P and is directed on the sample layer above a reflecting surface. Thereby the x - and y -components of the E -field are in the same phase.

Upon reflexion at the sample layer system/substrate (formed by the sample, SiO_x and Si) phase differences of the x - and y -components occur in dependence of the thickness and composition of the sample. As an image an ellipse with the pa-

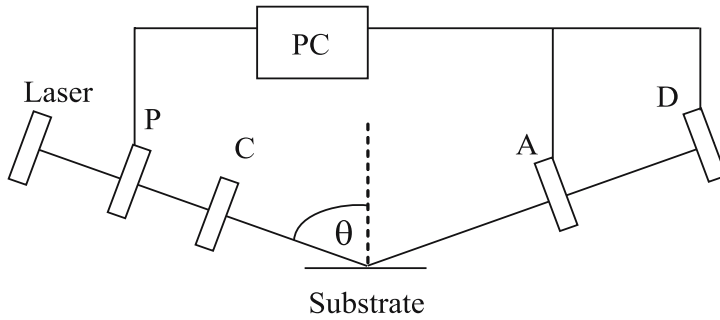
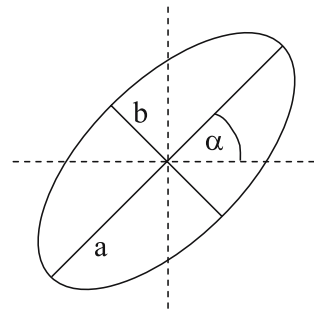


Fig. 3.17 Principle of ellipsometry (simplified)

Fig. 3.18 Ellipse parameters, used to calculate Δ and Ψ (see 3.17)



ram eters a , b and α is formed vertically with respect to the light propagation (Fig. 3.18). These ellipse parameters a , b , α can be determined by a rotatable analyser (A), which measures the intensities R_p and R_s (minimum intensity: b , maximum: a) and is correlated with the analyser (A) and the detector (D) via PC control. These parameters are in direct relation with the layer architecture and they deliver the important magnitudes Δ (phase parameter) and Ψ (amplitude parameter). Direct access to the Fresnel equations is obtained via (3.17):

$$\frac{R_p}{R_s} = \tan(\Psi)\exp(i\Delta) \tag{3.17}$$

3.3.1.2 Calculation of Parameters

Based on various models R_p and R_s are functions of the incident angle θ , the wavelength λ , the incremental thicknesses of phases 1, 2, 3 $d_{1,2,3}$, their refractive indices $n_{1,2,3}$, the absorption coefficients $k_{1,2,3}$, respectively. The calculations of these parameters is based on simulations using certain models, whereby $d_{1,2,3}$, $n_{1,2,3}$, $k_{1,2,3}$ and the layer topology are closely connected. From the measured psi, delta angles the parameters $n_{1,2,3}$, $k_{1,2,3}$, $d_{1,2,3}$ are iteratively determined (least square fit). Another setup is based on tunable elliptically polarized light (by 1/4-plate/compensator) which upon

reflexion produces linear polarized light in dependence of the sample system. Furthermore Spectroscopic Ellipsometry may be applied at variable angles of incidence (VASE, 350–750 nm) using variable λ . This increases the validity of ellipsometry, since the wavelength dependence allows further constraints on ellipsometric data.

3.3.1.3 Information Examples

Layer Thickness As important information from ellipsometry the thickness of the layer system d is obtained, if the refractive indices $n_{1,2,3}$ of the layer system are known. n_x and d are directly correlated one with another.

Surface Concentration The product of n and d is always constant, which is used for determining the adsorbed amount of polymer on the surface, if the refractive index increment dn/dc is known. Especially for in situ measurements in solvents this is very useful and the following equation (3.18) according to de Fejter [33] is used:

$$\Gamma = d_{\text{Polymer}} \times (n_{\text{Polymer}} - n_{\text{Solvent}}) / dn/dc \quad [\mu\text{g}/\text{cm}^2] \quad (3.18)$$

Hence ellipsometry can be used to monitor kinetics or isotherms of polymer and protein adsorption [34, 35] and multilayer deposition e. g. of polycations and silicates [36]. Generally, the detection limit of Ellipsometry is far below monolayer coverages ($d_{\text{MIN}} < 1$ nm).

Adsorption Kinetics In Fig. 3.19 the adsorption of BSA at unmodified and methylated silica surfaces is shown. Significantly, the higher protein adsorbed amount is obtained for the hydrophobic surface compared to the hydrophilic bare silica on. Note the high time resolution of in situ ellipsometry.

Polyelectrolyte Multilayer (PEM) Formation Figure 3.20 shows the consecutive layer deposition of PEI and PAC on Si ATR plates. The PEM was dried after each adsorption step and measured. After an initial lag phase until at about four layers (lateral growth) the PEM starts growing in the vertical direction. A quite good correlation with ATR-FTIR data could be obtained as seen in Fig. 3.20 (right).

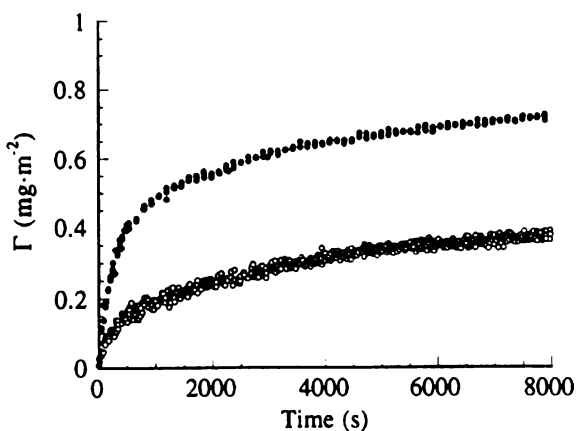


Fig. 3.19 Adsorption of the protein BSA at unmodified (lower curve) and methylated (upper curve) silica surfaces monitored in situ by ellipsometry (from Malmsten [35])

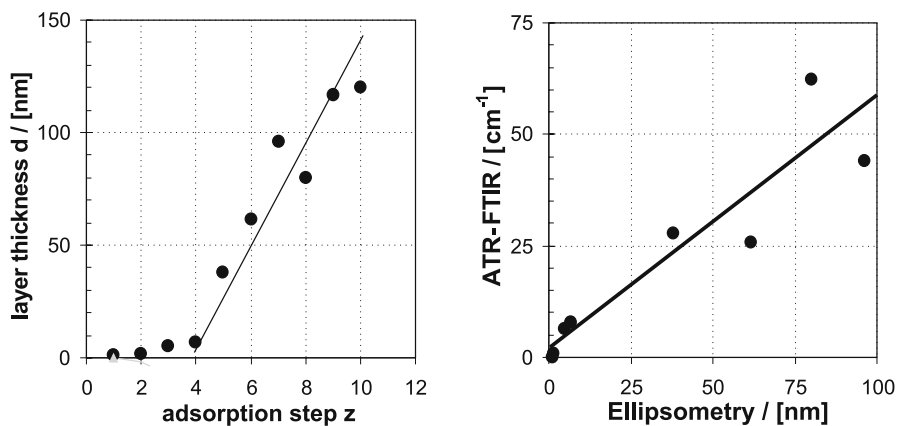


Fig. 3.20 (kindly measured by B. Mahltig) Deposition of consecutive PEI/PAC multilayers monitored by ellipsometry (left) and correlation to ATR-FTIR data (right)

3.3.2 Surface Plasmon Resonance (SPR)

Surface plasmon resonance (SPR) [37] is a non-destructive, probably the most sensitive, method for detecting layer formation or binding of (bio)molecules [38] at planar model surface.

3.3.2.1 Experimental Setup

In the shown configuration of Fig. 3.21 SPR is obtained by the specific interaction of an evanescent field with the gold layer (plasmon modes are excited in the gold layer). The exponentially decaying evanescent wave is formed upon total internal reflection of the incident light at the interface of a medium with a high and a medium with a low refractive index, respectively (see ATR-IR section). If the monochromatic incoming light is p-polarized (parallel with respect to the plane of incidence), free electrons within the gold layer oscillate and energy is absorbed at a certain angle of incident light, which is the SPR angle. Principally, the intensity of the reflected light is measured in dependence of the incident angle θ . If there is maximum excitation of the plasmon modes a minimum in intensity is measured at the detector (D), as seen in Fig. 3.22 (negative “band”). The SPR angle is strongly dependent on the refractive index of the sample being in contact to the gold layer/ surface. If material (polymer, proteins) is adsorbed onto the gold layer, the SPR angle will change due to the adsorbed amount. The adsorbed amount is a linear function of SPR angle shift, which might be equilibrated by gravimetry. The scanning mirror SPR apparatus measures the angle shift (mdeg) and the binding of material can be quantified. There is also a dependence on the refractive index of the bulk solution. For example an angle shift of $\Delta\theta_{\text{SPR}} = 120$ mdeg is related to a protein coverage

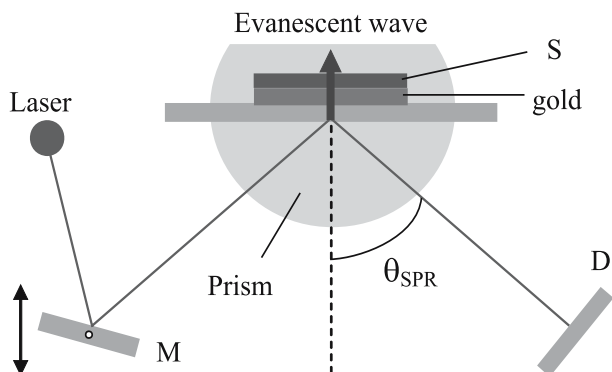
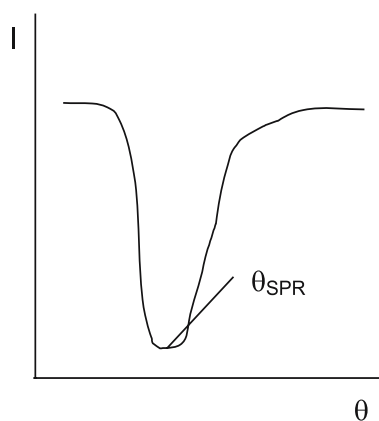


Fig. 3.21 Principle of the SPR experiment

Fig. 3.22 Plot of the intensity vs. incident angle, i. e. the resonance curve with minimum intensity at the resonant angle θ_{SPR}

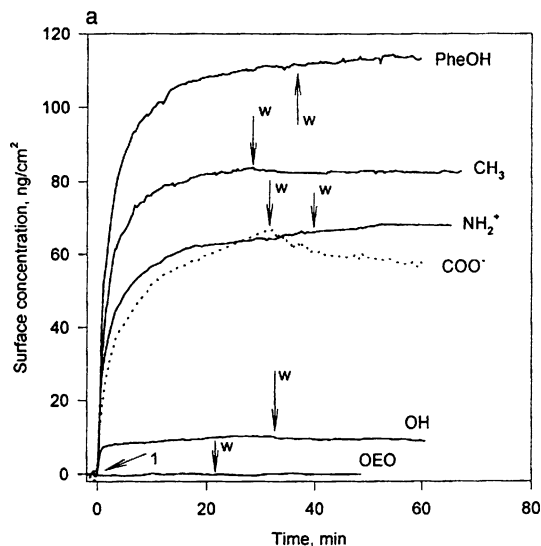


change of $\Delta\Gamma = 0.1 \mu\text{g}/\text{cm}^2$ or to the change of the bulk refractive index (gold + layer) of $\Delta n = 0.001$. The detection limit is given by the size of the analyte. For bound analytes of molecular weights below 100 Dalton Δn is too low for detection. Also d_p (see ATR-IR) of the evanescent wave ranging 300–400 nm limits the experiment, so that objects larger than 400 nm cannot be measured completely and the signal is then not linear to the adsorbed amount. For proteins the detection limit is below $1 \text{ ng}/\text{cm}^2$.

3.3.2.2 Information, Examples

Protein Adsorption In the Fig. 3.23 an example is shown for the adsorption of the protein BSA at gold surfaces, which were modified by self-assembled monolayers (SAM) of the alkyl thiol type (ω -substituted mercaptohexadecanes), where the ω -substituents were COO^- , OH, phenol (PheOH), NH_3^+ and hexa(ethylene oxide) (OEO) [39]. The individual adsorption curves (amount versus time) are given in Fig. 3.23. As a general trend the hydrophobic substituents cause the higher ad-

Fig. 3.23 Adsorption of the protein BSA at SAMs with various headgroups followed by SPR (from [39])



sorbed amounts compared to the hydrophilic ones. The highest adsorbed amount found for the PheOH substituent might be caused by specific interactions between the aromatic groups of both protein and SAM.

Polyelectrolyte Multilayer (PEM) Deposition In Fig. 3.24 the experimental data for the consecutive deposition of PSS and an ionene (structures given below) followed by SPR is shown [40]. For further analysis the intensity increase at a certain fixed angle is followed. In Fig. 3.24 (right) it is shown that around 10 layers give 10 nm PEM thickness and that there is a linear increase of the thickness with layer number z .

Biosensors Biosensors are devices for the detection of biomolecular interactions commonly on surfaces. Biosensors consist of an immobilized sensing element of

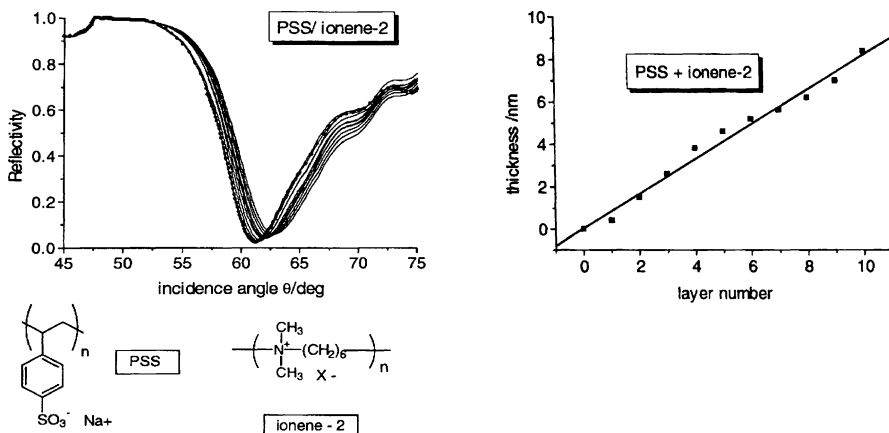


Fig. 3.24 PEM deposition of PSS and an ionene followed in situ by SPR (from [40])

biological origin incorporated into a physical signal transducer. The transduced signal is caused upon interaction between the immobilized biorecognition molecule, the sensing element, and the target analyte. Commonly, biomolecular interactions are studied using immunoassays (ELISA, RIA). Advantageously, SPR monitors binding events in real-time and it is not necessary to label the interacting biomolecules.

Table 3.2 Overview on selected vibrational spectroscopic and optical surface sensitive methods

Method	Abbreviation	Information	Detection limit
Transmission infrared spectroscopy	TRANS-IR	Molecular information on films, adsorbates (dry state). Direct access to surface concentrations [$\mu\text{g}/\text{cm}^2$] via the Lamber–Beer law, knowing the thickness d . Lacking sensitivity. Access to x - and y -axial polymer orientation.	$\Gamma_{\text{MIN}} \approx 0.375 \mu\text{g}/\text{cm}^2$ (PMI-P sample)
Attenuated total reflexion IR	ATR-IR	Molecular in situ detection of films and adsorbates on various surfaces (e. g. Si, Ge, diamond, polymer films) in contact to solution and in dry state. Quantification [$\mu\text{g}/\text{cm}^2$] via modified Lamber–Beer Law knowing d . Access to x -, y -, z -axial polymer orientation.	$\Gamma_{\text{MIN}} \approx 0.025 \mu\text{g}/\text{cm}^2$ (PMI-P sample)
Gracing incidence IR	GIR	Most sensitive IR method for detection of ultrathin films. Limited to gold substrates. No direct correlation between the measured absorbance A and the surface concentration. Access to z -axial polymer orientation	$\Gamma_{\text{MIN}} \approx 2 \mu\text{g}/\text{cm}^2$ (PMI-P sample)
Diffuse reflexion IR (Fourier transform)	DRIR, DRIFT	Molecular information on modifying layers on powdered samples (e. g. silica, granulate a.o.). Quantification not straightforward.	$\Gamma_{\text{MIN}} \approx 1/1600$ (w/w: PMI-P/silica)
(Surface enhanced) Raman spectroscopy	(SERS) RAMAN	Well adapted for polymer fibres, not for polymer films. Improvement by SERS.	$\Gamma_{\text{MIN}} \approx 20 \mu\text{g}/\text{cm}^2$ (SERS, Kieselgel)
Ellipsometry	ELL	An in situ detection of d of films and adsorbates on various surfaces (e. g. glass, Si, polymer films) in contact to solution/dry state. Quantification of Γ [$\mu\text{g}/\text{cm}^2$] via de Fejter approach.	$d_{\text{MIN}} < 1 \text{ nm}$
Surface plasmon resonance	SPR	An in situ detection of films and adsorbates on various surfaces (e. g. gold, polymer films) in contact to solution/dry state. Quantification [$\mu\text{g}/\text{cm}^2$] possible.	$\Gamma_{\text{MIN}} < 1 \text{ ng}/\text{cm}^2$ (proteins)

3.4 Summary

Table 3.2 gives a summary on the provided information and arbitrary detection limits (DL) like minimum detectable surface concentration (Γ_{MIN}) or thickness (d_{MIN}) of the spectroscopic and the optical methods collected in that contribution.

Acknowledgments

Some of the shown examples were part of research sponsored by German Research Foundation (DFG) within SFB 287.

References

IR Basics

1. H. Günzler, H. Heise, *IR-Spektroskopie* (VCH, Weinheim, 1996) & J.L. Koenig (ed.), *Spectroscopy of Polymers* (Elsevier, Oxford, 1999)

TRANS-IR

2. P.R. Griffith, J.A. De Haseth, Fourier Transform Infrared Spectroscopy, *Chem. Anal. Ser. Monogr. Anal. Chem. Appl.* Volume 83 (1986)
3. R. Zbinden, *IR-Spectroscopy of High Polymers* (Academic, New York, 1964)
4. U.P. Fringeli, M. Schadt, P. Rihak, Hs.H. Günthard, *Z. Naturforsch.* 31a, 1098–1107 (1976)
5. M. Müller, B. Keßler, K. Lunkwitz, *J. Phys. Chem. B* 107, 8189 (2003)

ATR-IR

6. N.J. Harrick, *Internal Reflection Spectroscopy* (Wiley, New York, 1967)
7. U.P. Fringeli, Hs.H. Günthard, in *Membrane Spectroscopy*, ed. by E. Grell (Springer, Berlin, 1981), p. 270–332 & U.P. Fringeli, in *Encyclopedia of Spectroscopy and Spectrometry*, ed. by J.C. Lindon, G.E. Tranter, J.L. Holmes (Academic, New York, 2000)
8. R.M. Gendreau, R.I. Leininger, S. Winters, R.J. Jacobsen, in *Biomaterials: Interfacial Phenomena and Applications*, ed. by S.L. Cooper, N.A. Peppas (eds), Advances in Chemistry Series 199 (American Chemical Society, Washington, D.C., 1982), p. 371
9. K.K. Chittur, D.J. Fink, R.I. Leininger, T.B. Hutson, *J. Coll. Interface Sci.* 111(2), 419 (1986)
10. S.S. Cheng, D.A. Scherson, C.N. Sukenik, *Langmuir* 11, 1190 (1995)
11. P. Frantz, S. Granick, *Macromolecules* 28, 6915 (1995)
12. S. Sukishvili, A. Dhinojwala, S. Granick, *Langmuir* 15, 8474 (1999)
13. M. Müller, C. Werner, K. Grundke, K.-J. Eichhorn, H.J. Jacobasch, *Microchim. Acta* 14, 671–674 (1997) & H.H. Bauer, M. Müller, J. Goette, H.P. Merkle, U.P. Fringeli, *Biochemistry* 33, 12276–12282 (1994)
14. M. Müller, T. Rieser, K. Lunkwitz, S. Berwald, J. Meier-Haack, D. Jehnichen, *Macromol. Rapid Commun.* 19(7), 333 (1998) & M. Müller, T. Rieser, K. Lunkwitz, J. Meier-Haack, *Macromol. Rapid Commun.* 20(12), 607–611 (1999)
15. M. Müller, I. Grosse, H.J. Jacobasch, P. Sams, *Tenside Surf. Det.* 35, 5 (1998)
16. G. Decher, J.D. Hong, J. Schmitt, *Thin Solid Films*, 210/211, 831 (1992)

17. M. Müller, in *Handbook of Polyelectrolytes and Their Applications*, ed. by S.K. Tripathy, J. Kumar, H. S. Nalwa, vol. 1 (American Scientific, Stevenson Ranch, CA, 2002), pp. 293–312
18. M. Müller, M. Briššová, T. Rieser, A.C. Powers, K. Lunkwitz, *Mater. Sci. Eng. C* 8–9, 167–173 (1999) & M. Müller, T. Rieser, P. Dubin, K. Lunkwitz, *Macromol. Rapid Commun.* 22(6), 390–395 (2001)
19. M. Müller, C. Werner, K. Grundke, H.J. Braun, K.J. Eichhorn, H.M. Buchhammer, U.P. Fringeli und H.J. Jacobasch, in *Werkstoffe für die Medizintechnik* (Ed. J. Breme), DGM-Informationsgesellschaft Verlag, Frankfurt (1997)
20. A. Elliott, E.J. Ambrose, *Nature* 165, 921 (1950) & T. Miyazawa, *J. Chem. Phys.* 32, 1647 (1960) & M. Byler, H. Susi, *Biopolymers* 25, 469 (1986)
21. M. Müller, *ETH Dissertation No 10422*, Eidgenössische Technische Hochschule, Zürich (1993) & M. Müller, R. Buchet, U.P. Fringeli, *J. Phys. Chem.* 100(25), 10810–25 (1996)
22. G. Wegner, *Mol. Cryst. Liq. Cryst.* 235, 1 (1993)
23. F.J. Schmitt, M. Müller, *Thin Solid Films* 310(1–2), 138–147 (1997) & D. Marsh, M. Müller, F.J. Schmitt, *Biophys. J.* 78(5), 2499–2510 (2000)

RAIR

24. E.E. Enriquez, E.T. Samulski, *Mat. Res. Soc. Symp. Proc.* 255, 423 (1992) & Y. Miura, S. Kimura, Y. Imanishi, J. Umemura, *Langmuir* 15, 1155 (1999)

DRIFT

25. F. Jones, J.B. Farrow, W.v. Bronswijk, *Langmuir*, 14 6512 (1998)

RAMAN

26. D.L. Andrews, *Perspectives in Modern Chemical Spectroscopy* (Springer, Berlin Heidelberg New York, 1990)
27. M.S. Dresselhaus, G. Dresselhaus, A. Jorio, *J. Phys. Chem. C.* (2007, ASAP Article)
28. M. Fleischmann et al., *Chem. Phys. Lett.* 26, 163 (1974)
29. J. Mink et al., *Microchim. Acta* 119, 129 (1995)
30. S. Stewart et al., *J. Raman Spectrosc.* 13, 225 (1992)
31. W. Zhang, B.S. Yeo, T. Schmid, R. Zenobi, *J. Phys. Chem. C.*, 111(4); 1733–1738 (2007)

Ellipsometry

32. R.M.A. Azzam, N.M. Bashara, *Ellipsometry and Polarized Light* (North Holland Press, Amsterdam, New York, 1977)
33. J.A. De Fejter, J. Benjamins, F.A. Veer, *Biopolymers* 17, 1759 (1978)
34. C.G. Gölander, E. Kiss, *JCIS* 121(1), 240 (1988)
35. M. Malmsten, *Coll. & Surf. B* 3, 297 (1995)
36. E.R. Kleinfeld, G.S. Ferguson, *Science* 265, 370 (1994)

SPR

37. H. Raether, in *Physics of Thin Films*, ed. by G. Hass, M.H. Francombe, R.W. Hoffman (Academic, New York, 1977) & B. Liedberg, C. Nylander, I. Lundström, Surface plasmon resonance for gas detection and biosensing, *Sens. Actuators* 4, 299–304 (1983) & K. Wellford, Surface plasmon-polaritons and their uses, *Opt. Quant. Electronics* 23, 1–27 (1991)
38. XanTec, <http://www.xantec.com>. Accessed 2007 & R.P.H. Kooyman, J. Kolkman, J. van Gent, J. Greve, Surface plasmon resonance immunosensors: sensitivity considerations, *Anal. Chim. Acta* 213, 35–45 (1988) & E. Stenberg, B. Persson, H. Roos, C. Urbaniczky, Quantitative determination of surface concentration of protein with surface plasmon resonance using radiolabeled proteins, *J. Coll. Interface Sci.* 143, 513–526 (1991)
39. V. Silin, H. Weetall and D.J. Vanderah, *J. Coll. Interface Sci.*, 185, 94 (1997)
40. R. Advincula, E. Aust, W. Meyer, W. Knoll, *Langmuir* 12, 3536 (1996)

Chapter 4

X-Ray Photoelectron Spectroscopy

Dieter Pleul¹ and Frank Simon²

^{1,2}Leibniz Institute of Polymer Research Dresden, Hohe Str. 6, 01069 Dresden, Germany, frsimon@ipfdd.de

Abstract X-Ray photoelectron spectroscopy is a highly surface sensitive technique, which can provide information on composition, binding and functionality of polymers at the surface. The aspect of information depth and surface charging is discussed as well as quantification and data interpretation.

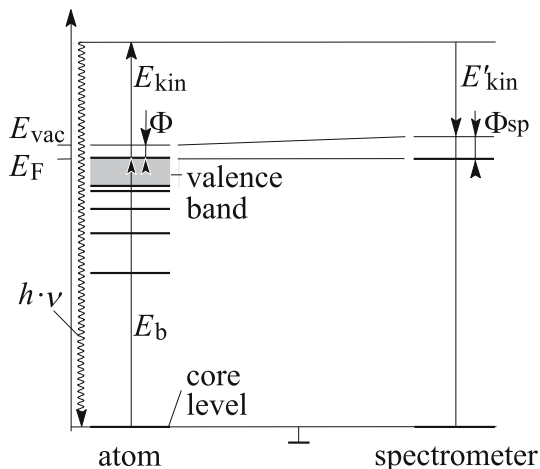
4.1 Introduction, History and Physical Principle

Today many thousands of publications are available which describe X-Ray photoelectron spectroscopy (XPS) as an analytical tool to study mostly solid surfaces. Already the enormous number of articles published in books and journals demonstrates that XPS is probably the most frequently applied analytical method in surface sciences. Its application is established in all fields of materials sciences (e. g. metals, ceramics, polymers and their composites), life sciences, electronic and several other industries [1].

XPS is an extremely surface sensitive method allowing us to identify and quantify the chemical elements in the surface region of a solid and give information on the binding states of these elements, their oxidation numbers or functionalities.

In 1905 Einstein explained Hertz's *photoelectric effect* (1887) and the results of Hallwachs' experiments (1888) by the *Lichtquantentheorie* (light quantum theory) and formulated the *Photochemische Quanten-Äquivalenzgesetz* (photo-chemical quantum equivalent law) (4.1):

$$h \cdot \nu = E_{\text{bind}} + E_{\text{kin}} + \Phi \quad (4.1)$$

Fig. 4.1 Principle of XPS

According to Einstein the light must also be considered as a flow of particles (*photons*) with a quantum energy $h \cdot \nu$ (incident photon energy), where h is the Planck constant and ν the frequency of the light. If the photons hit a target (Hallwachs used alkali metals) they have a particular probability to remove an electron from its orbital. This escaped electron was called *photoelectron*. To remove its orbital the electron has to get over its binding energy E_b . To leave the target surface the born photoelectron needs a small additional amount of energy (Φ) to transfer from the Fermi level (E_F) to the vacuum level (E_{vac}). Then the photoelectron has the kinetic energy E_{kin} (Fig. 4.1).

The discovery of (4.1) showed the way to apply the photoelectric effect as an analytical tool, because the binding energy of an electron is strongly related with the build-up of the electron orbitals of a particular chemical element. Hence, the possibility to determine the binding energy of escaped electrons opens the way to say from which elements the irradiated target is composed.

In 1954 Kai Siegbahn built the first practical X-Ray photoelectron spectrometer and presented the first photoelectron spectrum which was recorded from a common salt (NaCl) sample [2]. The peak maximum allowed the binding energy to be measured accurately. In the period 1955–1970 Siegbahn's group studied the chemical shift effect on core-level binding energies which is in polymer chemistry extremely important for the detection of functional surface groups. Siegbahn called his method *Electron Spectroscopy for Chemical Analysis* (ESCA), a name containing the fundamental physical principle and its fundamental goal. ESCA, XPS and the German abbreviation PES (*Photoelektronenspektroskopie*) can be considered as synonyms.

4.2 Instrumentation

Photoelectron spectrometer must be consisted of three basic units (Fig. 4.2). In order to fulfil (4.1) a light source providing photons with the well defined energy $h\nu$ is required. The primary energy has to be higher than the binding energies of the electrons which appear as photoelectrons in spectra. Ultraviolet light is only suited to release valence band electrons. Hence UPS (ultraviolet photoelectron spectroscopy) is applied to study the electron density and distribution in valence bands, their structures and super-positioning.

Core shell electrons can be released by X-Rays. A X-Ray source emits a white spectrum (Bremsstrahlung spectrum) which additionally contains intensive peaks of well defined energies (characteristic X-Ray radiations) (Fig. 4.2). Usually, for XPS the $K\alpha_{1,2}$ radiation of magnesium ($h\nu = 1253.6 \pm 0.35$ eV) or aluminium ($h\nu = 1253.6 \pm 0.45$ eV) is used. In order to enhance the energetic resolution of the spectrometer a crystal monochromator can be employed to cut a small line of the $K\alpha_1$ transition out.

The X-Rays pass the sample and there is a certain probability that photons release electrons which are now denoted photoelectrons. The actual aim of the spectrometer is to determine the kinetic energies of the photoelectrons escaping the sample surface. Usually in XPS a hemispherical analyser is used for this purpose. The photoelectrons which have passed the electron-optics of the spectrometer introduce a slit between two hemispheres. There an electric field is applied and forces the linearly moving photoelectrons on a circular path. The radius of this

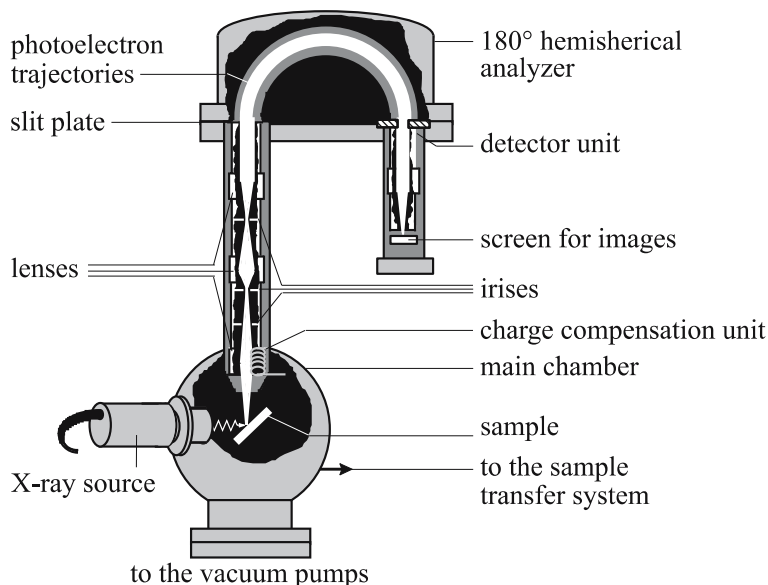


Fig. 4.2 Typical build-up of a simple photoelectron spectrometer

circular path depends on the applied field strength as well as the kinetic energy of the photoelectrons. At a given field strength only photoelectron with a definite kinetic energy can arrive the count unit (e.g. set of channeltrons) at the end of the hemispherical analyser. Hence, the variation of the field strength allows us to separate the photoelectrons concerning their different kinetic energies. In praxis, the field strength is mostly constant. A slit plate with an adjustable electric potential slows the photoelectrons with higher kinetic energies down to pass the hemispherical analyser and arrive at the count unit. In this case the voltage applied to the slit plate is a measure for the kinetic energy of the photoelectrons.

As mentioned above, the photoelectrons which have passed the hemispherical analyser are counted over a defined time interval. Hence the y-axis in the XPS spectra is indicated *count rate* and its unit is *cps* (counts per second). Today, mostly a series of channeltrons is used to count the photoelectrons.

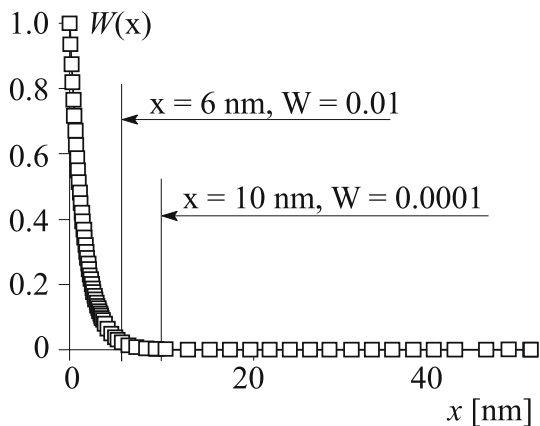
The fourth essential and fundamental module of all XPS spectrometers is the vacuum system requiring also a suitable sample transfer and handle system. To prevent interactions between photoelectrons and gas molecules which would result in a partial loss of the photoelectron's kinetic energy the base pressure in the analysis chamber must be better than 10^{-8} mbar. To produce and preserve the ultra-high vacuum different pumps have to work permanently.

Other spectrometer components may be used for special applications. All spectrometers are fitted with a sputter gun to clean sample surfaces under ultra-high vacuum conditions or record depth profiles by sputtering the sample layer by layer. For the measuring of electrically insulating samples, like most polymers and ceramics a unit is profitable (in the case of employing monochromated X-Rays it is essentially required) which is able to effectively compensate the electrostatic charging. Modern spectrometers offers the possibility to take images from the element distribution or the distribution of functional surface groups on a sample surface.

4.3 Information Depth

As mentioned above XPS is an extremely surface sensitive method. The spectral information appears from a depth of approximately 10 nm in maximum. Of course X-Rays penetrate the depth of the sample. Everywhere where X-Ray quanta interact with electrons there is a probability to release electrons. The photoelectrons produced in the depth of the sample have a high probability to interact with other electron and dissipate their kinetic energy fully or partly. If these inelastically scattered photoelectrons leave the sample surface and are introduced into the spectrometer they do not give a contribution to the spectroscopic information because their kinetic energies are insignificant for their origin. They will be found in the spectrum's background. Otherwise, photoelectrons generated near the sample surface do not have a high probability to interact with other electron orbitals. Hence, their kinetic energy can be used to determine the binding energy according to (4.1) and the counting of these photoelectrons contribute to the spectral information of the XPS spectrum.

Fig. 4.3 The probability W of a photoelectron which was generated in the depth x to contribution to the spectral information



The probability $W(x)$ of a photoelectron which was generated the depth x to contribute to the spectral information is well understood. Figure 4.3 shows a typical function $W(x)$ for polymer samples studied by means of Al $K\alpha$ X-Rays. It can be seen that, if we want to consider 99.99% of all photoelectrons escaping the sample surface as spectral information, we have an information depth of ca. 6 nm. Taking 99.9999% of all emitted photoelectrons into account we get information about ca. 10 nm, etc.

The fundamental parameter controlling the information depth is the mean free path of the electrons, λ , in the material under investigation. Besides the density of the material and the angle of emission, the parameter λ depends on the kinetic energy of the photoelectrons. Hence, different quantum energies $h\nu$, e. g. provided by different anode materials in the X-Ray source, cause various different depths. Using synchrotron beams this phenomenon can be exploited to record XPS spectra of high surface sensitivity.

Another way to enhance the surface sensitivity of the XPS method is to tilt the sample with the angle Θ under the electron-optical unit of the spectrometer. If the so-called *take-off angle* Θ is defined as angle between the surface normal of the sample surface and the electron-optical axis of the spectrometer the effective mean free path of the electrons, λ_{eff} corresponds to the cosine of Θ :

$$\lambda_{\text{eff}} = \lambda \cdot \cos(\Theta) \quad (4.2)$$

Below an example will be given where the so-called *angle-resolved XPS* (AR-XPS) technique was applied to study the orientation in molecular thin films.

4.4 Polymer and Other Non-Conducting Samples

Following the earlier and current literature it could be assumed that it is necessary to prepare special samples for XPS investigations. Mostly, polymer samples were cast as thin film on silicon wafers. But for many materials special preparation

procedures could result in samples which are very strange from their origin state. Today, the use of modern spectrometers allows us to record XPS spectra of samples of any shapes. Beside thin polymer films mostly it is also possible to study thick polymer sheets, grains, fibres, fabrics, foams or powders. To do this, one fundamental requirement is a charge compensation unit which effectively avoids the electrostatic charging of the non-conducting samples. The second fundamental requirement is the vacuum stability of the sample under investigation. Surprisingly, most polymer samples are very stable under ultra-high vacuum conditions. However, it must be taken into account that a polymer surface in vacuum can be different from the state in contact with the atmosphere. During vacuum generation additive and surface impurities may be removed partly or fully. In biomolecules and polyelectrolytes the loss of water is connected with dramatic changes in the build-up of surface region, denaturation reactions, changes in molecular orientations, conformations and a loss in the layer thickness are usual processes. In order to prevent such unwanted processes biomolecules and polyelectrolyte samples should be measured in the deep-frozen state which requires an additional cooling unit keep the sample in the deep-frozen state during evacuation and spectrum recording.

As mentioned non-even samples like powders, grains or fibres can be studied by XPS. But the more or less spherical shape of the sample surface causes an angular distribution of the effective mean free path of the electrons and consequently depth-depending information can be incorrectly.

4.5 Wide-Scan Spectra – Quantification and Interpretation

Figure 4.4 shows the wide-scan spectrum of a poly(3-hydroxybutyrate) layer spin-coated on a silicon wafer.

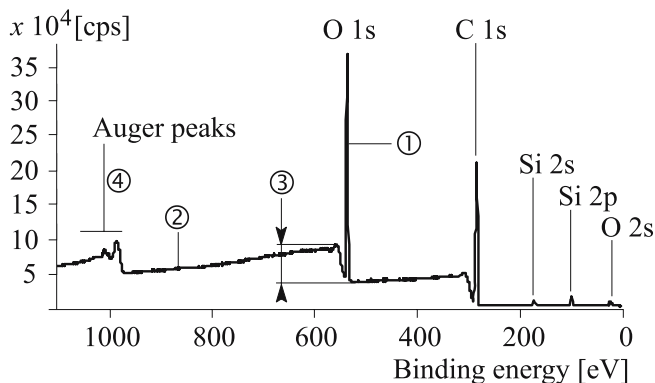
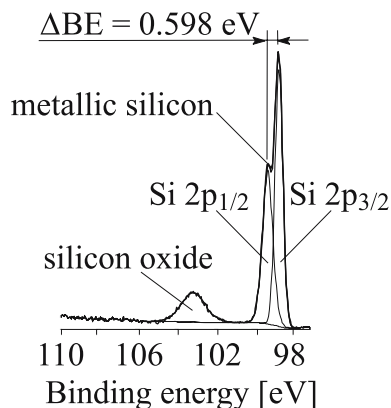


Fig. 4.4 Wide-scan XPS spectrum of poly(3-hydroxybutyrate)

Fig. 4.5 High-resolution Si 2p spectrum of a clean silicon wafer



The scan representing the count rates [cps] versus the binding energies [eV] shows all elements – without hydrogen – which are contained in the sample surface layer. The element peaks (⊙) show the presence of the expected elements carbon (as C 1s peak) and oxygen (as O 1s and O 2s peaks). Additionally, a small amount of silicon (as Si 2s and Si 2p peaks) was found on the sample surface appearing probably from the substrate material. The elements were identified by the binding energy position (BE) of their peaks, e.g. C 1s is expected at $BE \approx 285$ eV, O 1s at $BE \approx 532$ eV, etc. Elements of higher atomic numbers show various peaks in the wide-scan spectrum which can be used for a true element identification, e.g. $BE(\text{Au } 5p_{3/2}) \approx 54$ eV, $BE(\text{Au } 5p_{1/2}) \approx 72$ eV, $BE(\text{Au } 5s) \approx 108$ eV, $BE(\text{Au } 4f_{7/2}) \approx 83$ eV, $BE(\text{Au } 4f_{5/2}) \approx 87$ eV, $BE(\text{Au } 4d_{5/2}) \approx 334$ eV, $BE(\text{Au } 4f_{3/2}) \approx 352$ eV, $BE(\text{Au } 4p_{3/2}) \approx 546$ eV, $BE(\text{Au } 4p_{1/2}) \approx 644$ eV, etc. The width of the wide-scan spectrum is limited by the photon energy $h\nu$ of the X-Ray. Hence, not all electron orbitals of an element can contribute to the wide-scan spectrum.

The element peaks are named according to the photoelectron's origin, e.g. photoelectrons escaping the 1s orbital of carbon were found in the C 1s peak. The numbers 1, 2, 3, ... represent the main quantum number n of an electron orbital. The letters s, p, d, and f, indicate the orbital angular momentum l , where $l(s)=0$, $l(p)=1$, $l(d)=2$, and $l(f)=3$. Beside the orbital angular momentum an electron has also a spin momentum s which can be $+\frac{1}{2}$ or $-\frac{1}{2}$. The resulting total angular momentum j is a linear combination or the vector sum of l and s . The vector summation can be carried out in two ways, namely as $j-j$ coupling or Russell–Saunders $L-S$ coupling. The $j-j$ coupling has been established for XPS. Here, the orbital angular and spin momenta of a single isolated electron were vectorially added: $j = l + s$. The total angular momentum j is also given in the peak name as fraction number $1/2$, $3/2$, $5/2$ or $7/2$. According to the $j-j$ coupling all element peaks appearing from the p, d, and f orbitals are signed by a duplet structure with an energy difference ΔBE typical for each element (Fig. 4.5).

The element peaks stand out from the spectrum background (⊙). Its formation is the result of inelastically scattered photoelectrons which left the sample surface

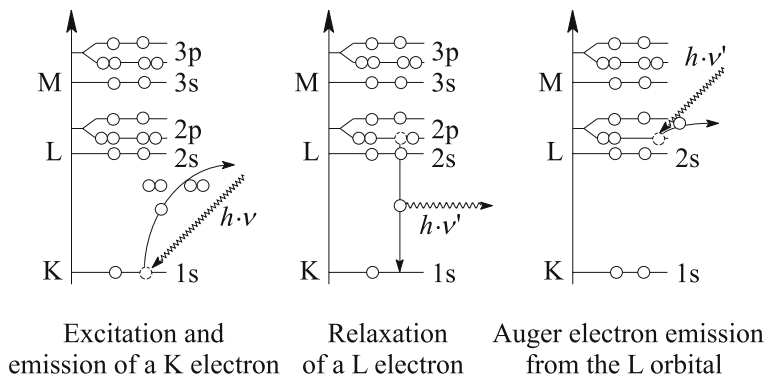


Fig. 4.6 The three steps of the *Auger* electron emission shown by a KLL emission process

and passed the spectrometer. Behind each element peak the inelastically scattered photoelectrons of the corresponding element cause a step in the count rate (③).

Furthermore, all XPS wide-spectra contains *Auger* peaks (④). The *Auger effect* is a relaxation process initiated by the primary photo-ionization step. If an electron left an inner orbital, there is a probability that an electron from a higher electron orbital is transferred to the free site in the lower-energy orbital. The energy difference can release a second electron, which is called *Auger electron* (Fig. 4.6). The Auger electron can also leave the sample surface with the kinetic energy E_{kin}' and pass the analyser unit. Of course, the detector cannot distinguish between electrons generated by photo-ionization or relaxation. Hence, both phenomena were observed in the XPS as well as AES spectra (*Auger electron spectroscopy*, AES is another surface sensitive technique using the *Auger effect* as fundamental principle). *Auger* peaks can be easily distinguished from photoelectron peaks. They appear in multiplets and normally they have a larger width. In spectra where the count rate is recorded versus the binding energy, the Auger peak position is changed by the use of another X-Ray source having a different primary energy. However, in spectra showing the count rate versus the Kinetic energy, the *Auger* peaks remain at their position while the position of the photoelectron peaks is changed. The reason of that phenomenon is, in contrast to the photoelectrons, the kinetic energy of the *Auger* electrons does not depend on the primary energy of the X-Ray source but on the energy which is released by the electron transfer from a higher occupied orbital to a unoccupied site in a lower level.

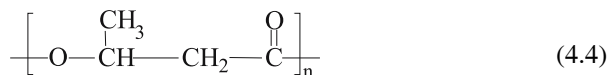
In addition to the qualitative determination of the surface composition of a sample, the XPS method allows us also to quantify: the elemental composition. This can be understood very easily. A high number of atoms of an element on the sample surface release more photoelectrons as an element with a low atomic concentration. The relationship between the number of atoms $n(X_i)$ of an element X_i and its corresponding spectral intensity $I(X_i)$ is not trivial:

$$I(X_i) = f[n(X_i), \eta_p, \sigma(X_i, i, h \cdot \nu), \lambda(E_{kin}), \cos(\Theta), A, T(E_{kin})] \quad (4.3)$$

Equation (4.3) consists of two parts. The first one contains parameters resulting from the interaction between the quantum and the electron orbitals, where η_p is the photon flux density, σ is the cross-section of photon interaction (depending on the element species X_i , the electron orbital i where the excitation takes place, and the quantum energy $h\nu$), and λ is the mean free path of the electrons (depending on E_{kin}). In order to estimate the values of this equation part complex models required. The second part of (4.3) contains parameter of the instrument, where A is the area of acceptance, Θ is the take-off angle of the sample, and T is the transmission function of the spectrometer which usually depends on the kinetic energy of the photoelectrons. As mentioned above, it seems extremely difficult to determine exactly all parameters contribute to the intensity $I(X_i)$. However, for analytical questions it is not meaningful to determine the absolute number $n(X_i)$ of an atom species in the sample surface. The matter of interest is the relative composition of the sample surface. The relative surface composition can be expressed by elemental or atomic ratios of the elements $[X_1]:[X_2]:[X_3]: \dots :[X_j]$. In the quotient $[X_1]:[X_j]$ the indefinable parameters of the first part of (4.3) can be combined in a so-called *relative sensitivity factor* (RSF). The take-off angle Θ and the area of acceptance A are equal for all elements X_i . The transmission function (transmission in dependence on the kinetic energy of passing electrons) can be experimentally determined for each spectrometer. The RSF values for the different orbitals of the elements can also be determined by simple experiments. The areas of the element peaks found in the XPS spectrum of a sample with well-defined stoichiometry (e. g. salts) must be multiplied with a factor (RSF) to equal the sample's stoichiometry. Usually, all RSF values were related to the fluorine's RSF which is set to one.

To determine the peak area of the element peaks in the wide-scan spectrum it is indispensable to separate the spectrum background which is formed by the inelastically scattered photoelectrons from the photoelectrons representing the spectral information. To subtract the spectrum background procedures according to Shirley [3] and Tougaard [4] have been established.

The elemental composition of the poly(3-hydroxybutyrate) layer in Fig. 4.4 was determined to $[C]=68.39$ at.%, $[O]=31.22$ at.%, and $[Si]=0.39$ at.%, which corresponds with atomic ratios of $[O]:[C]=0.456$ (according to the formula in (4.4) $[O]:[C]$ is expected to 0.5), and $[Si]:[C]=0.005$.



For all samples which were prepared under atmospheric conditions a small excess of carbon is observed appearing from the hydrocarbon's surface contamination. Traces of silicon may result from the substrate material (Si/SiO₂) or from siloxane impurities which are also typical for polymers prepared via wet-chemistry procedures. Here, angle-resolved XPS opens the way to clarify the origin of this unexpected element.

For many polymer samples the success of surface modification reactions can be evaluated by their changed surface composition. Furthermore, in many cases reaction mechanisms can be explained on the basis of quantitative surface analysis.

4.6 High-Resolution Element Spectra – Peak Deconvolution and Interpretation

Figure 4.5 shows a so-called *high-resolution spectrum* of a silicon wafer. Beside the metallic silicon, the spectrum shows a second, rather wide component peak appearing from the Si–O species. That example shows that XPS is also suitable to study the chemical environments of an elemental species. Surprisingly, to get information about the different bonds of an element or its oxidation state, usually the photoelectrons appearing from a core orbital are analysed. In contrast to the orbitals forming the valence band, these core shells are not involved in the chemical bonds to other atoms. But the formation of chemical bond influences the electron density on the atoms which form these bonds. Concerning the local electron densities it is a difference if a carbon atom is bonded to another carbon or to oxygen. In the first case the electron density is homogeneously distributed between the two carbon atoms. In the case of the formation of C–O bonds, the electron density on the carbon atom is strongly lowered because oxygen has a higher electronegativity. This state can be described by a positive partial charge on carbon ($C^{\delta+}$) and a negative partial charge on oxygen ($O^{\delta-}$). The photoelectrons escaped from the core levels of the positively charged carbon have to get over the additionally attractive Coulomb interaction by a lost of their kinetic energy. Hence, in the C 1s spectrum in addition to the component peak appearing from the C–C bonds a second component peak at a higher binding energy is observed.

According to the electron density distribution in the poly(3-hydroxybutyrate) molecule (4.4) four different chemical states of carbon (*A*, *B*, *C*, and *D*) are expected [in equation (4.5) the distribution of the electron density is schematically shown by the black arrows, the thick face indicates a high electron density]:



The corresponding C 1s spectrum (Fig. 4.7(a)) can be deconvoluted: into the expected four component peaks. The thick line in Fig. 4.7(a) is the measured C 1s spectrum containing the spectral information. After subtracting the spectrum background by Shirley's method the spectrum was mathematically deconvoluted into the four component peaks. The adding up of the component peaks give a master curve which can be fitted to the measured spectrum. Free parameters of the computer controlled fitting procedure are the component peak position (binding energy of the component peak maximum), the component peak height, the full width at

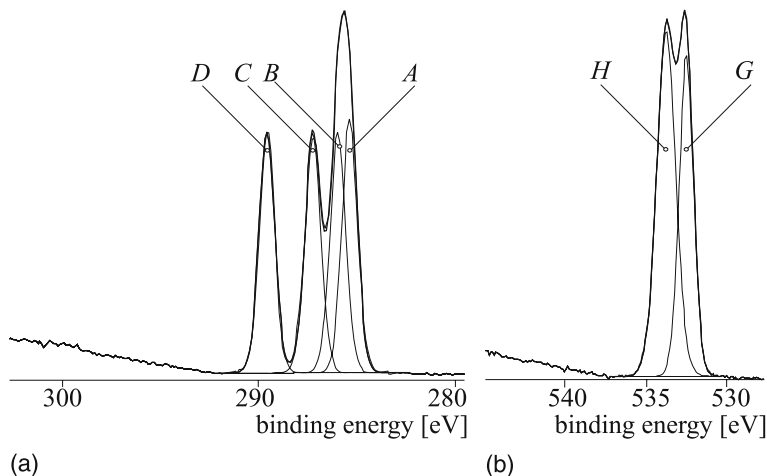


Fig. 4.7 High-resolved C 1s (a) and O 1s (b) spectrum of a poly(3-hydroxybutyrate) film spin-coated onto a silicon wafer

half maximum: of the component peak (FWHM), and the Gaussian–Lorentzian ratio (G/L) of the component peak. The fitting procedure can be considered as an approximation where the difference between the calculated master curve and the measured spectrum – indicated by the sum of least squares – should be small as much as possible.

In the case of poly(3-hydroxybutyrate) Fig. 4.7(a) shows that the master curve of the four component peaks excellently fit the measured spectrum. The chemical shifts (ΔBE) of the component peaks indicate the species of the differently bonded carbon atoms:

<i>A</i> : $\Delta BE = 0 \text{ eV}$	saturated hydrocarbons \underline{C}_xH_y	($BE = 285.00 \text{ eV}$),
<i>B</i> : $\Delta BE \approx 0.4 \text{ eV}$	$\underline{C}-C(O)-O-C$	($BE \approx 285.4 \text{ eV}$),
<i>C</i> : $\Delta BE \approx 1.3 \text{ eV}$	$O=C-O-\underline{C}$	($BE \approx 286.3 \text{ eV}$),
<i>D</i> : $\Delta BE \approx 3.7 \text{ eV}$	$O=\underline{C}-O-C$	($BE \approx 288.7 \text{ eV}$).

In Fig. 4.7(a) it can be seen that the ratio of the component peak areas $[B]:[C]:[D]$ equals the expected ratio $[B]:[C]:[D] = 1:1:1$. Component peak *A* shows the small excess of the hydrocarbon surface contamination noted also in the wide-scan spectrum. Furthermore, it can be seen that the two fit parameters FWHM and G/L have nearly the same values for all mathematical curves (FWHM ≈ 0.9 , $G/L \approx 0.3$). It is not surprising because all the photoelectrons of a certain carbon species have to pass the same electron optic and analyser in the spectrometer. Hence, the changes in the peak shape generated by the spectrometer (e. g. folding the Lorentzian distribution of the photoelectron emission by a Gaussian curve) is equal for all photoelectrons independent of their origins.

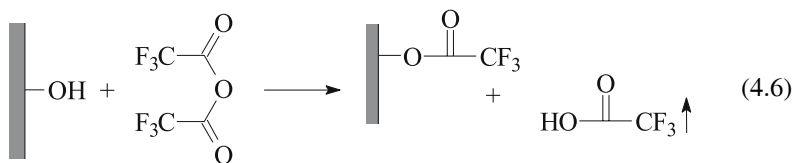
Equation (4.4) shows also two chemically different oxygen species forming the ester bond ($O=C-O$). Oxygen indicated by *G* has a double bond to carbon (carbonyl oxygen, $\underline{O}=C-O$), and the other oxygen species (*H*) has single bonds to

carbons (ether oxygen, $O=C-\underline{O}$). The double bond contains rather weakly bonded π -electrons which increase the electron density on the oxygen atom. Hence, the carbonyl oxygen is found at a lower binding energy as the single bonded ether oxygen (Fig. 4.7(b)). The ratio of the component peak areas $[G]:[H]$ equals the ratio $[G]:[H] = 1:1$ expected from (4.4) and (4.5).

In particular, in the case of polymers the discussion of the binding states of carbon can be very helpful for planning and controlling surface modification reactions and evaluate their success. The peak deconvolution procedure shows the kind and number of functional surface groups which can be act as reactive centres or anchors for grafting reactions. There is the fortunate position that the component peaks of the different carbon species or functional groups can be easily separated. Taking the quantitative information into account, mostly the assign of the component peaks to chemical structures has a high confidence.

4.7 Labelling – The Derivatization of Functional Groups for its Identification

The chemical shifts of the polymer relevant functional groups are listed in handbooks or databases of organic polymers or other materials [5–10]. The tables there show that the co-existence of certain functional groups or a high number of different functional groups on a polymer surface can make problems by the identification and assign of the functional groups. For example, ether ($\underline{C}-O-\underline{C}$) and alcohol groups ($\underline{C}-OH$) have the same interval of chemical shifts ($1.1 < \Delta BE < 1.7$ eV). The quantitative determination of the elemental ratio $[O]:[C]$ from the wide-scan spectrum and its comparison with the elemental ratio $[O]:[C]$ calculated from the deconvoluted C 1s spectrum may solve the identification problem because in the case of alcohol groups the ratio $[O]:[C]$ is 1:1, while ether groups give a ratio of 1:2.



An other way to identify reactive functional surface groups is their derivatization (*labelling*) with substances containing a heteroatom which is not present in the non-labelled sample surface. Those labelling agents should react selectively and sensitively with a high degree of coverage. Reactions which can be carried out in a gaseous atmosphere are preferred to such which must take place in solution.

A well established method to check the presence of alcohol groups is the derivatization reaction with trifluoroacetic anhydride (4.6). During its reaction the very reactive trifluoroacetic anhydride introduces fluorine in the sample surface. Immediately, after the gas phase reaction the labelled sample can be investigated by

Table 4.1 Compilation of established methods to label and identify functional surface groups

Surface functional group	Reagent	Unique element
C=C	Br ₂ in CCl ₄	Br
	OsO ₄	Os
O=C–OH (carboxylic acid)	AgNO ₃ in water	Ag
	Trimethylsilylimidazol	Si
C=O (carbonyl)	Gaseous hydrazine	N
	Gaseous HCl or hydrochloric acid	Cl
Epoxy	Gaseous (CF ₃ CO) ₂ O	F
	Gaseous (CF ₃ CO) ₂ O	F
–OH (alcoholic hydroxyl groups)	C ₃ F ₇ COCl in hexane	F
	AgNO ₃ in water	Ag
–SH (thiol)	Gaseous CS ₂	S
	Pentafluorobenzaldehyde	F
–NH ₂ (primary amine)	Pentafluorobenzaldehyde	F
	Pentafluorobenzaldehyde	F
–NR ₂ (amine)	Pentafluorobenzaldehyde	F
–C–O–O–H (hydroperoxide)	Gaseous SO ₂	S
Radicals [19]	Gaseous NO	N

means of XPS. The detection of the F 1s peak in the wide-scan spectrum indicates the presence of alcoholic groups in the non-labelled sample surface. However, it is necessary to note that this simple reaction is not a sensitive reaction only for alcohol groups. Epoxide and amino groups can also easily react with the fluorinated anhydride. Of course, the described reaction is not suitable for fluorinated polymers.

Table 4.1 shows a few of the established methods to label functional surface groups (for more information see [9–18]). As mentioned above it is necessary to prevent any side reactions via functional groups which are in competition with the offered labelling reagent.

Labelling reactions should not be used for the quantification of functionalities. The addition of bromine to a C=C double bond or the oxidation of C=C bonds with OsO₄ cannot be quantitative because the reaction space on the surface is limited. Furthermore, solvents (e.g. chlorinated alkanes or other organic liquids) may cause a swollen surface layer opening the access of the labelling reagent to functional groups which were originally situated in the sample depth. Nevertheless, labelling reactions are a powerful and widely applied tool to study the kind and reactivity of functional surface groups especially on plasma treated polymer surfaces [10, 11, 16, 18, 20].

4.8 Angle-Resolved XPS

As mentioned above angle-resolved XPS allows us to enhance the surface sensitivity of the XPS method. The practical use of this technique seems very simple and can be carried out on each XPS spectrometer. In order to change the *take-off* angle Θ , the sample must be tilted with regard to the electron optical axis of the spectrometer. The correlation between information depth and *take-off* angle is given in (4.2). All angle-resolved XPS studies require very smooth and even sample surfaces. Unevenness and roughness cause *take-off* angle-distributed spectral information corresponding with a distribution of the information depth. That phenomenon must be also considered by the interpretation of spherical surfaces of fibres, fabrics, powders and grains.

The technique can be used to study the migration of polymer blend components or the segregation of block copolymer segments or side chains to the sample surface [21–26].

In molecular thin adsorption films having a high degree of molecular order the orientation of the adsorbed molecules can be investigated. From the knowledge of the correlation between the relative peak intensity of an element i and the information depth d it is possible to calculate the elemental depth distribution for an assumed build-up of a surface layer.

This will be illustrated for an alkane phosphonic acids which was adsorbed on a titanium oxide substrate. The substrate material is indicated by Ti, the covering layer contains P and C. From the XPS spectra recorded for three different *take-off* angles ($\Theta = 0^\circ$, 45° , and 60°) it can be concluded that phosphonic acid group is attached to the titanium oxide substrate (Fig. 4.8(a)). The calculated depth distributions of the elements are shown in Fig. 4.8(b). As can be seen the Ti intensity is softened by the coating. Phosphorus is attached on the substrate surface, but its

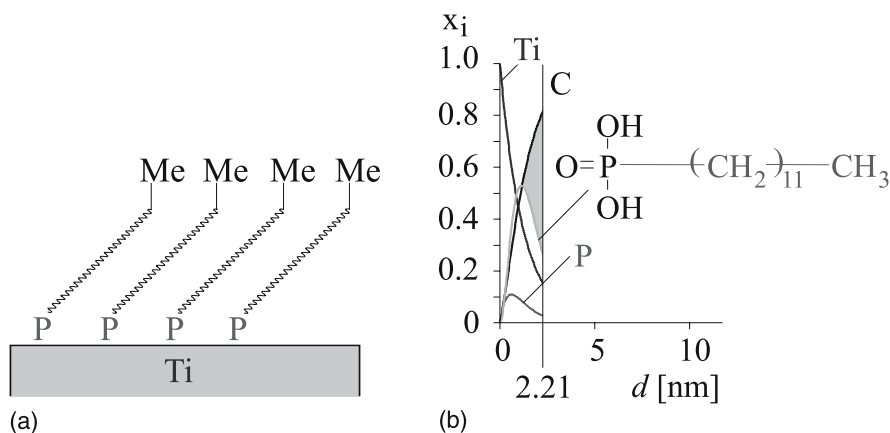


Fig. 4.8 Scheme of a self-assembly layer of an alkane phosphonic acid on a titanium oxide substrate (a) and the functional relationship between the element intensities and information depth for this layer build-up (b)

intensity is also softened by the outstanding hydrocarbons. For the applied coating (dodecane phosphonic acid) the fraction of carbon which is bonded to the phosphonic acid group corresponds to the given stoichiometry. The excess of carbon appears from surface hydrocarbon contamination. Obviously, the contamination layer is on the top of the sample surface, which indicates that a specific interaction between the phosphonic acid group and the titanium oxide overcompensate the adhesion forces of the non-specifically adsorbed contamination layer. The equilibrium layer thickness of the adsorbed dodecane phosphonic acid layer was determined to 1.1 nm. The comparison between the molecule length of the dodecane phosphonic acid molecule (1.536 nm) and its layer thickness shows that the molecules must be leaned at an angle of ca. 45°.

According to (4.7) XPS measurements with a fixed *take-off* angle Θ allow the determination the thickness d of a coating layer (containing the label element X_1) on a thick substrate material (with the label element X_2) [27]. In (4.7) $I(X_i)$ is the measured intensity of the element X_i in the sample layer or substrate, and $I_0(X_i)$ is the measured intensity of the element X_i of an infinitely thick sample.

$$\frac{I(X_1)}{I(X_2)} = \frac{I_0(X_1) \cdot \exp\left(1 - \left[-\frac{d}{\lambda(X_1) \cdot \cos \Theta}\right]\right)}{I_0(X_2) \cdot \exp\left[-\frac{d}{\lambda(X_1) \cdot \cos \Theta}\right]} \quad (4.7)$$

The variation of the *take-off* angle should not influence the resulting d value because the *take-off* angle is an adjusted value for the XPS experiment and not a the property of the prepared coating layer. However, in many cases a dependence of d on Θ is observed. This unexpected phenomenon can be explained by non-homogeneous coating films. Ruptured films, pin holes, or droplet formation lower the degree of coverage (φ) and cause a *take-off* angle depending shielding of the substrate element intensity $I(X_2)$. Opila et al. [28] introduced the degree of coverage as a second parameter in (4.7). In order to solve the two-parameter equation angle-resolved XPS measurements at two different *take-off* angles (in minimum) are required. The additional calculated parameter φ can be considered as a measure to evaluate the homogeneity of the coating layer.

4.9 Special XPS Techniques

During the last few years different techniques were developed to adapt the XPS method to special analytical requirements. One of the most important advances was the development of satisfactory working charge compensation units which allows the use of monochromatic X-Rays to record high-resolution XPS spectra of electrically non-conducting samples without any spectral distortions.

Below three special XPS techniques are briefly described.

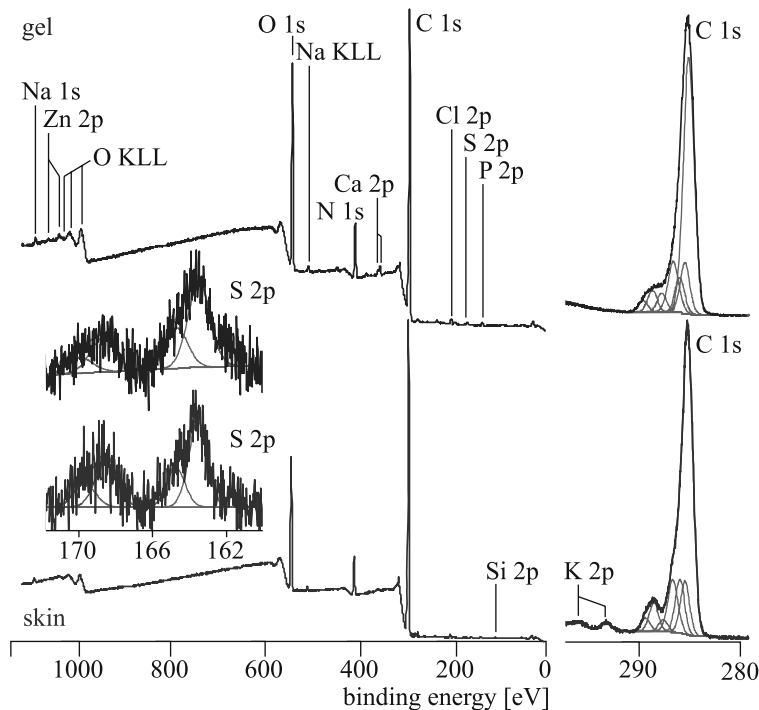


Fig. 4.9 XPS spectra of the skin and the skin's gel layer of a dolphin. The spectra were recorded employing the *kryo-XPS* technique [29]

4.9.1 *Kryo-XPS*

Biological materials (e. g. Fig. 4.9), polyelectrolytes and liquid samples seem unsuitable for XPS investigations because they may destroy the vacuum in the spectrometer or may be decomposed under vacuum conditions. An effectively working cooling unit of the sample transfer and manipulation system prevents a gassing or partial evaporation of the sample. Usually liquid nitrogen is used as cooling medium. In order to control the sample temperature the cooling state is additionally fitted with a heating. Hence, XPS spectra can also be recorded in dependence on temperature which can be the matter of interest to study thermally sensitive segregation processes or initiate chemical reactions.

4.9.2 *Small-Spot XPS*

The lateral resolution of an XPS spectrometer is rather low because it is very difficult to focusing the X-Ray beam. The beam diameter is reduced by its monochromator passage to ca. 1 mm. The size of many samples will be smaller than the radiated area.

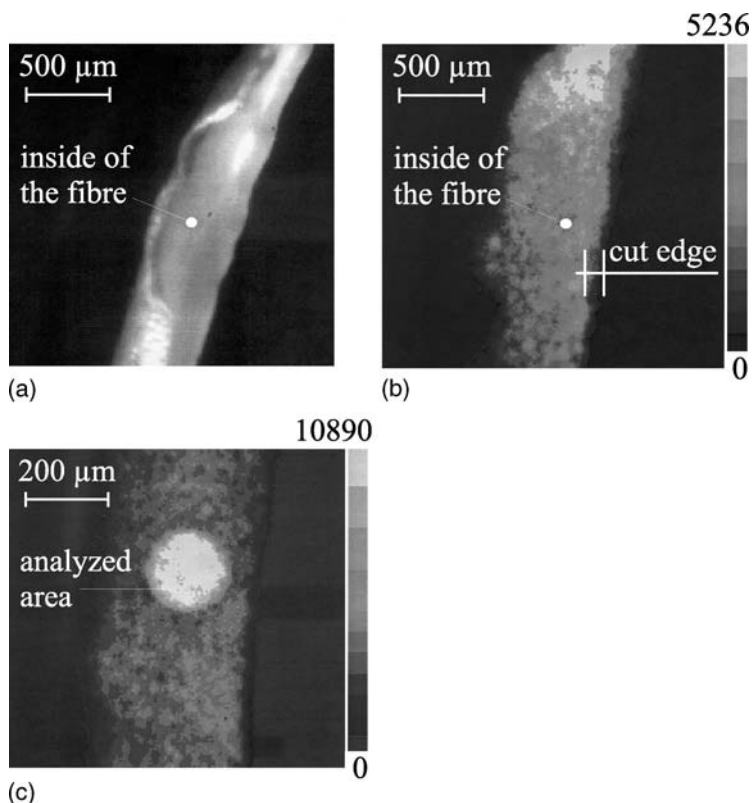


Fig. 4.10 Images of a hollow fibre cut in the middle along their length. Photograph of the fibre mounted on a sample holder under the analyser of the XPS spectrometer (a), S 2p XPS-image of the fibre (b), the same fibre, but now the iris is more closed to restrict the field of view (c) (the spectrometer can only see the pale area; the fibre can be seen is the result of the first exposure before the iris was closed)

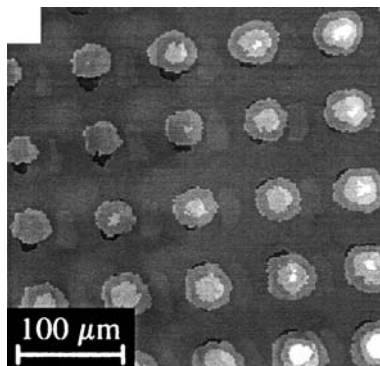
In order to solve this problem the area of acceptance can be reduced by an iris in the electron optic of the spectrometer. This procedure lowers also the transmission of the spectrometer. The lower count rate of photoelectrons must be compensated by a longer spectrum accumulation time.

Figure 4.10 illustrates the *small-spot* routine by a single hollow fibre of a dialysis membrane. The inside of the single fibre was studied by XPS after cutting the fibre along its length axis. Employing the *imaging* unit of the spectrometer the field of the spectrometer's view was visualized.

4.9.3 Imaging-XPS

Beside the visualization of the area of acceptance (measured area) the *imaging* mode can also be used to get information on the lateral distribution of elements or functional groups on the sample surface. As mentioned above the lateral resolution

Fig. 4.11 Spatially resolved XPS image of the lateral distribution of silver ions (the Ag 3d peak is pale) in a polyelectrolyte layer which was adsorbed onto a gold/11-mercaptoundecanoic acid structured silicon wafer surface. The Si 2p peak is depicted in black



of the XPS spectrometer is rather pure (for polymers ca. 10 μm), but the additional lateral information can be used to evaluate the success of complex reactions. The example in Fig. 4.11 shows a partly gilded silicon wafer. On the gilded areas a mercapto compound was adsorbed. The carboxylic group in ω -position of the mercapto compound should be the anchor for the adsorption of a cationically charged polymer which should be the bed for silver clusters. To prevent an adsorption of the polycation on the silica bars, the non-gilded silica surface was hydrophobized by a fluorinated silane. The composition of the sample as very complex, but the Fig. 4.11 shows that silver is only found on sites where gold/functionalized mercapto compounds/polycations were adsorbed. The silicon bars are free of silver clusters [30].

References

1. M.P. Seah, *Surf. Interface Anal.* 2, 222 (1980)
2. K. Siegbahn, K. Edvardson, *Nucl. Phys.* 1, 137 (1956)
3. D.A. Shirley, *Phys. Rev. B* 5, 4709 (1972)
4. H. Tokutaka, N. Ishihara, K. Nishimori, S. Kishida, T. Takbuchi, *Japan J. Appl. Phys. I* 29, 2512 (1990)
5. G. Beamson, D. Briggs, *High resolution of organic polymers: The Scienta ESCA 300 Database* (Wiley, Chichester, 1992)
6. J.F. Moulder, W.F. Stickle, P. Sobol, K.D. Bomben, J. Chastain, *PHI-Handbook of X-ray Photoelectron Spectroscopy* (Perkin-Elmer, Eden Prairie, 1992)
7. D. Briggs, M.P. Seah, *Practical Surface Analysis by Auger and X-Ray Photoelectron Spectroscopy* (Wiley, Chichester, 1990)
8. D.T. Clark, W.J. Feast, *Polymer Surfaces* (Wiley, New York, 1978)
9. K. Robinson, A. Carrick, *High resolution XPS spectra of polymers – a short compilation* (Kratos Analytical, Manchester, UK, 1992)
10. D.T. Clark, *Advances in ESCA applied to polymer characterization*, *Pure Appl. Chem.* 54, 415 (1982)
11. D.S. Everhart, C.N. Reilley, *Anal. Chem.* 53, 665 (1981)
12. D.S. Everhart, C.N. Reilley, *Surf. Interface Anal.* 3, 126 (1981)
13. D.S. Everhart, C.N. Reilley, *Surf. Interface Anal.* 3, 258 (1981)

14. J. Gardelle, D. Hercules, J. Amer. Chem. Soc. 105, 4536 (1984)
15. J.M. Pochan, L.J. Gerenser, J.F. Elman, Polymer 27, 1058 (1986)
16. A. Chilkoti, B.D. Ratner, Surf. Interface Anal. 17, 567 (1991)
17. T.A. Dang, R. Gnanasekaran, J. Vac. Sci. Technol. A9, 1406 (1991)
18. T.R. Gengenbach, X. Xie, R.C. Chatelier, H.J. Griesser, Evolution of the surface composition and topography of perfluorinated polymers following ammonia-plasma treatment, in *Plasma Surface Modification of Polymers, Relevance to Adhesion*, ed. by M. Strobel, C.S. Lyons, K.L. Mittal (VSP, Utrecht, 1994), p. 123
19. V.N. Vasilets, F. Simon, C. Werner, G. Hermel, D. Pleul, M. Nitschke, A. Menning, A. Janke, H.J. Jacobasch, J. Adh. Sci. Technol. 16, 1855 (2002)
20. J.F. Friedrich, Plasma modification of polymers, in *Polymer-Solid Interfaces*, ed. by J.J. Pireaux, P. Bertrand, J.L. Bredas (IOP, Bristol, UK, 1992), p. 443
21. T.G. Vargo, J.A. Gardella, J. Vac. Sci. Technol. A7, 1733 (1989)
22. J.J. Smith, J.A. Gardella, L. Salvati, Macromolecules 22, 4489 (1989)
23. M.B. Clark, C.A. Burkhardt, J.A. Gardella, Macromolecules 22, 4495 (1989)
24. S.C. Yoon, B.D. Ratner, Macromolecules 19, 1068 (1988)
25. D. Pospiech, K. Eckstein, L. Häußler, H. Komber, D. Jehnichen, K. Grundke, F. Simon, Macromol. Chem. Phys. 200, 1311 (1999)
26. A. Takahara, K. Takahashi, T. Kajiyama, J. Biomater. Sci. Polym. Ed. 5, 183 (1993)
27. C.S. Fadley, Progr. Surf. Sci. 16, 275 (1984)
28. R.L. Opila, J.D. Legrange, J.L. Markham, G. Heyer, C.M. Schroeder, J. Adh. Sci. Technol. 11, 1 (1997)
29. C. Baum, F. Simon, W. Meyer, L.G. Fleischer, D. Siebers, Biofouling 19, 181 (2003)
30. S. Spange, T. Meyer, I. Voigt, M. Eschner, K. Estel, D. Pleul, F. Simon, Poly(vinylformamide-co-vinylamine)/inorganic oxide hybrid materials, in *Polyelectrolytes with Defined Molecules Architecture I, Advances in Polymer Science*, vol. 165 (Springer, Berlin Heidelberg New York, 2003)

Monographs and Reviews

- D. Briggs, M.P. Seah, *Practical Surface Analysis by Auger and X-Ray Photoelectron Spectroscopy* (Wiley, Chichester, 1990)
- D.T. Clark, Advances in ESCA applied to polymer characterization, Pure Appl. Chem. 54, 415 (1982)
- G. Beamsom, D. Briggs, *High resolution of organic polymers: The Scienta ESCA 300 Database* (Wiley, Chichester, 1992)
- J.F. Moulder, W.F. Stickle, P. Sobol, K.D. Bomben, J. Chastain, *Handbook of X-Ray Photoelectron Spectroscopy* (Perkin-Elmer, Eden Prairie, 1992)
- K. Robinson, A. Carrick, *High resolution XPS spectra of polymers – a short compilation* (Kratos Analytical, Manchester, UK, 1992)
- T.L. Barr, Modern ESCA: The Principles and Practice of X-Ray Photoelectron Spectroscopy (CRC, Boca Raton, 1994)
- B.D. Ratner, Surface Characterization of Biomaterials, Progress in Biomedical Engineering, vol. 6 (Elsevier, Amsterdam, 1988)
- N.H. Turner, J.A. Schreifels, Surface analysis: X-Ray photoelectron spectroscopy and Auger electron spectroscopy. Anal. Chem. 64, 302R–320R (1992)

Chapter 5

Time-of-Flight Secondary Ion Mass Spectrometry

Dieter Pleul¹ and Frank Simon²

^{1,2}Leibniz Institute of Polymer Research Dresden, Hohe Str. 6, 01069 Dresden, Germany, frsimon@ipfdd.de

Abstract Static secondary ion mass spectrometry provides information on the molecular composition of the topmost layer of a sample. It is mostly used as a complementary technique to determine surface composition, surface contamination or surface segregation of components. The time-of-flight technique enables high mass resolution also at the higher mass values needed for polymers.

5.1 Introduction, History and Physical Principle

In the last decades secondary ion mass spectrometry (SIMS) has become important as a surface sensitive analytical technique in surface sciences. In the semiconductor and microelectronic industries the method is widely applied to try to find disturbing impurities or to visualize the microstructures using the contrast of different element species.

For polymers the SIMS method can be considered as a complementary tool in surface analysis. Often it can be profitably employed to get *molecular* information, while the electron spectroscopic methods (XPS and AES) give a rather element specific impression of polymer surfaces. From our point of view, SIMS should not be used as an exclusive technique for studying polymer surfaces because usually the recorded spectra seem very complex and their complete and correct interpretation need background information about the history of the sample's origin and composition. This opinion may be controversially discussed, but both former and recent literature show that SIMS is not the exclusively employed method to study real polymer surfaces. It is always applied in combination with XPS, surface sensitive techniques of the infrared spectroscopy, or other complement methods. Perhaps the multiplicity of the unsolved problems concerning the spectra interpretation – especially the unsatisfied quantification of the SIMS spec-

tra – could be the reason for a rather moderately increased application of the SIMS method in polymer sciences.

SIMS is based on the fact that charged atoms (ions) or molecules (molecule ions) are ejected from the surface of a solid under particle bombardment. The idea to use the ejected ions as analytical tool was found 65 years ago by Arnot and Milligan [1, 2]. They investigated, with the aid of a magnetic detection field, the secondary ion yield and energy distribution of negatively charged ions induced by positive ions. The fundamental for SIMS is the work by Herzog and Viehboeck, who also built the first primary ion source in 1949 [3]. The first complete SIMS spectrometers were constructed some ten years later. Semiconductor and thin film analysis by Beske and Werner were the first analytical application of SIMS [4, 5]. In 1969, Alfred Benninghoven from the university in Münster introduced the so-called *static* SIMS, which does not significantly destroy the sample surface, as a powerful tool in surface science [6–8]. His instrumental developments, particularly the time-of-flight detection technique, cause recognition of the extent of the SIMS method also for organic materials.

As mentioned above, SIMS requires the bombardment of a solid surface by charged (e. g. *primary ions*) or neutral particles of an energy range of some keV. During the surface bombardment, sputtering is one of the many processes happening during the particle/surface interaction. The sputter process is indicated by an implantation of the high-energy particles into the sample surface and an emission process initiated by an energy and momentum transfer to a limited sample volume around the point of particle impact [9]. The emission process include an electron and photo emission and an emission of surface particles. These particles are neutral atoms and molecules or charged simple ions and molecule ions which are emitted with a certain angular distribution. It can be assumed that all these surface fragments will escape in a highly excited state. Hence, changes of the fragment composition occur outside the sample surface, that means fragments can undergo decomposition reactions and neutral species can transferred into a charged state while charged species can be neutralized.

For the analytical application mainly the emitted charged species of the sputter process are the matter of interest. These species called *secondary ions* may be easily mass separated – or more correctly, separated according to their mass-charge ratio – by different physical principles (see below). The number of secondary ions were recorded in dependence on their molecular mass. The resulting spectrum can be considered as the key to interpret and understand the sample surface build-up. To prevent significant damage in the sample surface region during the bombardment the analytical SIMS technique for polymers or other organics should have a low sputter rate. This requirement is fulfilled by employing the *static* SIMS technique, where extremely low sputter rates were applied to remain a disturbing or decomposition of the surface (primary ion current density is in the range of 10^{-9} A cm⁻²). To get spectra in excellent quality the transmission of the static SIMS spectrometers has to be very high. The other available method with high sputter rates (primary ion current density is up to some A cm⁻²) – called

dynamic SIMS – is usually used to remove the sample surface and study the sample build-up layer by layer in the depth (depth profiling).

The most important feature of the static SIMS method is its extremely high surface sensitivity. The information depth is distinctly lower as for XPS and Auger electron spectroscopy. Virtually all secondary ions have their origin in the uppermost layer of the bombarded surface [9]. In the case of polymers Benninghoven introduced the term uppermost *monolayer*.

A fundamental problem of SIMS is the impossibility to quantify the spectral information reliably. The charge state of the emitted particles depends strongly on its origin chemical environment. This phenomenon, called the *matrix effect* is well known in all techniques of mass spectrometry. For SIMS different approximations, models and empirical procedures were applied to get quantitative information to compare samples exhibiting only small changes in their surface composition. But all these described ways to quantify SIMS results cannot be generalized [10].

5.2 Instrumentation

The physical principle of SIMS require three essential spectrometer parts. A source must provide a beam of accelerated primary particles which is focused onto the sample surface. The emitted secondary ions must be separated and detected according to their mass–charge (m/z) ratio. All the processes have to take place under ultra-high vacuum conditions. Hence, a set of components must provide and keep the excellent vacuum.

Mainly, the primary particles are positively (e.g. Ar^+ , Xe^+ , Ga^+) or negatively charged ions (O_2^-) provided by an ion source. A few spectrometers were fitted with sources providing uncharged γ -rays emitted from radioactive isotopes with an energy range of MeV [11].

According to the secondary ions mass separation and detection system three different types of spectrometers can be distinguished. Quadrupole, magnetic sector field, and time-of-flight detectors are widely applied in SIMS. Here, the time-of-flight (ToF) detection principle will be explained in detail. It is the most advanced SIMS technique and excellently suited to analytical applications. The high spectrometer transmission offers the possibility to work with very low sputter rates (static SIMS mode) which do not significantly change the sample surface over a couple of hours.

Figure 5.1 schematically shows the build-up of a ToF-SIMS spectrometer. The primary ion source provides argon ions (Ar^+) of an energy of 10 keV. The continuously generated beam is chopped into short pulses of ca. 200 ps by a buncher unit. The small ion packages bombard the sample surface and produce fragments which escape from the sample surface as neutral and charged particles. Usually only the charged particles (ions and molecule ions) were used to get the spectral information. But here it is necessary to note that during their flight exited neutral particles can be transferred into an ionic species or charged particles may be

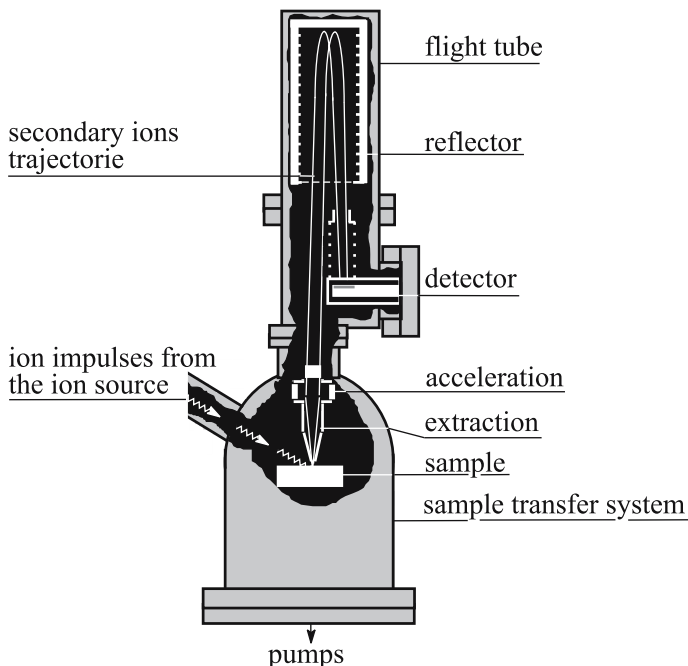


Fig. 5.1 Typical build-up of a time-of-flight secondary ion spectrometer

neutralized. It is also possible that double or higher charged ions can be produced. The charged fragments are introduced in the electrical field of the extraction unit of the ToF analyzer. The polarity of the electrical field can be selected by the operator. Hence, using the ToF-SIMS technique it is possible to collect the positively as well as negatively charged fragments and get *positive* and *negative SIMS spectra*. The secondary ions of the selected polarity have to pass a constant potential difference U . There each charge z of the fragments consume a constant amount of kinetic energy $E_{kin} = z \cdot e_0 \cdot U$ (e_0 = elementary charge). Then, the velocity (v) of a fragment depends on its mass-charge ratio (m/z):

$$E_{kin} = \frac{m}{2} \cdot v^2 = \frac{m}{2} \cdot \frac{s^2}{\Delta t^2} \quad (5.1)$$

The secondary ions have to pass the flight tube, were reflected on the reflection unit focussing the ion trajectories and compensating pathway differences and finally they were collected and counted on a channel plate working as detection system. The distance (s) is equal for all ions, but they need different times to pass the given way. Hence, a separation according to the masses of the fragments takes place and the detector unit register the different species depending on their molecular mass. The time interval (Δt) is defined by an impulse synchrony to the primary ion packages (start) and the arriving of the secondary ions in the detector. Employing (5.1) it is possible to calculate the mass-charge ratio (m/z) from the

measured *time of flight*. Finally, the dependence of the count rate [*cps*] on the *m/z* ratio [*amu* = atomic mass unit or *Dalton*] of the secondary ion is represented as a spectrum (Fig. 5.2).

The high transmission of the ToF-SIMS spectrometer is given by the detection of all produced secondary ions with the same (plus or minus) sign, while the other mass detector systems are only open for the passage of a certain mass over a fixed time span. Beside the use of extremely low sputter rates, it is also possible to detect traces of molecular or atomic species up to the fmol range.

5.3 Samples

For ToF-SIMS experiments smooth and even samples are required. Otherwise, the spectral mass resolution is negatively influenced by distance–time differences appearing from surface roughness, edges or other geometric defects on the sample surface. By using an additional electron gun delivering low energy electron impulses it is possible to investigate non-conducting samples, like polymers or ceramics. A fundamental requirement is the sample stability under ultra-high vacuum conditions. Sample cooling systems mentioned in the XPS chapter may be favourable for certain applications.

In order to enhance the yield of secondary ions it is profitable to prepare the samples on silver surfaces. During the bombardment silver ions can act as carriers for sample fragments. Using this preparation technique it is possible to detect also high-molecular mass fragments with a high intensity [12].

5.4 Time-of-Flight Secondary Ion Mass Spectra and Their Interpretation

Figure 5.2 shows a typical ToF-SIMS spectrum of the spin-cast polymer polystyrene on a silicon wafer.

In contrast to the common spectra of the thermal mass spectroscopy the ToF-SIMS spectra show a high number of peaks. Virtually each mass number is occupied by a peak. Some of these peaks are very small but often they must be taken into account to correctly understand and interpret the spectrum. Obviously, the discussion of SIMS spectra is not trivial and many peaks cannot be explained. Experience in thermal mass spectroscopy and the following the expected typical fragmentation reactions are helpful tools for understanding the SIMS spectra. As mentioned above a quantification does not consult for the interpretation.

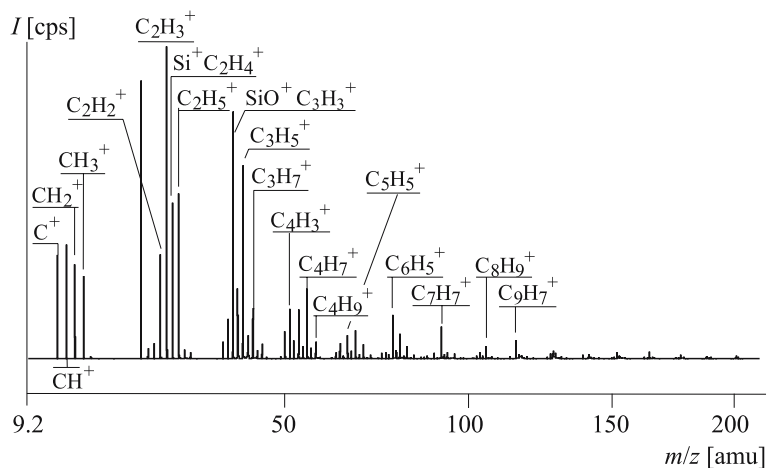


Fig. 5.2 Positive ToF-SIMS spectrum of a polystyrene film spin-cast on a silicon wafer

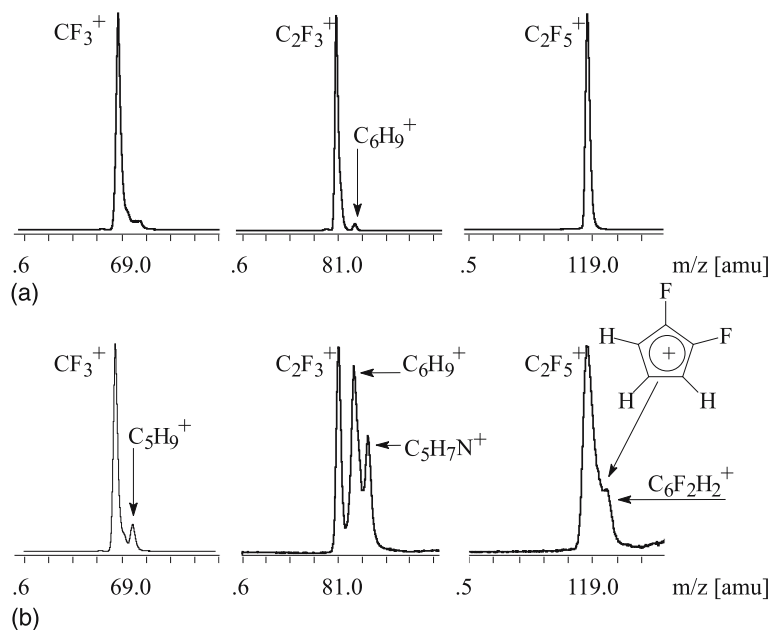


Fig. 5.3 High-resolution ToF-SIMS spectra of an unmodified (a) and a hydrogen plasma treated poly(tetrafluoroethylene) film (b). The peak maxima are listed in Table 5.1

In contrast to the quadrupole mass detection system the ToF principle provides an excellent mass resolution ($m/\Delta m > 10,000$) which can be used to confidently assign a recorded peak to its corresponding fragment structure. This is illustrated in Fig. 5.3 showing sections of ToF-SIMS spectra of an unmodified and hydrogen plasma modified poly(tetrafluoroethylene) film (see also Table 5.1).

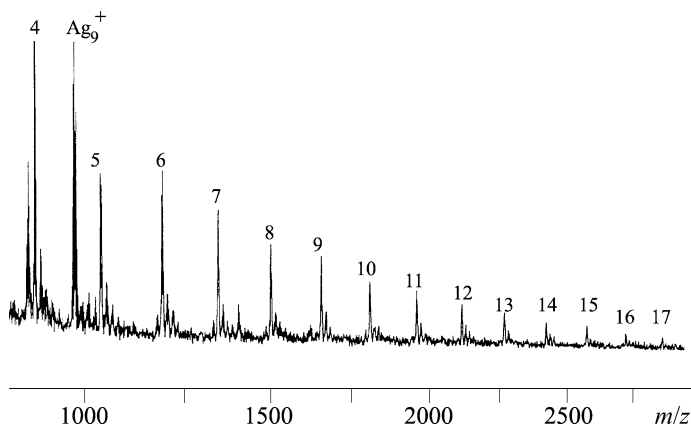


Fig. 5.4 Wide-scan ToF-SIMS spectrum of poly(vinyl naphthalene) spin-cast on silver. The numbers indicate the numbers of the monomer's repeat units n which form the molecule ions. All observed fragments contain one silver ion

Table 5.1 Comparison of measured peak maxima (see Fig. 5.3) and the calculated mass values for the assigned secondary ions

Ions	m/z Measured	m/z Calculated	Difference
CF_3^+	68.9873 amu	68.9952 amu	0.0079 amu
C_5H_9^+	69.0695 amu	69.0717 amu	0.0022 amu
C_2F_3^+	80.9888 amu	80.9952 amu	0.0064 amu
C_6H_9^+	81.0645 amu	81.0717 amu	0.0072 amu
C_2F_5^+	118.9858 amu	118.992 amu	0.0062 amu
$\text{C}_5\text{H}_2\text{F}_3^+$	119.0112 amu	119.0111 amu	0.006 amu
$\text{C}_6\text{H}_9\text{F}_2^+$	119.0659 amu	119.0685 amu	0.0026 amu

A second advanced feature of the ToF-SIMS method can be used to identify polymeric species. The mass range of the ToF-SIMS spectra is virtually not limited by the apparatus parameter. Hence, molecular masses of some thousands of Daltons may be observed [13]. In the case of polymers the *wide-scan* spectra show peak clusters appearing from the elimination of monomer units (Fig. 5.4).

Wide-scan ToF SIMS spectra were also used to determine the molecular mass and molecular mass distributions of low molecular mass polymers [14–16]. The polymer molecules with a low molecular mass have a high tendency to migrate to the polymer surface and form the top layer of the polymer which could make problems for polymer processing in the electronic industries [15, 16].

Of course, there are different methods to identify the species of a polymer, but for different analytical questions it can be useful in applying ToF-SIMS. The

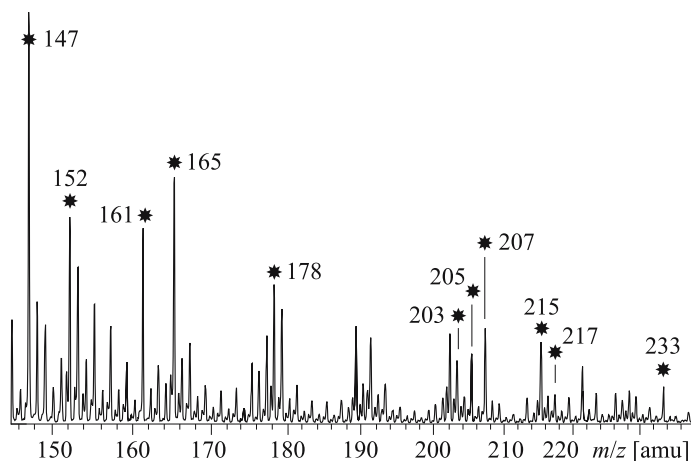


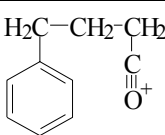
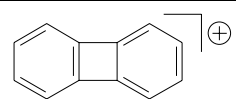
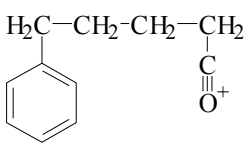
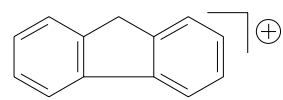
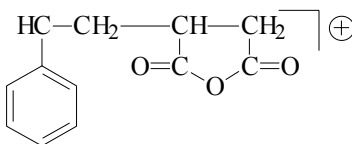
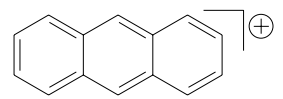
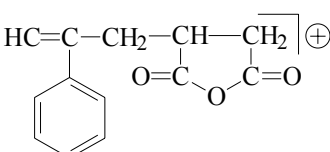
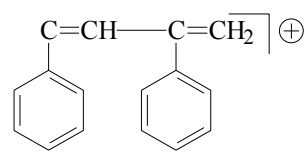
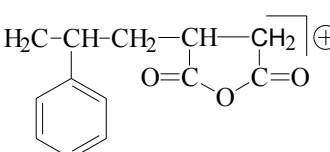
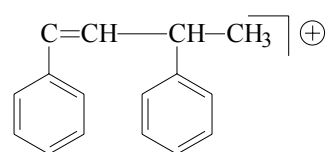
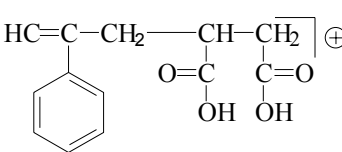
Fig. 5.5 ToF-SIMS spectrum of a maleic anhydride/styrene copolymer grafted from a polyethylene surface. The highlighted key peaks appear from fragments typical for polystyrene sequences and styrene bonded to maleic anhydride units. Table 5.2 shows the structure of the identified key peaks.

polymerization of copolymers on solid surfaces where a covalent bond between the insoluble substrate and the grown polymer brush is formed require surface sensitive techniques conveying a molecular picture about the build-up of the formed copolymers.

The example in Fig. 5.5 shows a section of a ToF-SIMS spectra recorded from a polyethylene surface which was grafted with maleic anhydride and styrene [17]. The questions which had to be answered were, are copolymers formed and is it possible find homo-polymerized poly(maleic anhydride) or polystyrene sequences in the grafted polymer chain? Different key peaks were identified and compared with structures which were recorded from pure polystyrene films. The formation of highly condensed aromatic systems ($m/z=152, 165, 178, 205$ and 207 amu) is typical for the SIMS spectra of polystyrene. The formation of those fragments require undisturbed sequences of homo-polymerized styrene. Hence, during the grafting-from reaction polystyrene sequences are formed. Other key peaks show that styrene is bonded to fragments appearing from the maleic anhydride ($m/z=147, 161, 203, 215, 217,$ and 233 amu).

These fragments indicate the presence of copolymerized species. In the complete spectrum we did not find any fragments of maleic anhydride-maleic anhydride units. It can be concluded that the coupling of maleic anhydride monomers does not take place.

Table 5.2 Identified fragments of the ToF-SIMS spectrum shown in Fig. 5.5

147	$\begin{array}{c} \text{H}_2\text{C}-\text{CH}_2-\text{CH}_2 \\ \\ \text{C} \\ \\ \text{O}^+ \end{array}$ 	152	
161	$\text{H}_2\text{C}-\text{CH}_2-\text{CH}_2-\text{CH}_2$ 	165	
203	$\begin{array}{c} \text{HC}-\text{CH}_2-\text{CH}-\text{CH}_2 \\ \quad \quad \\ \text{O}=\text{C} \quad \text{O} \\ \quad \quad \quad \\ \quad \quad \quad \text{C}=\text{O} \end{array}$ 	178	
215	$\begin{array}{c} \text{HC}=\text{C}-\text{CH}_2-\text{CH}-\text{CH}_2 \\ \quad \quad \\ \text{O}=\text{C} \quad \text{O} \\ \quad \quad \quad \\ \quad \quad \quad \text{C}=\text{O} \end{array}$ 	205	$\text{C}=\text{CH}-\text{C}=\text{CH}_2$ 
217	$\begin{array}{c} \text{H}_2\text{C}-\text{CH}-\text{CH}_2-\text{CH}-\text{CH}_2 \\ \quad \quad \\ \text{O}=\text{C} \quad \text{O} \\ \quad \quad \quad \\ \quad \quad \quad \text{C}=\text{O} \end{array}$ 	207	$\text{C}=\text{CH}-\text{CH}-\text{CH}_3$ 
233	$\begin{array}{c} \text{HC}=\text{C}-\text{CH}_2-\text{CH}-\text{CH}_2 \\ \quad \quad \\ \text{O}=\text{C} \quad \text{C}=\text{O} \\ \quad \quad \quad \quad \\ \quad \quad \quad \text{OH} \quad \text{OH} \end{array}$ 		

5.5 Imaging Time-of-Flight Secondary Ion Mass Spectroscopy

The point of impact of the ion beam has a small lateral resolution and can be easily controlled. This allows us to record series ToF-SIMS spectra from different points of a certain sample surface. From these recorded spectra the count rate of selected peaks can be shown according to their lateral origin. In other words, selected fragment species were represented as image of the sample surface. Driven from developments in the semiconductor and electronic industries the imaging technique have become a high relevance in the last ten years [18–20]. Special liquid metal ion sources (e. g. Ga^+) were developed to get high lateral resolutions which was connected with a loss of the mass resolution.

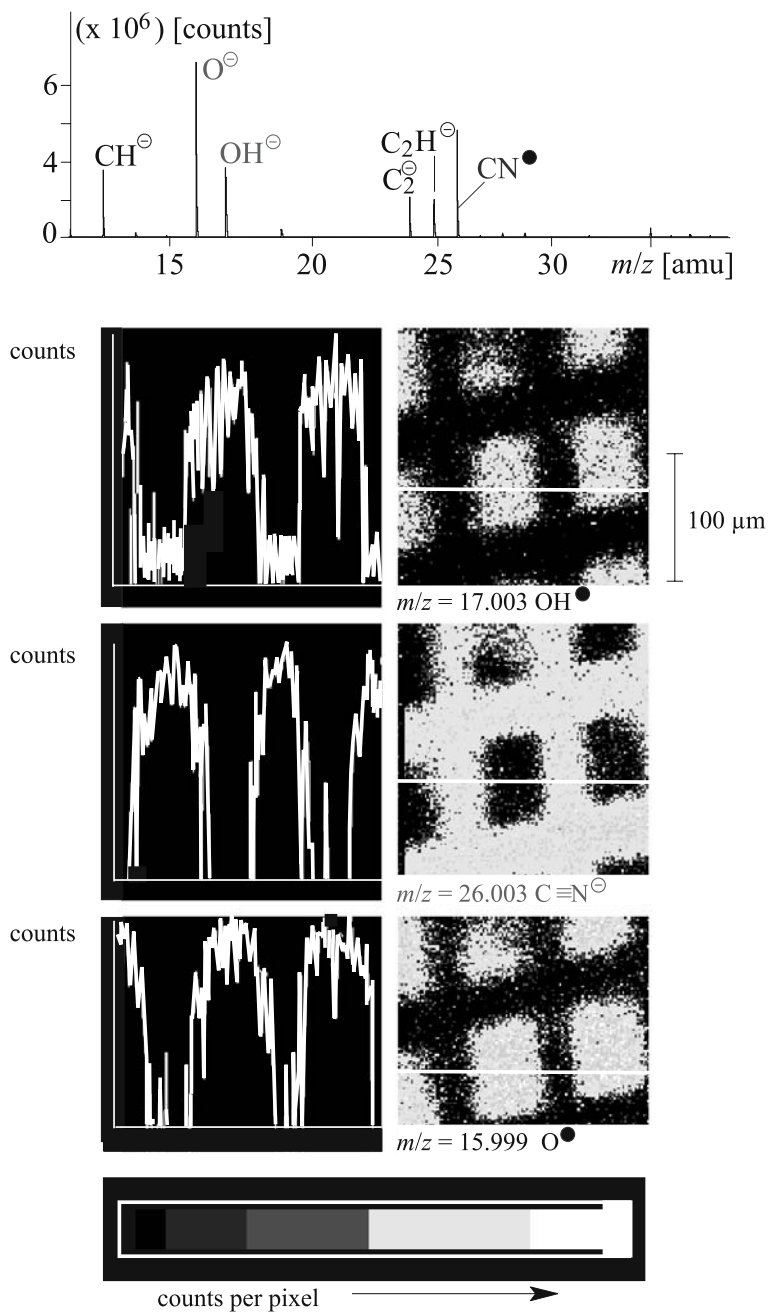


Fig. 5.6 ToF-SIMS spectrum (a) and image (b) of a silicon wafer coated with 3-aminopropyl-trichlorosilane. The coating layer was laterally structured in a micro-printing process

The example in Fig. 5.6 shows a silicon wafer which was laterally structured with an aminosilane. The ToF-SIMS fingerprint spectrum (Fig. 5.6(a)) shows some peaks which can be considered as key fragments for the amine compound (CN^- : $m/z = 26$ amu) and the silicon oxide layer (O^- : $m/z = 16$ amu, and OH^- : $m/z = 17$ amu). The corresponding images are shown in Fig. 5.6(b).

References

1. F.L. Arnot, J.C. Milligan, Proc. Roy. Soc. A156, 538 (1936)
2. F.L. Arnot, Proc. Roy. Soc. A158, 137 (1937)
3. R.F.K. Herzog, F. Viehboeck, Phys. Rev. 76, 855 (1949)
4. H.E. Beske, Z. Angew Phys. 14, 30 (1962)
5. H.W. Werner, H.A.M. DeGrefte, Vakuu-Technik 17, 37 (1968)
6. A. Benninghoven, Phys. Status Solidi 34, K169 (1969)
7. A. Benninghoven, Chem. Phys. Lett. 6, 616 (1970)
8. A. Benninghoven, Phys. Lett. A32, 427 (1970)
9. P. Sigmund, Rev. Roum. Phys. 17, 823–870, 969–1000, 1079–1106 (1972)
10. A. Benninghoven, F.G. Rüdener, H.W. Werner, Aspects of quantitative elemental SIMS analysis, in *Secondary Ion Mass Spectrometry* (Wiley, New York, 1987), pp. 277–328
11. H. Feld, R. Zurmühlen, A. Leute, B. Hagenhoff, A. Benninghoven, Secondary ion emission from polymer materials under keV ion and ^{252}Cf emission bombardment, in *Secondary Ion Mass Spectrometry (SIMS VII)*, ed. by A. Benninghoven, C.A. Evans, K.D. McKeegan, H.A. Storms, H.W. Werner (Wiley, New York, 1990), p. 219
12. D. Pleul, F. Simon, H.J. Jacobasch, Fresenius' J. Anal. Chem. 357, 684 (1996)
13. H. Feld, A. Leute, D. Rading, A. Benninghoven, G. Schmid, J. Am. Chem. Soc. 112, 8166 (1990)
14. D.E. Fowler, R.D. Johnson, D. VanLeyen, A. Benninghoven, Anal. Chem. 62, 2088 (1990)
15. K. Reihls, K. Kirchner, M. Voetz, M. Deimel, F.M. Petrat, D. Wolany, A. Benninghoven, Molecular weight determination of bulk polymer surfaces by static SIMS – Reaction dynamics of fragment ion formation, in *Secondary Ion Mass Spectrometry (SIMS X)*, ed. by A. Benninghoven, B. Hagenhoff, H.W. Werner (Wiley, New York, 1997), pp. 641–644
16. K. Reihls, Thin Solid Films 264, 135 (1995)
17. D. Pleul, S. Schneider, F. Simon, H.J. Jacobasch, J. Adh. Sci. Technol. 12, 47 (1998)
18. H. Rulle, D. Rading, A. Benninghoven, Imaging TOF-SIMS of Molecular Overlayers Limits of Lateral Resolution, in *Secondary Ion Mass Spectrometry (SIMS X)*, ed. by A. Benninghoven, B. Hagenhoff, H.W. Werner (Wiley, New York, 1997), pp. 153–156
19. D. Rading, V. Liebing, G. Becker, M. Mört, H. Fuchs, A. Benninghoven, Investigation of Electron Induced Damaging of Molecular Overlayers by Imaging ToF-SIMS. in *Secondary Ion Mass Spectrometry (SIMS XI)*, ed. by G. Gillen, R. Lareau, J. Bennett, F. Stevie (Wiley, New York, 1998), pp. 501–504
20. M. Deimel, H. Rulle, V. Liebing, A. Benninghoven, Appl. Surf. Sci. 134, 271 (1998)

Monographs and Reviews

- A. Benninghoven, F.G. Rüdener, H.W. Werner, *Secondary Ion Mass Spectrometry* (Wiley, New York, 1987)
- H. Düsterhöft, M. Riedel, B.K. Düsterhöft, *Einführung in die Sekundärionenmassenspektrometrie (SIMS)*, Teubner Studienbücher (Teubner, Stuttgart, Leipzig, 1999)

- J.C. Vickerman, A. Brown, N.M. Reed, *Secondary ion mass spectrometry – Principles and Applications* (Oxford Science, Clarendon Press, Oxford, 1989)
- D. Briggs, M.P. Seah, *Practical surface analysis*, vol. 2. *Ion and neutral spectroscopy* (Wiley, New York, 1992)
- F.A. Stevie, R.G. Wilson, D.S. Simons, M.I. Current, P.C. Zalm, *J. Vac. Sci. Technol.* B12, 2263 (1994)
- A. Benninghoven, *Surf. Sci.* 35, 427 (1973)

Chapter 6

Characterization of Polymer Surfaces by Wetting and Electrokinetic Measurements – Contact Angle, Interfacial Tension, Zeta Potential

Karina Grundke

Leibniz Institute of Polymer Research Dresden, Hohe Str. 6, 01069 Dresden, Germany,
grundke@ipfdd.de

Abstract The determination of the contact angle constitutes the most widely used surface characterization technique. It provides very valuable information on the wetting properties of the surface and is determined by the upper molecular layer at the surface. Looking more deeply into the background of the technique the interpretation is complex and some experimental guidelines should be followed when contact angles are used to calculate the interfacial tension of solid polymer surfaces. The zeta potential which is obtained from electrokinetic investigations provides information about the charge distribution at the polymer-liquid interface. By combining contact angle and zeta potential measurements conclusions can be drawn about the surface chemistry with regard to polar or non-polar functional groups as well as acidic or basic sites available at the outermost surface region and to the interaction of the solid surface with liquids and surface-active substances.

6.1 Introduction

The surface and interfacial properties of polymers play a key role in many technological processes, such as polymer processing and blending, coating and the reinforcement of polymers with fibres, or for their biocompatibility. All these processes are controlled by wetting and adhesion phenomena. Both are strongly influenced by adsorption processes. For example, the adsorption of organic contaminations is an undesirable effect, which diminishes the adhesive strength or wettability. In addition water is adsorbed which is ubiquitous under ambient conditions. Even on relatively hydrophobic polymer surfaces, condensed water is present which can give rise to capillary interaction and may alter the van der Waals forces of the solid surface. This is particularly important for the interaction of two solid surfaces at very small distances or in contact and will affect the adhesion forces considerably. A fundamental understanding of these forces including van der Waals, electrostatic, acid–base, or covalent interactions, is, therefore,

of considerable interest. Despite their importance, these macroscopic interfacial phenomena are still poorly understood. The development of theoretical models and experimental methods for the scientific elucidation of these phenomena is, therefore, a main task of the research in this field.

This chapter describes the theoretical background of surface characterization by two physico-chemical methods, *wetting* and *electrokinetic measurements*, and the progress in developing methods for the measurement of wetting and electrokinetic phenomena, and gives some examples of the application of *contact angle* and *zeta potential* measurements in polymer surface characterization. From these methods conclusions can be drawn about the surface chemistry with regard to polar or non-polar functional groups as well as acidic or basic sites available at the outermost surface region and to the interaction of the solid surface with liquids and surface-active substances.

Wetting involves the interaction of a liquid with a solid including the formation of a *contact angle* at the solid/liquid/fluid interface, the spreading of a liquid over a surface (displacing the fluid initially in contact with that surface), or the penetration of a liquid into a porous solid medium [1]. The importance of wettability in adhesion is well-known: the quality of adhesive bondings and coatings depends strongly on the spreading of these materials on the adherend or solid substrate. The reason is that for good adhesion to take place, the adhesive and the adherend must come into intimate contact. In this case, complete wetting is desirable where the liquid forms a thin film on the solid surface. By reducing the film thickness on a substrate several interesting phenomena occur depending on the chemical and physical properties of the solid–liquid system. If a critical film thickness is reached, the development of holes is often observed. This phenomenon is called *dewetting*.

A large number of wetting phenomena can be explained using the classical thermodynamic and mechanical description of capillarity which has been put forward by Gibbs, Laplace and Young in the nineteenth century. It deals with the macroscopic behaviour of interfaces rather than with the details of their molecular structure and is reviewed in the books of Adamson [2], Rowlinson and Widom [3], and Spelt and Neumann [4]. In the centre of the classical theory of capillarity is the notion of *interfacial tension* γ_{ij} which is the free energy necessary to increase the contact area between two different phases *i* and *j*. Surface free energies (i. e. *surface tensions*), especially of solid–vapour and solid–liquid interfaces, are important thermodynamic parameters to predict the wetting and adhesion properties of polymer materials including also their biocompatibility. Further, the adsorption of substances onto the solids is determined by the surface tension. It is a fundamental parameter of a solid since it depends directly on the binding forces of the material [2]. However, due to the lack of mobility of the molecules in a solid surface, solid surface tensions cannot be measured directly. Several independent approaches have been used in the past to estimate solid surface tensions, including direct force measurements [5–9], contact angles [10–17], capillary penetration into porous solid systems [18–21], sedimentation of particles [22, 23], solidification front interactions with particles [24–26], film flotation [27], gradient theory [28–30],

Lifshitz theory of van der Waals forces [31–33], and theory of molecular interactions [34–35].

Among these methods, contact angle measurements are believed to be the simplest and the most straightforward approach to obtain surface free energies of solids. In spite of the conceptual simplicity, experience has shown that the acquisition of thermodynamically significant and accurate contact angles requires painstaking effort regarding the quality of the solid surfaces (often solid surfaces are rough and chemically heterogeneous to some extent and swelling and reorientation of functional surface groups may occur in contact with the liquid), the purity of the measuring liquids (surfactant solutions or mixtures of liquids should not be used, since they would introduce complications due to preferential adsorption), and the skill of the experimenter, but also regarding the methodology and procedure. Different methods for measuring contact angles are available. The most widely used techniques are the Wilhelmy balance technique and the measurement of contact angles from sessile drops or adhering bubbles. Other methods, such as the capillary penetration of liquids into porous solid systems can also be very useful. The choice of a particular method depends on the geometry of the system and the size and the shape of the sample (flat surface, individual thin fibres, fibre bundles, particles, membranes).

Similar to contact angle measurements, *electrokinetic* or *zeta potential measurements* have long been used in colloid and surface chemistry to determine interaction energies between solid surfaces and contacting substances, mainly to calculate electrostatic interaction forces in lyophobic colloid systems. When a solid surface comes into contact with an aqueous electrolyte solution, an excess of positive or negative charges generally develops at the interface under equilibrium conditions due to the adsorption of charged species (cations or anions, polyelectrolytes or ionic surfactants) in competition to the adsorption of water or due to the ionization of specific functional groups on the surface (dissociation of acidic or basic surface groups). In these cases, the properties of an interface are governed to a large extent by the electrostatic interaction forces. These electrostatic forces can play a direct role in the behaviour of a two-phase system, e.g. creating repulsive or attractive forces between colloidal particles.

Generally, descriptions of the charge distribution at the solid–liquid interface are based on the model developed by Stern [36]. According to Stern, the charges at the solid surface are compensated by charges attributed partly to ions strongly adsorbed at the interface and partly to ions available at a greater distance from the interface due to their thermal movement. This double layer is divided into a fixed or Stern layer and a diffuse or Gouy layer. Today, a well-established model of the electrochemical double layer is the Gouy–Chapman–Stern–Grahame model [37].

The way in which the surface charge at an interface can be probed is through the measurement of electrokinetic phenomena that can be induced at an interface. If the solution is sheared relative to the solid surface, the “mobile” part of the double layer is separated from the “immobile” part and an electrical potential difference arises. The potential at this shear plane is called the electrokinetic or *zeta potential*.

Electrokinetic phenomena refer to dynamic processes that occur when viscous or electrical forces are applied to a charged solid–liquid interface. An externally applied electrical field causes a relative movement of solid and liquid phase (electrophoresis, electroosmosis), or the relative movement of solid and liquid phase generates an electrical potential or produces an electrical current (streaming potential/streaming current, sedimentation potential). In classical terms, electrokinetic phenomena can be described by the Navier–Stokes equation for steady laminar fluid flow to which an electrical body force term and the condition of continuity are added. This relation describes the balance of forces when external forces are applied to a charged interface. It gives insight into the type of information available from measurements of electrokinetic phenomena, namely information concerning net charge and/ or fluid properties near the solid–liquid interface or in other words electrokinetic phenomena depend on charge distribution and surface rheological properties.

Conclusions with regard to the occurrence of dispersion and acid–base interactions can be drawn from the results of zeta potential measurements using the Gouy–Chapman–Stern–Grahame model of the electrical double layer. Since adhesion forces are influenced by acid–base interactions or the adsorption of water at the interface, zeta potential measurements are suitable model experiments to predict interactions of the solid surface under investigation with other contacting substances.

6.2 Theoretical Background of Wetting and Electrokinetic Phenomena

6.2.1 Contact Angle, Interfacial Tension, Laplace and Young Equations

From the point of view of thermodynamic equilibrium, complete and partial wetting are two distinct equilibrium regimes. Complete wetting means that the contact angle between a liquid and a flat solid surface is zero ($\theta_c = 0$, Fig. 6.1(c)). In this case, the liquid forms a very thin film on the solid surface and the long range character of the molecular interactions must be taken into account [37–41].

Partial wetting occurs if the contact angle is finite ($\theta_c > 0$, Fig. 6.1(a) and (b)). The liquid does not spread down to a mesoscopic or a microscopic thickness. Thus, it can be described in terms of macroscopic quantities as will be discussed in this section. Partial wetting, with contact angles greater than 90° (Fig. 6.1(a)), are often called “non-wetting” situations when the liquid tends to ball-up and run off the surface easily.

In the case of partial wetting, the shape of a liquid drop is determined by a combination of surface tension and gravity effects. Surface forces tend to make drops spherical, whereas gravity tends to flatten a sessile drop or to elongate

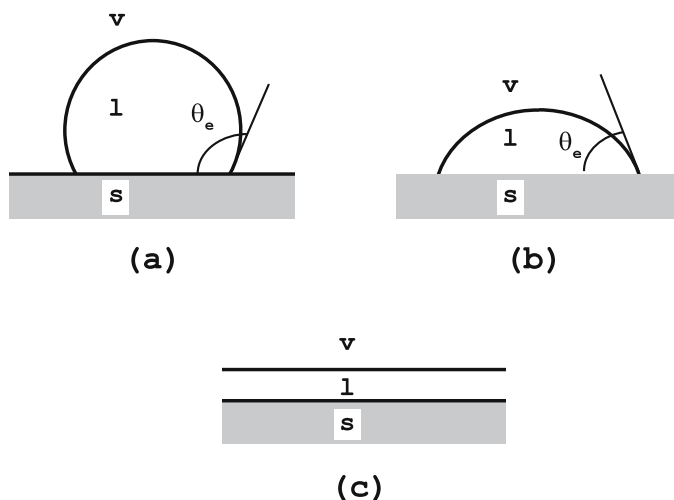


Fig. 6.1 Different wetting situations of a small droplet in contact with a solid surface, where (a) and (b) correspond to partial wetting ($\theta_c > 0$), and (c) corresponds to complete wetting ($\theta_c = 0$)

a pendant drop. The shape of the drop is governed by the Laplace equation of capillarity, as follows:

$$\Delta P = \gamma \left(\frac{1}{R_1} + \frac{1}{R_2} \right) \quad (6.1)$$

According to this well-known equation, the pressure difference ΔP across a liquid–fluid interface is related to its interfacial tension γ and curvature, where R_1 and R_2 are the principal radii of curvature. Derivations of this equation which describes the mechanical equilibrium condition for the liquid–fluid interface can be found in several textbooks (see for instance [2] and [4]). The Laplace equation is the basis for drop shape analysis techniques including a very powerful contact angle method based on axisymmetric drop shape analysis (see Sect. 6.3.1.1).

The equilibrium in the boundary region between two bulk phases can be treated mathematically, using either the concept of “surface tension” or the (mathematically) equivalent concept of “surface free energy”. Because of this mathematical equivalence both terms generally can be used interchangeably. Frequently, the term “surface tension” or “surface free energy” is used if one of the phases is a gas or a vapour. The term “interfacial tension” is often used to describe the tension between two immiscible liquids, i. e., water and oil. The terms “interfacial tension” or “interfacial free energy” are also used in a more general sense to describe the free energy of solid–liquid, solid–vapour, liquid–vapour and liquid–liquid interfaces.

The surface tension can be defined as a force per unit length [2]. If the value of this force per unit length is denoted by γ , then the work done in extending a movable side a distance dx is

$$\text{Work} = \gamma l dx \quad (6.2)$$

Since $l dx = dA$, it gives the change in area and (6.2) can be equally written as

$$\text{Work} = \gamma dA \quad (6.3)$$

Now, γ represents the work required by any reversible process to form a unit area of new surface. It is reported in dyne/cm or mN/m, but also in erg/cm² or mJ/m² which have the same numerical values.

According to the thermodynamics of interfaces, γ_{ij} can be written in terms of the surface excess free energy. That is, γ_{ij} is the change in surface excess free energy produced by a unit increase in area, either of a solid–vapour, solid–liquid, liquid–liquid or liquid–vapour interface, respectively. In general,

$$\gamma_{ij} = \left(\frac{\partial G}{\partial A_{ij}} \right)_{T,p,n} \quad (6.4)$$

or

$$\gamma_{ij} = \left(\frac{\partial F}{\partial A_{ij}} \right)_{T,V,n} \quad (6.5)$$

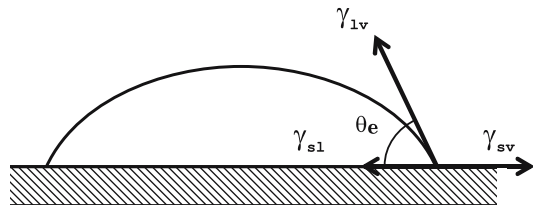
where G is the Gibbs free energy of the system and F the Helmholtz free energy, and A_{ij} the area of the interface between phases i and j . The subscript “ n ” denotes the assumption of adsorption equilibrium, in the case of multicomponent systems. In the thermodynamics of interface-containing systems both quantities, the Gibbs and the Helmholtz free energy are defined as excess quantities, drawing an imaginary and arbitrary dividing mathematical surface (Gibbs surface) between the two phases separated by the interface.

Three interfaces come into play if a liquid drop is deposited on a solid surface, and three interfacial tensions are involved: γ_{sv} , γ_{sl} , γ_{lv} , respectively the solid–vapour, solid–liquid, and liquid–vapour interfacial tensions. The mechanical equilibrium of the triple line fixes the value of the contact angle θ_e at which the liquid–vapour interface meets the solid plane defined by Young’s relation (Fig. 6.2):

$$\cos \theta_e = \frac{\gamma_{sv} - \gamma_{sl}}{\gamma_{lv}} \quad (6.6)$$

It should be noticed that Young’s law is valid even in the presence of gravity because it stems from a mechanical equilibrium condition on the contact line

Fig. 6.2 Young’s force balance giving the equilibrium contact angle

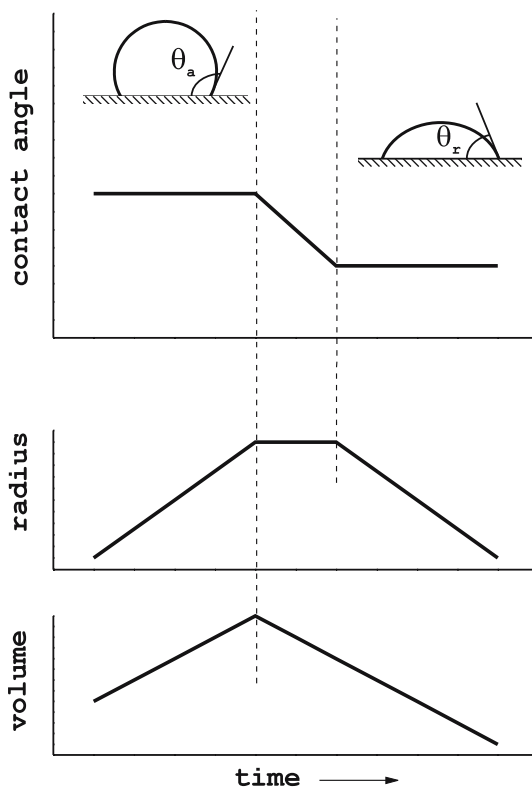


where the effect of body forces are vanishingly small. Gravity affects the shapes of sessile liquid drops in their central region where they are flattened, but not in a small region close to the contact line where the angle is given by Young's law. Nevertheless, there are several problems and limitations of Young's equation mainly due to the structure and constitution of the solid surface and the mutual interactions of the three phases in the close vicinity of the contact line.

6.2.1.1 Contact Angles on Imperfect Solid Surfaces

The derivation of the Young equation assumes that the solid surface is smooth, homogeneous, isotropic, insoluble, non-reactive and non-deformable. Then, a unique contact angle is expected for a given solid-liquid system. However, in contact angle experiments, a range of contact angles is usually obtained, and each contact angle gives rise to a mechanically stable liquid meniscus. In particular, when liquid is added to a drop on a solid or withdrawn from it, the contact angle is observed to increase or decrease, respectively. The maximum contact angle θ_a is called *advancing*, and the minimum θ_r is called *receding*. This behaviour is shown schematically in Fig. 6.3.

Fig. 6.3 Representations of advancing (θ_a) and receding (θ_r) contact angles: The maximum contact angle upon addition of liquid into a sessile drop is called advancing. The apparent contact angle decreases upon withdrawal of liquid, thus resulting in a minimum contact angle, which is known as the receding contact angle



The difference between the maximum (advancing) and the minimum (receding) contact angle is called *contact angle hysteresis*. In pioneering publications (reviewed in [4]) simple models were developed showing that multiple thermodynamic equilibrium states exist on rough and/or heterogeneous solid surfaces. The equilibrium state that corresponds to the absolute minimum in energy is the stable state; the others are metastable with energy barriers between them.

For the determination of the solid surface tension from contact angle data, it is important to use experimentally accessible contact angles which are Young contact angles. On ideal solid surfaces, there is no contact angle hysteresis and the experimentally observed contact angle is equal to θ_Y which is just the equilibrium contact angle θ_e . Since on real solid surfaces contact angle phenomena are very complicated the thermodynamic status of contact angles is often not clear and experimentally observed apparent contact angles, θ_{ap} , may or may not be equal to the Young contact angle θ_Y . Kwok and Neumann [43] considered the circumstances under which experimental contact angles may be used in conjunction with Young's equation, even if contact angle hysteresis is not negligible. They concluded that the experimental advancing contact angle, θ_a , on a smooth, but chemically heterogeneous solid surface can be expected to be a good approximation of θ_Y . While the receding angle on a heterogeneous and smooth surface can also be a Young contact angle, it is frequently found to be non-reproducible. Unlike the situation of the heterogeneous surface, contact angle hysteresis due to roughness precludes an interpretation in terms of solid surface tension. On a rough surface, no equality between θ_a and θ_Y exists. Wenzel (see, for example, [4]) was the first who discussed the *influence of surface roughness* on the apparent or macroscopic contact angle. He introduced a roughness factor, r_w , into the Young equation because he argued that, in the case of a rough solid surface, the interfacial tensions γ_{sv} and γ_{sl} should not be referred to the geometric area, but to the actual surface area. Thus, if

$$r_w = \frac{\text{true} \cdot \text{surface} \cdot \text{area}}{\text{geometric} \cdot \text{surface} \cdot \text{area}} \quad (6.7)$$

one obtains the so-called Wenzel equation

$$r_w (\gamma_{sv} - \gamma_{sl}) = \gamma_{lv} \cos \theta_w \quad (6.8)$$

and the following equation for the contact angle on a rough surface:

$$\cos \theta_w = r_w \cos \theta \quad (6.9)$$

The Wenzel contact angle is the equilibrium contact angle, θ_e , on a rough solid surface corresponding to the absolute minimum in the free energy of the system. Based on this equation it can be predicted that roughness should have a major effect on the contact angle and, hence, on the wettability of surfaces. Since the roughness factor is always greater than unity, equation (6.9) predicts that the Wenzel contact angle will increase with roughness if the contact angle on a smooth surface is greater than 90° and will decrease if it is less than 90° . It is important to note that this conclusion seemingly conflicts with experimental

observations: one finds that with increasing roughness, the advancing contact angle always increases and the receding contact angle decreases. Regarding these discrepancies one has to take into account that the Wenzel equation does not describe contact angle hysteresis and hence the relation between roughness and the phenomenon of hysteresis. In addition, since the physical feature affecting the Wenzel angle is the increased surface area of rough surfaces, no simple correlation is expected with surface roughness alone, as measured, for instance, by a profilometer.

Real surfaces are not only more or less rough. They can be heterogeneous and, therefore, can be composed by domains of different compositions with different wetting properties. Causes for domain structures are surface contaminations or phase separation. However, whereas the effect of roughness on the contact angle is well-known from many observations, the effect of chemical heterogeneity is more difficult to visualize. Cassie and Baxter, at first, calculated an apparent contact angle that represented the absolute minimum in the free energy of a system consisting of a composite surface made up of two types of patches. They obtained the following equation for the apparent contact angle on such a composite surface reviewed in many textbooks (see, for example, [4])

$$\cos\theta_c = a_1\cos\theta_1 + a_2\cos\theta_2 \quad (6.10)$$

where a_1 and a_2 are the fractional surface areas occupied by the two types of patches such that $a_1 + a_2 = 1$, and θ_1 and θ_2 are the corresponding intrinsic contact angles. θ_c is the Cassie contact angle or, like θ_w for a rough surface, the equilibrium contact angle for a heterogeneous solid surface. It should be pointed out that θ_w and θ_c will normally not be amenable to experimental determination [4]. The Cassie contact angle for a heterogeneous surface is only a conceptual measure of wettability and cannot be identified in practice.

6.2.1.2 Line Tension Approach

Another problem which is still an open one is the fact that the interfacial tensions that appear in Young's equation (6.6) are those evaluated far from the contact line. Young's equation ignores the three-phase molecular interactions at the line between the solid, liquid and fluid phases. The interfacial tensions at the contact line may have different values. The introduction of the line tension as a correction term that accounts for the three-phase molecular interactions was an attempt to solve this problem. It is assumed that line tension effects have important implications in a number of areas, as, for example, in heterogeneous nucleation or composite energetics of thin soap films. Depending upon the magnitude of the line tension and the characteristic length scale of the system, it may also have an impact on the wetting/spreading of liquids, spontaneous emulsification, and cell adhesion.

In complete analogy to the accepted thermodynamic definitions for pressure and surface tension, line tension is the one-dimensional analogue of surface tension, just as surface tension is the two-dimensional analogue of bulk pressure. On smooth, homogeneous, and horizontal solid surfaces, a liquid drop would form

a circle of contact with radius R and the corresponding corrected Young equation can be expressed as

$$\frac{\sigma}{R} + \gamma^{(lv)} \cos \theta_l = \gamma^{(sv)} - \gamma^{(sl)} \quad (6.11)$$

where R is the radius of the solid–liquid contact circle in the tangent plane of the solid and σ is the line tension [44]. If the drop is extremely large ($R \rightarrow \infty$), the corrected Young equation may be replaced by the classical Young equation

$$\gamma^{(lv)} \cos \theta_\infty = \gamma^{(sv)} - \gamma^{(sl)} \quad (6.12)$$

where θ_∞ is the contact angle for a large (infinite) drop. Rearranging (6.11) and (6.12) yields

$$\cos \theta_l = \cos \theta_\infty - \frac{\sigma}{\gamma^{(lv)}} \frac{1}{R} \quad (6.13)$$

If θ_l is measured as a function of R , a plot of $\cos \theta_l$ vs. $1/R$ permits one to determine both the contact angle θ_∞ at infinite radius, from the intercept, and the line tension, σ , from the slope. From (6.13) it can be concluded, that $\cos \theta_l$ should be a linear function of $1/R$, provided both the line tension and the liquid surface tension are constant.

Though the line tension is a well-defined thermodynamic quantity, there are still a large number of problems associated with determining both the magnitude and sign of the line tension. As proposed by Gaydos and Neumann [44], line tensions are positive with magnitudes of the order of 10^{-6} J/m for many solid–liquid–vapour systems. This implies that the effect of line tension is negligible in contact angle measurements for drops with a radius larger than a few millimetres. The methods for measuring contact angle, which will be discussed below, do not depend on line tension considerations [44].

6.2.1.3 Film Pressure Concept

Modification of the Young equation is also required if the interfacial tension of the solid–vapour interface is changed due to adsorption of species from the vapour. To solve this problem the film pressure concept was introduced [2]. The solid surface in a solid–liquid–vapour system may be modified by adsorption from the vapour phase. Depending on the liquid, non-volatile liquids or volatile liquids, one has to distinguish between “dry” wetting and “moist” wetting corresponding two extreme situations. In the case of dry wetting, the vapour pressure of the liquid is negligible and it is assumed that the liquid molecules, adsorbed on the solid surface, do not significantly change the surface properties during wetting. If moist wetting occurs the drop is in equilibrium with the vapour of the liquid [2] and usually a film of liquid is adsorbed on the solid surface. It may become thick and even macroscopic in the case of complete wetting. Since usually wetting processes take place under a more or less controlled atmosphere, the gas phase does not only

contain the vapour of the liquid, but also other gases. This effect of adsorption can be expressed by the following equation for the interfacial tension γ_{sv} of the modified solid surface:

$$\gamma_{sv} = \gamma_{sv}^0 - \pi_{e(sv)} \quad (6.14)$$

where γ_{sv}^0 is the surface tension of the bare solid and $\pi_{e(sv)}$ is the so-called “film pressure”. Since adsorption is a spontaneous process, the interfacial tension, γ_{sv} , after adsorption is lower than that of the bare solid. The term $\pi_{e(sv)}$ can be determined according to the following equation by measuring the adsorption of the vapour of the liquid:

$$\pi_{e(sv)} = RT \int_0^{P_{sat}} \Gamma(P) d \ln P \quad (6.15)$$

where $\Gamma(P)$ is the adsorbed amount of the vapour on the solid surface which can be measured by ellipsometry [1]. The film pressure can also be obtained from Derjaguin’s disjoining pressure isotherm [45]. The disjoining pressure $\pi(h)$ is a function of the film thickness. It can be expressed in terms of the Gibbs free energy per unit area of the film. According to Frumkin and Derjaguin the equilibrium macroscopic contact angle is a function of the disjoining pressure:

$$\gamma_{lv} \cos \theta_e = \gamma_{lv} + \int_0^{\infty} \pi(h) dh = \gamma_f(h) - \gamma_{sl} \quad (6.16)$$

where $\gamma_f(h)$ is the film tension. For infinite film thickness, $h = \infty$, $\cos \theta_e = 1$, $\pi(h) = 0$, and $\gamma_f(h) = \gamma_{lv} + \gamma_{sv}$.

It is assumed that the term $\pi_{e(sv)}$ is usually unimportant for non-wetting liquids [2], but it is quite possible that vapour adsorption can be important for more hydrophilic surfaces, particularly if $\gamma_{lv} \sim \gamma_{sv}$ or $\gamma_{lv} < \gamma_{sv}$. Unfortunately, one cannot distinguish the effect of vapour adsorption on the contact angle from other effects.

6.2.2 Wettability of Solid Surfaces

It is of great fundamental, but also practical interest to know how the contact angle depends on the chemical composition of both the solid and the liquid. The solids can be divided in two main types depending on the strength of bonding within the bulk: in hard solids (covalent, ionic, or metallic), and weak molecular solids (bound by van der Waals forces and hydrogen bonds) [38]. Due to the very different binding forces of these materials, the surface free energy at the solid–vacuum interface is also very different and is a fundamental parameter of a solid. Metals and inorganic materials have “high-energy” surfaces ($\gamma_s \sim 500\text{--}5000 \text{ mJ/m}^2$) and polymers (and also molecular liquids) have “low-energy” surfaces ($\gamma_s < 100 \text{ mJ/m}^2$). This difference in surface free energy causes solid surfaces to show different kinds of wetting

behaviour when brought into contact with a liquid. Although the wetting behaviour is determined by Young's equation (6.6), and hence by the relation between the three interfacial tensions, a simplistic argument using γ_{sv} and γ_{lv} can roughly predict the wetting behaviour. For a liquid with $\gamma_{lv} < \gamma_{sv}$, the total free energy would in general be minimized by maximizing the area of the liquid–vapour interface, and the liquid would wet the solid. However, if a liquid has $\gamma_{lv} > \gamma_{sv}$, the total free energy would in general be minimized by minimizing the area of the liquid–vapour interface and the liquid would partially wet the solid. Therefore, knowledge of γ_{sv} for a particular solid surface provides a means of gaining insight into the wetting behaviour of liquids on that surface.

6.2.2.1 Critical Surface Tension

The pioneering work goes back to Zisman [10]. The key observation made by Zisman and his coworkers was that for a given solid, the measured contact angles did not vary randomly as the liquid was varied. They found that for a homologous series of liquids (alkanes) and a given solid, $\cos\theta$ changed smoothly with γ_{lv} and suggested a straight-line relationship (Fig. 6.4). The extrapolation of this straight line to the point where $\cos\theta = 1$ yielded “the critical surface tension γ_c ”, i. e., the surface tension of a liquid which would just wet the solid completely. Using different types of liquids, such as homologous series of alkanes and alcohols, the contact angles changed with the liquid surface tension in a similar manner but the different series did not superimpose completely. However, in the case of simple

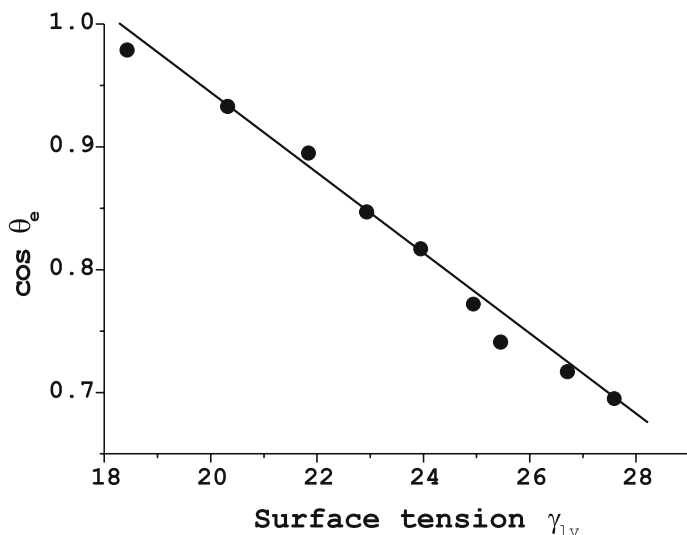


Fig. 6.4 A typical Zisman plot (cosine of θ vs. liquid surface tension) for a polytetrafluoroethylene (Teflon) surface in contact with liquid *n*-alkanes. The critical surface tension γ_c for this system is $\sim 18 \text{ mJ/m}^2$ (from [10])

liquids, such as alkanes where van der Waals forces are dominant, Zisman observed that γ_c is essentially independent of the nature of the liquid, and is a characteristic of the solid alone. Therefore, this empirical quantity was taken to be a measure for the experimentally inaccessible γ_{sv} . The variation in values of γ_c for different solid surfaces shows the same qualitative behaviour as one would expect of γ_{sv} and thus γ_c is a useful quantity for roughly characterizing the wetting behaviour of a solid surface [10, 38].

6.2.2.2 Geometric Mean Combining Rule

Based on Young's equation (6.6) different approaches were developed to determine the solid surface tension. The main difficulty is that Young's equation contains two non-measurable quantities, γ_{sv} and γ_{sl} , that cannot be measured independently. The strategy pursued by all approaches is, therefore, to express γ_{sl} in terms of the other two interfacial tensions, $\gamma_{sl} = f(\gamma_{sv}, \gamma_{lv})$, reducing the number of unknowns in the Young equation. Thus, the interfacial tension which is caused by the interaction between solid and liquid molecules has to be calculated from the knowledge of the surface properties of the solid and of the liquid phase. Strictly speaking, this is impossible. The available models are, therefore, empirically modified or they should be theoretically sound approximations.

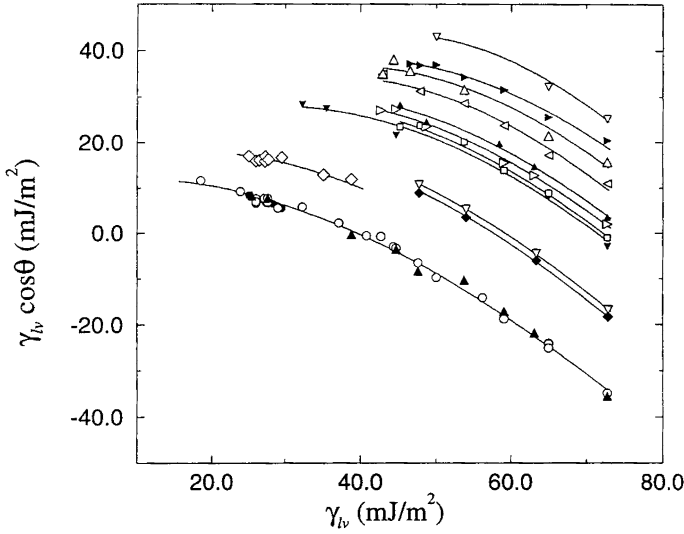
One such approximation that has proved to be very stimulating to research on contact angle phenomena was proposed by Girifalco and Good assuming that mainly van der Waals forces act between all molecules [46]. It is based on Berthelot's (geometric mean) combining rule. According to this rule the free energy of adhesion W_{sl}^a can be approximated in terms of the free energy of cohesion of the solid, W_{ss}^c , and the free energy of cohesion of the liquid, W_{ll}^c . Girifalco and Good modified the geometric mean combining rule by introducing an empirical correction factor called interaction parameter Φ .

$$\gamma_{sl} = \gamma_{sv} + \gamma_{lv} - 2\Phi\sqrt{\gamma_{sv}\gamma_{lv}} \quad (6.17)$$

This interaction parameter Φ is a characteristic of a given system that can be evaluated from molecular properties of the solid and the liquid phase. It was found to be very close to unity when dominant cohesive and adhesive forces were of the same kind.

6.2.2.3 Equation-of-State Approach for Solid-Liquid Interfacial Tensions

Based on experimental contact angle data, Neumann and coworkers have shown that the values of $\gamma_{lv}\cos\theta$ change systematically with γ_{lv} in a very regular fashion, from hydrophobic surfaces, such as polytetrafluoroethylene, to hydrophilic surfaces, such as poly(propene-*alt*-*N*-methylmaleimide), and that the patterns are independent of the experimental technique [43] (cf. Fig. 6.5).



●	FC-721-coated mica
○	FC-722-coated mica and wafer
▲	FC-725-coated wafer
◇	Teflon FEP
◆	hexatriacontane
▽	cholesteryl acetate
▼	poly(propene- <i>alt</i> - <i>N</i> -(<i>n</i> -hexyl)maleimide)
□	poly(<i>n</i> -butyl methacrylate)
▷	polystyrene
▲	poly(styrene-(hexyl/10-carboxydecyl 90:10)-maleimide)
◁	poly(methyl methacrylate/ <i>n</i> -butyl methacrylate)
△	poly(propene- <i>alt</i> - <i>N</i> -(<i>n</i> -propyl)maleimide)
▶	poly(methyl methacrylate)
▽	poly(propene- <i>alt</i> - <i>N</i> -methylmaleimide)

Fig. 6.5 Plots of $\gamma_{lv}\cos\theta$ vs. γ_{lv} for various solid polymer surfaces (from [43])

Thus, one can conclude that the values of $\gamma_{lv}\cos\theta$ depend only on γ_{lv} and γ_{sv} , i. e. $\gamma_{lv}\cos\theta$ is a function of γ_{lv} and γ_{sv} :

$$\gamma_{lv}\cos\theta = F(\gamma_{lv}, \gamma_{sv}) \quad (6.18)$$

Because of Young's equation (6.6), the experimental contact angles imply that γ_{sl} can be expressed as a function of only γ_{lv} and γ_{sv} :

$$\gamma_{sl} = F(\gamma_{lv}, \gamma_{sv}) \quad (6.19)$$

These experimental results are consistent with the equation of state approach for interfacial tensions [47]: A recent formulation of the equation-of-state can be written as

$$\gamma_{sl} = \gamma_{sv} + \gamma_{lv} - 2\sqrt{\gamma_{sv}\gamma_{lv}}e^{-\beta(\gamma_{lv}-\gamma_{sv})^2} \quad (6.20)$$

Combining (6.20) with the Young equation (6.6), one obtains

$$\cos\theta = -1 + 2\sqrt{\frac{\gamma_{sv}}{\gamma_{lv}}}e^{-\beta(\gamma_{lv}-\gamma_{sv})^2} \quad (6.21)$$

Thus, the solid surface tension can be determined from experimental contact angles and liquid surface tensions when β is known. β was determined experimentally for a given set of γ_{lv} and θ data measured on one and the same type of solid surface by least-squares analysis technique. A weighted mean β was calculated as $0.0001247 \text{ (m}^2/\text{mJ)}^2$ [47]. It was found that calculations of γ_{sv} values with slightly different β values have very little effect on the outcome [43]. However, it is still an open question of whether or not β in (6.21) is a “universal” constant, i. e. independent of the solid surface. Such a question can be addressed only after an even larger body of accurate contact angle data on various solids has been generated.

Recently, van Giessen, Bukman and Widom used a generalized van der Waals theory to model a diverse series of liquids on a low-energy substrate and to calculate the corresponding surface tensions and contact angles. The aim of this study was to investigate how the behaviour of $\cos\theta$ with γ_{lv} is related to molecular interactions [49]. Their results showed that it was indeed possible to reproduce behaviour similar to that seen in experiments (cf. Figs. 6.4 and 6.5), with the data for $\cos\theta$ plotted versus γ_{lv} falling in a narrow band which could almost be interpreted as a smooth curve. In their calculation, the width of the band depended on the ranges of the model parameters and on the details of the molecular structure. The main limitations of their model were its simplicity and the fact that they had to use a combining rule to estimate the interaction between the solid and the fluid.

Several other approaches have been developed to calculate the solid–vapour surface tension from contact angle measurements [50].

6.2.2.4 Surface Tension Component Approaches

The surface tension component approach was pioneered by Fowkes. He postulated that the total surface tension can be expressed as a sum of different surface tension components, each of which arises due to a specific type of intermolecular forces. Fowkes [see 11, 50] argued that in van der Waals systems, only dispersion forces could effectively operate across the interface. Therefore, he obtained

$$\gamma_{sl} = \gamma_{sv} + \gamma_{lv} - 2\sqrt{\gamma_{sv}^d\gamma_{lv}^d} \quad (6.22)$$

where γ_{sv}^d and γ_{lv}^d are the dispersion force components of the solid and liquid surface tension, respectively. Combining (6.22) with Young's equation (6.6), one obtains

$$\cos \theta = -1 + \frac{2(\gamma_{sv}^d \gamma_{lv}^d)^{1/2}}{\gamma_{lv}} \quad (6.23)$$

Equation (6.23) is known as the Girifalco–Good–Fowkes–Young equation. Using this equation the dispersion components of the solid or liquid surface tension were evaluated.

Owens and Wendt and Kaelble and others [see 50] argued that the “polar” interaction could be computed using the same geometric mean mixing rule as for the dispersion force interaction. One obtains the following equation:

$$\gamma_{sl} = \gamma_{sv} + \gamma_{lv} - 2\sqrt{\gamma_{sv}^d \gamma_{lv}^d} - 2\sqrt{\gamma_{sv}^p \gamma_{lv}^p} \quad (6.24)$$

where γ_{sv}^p and γ_{lv}^p are the polar force components of the solid and liquid surface tension. If the contact angles of at least two liquids, usually a polar and a non-polar liquid, with known γ_{lv}^d and γ_{lv}^p parameters are measured on a solid surface, the γ_{sv}^d and γ_{sv}^p parameters of that solid can be calculated by combining (6.24) with the Young equation. One obtains two equations with two unknowns. This concept of the “polar fraction” for the surface tension and the principle of “polarity matching” to optimize adhesion became a wide spread in many fields of applied surface science. However, the theoretical background of this approach is poor, especially concerning the assumption that the polar component of the surface tension can be calculated by a geometric mean combining rule from the internal polar cohesive forces. It can easily be proved that different sets of probe liquids lead to different polarity splits for a given solid.

Another approach using the concept of surface tension components was developed by Good, van Oss and Chaudhury [51]. According to this model, characteristic acid and base parameters of the surface tension may be determined from contact angle measurements. Three parameters are calculated, namely the Lifshitz–van der Waals component γ_i^{LW} , which contains the dispersion component, the electron donor component γ_i^- , and the electron acceptor component γ_i^+ , characterizing the solid surface tension. One has to use three liquids with known surface tension components, γ_{lv}^{LW} , γ_{lv}^- , γ_{lv}^+ , to measure the contact angles of these three liquids on the solid surface. It was found that most solids appear to be almost totally basic, including materials with known acidic character, such as poly(vinylchloride) and this therefore suggested that the consistency of the method should be checked [50]. We used contact angle measurements to determine the acid–base properties of treated carbon fibres according to this model [52]. The test liquids used were α -bromonaphthaline, which is a non-polar test liquid; water, which is considered as amphoteric test liquid in the literature [51]; and dimethylsulfoxide and formamide, which were used as model basic liquids in the literature [51]. However, according to Gutman's scale [53], the latter are also acidic. In other words, they are capable

of exerting both acidic and basic type of interactions. Depending on these test liquids we predicted different acid–base properties for the treated carbon fibres. From our measurements we concluded that formamide acted as an acid probe with the carbon fibres.

At present, no general consensus exists on the interpretation of contact angles in terms of solid surface tensions. The incompatibility of the two major schools, the equation-of-state approach [467] and the surface tension component approach [51] is rooted in the theory. Recent progress in the correlation of contact angles with solid surface tensions is summarized in a review by Kwok and Neumann [43].

6.2.3 Origin of Surface Charge, Electrical Double Layer, Zeta Potential

Excess charge at a polymer surface can originate from two sources, i. e. from the acid–base dissociation of ionizable functional groups, and/or from the specific adsorption of charged species. In Fig. 6.6, these possible charging mechanisms of polymer surfaces are shown schematically. A quantitative treatment of these mechanisms can be found in [54–58].

Polymer surfaces, which do not have dissociating surface groups, may still acquire a surface charge by preferential adsorption of one kind of ions from electrolyte solution. This process is described by Stern's theory [36] from which a relation was derived connecting the zeta potential and the adsorption free energies of anions Φ_- and cations Φ_+ [57]. The free energy of adsorption of a dissolved species on a solid can be calculated from its adsorption isotherm. In

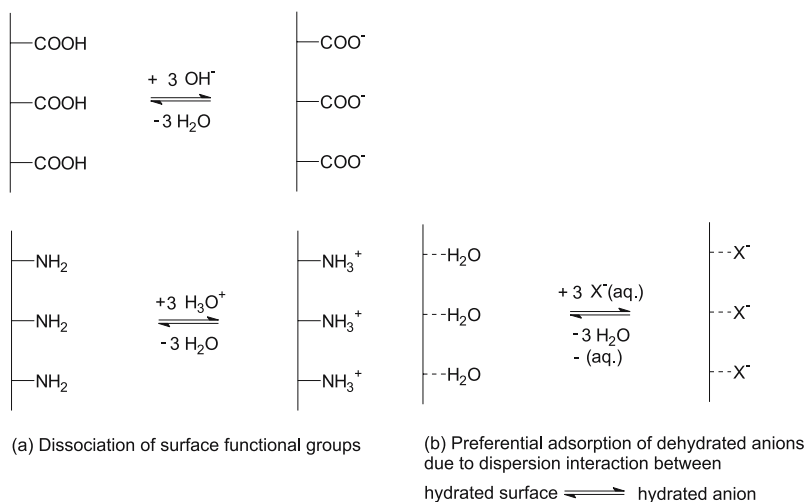


Fig. 6.6 Possible charge formation mechanisms at the polymer/electrolyte interface

the case of ions, it can be obtained by concentration dependent zeta potential measurements. Considering a solid in presence of a dilute 1-1 electrolyte solution, Sterns's equation [36] describes the charging of the solid surface, as follows:

$$\frac{\varepsilon}{4\pi\delta_0}(\Psi_0 - \zeta(c)) = \left(1 + \frac{1}{c} \cdot \exp\left(\frac{\Phi_- - F\zeta(c)}{RT}\right)\right)^{-1} - \left(1 + \frac{1}{c} \cdot \exp\left(\frac{\Phi_+ + F\zeta(c)}{RT}\right)\right)^{-1} \quad (6.25)$$

Φ_+ and Φ_- are the non-electrostatic components of the adsorption free energies for cations and anions, respectively. Ψ_0 is the surface potential, ζ the zeta potential, δ_0 the distance between the shear plane and surface, c the electrolyte concentration, R the gas constant, F Faraday's constant and T the absolute temperature.

The maximum value of the absolute value of $\zeta(c)$ occurs at

$$c_{\max} = \exp\left(\frac{\Phi_+ + \Phi_-}{2RT}\right) \quad (6.26)$$

and

$$\zeta_{\max} = \frac{\Phi_- - \Phi_+}{2F} \quad (6.27)$$

According to these relations the molar adsorption free energies Φ_+ and Φ_- can be calculated from the concentration, c_{\max} , and the maximum zeta potential ζ_{\max} from concentration dependent zeta potential measurements. As shown schematically in Fig. 6.7, most polymers show a parabolic dependence on concentration of electrolyte solutions. The extremum can be attributed to a maximum

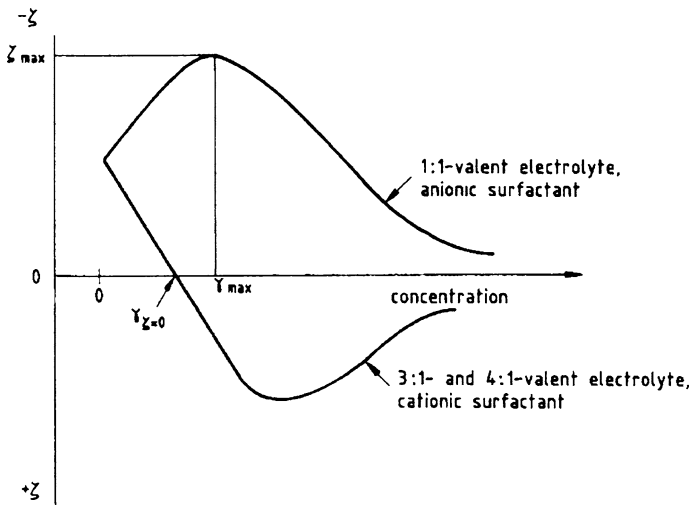


Fig. 6.7 The dependence of the zeta potential of negatively charged polymers on the concentration of electrolyte and ionogenic surfactant solutions

coverage of the surface with ions due to specific adsorption processes. At higher concentrations, the absolute potential is decreasing, because the electrostatic attraction of counterions is dominating in this regime and diminishes the potential difference between surface and bulk solution.

Assuming that anions are partially dehydrated and adsorbed in the so-called inner Helmholtz plane by dispersion interactions and that the hydrated cations are suitable as counter ions in the diffuse part of the double layer (cf. Fig. 6.8), the value of ζ_{\max} in KCl solutions should correspond with dispersion forces occurring at solid surfaces according to Jacobasch et al [59]. It was found that ζ_{\max} values of poly(acrylonitrile) fibres increase with increasing Hamaker constant when the porosity is kept constant and that they decrease with increasing porosity as expected from the microscopic theory of dispersion force [59].

Since adsorption of ions at the solid–electrolyte interface takes place in competition with the adsorption of water, it was often observed that the ζ_{\max} values in KCl solutions are lower the higher the hydrophilicity of the solid [59]. In many cases, ζ_{\max} correlated directly with the cosine of the contact angle between polymer and water. In other words, the lower the water contact angle and, hence, the hydrophilicity, the lower the ζ_{\max} values [59]. Experiments have shown that ζ_{\max} corresponds very well with the adhesion behaviour of solids due to dispersion forces. Examples are given in [60] for pigment soil adhesion on fibres and for reinforcement of polymers [61]. Weidenhammer and Jacobasch [57] concluded from zeta potential and AFM (Atomic Force Microscopy) measurements that there is an influence of adsorbing electrolyte ions on the adhesion of polymers, which

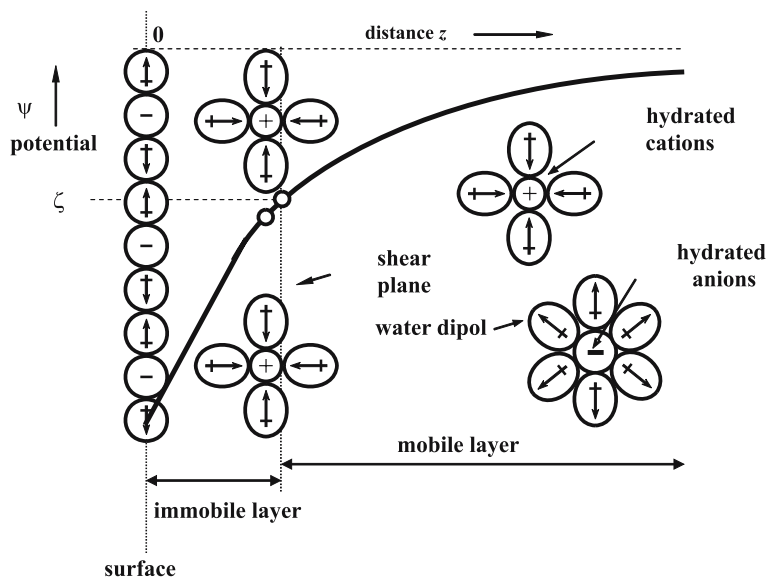


Fig. 6.8 Scheme of the electrical double layer according to the Gouy–Chapman–Stern–Grahame model

can be quantitatively characterized by zeta potential measurements. Hydroxyl anions adsorbed much stronger than chloride anions onto poly(etheretherketone) (PEEK) surfaces. The adhesion forces between PEEK surfaces and silicon nitride tips of the AFM are lower in KOH solution than in KCl solution corresponding to the different adsorption free energies of the anions. The larger the free energy of anion adsorption, the smaller was the attractive force between polymer surface and AFM probe. Complete surface coverage with anions yielded complete absence of attractive interaction.

Figure 6.8 shows a scheme of the electrical double layer based on the Gouy–Chapman–Stern–Grahame model. According to this model the electrical double layer is divided into three parts [37]. In the inner Helmholtz plane (IHP), the adsorbed charge carriers have lost fully or partially their hydration shell and are adsorbed strongly on the solid surface. The ions in the outer Helmholtz plane (OHP) are charged oppositely and have not lost their hydration shell. But, they are also strongly adsorbed via Coulomb forces. The remaining excess of charges is compensated by ions in the so-called diffuse or mobile layer. This model separates the counterion region of the double layer into a compact, surface-bound “Stern” layer, wherein potential decays linearly, and a diffuse region which obeys the Poisson–Boltzmann relation.

The mathematical treatment of the model according to Börner et al. [55] allows evaluation of the Brønsted acidity, basicity and adsorption properties of the solid

Table 6.1 Relations between the adsorption potentials Φ_i of H^+ and OH^- ions and the dissociation constants of basic and acidic surface groups (pK_A and pK_B values from [59])

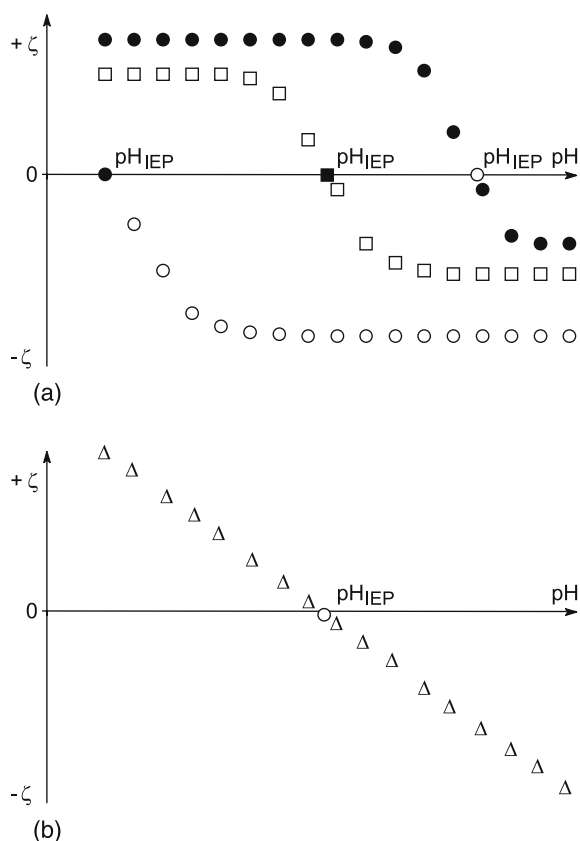
Physico-chemical properties of surface-modified polymers

<p style="text-align: center;">Acidic surface</p> $HX + H_2O \rightleftharpoons H_3O^+ + X^-$ $K_A = \frac{a[H_3O^+] \cdot a[X^-]}{a[HX]}$	<p style="text-align: center;">Basic surface</p> $Y + H_2O \rightleftharpoons HY^+ + OH^-$ $K_B = \frac{a[HY^+] \cdot a[OH^-]}{a[Y]}$
$\Delta G_i^0 = -R \cdot T \ln(K_i)$ $\downarrow \Delta G_i^0 \Big _{\zeta=0} = \Phi$ $\Phi_i = -R \cdot T \ln(K_i) \Big _{\zeta=0}$	
$\exp \left[-\frac{\Phi_{OH^-}}{R \cdot T} \right] = \frac{10^{-pK_A} \cdot a[H_2O]}{K_w \cdot l/mol}$	$\exp \left[-\frac{\Phi_{H^+}}{R \cdot T} \right] = \frac{10^{-pK_B} \cdot a[H_2O]}{K_w \cdot l/mol}$

surface from the zeta potential and the known properties of the aqueous electrolyte solution (pH value and ionic strength). This model assumes that the potential of the outer Helmholtz plane Ψ^{OHP} is approximately equal to the ζ potential. The parameters resulting from the solution of a set of equations by means of a stochastic trail and error procedure, which includes the measured function $\zeta = \zeta(\text{pH}, c^\infty)$ as input values (for more details see [55, 56, 58]), are the molar adsorption free energies of the ionic species Φ_{K^+} , Φ_{X^-} , Φ_{H^+} , Φ_{OH^-} , the capacity C^{HP} , and the charge density σ^{diffuse} . From the adsorption molar free energies Φ_{H^+} and Φ_{OH^-} , pK_a and pK_b values can be calculated (cf. Table 6.1). The latter values are parameters to describe the Brønsted acid–base properties of a surface, that means the dissociation of acidic and basic surface groups. It should be pointed out that the molar adsorption free energies, Φ_i , represent the non-electrostatic adsorption and do not describe the electrostatic influence on the adsorption equilibration between the charged surface and ionic species, i , from the liquid phase. Hence, Φ_i is a characteristic value to describe the adsorption equilibrium at the so-called isoelectric point.

It should be pointed out, that experimentally derived parameters from sophisticated models of electrokinetic phenomena should be considered as approximate values. One problem is the increase of the number of parameters needed in such

Fig. 6.9 Schematic representation of zeta potential versus pH plots for polymer/electrolyte interfaces. (a) ● dissociable basic functional groups, □ dissociable acidic and basic functional groups (amphoteric behaviour), ○ dissociable acidic functional groups. (b) Δ non-polar surface without dissociable functional groups



models to describe the electrokinetic phenomena, in particular electrokinetically inaccessible parameters, e. g. viscosity. Therefore, absolute quantitative values are not their essence. However, experimentally derived parameters from zeta potential measurements are related to surface charge in such a way as to provide useful information regarding the source and magnitude of surface charge.

Generally, the presence of acidic or basic functional groups corresponds with the ζ -pH plot, as is shown schematically in Fig. 6.9. The increase in negative zeta potential with increasing pH is due to the increased dissociation of acidic surface groups. In the case of basic groups, the number of positively charged groups increases with decreasing pH. Complete dissociation of acidic or basic functional groups is related to the plateau in the ζ -pH plot. Non-polar polymers yield ζ -pH plots without plateaus due to the lack of dissociable groups. The increase in negative zeta potential with pH is caused by the increasing adsorption of hydroxyl (OH^-) ions.

6.3 Experimental Techniques

6.3.1 Contact Angle Measurements: Sessile Drop or Adhering Bubbles, Wilhelmy Balance Technique, Capillary Penetration

6.3.1.1 Sessile Drop or Adhering Gas Bubble Techniques

The sessile drop or, alternatively, the adhering gas bubble method are the most commonly used techniques for flat surfaces. In these cases, the contact angles are measured from the drop profile, either by the *conventional goniometer-telescope* or the more sophisticated and advanced *axisymmetric drop shape analysis (ADSA)*.

Goniometer Technique.

Using this method, which is the most widely used procedure, the contact angle is determined simply by aligning a tangent with the sessile drop profile at the point of contact with the solid surface. Contact angles at both sides of the drop should be measured and averaged in order to achieve higher accuracy.

The results of this conventional goniometer technique are somewhat subjective and dependent on the experience of the operator. Although certain training procedures can be used to improve the reproducibility, the accuracy of this method is usually $\pm 2^\circ$ at the best. In general, placing a tangent to the sessile drops manually, e. g. by using a goniometer, is the most convenient method if high accuracy is not required. Advantages of this method are the very small quantities of liquid required and the small area of solid surfaces as small as a few square millimeters. We could show [48] that this procedure can produce misleading contact angle results, in terms of surface energetics. More details of this technique can be found in [4, 63].



Fig. 6.10 Commercial contact angle device (DSA 10, Fa. Krüss) for measurements with sessile droplets on planar solid surfaces

Axisymmetric Drop Shape Analysis-Profile (ADSA-P).

This technique, which is practiced by the present author, is a powerful method to determine simultaneously contact angles and liquid–fluid interfacial tensions from profiles of liquid drops. In addition to these two parameters, the drop volume and the drop surface area, as well as the drop radius, all with their corresponding 95 % confidence limits, are also output. Apart from local gravity and densities of liquid and fluid phases, the only information required by ADSA-P is several arbitrary but accurate coordinate points selected from the experimental drop profile. Assuming that the experimental drop is Laplacian and axisymmetric, ADSA-P finds a theoretical profile, based on the Laplace equation of capillarity (cf. 6.1), that best matches the drop profile extracted from an image of a real drop. The best fit identifies the correct surface/interfacial tension from which the contact angle can be determined by a numerical integration of the Laplace equation.

With respect to low-rate dynamic contact angle measurements by ADSA-P, liquid is supplied to the sessile drop from below the solid surface using a motorized syringe device as can be seen schematically in Fig. 6.11. It is a good strategy

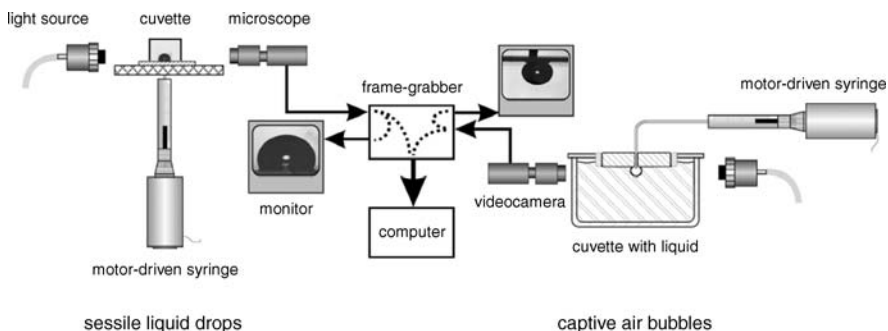


Fig. 6.11 Experimental set-up for ADSA-P contact angle measurements using sessile liquid drops or captive air bubbles: A CCD camera is mounted on a microscope. The video signal of the sessile drop or captive bubble is transmitted to a digital video processor, which performs the frame grabbing and digitization of the image. A SPARCstation or PC computer is used to acquire images from the image processor and to perform the image analysis and computation

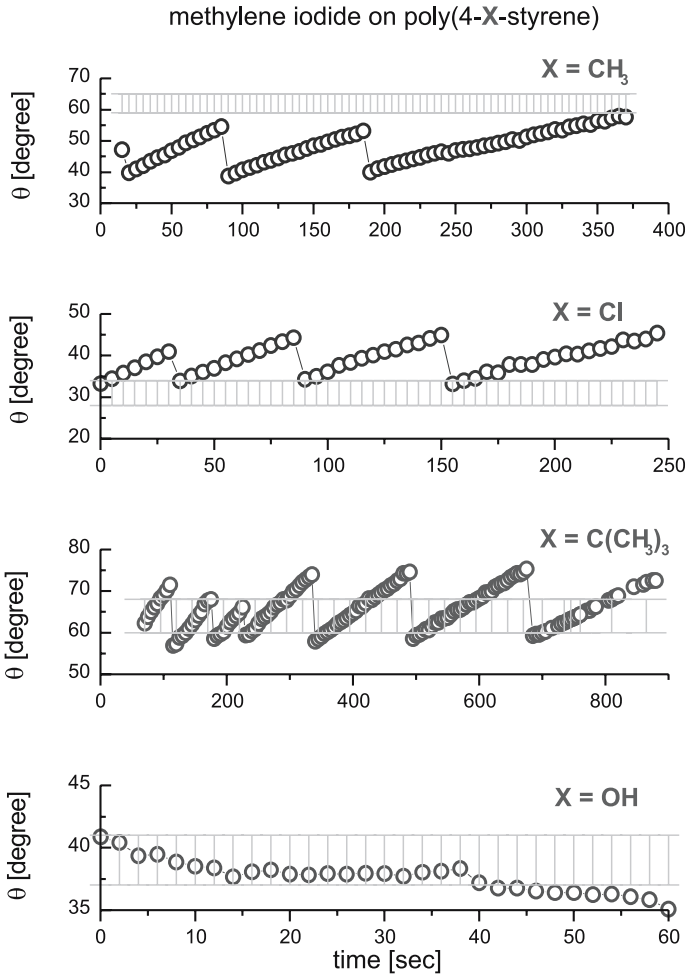


Fig. 6.12 Advancing contact angles of methylene iodide measured by ADSA-P on different poly(4-X-styrene) films in comparison with the mean advancing contact angles determined by a conventional goniometer technique (bar graph). Only ADSA-P reveals slip/stick contact angle behaviour and time dependent changes of the advancing contact angle due to swelling and partial dissolution

[21, 48] first to deposit a drop of liquid on a given solid surface covering a small hole, which is needed to supply liquid from below. This experimental procedure is necessary since ADSA-P determines the contact angles based on a complete and undisturbed drop profile. While the drop is growing at very slow motion of the three-phase contact line, a sequence of images is recorded by the computer (typically 1 image every 2–5 seconds). Since ADSA-P determines the contact angle and the three-phase contact radius simultaneously for each image, the advancing and receding dynamic contact angles as a function of the three-phase contact radius

(i. e. location on the surface) can be obtained. Furthermore, the liquid surface tension is determined for each image, and can also be recorded. Details of the ADSA methodology, including background mathematical analysis, fundamental equations and optimizations are given elsewhere [4, 62–68]. ADSA-P can achieve an accuracy of $\pm 0.05 \text{ mJ/m}^2$ or better for surface tension and $\pm 0.2^\circ$ or better for contact angles.

ADSA-P has several advantages over traditional methods:

1. Since the coordinates of the drop apex are optimization parameters, the drop can be measured from any convenient reference frame, and all measured points on a drop profile are equally important. Only the density difference across the interface, the magnitude of the local gravity acceleration, and several arbitrary coordinate points selected along the drop profile are required as input parameters.
2. There is no restriction on the drop size, the surface tension and the contact angle, as long as the latter is not close to zero.
3. Besides interfacial tensions and contact angles, volume, surface area and radius of curvature are also output of ADSA-P.

An important advantage of this procedure for polymer surface characterization is that the quality of the surface is checked indirectly by means of the measured contact angles. If a solid surface is not very smooth, irregular and inconsistent contact angle values will be seen as a function of the three-phase contact line. Contact angle complexities, such as slip/stick contact angle behaviour, caused by swelling processes or partial dissolution of the surface of non-inert polymer materials, can also be revealed by this contact angle technique [48, 63] (Fig. 6.12).

6.3.1.2 Wilhelmy Balance Technique

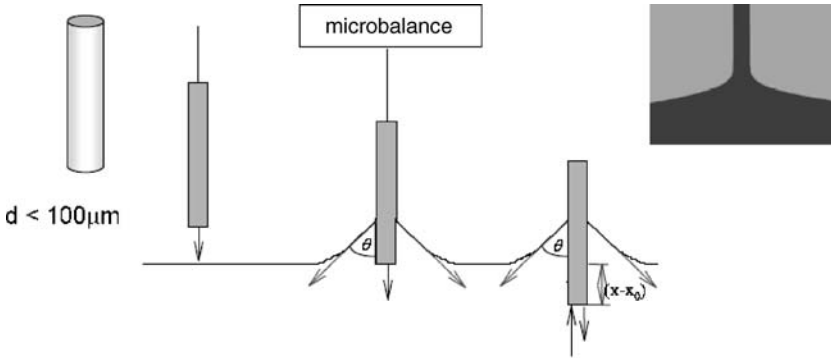
The Wilhelmy balance method is an excellent technique to measure contact angles indirectly on a flat plate of known perimeter of the plate cross-section or on thin fibres of known perimeter. In the classical Wilhelmy balance experiment the force F measured by an electrobalance is the sum of gravitational, interfacial, buoyancy, and hydrodynamic forces:

$$F = m g + p \gamma_{lv} \cos \theta + (x - x_0) A \Delta \rho g + p (x - x_0) \tau_0 \quad (6.28)$$

where mg is the weight contribution of the solid sample, p is the perimeter of the sample in contact with the liquid, γ_{lv} is the liquid–vapour surface tension, θ is the contact angle of the liquid lens on the solid sample, $(x - x_0)$ is the immersion depth, $\Delta\rho$ is the density difference between the liquid and air phase, g is the (local) gravitational acceleration, and τ_0 is the shear stress. In the case of low-molecular liquids, shear forces can be neglected. For thin fibres (diameters less than $100 \mu\text{m}$), the buoyancy force can also be ignored and the following simple equation results:

$$\gamma_l \cos \theta = \Delta m g / p = F / p \quad (6.29)$$

The perimeter p of the sample can be determined by using a liquid of known surface tension for which the contact angle is zero. The contact angle θ of another



$$F = m g + U \gamma_1 \cos\theta + (x-x_0) A \rho g + U (x-x_0) \tau_0$$

$$\gamma_1 \cos\theta = \Delta m g/p = F/p$$

Fig. 6.13 Scheme of the force measurement in a Wilhelmy balance experiment.

liquid with known surface tension γ_{lv} can then be determined by measuring the force per unit length of the perimeter p .

In the special case, when the contact angle is zero and the perimeter is known, the measured force is related directly to the liquid surface tension. Details of the technique can be found in [62]. Several drawbacks of the method should be mentioned. The high sensitivity of the electrobalance employed in the Wilhelmy experiment can be exploited only if the perimeter is constant. In addition, the plate must have the same composition and morphology at all surfaces: front, back, and

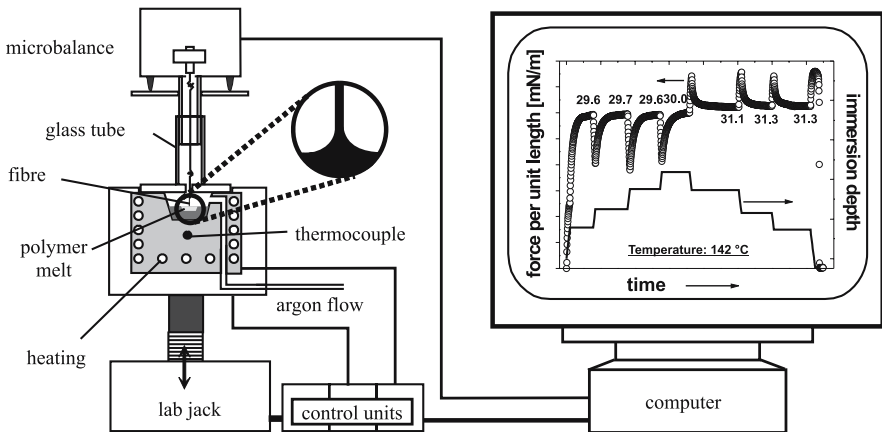


Fig. 6.14 Experimental set-up of a Wilhelmy balance device to determine contact angles and liquid surface tensions at room and elevated temperatures

both edges. This condition may be difficult to meet, particularly if one wants to investigate films or anisotropic systems. Swelling of the solid may also become a problem because it may change the perimeter in an uncontrollable manner. Finally, adsorption of the vapour of the liquid at various parts of the gravimetric system may change the balance output.

An advantage of the Wilhelmy balance method is its very high sensitivity. It provides very accurate advancing and receding contact angles, free of operator subjectivity. Several commercial instruments are available consisting of a microbalance and a motor driven movable table, on which the liquid container is placed. An experimental setup of a home-made device is shown in Fig. 6.14. This apparatus can also be used for contact and surface tension measurements at elevated temperatures.

6.3.1.3 Capillary Penetration Technique

It is well-known that serious problems arise when contact angles of sessile liquid drops are measured directly on the surfaces of porous materials, such as membranes or powders. Surface roughness, heterogeneity, and the penetration of the liquid drop into the porous material may affect the measured contact angles, causing meaningless angles in terms of Young's equation and hence in terms of a surface energetic interpretation of the contact angle data. At present, many authors follow another concept to determine contact angles on porous materials. They use an indirect method based on the capillary penetration of liquids. The use of the Washburn equation (6.30) and (6.31) has been extended from cylindrical capillaries to powders to determine dynamic liquid contact angles measuring the penetration rates of liquids into powder packings [69]. The Washburn equation describes the flow in a single capillary, provided the effects of slip, gravity and inertial effects can be neglected, and there are no external pressure gradients:

$$\frac{dh}{dt} = \frac{r\gamma_{lv} \cos \theta}{4\eta h} \quad (6.30)$$

After integration one obtains

$$h^2 = \frac{rt}{2\eta} \gamma_{lv} \cos \theta \quad (6.31)$$

where h is the height of the liquid front at a certain time t , r is the capillary radius, and η is the viscosity of the liquid. The powder (uniformly packed into a tube) is modelled as a bundle of capillary tubes so that the plot of h^2 over t should be linear. Other models propose that the powder can be represented by a bundle of capillaries with an added tortuosity factor. If it is assumed that a liquid completely wets the powder packing, $\cos \theta = 1$, the value of \bar{r} (the average equivalent pore radius) can be obtained. Then, for the same packing, from measurements with other liquids, values of $\cos \theta$ can be determined. In this way, an "effective"

wettability can be found, “effective” because it is derived from the capillary tube model of porous media and not by direct measurements. This procedure reveals a main deficiency of this approach. It is the fact (cf. 6.31) that only the product $r\cos\theta$ can be elucidated and not r or $\cos\theta$ separately. Nevertheless, these contact angles have been often used to determine the solid surface tension of porous materials [70–72]. This procedure is dubious because, as was mentioned above, it can be expected that these contact angles are apparent contact angles which are affected by the geometry (roughness and porosity) of the porous medium, as for example the local inclination angles of the capillary walls. Only in a cylindrical capillary of smooth and homogeneous walls the calculated θ coincides with the intrinsic contact angle. In general it has been found that capillary penetration experiments tend to overestimate the contact angles compared to directly measured contact angles on smooth surfaces of the same material. For example, the contact angle of hexadecane was calculated to be $\theta=88^\circ$ for a PTFE (polytetrafluoroethylene) powder using the Washburn equation [73]. On a flat and smooth PTFE surface, this contact angle is well known to be 46° . Obviously, the former value only reflects the contact angle/wettability of hexadecane on “rough” PTFE powder, which is meaningless for energetics calculations in conjunction with the Young equation. A second example: for an organic liquid on cellulose fibres, the intrinsic contact angle may very well be close to zero. However, from capillary penetration experiments using filter papers of cellulose fibres, $\cos\theta$ comes out to be far from unity [74]. Thus, it can be concluded that experimentally determined contact angles of porous materials do not reflect material properties of the surface; rather, they reflect morphological ones. In addition, if the rate of motion of the three-phase line is relatively high it cannot be excluded that the “dynamic” contact angles calculated from capillary penetration experiments differ from static advancing contact angles. It is well-known that they can be quite different at higher velocities of the moving meniscus [75].

For that reason, another strategy was pursued to characterize the wettability of porous media [73]. This strategy is also based on a modified Washburn equation. By plotting $K\gamma_{lv}\cos\theta$ versus the liquid surface tension γ_{lv} , the solid surface tension, γ_{sv} , can be directly derived from these curves. $K\gamma_{lv}\cos\theta$ can be obtained indirectly from capillary penetration experiments, when the liquid properties and the penetration velocities are known (K is an unknown parameter that depends on the geometry of the porous medium). This approach is based on the following considerations:

If the Washburn equation (6.31) describing the flow in a single capillary is used one can replace h by the weight M of the liquid which penetrates into the capillary:

$$M = \rho V = \rho h A \quad (6.32)$$

where A is the cross-sectional area of the capillary and ρ is the density of the liquid. It follows that

$$\frac{M^2}{\rho^2 A^2} = \frac{r}{2} \frac{t}{\eta} \gamma_{lv} \cos\theta \quad (6.33)$$

and by rearranging

$$\gamma_{lv} \cos \theta = \left[\frac{2}{A^2 r} \right] \left[\frac{\eta}{\rho^2} \right] \left[\frac{M^2}{t} \right] \quad (6.34)$$

where $\left[\frac{2}{A^2 r} \right]$ is a factor representing the geometry of the capillary, $\left[\frac{\eta}{\rho^2} \right]$ reflects properties of the test liquid and $\left[\frac{M^2}{t} \right]$ is determined in the experiment.

In the case of powder packings or other porous solids, such as membranes, the geometry of the capillary system is not known. The value of $\left[\frac{2}{A^2 r} \right]$ in (6.34) is therefore replaced by an unknown factor $\frac{1}{K}$, i. e.,

$$\gamma_{lv} \cos \theta = \frac{1}{K} \left[\frac{\eta}{\rho^2} \right] \left[\frac{M^2}{t} \right] \quad (6.35)$$

or

$$K \gamma_{lv} \cos \theta = \left[\frac{\eta}{\rho^2} \right] \left[\frac{M^2}{t} \right] \quad (6.36)$$

This modified Washburn equation is valid with the following assumptions:

- (1) laminar flow predominates in the pore spaces;
- (2) gravity can be neglected; and
- (3) the geometry of the porous solid is constant.

The quantity $\left[\frac{M^2}{t} \right]$ can be determined by measuring the weight M of a penetrating liquid into a porous solid as a function of time t using a tensiometer. Figure 6.15 shows the experimental set-up for the capillary penetration measurements [73]. Similar arrangements for capillary penetration tests were used by Bruil [18], Cheever [19], and Kilau [20]. The powder is packed in a glass tube at which the lower end is closed with a glass filter or with a membrane that is removed after each experiment. Considerable care is necessary to obtain a constant and homogeneous powder packing. A precisely weighed quantity of the powder has to fill up to the same height in the glass tube by manually tapping the powder. The filled columns are attached to an electrobalance and brought into contact with several test liquids. Their penetration velocities are determined by measuring the weight gain with the electrobalance as a function of time.

If M is plotted versus \sqrt{t} the experimental quantity $\left[\frac{M^2}{t} \right]$ can be obtained by determining the slope of the linear part of these plots. There are two basic

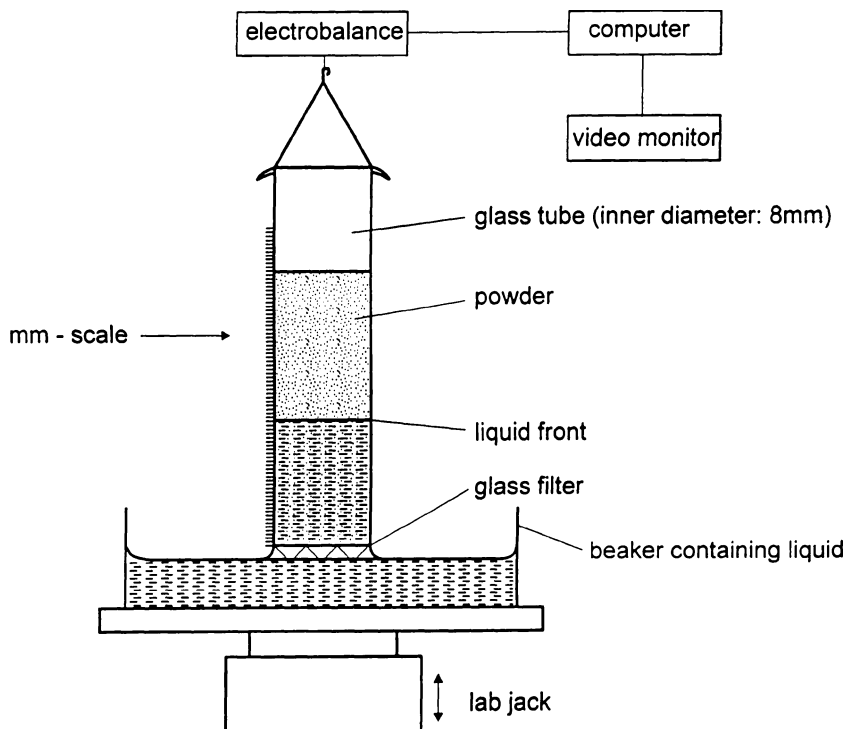


Fig. 6.15 A schematic of the set-up for capillary penetration experiments

requirements that the test liquids must satisfy in order to be used for capillary penetration experiments: (1) they should be chemically inert with respect to the porous material of interest; and (2) the range of the surface tension γ_{lv} of the test liquids should cover the anticipated surface tension of the powder. Experimental results obtained for powders and membranes consisting of hydrophobic and hydrophilic polymer materials show that an extremum (maximum) exists when the values $K\gamma_{lv}\cos\theta$ are plotted against the surface tension of the liquids γ_{lv} , at a value of $\gamma_{lv} = \gamma_{lv}^*$ [73, 76, 77]. It can be argued that the surface tension can then be determined as $\gamma_{sv} = \gamma_{lv}^*$. As an example, Fig. 6.16 shows the results for a PTFE (Teflon 807-N) powder. The maximum occurs at $\gamma_{lv}^* = 20.4 \text{ mJ/m}^2$. Thus, the γ_{sv} value of the PTFE particles would be 20.4 mJ/m^2 . Knowing the value of γ_{sv} and γ_{lv} for a given liquid, the equation-of-state for solid-liquid interfacial tensions (6.21) can be used to predict the contact angle, θ , of this liquid on the solid material. In the case of PTFE powder, a water contact angle of 104° is predicted ($\gamma_{lv} = 72.5 \text{ mJ/m}^2$ for water). Remarkably, this is exactly what one would observe on a smooth Teflon surface. Further polymer powders, as for example polypropylene, polyethylene, and polystyrene, were investigated [77] and it was found that the derived γ_{sv} values are in good agreement with the γ_{sv} values obtained from contact angle measurements on flat and smooth solid surfaces of the same materials.

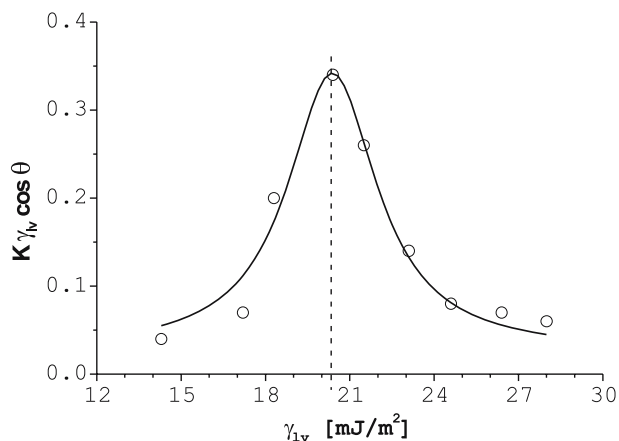


Fig. 6.16 A plot of $K\gamma_{lv}\cos\theta$ versus γ_{lv} for PTFE (Teflon 807-N) powder packings using nine test liquids reproduced from [73]

Although the packed powder bed certainly does not represent a flat and smooth solid surface, the derived value for γ_{sv} is that obtained by contact angle measurements on a flat and smooth surface. It is well known that even a highly compacted hydrophobic powder, presenting a seemingly flat and smooth solid surface, does not yield the same contact angle as truly smooth and coherent solid surfaces. It appears that an indirect method, such as capillary penetration, may provide much more relevant information concerning the solid surface energetics than direct contact angle measurements on imperfect solid surfaces.

Since only the product $K\cos\theta$ can be elucidated and not K or $\cos\theta$ separately in capillary penetration experiments, K which reflects the geometry of the porous medium may change in a non-predictable way during the penetration of different liquids and, hence, the shape of the curve $K\gamma_{lv}\cos\theta$ vs. γ_{lv} . From experiments with microporous expanded PTFE membranes of different pore geometries it could be concluded that information about the geometric constant K is not needed. The position of the maximum, which is expected to reflect the solid surface tension γ_{sv} of the porous material was not affected by the different geometries of the membranes [76].

Figure 6.17 shows that the above described approach is not only applicable to hydrophobic surfaces but also to very hydrophilic surfaces, such cellulose membranes [73]. As in the case of the PTFE powder (Fig. 6.16) we obtain curves with a maximum if $K\gamma_{lv}\cos\theta$ versus the surface tension γ_{lv} of the test liquids is plotted. It can be seen that the unmodified cellulose capillary membrane (hollow fibre) indicates the highest γ_{sv} value whereas the modified types have a lower γ_{sv} , i. e. a less hydrophilic surface. We can predict a water contact angle of 59° for an ideally smooth unmodified cellulose hollow fibre CUPROPHAN, if we input $\gamma_{sv} = 48 \text{ mJ/m}^2$ and $\gamma_{lv} = 72.5 \text{ mJ/m}^2$ for water in (6.21). It has to be considered that processing agents are applied during the manufacture of the CUPROPHAN fibres, which can be expected to influence even the surface properties of the unmodified cellulose material. By chemical modification of the cellulose, the γ_{sv} could be

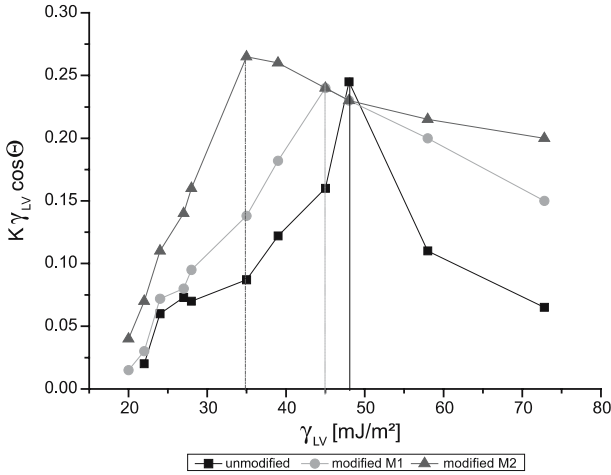


Fig. 6.17 A plot of $K\gamma_{LV}\cos\theta$ versus γ_{LV} for different cellulose membranes (■ unmodified Cellulose CUPROPHAN; ● chemically modified cellulose M1; ▲ chemically modified cellulose M2)

decreased to 35 mJ/m², as can be seen from Fig. 6.17; a water contact angle of 80° can be predicted for this modified cellulose material by (6.21).

6.3.2 Zeta Potential Measurements: Particle Electrophoresis, Electro-Osmosis, Streaming Potential, Sedimentation Potential

The zeta potential can be determined experimentally either by measuring the relative movement of solid and liquid phase induced by an externally applied electric field, in the case of electrophoresis and electroosmosis, or by measuring the strength of an electric field generated by the relative motion of solid and liquid phase, in the case of streaming potential and sedimentation potential. The different experimental techniques are summarized in Table 6.2 including the basic equations to determine the zeta potential from the measured experimental quantities.

Particle electrophoresis is the most frequently employed experimental technique. The electrophoretic mobility v can be measured within a wide range of particle diameters. The observation of particle movement by standard microscope permits the characterization of particles with diameters ranging from 0.5 μm to 5 μm . In the experiment, an averaged electrophoretic velocity v is determined and the zeta potential is calculated by the simple Smoluchowski equation [78] as follows

$$\zeta = \frac{v\eta}{E\epsilon_0\epsilon_r} \quad (6.37)$$

where η is the viscosity of the liquid, E the external electric field, and ϵ_0 and ϵ_r are the permittivities of the free space and the liquid, respectively. Although the

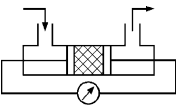
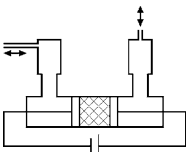
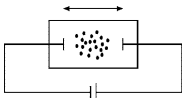
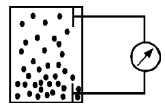
Smoluchowski equation does not reflect the surface conductivity, it has been used widely for the semiquantitative interpretation of electrokinetic measurements.

The application of laser doppler electrophoresis based on light scattering to determine particle velocities enables the determination of the zeta potential of particles with diameters between 10 nm and 10 μm . These methods are used in contemporary commercially available analytical particle electrophoresis apparatus, such as the “Malvern Zeta-Sizer”. For concentrated dispersions, where conventional electrophoretic methods are inappropriate, mass transport analysis or acoustophoresis can be applied. The disadvantage of the latter method is that it is not appropriate to systems having low density differences between the particles and suspending liquid.

For porous and fibrous materials, it is often most convenient to measure *electroosmosis* across a packed bed or plug [79]. In this case, bulk electroosmotic fluid flow dV/dt must be measured directly in an open circuit (cf. Table 6.2), or the pressure difference measured across a closed cell.

The zeta potentials of coarse powders, fibres, plates, sheets, membranes, etc. were determined mainly by *streaming potential measurements* [54]. Since the determination of the zeta potential depends on the existence of single capillaries or capillary bundles their length to cross-sectional area ratio L/Q has to be determined and the streaming potential U_{Sr} has to be measured as a function of the pressure decay in the capillary (capillary bundle) (cf. Table 6.2).

Table 6.2 Electrokinetic techniques to determine the zeta potential (reproduced from [82])

Method	Streaming potential	Electro-osmosis	Electrophoresis	Sedimentation potential
Measured quantity	dU/dp	dV/dt	v	U
Equation	$\zeta = \frac{dU_{Sr}}{dp} \frac{\eta}{\varepsilon\varepsilon_0} \frac{L}{QR}$	$\zeta = \frac{dV/dt}{U} \frac{\eta}{\varepsilon\varepsilon_0} \frac{L}{Q}$	$\zeta = \frac{v}{E} \frac{\eta}{\varepsilon\varepsilon_0}$	$\zeta = \frac{3\eta\lambda U_{sd}}{\varepsilon\varepsilon_0 r^3 d\rho ng}$
Scheme of the measuring cell				
Application	Fibres, powders, plates, films	Fibres, powders	Powders, suspensions, dispersions, emulsions	Powders, suspensions, dispersions

ζ is the zeta potential, U_{Sr} the streaming potential, p the pressure, η the viscosity, ε the dielectric constant, L and Q the capillary length and cross-section area, R the electric resistance, dV/dt the electroosmotic volume flow, U the externally applied voltage, v the particle velocity, E the field strength, U_{sd} the sedimentation potential, λ the specific conductivity, $d\rho$ the difference of the density of the liquid and the particles, r and n the radius and the number of the particles, and g the force of gravitation

In the past, discredit was brought upon the zeta potential as, allegedly, not clearly defined measure [80, 81]. This situation was mainly due to insufficient experimental conditions and the disregard of the effect of several influencing factors caused by the device and/or the materials. Today, automatically working devices are commercially available that provide reproducible results when they are appropriately used [82, 83]. In the literature, one can find several papers that have been contributed to a better understanding of electrokinetic phenomena and to a broader use of electrokinetic methods [56, 57, 84].

References

1. K. Grundke, Wetting, Spreading and Penetration, in *Handbook of Applied Surface and Colloid Chemistry*, ed. by K. Holmberg, vol. 2, chap. 7 (2002), pp. 119–142
2. A.W. Adamson, *Physical Chemistry of Surfaces*, 5th edn. (Wiley, New York, 1990)
3. J. Rowlinson, B. Widom, *Molecular Theory of Capillarity* (Oxford University Press, Oxford, 1982)
4. A.W. Neumann, J.K. Spelt, *Applied Surface Thermodynamics*, Surfactant Science Series 63 (Marcel Dekker, New York, 1996)
5. B.V. Derjaguin, V.M. Muller, Y.P. Toporov, J. Colloid Interface Sci. 73, 293 (1980)
6. K.L. Johnson, K. Kendall, A.D. Roberts, Proc. R. Soc. (London) A324, 301 (1971)
7. H.K. Christenson, J. Phys. Chem. 90, 4 (1986)
8. P.M. Claesson, C.E. Blom, P.C. Horn, B.W. Ninham, J. Colloid Interface Sci. 114, 277 (1986)
9. R.M. Pashley, P.M. McGuiggan, B.W. Ninham, D.F. Evans, Science 229, 1088 (1985)
10. W. Zisman, Relation of the equilibrium contact angle to liquid and solid constitution, in *Contact Angle, Wettability and Adhesion*, ed. by F.M. Fowkes, Adv. Chem. Ser. 43, (American Chemical Society, Washington, D.C., 1964), pp. 1–51
11. F.M. Fowkes, Ind. Eng. Chem. 12, 40 (1964)
12. O. Driedger, A.W. Neumann, P.J. Sell, Kolloid-Z. Z. Polym. 201, 52 (1965)
13. D.K. Owens, R.C. Wendt, J. Appl. Polym. Sci. 13, 1741 (1969)
14. A.W. Neumann, R.J. Good, C.J. Hope, M. Sejjal, J. Colloid Interface Sci. 49, 291 (1974)
15. C.J. van Oss, M.K. Chaudhury, R.J. Good, Chem. Revs. 88, 927 (1988)
16. J.K. Spelt, D. Li, The equation of state approach to interfacial tensions, in *Applied Surface Thermodynamics*, ed. by A.W. Neumann, J.K. Spelt, Surfactant Science Series 63 (Marcel Dekker, New York, 1996), pp. 239–292
17. R.J. Good, C.J. van Oss, The modern theory of contact angles and the hydrogen bond components of surface energies, in *Modern Approaches to Wettability – Theory and Applications*, ed. by M.E. Schrader, G.I. Loeb (Plenum, New York, 1992), pp. 1–27
18. H.G. Bruil, Colloid Polym. Sci. 252, 32 (1974)
19. G.D. Cheever, J. Coat. Technol. 55, 53 (1983)
20. H.W. Kilau, Colloid Surf. 26, 217 (1983)
21. K. Grundke, T. Bogumil, T. Gietzelt, H.-J. Jacobasch, D.Y. Kwok, A.W. Neumann, Prog. Colloid Polym. Sci. 101, 58 (1996)
22. E.I. Vargha-Butler, E. Moy, A.W. Neumann, Colloids Surf. 24, 315 (1987)
23. D. Li, A.W. Neumann, Wettability and surface tension of particles, in *Applied Surface Thermodynamics*, ed. by A.W. Neumann, J.K. Spelt, Surfactant Science Series 63 (Marcel Dekker, New York, 1996), pp. 509–556
24. S.N. Omenyi, A.W. Neumann, J. Appl. Phys. 47, 3956 (1976)
25. J. Cisse, G.F. Bolling, J. Crystal Growth 11, 25 (1971)
26. K.H. Chen, W.R. Wilcox, J. Crystal Growth 40, 214 (1977)
27. D.W. Fuerstenau, M.C. Williams, Colloid Surf. 22, 87 (1987)

28. S.J. Hemingway, J.R. Henderson, J.R. Rowlinson, *Faraday Symp. Chem. Soc.* 16, 33 (1981)
29. R. Guermeur, F. Biquard, C. Jacolin, *J. Chem. Phys.* 82, 2040 (1985)
30. B.S. Carey, L.E. Scriven, H.T. Davis, *AIChE J.* 26, 705 (1980)
31. H.C. Hamaker, *Physica* 4, 1058 (1937)
32. J.N. Israelachvili, *Proc. R. Soc. London A* 331, 39 (1972)
33. A.E. van Giessen, D.J. Bukman, B. Widom, *J. Colloid Interface Sci.* 192, 257 (1997)
34. D.E. Sullivan, *J. Chem. Phys.* 74, 2604 (1981)
35. D.V. Matyushov, R. Schmid, *J. Chem. Phys.* 104, 8627 (1996)
36. O. Stern, *Z. Elektrochemie* 30, 508 (1924)
37. D.C. Grahame, *J. Chem. Phys.* 16, 1117 (1948)
38. P.G. de Gennes, Wetting: statics and dynamics, *Rev. Mod. Phys.* 57, 827–863 (1985)
39. L. Leger, J.-F. Joanny, Liquid spreading, *Rep. Prog. Phys.* 55, 431–486 (1992)
40. A.-M. Cazabat, How does a droplet spread? *Contemp. Phys.* 28, 347–367 (1987)
41. B.V. Derjaguin, N.V. Churaev, *Wetting Films* (Nauka, Moscow, 1984)
42. M.P. Valignat, M. Voue, G. Oshanin, A.M. Cazabat, Structure and dynamics of thin liquid films on solid substrates, *Colloid Surf. Part A* 154, 25–31 (1999)
43. D.Y. Kwok, A.W. Neumann, Contact angle measurement and contact angle interpretation, *Adv. Colloid Interface Sci.* 81, 167–249 (1999)
44. J. Gaydos, A.W. Neumann, Line tension in multiphase equilibrium systems, in *Applied Surface Thermodynamics*, ed. by A.W. Neumann, J.K. Spelt, Surfactant Science Series 63 (Marcel Dekker, New York, 1996), pp. 169–238
45. B.V. Derjaguin, N.V. Churaev, V.M. Muller, *Surface Forces* (Consultants Bureau, New York, 1987)
46. L.A. Girifalco, R.J. Good, *J. Phys. Chem.* 61, 904 (1957)
47. J.K. Spelt, D. Li, The equation of state approach to interfacial tensions, in *Applied Surface Thermodynamics*, ed. by A.W. Neumann, J.K. Spelt, Surfactant Science Series 63 (Marcel Dekker, New York, 1996), pp. 239–292
48. D.Y. Kwok, T. Gietzelt, K. Grundke, H.-J. Jacobasch, A.W. Neumann, Contact angle measurements and contact angle interpretation: I. Contact angle measurements by axisymmetric drop shape analysis and a goniometer sessile drop technique. *Langmuir* 13, 2880–2894 (1997)
49. A.E. van Giessen, D.J. Bukman, B. Widom, Contact angles of liquid drops on low-energy solid surfaces, *J. Colloid Interface Sci.* 192, 257–265 (1997)
50. J.C. Berg, Role of acid–base interactions in wetting and related phenomena, in *Wettability*, ed. by J.C. Berg, Surfactant Science Series 49 (Marcel Dekker, New York, 1993)
51. R.J. Good, C.J. van Oss, The modern theory of contact angles and the hydrogen bond components of surface energies, in *Modern Approaches to Wettability – Theory and Applications*, ed. by M.E. Schrader, G.I. Loeb (Plenum, New York, 1992), pp. 1–27
52. H.-J. Jacobsch, K. Grundke, P. Uhlmann, F. Simon, E. Mäder, *Composite Interfaces* 3, 293 (1996)
53. V. Gutman, *The Donor–Acceptor Approach to Molecular Interactions* (Wiley Interscience, New York, 1980)
54. H.-J. Jacobasch, *Prog. Organic Coatings* 17, 115 (1989)
55. M. Börner, H.-J. Jacobasch, F. Simon, N.N. Churaev, I.P. Sergeeva, V.D. Sobolev, *Colloid Surf. A* 85, 9 (1994)
56. S. Simon, H.-J. Jacobasch, S. Spange, *Colloid Polym. Sci.* 276, 930 (1998)
57. P. Weidenhammer, H.-J. Jacobasch, *J. Colloid Interface Sci.* 180, 232 (1996)
58. F. Simon, Dissertation, F.-Schiller University Jena (1993)
59. H.-J. Jacobasch, K. Grundke, S. Schneider, F. Simon, *J. Adhesion* 48, 57 (1995)
60. H.-J. Jacobasch, *Oberflächenchemie faserbildender Polymerer* (Akademie-Verlag, Berlin, 1984)
61. M. Rätzsch, H.-J. Jacobasch, K.-H. Freitag, K. Grundke, G. Hermel, *J. Adhesion Sci. Technol.* 3, 595 (1989)

62. D.Y. Kwok, A.W. Neumann, Contact angle techniques and measurements, in *Surface characterization methods, principles, techniques, and applications*, ed. by A.J. Milling (Marcel Dekker, New York, 1999), pp. 37–86
63. A. Augsberg, K. Grundke, K. Pöschel, H.-J. Jacobasch, A.W. Neumann, *Acta Polym.* 49, 417 (1998)
64. M. Wulf, K. Grundke, D.Y. Kwok, A.W. Neumann, *J. Appl. Polym. Sci.* 77, 2493 (2000)
65. D.Y. Kwok, C.N.C. Lam, A. Li, K. Zhu, R. Wu, A.W. Neumann, *Polym. Eng. Sci.* 38, 1675 (1998)
66. D.Y. Kwok, A. Leung, A. Li, C.N.C. Lam, R. Wu, A.W. Neumann, *Colloid Polym. Sci.* 276, 459 (1998)
67. P. Cheng, D. Li, L. Boruvka, Y. Rotenberg, A.W. Neumann, *Colloid Surf.* 93, 169 (1983)
68. O.I. del Rio, A.W. Neumann, *J. Colloid Interface Sci.* 196, 136 (1997)
69. J. Van Brakel, P.M. Heertjes, Capillary rise in porous media, Part I, A problem, Part II, Secondary phenomena, Part III, Role of contact angle, *Powder Technol.* 16, 75–96 (1977)
70. P.M. Costanzo, R.F. Giese, C.J. van Oss, *J. Adhes. Sci. Technol.* 4, 267 (1990)
71. C.J. van Oss, R.F. Giese, Z. Li, K. Murphy, J. Norris, M.K. Chaudhury, R.J. Good, *J. Adhes. Sci Technol.* 6, 413 (1992)
72. E. Chibowski, L. Holysz, *Langmuir* 8, 710 (1992)
73. K. Grundke, T. Bogumil, T. Gietzelt, H.-J. Jacobasch, D.Y. Kwok, A.W. Neumann, Wetting measurements on smooth, rough and porous solid surfaces, *Progr. Colloid Polym. Sci.* 101, 58–68 (1996)
74. A. Marmur, R.D. Cohen, Characterization of porous media by the kinetics of liquid penetration: the vertical capillaries model, *J. Colloid Interface Sci.* 189, 299–304 (1997)
75. T.D. Blake, Dynamic contact angles and wetting kinetics, in *Wettability*, ed. by J.C. Berg, Surfactant Science Series 49 (Marcel Dekker, New York, 1993), pp. 251–309
76. J. Tröger, K. Lunkwitz, K. Grundke, W. Bürger, Determination of the surface tension of microporous membranes using wetting kinetics measurements, *Colloid Surf. A* 134, 299–304 (1998)
77. K. Grundke, A. Augsberg, On the determination of the surface energetics of porous polymer materials, *J. Adhes. Sci. Technol.* 14, 765–775 (2000)
78. R.J. Hunter (ed.) *Zeta Potential in Colloid Sciences* (Academic, New York, 1981)
79. S.S. Dukhin, B.V. Derjaguin, *Electrokinetic Phenomena*, Surface and Colloid Science Series, vol. 7, ed. by E. Matijevic (Wiley, New York, 1974)
80. H. Sonntag (ed.) *Lehrbuch der Kolloidwissenschaft* (VEB Deutscher Verlag der Wissenschaften, Berlin, 1977), p. 99
81. H. Hintze, M. Stintz, S. Ripperger, *Chem. Ing. Technol.* 71, 338 (1999)
82. C. Bellmann, C. Klinger, A. Opfermann, F. Böhme, H.-J. Adler, *Prog. Organic Coatings*, 44, 93 (2002)
83. H.-J. Jacobasch, F. Simon, C. Werner, C. Bellmann, *Technisches Messen* 63, 439 (1996)
84. R. Zimmermann, S. Dukhin, C. Werner, *J. Phys Chem. B* 105, 8544 (2001)

Chapter 7

Mechanical Properties of Polymers at Surfaces and Interfaces

Konrad Schneider

Leibniz Institute of Polymer Research Dresden, Hohe Str. 6, 01069 Dresden, Germany,
schneider@ipfdd.de

Abstract Mechanical properties are highly relevant for the use of polymers in many practical cases. Interfacial aspects are important during fracture also of bulk materials, where for instance microvoids, cracks and crazes are formed. The measurement of interface and thin film mechanical properties and adhesion requires special techniques, which include peel, blister and blade cutting test. Surface properties like hardness, scratch resistance or surface modulus are determined by nanoscratch, nanoindentation and AFM tapping test, while interactions between solid interfaces are determined from surface force, colloidal probe or AFM force–distance measurements.

7.1 Introduction

Mechanical properties are probably the most important ones to be considered in many polymer applications. Thereby the mechanical behaviour varies from stiff and brittle to extremely flexible. Additionally a strong temperature and load rate dependence of the properties is well documented.

On the other hand, for practical applications the behaviour is often necessary to be defined under special geometrical conditions, near the surface, or in very small specimen. Therefore, a large set of mechanical tests has been established for the characterization and description of the mechanical behaviour of polymers.

The deformation mechanisms of polymers have been under immense study for almost half a century, but yet no general conclusion has been drawn concerning how and when polymers deform. However, in many cases certain knowledge is gained.

In the following, a set of aspects of mechanical tests is presented and shortly discussed in note form. A detailed presentation can be found in the literature [4–9, 11–18, 20–22].

Each surface contact stresses also the bulk material under the surface with its specific deformation behaviour. For a comprehensive understanding of mechani-

cal interactions on surfaces always this deformation of the underlying bulk material must be taken into consideration.

Generally, there are different kinds of surface interactions. New surfaces can be established by fracture of a polymer material or by interfacial failure. To characterize these cases some comments about the fracture mechanics will follow. – On the other hand, mechanical interaction can take place on a pure surface. The effects on different scales and their characterization are described in a second step.

7.2 Overview of Mechanical Bulk Behaviour

Due to the variety of structures and the respective local possibilities of molecular rearrangement under load polymers show a widespread spectrum of mechanical properties. Typical stress–strain curves for the tensile test under room temperature are shown in Fig. 7.1.

Besides tension, mechanical characterization is also convenient under shear and compression modes. The behaviour is partially analogous, and under special conditions to a certain extent the results can be converted to each other.

Typical internal structures of homopolymers – amorphous, semi crystalline and cross-linked polymers – show characteristic mechanical behaviour.

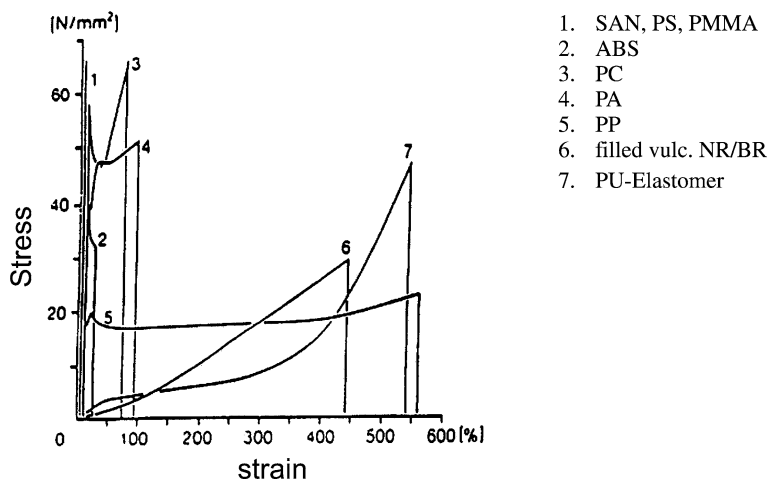


Fig. 7.1 Variety of stress–strain curves of polymers under tension with some characteristic material as example for the behaviour

The mechanical properties of *amorphous polymers* are strongly temperature dependent. At low temperatures the chain mobility is frozen, the material is stiff and in many cases brittle (cf. PS, PMMA). At higher temperatures, approaching the glass transition temperature, the chain mobility increases locally and may

finally allow global rearrangement. At this instance, the modulus drops down firstly and the stress–strain curve flattens with increasing the load. At high stresses some amorphous polymers can be deformed plastically. After a yield stress threshold an irreversible deformation takes place (cf. PC).

The behaviour of amorphous polymers at low deformations can be well described within the frame of linear viscoelasticity. This theory describes the transition from elastic behaviour at low temperatures (linear-elastic region with reversible deformation, stress and strain are proportional, $\sigma \sim \epsilon$, modulus $E = d\sigma/d\epsilon$ and the Poisson ratio $\mu_n = -d\epsilon_n/d\epsilon$) to the viscous one at elevated temperatures (where the stress is proportional to the strain rate, $\sigma \sim d\epsilon/dt$).

Between the elastic low- and the viscous high-temperature behaviour the amorphous polymers have their glass transition with strong time- and temperature-dependent behaviour, which can be demonstrated in two very simple experiments, see Fig. 7.2.

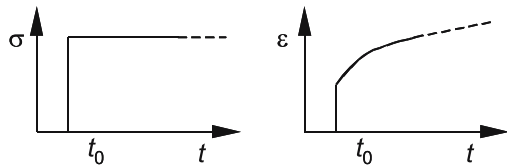
Similar studies may be carried out in a dynamic mode, applying a sinusoidal displacement and measuring the resulting restoring force. The ratio between stress and strain can be described with a complex modulus M^* . The real part of this modulus describes the storage, while the imaginary part describes the loss of energy during a test. The phase shift between stress and strain, δ , is conventionally used as loss factor $\tan \delta$.

The time- and the frequency-dependent behaviour can be transformed into each other.

The ratio between the instantaneous response to the time dependent as well as the time dependence are strongly temperature dependent.

Figure 7.3 shows an example of the temperature dependent shear compliance of PMMA.

creep test:
compliance
 $C(t) = \epsilon(t)/\Delta\sigma(t = 0)$



stress relaxation:
relaxation modulus
 $M(t) = \sigma(t)/\Delta\epsilon(t = 0)$

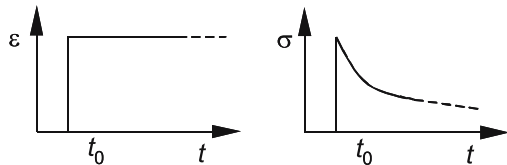


Fig. 7.2 Time-dependent mechanical response: Creep test and stress relaxation within the frame of linear viscoelasticity

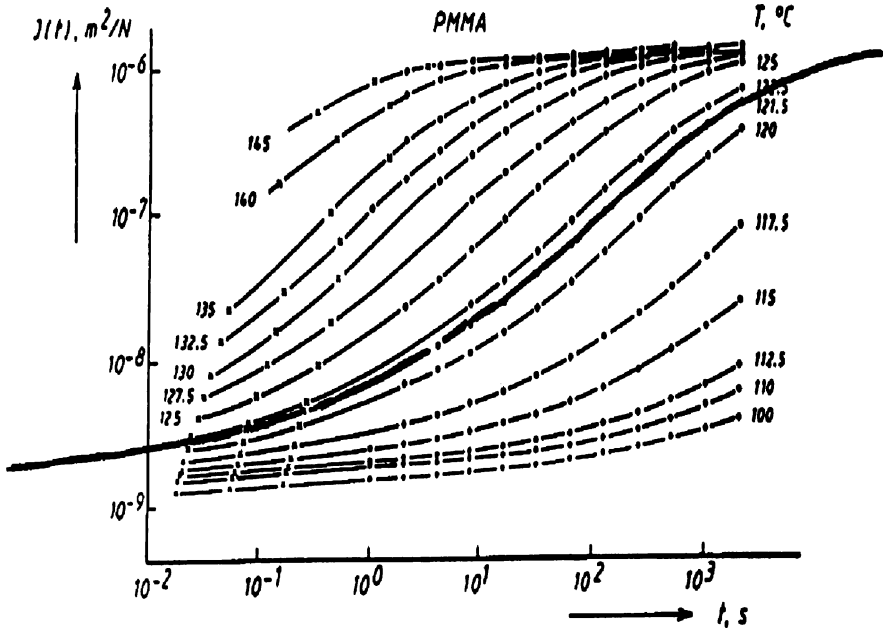


Fig. 7.3 Shear compliance $J(t)$ of PMMA in dependence of temperature with the master curve (bold)

Experience shows, that a master curve can be constructed shifting the time- or frequency-dependent compliances or moduli to superposition. This can be described as

$$M^*(\log \omega, T) = a_T(T) * F(\omega/\omega_0) \text{ or } M^*(\log t, T) = a_T(T) * F(t/t_0) \quad (7.1)$$

with a shift factor a_T , which can be described by the well known WLF equation (according to Williams, Landel and Ferry)

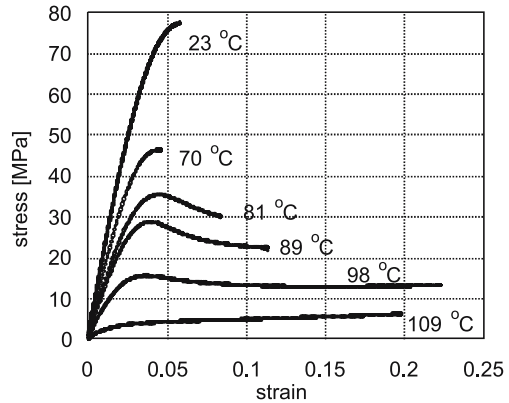
$$\log a_T = C_1 (T - T_0) / (C_2 + T - T_0) = \log (\omega/\omega_0). \quad (7.2)$$

At temperatures well above the glass transition the chains obtain increased mobility and their motion can be well described by the reptation model of Edwards and de Gennes.

Some polymers are, due to their regular structure, able to crystallize to a certain extent, yielding *semicrystalline polymers*. Crystallization takes place at temperatures well below the melting temperature with internal or external, e.g. stress induced, nucleation. Crystallization behaviour is strongly temperature dependent and freezes when the system reaches the glass transition. The overall mechanical properties of a semicrystalline polymer are strongly dependent on the degree of crystallinity as well as the size and orientation distribution of the crystallites.

The chains between the crystallites remain amorphous. They are in their dynamical behaviour slightly restricted by the crystallites, mainly in the immediate surrounding of it. This may increase the glass transition temperature slightly. If re-crystallization occurs the dynamical behaviour can be changed drastically.

Fig. 7.4 Influence of temperature on the whole stress–strain curve of an epoxy resin



In particular the behaviour during plastic deformation is strongly determined by changes in the confinement of amorphous chain segments by the crystallites due to recrystallization.

A quite different class of polymers are the chemically *cross-linked polymers*. They range from the highly cross-linked resins like epoxies to the extremely flexible low cross-linked **elastomers**. The behaviour of the highly cross-linked materials is comparable with that of semi crystalline materials with the difference, that the network nodes are fixed. The cross-linking density strongly determines the overall behaviour. The chains within the network behave like small amorphous chains. Due to cross-linking the overall shape of the material also remains stable at higher temperatures. The temperature dependent stress–strain curves of a fully cured epoxy are shown in Fig. 7.4. With increasing temperature the modulus drops down as well as the strength, but at the same time the strain at failure increases. A change in the strain rate has a similar influence, like discussed above, but to a much lower degree.

Low cross-linked polymers show *entropic elastic behaviour* above the glass transition. The restoring force on an external load has a low energetic, and a high entropic component. This leads to a steady increasing slope of the stress–strain curve (cf. Fig. 7.1).

In some cases polymers show *plastic deformation* (see PA and PP in Fig. 7.1). Above the yielding point irreversible deformation at constant stress occurs. In many cases the tensile specimen necks, the remaining cross-section after yielding being only a fraction of the initial one. The underlying processes may be different. Well described in the literature are shear yielding and craze formation. In shear yielding macromolecules are oriented in the stress field and may slide to one another. The local orientation of the chains together with molecular structure can enable stress induced crystallization. This would give an anisotropic semicrystalline material with comparable high modulus and strength. In the case of crazing a large number of cracks perpendicular to the loading direction establish, bridged by extended polymer chains in the form of nanofibrils.

7.3 Fracture Mechanical Characterization of Polymers and Composites

Due to the widespread fracture behaviour a general description largely independent on specific geometry and experimental conditions (the dependence on the strain rate $\dot{\epsilon}$ and the temperature T persist on) is sought. This characterization of toughness was developed initially based on the *linear-elastic fracture mechanics (LEFM)* [25]. In general sharp notches can be used as stress concentrators for crack initiation. This prevents the random stress concentration by inhomogeneities (e. g. material defects, discontinuities in design). Mainly three different modes of load and failure at cracks were distinguished: Tension, crack opening; in-plane shear, sliding; out-of-plane shear, tearing, see Fig. 7.5.

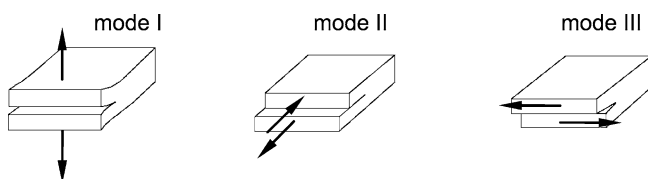


Fig. 7.5 Load at the different crack modes I, II and III

There exist two ways to characterize crack initiation and propagation: Via a critical stress or the energy release rate.

7.3.1 Stress Intensity-(K-)Factor

The state of stress in the vicinity of a crack tip/notch can be characterized by a stress intensity factor K as

$$K = \sigma_N (\pi a)^{1/2} f(a/W) \quad (7.3)$$

with the geometry function $f(a/W)$, where a is the depth of the notch, W the sample thickness and so $(W-a)$ the ligament length. The functions $f(a/W)$ are published for several geometries in the literature. Based on linear theory the stresses at the crack tip are infinity but in reality there is always a plastic zone at the crack tip that limits the stresses to finite values.

Crack propagation starts if stress concentration at the notch or crack tip exceeds a critical values $K_i \geq K_{ic}$ (fracture toughness, $i = I, II, III$ according to the mode of load).

7.3.2 Energy Release Rate

At crack propagation also with non-negligible elastic–plastic behaviour a decrease of the elastically stored energy dU at constant strain λ is observed due to the extension of the fractured surface by dA and the increasing compliance. The energy release rate G is defined as

$$G = - \left. \frac{dU}{dA} \right|_{\lambda} \text{ at constant strain } \lambda; \tag{7.4}$$

The interrelation between K and G depends on the deformation state:

plane stress
$$K_c^2 = E G_c \tag{7.5}$$

plane strain (independent on sample geometry)

$$K_c^2 = \frac{E G_c}{1 - \nu^2} \tag{7.6}$$

Crack propagation occurs crossing the crack resistance, characterized by the critical energy release rate G_{ic} .

Within the yielding or elastic plastic fracture mechanics several procedures have been developed for describing the (partially) plastic behaviour at the crack tip. The *CTOD concept* (*crack tip opening displacement*) describes ductile behaviour of the material in front of the crack tip. The extent is determined by a small scale yielding stress σ_{ys} .

The stress intensity factor is

$$K_{ic}^{CTOD} = (m \sigma_{ys} \delta E)^{1/2} \tag{7.7}$$

with the dimensionless constraint factor m . For nonhardening materials and plane stress it is $m = 1$.

Fig. 7.6 Scheme of crack propagation to be described by the CTOD concept

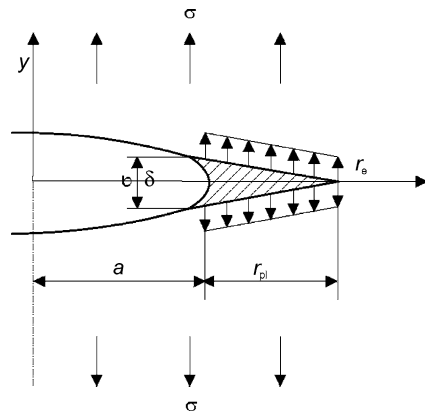
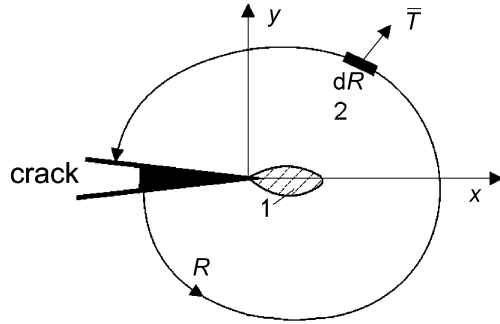


Fig. 7.7 Scheme of the crack propagation described by the J -integral concept



The J -integral concept uses a path-independent line integral in the elastic deformed region around the plastic deformed region with the crack tip as

$$J = \int_R \left(W \, dy - T_{ij} n_j \frac{\partial u_i}{\partial x} \, ds \right) \quad (7.8)$$

where W is the elastic energy density, T_{ij} the stress tensor, n_j the normal of the arbitrary contour R around the crack tip and u the displacement vector, to describe fracture. It represents the *strain energy release rate of nonlinear elastic materials*.

Comparing with the CTOD concept follows that

$$J = \frac{K^2}{E} = m \sigma_{ys} \delta \quad (7.9)$$

with constraint factor m .

Compared with elastical material behaviour the J -integral becomes equivalent to the energy release rate described above.

7.3.3 The Concept of Crack Resistance-(R)-Curve

Cracks are in many cases introduced by stable crack propagation. The aim of the crack resistance curve is the observation of J -integral, or crack opening displacement δ over the crack propagation δa (J_R - resp. J_δ -curve).

It consists of the blunting line (blunting of crack tip), the establishment of a stretching zone and crack propagation line.

The crack resistance resp. J -integral is dependent on load state (mode I, II, III), stress and energy criteria (linear-elastic or elastic-plastic fracture mechanics), blunting and stable crack propagation.

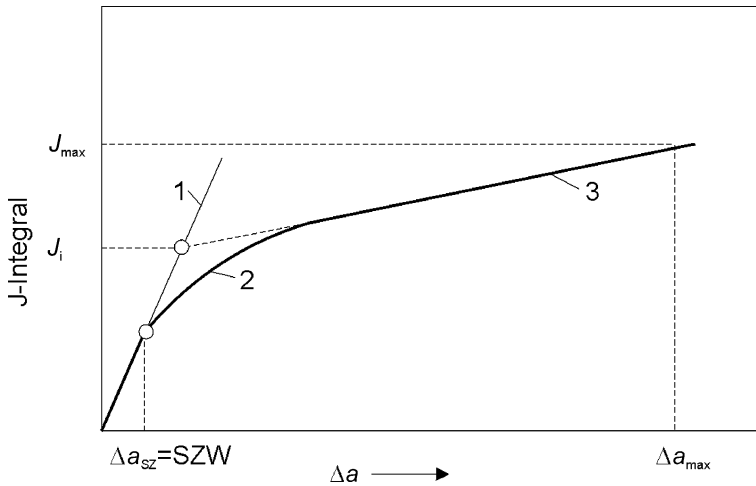


Fig. 7.8 Crack resistance curve with the blunting line (1), the establishment of a stretching zone (2) and the propagation line (3)

7.3.4 Stress–Strain Situation and Failure in Heterogeneous Systems

Bimaterials, composites (e. g. fibre or particle reinforced), compounds (filled, pigmented materials) and blends are characterized by complex stress and strain (fields) at the interface with certain stress tips. According to the situation described above adhesive and cohesive failure may occur.

To characterize the relative complex behaviour in the bulk methods of direct stress measurement (e. g. by photoelasticity) or strain measurement (e. g. by Raman microscopy) are powerful tools.


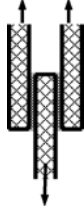
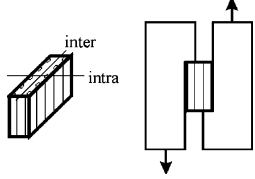

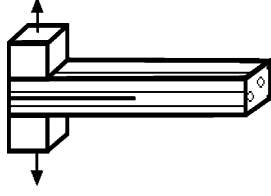
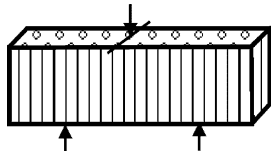
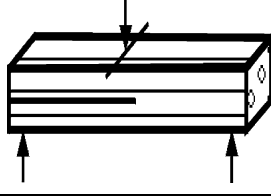
7.3.5 Characterization of Interlaminar Strength in Composites

On macroscopical scale several fracture mechanical tests for composites/bonds were established to characterize adhesion. Some of them are summarized in Table 7.1.

Table 7.1 Schema of commonly used arrangements to characterize interlaminar strength in composites

Method	Sample configuration	Property
Transversal tensile test (see also Stud Pull Bonding) Agent Test (Stirnabreißversuch) tack test (pull off test)		Transversal modulus Transversal strength (mode I)

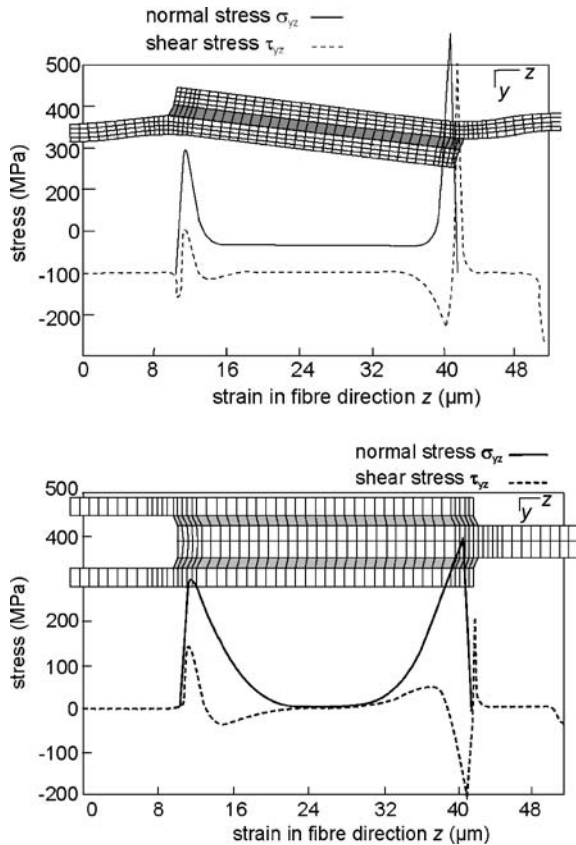
Table 7.1 (continued)

Method	Sample configuration	Property
Single lap shear test		Apparent shear strength (mode II)
Double lap shear test		Apparent shear strength (mode II)
Compression Shear Test (CST)	 inter intra	Apparent shear strength (mode II)
SEN (Single Edge Notched Test) [intralaminar]		G_{Ic}
DCB (Double Cantilever Beam Test) [interlaminar] tapered DCB specimen: constant compliance due to change in thickness of beams with crack length		G_{Ic}
BEND (Bending)		Transversal strength (mode I)
ENF (End Notched Flexure Test) [interlaminar]		G_{IIc}

7.3.6 Some Remarks on Shear Tests

Though widely used by many practitioners, the analysis of the *single lap shear test* is extremely complex particularly if there is any flow in the bonding medium. Since the nature of failure is by both plastic and elastic extensions, and the nature can change as a function of relative travel distance of the two bonded faces. It is not recommended for thin films but apparently has some value for organic bonding agents. The *double lap shear test* is an advancement of the single lap shear test to get a relatively pure shear load of the interphase. The evaluation occurs mostly by the shear lag model, estimating an apparent shear strength dividing the total load by the total area under shear stress.

Fig. 7.9 Geometry of the loaded region in single and double shear lap tests as well as the stress distribution (from [1])

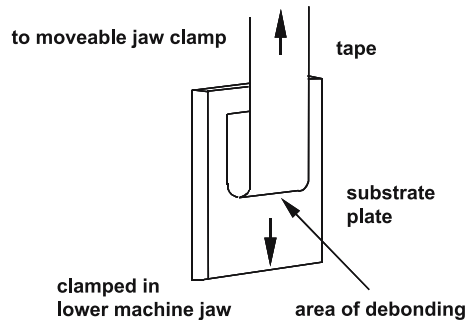


7.4 Characterization of Surface Forces and Adhesion

7.4.1 Peel Test

The peel test is mostly used to characterize the adhesion of tapes or films on substrates. A bonded assembly of two adherents is prepared under specific conditions using the adhesive under test. The adherents are then pulled apart at a substantially steady rate and angle, starting at the open end of the bond, in such a way that separation occurs progressively along the length of the bonded adherents. (Recommended dimensions of the bonded surface 25 mm width, length of 150 mm by ISO 8510-1 [23]). From the curve of force versus grip separation the average peel force is determined. The force per width of bonded area is evaluated.

Fig. 7.10 General arrangement of the peel test



- A primary use of both the 90° and 180° tests is the measurement of adhesion in the tapes and labels industry.
- The 90° rigid substrate coating peel test is executed by bonding an extremely high-strength peel tape material, and then peeling at an exact 90° angle. The angle is maintained by a slider that is pulled along simultaneously with the pull-up rate, while continuously recording the progressive peel force.
- 90° Flexible substrate peel test (German Wheel): By mounting the sample on the periphery of a free running German Wheel, the coating is peeled from the substrate.
- 180° Back Peel Test: Here the sample is attached to a fixed to a vertical mount.
- Peel resistance of high-strength adhesive bonds – Floating roller method (ISO 4578 [24]) – The angle is self-adjusting by a special equipment.

If the components are stiff enough there is no stretching of it and the measured way of the machine is equal to the debonding length.

In detail, the peel work is the sum of the following components:

1. Surface energy that results from the creation of two free surfaces (energy of “dewetting”). This term is also referred to as the intrinsic work of adhesion (or cohesion).

2. Bulk energy that dissipates into the stripping member.
3. Strain energy in the newly detached strip.

The intrinsic work of adhesion (or cohesion) is independent of the peel rate (speed) if no viscoelastic effects occur, peel angle, thickness of the adhesive and thickness of the stripping member. Its values vary from 0.07 J/m² for hydrocarbon van der Waals interactions to 2 J/m² for a system with covalent bonding as part of the adhesion.

The work of fracture can be several orders of magnitude greater than the intrinsic work of adhesion. This raises some questions: Does this mean the peel test is inappropriate? or better still, Does this mean that the intrinsic work of adhesion isn't a practical issue, and that in a practical application we want more than the work of adhesion?

7.4.2 Blister Tests

The blister test is used to characterize the adhesion between a substrate and a flexible layer by creating and enlarging a blister between both. Generally different geometries were established, overviewed in Table 7.2.

Table 7.2 Different arrangements of commonly used blister tests

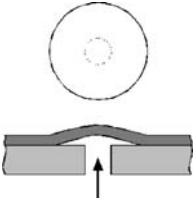
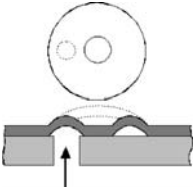
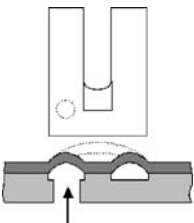
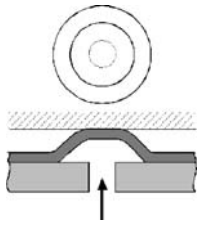
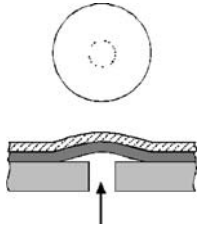
Standard blister test		$G = \frac{3}{32} \frac{(1-\nu^2)p^2 r}{E} \left(\frac{r}{t}\right)^3$ <p>derived by Williams for bending of a thick plate,</p> <p>or $G = \left(\frac{p^4 r^4}{17.4 E t}\right)^{1/3}$</p>
Island blister test		<p>derived from Gent and Lewandowski, based on stretching of a thin membrane</p> <p>Very strong influence of G on geometry, especially compared with the peninsula blister test</p>
Peninsula blister test		$G = \frac{p^2 a^4}{18 D} \quad \text{with} \quad D = \frac{E t^3}{12(1-\nu^2)}$ <p>a is the strip width, D the plate rigidity, and t the thickness of the blister (derived from Dillard and Bao, based on the plate theory)</p>

Table 7.2 (continued)

<p>Constrained blister test</p>		$G = \frac{p^2 R^4}{16 D} \left[\frac{(b^4 - 1) \ln(b) - (b^2 - 1)^2}{b^2 - 1 - 2 \ln(b)} \right]^2$ <p>with supported radius b and the plate rigidity</p> $D = \frac{E t^3}{12 (1 - \nu^2)}$ <p>t is the thickness of the blistered film, the gap between film and upper constraint</p> $H = \frac{p^2 R^4}{64 D} \left[\frac{b^6 - 5b^4 + 7b^2 - 3 + 2 \ln(b)(3b^4 - 2b^2 - 1) - 8b^4 \ln(b)^2}{b^2 - 1 - 2 \ln(b)} \right]$
<p>Inverted blister test</p>		<p>with $G = pH$ for steady state energy release at great blisters, due to Jensen and Cochelin Derived by Fernando and Kinloch</p>

7.4.3 Blade Cutting Test (Hesiometer)

The operating principle of the blade cutting (hesiometer) or razor blade test is to establish a wedge-shaped splitting plane at a layer interface, project that opening forward and measure the energy required to separate the coating from the structure below it.

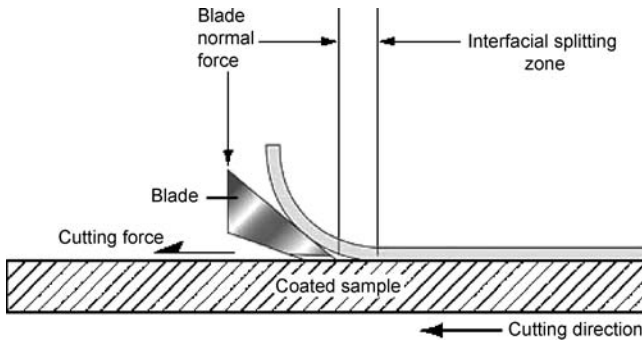


Fig. 7.11 Arrangement of the blade cutting test (Quad Group Inc., Spokane, WA)

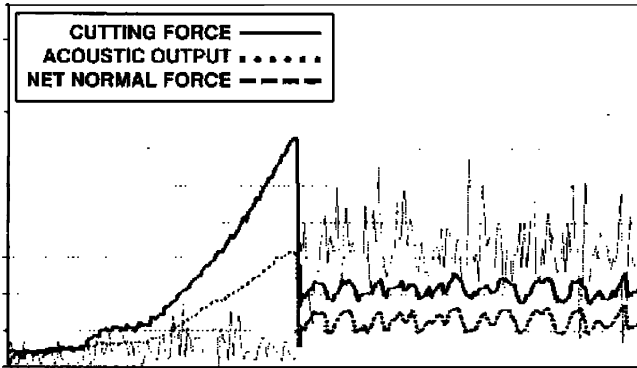


Fig. 7.12 Typical blade cutting plot (hesiometer), arbitrary units on the axes

The diagram shows a strong increase of the cutting forces penetrating the coating (left part of the curve). If the blade comes in contact with the substrate, a drop in cutting and normal force curve is obtained.

7.4.4 The Adhesion Scratch Test (Diamond Scratch Test, Stylometer), Nanoscratch Test

The adhesion scratch test is currently the most commonly used method of assessing coating adhesion. The method is reproducible and capable of generating stresses which exceed the interfacial bond strength of thin well adhering films.

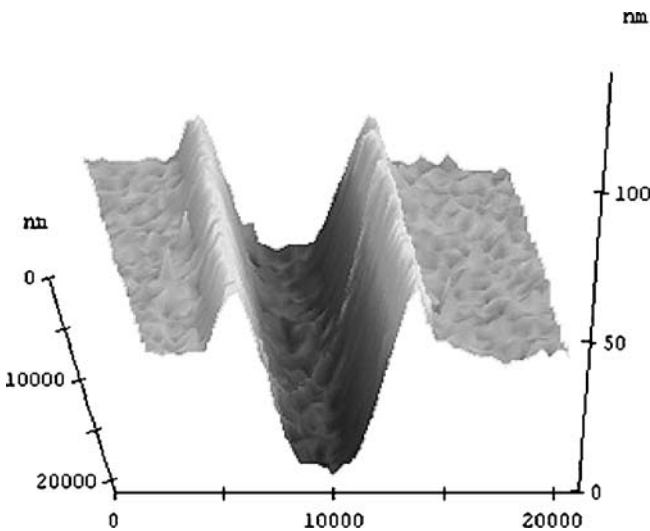


Fig. 7.13 Nanoscratch, visualized by a SFM

The test is easily performed: a loaded stylus (spherical diamond) is drawn across a coated surface under an increasing normal load until some well defined failure occurs at the critical load. During the test, both the vertical force (F_v) applied to the indenter and the horizontal force (F_H) required to move the stage under the indenter are recorded, and where applicable the acoustic energy output. A plot of the effective coefficient of friction (F_H/F_v) as a function of applied load then allows critical failure events and changes in the failure mechanisms to be identified. These events can then be observed microscopically (via light or scanning electron microscopy) to assess the type of failure mode.

The failure force is a measure of relative adherence for samples of similar character and thickness. It is believed that techniques can be developed to measure coating tensile strength, elastic limit, scratch resistance, friction coefficient and other physical properties, if the very complex behaviour of deformation of the adhering layer is understood.

7.4.5 Nanoindentation Test

The nanoindentation device pushes a calibrated diamond indenter (perpendicular) into a specimen surface at a controlled loading rate. The penetration depth as a function of the applied load is recorded continuously during a complete cycle of loading and unloading. Different experimental setups are possible, from a pendulum pivoted on bearings which are essentially frictionless with a coil producing motion of the indenter towards the specimen and into the specimen surface up to setups on the basis of a scanning force microscope (SFM).

A frequently used indenter is a Berkovitch diamond, a three-sided pyramid, because it can be machined down very accurately to a very sharp tip with a curvature radius of one half of a nanometer. Resolutions in the order of up to $0.1 \mu\text{N}$ and 0.1 nm for the load and displacement respectively, are usual. Load range is up to 1 N .

The instruments are mostly equipped with high magnification microscopes to enable high precision selection of any area of very small specimens. With this experiment *hardness* and *Young's modulus* can be determined. Furthermore, the *fracture toughness* can be deduced by the use of indentation fracture theories, based on relating the length of cracks produced during indentation to the applied load.

Fig. 7.14 SEM image of a Berkovich indent

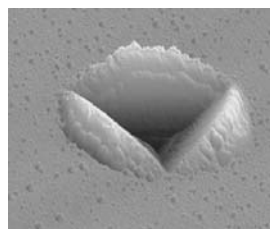


Fig. 7.15 Illustration of the indentation geometry at maximum load for an ideal conical indenter

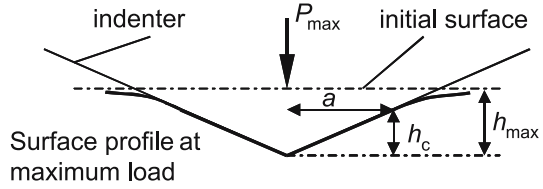
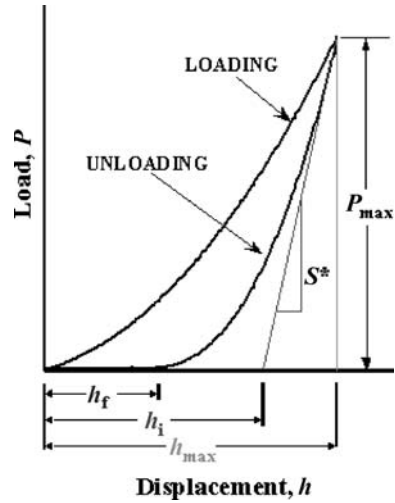


Fig. 7.16 Schematically indentation load–displacement curve of a nanoindentation test, h_{max} is the maximal displacement, h_f the final depth, h_i the intercept displacement



Upon initiation of unloading, the load does not suddenly fall to zero, i.e. the unloading curve is not horizontal; instead the elastic component of the displacement starts to recover so that contact between the material surface and the indenter is still maintained. As the load is decreased the elastic displacement continues to recover until at zero load the displacement reaches a final value. The *micro-hardness*, H , can be determined by measuring the peak load and dividing this by the projected area of the impression, A . A is defined as the product of the indenter shape factor, k , and the square of the contact depth at peak load, h_{max} .

$$H = \frac{P_{max}}{kh_{c,max}^2} \tag{7.10}$$

For measurement of the *Young's modulus*, the unloading portion of the depth–load curve is analysed according to Sneddon's relation. This relation is independent of the indenter geometry.

$$E_r = \frac{\sqrt{\pi}}{2} \frac{S}{\sqrt{kh_{c,max}^2}} \tag{7.11}$$

where S is the stiffness and E_r is the reduced modulus defined by:

$$E_r = \frac{(1-\nu^2)}{E} + \frac{(1-\nu_i^2)}{E_i} \quad (7.12)$$

which includes Poisson's ratios and Young's moduli of the specimen and the indenter (the latter subscripted i).

Recently, it has been demonstrated that the *fracture toughness* K_c can be measured using very small specimen by the indentation fracture method. Here no special specimen geometry is required. The test relies, however, upon the indentations to produce a crack system by semi-brittle failure mode, i. e. typically radial or median cracks. The fracture toughness can then be determined from the crack size if the fracture mode is well understood. SEM analysis can be used to validate the nanoindentation crack lengths necessary for calculation of the fracture toughness. This latter method has also been adopted for measuring the fracture toughness of single crystals using the nanoindentation device with a Berkovitch indenter.

Based upon radial and median cracks, several expressions for toughness have been proposed. A generalized form of these expressions is given by:

$$K_c = x_v \left(\frac{a}{l} \right)^k \left(\frac{E}{H} \right)^n \frac{P}{c^{*3/2}} \quad (7.13)$$

where x_v is a calibration factor, (a/l) is the ratio of crack length to impression size, $c^* = (a+l)$ is the crack size as measured from the centre of the impression, and k and n are power indices. This method relies upon the factor $P/c^{*3/2}$ to be constant for a given material for the fracture toughness to be determined.

7.4.6 Surface Force Measurement: Surface Force Apparatus/MASIF

The surface force apparatus (SFA) or MASIF (measurement and analysis of surface and interface forces) measures the force acting between two surfaces coming into contact. It can be realized by two crossed cylinders of mica sheets, or by a sphere against a flat surface, which is mathematically equivalent. The surfaces are prepared or modified by the systems under interest.

The contact between a sphere and a flat surface can be modelled in different ways.

The *Hertz model* describes the contact of a hard sphere with radius R on a stiff surface in vacuum without adhesion ($\gamma_{12}=0$), only elastic deformation of the surface. With a elasticity modulus K of the hard sphere the contact radius becomes

$$a = \sqrt[3]{\frac{RF}{K}} \quad (7.14)$$

Beyond the Hertz model the *JKR* theory (Johnson, Kendal, Roberts) for large soft objects takes adhesive deformation of the sphere in vacuum into account. For the contact radius a_0 in the unloaded position and the pull-off force F_s follows

$$a_0(F=0) = \sqrt[3]{\frac{12\pi R^2 \gamma_{12}}{K}} \quad F_s = -F_{adhesion} = -3\pi R \gamma_{12} \quad (7.15)$$

Fig. 7.17 Contact between a sphere and a flat surface according to the Hertz as well as the JKR model: Elastic deformation of the sphere without and with adhesive interaction

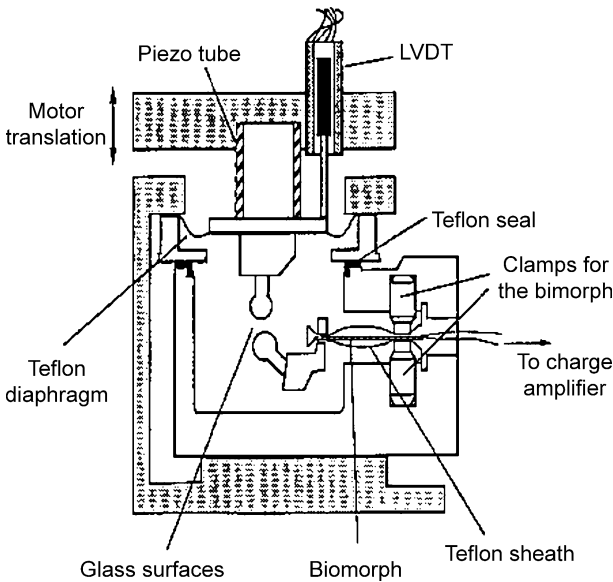
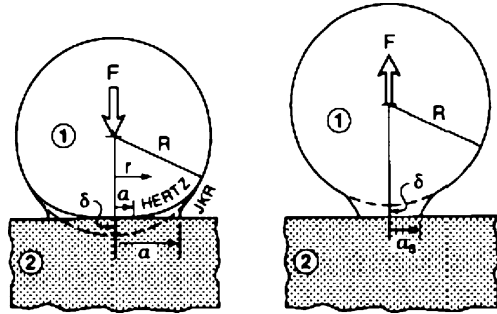
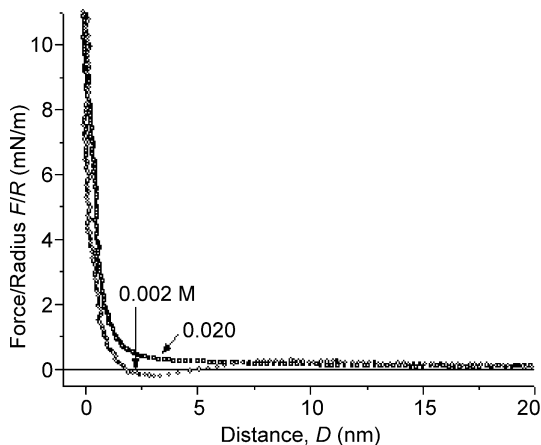


Fig. 7.18 Schematic drawing of the bimorph surface forces apparatus (from [2])

Fig. 7.19 Force (normalized by radius of curvature) vs. distance function of two polystyrene surfaces in surfactant solutions, at and below the cmc (0.020 M) [3]



The *DMT* theory (Derjaguin, Muller, Toparov) for small hard objects gives

$$F_{adhesion} = 4\pi\gamma R \quad (7.16)$$

A possible realization of the MASIF apparatus is shown in Fig. 7.18. One of the spheres under investigation is mounted on a bimorph, used as force sensor, the other on a piezo tube used for distance control between the spheres.

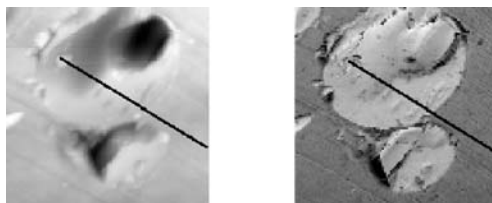
7.4.7 Force Measurement by AFM/SFM

Force modulation microscopy as speciality of surface force microscopy monitors the damping of cantilever oscillation due to energy dissipation in sample surface. It is correlated to elastic properties of the surface (compare also phase modulation). Hard surface provide weak damping, soft surfaces give strong damping.

Similarly in contact mode from the penetration of the hard cantilever tip into the specimen the stiffness of the sample can be estimated, if the elastic constant of the cantilever is known.

The force versus distance curves provide information on adhesive and surface forces.

Fig. 7.20 Topography and stiffness image of a glass fibre composite (microtomed specimen), along the black line, e. g. the step in stiffness can clearly be estimated [19]



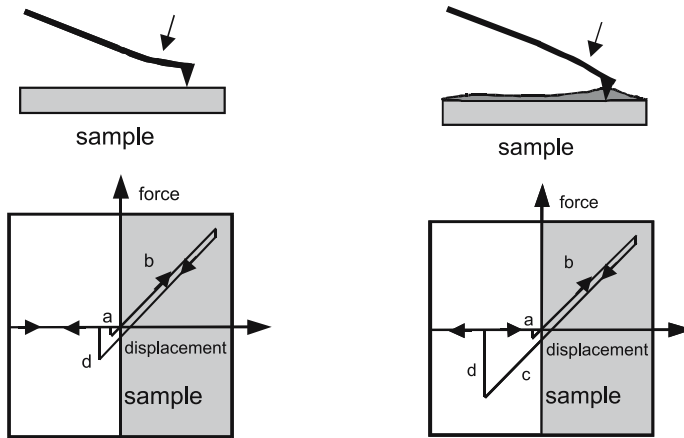


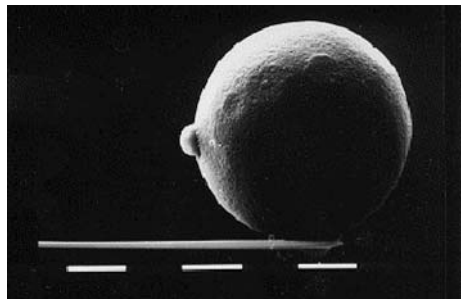
Fig. 7.21 Typical force–distance curves for the characterization of adhesive forces. Left – van der Waals interaction only, right – surface with thin water film: (a) jump in, (b) deflection due to surface stiffness, (c) cantilever deflection due to capillary forces of the water film, (d) jump out

7.4.8 Colloidal Probe Techniques with the SFM

Mounting a particle under investigation on the tip of a SFM, the deflection of the cantilever reflects the forces acting on the particle approaching a surface. In this way surface forces in the sub- μm -range can be studied similar to the SFA. Dependent on the operation mode of the SFM different interactions can be estimated (e. g. adhesion, friction).

It is obvious that in this case a detailed knowledge of the geometry and mechanical deformation behaviour of the probe is necessary to interpret the experimental findings.

Fig. 7.22 Scanning electron micrograph showing a cellulose sphere attached to an AFM cantilever. In this case the sphere was used in a friction study. The white scale bars are 10 micrometers (from <http://www.kemi.kth.se/organisation/annual/1999/surf.html>)



References

1. A. Hampe, O. Hoyer, J. Munschau, K. Schumacher, C. Marotzke, Messung der Scherfestigkeit von Faserverbunden, *Forschung Aktuell* **27–29** (7) 18, 19 TU Berlin (1990)
2. P.M. Claesson, T. Ederth, V. Bergeron, M.W. Rutland, *Adv. Coll. Interface Sci.* **67**, 119 (1996)
3. H.-J. Jacobasch, F. Simon, P. Weidenhammer, Adsorption of ions onto polymer surfaces and its influence on zeta potential and adhesion phenomena. *Coll. Polym. Sci.* **276**, 434 (1998)
4. B. Carlowitz (ed.), *Kunststoff-Handbuch*. Band: Die Kunststoffe – Chemie, Physik, Technologie (Hanser, Munich, 1990), pp. 145–169
5. R.M. Christensen, *Theory of Viscoelasticity* (Dover, Mineola, NY, 2003)
6. N.E. Dowling, *Mechanical Behavior of Materials* (Prentice-Hall, Upper Saddle River, NJ, 1998)
7. U. Eisele, *Introduction to Polymer Physics* (Springer, Berlin Heidelberg New York, 1990)
8. W. Goldsmith, *Impact: The Theory* (Dover, Mineola, NY, 2001)
9. D. Haarer, H.W. Spiess (ed.), *Spektroskopie amorpher und kristalliner Festkörper* (Steinkopff, Darmstadt, 1995)
10. G. Kämpf, *Charakterisierung von Kunststoffen mit physikalischen Methoden* (Hanser, Munich, 1982)
11. A.J. Kinloch, *Adhesion and Adhesives: Science and Technology* (Kluwer Academic, 2 Dordrecht, 1987)
12. A.J. Kinloch, R.J. Young, *Fracture Behaviour of Polymers* (Kluwer Academic, Dordrecht, 1993)
13. S. Matsuoka, *Relaxation Phenomena in Polymers* (Hanser, Munich, 1992)
14. T. Murayama, *Dynamic Mechanical Analysis of Polymeric Material* (Elsevier Scientific, Amsterdam, 1978)
15. L.E. Nielsen, *Mechanical Properties of Polymers and Composites* (Marcel Dekker, New York, 1993)
16. G.W. Scherer, *Relaxation in Glass and Composites* (Wiley, New York, 1986)
17. H. Schmiedel (ed.), *Handbuch der Kunststoffprüfung* (Hanser, Munich, 1992), pp. 80–111
18. K. Schneider, V. Herrmann, Semi-quantitative mechanical characterisation of fibre composites in the sub-micron-range by SFM. *Composites Part A* **32**, 1679–1687 (2001)
19. L.C.E. Struik, *Internal Stresses, Dimensional Instabilities and Molecular Orientations in Plastics* (Wiley, Chichester, 1990)
20. F.R. Schwarzl, *Polymermechanik* (Springer, Berlin Heidelberg New York, 1990)
21. I.M. Ward, D.W. Hadley, *An Introduction to the Mechanical Properties of Solid Polymers* (Wiley, New York, 1993)
22. ISO 8510-1: 1990, Adhesives – Peel test for a flexible-bonded-to-rigid test specimen assembly – Part 1: 90 degree peel
23. ISO 4578: 1997, Adhesives – Determination of peel resistance of high-strength adhesive bonds – Floating-roller method
24. W. Grellmann, S. Schneider (eds.), *Deformation and Fracture Behaviour of Polymers* (Springer, Berlin, Heidelberg 2001)

Chapter 8

Interfaces Between Incompatible Polymers

Peter Busch¹ and Roland Weidisch²

¹JCNS-FRMII, TU-München, Lichtenbergstr. 1, 85747 Garching, Germany,
p.busch@fz-juelich.de

²Friedrich-Schiller-Universität Jena, Institut für Materialwissenschaft und Werkstofftechnologie,
Löbdegraben 32, 07743 Jena, Germany, roland.weidisch@uni-jena.de

Abstract Many polymers are incompatible with each other and form phase segregated morphologies in binary blends and copolymers. Properties are largely determined by an interplay between morphologies, interfaces and properties of components. Neutron and X-Ray reflectometry are powerful techniques to determine the interface width between homopolymers, polymer blends, components of block copolymers and other organic materials. The techniques are described, several examples are discussed and compared with real space methods.

8.1 Introduction

Heterogeneous polymers such as polymer blends and copolymers are important for applications in industry because they have the potential for the design of materials with tailored properties. For industrial applications it is often demanded to have the combination of different properties which can only hardly be achieved by a single polymer component. A prominent example is polystyrene (PS), which is a stiff material, but relatively brittle, what makes it inappropriate for many applications. However, a blend of it with rubbers, e. g. polybutadiene, meets the criterion of a tough material with a still large stiffness. Another problem arises from the mixing of different polymers. Because of the incompatibility of many polymers they tend to demix. In order to design new materials with special properties an understanding of the mixing behaviour is necessary, what can be done by studying the interfaces between the two components. Special techniques have to be used to understand the interplay between morphology, interfaces, and mechanical properties of polymers. Without any knowledge of compatibility and interfaces of polymers it is not possible to combine the advantages of different polymers.

With block copolymers, which are discussed in another chapter of this book, macroscopic phase separation can be avoided and the properties of incompatible

polymers can be combined in an elegant way. However, for the understanding of the properties of these materials, the knowledge about the degree of phase separation is important. This can also be investigated by studying their interfaces in appropriate model systems. The interfacial behaviour is fundamental to the bulk properties of the system, and consequently to the applications of the polymers. For instance adhesion, miscibility, compatibilization, welding, surface wetting, blend morphology, mechanical strength, etc. are all controlled by interfacial behaviour. The characterization and understanding of these properties on a microscopic level are therefore of vital importance.

Several techniques can be applied for the study of polymer interfaces, e. g. direct imaging by electron microscopic techniques. However, better resolution can be achieved by reflectometry techniques either with X-Rays or neutrons. For reflectometry the samples are transferred into thin films (typical thicknesses are smaller than a few 100 nm) on a reflective substrate and the reflected intensity is measured in dependence of the incident angle. This reflectivity can be compared with calculated reflectivities for appropriate models and information about the density profile along the film normal can be developed. X-Ray reflectometry has the advantage that it can be done in many cases in a laboratory either with a sealed tube or a rotating anode. Only in special cases the high intensity of synchrotrons is needed. However, in certain cases neutron reflectometry has been proven to be of considerable advantage, mainly of two reasons.

First, as X-Rays are scattered by the electrons from the samples the contrast in electron density between different regions is probed. For many polymer systems the electron density is relatively similar and therefore the scattering is weak. Neutrons are scattered by the nuclei of the polymers. As neutrons possess a spin, the interaction with the nuclei are very different for different elements and even different isotopes of the same element can possess sufficient contrast to induce sufficient scattering. In polymer science often the large difference in the scattering properties between hydrogen and deuterium is used. By substituting the hydrogen atoms of specific groups or components by deuterium allows to tune the contrast in a controlled manner without changing the chemistry and the physical properties of a given system significantly. So the potential of neutron reflectometry is larger than for X-Rays due to the possibility of labeling whole molecules or specific sections of the polymer by deuteration and produce a large contrast variation with the normal hydrogenous molecules around it. Also polymers at the air/liquid or liquid/liquid interface can be measured by adjusting the scattering properties of the liquid by contrast variation and contrast matching techniques.

A second advantage of neutron reflectometry is that the neutrons have a low absorption and can travel over relatively large distances through many materials which are opaque for X-Rays. This offers a higher flexibility for designing experiments to access certain interfaces. For example an adsorbed layer at the interface between a silicon substrate and a solvent can be hardly measured by X-Ray reflectometry due to the additional liquid/air interface. With neutrons one can circumvent this problem by guiding the incident beam through the silicon substrate and measuring the reflected intensity scattered from the liquid silicon interface.

In the next section a short introduction to polymer interfaces will be given and the most important thermodynamic parameters which contribute to the free energy will be discussed. Then follows a section about the basic experimental principles of reflectometry techniques and the theoretical concepts to explain the experimental results will be discussed. Finally applications of X-Ray and neutron reflectometry on thin films or layers will be presented and compared with other techniques like electron microscopy or AFM.

8.2 Theory

Most incompatible polymers show interfaces in the range of 1–50 nm, depending on compatibility. During the mixing process, the incompatible polymers interpenetrate at temperatures above the glass transition. The interfacial width generally increases in time, reaching an equilibrium value, which is determined by the Flory–Huggins interaction parameter χ . From a detailed knowledge of the interaction parameter one can expect to obtain a better understanding of polymer miscibility. Furthermore, the χ -parameter is also correlated to the interface width which allows to tailor specific interfaces for special uses. For polymer blends the free Gibbs mixing energy can be described by a lattice model. The single A- and B-units are considered to have the same volume and they occupy the cells of a regular lattice. In general the free mixing energy can be formulated like

$$\Delta G = \Delta H - T\Delta S \quad (8.1)$$

Here ΔG is the free mixing energy, ΔH the mixing enthalpy, T the temperature and S the mixing entropy.

The free mixing energy is thus consisting of two parts, one is the enthalpic part and the second is the entropic part. Following the approach of Flory and Huggins [1] the two contributions can be expressed by

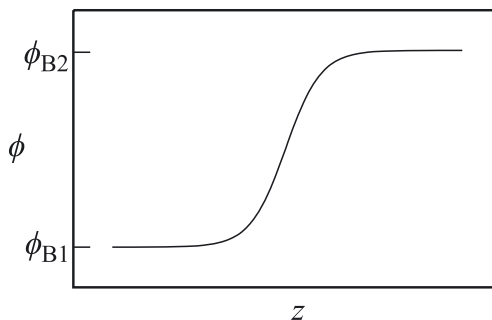
$$\Delta H = nk_B T \chi \phi_1 \phi_2 \quad (8.2)$$

$$\Delta S = -nk_B \left(\frac{\phi_1}{N_1} \ln \phi_1 + \frac{\phi_2}{N_2} \ln \phi_2 \right) \quad (8.3)$$

where ϕ_1 , ϕ_2 are the volume fractions, N_1 , N_2 the degrees of polymerization of polymer 1 and 2, respectively, and χ is the Flory–Huggins interaction parameter.

The entropic part is associated with the motion of the centre of mass of the polymer molecules and is therefore called translational entropy. This contribution favours always mixing. However, due to the large molecular weights of polymers,

Fig. 8.1 Schematic representation of the density profile of an interface between incompatible polymers depending on the volume fraction of polymer B₁ and B₂ at equilibrium. z is a coordinate perpendicular to the interface



it is usually very small. The enthalpic part can be either positive or negative depending on the compatibility of the two polymers and dominates in many cases the mixing behaviour. Most polymers have unfavourable interactions resulting in a large interaction parameter. Therefore, the free mixing energy ΔG is positive, leading to macrophase separation or two phases in polymer blends. Depending on the value of the interaction parameter incompatible polymers form an equilibrium interfacial profile where the interface width a_i depends on the Flory–Huggins parameter χ . The general concentration profile of the interface for a two phase polymer blend is shown in Fig. 8.1.

Thermodynamic properties can be calculated by several theoretical approaches which differ in the assumptions being made and the mathematical techniques being used. More assumptions included in a specific theory leads often to more accurate results, which agree better with the experimental data. However, this is in many cases also accompanied with more complex formulas and expressions. One of the most basic theory is the mean field theory which assumes a homogeneous, mean field everywhere in the sample, neglecting fluctuations, excluded volume or finite size effects. Using the following approach an analytical solution for the volume fraction profile at an interface between two incompatible blends can be calculated [2]:

$$\phi(z) = \frac{1}{2} \left(1 + \tanh \left(\frac{2z}{a_1} \right) \right) \quad (8.4)$$

with volume fraction ϕ , z as coordinate perpendicular to the interface and a_1 being the interfacial width. In the case of incompatible polymer blends the interfacial width can often be calculated by using the following equation:

$$a_1 = \frac{2b}{\sqrt{6\chi}} \quad (8.5)$$

where b is the characteristic segment length.

This calculation gives a useful tool to calculate volume fraction profiles and interfacial width for polymer blends based on neutron reflectometry. Furthermore, (8.5) clearly demonstrates that polymer–polymer miscibility is directly correlated

with interfacial width. The interfacial width a_i decreases with increasing incompatibility, expressed by the interaction parameter χ . However, this correlation does not include complex phenomenon such as surface roughness, chain end effects, compositional fluctuations at the interface or molecular weight distribution. These effects may influence the nature of interface formation in a very complex manner, as will be discussed later in this chapter.

In the following paragraph we will present the experimental and theoretical concepts of neutron reflectometry.

8.3 Neutron Reflectometry

Numerous techniques have been applied to investigate the surface and interfacial behaviour of polymers. However, the accuracy of the experimental data required in order to obtain reliable information about the interfacial properties requires special techniques and the associated instrumentation. One technique which has gained significant importance within the polymer community over the last two decades is specular neutron reflectometry. The reasons for this popularity are partly due to the development and advances in the reflectometers, but are mostly associated with the simple fact that neutron reflectometry is very sensitive to the interfaces between polymer/polymer, but also polymer/liquid interfaces.

To probe interfacial properties like interfacial thickness or interdiffusion of blends of incompatible polymers or diblock copolymers the systems are transformed into a thin film serving as a model system [3]. With reflectometry then the density profile along the film normal can be determined with accuracy on a sub-nanometre length scale. This kind of information is also given by X-Ray reflectometry and to some degree also by light ellipsometry, however, reflectometry experiments performed with neutrons goes beyond those other radiation sources due to the possibility of deuteration and the lower absorption coefficients as has already mentioned in the introduction.

Neutron scattering experiments are performed in neutron research reactors. Only relatively small thermal powers are needed (10–60 MW typically), as the major goal is not to produce as many neutrons as possible but a high neutron flux density. The neutrons produced are collected and guided into large experimental halls, where they can be accessed by different beamlines. Examples for neutron research reactors are the Institute Laue–Langevin (ILL) in Grenoble, the National Institute of Science and Technology (NIST) in Washington and the Forschungsreaktor München II, which started to work recently in Spring 2004.

One example for a neutron reflectometry beamline is the beamline ADAM at ILL. The setup of this station is sketched in Fig. 8.2 [4]. The incoming bunch of neutrons has a wide spread of thermal energies as well as a large divergence. The desired energy wavelength must be selected by monochromators, which are typically choppers or graphite crystals. The neutron beam is collimated by slits to

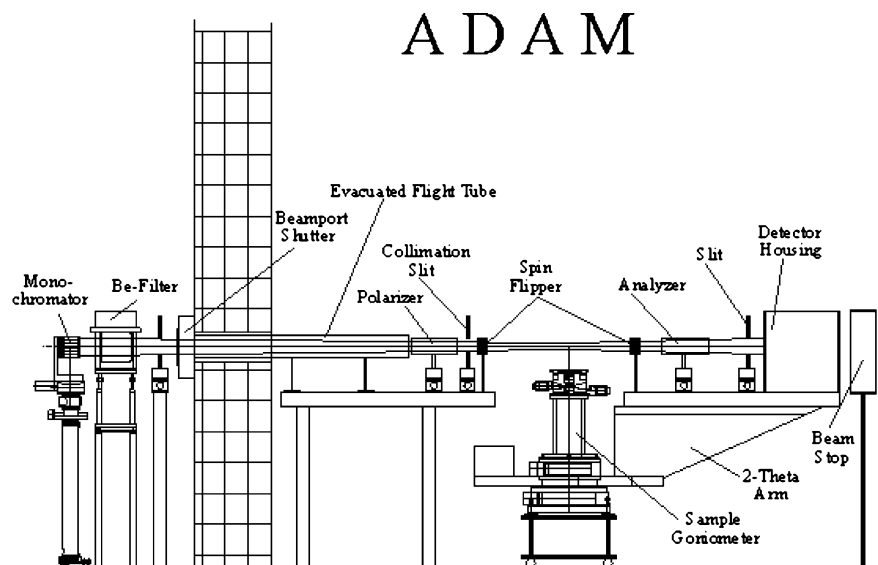


Fig. 8.2 Experimental setup of the reflectometer ADAM at the ILL in Grenoble. The incoming beam is monochromatized and – after passing an evacuated flight tube – collimated by a slit. The sample is mounted on a goniometer to adjust the angle of incidence. The detector is mounted on a 2θ arm and is moved twice the angle of incidence to record the specular reflected intensity. Image from [4]

a finite size and a small divergence before it hits the sample surface and the reflected intensity is collected by a detector, which is often a helium gas detector.

Even though X-Rays and neutrons are quite different in nature (X-Rays are photons, whereas neutrons are particles), the scattering theory for both is very similar. This is due to the wave behaviour of neutrons and therefore neutrons can be treated to a good approximation like electromagnetic waves in classical optics. With only a few minor modifications, neutron waves are able to reflect, refract and interfere following according to standard optical rules and the formalism is quite similar for X-Rays and neutrons.

A full discussion of the theory of reflection is beyond the scope of this book and the reader is referred to further literature [5, 6]. However, it is necessary to include a brief description of the basic concepts since an understanding of them is essential in the interpretation of reflectivity data. The following explanations will be made for neutron reflectometry, but are also valid for X-Ray reflectometry unless stated explicitly.

First we will consider the reflection from an infinitely sharp substrate, characterized by its refractive index n . The refractive index can be written as

$$n = 1 - \frac{\lambda^2}{2\pi} b\rho_n + i \frac{\lambda}{4\pi} \mu_n \quad (8.6)$$

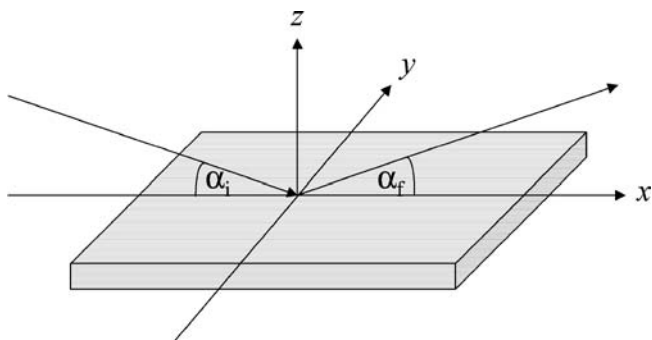


Fig. 8.3 Schematic representation of the general setup used for reflectometry. The beam impinges at a glancing angle α_i and is specularly reflected under an exit angle $\alpha_f = \alpha_i$

where b is the scattering length (for X-Rays this is the classical electron radius a), ρ_n the number density of nuclei (for X-Rays the electron density) and μ_n the linear absorption coefficient for neutrons. The product $b\rho_n$ is called the scattering length density. The particle density ρ_n is the analogon to the electron density ρ_e in X-Ray reflectometry and for b the classical electron radius r_e is used. This equation is often abbreviated by $n = 1 - \delta + i\beta$. δ is the dispersion term and β the absorption term of the refractive index of a given material.

If an incident beam impinges from air at an infinitely sharp substrate with refractive index n under a glancing angle of incidence α_i most of the intensity will be specularly reflected under an exit angle α_f , where $\alpha_i = \alpha_f$, as sketched in Fig. 8.3 The reflectivity is defined as the ratio of the reflected intensity to that of the incident beam and is usually presented by the momentum transfer \mathbf{q} . In general \mathbf{q} is a three-dimensional vector with components in x , y and z . However, it is only the z -component q_z which contributes to the specular reflectivity $R(q_z)$ [7]. Thus it contains the information about the density profile along the film normal. The momentum transfer q_z is connected to the incident angle α_i by the relation

$$q_z = 2k_z \sin \alpha = \frac{4\pi}{\lambda} \sin \alpha \quad (8.7)$$

The reflectivity R can be derived from Snell's law and the Fresnel equations, considering the complex index of refraction (8.6), to read as

$$R(q_z) = \left[\frac{1 - \sqrt{1 - (q_c / q_z)^2}}{1 + \sqrt{1 - (q_c / q_z)^2}} \right]^2 \quad (8.8)$$

where q_c is the momentum transfer associated with the critical angle of total reflection α_c , which is related to the dispersion term by $\alpha_c \approx \sqrt{2\delta}$. Equation (8.8) is also known as the Fresnel reflectivity and is often denoted as R_F [7].

As mentioned above, the Fresnel reflectivity is calculated for an infinitely sharp interface between two media, e. g. a substrate and air. In real cases an interface always possesses a certain roughness, which has to be considered. Usually exponential error functions are used to take this into account. However in certain cases also specific analytical profiles are used to describe the nature of an interface, as will be outlined later in this chapter.

It should be mentioned, that in general it is not possible to calculate from a measured reflectivity a concentration profile directly. As the reflectivity is the square of the amplitude of the scattered waves any information about the phases is lost. This is well known as the “phase problem” in scattering physics. However, from the general shape of the measured curve some first conclusions about, e. g. film thickness, number of layers and their thickness in a multilayer system can be estimated. This information can be used to develop a model of the density profile that is used to calculate a reflectivity which can be compared with the experimental results. Optimization of the model is necessary to bring the measured and the calculated reflectivities into good agreement. Often also information obtained by other, complementary techniques is helpful to develop a reasonable model. The strategy for the interpretation should be demonstrated at selected examples in the following section. These examples should also show that reflectivity and especially neutron reflectometry is a powerful tool to find solutions to problems which are important in polymer science.

8.4 Applications

8.4.1 Homopolymers

In this section examples will be given for the applications of reflectometry for polymer systems. We will start with two X-Ray reflectometry experiments to show some general concepts of reflectometry. Then neutron reflectometry studies will be presented, where the interfacial width of polymer blends and block copolymers, but also surface induced ordering phenomena at the film interfaces have been studied. An example of neutron reflectometry at the solid/liquid interface should show that also density profiles with a gradual shape can be investigated. Finally, neutron reflectometry will be compared with AFM-nanotomography, which is a 3D-visualization technique sensitive to local details in thin film geometry.

Figure 8.4 shows an X-Ray reflectivity curve of a homogeneous polystyrene film on a glass substrate [8] in dependence of the wave vector k_z . The experimental data are given by points. Several representative features can be seen immediately. First of all, there are regular oscillations, which are commonly called Kiessig fringes, named after H. Kiessig who first observed them in metal films [9]. They originate from the interference of the beams reflected at the two interfaces. From the distance between adjacent minima $\Delta q_z = 2k_z = 2\pi/D_{\text{film}}$ the film thickness can be estimated. Thus, the thicker the films, the distance between the minima will be smaller.

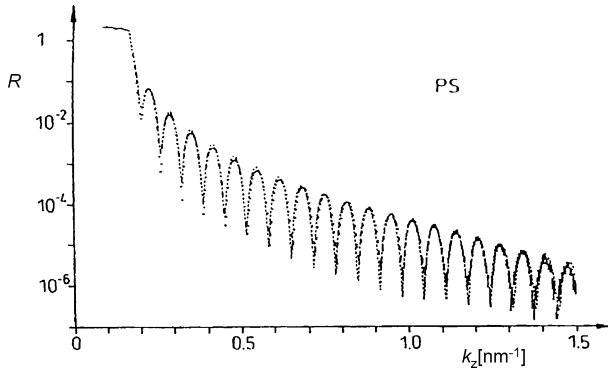


Fig. 8.4 X-Ray reflectivity of a homogeneous polystyrene film on glass [8]. A model fit (dashed line) yields the film thickness (49.3 ± 0.1 nm) as well as the surface roughness (0.3 ± 0.1 nm at the film surface and 0.6 ± 0.1 nm at the film substrate interface). The roughness of the film interfaces have been determined by assuming error functions

Furthermore, a plateau at low k_z can be seen. This is due to total external reflection of the X-Ray beam, i. e. the beam penetrates the polymer film only in a very thin layer at the top and all the incoming intensity is specularly reflected. Above a certain value of k_z the reflectivity drops drastically, which follows from an expansion of (8.8). This value ($\approx 0.18 \text{ \AA}^{-1}$) is connected to the critical angle of the substrate α_c . The critical angle of the polymerfilm, which is usually smaller for polymers, gives rise to a second, lower plateau at lower k_z values. Due to the logarithmic presentation this second plateau is often too weak to be visible. For a smooth substrate it follows that the decay follows a k_z^{-4} power law, whereas roughness from the films interfaces changes this slope.

The reflectivity can be calculated either by the matrix technique [5, 10] or the Parratt algorithm [11]. By using the matrix technique one considers that the film is made up by N interfaces. Then a transfer matrix is considered for each layer, which connects the fields at a given interface j with those at the next interface, $j-1$. After N matrix multiplications the reflected amplitude can be calculated and by squaring the amplitude the reflectivity is obtained. The Parratt algorithm is a recursive approach, where the ratio of the reflectivity and the transmittivity in each layer can be calculated from those of the layer below considering the Fresnel coefficient at the interface between them. Also the surface roughness is considered by assuming error functions.

The line in Fig. 8.4 is the calculated reflectivity based on a model which assumes a homogeneous polystyrene film on a semi-infinite silicon substrate. From the modeling of this fit the thickness of the polystyrene layer (49.3 ± 0.1 nm), the roughnesses of the substrate/film (0.6 ± 0.1 nm) and the film/air interface (0.3 ± 0.1 nm) can be calculated with subnanometer resolution.

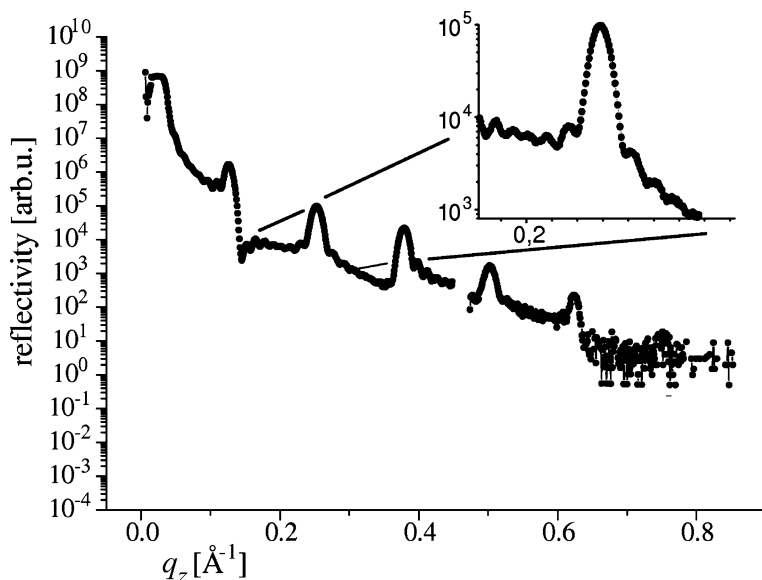


Fig. 8.5 X-Ray reflectivity of multilamellar bilayers of DMPC in the fluid L_{α} phase [12] on silicon. The sample consists of eight bilayers which give rise to Bragg peaks which are superimposed over the Kiessig fringes from the total film thickness, which appear more clearly in the inset

In the case described above the polymer film was homogeneous and had no internal structure, so the reflectivity arises purely from the scattering at the two films interfaces.

For films with a regular internal structure along the film normal, e. g. alternating multiple layers, the interfaces between these layers give rise to additional scattering, superimposed to the Kiessig fringes originating from the total film thickness. Prominent examples for multilayer systems are membranes of amphiphilic phospholipids which form bilayers. In thin film geometry these bilayers form a stratified structure, which can be studied by X-Ray reflectometry. Figure 8.5 shows an X-Ray reflectivity curve of a multilamellar membrane of 1,2-dimyrisoyl-sn-glycero-3-phosphatidylcholine (DMPC) [12]. DMPC is an amphiphilic lipid with a polar head group and a nonpolar tail. Thus the electron contrast is still sufficiently large to give reliable information from X-Ray reflectometry. In the thin film geometry the interfaces of the bilayers are oriented parallel to the films interfaces. Therefore, there is an alternating electron density profile along the film normal. This inner structure of the film leads to a superposition of interference at the inner and the outer interfaces resulting in additional Bragg peaks superimposed to the Kiessig fringes emanating from the films interfaces. In Fig. 8.5 it can be seen that the Bragg peaks are very pronounced and the high frequency Kiessig fringes can be observed more clearly in the magnification in the inset.

8.4.2 Polymer Blends

As stated in (8.5), for incompatible polymer systems like blends or block copolymers the mixing properties are related to the Flory–Huggins parameter via the interfacial thickness. Thus a measurement of the interfacial thickness can provide important information about the thermodynamic properties. One drawback for these materials is that often the electron density is very similar and one does not obtain reliable information from X-Ray reflectivity curves, even with synchrotron radiation. In these cases neutron reflectometry has proven to be a powerful technique because of the possibility to enhance the contrast simply by deuteration of one of the components, without changing the chemical or physical properties significantly.

The interface of two incompatible polymers in a blend is related to the Flory Huggins parameter χ and the statistical segment length b according to (8.5). This equation was obtained by a mean field approach, where an infinite chain length was assumed. Thus, for large molecular weight it is possible to calculate χ by (8.5), if the segment length b is known. In order to consider the effect of finite chain lengths for moderate or lower molar masses several expressions have been developed. A detailed discussion and comparison can be found in [13]. One approach which considers the slope at $\phi(z)=0.5$ has been calculated by [2]:

$$a_i = \frac{2b}{\sqrt{6 \left(\chi - 2 \ln 2 \left(\frac{1}{N_1} + \frac{1}{N_2} \right) \right)}} \quad (8.9)$$

where N_1 and N_2 are the degrees of polymerization of the two components respectively. This expression describes the interdigitation of incompatible polymers.

Schubert and Stamm investigated blends of PS and poly(methyl methacrylate) (PMMA) following this approach [14]. They prepared five bilayers with deuterated PS on top of PMMA, where the molar mass of PMMA was varied. The samples have been measured as cast and annealed. The latter was done to achieve the equilibrium interfacial thickness. The equilibrium interfacial thickness measured after annealing has an additional contribution from long range lateral roughness and waviness. This contribution will be seen on a relatively large length scale whereas interdiffusion of polymers as calculated by (8.9) takes place on a molecular length scale (several nanometres). Therefore, the authors assumed, that they can be separated by

$$a_i = \sqrt{(a_i^c)^2 - (a_i^0)^2}, \quad (8.10)$$

where a_i^c is the equilibrium interfacial thickness, a_i^0 is the contribution due to interfacial roughness, present before annealing and a_i the interfacial thickness due to incompatibility. a_i^0 is the dominating contribution in the as cast sample and can thus be obtained by analyzing the reflectivity curve from these samples.

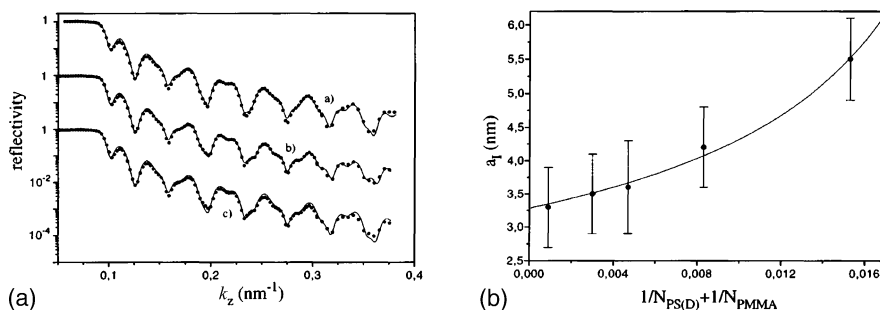


Fig. 8.6 (a) Neutron reflectivity data (●) and calculated fits (curves) for a blend of PS and PMMA before (a) and after (b) annealing. The experimental curve in (c) is identical to be, but fitted with the same roughness than in a). Interfacial width (●) of PS and PMMA with variation in the molar mass of PMMA. The line is a fit through the data based on (8.9) and yields an interaction parameter $\chi_{S/MMA} = 0.0326 \pm 0.0058$, as well as a segment length $b = (0.73 \pm 0.13)$ nm. Taken from [14]

Figure 8.6(a) shows the reflectivity curves before (a) and after (b) annealing. The values taken in the fits through the data have been determined to be (3.0 ± 0.4) nm for curve (a) and (4.6 ± 0.4) nm for curve (b). To demonstrate the accuracy of the technique, through curve (c), which is the same than curve (b), a model fit with the roughness parameter of curve (a) (3.0 nm) is drawn. It can be seen that the quality of the fit shown in (b) is much better than in (c). Thus the reflectivity is very sensitive to relatively small changes in interfacial width during annealing or other treatments of the polymer films.

The data for the interfacial widths a_1 are plotted in Fig. 8.6(b) in an appropriate way against the degrees of polymerization and a fit through the data on the basis of (8.9) yields the Flory–Huggins interaction parameter χ and the statistical segment length b . In this particular case values of $\chi_{S/MMA} = 0.0326 \pm 0.0058$ and $b = (0.73 \pm 0.13)$ nm have been found. Comparison with values obtained by other authors with different techniques like small angle neutron scattering [15], light scattering [16], fluorescence spectroscopy [17] demonstrate, that the experimental values obtained by this technique are in very good agreement with the values obtained by these other techniques. This shows, that by determining the interfacial properties from neutron reflectometry can give also information about important thermodynamic properties, which are not directly related to the density profile along the film normal.

8.4.3 Block Copolymers

As described in another chapter diblock copolymers undergo microphase separation to form regular structures like e. g. lamellae. In thin films there is often a preferential adsorption of one of the two blocks to the films interfaces, leading to

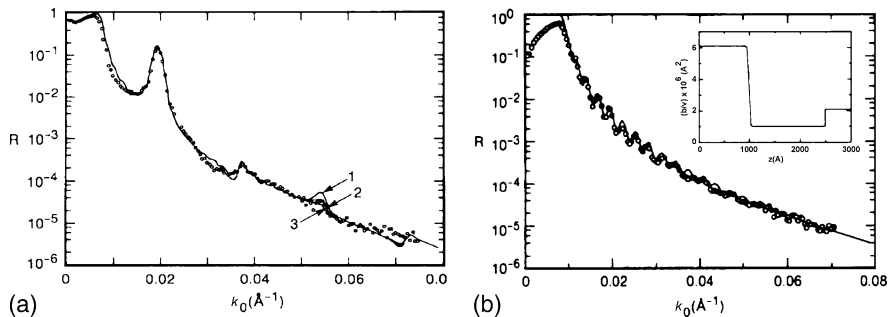


Fig. 8.7 (a) Neutron reflectivity curve (symbols) of a lamellar PS-*b*-D-PMMA diblock copolymer with molar mass of 30 kg/mol (Anastasiadis et al. 1989). The Bragg peaks correspond to the repeat period of the lamellae. The lines are model fits to the data and interfacial thicknesses of (1) 5.2 nm, (2) 5.4 nm and (3) 5.6 nm have been used. (b) The reflectivity of a bilayer of a deuterated PS film on top of a PMMA layer gives the same interfacial thickness [19]

a parallel orientation of the lamellae. Figure 8.7(a) shows the neutron reflectivity of a thin film of a lamellar PS-*b*-D-PMMA diblock copolymer [18]. Here D denotes that the PMMA block is deuterated. The alternating PS and PMMA lamellae have a thickness of 9.1 and 8.4 nm and the total film thickness was 149 nm. Also for this film a multilayer system is present and thus the curve has a similar shape than the curve in Fig. 8.5. The high frequency oscillations from the total film thickness are very weak. The lamellar structure gives rise to three pronounced Bragg peaks. The peak at $k_0 \approx 0.05 \text{ \AA}^{-1}$ is very sensitive to slight changes of the interfacial thickness. The three different lines in Fig. 8.7(a) are the results of model fits, where only the interfacial thickness was varied to be (1) 5.2 nm, (2) 5.4 nm and (3) 5.6 nm. As curve (2) gives the best description of the data, the interfacial thickness could be determined with a very high accuracy to be $5.4 \pm 0.2 \text{ nm}$.

In diblock copolymers the two blocks are chemically linked at the interfaces. As the interfacial thickness (8.5) is a purely enthalpic property the interfacial width for a blend of the two homopolymers is expected to be identical. This has been proven by the same authors [19], who investigated a thin layer of deuterated PS (99 nm) on top of a much thicker PMMA film ($\sim 200 \text{ nm}$) on silicon. Due to the thickness of the bottom layer the frequency of the oscillations of this layer was too large to be resolved with the setup used. In this way only the reflection of the polymer/polymer and the polymer/air interfaces contribute to the reflectivity. This has been done by the authors, because they were only interested in the interface between the two incompatible polymers. The sample has been annealed for sufficient time to assure that the interface is at equilibrium.

Figure 8.7(b) shows the neutron reflectivity data for this sample. The line is a fit which is calculated from the density profile shown in the inset. A very smooth surface with a roughness of only 0.4 nm has been found in this case. The interface between the two layers could be well described by a hyperbolic tangent profile as

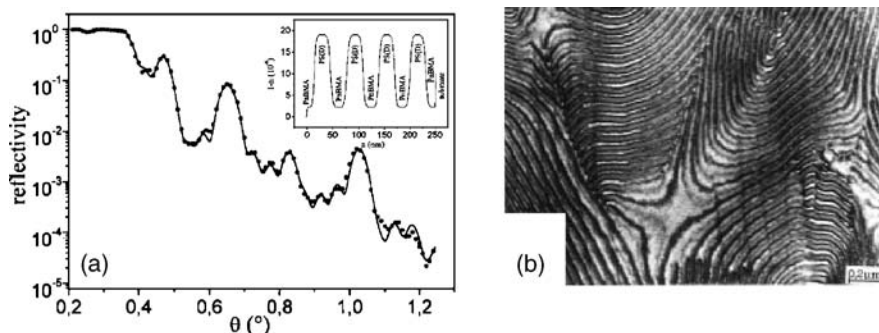


Fig. 8.8 (a) Neutron reflectivity curve (●) and calculated fit (line) according to the model sketched in the inset for a thin film of a D-PS-*b*-PnBMA diblock copolymer. (b) Cross-sectional TEM image of the same sample. Both images are taken from [20]

expressed by (8.4). This resulted in an interfacial width of 5.0 ± 0.5 nm which is in agreement with the results obtained for the copolymers.

A comparison of neutron reflectometry with electron microscopy has been performed by Schubert et al. [20]. Electron microscopy is a direct visualization technique, which is sensitive to regions of different electron density inside the material. For polymers different staining procedures with heavy metal compounds are commonly used, where the different compounds have different sensitivity to specific groups.

In the study of Schubert et al. [20] a lamellar PS-*b*-PnBMA (PBMA: poly(*n*-butyl methacrylate)) diblock copolymer has been used and the staining agent was RuO₄. RuO₄ is commonly a selective staining agent for PS, but it has been shown that by using short staining times (5 minutes instead of 30–45 min) RuO₄ goes only to the interfaces. Thus it can be also applied to study the interfacial widths of diblock copolymers by TEM [21, 22].

Figure 8.8(a) shows the neutron reflectivity of a thin film of a lamellar D-PS-*b*-nPBMA diblock copolymer, while in Fig. 8.8(b) a TEM micrograph of a cross-section from a bulk sample of the same polymer can be seen. Both the Kiessig fringes from the total film thickness and the Bragg peaks of the lamellae can be clearly observed in the neutron reflectivity. From the fit through the data a lamellar thickness of about 60 nm can be found which is in very good agreement with the long period found in the TEM image, where (60 ± 5) nm could be found. Also the interfacial widths found in TEM coincides with (8 ± 2) nm with values found in the reflectometry experiments. However, as the accuracy of neutron reflectivity allows to determine both the lamellar period and the interfacial width with much better resolution, differences in the lamellar thickness of less than 2 nm and for the interfacial width of 0.7 nm can be resolved if the sample is annealed to elevated temperatures. This is far beyond the resolution of TEM. Furthermore, for TEM the sample has to undergo a sophisticated preparation including staining, cutting etc. making it impossible to perform temperature dependent experiments with the same specimen.

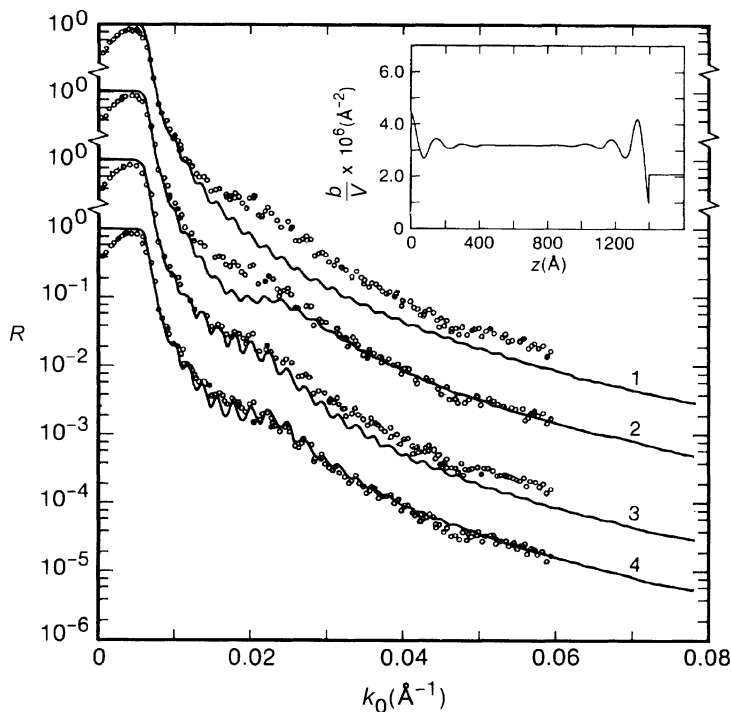


Fig. 8.9 Neutron reflectivity from a D-PS-*b*-PMMA diblock copolymer film annealed at 170°C for 24 h. Four different models have been used to calculate the reflectivity: (1) a homogeneous density profile; (2) exponentially damped cosine profile from the air/film surface; (3) exponentially damped cosine profile from the film/substrate surface; and (4) a damped profile from both surfaces. The inset shows the density profile for curve (4). For clarity the four curves have been shifted by a factor of ten [18]

It should be noted that the interfacial thickness of PS-*b*-PnBMA is much larger than that of the PS-*b*-PMMA sample presented in Fig. 8.7, even though the molar mass is more than eight times higher. As for higher molar masses the incompatibility usually increases, the interfacial width is expected to be smaller for this specimen. The reason for this large value is the small χ -parameter between PS and PnBMA.

Up to now only systems with sharp interfaces and well defined interfacial properties have been discussed. We will go beyond those systems in a sense that the density profile can be described by a damped oscillation at the films interfaces and a constant scattering length density between. Such a case has been reported by [18], who investigated a D-PS-*b*-PMMA diblock copolymer above its order-disorder transition (ODT) temperature. Below this temperature the two blocks undergo microphase separation in bulk, while above they become miscible and form a homogeneous mixture.

Figure 8.9 shows the neutron reflectivity of a D-PS-*b*-PMMA sample with a molar mass of 30 kg/mol. The data were obtained at a temperature of 170°C and

thus well above the ODT temperature, which has been found for this particular sample to be 65°C [15]. At this temperature complete mixing and therefore the reflectivity calculated from a model of a film with a homogeneous density profile, similar to that used in Fig. 8.4 would be expected.

A calculated reflectivity based on a model with a homogeneous density is shown as curve 1 in Fig. 8.9. Clearly the calculated reflectivity does not describe the experimental data satisfactory. In thin film geometry the two interfaces can affect the morphology of the mixed diblock copolymers. Considering the difference of the surface tensions between PS and PMMA [23] and the affinity of the polar PMMA block to the substrate, it is reasonable to assume an excess concentration of one block on either one or both interfaces. This would inevitably mean that the interfaces would induce a microphase separation and therefore the authors described the density profile at the two interfaces by a damped sinusoidal oscillation:

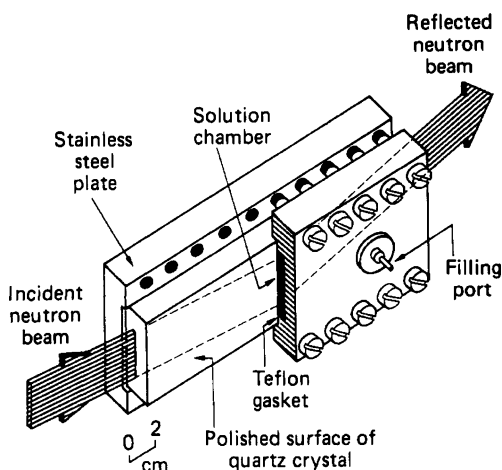
$$\phi(z) = \phi_e e^{-z/\xi} \cos(2\pi z/L) + \langle \phi \rangle, \quad (8.11)$$

where ξ is the correlation length, L is the period, ϕ_e is the excess concentration of PS at one interface and $\langle \phi \rangle$ is the average correlation length.

The calculated reflectivity with $L=15$ nm and $\xi=9.5 \pm 0.7$ nm and a concentration of PS $\langle \phi \rangle + \phi_e = 0.65$ at the film surface is shown as curve 2. Since the values chosen for L and ξ are the values of the lamellar thickness and the correlation length in bulk they can be taken as material parameters. At low k_z the description is still not good. However at large k_z the agreement with the experimental data is quite good. This points to the enrichment of PS at the film surface. This is a reasonable assumption as the surface tension of PS is smaller than that of PMMA [23].

On the other hand, it is well known, that the polar PMMA block has a strong affinity to the polar SiO_x layer which usually covers the silicon substrate, while the interaction of that layer with PS is rather weak. Thus, there is a preferential

Fig. 8.10 Schematic diagram for a sample cell for neutron reflectivity in liquid environment. The beam enters the solid/liquid interface through the substrate. Taken from [24]



adsorption of the PMMA block to the substrate. A calculated reflectivity which assumes a concentration of PMMA at the film/substrate interface of 1 and $L = 15$ nm and $\xi = 9.5 \pm 0.7$ nm is shown as curve 3. Here the agreement between the calculated and the measured reflectivity is good at low k_z values, while it is poor at large k_z . The combination of both attempts is shown as curve 4, which has been calculated assuming the density profile shown in the inset. A good agreement between the calculated and the measured reflectivity can be observed. The peculiarity of this experiment is that the surface potentials are strong enough to induce an ordering of diblock copolymers in the disordered state, where the two blocks are miscible.

8.4.4 Organic Films and Polymer Brushes

Usually, X-Ray reflectivity experiments are performed on thin solid or liquid films on a solid or liquid substrate, where the upper surface of the film is exposed to air. Investigations of a thin layer adsorbed to the substrate, while it is in solution of water or an organic solvent are obscured by refraction at the air/liquid interface and absorption of the liquid medium, which is usually in the order of mm. With neutron reflectometry this drawback can be circumvented due to the low absorption of neutrons by many materials. Neutrons might travel even through materials like silicon over about 200 mm with a transmission of around 0.6. Thus, a cell can be constructed, where the incoming beam can enter from the silicon substrate. Then the reflectivity from the solid/liquid interface can be recorded and a thin adsorbed layer can be investigated.

A typical liquid cell for neutron reflectometry has been described by Satija et al. [24] (see Fig. 8.10). Large single crystals of silicon (typically $100 \times 50 \times 25$ mm) mounted on stainless steel or teflon plates are typically used. The large thickness compared to the thin silicon wafers usually used for reflectivity experiments is required, because the beam enters through the side of the substrate at nearly 90° . Under these large incident angles refraction effects at the air/silicon interface can be neglected. The beam height is chosen relatively large to compensate the absorption which is still considerable. A teflon gasket is placed on top with a thin slit which serves as a solution chamber. The solution is injected through two small filling ports. Either the adsorption of the solute can be investigated or previously adsorbed or chemically anchored polymers in various environments. Examples for the latter case are investigations of the solvent quality of the swelling behaviour of polymer brushes.

Polymer brushes are polymers, which are grafted with one end to the surface. The distance between adjacent grafting points is considerably smaller than the radius of gyration of the molecules in the melt. In this case, a steric repulsion leads to stretching of the molecules normal to the substrate surface, which makes the surface similar to a conventional brush. In solution the brushes can be swollen in a good solvent, just like polymers in bulk are swollen. The solvent diffuses into

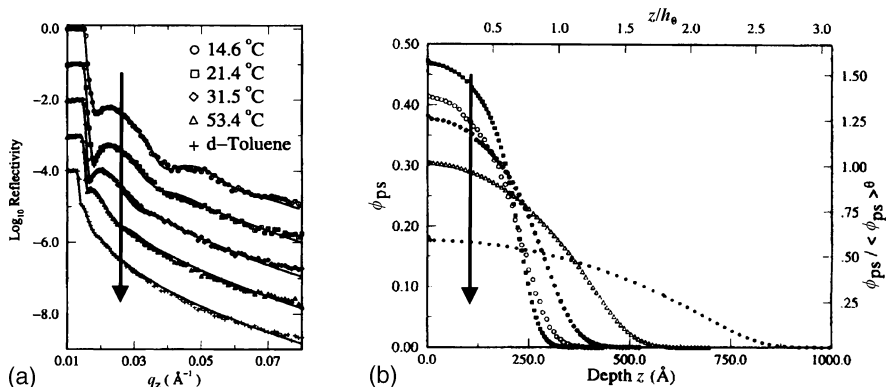


Fig. 8.11 Neutron reflectivity profiles (a) and density profiles along the substrate normal (b) for a polystyrene brush for different solvent quality [25]. The results are for deuterated cyclohexane, which is a θ -solvent for PS (i. e. the solvent quality increases with temperature), and for deuterated toluene, which is a good solvent. Solid lines in (a) are reflectivities calculated from the brush profiles in (b). The arrows indicate increasing solvent quality

the brush and due to space filling conditions the polymers stretch even more away from the surface. Thus the thickness of the brush increases while being swollen. This has been investigated in dependence of solvent quality by Karim et al. with neutron reflectometry [25].

In this study the authors investigated a polymer brush consisting of polystyrene with a molar mass of $M_w = 105$ kg/mol. The thickness of the dry film was measured before by X-Ray reflectivity to be about 10 nm and the distance between grafting points was 4 nm [25]. When the brush is exposed to toluene, which is a good solvent for PS, the brush is swollen by toluene. To achieve good contrast, deuterated toluene was chosen in this particular case. The reflectivity indicates a swelling to approximately 82 nm (see Fig. 8.11(a), bottommost curve). Note that this is more than eight times the initial brush thickness and more than nine times the radius of gyration of the respective polymer in the melt!

In Fig. 8.11(b) the density profile used to calculate the reflectivity for this particular sample. It has a parabolic profile, which is consistent with theoretical predictions made by self consistent field theory (SCF) [26,27] and Monte Carlo simulations [28].

Furthermore, for θ -conditions the density profile, which gives the best fit to the data can be described by an analytical expression, motivated by SCF calculations [26, 27]

$$\phi(z) = \begin{cases} \phi_s \left[1 - (z/h)^2 \right]^\alpha, & z < h \\ 0, & z > h \end{cases} \quad (8.12)$$

Here, ϕ_s is the volume fraction of the polymer at the silicon oxide surface, h is a cut-off thickness of the profile and α is a characteristic exponent for a given

profile. Around the θ -temperature this exponent lies between 0 and 1 and at the θ -temperature it is equal to one half. For good solvent conditions α is equal to 1, which results again in a parabolic density profile which has been found for toluene. All these results are in good agreement with the results predicted by theory. Thus, neutron reflectometry can give valuable proofs of modern theories of specific polymer systems in great detail, which is hardly possible with other techniques. In this way this technique can contribute to a better understanding of the properties of new polymer systems and help to develop materials with specific properties.

There are, however, a few restrictions to either X-Ray or neutron reflectometry which should be quoted here: (i) only information about the density profiles along the film normal can be recorded and (ii) only an overall averaged intensity is measured. Thus, with these techniques no information about local details can be gained and information about structures in the film plane cannot be made without assumptions or further information obtained by other techniques. Furthermore, it is inherent to nearly all reciprocal space techniques that the measured intensity is the square of the scattered amplitude and therefore the information about the phase is lost. This fact is well known as the “phase problem” in scattering. All calculated models discussed above were fitted on the basis of reasonable models and compared with the measured data, since it is not possible to calculate a density profile from the measured data directly. Furthermore it has been shown that different models can lead to very similar reflectivity curves [29]. Therefore one has to choose the models for calculating reflectivities very carefully and often other complementary techniques have to be taken into account. One relatively new technique which combines several of the above discussed restrictions is the recently developed nanotomography, which has been developed by Magerle [30]. This technique should be discussed in the next section.

8.4.5 Comparison with Real Space Techniques

Nanotomography is a combination of three steps which have been developed independently in a broad range of different fields of science. The first step is simply the imaging of the surface of a structured polymer film by atomic force microscopy (AFM), which is discussed in another chapter in this book. AFM is a surface sensitive technique. Thus, AFM alone can not deliver the full information about the three dimensional structure of the thin film. In a second step a thin layer is removed by plasma etching in a similar manner than Harrison et al. [31] on stained PS-*b*-PI (PI stands for polyisoprene). Then the surface is scanned at the same area. In this way the morphology of the film in well controlled depths can be recorded. Repeating this process several times delivers a set of images in equidistant depths of the film. Finally, this set of images can be combined using special computer techniques which also have been described elsewhere [32] to reveal a three-dimensional image of the film.

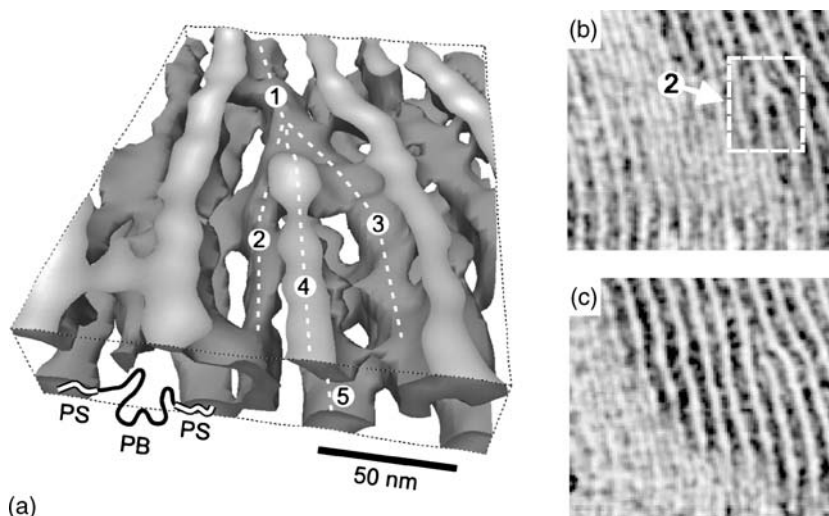


Fig. 8.12 (a) Three-dimensional image of a thin film of a PS-*b*-PB-*b*-PS triblock copolymer reconstructed from single AFM images like those shown in (b) and (c). [30]. The region shown in (a) is marked by the rectangle in (b)

Magerle applied this procedure to thin films of cylindrical PS-*b*-PB-*b*-PS triblock copolymers (PB stands for polybutadiene). The cylinders were oriented parallel to the films interfaces. The total film thickness was 140 nm, and by removing layers with an average thickness of 7.5 ± 0.2 nm he recorded a set of about 20 images at different depths. As the etching step for each was smaller than the intercylinder distance (42 nm), it was possible to find the same position on the sample after each etching step.

The reconstructed image obtained in this way is shown in Fig. 8.12(a). The image focuses on a defect located in the centre. In Fig. 8.12(b) and (c) the two-dimensional images are shown. Images like this have been frequently shown in transmission electron micrographs. However, there only the two-dimensional projection of three-dimensional images and from only one image the branching of either the matrix or the cylinder can be seen. In the three-dimensional image the details of this structure becomes more evident. The cylinder 1 is branching into two cylinders 2 and 3. Furthermore, above and below the branching point, two cylinders (4 and 5) are emerging and lie in between the cylinders 2 and 3. These structural details could not be clearly seen from the two-dimensional projections alone. The resolution of the image (about 10 nm) is limited by (i) the etching depth along the film normal and (ii) by the finite tip radius (~ 10 nm).

A comparison of this technique with reflectometry is mandatory, as it seems at a first glance that it gives more direct and more detailed information about the structure in thin diblock copolymer films and is therefore superior to reflectometry.

With nanotomography local details can be revealed whereas neutron reflectometry is a technique which averages over the whole sample surface. Thus, the structure revealed by nanotomography recovers the details of the local structure,

but it cannot be concluded that the film as a whole is inhomogeneous and can consist of domains with some tenth of micrometres or more of totally different structures. It is for example not possible to confirm with a single three-dimensional image that the cylinders are oriented parallel throughout the whole film or whether there are other regions with a perpendicular orientation of the cylinders. A set of many images, statistically distributed over the whole film would be necessary, which would be very time consuming. With reflectometry a technique, which is an averaging technique over the whole film, a single experiment could confirm the parallel orientation.

Another advantage of reflectometry over nanotomography is that reflectometry is a non destructive technique and experiments can be performed before and after annealing to elevated temperatures on the same specimen. Also the depth profile of a polymer brush in a swollen state can be recorded with neutron reflectometry, which is impossible with nanotomography.

Furthermore, the resolution (~ 10 nm) is much lower than for reflectometry (< 1 nm) or even electron microscopy (~ 2 nm, see above), so that parameters like the interfacial width can be only determined by reflectometry with great accuracy.

In summary, nanotomography can reveal local details as a picture in real space, while reflectometry techniques can provide globally averaged information in reciprocal space. The focus of both techniques is quite different and so are the informations the two techniques deliver. This example shows, that imaging techniques in real space can give in some cases complementary information to results got by reflectometry. However, the high accuracy and flexibility of neutron reflectometry makes it an indispensable tool to study interfaces as well as concentration gradients in thin polymer films and layers.

8.5 Conclusion

It has been shown that neutron reflectometry is a powerful technique to study the interfaces of incompatible polymers with a resolution well below a nanometre. The polymers are prepared as bilayers into a thin film and the density profile along the film normal is recorded. The reflectivity of a reasonable model can be calculated and compared with the experimental data. Optimization of the model calculation can deliver information about the thickness of the layers, but also about roughness and thermodynamic important parameters like the interfacial width between the incompatible polymers can be determined and compared with theoretical models with an accuracy which is difficult or rather impossible to achieve with other techniques like, e. g. TEM. Furthermore, with neutron reflectometry temperature dependent measurements and experiments under complex environments, like polymer brushes in solution can be performed.

Financial Support from the Heisenberg-Stipendium is gratefully acknowledged by R. Weidisch. We thank Dirk W. Schubert for the fruitful cooperation during neutron reflectometry experiments at the GKSS Forschungszentrum in Geesthacht.

References

1. Flory PJ (1971) Principles of Polymer Chemistry. Cornell University Press, Ithaca, New York
2. Broseta D, Fredrickson GH, Helfand E, Leibler L (1990) *Macromolecules* 23: 132
3. Stamm M (1992) Reflection of Neutrons for the Investigation of Polymer Interdiffusion at Interfaces. In: Sanchez IC, Fitzpatrick LE (eds) *Physics of Polymer Surfaces and Interfaces*. Butterworth-Heinemann, Boston, p 163
4. ADAM (2007) <http://www.ep4.ruhr-uni-bochum.de/adam/> Accessed 2007
5. Lekner J (1987) *Theory of Reflection*. Martinus Nijhoff, Dordrecht
6. Higgins JS, Benoit HC (1994) *Polymers and Neutron Scattering*. Clarendon, Oxford
7. Tolan M (1999) *X-Ray Scattering from Soft-Matter Thin Films*. Springer, Berlin Heidelberg New York
8. Foster M, Stamm M, Reiter G, Hüttenbach S (1990) *Vacuum* 41: 1441
9. Kiessig H (1931) *Annalen der Physik* 10: 769
10. Abelès F (1950) *Ann. Physique (Paris)* 5: 596
11. Parratt LG (1954) *Phys Rev* 95: 359
12. Salditt T, Li C, Spaar A, Mennicke U. (2002) *Eur Phys J E* 7: 105
13. Stamm M, Schubert DW (1995) *Annu Rev Mater Sci* 25: 325
14. Schubert DW, Stamm M (1996) *Europhys Lett* 35: 419
15. Russell TP, Hjelm RP, Seeger PA (1990) *Macromolecules* 23: 890
16. Fukuda T, Nagata M, Inagaki H (1986) *Macromolecules* 19: 1411
17. Tcherkasskaya O, Ni S, Winnik MA (1996) *Macromolecules* 29: 610
18. Anastasiadis SH, Russell TP, Satija SK, Majkrzak CF (1989) *Phys Rev Lett* 62: 1852
19. Anastasiadis SH, Russell TP, Satija SK, Majkrzak CF (1990) *J Chem Phys* 92: 5677
20. Schubert DW, Weidisch R, Stamm M, Michler GH (1998) *Macromolecules* 31: 3743
21. Arnold M, Poser S, Fischer H, Frank W, Utschick H (1994) *Macromol Rapid Commun* 15: 949
22. Fischer H (1994) *Polymer* 35: 17
23. Wu W (1982) *Polymer Interface and Adhesion*. Marcel Dekker, New York
24. Satija SK, Maykrzak CF, Russell TP, Sinha SK, Sirota EB, Hughes GJ (1990) *Macromolecules* 23: 3860
25. Karim A, Satija SK, Douglas JF, Ankner JF, Fetters LJ (1994) *Phys Rev Lett* 73: 3407
26. Milner ST, Witten TA, Cates ME (1989) *Macromolecules* 22: 853
27. Zhulina EB, Borisov OV, Pryamitsyn VA, Birshtein TM (1991) *Macromolecules* 24: 140
28. Lai PY, Binder K (1992) *J Chem Phys* 97: 586
29. Pedersen JS, Hamley IW (1994) *J Appl Cryst* 27: 36
30. Magerle R (2000) *Phys Rev Lett* 85: 2749
31. Harrison C, Park M, Chaikin P, Register RA, Adamson DH, Yao N (1998) *Macromolecules* 31: 2185 and *Polymer* 39: 2733
32. Brown LG (1992) *ACM Comput Surv* 24: 325

Chapter 9

Liquid–Liquid and Liquid–Vapor Interfaces in Polymeric Systems

Marcus Müller

Institut für Theoretische Physik, Georg-August Universität, Friedrich-Hund-Platz 1,
37077 Göttingen, Germany, mmueller@theorie.physik.uni-goettingen.de

Abstract Surfaces and interfaces of polymers can be described by theory and simulations at different length scales. In this contribution polymer–polymer interfaces and kinetics of phase separation in binary polymer blends are presented in the framework of self-consistent field theory. Interface width, profiles and fluctuations are critically discussed. Surfaces are described as the special case of phase separation of a polymer melt and its vapour. Wetting and thin film stability then can also be calculated.

9.1 Introduction

Interfaces and surfaces in polymeric systems are ubiquitous: Similar to metallic alloys one often blends different types of polymers to combine the characteristics of both materials [1]. Unfortunately, long macromolecules tend not to mix, because a minuscule repulsion between different monomeric units largely outweighs the entropy gain upon mixing. Thus, the blend phase separates into domains, in which one of the components is enriched and the other is depleted. Those spatially segregated regions are separated by interfaces. On a larger length scale, one can conceive the material as an ensemble of interfaces. The structure and thermodynamics of internal interfaces between different polymers determine many practically important properties [2]: The smaller the interface tension, for instance, the smaller is the typical domain size obtained when the blend is extruded [3]; the larger the width of the interface, the more entanglements are formed across these inner interfaces and the better are the mechanical properties of the composite material [4, 5].

At the outer surfaces of a polymeric material another type of spatial inhomogeneity occurs, where the dense polymeric phase is in contact with its vapor (or vacuum) or with the surface of another material (e. g. a silicon wafer). The properties of these outer surfaces determine much of the appearance of polymeric mate-

rials (e. g., gloss, adhesion, or wettability) and have attracted abiding interest for they determine the stability of thin polymeric coatings.

Quite different theoretical techniques [6–19] have been employed to describe internal interfaces between two unmixed liquid domains and the outer surface between a liquid (or glassy) polymer and its vapor. The main difference can be traced back to the strength of the interactions on the scale of the monomeric units. In a binary polymer blend, the repulsion between the different components (in units of $k_{\text{B}}T$) often is parameterized by the Flory–Huggins parameter. For typical blends, the Flory–Huggins parameter is only of the order 10^{-2} – 10^{-4} . Hence, the interface between two immiscible polymers is rather broad; its (intrinsic) width is much larger than the size of monomeric unit. Therefore, interfaces in polymer blends exhibit a rather universal behavior, which does not depend on the detailed structure of the monomeric units but can be described by a few coarse-grained parameters, the incompatibility per chain, χN , and the size of the polymeric coil, R_{c} . At a surface, however, the forces that act on a monomeric unit are on the order of the thermal energy scale, kT , itself and hence the characteristic length scale of the density profile is the size of the monomeric units. In this case, the detailed packing of the monomeric units and the local molecular architecture are important and the behavior cannot be described by only a few coarse-grained parameters.

This chapter is organized as follows: First, we shall discuss phase separation and interfaces in binary polymer blends. We give some background, discuss the phase behavior and interface properties, and briefly describe the self-consistent field (SCF) theory. Then, we present some results on polymer–polymer interfaces and the kinetics of phase separation in binary polymer blends. Subsequently, we turn to the discussion of polymer surfaces. The starting point is the phase separation between a dense polymeric liquid (melt) and its vapor. For the theoretical approach to be accurate, one needs an accurate equation of state, to include the detailed molecular architecture on the length scale of the monomeric units, and a non-local interaction functional to describe the fluid-like packing of the monomeric units. We discuss how the theoretical approach can be used to calculate the wetting properties and stability of thin films.

9.2 Interfaces in Binary Polymer Blends

We consider a melt of two chemically distinct polymers, A and B. In the vicinity of the critical point, where the blend just begins to separate into A-rich and B-rich domains, the width of the interface is much broader than the polymer size, and the behavior of polymer mixtures is qualitatively similar to a near-critical blend of small molecules or a metallic alloy. If one increases the incompatibility between the two species, the interface width decreases and, in the strong segregation limit, the interface width is much smaller than the polymer size but much larger than the size of a monomeric units. This limit is characteristic for extended macromole-

cules, and many properties of interfaces in a dense, liquid polymer blend can be qualitatively characterized by loops that polymers form into the opposite domain.

The bulk phase behavior is a prerequisite for understanding the properties of spatially inhomogeneous systems. For a dense, incompressible polymer mixture of two components the excess free energy of mixing per monomeric unit can approximately be described by the Flory–Huggins form [20, 21]:

$$\frac{F}{\rho V k T} = \frac{\phi}{N_A} \ln \phi + \frac{1-\phi}{N_B} \ln(1-\phi) + \chi \phi(1-\phi) \quad (9.1)$$

ρ in (9.1) denotes the monomer number density. The first term presents the entropy of mixing which scales like the number of polymers, while the last term represents the repulsion between unlike polymers. It is proportional to the number of monomeric units, and the Flory–Huggins parameter, χ , describes the repulsion between unlike monomeric units. For simplicity, we assume in the following a symmetric polymer blend, where both species have the same chain length, $N=N_A=N_B$. Due to the connectivity of the monomeric units the translational entropy is a factor of $1/N$ smaller than the energy of mixing. Note that this free energy does not contain any entropic contributions which may arise from the dependence of the molecular conformations on the composition of the blend. Nevertheless, this very simple free energy of mixing can rationalize the experimental observation that mixtures of long macromolecules tend to phase separate.

In the original description of Flory and Huggins the χ -parameter is related to the enthalpic repulsion between the different monomeric units. In many circumstances, however, the assumption that there are no entropic contributions to the free energy of mixing is not fulfilled and also the literal identification of the enthalpic term is problematic, e. g., only the interactions between different molecules contribute to the energy of mixing. Nevertheless, the Flory–Huggins parameter provides a rather successful and commonly used quantification of the repulsion between unlike monomeric units, if it is extracted by comparing the predictions of the Flory–Huggins theory [or the self-consistent field (SCF) theory] to experiments in the parameter range where long-range composition fluctuations (i. e., critical fluctuations of Ising type or capillary waves at interfaces) do not invalidate the mean field approach [22–24].

A common experimental procedure is to extract the Flory–Huggins parameter from the inverse scattering of composition fluctuations in the one-phase region far away from the critical point. This is illustrated by simulations of a binary polymer blend in the framework of the bond fluctuation model [25] in Fig. 9.1. In this coarse-grained polymer model, an effective segment corresponds to a few chemical repeat units and it is represented by a cube on a lattice. It blocks all eight corners of the cube from double occupancy. Segments along a polymer are connected via one of 108 bond vectors; this represents the connectivity along the backbone of the polymer. The two species of a blend repel each other via a square-well potential that is extended over the nearest 54 lattice sites. Like segments attract each other while unlike ones repel each other with a strength ϵ . Although the Flory–

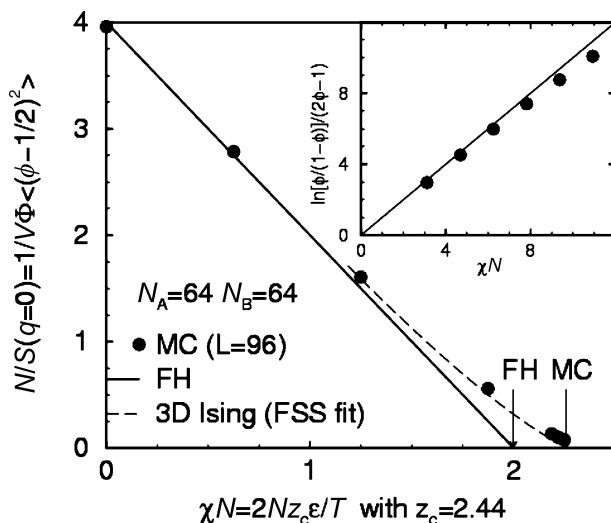


Fig. 9.1 Inverse collective structure factor at zero wave vector as a function of incompatibility. Symbols correspond to the results of computer simulations of the bond fluctuation model (chain length $N=32$), while the straight line is the prediction of the Flory–Huggins theory for composition fluctuations. It describes the data far above the critical point in the one-phase region. The Flory–Huggins theory, however, underestimates the critical value of the Flory–Huggins parameter and there are deviations from the linear behavior that marks the Ising critical behavior. The dashed line shows the finite size scaling extrapolation of the scattering intensity showing 3D Ising critical behavior, $N/S(q) \sim (\chi N - \chi_c N)^{-\gamma}$ with an Ising critical exponent $\gamma=1.24$

Huggins parameter is not straightforwardly related to molecular interaction (or the square-well depth, ϵ , of the potential between segments in the bond-fluctuation model) [22–24], but also includes correlations (e.g., packing effects) on short length scales, this identification of the Flory–Huggins parameter yields a consistent parameterization of blend immiscibility, and the Flory–Huggins free energy of mixing provides an excellent starting point to describe spatially inhomogeneous systems like interfaces in polymer blends or the self-assembly of diblock copolymers.

9.3 Self-Consistent Field (SCF) Theory

The idea of the mean field theory is to replace the original problem of chains interacting with their neighbors, by a single chain in an effective field [6–12]. This effective field should mimic the effect of the surrounding molecules. It comprises two contributions: On one hand, there acts a repulsion between unlike species which is proportional to the Flory–Huggins parameter. On the other hand, there is

a local pressure field, ξ , that restores the constant density throughout the system. The field acting on a monomeric unit of type A is

$$w_A = \chi\phi_B + \xi \quad (9.2)$$

and a similar expression holds for type B. The fields, w_A and w_B , depend on the local concentration of the species. The local concentration, in turn, is determined by the distribution of a single chain in the external fields. To this end, one has to solve the single chain problem in the external field and calculate the thermal average of the density a single chain creates in the external field. This is the computationally most intensive part, because the polymer can adopt many different conformations. The pressure field is adjusted such that the sum of the two compositions equals unity throughout the system. The calculation is iterated until the densities created by the single chains in the external field and the relation between the field and the density [cf. equation (9.2)] are self-consistently fulfilled.

Since interfaces in polymer blends are broad compared to the size of the monomeric units, one often utilizes the Gaussian chain model [26]. This coarse-grained description does not capture the behavior on the short length scales (e. g., bond angles or distribution of torsions), but it allows for an efficient calculation of the single chain partition function in an external field in terms of a modified diffusion equation. In the limiting cases of very small and very large fields – the weak and the strong segregation limit, respectively – explicit analytical expression can be obtained.

In the strong segregation limit, polymers form loops across the interface into the opposite domain. Each loop carries a free energy on the order of $k_B T$. Each monomeric unit in such a loop yields a contribution $\chi/k_B T$. Therefore, a typical loop contains $1/\chi$ monomeric units. If we assume that this number is large enough, such that a loop can be described by the Gaussian statistics of the polymer on the coil size, R , the spatial extension of such a loop is $w_{SSL} = R/(6\chi N)^{1/2}$. The numerical factor 6 is just introduced to reproduce the result for the interface width of the SCF theory in the strong segregation limit [7]. By the same token, one can estimate the interface tension σ . The number of monomeric units in the interface region per units area is ρw , where ρ is the monomer number density. Each monomeric unit contributes χ to the interface free energy, thus we obtain $\sigma_{SSL} = \rho R/N (\chi N/6)^{1/2}$ – a result that becomes correct in the limit of large χN [27].

The SCF theory provides numerical results over the entire range of incompatibilities and also yields detailed information about segmental profiles and the orientation of the spatially extended molecules on different length scales. It also can be generalized to different chain architectures, like block-copolymers or branched structures.

9.4 Excess Quantities

In the following, we present a brief comparison between the predictions of the SCF theory and computer simulations of a symmetric binary polymer blend in the framework of the bond-fluctuation model. Two interface properties can be distinguished: (i) excess properties, like the interface tension or the adsorption of solvent or block-copolymers at the interface that do not make reference to the explicit location of the interface, and (ii) profiles of various quantities across the interface.

In Fig. 9.2 we show the interface tension, σ , as a function of the incompatibility χN for different chain lengths N . The values are normalized by the prediction in the strong segregation limit. They approach the simple scaling limit with a $1/\chi N$ correction. The magnitude of this correction agrees with the SCF theory and calculations by Semenov [27].

Such a $1/\chi N$ correction is the typical form of corrections to the strong segregation limit. Note, that there are notable corrections to the strong segregation limit even at $\chi N > 50$, and that one has to account for these corrections to the simple analytical expressions when quantitatively comparing simulations or experiments to the predictions of the SCF theory. The good agreement in Fig. 9.2 shows that the SCF theory accurately predicts the interface tension, once the Flory–Huggins parameter has been determined from the thermodynamics of the bulk.

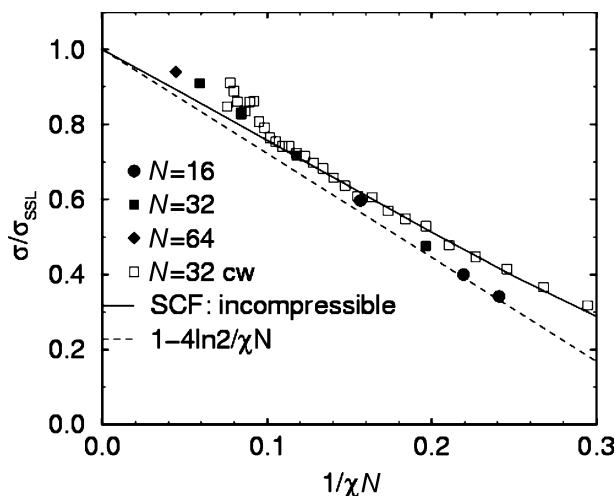


Fig. 9.2 Ratio of the measured interface tension, σ , and the simple analytical expression in the strong segregation (SSL) limit. Closed symbols correspond to chain length $N = 16, 32$ and 64 , and they have been obtained from grand canonical computer simulations monitoring the probability distribution of the composition. Open symbols have been extracted from the Fourier spectrum of capillary waves. The solid line corresponds to the prediction of the SCF theory, while the dashed line shows the result of a first correction to the strong segregation limit found in [27]. Adapted from [28, 29]

9.5 Interface Fluctuations

While the comparison of excess quantities is straightforward, the calculation of profiles is a rather delicate matter. In the SCF theory, one calculates the spatial variation of a quantity, e. g., the composition, as a function of the distance from the location of the interface. In the SCF calculations, however, the interface is strictly flat. This is in marked contrast to experiments or simulations, where the local position of the interface fluctuates: thermal fluctuations give rise to capillary waves [30]. A snapshot of the local interface position obtained from the simulation of a binary polymer blend is depicted in Fig. 9.3.

These fluctuations give rise to a broadening of interface profiles and a dependence of the profiles on the lateral size, L , over which the profile is averaged. For the apparent width of the interface, w , one obtains [28]

$$w^2 = w_0^2 + \frac{kT}{4\sigma} \ln \frac{L}{B_0} \quad (9.3)$$

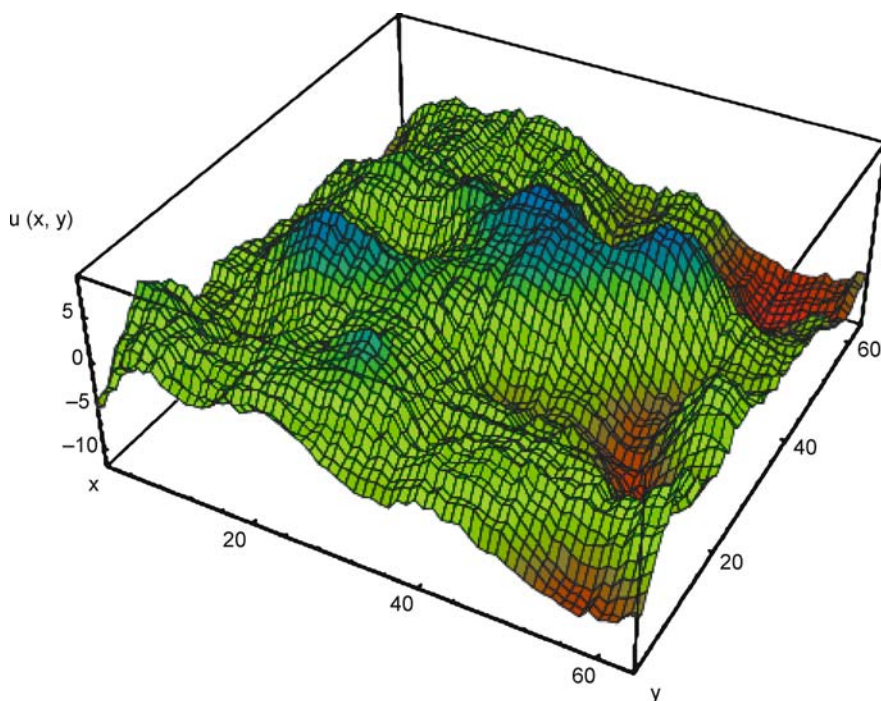


Fig. 9.3 Snapshot of the local interface position from a computer simulation of a binary polymer blend in the framework of the bond-fluctuation model with chain length $N=32$. The local interface position was estimated by an integral criterion applied to a lateral patch of the system of size $B \times B$. Adapted from [28]

where w_0 is the “intrinsic width” of the interface which does not include capillary waves and can be calculated by SCF theory, while the latter term describes the broadening by interface fluctuations. The lateral length, B_0 , describes the rather subtle cross-over between short-ranged fluctuations that contribute to the “intrinsic profile” and long-ranged capillary waves. Typically one obtains from experiments or simulations only the dependence of the width, w , on the systems size, L , but one cannot measure the “intrinsic width”, w_0 , and the lateral cut-off, B_0 , independently. This dilemma seriously hampers the quantitative comparison between profiles calculated from a mean-field theory (like the SCF theory) and experiments or simulations.

Binary polymer blends offer a unique opportunity. Due to the extended structure of the macromolecules and the rather universal behavior of interfaces in binary polymer blends, one expects the SCF theory to provide a quantitatively accurate description of the “intrinsic profile”. Thus, by comparing simulations and SCF theory and adjusting the lateral length scale, L , such that both profiles match, one can determine the short-length scale cut-off, B_0 . This yields the value $B_0 = 3.8w_0$ in good agreement with the prediction of Semenov [31, 32], $B_0 = \pi w_0$.

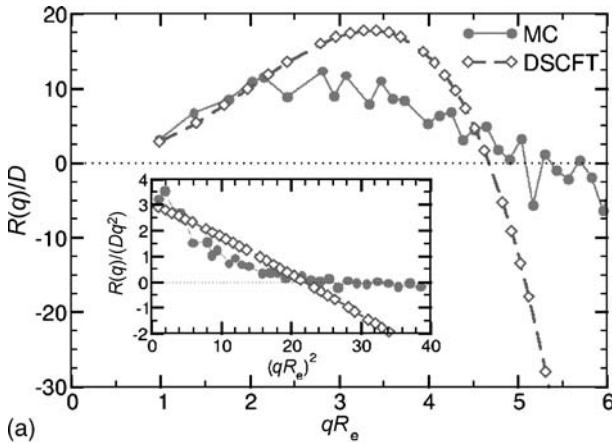
9.6 Kinetics of Phase Separation

In many circumstances, the phase separation is incomplete and does not reach equilibrium, i. e., there are not just simply two macroscopic domains into which the incompatible polymer species segregate, but the material consists of several domains on the size of micrometers separated by an assembly of interfaces. On larger length scales (say millimeters) the material appears homogeneous. The morphology depends on the history of the material, and the kinetics of phase separation is important.

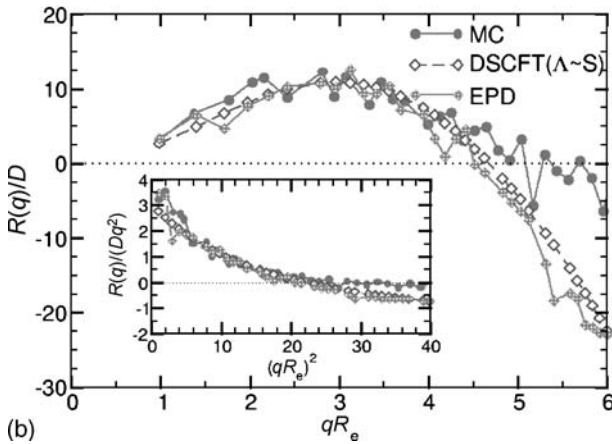
In the early stages of phase separation [33–35], two pathways can be distinguished. The mixture may spontaneously phase separate (spinodal decomposition), and concentration fluctuations start to grow in the entire system. Alternatively, the phase separation may proceed via a thermally activated process, the nucleation of drop of the new phase. Which one of the two limiting pathways will be followed depends on the bulk thermodynamics. At the later stages, the domains grow and the morphology coarsens. In this later time regime, hydrodynamics of the polymeric fluid is important. The kinetics of phase separation determines the morphology of the blend and, thereby, many mechanical properties of the multi-component material.

In the following, we shall briefly discuss the spinodal decomposition in binary polymer blends, and focus on how the diffusive dynamics of the polymer molecules influences the kinetics of collective concentration fluctuations that exponentially grow in the initial regime [33, 34].

$$S(q, t) = S(q, 0) \exp(R(q)t) \quad (9.4)$$



(a)



(b)

Fig. 9.4 (a) Growth rate of the collective structure factor in response to a quench from the one-phase region ($\chi N=0.314$) into the miscibility gap, $\chi N=5$. Circles present the results of Monte Carlo simulations in the bond-fluctuation model for chain length $N=64$, while diamonds show the prediction of the dynamic SCF theory using a local Onsager coefficient. The inset shows the ratio between the growth rate and q^2 – the Cahn plot. The results of the dynamics SCF theory fall onto a straight line, while deviations from such a linear behavior indicate non-local contributions to the Onsager coefficient. (b) The same comparison but with a dynamic SCF theory that employs a non-local Onsager coefficient appropriate for Rouse dynamics in a spatially homogeneous system and External Potential Dynamics (EPD). Adapted from [36]

where $S(q,0)$ denotes the equilibrium collective structure factor of composition fluctuations in the initial stage (i. e., the one-phase region at $\chi N < 2$) and $R(q)$ denotes the growth rate of composition fluctuations with wave vector, q . Long-wavelength fluctuations grow spontaneously, there is a maximum of the growth

rate at q_{\max} , and short-wavelength fluctuations with $q > q_{\max}/2^{1/2}$ do not spontaneously grow.

How does the dynamics of the individual molecules influence the growth of spontaneous composition fluctuations? The SCF theory can also be extended to the dynamics. The idea is to calculate the free energy of a composition fluctuation or a specific distribution of densities with the SCF theory. At this stage, one assumes that the density is the slowest variable and the chain conformations are in equilibrium with the instantaneous distribution, $\phi(r,t)$. From the free energy, $F[\phi]$, one can calculate the chemical potential, $\mu = \delta F / \delta \phi$. In equilibrium the chemical potential is constant throughout the system; in a non-equilibrium situation, a spatial variation of the chemical potential gives rise to a current, J (model B according to [37])

$$J(r,t) = \int dr' \Lambda(r-r') \nabla \delta F / \delta \phi(r') \quad (9.5)$$

The Onsager coefficient, Λ , relates the gradient of the chemical potential to the current, and it encodes the dynamics of the molecules. In general, it is non-local, because the gradient of the chemical potential acts like a thermodynamic force on a segment at position, r' , and this force is transmitted along the backbone of the molecules and gives rise to a current at position r .

A current results in a change of the local density, and both are related via the continuity equation:

$$\frac{\partial \phi(r,t)}{\partial t} = -\nabla J(r,t) \quad (9.6)$$

The neglect of forces along the backbone of the molecule corresponds to a local Onsager coefficient, $\Lambda \sim D \delta(r-r')$, where D is the self-diffusion coefficient of the molecules' center of mass. If the dynamics of the single molecules is described by the Rouse model, the Onsager coefficient is proportional to the single chain structure factor, and there exists also an explicit expression for reptation dynamics [38–40]. It is important to note that a simple expression for the Onsager coefficient exists only in a spatially homogeneous system. If interfaces are present, the chain conformations are distorted in their vicinity (e.g., chain ends enrich at the center of the interface, and molecules align parallel to the interface), and one would have to calculate the single chain correlations explicitly. This is often impracticable and, therefore, many calculations utilize the approximation of a local Onsager coefficient.

Figure 9.4(a) compares the growth rate, $R(q)$, of the collective structure factor obtained from dynamic SCF calculations utilizing a local Onsager coefficient with the results of Monte Carlo simulations in the bond-fluctuation model [36]. The simulations use chain length $N=64$ which is a compromise: For longer chains, the SCF theory would be more accurate in predicting the equilibrium properties, but also the dynamics would cross-over to the more complex, reptation dynamics. In both, the dynamic SCF calculations and the computer simulations, we study a quench from the one phase region, $\chi N=0.314$, into the miscibility gap, $\chi N=5$.

As one can observe in panel (a), the dynamic SCF theory with a local Onsager coefficient grossly overestimates the growth rate and it also predicts a too large wavevector, q_{\max} , of the fastest growing mode.

Alternatively, one can use a non-local Onsager coefficient that corresponds to Rouse-like dynamics or, equivalently, propagate the external field, w_A , instead of the density ϕ_A – a method called external potential dynamics [18, 36, 41, 63]. The results are presented in Fig. 9.4(b) and compare much better with the data from the computer simulations. This illustrates that it is important to take due account of the dynamics of the underlying molecules when one predicts the early stages of phase separation and that the dynamic SCF theory utilizing the appropriate, non-local Onsager coefficient is able to quantitatively predict the behavior during the early stages. Recently particle-based dynamic SCF calculations have been devised that explicitly propagate a large ensemble of single chain conformations in external fields. These “single chain in mean field” simulations do not require an Onsager coefficient and do not assume the chain conformations to be in equilibrium with the instantaneous density distribution. In the case of spinodal decomposition they yield similar results as the EPD theory but they can also be applied to systems with strong dynamic asymmetries (e. g., evaporation of solvent from a thin polymer film [42] or the ordering of diblock copolymers where the blocks differ in their mobility [43]).

9.7 Liquid–Vapor Interfaces

9.7.1 Phase Behavior, Packing Effects and Density Functional Theory

The phenomenology of liquid–liquid phase separation in dense binary polymer blends and liquid–vapor coexistence in polymers (or incompressible polymer + solvent mixtures) is similar. In fact, the Flory–Huggins theory [cf. equation (9.1)] has been employed to describe incompressible polymer + solvent mixtures by setting the chain length of the solvent to unity. This reproduces many, qualitative features of the liquid–vapor (or polymer + solvent) separation, namely the critical density is low, $\phi_c \sim 1/N^{1/2}$, and the critical temperature approaches a chain length independent limit, the Θ temperature, with a $1/N^{1/2}$ correction.

We shall point out, however, two important differences:

1. Instead of an incompressible polymer + solvent mixture, one often regards a pure polymer system where different monomeric units attract each other. These interactions are effective attractions which result from the fact that monomeric units attract each other more strongly than the attractions between monomeric units and solvent are. While such a compressible one-component system yields qualitative similar phase diagrams, there is an important difference: In the Flory–Huggins description the third and higher order virial coefficients exclu-

sively stem from the entropy of mixing (and therefore they are not independent), while in the compressible one-component system higher order virial coefficients are generated by the interaction of the monomeric units. This is a more realistic description which we shall adopt in the following.

2. In contrast to a binary polymer blend, where the interactions on the scale of a monomeric units are typically small, $\chi \sim 1/N$, at the onset of phase separation, the interactions in an incompressible polymer + solvent mixture are on the order of $k_B T$. Thus, the characteristic (“intrinsic”) width of interfaces in polymer + solvent systems is on the order of the monomeric units itself. Therefore, details of the molecular architecture and the local fluid packing matters. Polymer + solvent mixtures cannot be described by a few, coarse-grained parameters (like the Flory–Huggins parameter) and generally, one cannot expect the same degree of universality than in binary polymer blends.

Since the characteristic length scales are comparable to the extension of a statistical segment, one has to incorporate more of the structural details on short length scales. Intramolecular correlations can be incorporated into the theory by using explicit chain conformations. Similar to the SCF theory for polymer blends, the problem of many interacting molecules is replaced by that of a single molecule in an external field. The single chain problem can be solved numerically by a partial enumeration [11] over a large sample (10^7 conformations) of explicit single chain conformations. By virtue of the independence of the single chains, this can conveniently be performed on a parallel computer. The single chain conformations can be extracted from simulations of the bulk system or from a molecular-modeling approach. In this way one can take all the details of the chain architecture on all length scales fully into account.

The dependence of the phase diagram of a bead–spring Lennard-Jones polymer on chain length, N , is presented in Fig. 9.5. As expected from the Flory–Huggins description, the critical point approaches a finite, chain length independent temperature, the Θ temperature, and the critical density decreases as we increase the chain length. In addition to the simulation results, the figure also displays results from an analytical, liquid-state approach – Wertheim’s perturbation theory [44–46]. This approach uses a fluid of unconnected particles interacting via a Lennard-Jones potential as reference fluid and, then, calculates the effect of bonding to first order in thermodynamic perturbation theory. Thus, it incorporates the local packing of the Lennard-Jones monomeric units and yields a much more detailed description of the thermodynamics than the Flory–Huggins approach. Being a mean field theory, however, Wertheim’s perturbation theory also overestimates the critical temperature, but it provides a rather accurate description of the density of the polymer liquid that coexists with its vapor of vanishingly small density.

In computer simulations, one can use similar techniques to calculate the phase diagram and interface properties as in binary polymer blends [24, 47, 48]. For instance, the interface tension can either be obtained from the probability distribution of the density in the grand canonical ensemble or from the spectrum of capillary waves extrapolating the data to vanishingly small wave vector, q . In contrast to

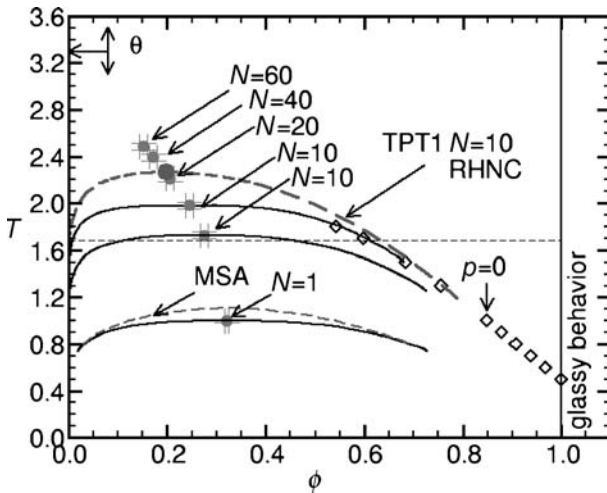


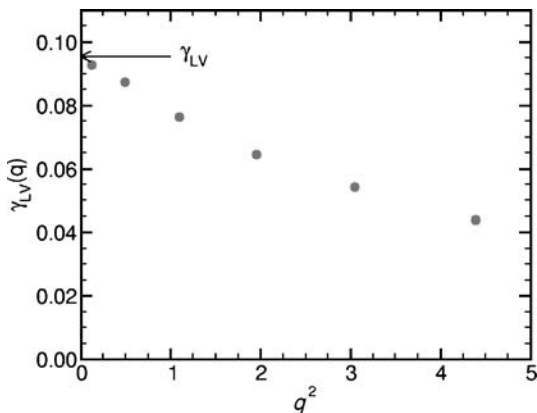
Fig. 9.5 Phase diagram of a bead–spring polymer model. Polymer segments interact via a Lennard–Jones potential that is cut-off at $r_c = 2 \cdot 2^{1/6} \sigma$, where σ denotes the length scale of the Lennard–Jones potential. Segments along the backbone are bonded via a non-linear spring (FENE potential). The complete phase diagram (critical point and bimodal) obtained from grand canonical Monte Carlo simulations are shown as full lines, while the corresponding results from Wertheim’s perturbation theory are presented by dashed lines. The figure also includes the critical points from MC simulations of longer chains, which tend towards the Θ temperature (indicated by an arrow). Diamond present the results of constant pressure simulations and indicate the densities that correspond to vanishing pressure (a good approximation for the coexistence curve at low temperatures). Adapted from [44]

binary polymer blends, however, the tension extracted from the spectrum of capillary waves exhibits a marked wave vector-dependence: Fluctuations on shorter length scales cost less free energy than one would expect from the capillary wave Hamiltonian. Formally, this corresponds to a negative bending rigidity of the interface which has also been predicted by Mecke and Dietrich [49].

Additionally, also local correlations between segments have to be incorporated into the theoretical approach. This can be done by replacing the Flory–Huggins interaction excess free energy $\Delta F = kT\rho \int dr \chi \phi_A \phi_B$ by a weighted density functional. In a fluid, one has to distinguish two effects: On one hand, the harsh, short-range repulsion between the segments are responsible for packing correlations, i. e., density oscillations around a reference segment. On the other hand, there are longer-range attractions which lead to the liquid–vapor phase coexistence. In our calculations we use a weighted-density Ansatz for the excess free energy functional [13–17, 19, 50–53]

$$\Delta F = \int dr \phi \left(g_{hc}(\bar{\phi}_{hc}) + g_{att}(\bar{\phi}_{att}) \right) \tag{9.7}$$

Fig. 9.6 Wave vector dependence of the liquid–vapor interface tension as extracted from the Fourier spectrum of interface fluctuations in an off-lattice bead–spring model (length scales are measured in units of the Lennard-Jones diameter, σ , and energies in units of $k_B T = 1.68\epsilon$). In agreement with theoretical predictions we find a reduction of the effective interface tension with growing wave vector (negative bending rigidity of the interface). In the limit $q \rightarrow 0$, the value extracted from the Fourier spectrum agrees with the value obtained from grand canonical simulations. Adapted from [16]



The bulk thermodynamics is only determined by the sum of the two functions, $g_{hc} + g_{att}$. This can be calculated by Wertheim's perturbation theory. g_{hc} describes the thermodynamics of the fluid without attractions, and this also can be obtained from Wertheim's theory using a purely repulsive fluid of unconnected segments as reference. The weighted density are defined by

$$\bar{\phi}_{hc} = \int dr w_{hc}(r - r') \phi(r') \quad (9.8)$$

where w_{hc} has the spatial range of the harsh repulsion and its integral is normalized to unity. A similar definition holds for w_{att} , but the range is comparable to the spatial extension of the attraction between monomers. Fortunately, the results of the calculations are not very sensitive to the detailed shape of these weighting functions as long as their spatial extent characterizes the short-ranged repulsion and longer-ranged attraction, respectively. Ideally, one would use the direct correlations functions as calculated by P-RISM theory for the system with only repulsive interactions for w_{hc} and the difference between this result and P-RISM calculation [54] for the full system for w_{att} .

Using the detailed chain conformations and the weighted density functional, one accurately takes account of the local fluid-like structure of the polymeric liquid. Using Wertheim's thermodynamic perturbation theory one accurately describes the bulk thermodynamics. This allows us to describe the behavior of polymers at liquid–vapor interfaces and surfaces of a melt in contact with a solid substrate.

9.7.2 Wetting and Stability of Thin Films

Calculating the liquid vapor interface tension γ and the surface tension of the liquid and the vapor in contact with a solid substrate, γ_{lw} and γ_{vw} , respectively, one can estimate the contact angle of a macroscopic drop via Young's equation [55]

$$\cos \Theta = \frac{\gamma_{vw} - \gamma_{lw}}{\gamma} = \frac{\Delta\gamma}{\gamma} \quad (9.9)$$

This equation also proves very useful for estimating contact angles of macroscopic droplets from computer simulations [17, 48, 53].

In Fig. 9.7 we plot the contact angle of a polymer drop that consists of short bead–spring polymers on top of a surface. The surface attracts the polymer segments with a long-ranged attraction which decays like the inverse cube of the distance and which is characterized by a strength ϵ_{wall} (Hamaker constant).

The figure presents the results of the computer simulations and DFT (density functional theory) calculations. The two sets of DFT calculations both use the explicit chain conformations extracted from the simulations of a bulk liquid and an accurate equation of state from Wertheim's perturbation theory [44]. In one calculation we used the weighted density functional of (9.7) to describe the interactions between segments, but in the other calculation we used just a single term with a single weighting function for both, the harsh repulsive and the longer-ranged attractive part. The quantitative comparison shows that the former can describe the simulation data, while there are rather pronounced deviations for the latter version of the DFT calculations.

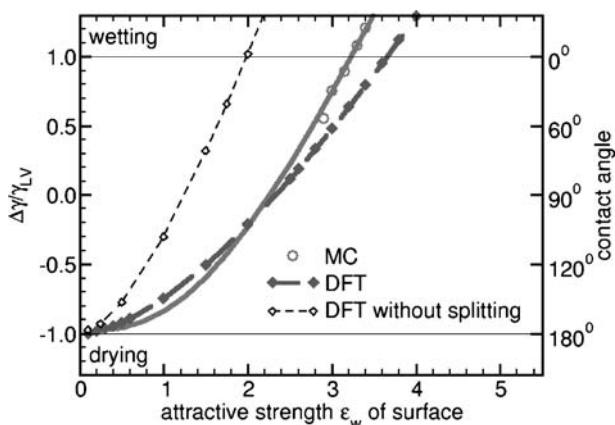


Fig. 9.7 Contact angle of a macroscopic droplet of a polymer on a solid substrate as obtained from Young's equation. Both the results of Monte Carlo simulations of a bead–spring model with chain length $N=10$, and density functional calculations (DFT) are shown. The data illustrate that it is important to split the density functional into a harsh repulsive contribution and a longer-ranged attractive one. Without this splitting the DFT cannot quantitatively predict the surface and interface tensions. Adapted from [17]

9.7.3 Explicit Solvent

One advantage of the DFT calculations is that one can extend them to a variety of more complicated systems which are very time-consuming to investigate by computer simulations.

Recently it was suggested to expose thin polymer films to solvent vapor to facilitate the equilibration. The solvent might act as a plasticizer and significantly speed-up the diffusion of the polymer in the thin film [57–60]. Thus, such a vapor treatment might be a promising alternative to tempering at elevated temperatures. Often it is assumed that the solvent distributes homogeneously in the film (dilution approximation). Generally, however, the solvent exhibit some tendency to enrich at the liquid–vapor interface or the surface to the substrate. Such enrichment will influence the interface and surface structure [61] and thereby it might modify the stability of the polymer film.

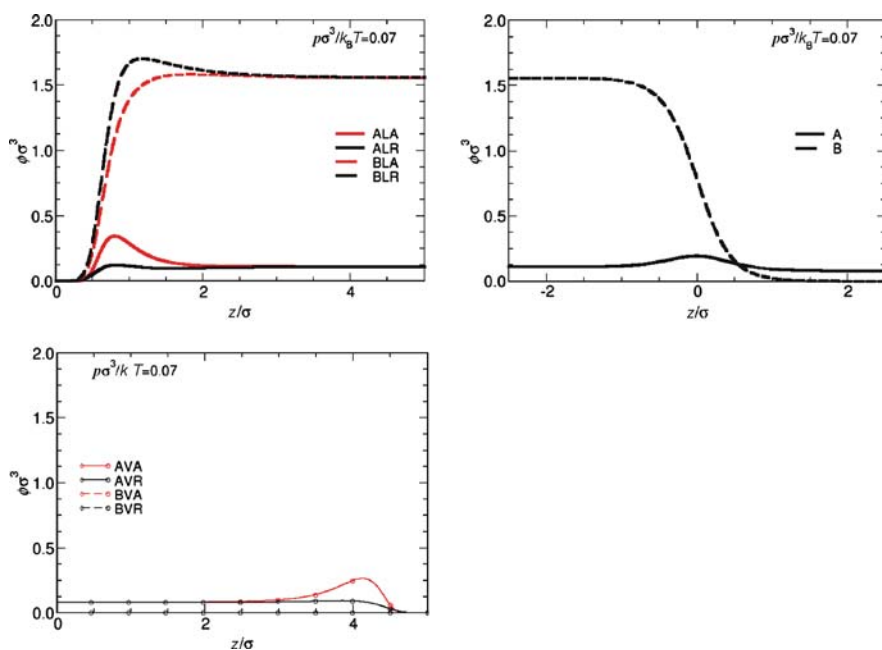


Fig. 9.8 Profiles of polymer + solvent mixture obtained from DFT calculations. The upper left panel shows the profiles of the polymer-rich phase in the vicinity of the wall at rather low vapor pressure. In this case not much solvent dissolves into the polymer melt. The two sets of curves correspond to a surface that attracts the polymer (black) and a surface that attracts both, the polymer and the solvent (red). The right panel presents the profiles across the liquid–vapor interface. Note the enrichment of solvent at the interface. The polymer density in the vapor in vicinity of the surface. The lower panel shows the profiles of the vapor in vicinity of the surface. The polymer density in the vapor is vanishingly small. The solvent is enriched at the surface that attracts not only the polymer but also the solvent. The free energy costs of these three interfaces determine the stability of a polymer film in equilibrium with solvent vapor. Adapted from [56]

In Fig. 9.8 we present the profiles of the polymer and the solvent in the vicinity of the substrate and at the liquid vapor interface. Two substrates were considered: The first substrate only attracts the polymer. As we increase the vapor pressure, the solvent density increases both in the polymer liquid as well as in the vapor. No enrichment of solvent builds up at the substrate, neither in the vapor nor in the liquid phase. Thus the difference in the surface tensions, $\Delta\gamma$, does not depend strongly on the vapor pressure. We observe, however, an enrichment of solvent at the liquid–vapor interface. This interfacial excess of solvent will diverge (interfacial wetting) if we approach the triple point (if it exists) where the dense polymer coexists with a solvent vapor and a liquid of solvent. This is a quite common phase behavior in compressible ternary systems (type III in the classification of Konynenburg and Scott [62]). It occurs if there is a liquid–vapor phase coexistence of the solvent in the temperature and pressure range of interest and the liquid–solvent is only partially miscible with the dense polymer. The enrichment of solvent at the liquid–vapor interface might cause a rather substantial reduction of the interface tension and it leads to a reduction of the contact angle or a stabilization of the polymer film.

The second substrate attracts the solvent, and this gives rise to a pronounced enrichment of solvent at the surface in contact with the polymer melt and in contact with the vapor. Both effects tend to destabilize the polymer film. The enrichment of the solvent at the surface in the vapor phase decreases the surface tension γ_{vw} . At the surface in contact with a melt, the enrichment layer of solvent displaces the polymer from the surface. Thus, the polymer benefits less from the attractions between surface and polymer segments and the surface tension γ_{lw} increases. Both effects decrease $\Delta\gamma$ and can compensate or, at large vapor pressure, even outweigh the decrease of the interface tension. Thus, if the substrate attracts the solvent, increasing the solvent pressure might lead to a destabilization of the polymer film and re-entrant dewetting as a function of vapor pressure [56].

9.8 Outlook

We have described the similarities and differences in the theoretical description of interfaces in binary polymer blends and polymer solutions. Since the characteristic length scale of interfaces in polymer blends is much larger than the width of the surface of a polymer melt or solution in contact with its vapor or a solid substrate, the properties of blends exhibit a large degree of universality and, within mean field theory, are characterized by only two parameters, the incompatibility of the molecules and their size.

This behavior is in marked contrast to narrow profiles of outer polymer surfaces. In order to quantitatively describe the properties of liquid–vapor surfaces, three ingredients are necessary:

1. an accurate description of the equation of state,
2. an accurate description of the fluid-like packing and

3. the incorporation of the detailed chain architecture on short length scales. We have outlined how these ingredients can be incorporate into the theoretical approach and have compare the theory with computer simulations of a bead-spring model [16, 17, 53].

We have illustrated its usefulness by investigating the stability of polymer films in equilibrium with an explicit solvent [56]. Depending on whether or not the substrate favors the solvent, such a solvent treatment might destabilize or stabilize the thin polymer film, respectively.

As the properties of liquid–vapor interfaces and the behavior at solid substrates depend on details on short length scales they pose a challenge to a theoretical description but also a much richer behavior can be expected. In order to learn more about the properties on large length scales, the generalization of the approach to study the dynamics of interface formation would be interesting. In the case of a binary polymer blend, we have illustrated that the dynamic SCF theory is able to quantitatively describe the early stages of phase separation [36, 63] (where interfaces form and hydrodynamics effects are not yet important), if one uses an Onsager coefficient that duly accounts for the propagation of forces along the backbone of the molecules. Recently developed particle-based dynamic SCF simulations are particularly promising techniques to study the early stages of phase separation in multi-component polymer systems with strong spatial or dynamic asymmetries [42, 43]. In polymer solutions, a much richer behavior can be expected because of the possibly large dynamic asymmetry between the polymer and the solvent.

Acknowledgements

It is a great pleasure to thank K. Binder, J.J. de Pablo, E.W. Edwards, K. Ch. Daoulas, Y.C. Lin, L. Gonzalez MacDowell, P. Nealey, E. Reister, F. Schmid, G.S. Smith, M.P. Stoykovich, A. Werner, and A. Yethiraj for very enjoyable collaborations and stimulating and fruitful discussions. Financial support was provided by the DFG under grant Mu1764/3 and the Volkswagen foundation. The calculations would not have been possible without a generous allocation of computing time at the NIC, Jülich, the HLR Stuttgart and the computing center at the Johannes Gutenberg Universität, Mainz.

References

1. Paul DR, Newman S (1978) *Polymer Blends*. Academic, New York
2. Stamm M, Schubert DW (1995) *Ann Rev Mater Sci* 25:325
3. Tucker CL, Moldenaers P (2002) *Ann Rev Fluid Mech* 34:177
4. Brown HR, Char K, Deline VR, Green PF (1993) *Macromolecules* 26:4155

5. Schnell R, Stamm M, Creton C (1999) *Macromolecules* 32:3420
6. Helfand E, Tagami Y (1972) *J Chem Phys* 56:3592
7. Helfand E (1975) *J Chem Phys* 62:999
8. Scheutjens JM, Fleer GJ (1979) *J Chem Phys* 83:1619
9. Noolandi J, Hong KM (1981) *Macromolecules* 14:727
10. Shull KR (1993) *Macromolecules* 26:2346
11. Szleifer I, Carignano MA (1996) *Adv Chem Phys* 94:742
12. Matsen MW, Schick M (1995) *Phys Rev Lett* 74:4225
13. Woodward CE (1991) *J Chem Phys* 94:3184
14. Woodward CE, Yethiraj A (1994) *J Chem Phys* 102:5499
15. Yethiraj A (1998) *J Chem Phys* 109:3269
16. Müller M, MacDowell LG (2000) *Macromolecules* 33:3902
17. Müller M, MacDowell LG, Yethiraj A (2003) *J Chem Phys* 118:2929
18. Müller M, Schmid F (2005) *Adv Polym Sci* 185:1
19. Patra CN, Yethiraj A (2003) *J Chem Phys* 118:4702
20. Flory PJ (1941) *J Chem Phys* 9:660
21. Huggins ML (1941) *J Chem Phys* 9:440
22. Müller M, Binder K (1995) *Macromolecules* 28:1825
23. Müller M (1995) *Macromolecules* 28:6556
24. Müller M (1999) *Macromol Theory Simul* 8:343
25. Carmesin I, Kremer K (1988) *Macromolecules* 21:2819
26. Edwards SF (1965) *Proc Phys Soc* 85:613
27. Semenov AN (1996) *J Phys II* 6:1756
28. Werner A, Schmid F, Müller M, Binder K (1999) *Phys Rev E* 59:728
29. Schmid F, Müller M (1995) *Macromolecules* 28:8639
30. Buff FP, Lovett RA, Stillinger FH (1965) *Phys Rev Lett* 15:621
31. Semenov AN (1993) *Macromolecules* 26:6617
32. Semenov AN (1994) *Macromolecules* 27:2732
33. Cahn JW, Hilliard JE (1958) *J Chem Phys* 28:258
34. Cahn JW, Hilliard JE (1959) *J Chem Phys* 31:668
35. Cook HE (1970) *Acta Metall* 18:297
36. Reister E, Müller M, Binder K (2001) *Phys Rev E* 64:041804
37. Hohenberg PC, Halperin BI (1977) *Rev Mod Phys* 49:435
38. deGennes PG (1980) *J Chem Phys* 72:4765
39. Pincus PJ (1981) *J Chem Phys* 75:1996
40. Binder K (1983) *J Chem Phys* 79:6387
41. Maurits NM, Fraaije JG (1997) *J Chem Phys* 107:5879
42. Müller M, Smith GS (2005) *J Polym Sci Polym Phys B* 43:934
43. Edwards EW, Stoykovich MP, Müller M, Solak HH, de Pablo JJ, Nealey P (2005) *J Polym Sci B* 43:3444
44. MacDowell LG, Müller M, Vega C, Binder K (2000) *J Chem Phys* 113:419
45. Wertheim MS (1987) *J Chem Phys* 87:7323
46. MacDowell LG, Müller M, Virnau P, Binder K (2002) *J Chem Phys* 117:6360
47. Müller M, Schick M (1996) *J Chem Phys* 105:8885
48. Müller M, Binder K (1998) *Macromolecules* 31:8323
49. Mecke KR, Dietrich S (1999) *Phys Rev E* 59:6766
50. Curtin WA, Ashcroft NW (1985) *Phys Rev A* 32:2909
51. Van Swol F, Henderson JR (1991) *Phys Rev A* 43:2932
52. Katsov K, Weeks JD (2001) *J Phys Chem B* 10:6738
53. Müller M, MacDowell LG (2003) *J Phys Condens Matter* 15:609
54. Schweizer KS, Curro JG (1997) *Adv Chem Phys* 98:1
55. Young T (1805) *Philos Trans R Soc London* 57:827
56. Lin YC, Müller M, Binder K (2004) *J Chem Phys* (in press)
57. Kim G, Libera M (1998) *Macromolecules* 31:2569

58. Kim SH, Misner MJ, Xu T, Kimura M, Russell TP (2004) *Adv Mater* 16:226
59. Fukunaga K, Elbs H, Magerle R, Krausch G (2000) *Macromolecules* 33:947
60. Fukunaga K, Hashimoto T, Elbs H, Krausch G (2002) *Macromolecules* 35:4406
61. Müller-Buschbaum P, Gutmann JS, Wolkenhauer M, Kraus J, Stamm M, Smilgies D, Petry W (2001) *Macromolecules* 34:1369
62. Van Konynenburg P, Scott RL (1980) *Philos Trans Soc London Series A* 298:495
63. Reister E, Müller M (2003) *J Chem Phys* 118:8476

Chapter 10

Plasma Modification of Polymer Surfaces and Plasma Polymerization

Mirko Nitschke

Leibniz Institute of Polymer Research Dresden & Max Bergmann Center of Biomaterials
Dresden, Hohe Str. 6, 01069 Dresden, Germany, nitschke@ipfdd.de

Abstract An ionized medium consisting of electrons, ions and possibly of neutrals and photons, which meets some additional criteria, is called a plasma. According to this definition, the term plasma covers a wide range of phenomena. Low pressure plasmas, as discussed here, are universal tools for surface treatment. Depending on the process parameters and the process gas material loss or material deposition can predominate. In the intermediate case a shallow surface layer is modified with respect to its chemical and/or physical properties.

In the first part of this chapter low pressure plasma surface modification of polymeric materials is discussed. The second part introduces the deposition of thin polymer films by means of plasma polymerization.

10.1 Plasma Modification of Polymer Surfaces

10.1.1 Why Use Low Pressure Plasma?

Advantages

- Elementary processes with high activation energies of several electron volts are possible in low pressure plasmas without elevated gas (ion, neutral) temperatures. There is almost no thermal load for sensitive polymer materials during low pressure plasma treatment.
- While the chemical structure of a shallow surface layer can be changed significantly, the bulk properties remain unchanged.
- An extremely wide range of surface modifications can be obtained with different low pressure plasmas.
- The amount of toxic byproducts is low compared to other methods.

Disadvantages

- Because of the high vacuum necessary, low pressure plasma applications are quite expensive.
- Due to the multitude of elementary reactions occurring simultaneously, it is impossible in most cases to calculate in detail the physical and chemical behavior of a plasma. This applies especially to plasma–surface interactions.
- It is difficult to restrict the variety of functional groups formed in a plasma treatment to a well defined set of species.
- Scaling up a plasma process from laboratory size to industrial dimensions is far from a straight forward procedure.
- It is difficult to replace batch processes by continuous processes (air to air processes).

10.1.1.1 How to Overcome These Problems

- The high expenses for plasma equipment will decrease when this technique becomes more popular, especially in industry scale applications. On the other hand, the costs for wet chemistry processes will exceed those for plasma processes with higher waste disposal expenses.
- The increasing power of computer systems allows nowadays the creation of complex models to predict real plasma processes. Especially with the use of Monte Carlo codes, an adequate treatment of a wide range of elementary processes in the plasma volume, the plasma sheath and the surface region can be done. Nevertheless, there is a significant lack of necessary input values like rate constants, cross-sections and sticking coefficients.
- With a better knowledge of elementary processes, especially at the polymer surface, the choice of process parameters will become less empirical. This also covers the problem of a poor selectivity of plasma processes with regard to the range of formed species. Another approach to a more uniform surface chemistry is to combine the plasma process with pre or post plasma treatments.
- A solution for problems related to reactor scaling will become available with future progress in simulation techniques. In contrary, the problem of continuous air to air plasma processing of polymers is a more serious one. There is a strong contradiction of the polymer inherent outgasing tendency and the requirement of a clean process. This will possibly restrict the application of more sophisticated plasma treatments to batch processes with limited material throughput.

10.1.2 How to Apply Low Pressure Plasma

10.1.2.1 Plasma Parameters

When a polymer is immersed into a plasma the interaction processes are governed by internal plasma parameters.

- Type of species present in the plasma
- Spatial distributions
- Energy distributions
- Directional distributions

The internal plasma parameters are determined in a complex way by external plasma parameters (process parameters, accessible for the user).

- Reactor geometry
- Type of excitation
- Applied power
- Process gas
- Gas pressure
- Gas flow

Consequently, for a given application, a specific reactor design and an appropriate set of process parameters are necessary.

10.1.2.2 Plasma Generation and Reactor Design

For plasma generation on a laboratory scale electrical gas discharges are used. An AC excitation is necessary for the treatment of insulating materials like polymers. The most popular excitation frequencies are in the radio frequency (RF) and the micro wave (MW) range. In the case of MW excitation an additional magnetic field can be applied to meet the criterion for electron cyclotron resonance (ECR):

- The setup for RF excitation is the most simple one. In the case of a capacitively coupled RF discharge two electrodes are mounted into a vacuum chamber. A process gas with a typical pressure of a few pascal is introduced. When the RF voltage exceeds a certain value the discharge ignites. This value is generally within the range of some hundred volts depending on gas, pressure and reactor geometry.
- In the case of MW excitation no electrodes are necessary. A higher degree of ionization is achieved for MW discharges in general and especially for MW-ECR discharges. The use of the ECR effect is restricted to pressures < 1 Pa. A setup with a MW excitation is more complicated and more expensive compared to one using RF.

For a given type of plasma excitation, the position of the sample in the reactor volume is an important parameter. This applies to the surface modification of polymers and especially to the case of plasma polymerization discussed below:

- When the sample is placed directly in the excitation volume of the discharge, there is a relatively high flux of active particles to the treated surface. Moving the sample away from the discharge (remote plasma position, afterglow) decreases the flux and restricts the variety of active particles to long-living species. Depending on the reactor geometry, the sample can be shielded from the action of vacuum ultraviolet radiation.
- In the case of capacitively coupled RF discharges significant self bias voltages can appear at the treated surface when the sample is placed on the powered electrode. This leads to high ion energies up to several hundred electron volts.

10.1.2.3 The Variety of Effects

During low pressure plasma treatment a shallow surface layer of the polymer of some 10 nm is modified due to the action of energetic particles and vacuum ultraviolet radiation. The surface modification can be understood as a dynamic equilibrium of competing functionalization and degradation processes.

There are effects, common to almost all plasma processes, such as hydrogen loss and overall material ablation. Other effects are characteristic for the specific type of plasma, such as the introduction of functional groups containing foreign atoms. To illustrate the complexity of plasma surface modification, some experimental observations are given here:

- Low pressure plasma treatment usually leads to the simultaneous formation of different functional groups (e. g. carbonyl and hydroxyl groups in an oxygen discharge).
- Functional groups formed in a plasma treatment can migrate to the subsurface. As a result, the number of accessible functional groups may decrease over time.
- Stable radicals formed at the polymer surface can cause post plasma reactions on different time scales.
- A plasma treatment can cause graphitization of a polymer surface, which strongly affects the electrical conductivity.

All these effects and many others depend on the type of plasma and the plasma parameters. A particular effect can be pronounced or suppressed by an appropriate choice of the experimental conditions. For that purpose, a set of diagnostic techniques is necessary.

10.1.2.4 Diagnostic Techniques

Due to the fact, that the modification effects at the polymer surface can not be derived in detail from the knowledge of external process parameters, the following strategy is used:

- Internal plasma parameters are measured. When correlations are found between process parameters and internal plasma parameters, surface effects can be predicted at least qualitatively.
- Specific surface effects expected from the behavior of the plasma have to be proved or to be disproved with adequate surface diagnostic techniques.

Table 10.1 Diagnostic techniques (most popular methods mentioned first)

Plasma diagnostics	Surface diagnostics
Langmuir probe diagnostics	X-Ray photoelectron spectroscopy
Optical emission spectroscopy	Fourier transform infrared spectroscopy
Mass spectroscopy	Contact angle goniometry
Energy dispersive mass spectroscopy	Atomic force microscopy
Laser induced fluorescence	Fluorescence labelling
Calorimetry at catalytic surfaces	Secondary ion mass spectroscopy
	Streaming potential measurement

10.1.3 Examples

In many cases the main purpose of low pressure plasma polymer modification is a more hydrophilic surface. In the initial phase of the plasma treatment the wettability is improved significantly. When the equilibrium between functionalization and degradation (etching) is reached, the value of the contact angle becomes constant (Fig. 10.1).

Due to different reasons (polymer chain mobility, post plasma reactions with the ambient air) the obtained effect is not stable (hydrophobic recovery). However, on a long time scale, most materials remain more hydrophilic than before the plasma treatment (Fig. 10.2).

To avoid the hydrophobic recovery, the plasma-activated surface can be used to graft or to adsorb other polymers immediately after treatment. Here, the adsorption of a polyelectrolyte is shown. As a result, a more hydrophilic and more stable surface modification is obtained (Fig. 10.3).

Fig. 10.1 Static water contact angle of NH_3 plasma treated FEP. Reprinted with permission from [1]

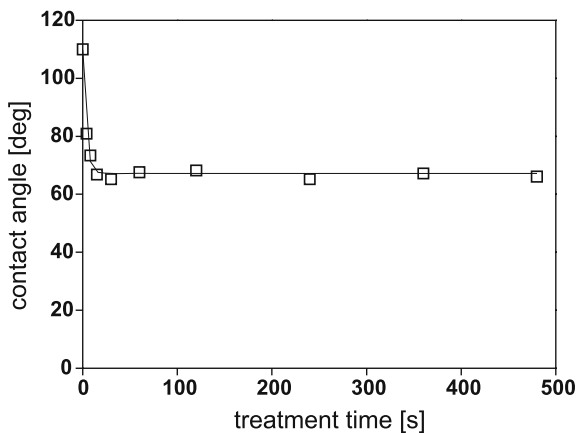


Fig. 10.2 Advancing (solid lines) and receding (dashed lines) water contact angles of NH_3 plasma treated FEP (squares) compared to untreated FEP (circles). Reprinted with permission from [1]

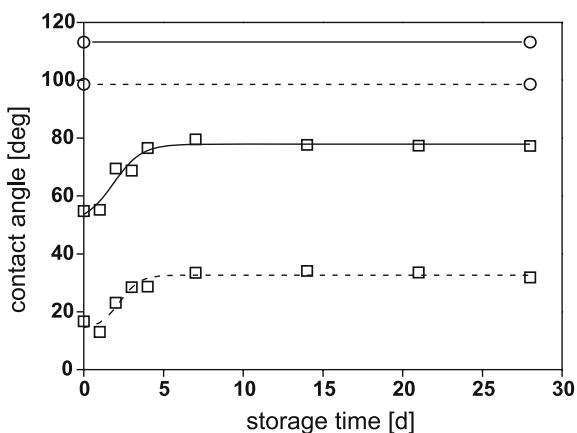
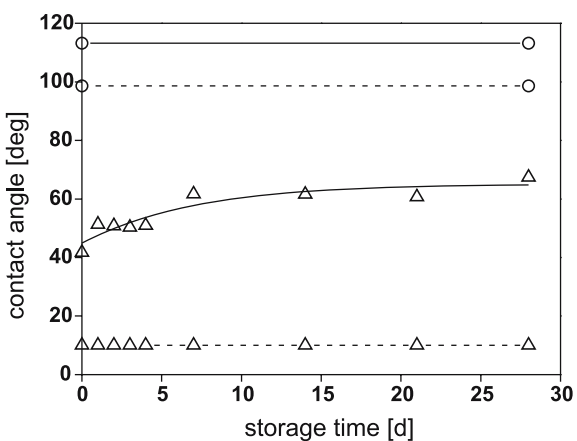


Fig. 10.3 Advancing (solid lines) and receding (dashed lines) water contact angles of NH_3 plasma treated and poly(sodium 4-styrenesulfonate) exposed FEP (triangles) compared to untreated FEP (circles). Reprinted with permission from [1]



In other applications, the purpose of low pressure plasma treatment is to provide a particular type of functional group on the polymer surface. In this case more sophisticated surface sensitive analytical techniques are necessary. For semi-quantitative results Fourier transform infrared (FTIR) attenuated total reflection (ATR) spectroscopy can be applied. Quantitative results can be obtained by X-Ray photoelectron spectroscopy combined with labelling techniques (Figs. 10.4–10.7).

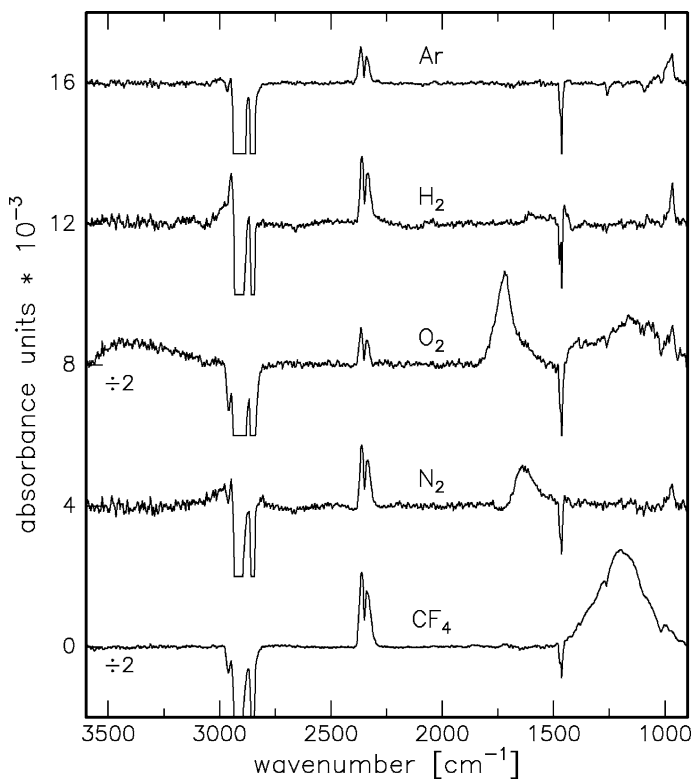


Fig. 10.4 FTIR-ATR difference spectra for the treatment of polyethylene in Ar, H_2 , O_2 , N_2 and CF_4 plasmas. Reprinted with permission from [2]

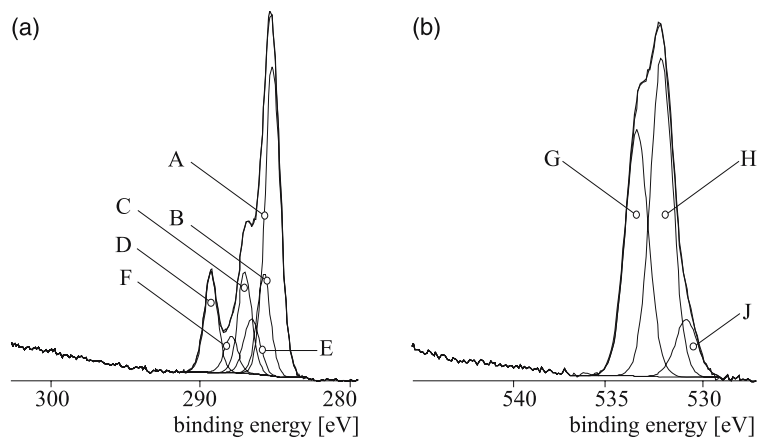
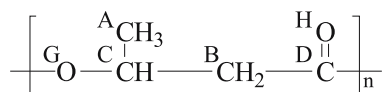
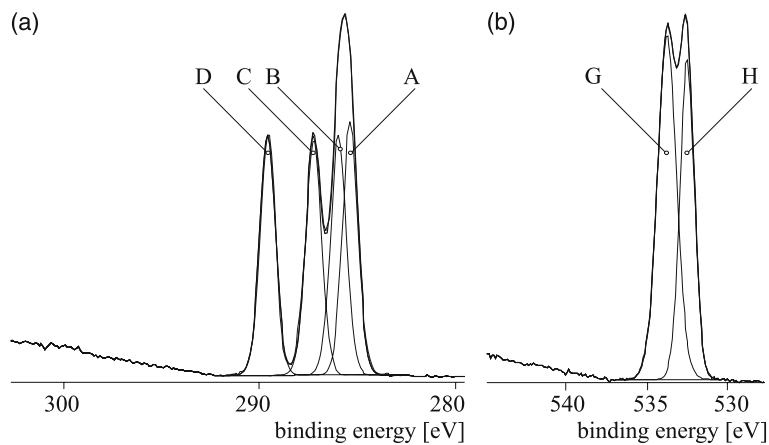


Fig. 10.5 XPS C_{1s} and O_{1s} spectra of poly(3-hydroxybutyrate) before (top) and after NH_3 plasma treatment (bottom). Reprinted with permission from [3]

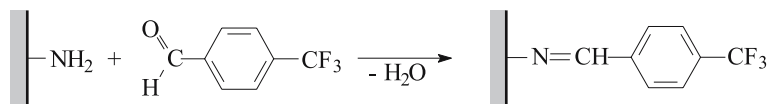


Fig. 10.6 Labelling of NH_2 groups with trifluoromethyl benzaldehyde (TFBA)

Fig. 10.7 Total nitrogen content (squares) and nitrogen in NH_2 groups (circles) after plasma treatment as determined by XPS and TFBA labelling. Reprinted with permission from [3]

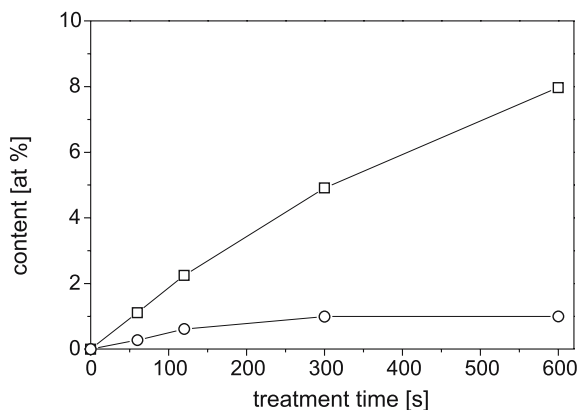


Table 10.2 Examples of polymer surface modification by low pressure plasma

Plasma	Application
Ar, He, H_2	Surface cross-linking, generation of radicals for grafting processes, plasma immobilization of pre-deposited molecules or thin films
O_2 , CO_2 , H_2O	Improvement of the wetting behavior, generation of $\text{C}=\text{O}$, $\text{O}-\text{H}$, etc.
NH_3	Improvement of the wetting behavior, generation of NH_2 groups
CF_4	Fluorination

10.2 Plasma Polymerization

10.2.1 Why Use Plasma Polymerization?

Electrical gas discharges can initiate monomers to form polymeric products. When a low pressure plasma is operated under appropriate conditions with a substance like styrene or acrylic acid as a process gas, the formation of thin polymer films on the reactor walls is observed. This effect is called plasma polymerization.

The concept of atomic polymerization (one of the proposed mechanisms for plasma polymerization) suggests, that the elemental reactions are the fragmentation of monomer molecules, the formation of radical sites and the recombination of the activated fragments (in the gas phase as well as in the growing film).

According to this concept, plasma polymerization is not restricted to unsaturated monomers as used in conventional polymerization. This was proven in many experiments with process gases consisting of saturated organic molecules. For example, plasma polymerization leads to similar results when a unsaturated monomer is replaced by its saturated counterpart.

Advantages

- The variety of organic substances that can serve as a monomer makes plasma polymerization an extremely versatile tool for the deposition of polymeric thin films.
- Functional groups of the monomer can be transferred into the plasma polymer film.
- Due to the adjustable degree of cross-linking, plasma polymers can have exceptional mechanical properties.
- Plasma polymers can be prepared as thin as a few nanometres while the films are pin hole free and have good adhesion to most substrates.
- Vertical gradients of the film properties can be obtained by changing the process parameters *during* the deposition process.

Disadvantages

The major disadvantages of plasma polymerization are the same as those mentioned for low pressure plasma surface modification.

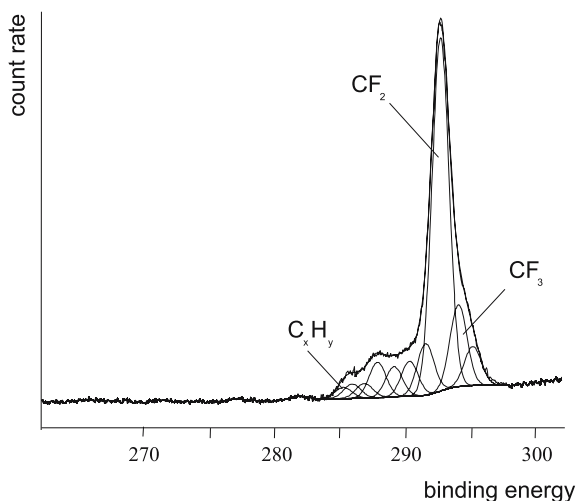
10.2.2 How to Apply Plasma Polymerization

A number of process parameters allows to adjust the deposition rate and the properties of the obtained thin film:

- Depending on the monomer, hydrocarbon, fluorocarbon or silicon organic films can be fabricated. The process gas can be either a pure monomer gas or a small amount of monomer mixed with a carrier gas (e. g. argon).
- Pressure and flow rate of the process gas are essential parameters to control plasma polymerization. The deposition rate passes through a maximum when a monomer sufficient regime is gradually shifted into a monomer deficient regime.
- The applied power determines the degree of fragmentation of the process gas. This can change the properties of the obtained polymer film over a very wide range. For example, the film obtained by plasma polymerization of hexamethyldisiloxane can vary from a low molecular weight silicone polymer to silicon oxide depending on the applied power.
- The structure of the obtained film can be altered significantly when the position of the substrate is changed from inside the plasma excitation volume to a remote position in the outward gas flow. This is due to gas phase reactions of activated species and differences with respect to flux and energy of ions hitting the growing film. Beyond that, a remote substrate position can be shielded from high energy vacuum ultraviolet photons emitted by the plasma.
- Flux and energy of the ion bombardment at the substrate position can be changed by electrical potentials (bias voltages). This allows to control the deposition rate and the structure of the plasma polymer film.

10.2.3 Example

Fig. 10.8 XPS C_{1s} spectrum of a plasma polymer film obtained from a RF discharge operated with a mixture of argon and C_2F_4 . Contrary to most plasma polymers, the film has a structure close to PTFE, characterized by a low degree of cross-linking. Reprinted with permission from [4]



10.3 Recommended Literature

There is a huge amount of literature on low pressure plasma techniques. Some text books and review articles are recommended here. The book by Chapman [5] gives an easy to read introduction to low pressure plasma (DC, RF). Microwave plasmas are discussed in detail in the book by Ferreira and Moisan [6]. Selected techniques of polymer surface modification and characterization are presented by Chan [7, 8]. By comparison, the book by Sabbatini and Zambonin [9] covers a wider range of techniques but it is not exclusively dedicated to plasma induced surface effects. Briggs and Seah [10] give a general introduction to X-Ray photoelectron spectroscopy (XPS) while the book by Beamson and Briggs [11] addresses the specific problems of XPS polymer characterization. Beyond XPS, infrared (IR) spectroscopy is one of the most popular techniques to study plasma modified polymer surfaces. The book by Garton [12] is an excellent introduction to this method. Among the surface sensitive IR sampling techniques attenuated total reflection (ATR) is especially important. This subject is covered in depth by Harrick [13]. General introductions to plasma polymerization are given by d'Agostino, Biederman and Inagaki [14–16].

References

1. Lappan U, Nitschke M, Pleul D, Simon F, Uhlmann S (2001) Polyelectrolyte adsorption on NH_3 plasma treated poly(tetrafluoroethylene-co-hexafluoropropylene) (FEP). *Plasmas Polym* 6:211–220
2. Nitschke M, Meichsner J (1997) Low pressure plasma polymer modification from the FTIR point of view. *J Appl Polym Sci* 65:381–390
3. Nitschke M, Schmack G, Janke A, Simon F, Pleul D, Werner C (2002) Low pressure plasma treatment of poly(3-hydroxybutyrate) – toward tailored surfaces for tissue engineering scaffolds. *J Biomed Mater Res* 59:632–638
4. Nitschke M, Menning A, Werner C (2000) Immobilization of PEO-PPO-PEO triblock copolymers on PTFE-like fluorocarbon surfaces. *J Biomed Mater Res* 50:340–343
5. Chapman B (1980) *Glow Discharge Processes*. Wiley, New York
6. Ferreira C, Moisan M (1993), *Microwave Discharges*. Plenum, New York
7. Chan CM (1994) *Polymer Surface Modification and Characterization*. Hansa, München
8. Chan CM, Ko TM, Hiraoka H (1996) Polymer surface modification by plasmas and photons. *Surf Sci Rep* 24:1–54
9. Sabbatini L, Zamboni PG (1993) *Surface Characterization of Advanced Polymers*. VCH, Weinheim
10. Briggs D, Seah MP (1990) *Practical Surface Analysis* vol. 1. Wiley, New York
11. Beamson G, Briggs D (1992) *High Resolution XPS of Organic Polymers*. Wiley, New York
12. Garton A (1992) *Infrared Spectroscopy of Polymer Blends, Composites and Surfaces*. Hanser, München
13. Harrick NJ (1975) *Internal Reflection Spectroscopy*. Interscience, New York
14. d'Agostino R (1990) *Plasma Deposition, Treatment and Etching of polymers*. Academic, San Diego
15. Biederman H, Osada Y (1992) *Plasma Polymerization Processes*. Elsevier, Amsterdam
16. Inagaki N (1996) *Plasma Surface Modification and Plasma Polymerization*. Technomic, Lancaster

Chapter 11

Grafting on Solid Surfaces: “Grafting to” and “Grafting from” Methods

Sergiy Minko

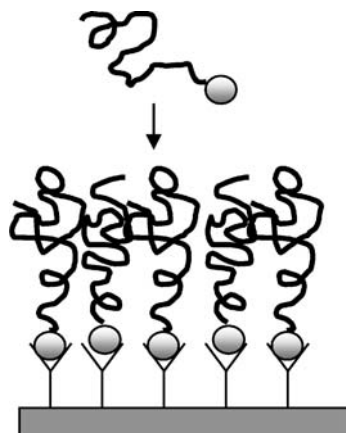
Department of Chemistry and Biomolecular Science #5810, Clarkson University,
8 Clarkson Ave., Potsdam, NY 13699, USA, sminko@clarkson.edu

Abstract The grafting of polymer brushes to a solid surface provides a versatile tool for surface modification and functionalization. End-functionalized polymer chains may be grafted to the solid substrate (grafting to) or the grafting reaction can proceed by polymerization from the surface (grafting from). In both cases a thin polymer brush layer on the solid surface is formed, which determines the surface properties. The use of mixed brush layers is described, which provide switching and adaptive surface properties. A combination of surface roughness with mixed brushes can provide switchable ultra-hydrophobic surfaces.

11.1 Introduction

The composition and behavior of surfaces and interfaces plays a pivotal role in dictating the overall efficiency of a majority of materials and devices. For instance, control of surface and interfacial properties is critical in many traditional areas of science and technology such as colloid stabilization, adhesion, lubrication, rheology, immobilization of catalysts, and generation of multiphase materials [1–5]. Beside the traditional fields the surface modification has recently found use in bioengineering, nonlinear optics, (bio)sensors, nanopatterning, molecular recognition, waveguides, and electronic microcircuit processing. A promising means to optimize the surface properties is via deposition of thin polymer layers tethered to the surface that possesses appropriate physical and chemical properties [6, 7]. This is why solid surface modification with thin polymer films has gained great interest.

Fig. 11.1 Schematic illustration of end tethered polymer chains forming brush-like layer

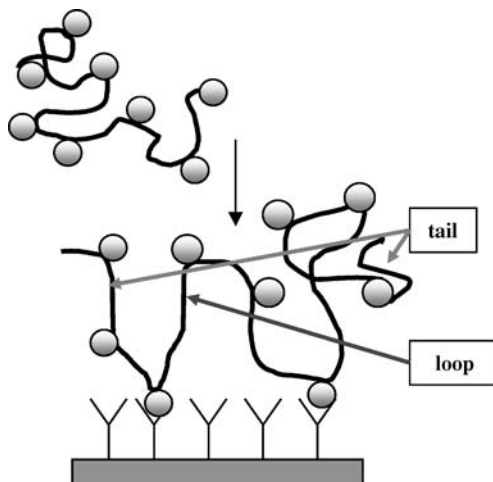


Several commonly used methods of thin film preparation on solid substrates should be mentioned. These are polymer deposition by spin casting, precipitation, Langmuir–Blodgett technique, polymer adsorption and chemical grafting of polymers. It is necessary to highlight that grafting techniques have advantages over others because of several reasons [8]. They include easy and controllable introduction of polymer chains with a high surface density, precise localization of the chain at the surface, and long stability of the grafted layers. The most substantial additional advantage is the possibility to graft several different polymers to the same substrate. In this scenario the chemical grafting prevents macro-phase separation and properties of the film are benefited from the combination of different functional ingredients.

The simplest and most investigated example (Fig. 11.1) of tethered polymer chains that are connected to the solid substrate by one chain end may be definitely distinguished from other grafted polymer layers, since they form polymer brushes if relatively high grafting density is reached. Brush-like layers are formed due to the excluded volume effect, when the substrate is completely covered with a relatively dense monolayer of grafted chains stretched normal to the support. There are several major parameters that control the brush properties: grafting density, chain length, and chemical composition of the chains. One can regulate properties of the brush by tuning the parameters which can be predicted by simple scaling relationships.

There is an alternative possibility to graft polymer chains to a solid substrate using side chain functional groups (one or more). In this case the grafted chains is “split” on several parts between grafting points forming loops or tails with behavior similar to brush-like layer (Fig. 11.2). Thus, we consider here the case of end-tethered chains when theoretical treatment is much more straightforward.

Fig. 11.2 Schematic illustration of the polymer chain grafted via side functional groups. Loops and tails behave similar to polymer brush



11.2 Behavior of Polymer Brushes

11.2.1 Homopolymer Brushes

In the diluted regime tethered polymer chains appear as mushroom like structures in good solvent (Fig. 11.3(a)), or as pancake like structures in poor solvent (Fig. 11.3(b)) if the interaction with the substrate is stronger than with the solvent. In semi-diluted regime grafted chains interact with neighbors. This interaction results either in stretching away from the substrate in good solvent or in the forma-

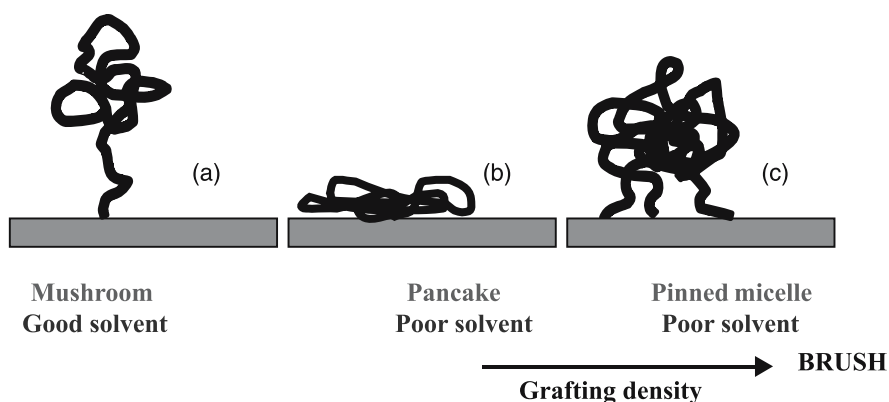


Fig. 11.3 Schematic illustration of different morphologies formed by tethered polymer chains on solid substrate in surface diluted regime: mushrooms in good solvent (a), pancake in poor solvent (b), and in surface semi-diluted regime: pinned micelle in poor solvent (c). Further increased of the grafting density brings the brush regime

tion of pinned micelles (clusters) in poor solvent (Fig. 11.3(c)). Further increase of grafting density brings the brush regime (Fig. 11.1).

Polymer brushes have been the subject of extensive theoretical study [9–19]. In studies of phase behavior of brushes, it was shown that properties of grafted chains interacting with a solvent are fundamentally different from those of free chains in solution. Brush thickness (h) scales linearly with the degree of polymerization (N). Simulations and experiments confirmed the scaling laws connecting degree of polymerization and grafting density (σ) with the brush thickness. The

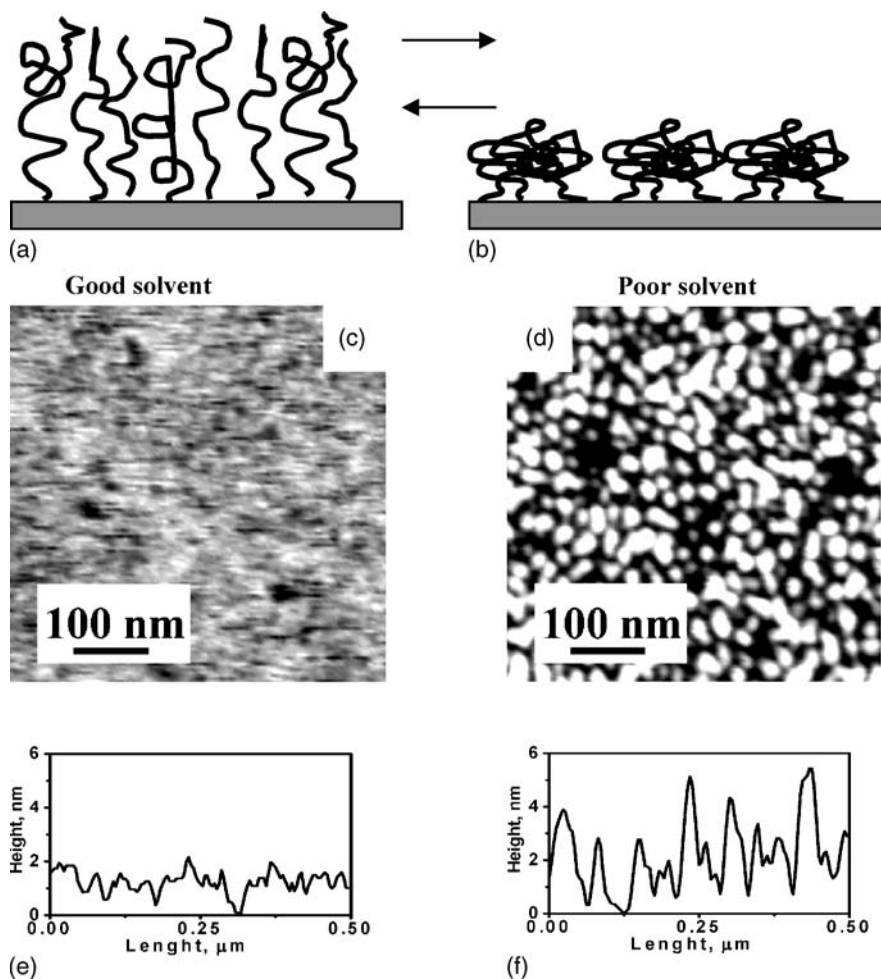


Fig. 11.4 Morphology of the polymer brush in solvent. Schematic illustration of the brush layer: smooth in good solvent (a), rough with pinned micelles in poor solvent (b). AFM images of polystyrene brush grafted on a Si-wafer after treatment with toluene (good solvent) (c), after treatment with ethanol (poor solvent) (d) and corresponding cross-section from the images (e) and (f), respectively. AFM images were obtained by Dr. Ionov

structure of brushes in a solvent results from a balance between the elastic energy of grafted chains, taken as entropic springs $f_1 \approx kTRg^{-2}$ ($Rg \approx N^{1/2}a$, where Rg and a is the chain size and monomer size, respectively) and the osmotic pressure proportional to segment density in the brush ($N\sigma/h$) $f_2 \approx kTvN(N\sigma/h)$, where v is the excluded volume parameter, which measures the strength of the repulsion between chains units. Thus, $\Delta f = f_1 + f_2$. Minimization with respect to the brush height results in:

$$h \approx N(v\sigma a^2)^{1/3}; f = kTN(v\sigma a^{-1})^{2/3}.$$

Note that the height of the brush grows linearly with N , while the unstretched chain dimension Rg only grows as $N^{1/2}$.

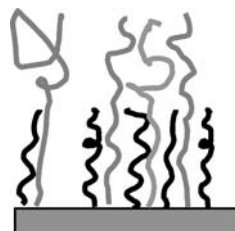
In a good solvent the brush is homogeneous parallel to the grafting surface (Fig. 11.4(a)). In contrast, for the case of a brush immersed in a poor solvent, the lateral symmetry of the brush is broken and chains segregate into nanoscopic domains (the pinned micelles) (Fig. 11.4(b)).

The size of the domains depends on grafting density and scales with chain length. At very high grafting density intermolecular interactions cannot compensate the loss of entropy and the brush appears as a very smooth polymer film. Computer simulations and analytical works suggested the possibility of lateral instabilities in the segment density of polymer brush in poor solvent. The theoretical data were proved with experiments (Fig. 11.4(c)–(f)).

11.2.2 Bidisperse Polymer Brushes

Recently, researchers have shifted the emphasis to heterogeneous brushes composed of two different polymers, because amphiphilic materials offer more possibilities and variations for the theoretical study and fabrication of functional materials. Analysis of binary brushes composed of two polymers of the same chemical structure and different molecular weights was performed in theoretical [19–27] and experimental studies [28–36]. The theories predicted and the experiments proved the stratification of the bidisperse brushes. The bottom of the brush is composed of short and long chains forming a mixed region, while the top of the film is occupied by the long chains (Fig. 11.5). The volume fraction of the longer chains increases with increasing distance to the substrate plane until a top region purely composed of the longer chains is approached.

Fig. 11.5 Schematic illustration of the stratification in the bidisperse homopolymer brush



11.2.3 Mixed Polymer Brushes

When typical homopolymer brushes are synthesized, only one polymer material is grafted to the surface to target some specific property such as wettability, colloidal stability, adhesion, friction, biocompatibility, conductivity or adsorptivity. However, further advance in polymer films imposes requirements for the surface and interfacial modifications that frequently are in conflict: a given material, depending on the conditions under which it is utilized, has to have adhesion to different surfaces, has to be hydrophobic or hydrophilic, conductive or nonconductive, deliver or adsorb some species, etc. An effective means to build an adaptive polymer layer is fabrication of a mixed polymer brush (Fig. 11.6) by combination in one grafted layer polymers of different nature. Then, each component of the nanostructured heterogeneous layer will play its specific role and support versatile behavior of the surface. Moreover, the combination of two or more polymers in the brush acts not as a simple addition of different functions, but it affects a specific morphology of the film driven by a subtle interplay between increased numbers of interactions. Therefore, we should emphasize the difference between a brush of a random copolymer when different functions can be combined in the same polymer chain by random distribution of two or more different monomer units in the polymer molecule and binary or multi-component brushes with different homopolymers randomly grafted to the same substrate. The principle difference is introduced by structure of the film when different end-attached polymer chains can segregate into nanoscopic domains effecting a unique morphology of the film.

The properties of mixed brushes were recently theoretically analysed [37–44]. It was shown that the brush morphology is affected by the interplay between lateral and perpendicular to the substrate phase segregation governed by solvent quality.

Fig. 11.6 Mixed polymer brush

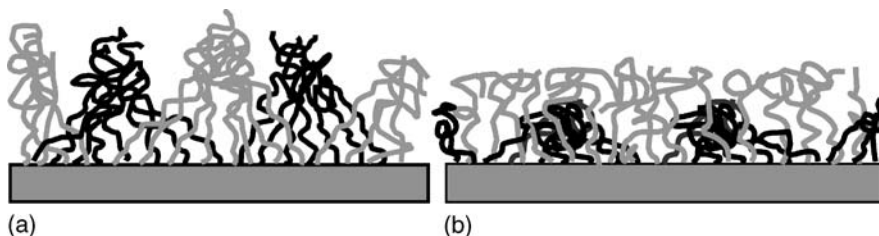


Fig. 11.7 Schematic illustration of two possible morphologies of mixed brush irreversibly grafted to solid substrate (cross-section of the layer): in a nonselective solvent (a), in a solvent poor for the black chains (b)

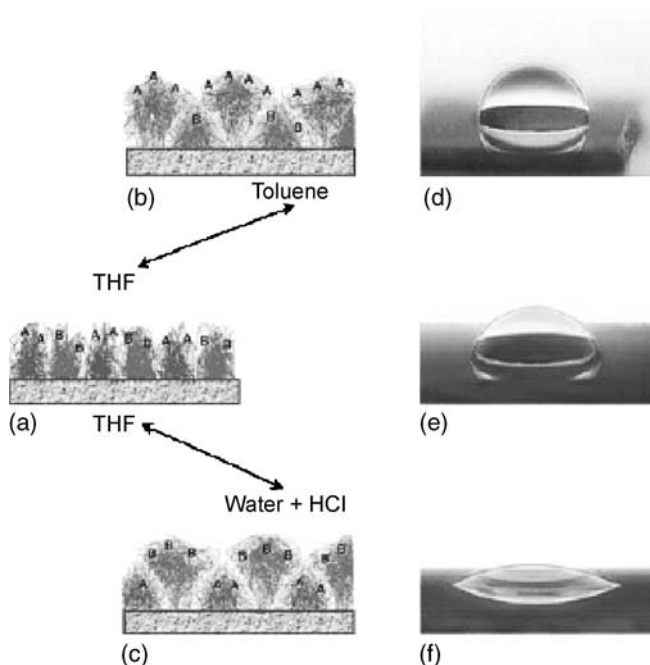


Fig. 11.8 Wetting of the heterogeneous polymer brush composed of polystyrene and poly(2-vinylpyridine) chains

The lateral segregation of the mixed brush is dominant in nonselective solvent and results in a ripple morphology (Fig. 11.7(a)), when both polymers form lamellar-like structure with parallel to the substrate orientation (lamellar of both polymers approach polymer brush–substrate and polymer brush–solvent interfaces). In this case both polymers are present on the surface and surface properties of the film are effected by the combination of functional groups of both polymers. In selective solvent the unfavorable polymer form clusters embedded in the continuous phase (dimple morphology) of the second polymer (Fig. 11.7(b)). This “dimple morphology” results in an enhanced concentration of the second polymer on the top of the layer. In other words, in addition to lateral segregation the film undergoes layered segregation. In this case the surface properties of the film are determined by polymer which occupies the top layer. Such mechanism affects the adapting and switching properties of the thin film that can change morphology and surface energetic state and functionality upon exposure to controlled environment. These brushes, composed of two (or more) distinct species of homopolymers, may change wettability and adhesion in response to variation of environment.

This concept is illustrated in Fig. 11.8. At least two different polymers A and B are grafted to a solid substrate and form a mixed polymer brush (Fig. 11.8(a)). The ratio between chain length of the polymers A and B, composition of the brush and nature of the polymer chain functional groups affect the layer properties: roughness, wettability, reactivity, adhesion to another materials, biocompatibility etc. It

is clear that interplay with above-mentioned parameters of the mixed brush allows a wide variety of diverse surface properties. Besides the mixed brush has unique capability to change properties based on a change of environment. Let us assume that initial stage (Fig. 11.8(a)) was obtained in a nonselective solvent with respect to both polymers A and B. Both polymers form laterally segregated lamellar-like structures and are exposed to the solvent phase. Then a change of environment by addition of a selective solvent (e. g. for polymer A), or change of pH (if one or both A and B are sensitive to pH) brings out selective swelling of the polymer A, and collapse of chains of the polymer B (Fig. 11.8(b)). Additionally to lateral segregation we obtain layered segregation. If we use a selective solvent for polymer B the inverse behavior of the layer is expected (Fig. 11.8(c)). Degree of coverage of the top of the brush by one of the polymers depends on composition of environment and layer structure. This can be adjusted very precisely to a desired value. Consequently, one may obtain the desired composition of the top layer with respect to A and B functional groups as a response to the composition of environment (liquid or a gas phase). Rapid evaporation of solvent freezes the film morphology and in this way the segregated phases are kinetically stabilized by the glassy state of the polymers. Nevertheless, upon exposure to other solvent or heating above glass transition temperature the morphology can be switched again. If in our case A is a hydrophilic and B is a hydrophobic polymer we may expect switching between hydrophilic and hydrophobic properties of the polymer film as it is shown in Fig. 11.8(d)–(f). It is noteworthy that different possibilities to freeze the particular morphology (for example chemical cross-linking) may be explored.

The above-mentioned switching properties of the mixed brushes have been studied experimentally using contact angle measurements, XPS, XPEEM and SPM [45–49]. The kinetics of switching was investigated with contact angle method. Switching time varies with grafting density and solvent quality from seconds to hours. Numerous morphologies of the thin films were observed with SPM investigations. Experiments prove that upon exposure to different solvents,

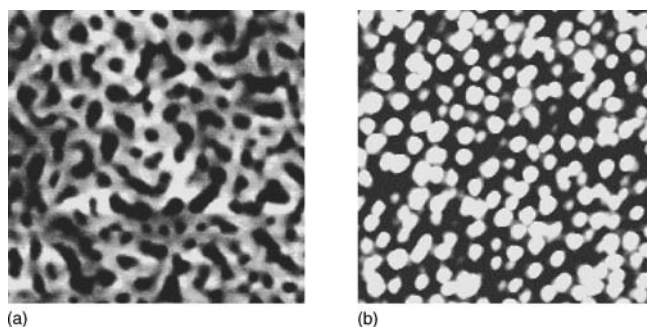


Fig. 11.9 Scanning probe microscopy images for the surface reconstruction of the mixed PS/PMMA brush upon exposure to: nonselective solvent (THF) resulting in a ripple morphology (a); selective for PMMA solvent (acetone) resulting in a dimple morphology (b). Obtained by Dr. Usov

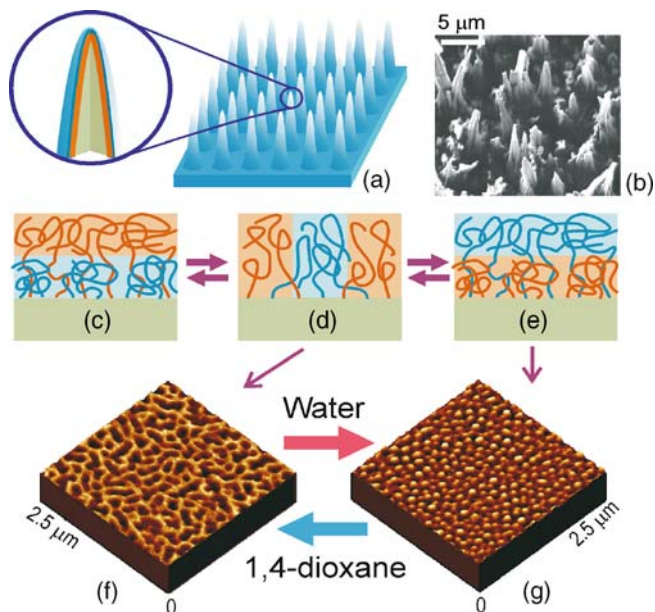


Fig. 11.10 Two-level structure of self-adaptive surfaces (SAS): Schematic representation of needle-like surface morphology of the PTFE surface (first level) (a) and SEM image of the PTFE film after 600 s of plasma etching (b). Each needle is covered by a covalently grafted mixed brush which consists of hydrophobic and hydrophilic polymers (second level) depicted schematically in panel (c-e). Its morphology results from an interplay between lateral and vertical phase segregation of the polymers which switches the morphology and surface properties upon exposure to different solvents. In selective solvents the preferred polymers preferentially occupies a top of the surface (c and e) while in non-selective solvents, both of polymers are present in the top layer (d). The lower panels (f and g) show AFM images (model smooth substrate) of the different morphologies after exposition to different solvents. Obtained by Dr. Motornov

the film morphology reversibly switches from “ripple” to “dimple” structures (Fig. 11.9) as well as the surface energetic state switches from hydrophobic to hydrophilic. For example, the mixed brush prepared from polystyrene (PS) and poly(2-vinylpyridine) (P2VP) shows switching of wettability evaluated by water contact angle from 90° (upon exposure to toluene) to 20° after acidic water.

Recently the strategy of mixed brushes was extended to polymeric substrates with controlled roughness [50]. Two-level structured surfaces were designed and fabricated for reversibly switching from hydrophilic to ultra-hydrophobic states upon external stimuli (Fig. 11.10). The first level is organized by a periodic needle-like morphology of the polymer substrate. The second level of structure is represented by the mixed brush grafted onto the needles. Such a morphology forms a composite surface which substantially amplifies the switching effect of the mixed brush allowing to switch wettability from complete wetting to ultra-hydrophobic properties (water contact angle 160°) (Fig. 11.11). These experiments demonstrate that mixed polymer brushes offer numerous possibilities to

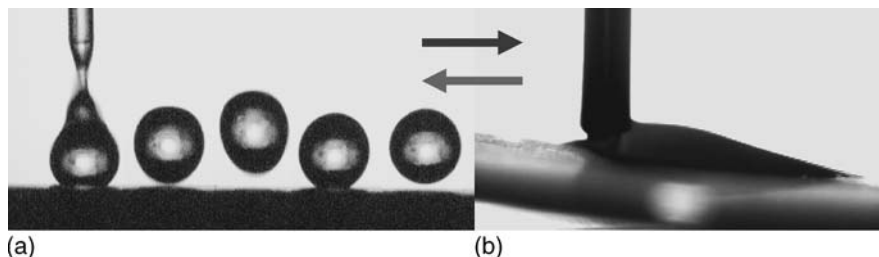


Fig. 11.11 Photograph of a water drop deposited onto the SAS: the stroboscopic image shows that a water drop jumps and rolls on the ultra-hydrophobic surface obtained after exposure of the sample to toluene (a). In contrast, exposure to acidic water switches the sample to a hydrophilic state and the water drop spreads on the substrate (b). Obtained by Dr. Motornov

explore the phenomenon of incompatibility of different polymers and their selective interaction with controlled environment.

11.2.4 Block-Copolymer Brushes

We should highlight an alternative approach to prepare switchable brush-like layers. This approach is based on grafting of block-copolymers. Zhao and Brittain and coworkers [51–55], Mattyjaszewski et al. [56] and Husseman et al. [57] synthesized tethered block copolymer brushes by cationic and “living” radical polymerization. It was shown that the synthesized films had ability to change their morphology and wettability in response to variation of environment [51–55]. Although, in block-copolymer and mixed brushes the switching of morphology (Fig. 11.12) and surface energetic state upon exposure to controlled environment is effected by similar driving forces and those brushes exhibit similar behavior we should mention the difference in structure and synthetic routes to fabricate the

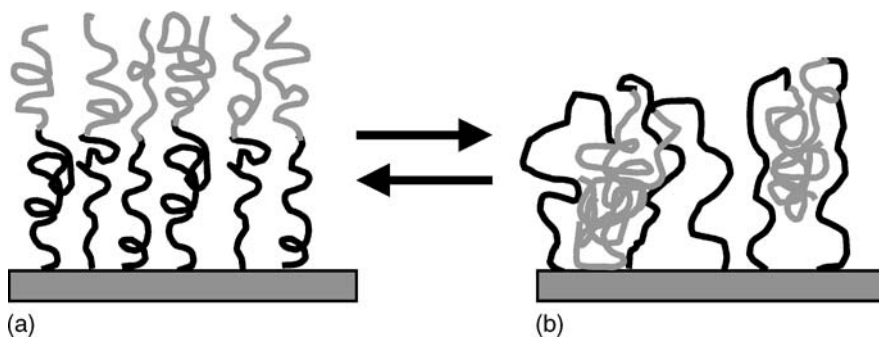


Fig. 11.12 Block-copolymer brush in nonselective solvent (a) and in solvent selective for the black chains (b)

brushes. It is important to approach further progress in the development of both methods for the fabrication of switchable polymer films.

Consequently, changing the parameters of the brush allows: (1) to tune interaction of the brush with solvent, other polymer molecules, other brushes and colloidal particles in solution; (2) to regulate morphology of the polymer film. These options have attracted great fundamental and practical interests for regulation of wettability, colloidal stability, adhesion, friction, biocompatibility, conductivity or adsorptivity, and surface patterning.

11.3 Synthesis of Polymer Brushes

The chemical grafting of polymer brushes can be accomplished by either “grafting to” and “grafting from” methods. According to “grafting to” technique, end-functionalized polymer molecules react with complementary functional groups located on the surface to form tethered chains. However, only a limited amount of the polymer can be tethered onto the substrates by the grafting to approach. The attaching polymer chains have to overcome the activation barrier, which appears as soon as the earlier attached chains begin to overlap. The “grafting from” technique utilizes the polymerization initiated from the substrate surface by attached (usually by covalent bonds) initiating groups. Molecules of a monomer penetrate through the already grafted polymer layer easily and significant grafted amounts can be reached. This technique was used for the preparation of thick grafted layers of high grafting density on the surface. Anionic [58], cationic [59, 60], controlled [61, 62] and conventional [63, 64] free radical polymerizations have been successfully used to synthesize tethered polymer layers on solid substrate surfaces. By appropriate choice of initiating system, temperature, monomer nature and concentration, it is quite possible to find conditions for synthesis of the layers possessing different morphology, thickness and composition [6]. Thus, fine-tuning of the layer properties is possible.

11.3.1 *Modification of Solid Substrate*

Grafting of polymers using “grafting to” or “grafting from” methods can be performed if the appropriate reactive groups are located onto the solid substrate. Different methods were developed to immobilize appropriate functional groups on the surface of inorganic or polymer substrates. Modification of surfaces of materials from inorganic oxides usually is based on reaction with surface hydroxyl groups. The most known approach comprises covalent grafting of σ -functional alkoxy- or chloro-silanes. For gold substrates σ -functional thiols found broad applications. Modification of polymer surfaces depends on reactivity of functional groups in polymer chains. If the direct chemical reaction between the appropriate modifier

Fig. 11.13 Modification of Si-wafer with ω -epoxy silane

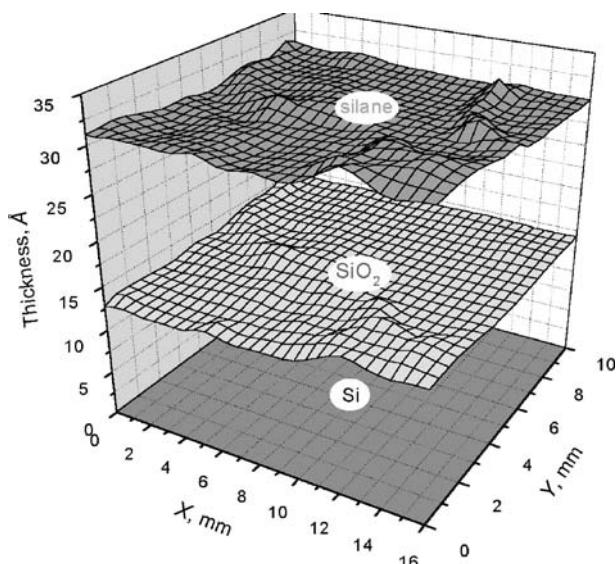
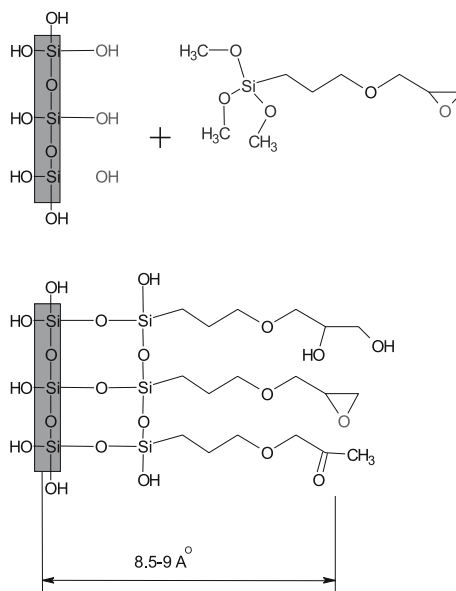
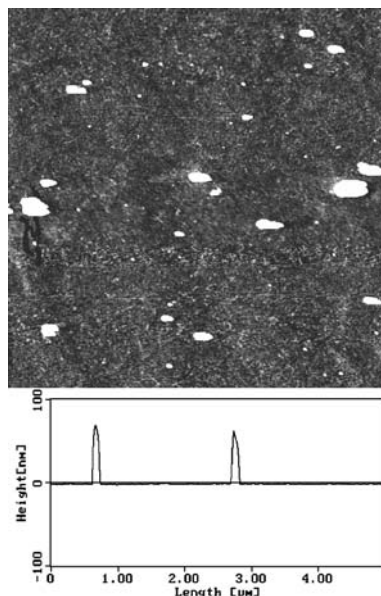


Fig. 11.14 Ellipsometric image of the native SiO₂ and covalently grafted GPS layer on the surface of Si-wafer. Obtained by Dr. Ussov

and polymeric substrate is not effective the polymer surface is activated using plasma treatment, UV- or γ -irradiation, chemical oxidation, etc to introduce reactive functional groups ($-\text{OH}$, $-\text{NH}_2$, $-\text{COOH}$, etc.) onto the polymeric substrate. Afterwards the functional groups can be involved in further chemical reactions to attach molecules of an appropriate modifier or polymer.

Fig. 11.15 AFM-image and cross-section of GPS layer. Obtained by Dr. Usov



As an example we consider surface modification of a Si-wafer with 3-glycid-oxypolytrimethoxysilane (GPS) (Fig. 11.13). The Si-wafer is covered with a native SiO_2 layer (usually 1.5 nm thick) with a high density of $-\text{OH}$ groups on the surface. Those $-\text{OH}$ groups are used for chemical grafting of alkoxy silane molecules. GPS is hydrolyzed by traces of water dissolved in toluene and reacts with surface hydroxyl groups as it is shown in Fig. 11.13.

The GPS layer thickness determined with ellipsometry and morphology of the layer studied with AFM are presented in Figs. 11.14 and 11.15, respectively. Although, the GPS layer thickness is consistent with a monolayer of the silane molecules the AFM image demonstrates formation of small clusters which originate from precipitation of poly-GPS particles due to the side reaction of GPS polymerization in solution. IR and XPS spectra provide evidence for the fraction of hydrolyzed or even oxidized epoxy-functional groups of GPS. Those side reaction is very typical for surface modification with functional silanes. The resulting layer with functional groups can be used for the next steps of grafting of polymers.

11.3.2 “Grafting to” Method

Grafting of the end-functional polymer via chemical reaction of the end-functional group with the functional groups on the modified substrate can be performed in solution of the polymer or from the polymer melt. As an example we consider grafting of carboxyl terminated polystyrene PS-COOH to the Si wafer modified with GPS. PS-COOH was dissolved in toluene to prepare 1 % solution. The thin

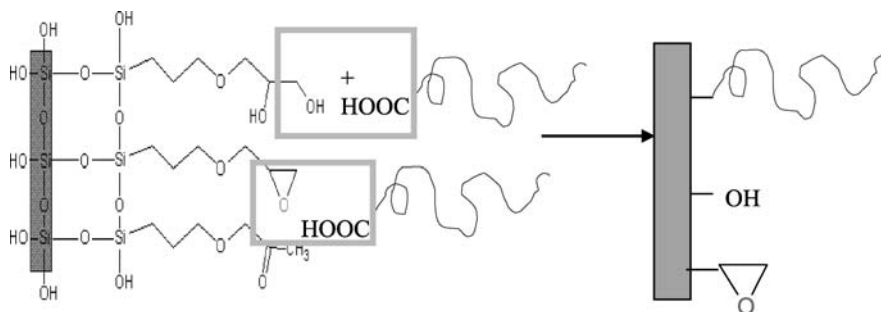


Fig. 11.16 Scheme of grafting of carboxyl-terminated polystyrene to the Si wafer modified with GPS

polymer film (50 nm) of PS–COOH was spin coated on the surface of the Si wafer and heated in a vacuum oven at 150°C for several hours. Heating above the glass transition temperature enhance mobility of PS segments and in this way accelerates the diffusion limited reaction of grafting. At this temperature end carboxyl groups react with epoxy or hydroxyl functional groups on the surface resulting in chemical grafting of the polymer via ester groups (Fig. 11.16).

11.3.3 “Grafting from” Method

This approach refers to the method of synthesis of a covalently attached polymer in situ on the solid substrate. Almost all known mechanisms for polymer synthesis can be employed for “grafting from” approach. The same first step of substrate surface modification (as in the case of “grafting to” method) is usually required to introduce initiator of polymerization onto the solid surface. Appropriate initiator is covalently attached to the surface depending on polymerization mechanism selected for grafting. For conventional radical polymerization either azo-initiators, peroxide- or photo- initiators are attached to the solid substrate. Peroxide initiators can be synthesized directly on the polymeric substrates using plasma, UV irradiation or ozone treatment of the surface. In the same manner applying external field or reactive species a solid substrate can be prepared for different polymerization mechanism: polycondensation, carbocationic, anionic, ring-opening metathesis polymerization. The most attempts reported in literature were done with conventional and controlled radical polymerization methods. Here we consider some examples of conventional radical polymerization for synthesis of mixed polymer brushes and controlled radical polymerization for synthesis of homopolymer and block-copolymer brushes. Those both directions seem to be most promising for development of new functional and responsive materials.

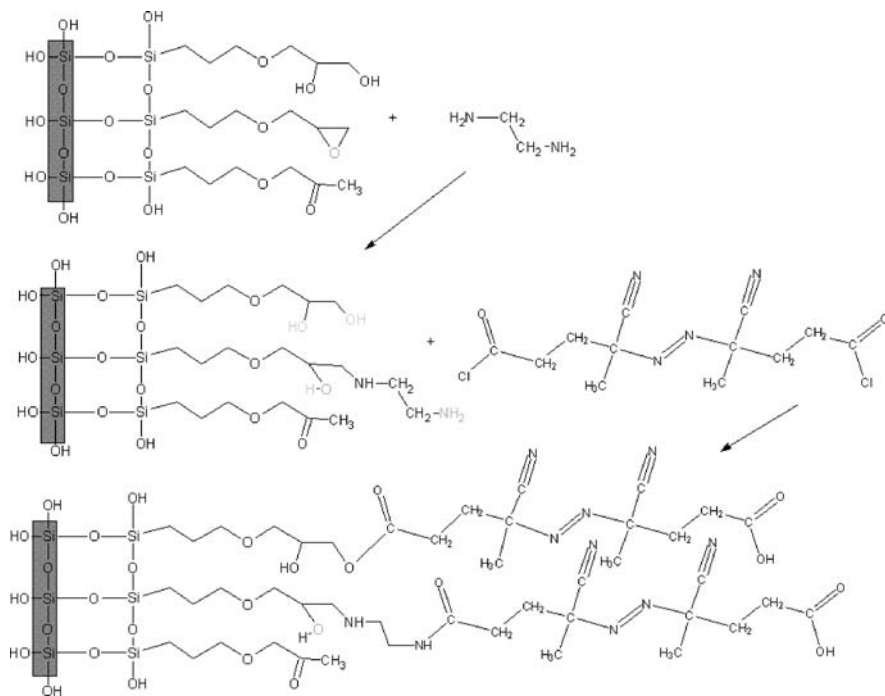


Fig. 11.17 Grafting of azo-initiator to the surface of Si wafer modified with GPS

11.3.4 Synthesis of Mixed Brushes

It is necessary to highlight that little experimental work has been done on synthesis and characterization of the mixed polymer brushes. Actually few articles on the topic are available [44–49].

The method of binary brush synthesis utilizing “grafting from” approach was recently reported in literature [45]. The procedure includes the introduction of the azo-initiator onto a Si wafer (Fig. 11.17). In the next step the grafting of styrene is initiated from the solid substrate by the chemisorbed azo-initiator (Fig. 11.18). The PS layer growth is detected by in situ ellipsometric measurements. In the third step the styrene solution is exchanged for 2-vinylpyridine solution and P2VP is grafted under similar conditions using the residual initiator and the still free places remaining in the first grafted layer. The ratio between grafted PS and P2VP is varied by a change of the duration of the grafting reaction of the respective monomer. In this way mixed polymer brushes of thickness 10–100 nm consisting of two different polymers polystyrene and poly(2-vinylpyridine) of the same molecular weight (2.5×10^5 g/mol) were synthesized. The composition of the top layer in different media is controlled by the composition and molecular weight of the two polymers in the coating.

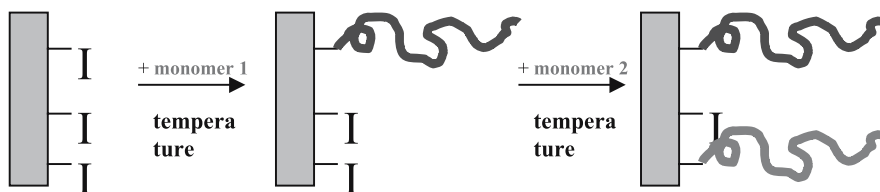


Fig. 11.18 Two-step grafting procedure for synthesis of binary mixed brush

11.3.5 Controlled Synthesis of Polymer Brushes by “Living” Free Radical Polymerization

The disadvantages of the conventional radical polymerization comprise such difficulties as molecular weight control and high polydispersity of polymer chains being formed. These typical reasons are also supplemented with some specific problems connected to the synthesis of polymer initiated from the surface. Namely, high concentration of active radicals and rapidly growing polymer chains in the confined interfacial region provoke cross-linking reactions, chain transfer to already grafted polymer and autoacceleration of the grafting due to Trommsdorff effect resulting in heterogeneous grafting [63, 65]. It is necessary to point out that another radical based polymerization technique, namely controlled/“living” free radical polymerizations, has a number of advantages over traditional free radical procedures [55, 57, 62]. The main advantages that a “living” process provides for the synthesis are reliable control over the polymer molecular weight and narrow polydispersities. Thus, the nature of the polymerization process permits structural characteristics of the grafted polymer brush to be readily varied and controlled. An added benefit is the frontal character of the chain growth on the surface. In this manner all chains have very close history that may be translated in more predictable cooperative behavior of the chains and make the brush nearly “defect free”. Numerous effective approaches are reported for synthesis of homogeneous polymer brushes by “living” free radical polymerization [66–88].

Husseman et al. [61, 89] have demonstrated that initiator functionalized surfaces, suitable for both alkoxyamine and atom transfer radical polymerization (ATRP) living free radicals procedures, can be readily prepared. They are stable to prolonged storage, and can be used for the controlled synthesis of polymeric brushes. The use of “living” free radical chemistry permitted the accurate control of molecular weight or thickness of the brush while maintaining low polydispersity. It was noted that different functional monomers could be polymerized utilizing the same synthetic approach to the brush synthesis.

Matyjaszewski et al. [62] reported about ATRP of styrene and acrylates from silicon wafer modified with an initiator layer composed of 2-bromoisobutyrate fragments. In the presence of the proper ratio of activating and deactivating transition metal species, controlled radical polymerizations of styrene were observed

when the thickness of the layer constituting of chains grown from surface increased linearly with the molecular weight of the chains obtained in solution in identical experiment.

Boyes et al. [55] successfully synthesized and characterized a tethered triblock copolymer by sequential monomer addition to a self-assembled monolayer of (11-(2-bromo-2-methyl)propynyl)oxy) undecyltrichlorosilane. The block copolymer brushes were prepared using ATRP. Upon treatment with different solvents, the tethered triblock copolymer brushes exhibited reversible changes in surface properties.

De Boer et al. [90] developed a method for chemically modifying a surface with a grafted iniferter monolayer, which can be used for a “living” free radical photopolymerization. By using process developed, it was possible to control the length of the grafted polymer chains and therefore the layer thickness up to approx. 100 nm. Also, single layer grafted block copolymers were obtained by subsequent polymerization of styrene and methyl methacrylate monomers.

Tsujii et al. [91] studied mechanism and kinetics of reversible addition fragmentation chain transfer technique (RAFT) initiated from solid surface. It was proved that RAFT could be also used for the synthesis of polymer brushes. RAFT has been successfully applied to synthesize various polymer brushes by Baum and Brittain [92]. Styrene, methyl methacrylate, and *N,N* dimethylacrylamide brushes were prepared under RAFT conditions using silicate surfaces that were modified with surface-immobilized initiators.

References

1. Wool RP (1995) Polymer interfaces: structure and strength. Hunser/Gardner, New York
2. Koberstein JT (ed) (1996) Polymer surfaces and interfaces. MRS Bull Jan:16
3. Israelachvili J (1992) Intermolecular and surface forces. Academic, New York
4. Ratner B (1993) New ideas in biomaterials science – a path to engineered biomaterials. J Biomed Mater Res 27:837
5. Napper DH (1983) Polymeric stabilization of colloidal dispersions. Academic, London
6. Zhao B, Brittain WJ (2000) Polymer brushes: surface-immobilized macromolecules. Prog Polym Sci 25:677
7. Halperin A, Tirrell M, Lodge TP (1992) Adv Polym Sci 100:31–71
8. Uyama Y, Kato K, Ikada Y (1998) Surface modification of polymers by grafting. Adv Polym Sci 137:1
9. Alexander SJ (1977) J Phys (Paris) 38:983–987
10. de Gennes P-J (1976) J Phys (Paris) 37:1443
11. de Gennes P-J (1980) Macromolecules 13:1069
12. Cantor R (1981) Macromolecules 14:1186
13. Grest GS, Murat M (1993) Macromolecules 26:3108
14. Zhulina EB, Borisov OV, Priamitsyn VA (1990) J Colloid Interface Sci 137:495
15. Grest GS, Murat M (1993) Macromolecules 26:3108
16. Milner ST, Witten TA, Cates ME (1988) Macromolecules 21:2610
17. Likhtman AE, Anastasiadis SH, Semenov AN (1999) Theory of surface deformations of polymer brushes in solution. Macromolecules 32:3474
18. Sidel K, Netz RR (2000) Macromolecules 33:634

19. Yeung C, Balazs AC, Jasnow D (1993) *Macromolecules* 26:1914
20. Milner ST, Witten TA, Cates M (1989) *Macromolecules* 22:853
21. Birstein TM, Liatskaya YV, Zhulina EB (1990) *Polymer* 31:2185
22. Chakrabarti A, Toral R (1990) *Macromolecules* 23:2016
23. Dan T, Tirrell M (1993) *Macromolecules* 26:6467
24. Lai PY, Zhulina EB (1992) *Macromolecules* 25:5201
25. Spontak RJ (1994) *Macromolecules* 27:6363
26. Skvortsov AM, Klushin LI, Gorbunov AA (1997) *Macromolecules* 30:1818–1827
27. Borovinskii AL, Khohlov AB (1998) *Macromolecules* 31:1180
28. Klein J, Kamiyama Y, Yoshizawa H, Israelachvili JN, Fetters LJ, Pincus P (1992) *Macromolecules* 25:2062
29. Kumacheva E, Kölein J, Pincus P, Fetters LJ (1993) *Macromolecules* 26:6477
30. Dhoot S, Watanabe H, Tirrell M (1994) *Colloid Surf* 86:47
31. Dhoot S, Tirrell M (1995) *Macromolecules* 28:3692
32. Gao Z, Ou-Yang HD (1993) *ACS Symp Ser* 532:70
33. Mayes AM, Russell TP, Deline VR, Satija SK, Majkrzak CF (1994) *Macromolecules* 27:7447
34. Kent MS, Factor BJ, Satija S, Gallagher P, Smith GS (1996) *Macromolecules* 29:2843–2849
35. Levicky R, Koneripylli N, Tirrell M, Satija SK (1998) *Macromolecules* 31:2616
36. Goedel WA, Luap C, Oeser R, Lang P, Braun C, Steitz R (1999) *Macromolecules* 32:7599–7609
37. Marko JF, Witten TA (1991) *Phys Rev Lett* 66:1541
38. Lai P-Y, Binder KJ (1992) *Chem Phys* 97:586
39. Lai P-Y (1994) *J Chem Phys* 100:3351–3357
40. Brown G, Chakrabarti A, Marko JF (1994) *Europhys Lett* 25:239–244
41. Soga KG, Zuckermann MJ, Guo H (1996) *Macromolecules* 29:1998–2005
42. Zhulina E, Balazs AC (1996) *Macromolecules* 29:2667–2673
43. Müller M (2002) *Phys Rev E* 65:030802(R)
44. Minko S, Müller M, Usov D, Scholl A, Froeck C, Stamm M (2002) *Phys Rev Lett* 88:035502
45. Sidorenko A, Minko S, Schenk-Meuser K, Duschner H, Stamm M (1999) Switching of polymer brushes. *Langmuir* 15:8349
46. Minko S, Usov D, Goreshnik E, Stamm M (2001) *Macromol Rapid Commun* 22:206
47. Minko S, Patil S, Datsyuk V, Simon F, Eichhorn K-J, Motornov M, Usov D, Tokarev I, Stamm M (2002) Synthesis of adaptive polymer brushes via “grafting to” approach from melt. *Langmuir* 18:289
48. Minko S, Luzinov I, Patil S, Datsyuk V, Stamm M (2001) Tuning morphology and surface properties of smart polymer coatings from mixed polymer brushes. *ACS Proc PMSE Div* 85:314
49. Draper J, Luzinov I, Tokarev I, Minko S, Stamm M (2002) Morphology and wettability of hybrid polymer brushes. *ACS Proc PMSE Div* 87:187
50. Motornov M, Minko S, Nitscke M, Grundke K, Stamm M (2002) Hierarchically structured self-adaptive surfaces. *Polymer Preprints* 43(2):379
51. Zhao B, Brittain WJ (1999) Synthesis of tethered polystyrene-block-poly(methyl methacrylate) monolayer on a silicate substrate by sequential carbocationic polymerization and atom transfer radical polymerization. *J Am Chem Soc* 121(14):3557
52. Sedjo RA, Mirous BK, Brittain WJ (2000) Synthesis of polystyrene-block-poly(methyl methacrylate) brushes by reverse atom transfer radical polymerization. *Macromolecules* 33(5):1492–1493
53. Zhao B, Brittain WJ (2000) Synthesis, characterization, and properties of tethered polystyrene-b-polyacrylate brushes on flat silicate substrates. *Macromolecules* 33(23):8813
54. Zhao B, Brittain WJ, Zhou W, Cheng SZD (2000) AFM study of tethered polystyrene-b-poly(methyl methacrylate) and polystyrene-b-poly(methyl acrylate) brushes on flat silicate substrates. *Macromolecules* 33:8821

55. Boyes SG, Brittain WJ, Weng X, Cheng SZD (2002) Synthesis, characterization, and properties of ABA type triblock copolymer brushes of styrene and methyl acrylate prepared by atom transfer radical polymerization. *Macromolecules* 35(13):4960
56. Matyjaszewski K, Miller PJ, Shukla N, Immaraporn B, Gelman A, Luokala BB, Siclován TM, Kickelbick G, Vallant T, Hoffmann H, Pakula T (1999) Polymers at interfaces: using atom transfer radical polymerization in the controlled growth of homopolymers and block copolymers from silicon surfaces in the absence of untethered sacrificial initiator. *Macromolecules* 32(26):8716
57. Husseman M, Malmstrom EE, McNamara M, Mate M, Mecerreyes D, Benoit DG, Hedrick JL, Mansky P, Huang E, Russell TP, Hawker CJ (1999) Controlled synthesis of polymer brushes by "living" free radical polymerization techniques. *Macromolecules* 32(5):1424
58. Jordan R, Ulman A, Kang JF, Rafailovich MH, Sokolov J (1999) Surface-initiated anionic polymerization of styrene by means of self-assembled monolayers. *J Am Chem Soc* 121:1016
59. Zhao B, Brittain WJ (2000) Synthesis of polystyrene brushes on silicate substrates via carbocationic polymerization from self-assembled monolayers. *Macromolecules* 33:342
60. Jordan R, West N, Ulman A, Chou Y-M, Nuyken O (2001) Nanocomposites by surface-initiated living cationic polymerization of 2-oxazolines on functionalized gold nanoparticles. *Macromolecules* 34:1606
61. Husseman M, Malmstrom EE, McNamara M, Mate M, Mecerreyes D, Benoit DG, Hedrick JL, Mansky P, Huang E, Russell TP, Hawker CJ (1999) Controlled synthesis of polymer brushes by "living" free radical polymerization techniques. *Macromolecules* 32:1424
62. Matyjaszewski K, Miller PJ, Shukla N, Immaraporn B, Gelman A, Luokala BB, Siclován TM, Kickelbick G, Vallant T, Hoffmann H, Pakula T (1999) Polymers at Interfaces: Using atom transfer radical polymerization in the controlled growth of homopolymers and block copolymers from silicon surfaces in the absence of untethered sacrificial initiator. *Macromolecules* 32:8716
63. Luzinov I, Minko S, Senkovsky V, Voronov A, Hild S, Marti O, Wilke W (1998) Synthesis and behavior of the polymer covering on a solid surface: 3. Morphology and mechanism of formation of grafted polystyrene layers on the glass surface. *Macromolecules* 31:3945
64. Prucker O, Ruhe J (1998) Polymer layers through self-assembled monolayers of initiators. *Langmuir* 14:6893
65. Luzinov I, Voronov A, Minko S, Kraus R, Wilke W, Zhuk A (1996) Encapsulation of fillers with grafted polymers for model composites. *J Appl Polym Sci* 61:1101
66. Kim J-B, Bruening ML, Baker GL (2000) Surface-initiated atom transfer radical polymerization on gold at ambient temperature. *J Am Chem Soc* 122:7616
67. Shah RR, Mecerreyes D, Husemann M, Rees I, Abbott NL, Hawker CJ, Hedrick JL (2000) Using atom transfer radical polymerization to amplify monolayers of initiators patterned by microcontact printing into polymer brushes for pattern transfer. *Macromolecules* 33:597
68. Ejaz M, Yamamoto S, Tsujii Y, Fukuda T (2002) Fabrication of patterned high-density polymer graft surfaces. I. Amplification of phase-separated morphology of organosilane blend monolayer by surface-initiated atom transfer radical polymerization. *Macromolecules* 35:1412
69. Ejaz M, Yamamoto S, Ohno K, Tsujii Y, Fukuda T (1998) Controlled graft polymerization of methyl methacrylate on silicon substrate by the combined use of the Langmuir-Blodgett and atom transfer radical polymerization techniques. *Macromolecules* 31:5934
70. Ejaz M, Tsujii Y, Fukuda T (2001) Controlled grafting of a well-defined polymer on a porous glass filter by surface-initiated atom transfer radical polymerization. *Polymer* 42:6811
71. Tsujii Y, Ejaz M, Yamamoto S, Fukuda T, Shigeto K, Mibu K, Shinjo T (2002) Fabrication of patterned high-density polymer graft surfaces. II. Amplification of EB-patterned initiator monolayer by surface-initiated atom transfer radical polymerization. *Polymer* 43:3837
72. Yamamoto S, Ejaz M, Tsujii Y, Fukuda T (2000) Surface interaction forces of well-defined, high-density polymer brushes studied by atomic force microscopy. 2. Effect of graft density. *Macromolecules* 33:5608

73. Meyer U, Svec F, Frechet JMJ, Hawker CJ, Irgum K (2000) Use of stable free radicals for the sequential preparation and surface grafting of functionalized macroporous monoliths. *Macromolecules* 33:7769
74. Ejaz M, Ohno K, Tsujii Y, Fukuda T (2000) Controlled grafting of a well-defined glycopolymer on a solid surface by surface-initiated atom transfer radical polymerization. *Macromolecules* 33:2870
75. Jones DM, Huck WTS (2001) Controlled surface-initiated polymerizations in aqueous media. *Adv Mater* 13(16):1256
76. Xiao D, Wirth MJ (2002) Kinetics of surface-initiated atom transfer radical polymerization of acrylamide on silica. *Macromolecules* 35:2919
77. Jayachandran KN, Takacs-Cox A, Brooks DE (2002) Synthesis and characterization of polymer brushes of poly(N,N-dimethylacrylamide) from polystyrene latex by aqueous atom transfer radical polymerization. *Macromolecules* 35(11):4247–4257
78. Luo N, Hutchison JB, Anseth KS, Bowman CN (2002) Surface-initiated photopolymerization of poly(ethylene glycol) methyl ether methacrylate on a diethylthiocarbamate-mediated polymer substrate. *Macromolecules* 35:2487
79. Mori H, Boker A, Krausch G, Muller AHE (2001) Surface-grafted hyperbranched polymers via self-condensing atom transfer radical polymerization from silicon surfaces. *Macromolecules* 34:6871
80. Jones DM, Brown AA, Huck WTS (2002) Surface-initiated polymerizations in aqueous media: effect of initiator density. *Langmuir* 18:1265
81. Robinson KL, de Paz-Banez MV, Wang XS, Armes SP (2001) Synthesis of well-defined, semibranched, hydrophilic-hydrophobic block copolymers using atom transfer radical polymerization. *Macromolecules* 34:5799
82. Perruchot C, Khan MA, Kamitsi A, Armes SP, von Werne T, Patten TE (2001) Synthesis of well-defined, polymer-grafted silica particles by aqueous ATRP. *Langmuir* 17:4479
83. Cheng G, Boker A, Zhang M, Krausch G, Muller AHE (2001) Amphiphilic cylindrical core-shell brushes via a “grafting from” process using ATRP. *Macromolecules* 34:6883
84. Huang W, Kim J-B, Bruening ML, Baker GL (2002) Functionalization of surfaces by water-accelerated atom-transfer radical polymerization of hydroxyethyl methacrylate and subsequent derivatization. *Macromolecules* 35:1175
85. Kong X, Kawai T, Abe J, Iyoda T (2001) Amphiphilic polymer brushes grown from the silicon surface by atom transfer radical polymerization. *Macromolecules* 34:1837
86. Carrot G, Diamanti S, Manuszak M, Charleux B, Vairon J-P (2001) Atom transfer radical polymerization of n-butyl acrylate from silica nanoparticles. *J Polym Sci Part A Polym Chem* 39:4294
87. Böttcher H, Hallensleben ML, Nuß S, Wurm H (2000) ATRP grafting from silica surface to create first and second generation of grafts. *Polym Bull* 44:223
88. Min K, Hu J, Wang C, Elaissari A (2002) Surface modification of polystyrene latex particles via atom transfer radical polymerization. *J Polym Sci Part A Polym Chem* 40:892
89. Hussemann M, Morrison M, Benoit D, Frommer J, Mate CM, Hinsberg WD, Hedrick JL, Hawker CJ (2000) Manipulation of surface properties by patterning of covalently bound polymer brushes. *J Am Chem Soc* 122:1844
90. de Boer B, Simon HK, Werts MPL, van der Vegte EW, Hadziioannou G (2000) “Living” free radical photopolymerization initiated from surface-grafted iniferter monolayers. *Macromolecules* 33(2):349–356
91. Tsujii Y, Ejaz M, Sato K, Goto A, Fukuda T (2001) Mechanism and kinetics of RAFT-mediated graft polymerization of styrene on a solid surface. 1. Experimental evidence of surface radical migration. *Macromolecules* 34(26):8872
92. Baum M, Brittain WJ (2002) Synthesis of polymer brushes on silicate substrates via reversible addition fragmentation chain transfer technique. *Macromolecules* 35(3):610

Chapter 12

Surface Modification by Adsorption of Polymers and Surfactants

Cornelia Bellmann

Leibniz Institute of Polymer Research Dresden, Hohe Str. 6, 01069 Dresden, Germany,
bellmann@ipfdd.de

Abstract The adsorption of surface-active molecules at a solid/liquid interface provides a versatile tool for modification and structuring of polymer surfaces. In particular, other polymers, ions or charged or uncharged tensides may be used for the adsorption process. The adsorption process itself and the formation of structured or homogeneous thin layers are discussed in detail. In some cases adsorbed molecules are used as coupling agents for adhesion promotion with a polymer matrix.

12.1 Introduction

The modern and also reasonable way to get new polymer materials with special properties is the modification of commercial polymers. In many cases multiphase systems will be developed for new properties like higher strength, lower density, and so on. Other systems need changes of the surface properties to open up new operating ranges such as biocompatibility, hydrophilicity, hydrophobicity, adhesion characteristics, corrosion and friction properties, etc. On the other hand, polymer and surfactant layers, respectively, extend the operating field of this class of materials at inorganic surfaces.

Both the control of interaction forces in multiphase systems and the control of surface properties need modification steps on solid surfaces. Normal physical and chemical treatments are possible. The adsorption of surface-active molecules at a solid/liquid interface is a neat possibility for modification and structuring of surfaces and compared with other treatments the apparatus involved is very simple and the scope for modifications is very high.

The adsorption of soluble polymers or surfactants at solid/liquid interfaces is a highly complex phenomenon with a vast number of possible configurations of the molecules at the surface. Previous analyses of polymer and surfactant adsorption have ranged in sophistication from very simple applications of standard models

derived for small molecules, to detailed statistical-mechanical treatments of the process. The effect of the adsorption processes, shown by the resulting surface properties (stability, chemical and physical properties), strongly depends on the adsorption mechanism described by adsorption isotherms and the nature of the effective interaction forces.

The use of the simplest models, such as the Langmuir isotherm, neglects variations in molecular configuration and assumes, in effect that there is a single, “average” configuration of a molecule at the surface. In particular, the configuration is considered to be independent of the extent of coverage of the surface: a single molecule on an otherwise bare surface occupies the same area as an individual molecule on a surface saturated with polymers.

New complicated models are developed to explain adsorption processes of such molecules. But, nevertheless, in industrial applications simple models are in demand to control adsorption.

Of course there is a big difference in the two species of molecules we want to study: polymer chains with a statistical distribution of charges or surfactants, smaller molecules with a hydrophobic and a hydrophilic part and also complexes of these two species.

This chapter on adsorption processes of soluble polymers and surfactants does not lay claim to completeness. It should be seen as an introduction to this subject. At the end of the chapter the reader can find a compilation of special literature for deeper understanding.

12.2 Fundamentals

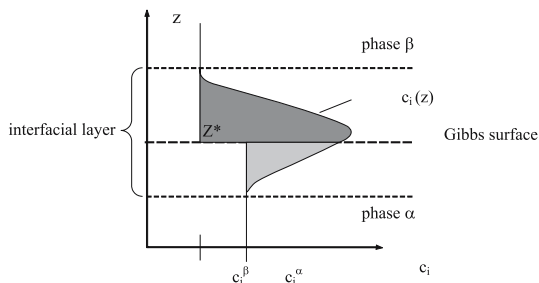
The change in concentration of a given substance i at the interface as compared with the neighbouring phase is referred to adsorption [1]. Depending on the type of phases in contact, we can consider these processes in the following systems: liquid–gas, liquid–liquid, solid–liquid and solid–gas. In this treatise we confine discussion to solid–liquid systems. Parfitt and Rochester [2], and Ottawil et al. [3] gave overviews of adsorption processes on solid/liquid interfaces.

It is not possible to determine the concentration of substance i at the interface layer experimentally. Hence, for quantitative determination of the adsorbed amount different reference systems were developed. The most used concept is the Gibbs concept. It deals with an introduced interfacial excess quantity n_i^σ [4] (see Fig. 12.1).

$$n_i^\sigma = n_i(\text{real}) - n_i(\text{reference}) = n_i - (c_i^\alpha V^\alpha + c_i^\beta V^\beta) \quad (12.1)$$

where $n_i(\text{real})$ is the real amount of substance in the system and $n_i(\text{reference}) = (c_i^\alpha V^\alpha + c_i^\beta V^\beta)$ is the imaginary amount of the reference system, characterized by the Gibbs dividing surface.

Fig. 12.1 Definition of the interfacial excess quantity n_i^σ in terms of a Gibbs dividing surface in the level of $z=Z^*$ [14]



From the thermodynamic point of view adsorption is going on if the free enthalpy G of the system decreases by adsorption. The change of the free enthalpy ΔG is given by the change of the enthalpy ΔH and the entropy ΔS [5].

$$\Delta G = \Delta H - T\Delta S \quad (12.2)$$

Corresponding to existing interaction forces, the free enthalpy of adsorption can be divided in two components, the electrostatic (ΔG_{elec}) and nonelectrostatic interactions (ΔG_{spec}) [6]. The nature of these interaction forces controls the properties of the adsorbed layer and with it the character of the modified surfaces.

The driving forces of adsorption processes are discussed generally by Israelachvili [7], Lyklema [8], Rouquerol and co-workers [9], Bruch and co-workers [10]. Especially for surfactants Rosen [11] described surfactant-specific interactions.

The adsorption mechanism by Rosen, especially in the case of surfactants is:

- Ion Exchange: replacement of counter ions of the double layer by similar charged surfactant ions
- Ion Pairing: Adsorption of surfactant ions by electrostatic interactions to counter ions
- Acid–Basic Interaction: Via either hydrogen-bond formation between substrate and adsorbate
- Adsorption by polarization of π -electrons: Interactions between aromatic molecule groups and positive charges at the adsorbent
- Adsorption by disperse forces
- Hydrophobic Bonding: attractive interactions between hydrophobic groups of the surfactant molecules and the solvent molecules near the interface/entropy effect

Israelachvili [7] completed the list given in Table 12.1 by some common interaction forces and some information about the expected energy of these interactions. The differences of interaction-energy-induced competitive adsorption processes are noted in many systems.

Table 12.1 Molecule–molecule interaction forces by Israelachvili [7]

Interaction parameter	Interaction energy (kJ/mol)
Covalent or chemical bonding forces	200–800
Charge–charge	600–1000
Interactions between polar molecules	< 40
Dispersion forces	~ 1
Hydrogen bonding	10–40
Hydrophobic interactions	< 20
Hydrophilic interactions	

Depending on the nature of these interactions we distinguish between chemisorption and physisorption. In the literature we found many different descriptions of these two kinds of adsorption and intermediate cases. In general, adsorption in which forces involved are valence forces of the same kind as those operating in the formation of chemical compounds is called chemisorption, and adsorption in which the forces do not involve a significant change in the electronic orbital patterns of the species involved is called physisorption. The term ‘van der Waals adsorption’ is synonymous with physical adsorption, but its use is not recommended [12].

In consideration of the kind of bonding chemisorption processes in general are not reversible, interactions are mostly specific, the temperature coefficient is positive, and the adsorption enthalpy $\Delta H > 80$ kJ/mol, whereas physisorption processes are reversible with non-specific interactions, a negative temperature coefficient, and an adsorption enthalpy $\Delta H < 80$ kJ/mol [13].

The adsorption process of solutions should be considered as an equilibrium process. Hence, one quantitative description of adsorption of solved molecules onto solid surfaces is given by adsorption isotherms. In this, the coverage rate Θ will be described as a function of adsorption enthalpy ΔG_{ads}^0 , the concentration of the solved substance c_i , as well as characteristic values for the interaction forces between the adsorbent molecules, e.g. β as the adsorption coefficient. The coverage rate Θ for both monolayer and multilayer adsorption is defined as the ratio of the amount of adsorbent substance to the monolayer capacity. In combination with the Gibbs concept of interfacial excess quantity the Stern-Graham equation [14] describes the general correlation of Θ and ΔG_{ads}^0 :

$$\Gamma_s = 2rc_i^{\frac{1}{2}} \exp\left(-\frac{\Delta G_{\text{ads}}^0}{RT}\right) = f(\Theta) \quad (12.3)$$

with Γ_s = specific interfacial excess quantity and r = radius adsorbate.

In the past, a multiplicity of adsorption isotherms are derived. Jacobasch summarized the most used isotherms in [15], which describe the adsorption of solved substances at solid surfaces.

A variety of shapes of adsorption isotherm have been reported. They were classified by Giles et al. [16], and later a theoretical basis was given to the classification adopted [17].

The L (Langmuir) class is the most common and can be described by the Langmuir equation. Interactions between adsorbate molecules are negligible.

The application of the classic Langmuir isotherm (L/2) is accurate under these circumstances only:

1. In the case of low concentration the adsorption is indirectly proportion to the concentration of the adsorptive. This means that in this range the Henry law is realized.
2. In the case of high concentration the adsorption is independent of the concentration, the maximum coverage is reached.
3. In the range of medium concentration $1/n^a$ vs. $1/c^1$ is a linear function.

Deviations from this isotherm will happen if the interaction forces between adsorbent and adsorbate are strong like:

- electrostatic interactions (criterion 1 is not realized) – these forces dominate in the case of surfactants and polyelectrolytes,
- non-ideal behaviour of the adsorbate, for example multilayer adsorption (criterion 2 is not realized),
- during measuring, conditions of equilibrium are not achieved.

Normally, we can say: the Langmuir law is only applicable in the case of physisorption and especially in the case of van der Waals interactions. A special variant of the L class is the H class with very high affinity of adsorptive to adsorbance.

The H class represents high interaction forces between adsorbate molecules. In this case we speak about cooperative adsorption describable by the Frumkin equation [15], (Table 12.2) for instance.

In the case of penetration of adsorbate molecules in the surface region of the solid, isotherms of the C class can be observed.

Table 12.2 Isotherms to describe the adsorption of solved substances at solid surfaces [15]

Isotherm	Equation	
General formula	$a \cdot \beta = a \cdot \exp(-\Delta G_{\text{ads}}^0 / RT) = f(\theta)$	(12.4)
Henry	$a \cdot \beta = \theta$	(12.5)
Freundlich	$a \cdot \beta = \theta^{-n}$	(12.6)
Langmuir	$a \cdot \beta = \frac{\theta}{1-\theta}$	(12.7)
Viral	$a \cdot \beta = \theta \exp[-2a\theta]$	(12.8)
Frumkin	$a \cdot \beta = \theta(1-\theta)^{-1} \exp(-2a\theta)$	(12.9)
Damaskin	$a \cdot \beta = \theta(1-\theta)^{-n} \exp(-2a\theta)$	(12.10)
Volmer	$a \cdot \beta = \theta(1-2\theta)^{-1} \exp[2\theta(1-2\theta)^{-1}]$	(12.11)

(a = activity of the dissolved adsorptive, β = adsorption coefficient, n = constant)

In the case of long-chain molecules like polymers of effects from the adsorbed molecules must be observed:

- Configuration effects [18]
- Aggregation effects, micelles [19], multilayer adsorption
- Molar weight, chain stiffness [19]
- Surface charges [20]
- Competitive adsorption of solvent molecules

In all cases, the knowledge of the adsorption isotherms and with it of the mechanism of adsorption is essential for specific modifying processes of solid surfaces.

But, the adsorption process depends not only on the nature of the adsorptive. The solid surface and the solvent also have significant influence on the adsorption process.

12.2.1 The Role of the Solid Surface

In any case, chemical properties of the solid surface, like functional groups, charge density, polarity, surface energy, surface morphology (roughness, degree of crystallinity), and surface contaminations influence the adsorption process. The chemical nature of the surface determines the strength of the interaction forces between the surface and the adhesive. In many cases pre-treatment is done to prepare the surface for adsorption, especially to increase the effective interaction forces.

The influence of the porosity of the surface depends on the size and the shape of the single pores. On the other hand, the size and the nature of the adhesive are equally important for observed effects. If we have small pores and small molecules like N_2 we note capillary condensation in such pores. On the other hand, we use porous systems for size-exclusion chromatography to separate molecules with different molar masses. This means that the size of the single pore should correspond to the size of the adhesive molecule or associate.

Finally, the structure of the adsorption layer depends on the quality of the surface: Is it homogeneous or heterogeneous and what is the nature of the heterogeneity?

12.2.2 The Role of the Solvent

One point is the solubility of the adsorptive in the used solvent. We can distinguish good and poor solvents and some transient states in-between. If we record low solubility we can expect strong adsorption. In such systems the interaction forces between the adsorptive and the surface are higher than between adhesive

and solvent. The adsorption process is favoured. When we record high solubility weak adsorption takes place. Here, we find the opposite situation [13].

Another point is the structure of the adhesive in the solution: formation of associates like surfactant micelles or polyelectrolyte complexes, coiled or linear chains and so on. In such cases the nature of the interaction forces is the reason for changes of this structure during the adsorption process. In some cases the same structure can be found at the solid surface, in other cases the associates decompose and single molecules will be adsorbed. This behaviour depends not only on the used solvent. In this case, the solid surface also plays an important role.

Finally, transport phenomena in the solution impact the process of adsorption. For adsorption the concentration of adsorptive molecules should increase near the interface. The driving force of this procedure is the diffusion force. Adsorption velocity and diffusion rate are in competition.

12.2.3 Influence of the Third Substance

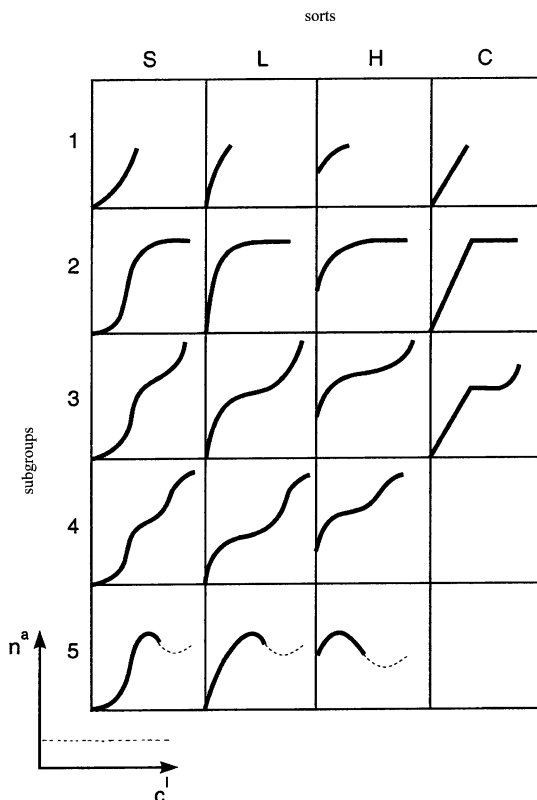
Under real conditions no 'clean' solid surfaces are available. Depending on the surface energy of the system's gaseous molecules, water and other partly organic impurities will be found. The adsorption processes in these cases are mostly the change from smaller adsorbed molecules to larger ones. In protein adsorption Vroman [21] described this effect of molecular size, which was called later on by his name. Such effects are based on nearly the same interaction forces between adsorbent and adsorbate. When different interaction forces take effect, molecules with higher affinity to the substrate replace molecules with lower affinity. Such molecules that will be adsorbed in the end of this process will dominate the resulting surface properties.

12.2.4 Adsorption of Uncharged Macromolecules

It is assumed that there is a big difference between adsorption of small molecules and macromolecules. The structure of macromolecules allows a large number of configurations. In this case a high entropy loss but also a large decrease of energy determines the adsorption process of macromolecules [22].

Depending on current conditions, a large variety of adsorption isotherms can be experimentally obtained. The principal adsorption characteristics of neutral macromolecules are demonstrated in Fig. 12.2/2H. Such an isotherm curve is known as a typical high-affinity adsorption isotherm. In this case the first molecules adsorb so strongly that the solution is depleted till below the limit of experimental detectability [8]. At high solution concentration a pseudo-plateau is obtained that strongly depends on molar mass [19].

Fig. 12.2 Classification of isotherm shapes [16] (c^1 = concentration in solution, n^a = number of adsorbed molecules)

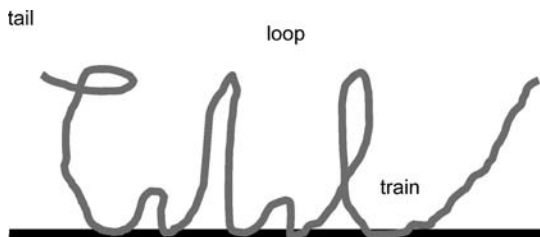


In recent years, many theoretical solutions of the adsorption process of macromolecules were developed [19]. For practical applications qualitative characteristics of macromolecule adsorption should be observed [22]:

- Macromolecule adsorption isotherms have a high-affinity character.
- Adsorption increases with decreasing solvent quality.
- Adsorption increases with molecular weight in a poor solvent, and is rather insensitive to molecular weight in a good solvent.
- The influence of temperature is small or absent.
- Adsorption of macromolecules is a slower process than adsorption of small molecules and it depends on the molecular weight distribution.
- Effects of configuration and aggregation changes influence the adsorption process (influence of molecular stiffness) just like the heterogeneous composition of the macromolecule. In this case, parts of high affinity and parts of low affinity control the structure of the adsorbed molecule.

A first theoretical model of macromolecule adsorption was developed by Simah and co-workers in 1953 [23]. In these models the segment–surface interactions and the conformation statistics of an adsorbed molecule, consisting of

Fig. 12.3 Structure of adsorbed molecular chain



trains, loops and tails is described (Fig. 12.3). Interaction forces between segments and different molecules are neglected. But new concepts include such interactions.

In comparison, these models based on the self-consistent mean field consider the total ensemble of chains and give the thermodynamic equilibrium between surface and bulk phase [19].

Especially interesting adsorption behaviour is demonstrated by block copolymers. Usually one block is preferentially adsorbed as an anchor. The other block, with lower adsorption affinity, is excluded from the surface and forms dangling tails into the solution. A brushlike structure is formed with a solvated shell. The resulting conformation is determined by the solvent, which can be selective or non-selective for one part, and by the lengths of the blocks [24]. Such special adsorption effects are of particular interest because of the wide range of applications.

12.2.5 Adsorption of Polyelectrolytes and Polyampholytes

For charged macromolecules the situation is much more complicated. Influencing variables like charge density of the adsorptive, surface charge of the adsorbent, ionic strength and pH of the solution affect additionally the adsorption process of polyelectrolytes. Resulting electrostatic interaction forces are very strong and do not follow the regularity of isotherms described above. Scheutjens and Fleer [25] included the dependency of the adsorption on adsorption energy, solvent quality, salt concentration and surface charge in their adsorption model.

Polyelectrolytes have, apart from the chemical contribution, an electrostatic part in their Gibbs energy of adsorption. With an uncharged surface this electrostatic effect opposes the accumulation of the polyelectrolyte. In the case of charged surfaces, the electrostatic component in the adsorption energy is observed, which may be positive or negative, depending on the charge signs. Indifferent electrolytes screen all electrostatic interactions, both the intermolecular repulsion and the segment–surface interaction, so that they have at least two – often opposing – effects.

Cohen Stuart and co-workers [26] summarized different theoretical models of ion, polyelectrolyte, and polyampholyte (special protein) adsorption.

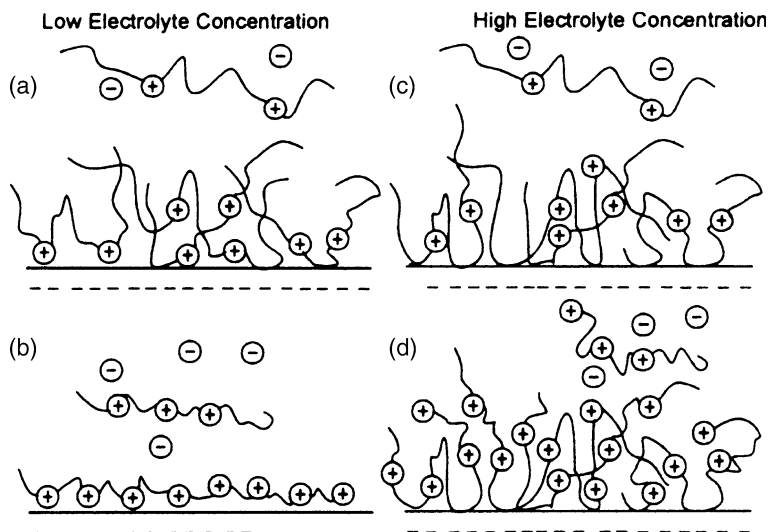


Fig. 12.4 Conformation models of adsorbed polyelectrolytes: (a, c) macro-ions of low charge density; (b, d) macro-ions of high charge density [19].

The principal characteristics of the adsorption of polyelectrolytes of various charge densities onto surfaces of different charge in solutions of low or high ionic strength obtained from theoretical treatments are presented as structure models in Fig. 12.4 [19].

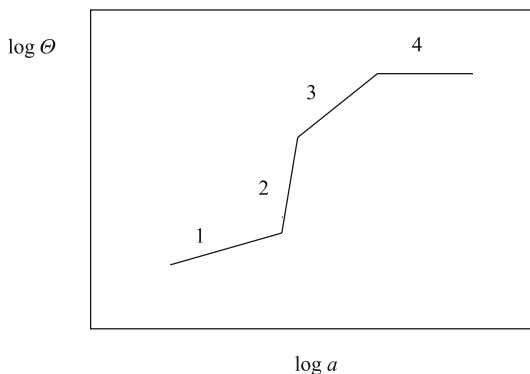
Polyelectrolyte adsorption gives us the opportunity for controlling surface charges of solids and plays an important role for setting of special surface properties like biocompatibility, dispersion stability as well as others.

12.2.6 Adsorption of Surfactants

Surfactants are surface-active molecules with one hydrophobic and one hydrophilic part. Depending on the character of the hydrophilic group of surfactant molecules we distinguish between ionic and non-ionic surfactants. The hydrophobic part of such molecules is in most cases a longer, branched or linear alkyl chain. Surfactants are characterized by aggregation in solution and at interfaces. Results are micelles in solution and structured surfactant films at interfaces and in the end local enrichment of surfactants at the solid/liquid interface. The driving force of adsorption is the decrease of surface tension in the case of surfactant adsorption [14].

A typical adsorption isotherm of surfactants can be divided into 4 parts (Fig. 12.5): Region 1 is the Henry range and represents adsorption of isolated molecules. In region 2 aggregates are formed on the surface “head-on”. The difference in slope of parts 2 and 3 can only be interpreted as a transition from “head-

Fig. 12.5 Typical adsorption isotherm of an ionic surfactant (schematic) [27]



on” aggregates to aggregates containing “head-on” and head-out” surfactant molecules. Above the c.m.c. (critical micellization concentration) further increase in surfactant concentration in solution does not induce an increase in adsorption density [27]. In the case of non-ionic surfactants the slope between regions 2 and 3 is not different.

As described above, adsorbed surfactant films at interfaces will be structured because of their property to aggregate. The special structures of these films depend on the surface properties of the adsorbent.

Different publications [28] refuted the idea of continuous surfactant mono or multilayers being deposited at a solid/liquid interface. This can be expected in the case of low surfactant concentration. But, on the contrary, surfactants do form ordered structures on solids in solutions at concentrations well above the c.m.c., so-called self-assembled layers (Fig. 12.6). Their structure depends mainly on the hydrophilicity or hydrophobicity of the solid surface and less on the ionicity of the surfactant. Structures similar to those formed in solutions above the c.m.c. (micelles, lamellar phases) have been observed by some authors below c.m.c. The reason is the higher concentration of the surfactants near the solid surface because of their surface activity. On hydrophobic model surfaces, such as graphite, extended half-cylinders/hemimicelles are postulated that provide the greatest possible contact area between the hydrophobic part of the surfactant (carbon chains) and the surface (Fig. 12.6a) [29]. Two models exist for hydrophilic surfaces (mica, silica) (Fig. 12.6b) [29, 30]: rodlike micelles or monolayers topped with half-cylinders. The latter model provides the maximum contact between the hydrophilic head group of the surfactant and the hydrophilic solid surface. In addition, this structure compensates for the repulsive forces between the single adsorbed surfactant molecules.

Ionic surfactants are normally incorporated in the stern layer of the solid surface by coulomb interaction. In most cases specific interaction complete the adsorption forces. Additionally, hydrocarbon chains of adsorbed surfactants interact with each other because of their tendency to be expelled from water. In the end, changes of the surface energy and of interaction forces at the interface result from adsorption of surfactants onto the solid surface.

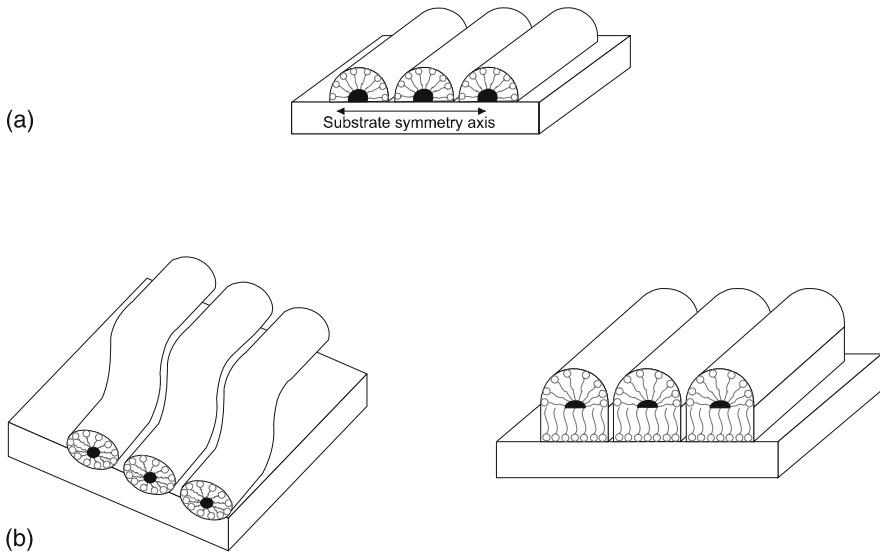


Fig. 12.6 Models of layers of a cationic surfactant at solid/liquid interfaces. **(a)** Hydrophobic substrate (graphite). Hemicylindrical aggregates by Manne and Gaub [22]. **(b)** Hydrophilic substrate (mica, silica): *(left)* flexible cylindrical aggregates by Manne and Gaub [22]; *(right)* monolayers topped with hemicylinders by Johnson and Nagarajan [23]

12.3 Selected Methods for Investigation of Adsorption Processes

Normally, the adsorption process can be characterized by adsorption isotherms or by the resulting surface properties of the adsorbent. We can subdivide the known methods into direct and indirect (Tables 12.3 and 12.4).

Direct methods (Table 12.3) observe the changes at the solid surface during or after adsorption process while indirect methods (Table 12.4) investigate the chan-

Table 12.3 Direct measurements of adsorption processes

Thermodynamic methods	Spectroscopic methods	Imaging methods [37]
<ul style="list-style-type: none"> • Microcalorimetry [9, 31] • Volumetry, gravimetry • Inverse gas chromatography [32] • Electrokinetics [8, 27], see Chapt. 5 • Wetting measurements [33], see Chapt. 5 	<ul style="list-style-type: none"> • Infrared spectroscopy (ATR-FTIR) [34], see Chapt. 3 • Surface plasmon resonance spectroscopy [35], see Chapt. 3 • Fluorescence spectroscopy • X-Ray photoelectron spectroscopy [34], see Chapt. 4 • Spectroscopic ellipsometry [36], see Chapt. 3 	<ul style="list-style-type: none"> • Brewster-angle microscope • Scanning electron microscopy • Atomic force microscopy

Table 12.4 Indirect methods to investigate adsorption processes

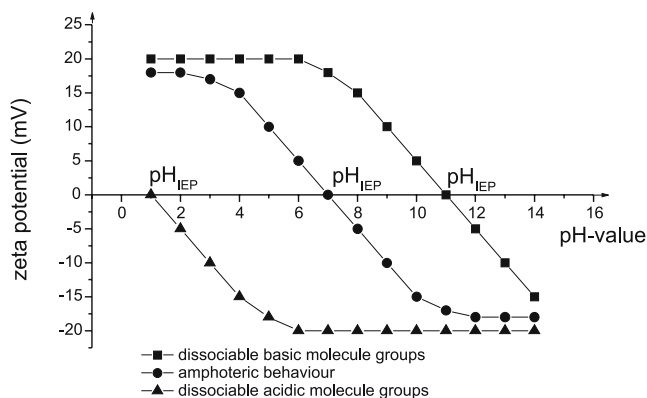
Methods	Measuring effect
• Adsorbed amount: potentiometric titration, TOC	• Concentration of surfactant in solution
• Particle charge detector	• Determination of surface charge density

ges in the liquid phase (for example, the decrease of the concentration of the adsorptive/depletion effect). With such results it is possible to conclude the amount of adsorbate indirectly.

The principles of all the mentioned methods can be found in the noted references. Some of them are also described in other chapters of this book.

One of the not so usual methods of characterizing adsorption processes is the electrokinetic method. With this method adsorption processes can be observed directly or the resulting surface properties after adsorption can be investigated. The fundamentals of this method can be found in refs. [38, 39].

Electrokinetic phenomena can be observed by the contact of a solid surface with a polar liquid medium, because of the existence of an electric double layer at the solid/liquid interface. The potential on the surface of a solid in contact with a polar medium is governed, according to Lytlema [43], by dissociation of surface groups, preferential adsorption of cations or anions, adsorption of polyelectrolytes or surfactants, isomorphic substitution of ions, and lastly accumulation or depletion of electrons. Generally, descriptions of the charge distribution at the interface are based on the model developed by Gouy and Chapman and completed by Stern and Grahame (GCSG model) [38, 39]. The electric double layer, which is based on the GCSG model, consists of two regions: a fixed layer and a diffuse layer. Between these two parts lies a “surface of shear” or “slipping plane”. Externally used electrical or mechanical forces cause a relative movement between the fixed part

**Fig. 12.7** Acid–base surface properties – electrokinetic investigations [40]

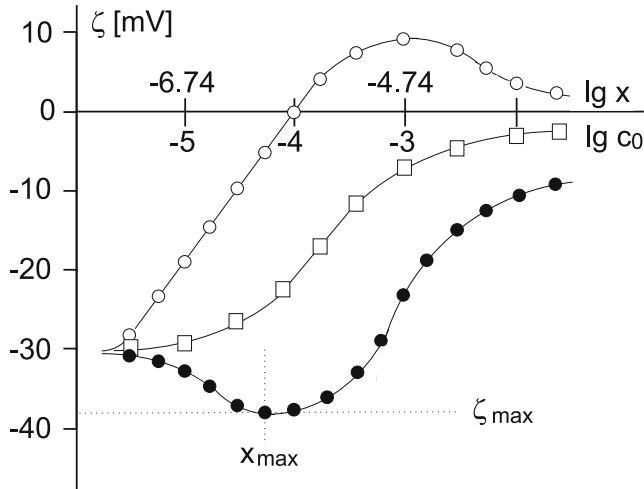


Fig. 12.8 Adsorption processes – electrokinetic investigations [41]

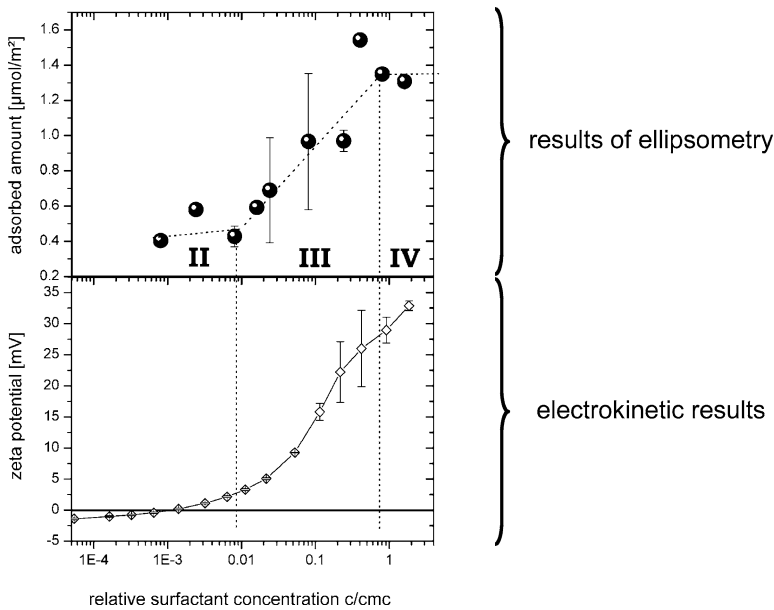


Fig. 12.9 Comparison of electrokinetic and ellipsometry results of surfactant adsorption [42]

and the diffuse part. The potential at this surface is called the electrokinetic or zeta (ζ) potential. According to the formation mechanism of the double layer characterization of solid surfaces is possible. According to Jacobasch [39] mainly acid-base properties at the solid surface can be determined (see Fig. 12.7).

On the other hand, adsorption processes can be investigated directly (Fig. 12.8) with the help of electrokinetics.

If charged species are adsorbed onto a solid surface apparent “adsorption isotherms” can be measured with electrokinetics. This can be shown by the results of surfactant adsorption onto polymer films (Fig. 12.9).

The main method of electrokinetics for measuring adsorption processes is the method of streaming potential [39,44]. In this case solid surfaces are fixed and should build one or more streaming canals to pump the measuring solution through this canal. Depending on the actual pressure drop a streaming potential can be detected. Measured streaming potentials (U_s) vs. pressure drop (p) are the base of calculation of electrokinetic potential (ζ) by the Smoluchowski equation:

$$\zeta = \frac{dU_s}{dp} \frac{\eta}{\epsilon \epsilon_0} \frac{L}{QR} \quad (12.12)$$

where η is the viscosity and ϵ the dielectric constant of the measuring fluid, ϵ_0 is the electric constant, L and Q are the length and cross-sectional area, respectively, of the streaming canal and R is the electrical resistance in the system.

12.4 Applications

The technological, environmental and biological importance of adsorption can never be in doubt. Its practical applications in industry and environmental protection are of paramount importance.

One of the classical application fields are colloidal systems. With the help of adsorption layers the dispersion stability of colloidal systems can be controlled [45,46]. Here, we have two possibilities to stabilize such systems: steric or/and electrostatic. In the other case, flocculate processes can be controlled. With the help of special adsorbable molecules, normally polyelectrolytes or polyelectrolyte complexes, the surface of the disperse phase will be modified in this direction.

In nearly all composite materials the properties of these materials depend on the interaction forces between the adhesion reactants. Here, we are also able to regulate these forces with the help of such adsorption layers. In such systems special coupling agents are included in the adsorption layer to achieve high adhesive strength.

In the field of coatings the interaction forces between the substrate and the coating could be influenced with adsorbates in the interaction layer. The aim in all cases is a very stable coating layer.

Other applications are papermaking, food industry, catalysis, selective material separation, medical systems, textile industry, cleaning processes and so on.

12.4.1 Adsorption of Surfactants

Chemical mechanical planarization (CMP) is an important processing step of semiconductor manufacture. Shrinking dimensions in semiconductor wafer processing have led to an increased need for CMP. The process is used to remove metal and oxide layers from the wafer and to generate smooth, flat surfaces.

After processing, the surface should have a very high quality. Scratching and scale effects on the wafer surface must be prevented. Afterwards, the surface has to be cleaned until it is residue-free, i.e. the used abrasive particles must be removed completely.

The most important part of the CMP process is the slurry that is made of solid particles suspended in an aqueous medium. The quantity of abrasive particles and additives depends on the particular application of the slurry. For example, high-facing oxide processes need slurries containing abrasive powder between 10 and 30 per cent by weight. The polishing process is mainly one of mechanical milling. Slurries for metal polishing contain additives to attack the metal by oxidation and approximately 1 to 3 per cent by weight of polishing powder to remove the products of the chemical reaction. Buffering agents and surfactants complete the slurry formulation.

The aim of such polishing processes is a very smooth surface without any surface defects. This means that the particles in the slurry should be very small (~200 nm diameter and smaller) and should not coagulate before and during the process. The hardest conditions are during the polishing process because of the high shearing forces. We therefore need strong repulsive interaction forces between two particles. On the other hand we need strong repulsive forces between the wafer surface and grinding medium to hinder particle adhesion to the wafer surface.

In ref. [47] the influence of surfactants on this process was shown. For this investigation we selected substances with the same chain length for the sake of better comparison.

In the case of cationic surfactants (dodecyl trimethyl ammonium bromide/DDTMABr), it might be expected that the head groups of the substance would bind onto the hydrophilic anionic wafer surface and the hydrophobic chain would determine surface properties. The adsorption process follows the adsorption isotherm in Fig. 12.5. The result is a structured double layer or special forms such as cylinders or rods described in Fig. 12.6 (b) [see Sect. 12.2.6].

This layer has a space effect and inhibits the particle adsorption on the wafer surface in addition to the repulsive electrostatic forces of the head groups. Such spacers are necessary to inhibit agglomeration processes in the case of strong shear forces. It is also necessary, however, to remove these surface-active substances from the wafer surface afterwards. Otherwise they interfere with the adhesion of the next layer on the electronic component.

In our experiments we found a strong adsorption at the wafer surface. We recorded a charge reversal at the surface. This supports the discussed adsorption

mechanism above. But we were also able to show (Fig. 12.10) that it is possible to remove the surfactant completely. After cleaning the zeta potential is nearly the same ($\zeta = -4.2$ mV) as at the beginning of the adsorption ($\zeta = -1.1$ mV).

With anionic substances (sodium dodecyl sulfate/NaDDS), the surfactant is adsorbed at the surface of the alumina particles (Fig. 12.11), not at the wafer surface (Fig. 12.10).

But at high surfactant concentrations ($> 10^{-4}$ mol/l) we note an increase in the negative zeta potential value. This can only be explained by dispersion attraction forces between the wafer surface and the surfactant.

Like the effect of detergents in cleaning processes of textiles, etc., the dirt (in our case the alumina) is kept away from the solid surface (in our case the wafer) [48] with the help of the anionic surfactants (flotation effect). This effect did not influence the subsequent coating steps. But the problem in this case is the stability of the slurry. Concentrations of about 10^{-4} mol/l initiate the agglomeration process (Fig. 12.11). This effect depends not only on the point of zero charge (pzc) when electrostatic repulsive forces are stopped. It also seems that the maximum particle size corresponds to the maximum concentration of surfactant adsorption.

In the case of a non-ionic surfactant (Marlipal 013/100/Hüls) only hydrophobic or steric interactions are expected. The adsorption process indicates uncharged surfaces.

The adsorption process of surfactants described by the special adsorption isotherm (Fig. 12.3) indicates a strong dependence of adsorption energy by chain interaction of the surfactant hence the role of the hydrocarbon chain should be

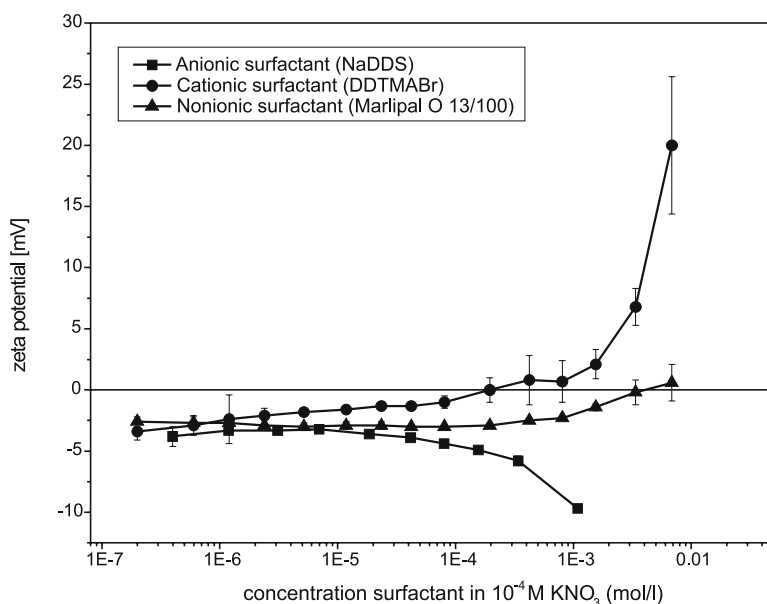


Fig. 12.10 Surfactant adsorption on copper surfaces [47]

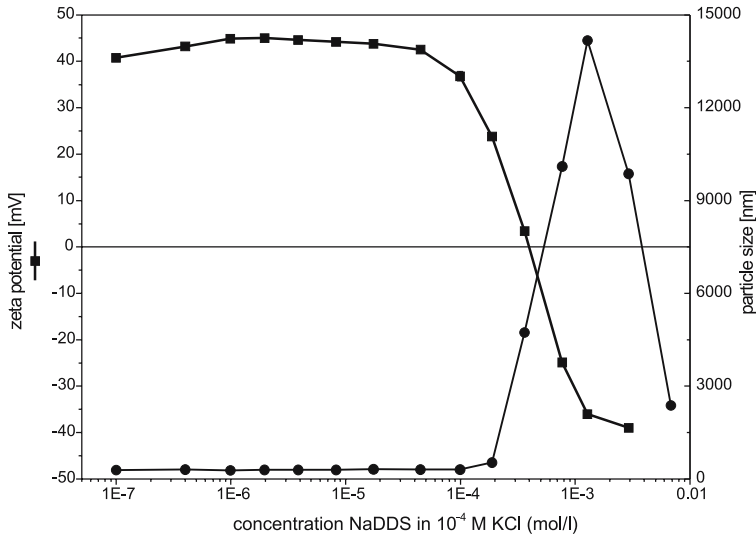


Fig. 12.11 Surface adsorption on alumina particle surfaces and agglomeration process [47]

studied. Fuerstenau [49] described the influence of the hydrophobic chain extensive in 1971. It can be shown by different points of zeta potential reversal (pzs) dependent on the chain length with the help of electrokinetic measurements. We were able to verify such results (Fig. 12.12).

According to Fürstenau [49] the number of carbon atoms in the chain should directly relate to the adsorption behaviour. If all other specific adsorption effects are negligible, then above the hemimicelle concentration the adsorption density Γ_δ of surfactant ions in the Stern layer δ is given by

$$\Gamma_\delta = 2rC \exp\left(\frac{-zF\Psi_\delta - N\Phi}{RT}\right) \quad (12.13)$$

where r is the effective radius of the adsorbed surfactant ion, C is the bulk concentration, z is the ion charge, Ψ_δ is the potential in the plane δ of the double layer, N is the number of carbon atoms in the alkyl chain, Φ is the molar cohesive free energy per mol of CH_2 groups in the chain, R is the gas constant, and T is the temperature.

Equation (12.13) shows that the amount of adsorbed surfactant should depend strongly on the chain length, once the hemimicelle concentration is exceeded. This approach includes that after association of the alkyl chains the zeta potential is reduced to zero. In this case, the function N versus C at the point of pzs should be linear, with a slope equal to $\Phi/2.3RT$.

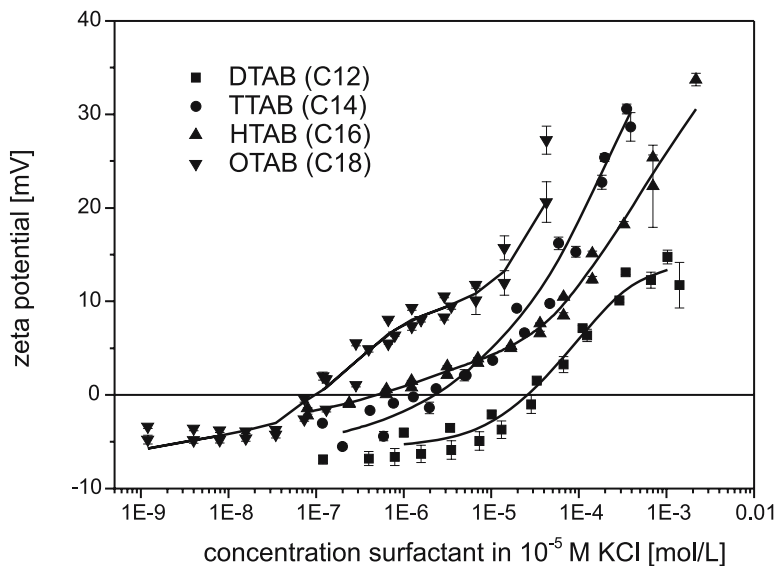


Fig. 12.12 Adsorption of surfactants with different chain length (D=dodecyl, T=tetradecyl, H=hexadecyl, O=octadecyl) [50]

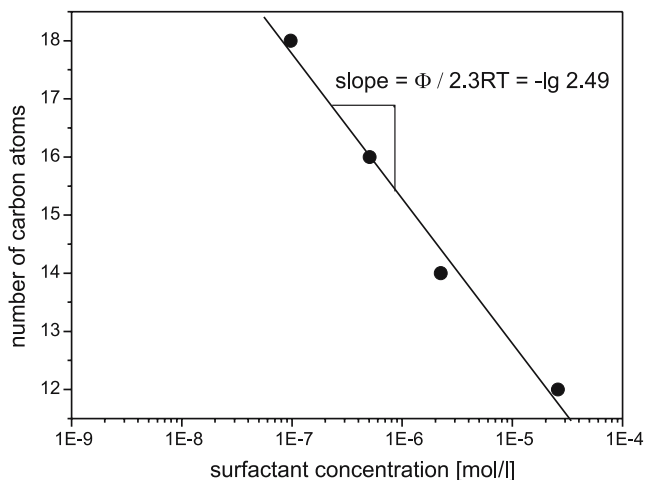


Fig. 12.13 Chain length versus concentration at pzc (correlation coefficient=0.99333) [50]

Figure 12.13 shows such a plot for alkyltrimethylammonium ions adsorbed on polymer surface, and from this plot Φ is calculated to be $-0.91RT$. Studies of micelle formation have resulted in values of Φ of -1.0 to $-1.1RT$ per mole of CH_2 groups [49]. The value that we obtained is of the same order of magnitude. In our analysis we could not include the influence of the trimethyl group, which can

explain the slightly lower value for the determined Φ . These results validate the Stern approach and the physical uniqueness of the zeta potential.

Such influential parameters are a nice possibility to control surface properties by different surfactants.

12.4.2 Adsorption of Polyelectrolytes

Hydrophobic polymers are commonly used for the preparation of micro- or ultra-filtration membranes due to their high mechanical strength and long lifetime. But hydrophobic surfaces are likely to adsorb biological substances like proteins and natural organic matter, caused by hydrophobic interactions between feed components and the membrane surface. This so-called fouling process is one of the major factors limiting the use of membranes. In [51] Meier-Haack prepared membranes with designed surfaces by adsorption of polyelectrolyte multilayer systems. A smart method to obtain hydrophilic and charged surfaces is given by the layer-by-layer adsorption of oppositely charged polyelectrolytes and the build-up of polyelectrolyte multilayer complexes on polymeric substrates, which has been initiated by Decher et al. [52]. Figure 12.14 shows the electrokinetic properties of a commercial polypropylene membrane after grafting with 3.3 wt.% poly(acrylic acid) (PAAC), after grafting and complexation with poly(dimethyldiallyl-ammoniumchloride) (PDADMAC), and after grafting and complexation with PDADMAC/PAAC. The changes of surface charges by different layers are seen by the changes of the IEP (isoelectric point). In the case of PAAC negative acid groups dominate the surface of the membrane, while in the case of PDADMAC positive basic groups dominate the surface. The next layer of PAAC shifted the

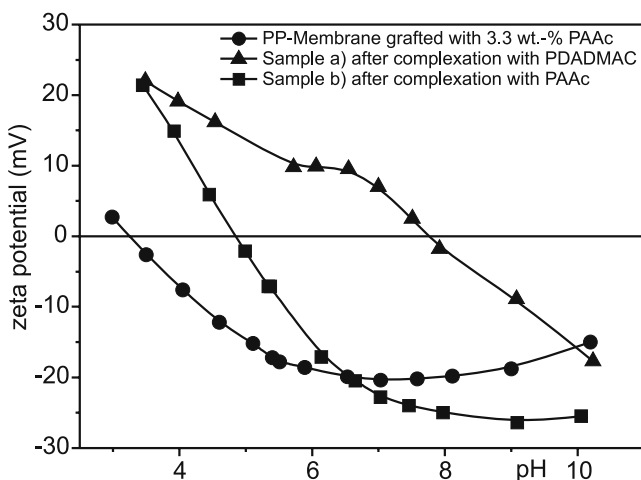


Fig. 12.14 Polyelectrolyte modification of polypropylene microfiltration membrane [51]

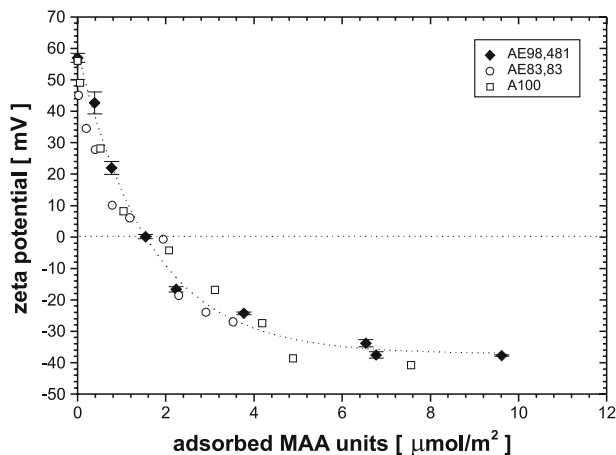


Fig. 12.15 α -alumina with adsorbed DBCPs (AE98,481 and AE83,83 and PMAA homopolymer (A100) as a function of the number of adsorbed MAA units at pH 4.5) [53]

IEP toward lower values but not toward the IEP of the first layer. In this case, the use of electrokinetics gave us not only information about the adsorption mechanism but also about the most important resulting property of the surface.

Water-soluble diblock copolymers (DBCPs) with a polyelectrolyte block are used as highly efficient dispersants for oxide ceramic powders in aqueous media (ceramic industry). In [53] the authors described the adsorption of polyelectrolytes as components of block copolymers on aluminium oxide surfaces. The stability of powder particles in an aqueous dispersion is a complex function of the polymer properties; among others in particular molecular weight, the block-length distribution and the ionic nature of the polymer, as well as the nature of the powder surface, pH value and ionic strength of the medium. Therefore P[MAA-b-PEO] was synthesized by sequential anionic polymerization of tert-butylmethacrylate (TBMA) and ethylene oxide (EO), followed by polymer analogous conversion of the PTBMA into poly(methacrylic acid) (PMAA) blocks.

It was found that the IEP of the particle surface strongly depends on the amount of the adsorbed DBCP. But the results in Fig. 12.15 indicate no influence of the non-ionic PEO block on the electrokinetic behaviour of the alumina particles in diluted suspensions. The change of zeta potential of the alumina particles due to the DBCP adsorption is therefore only a function of the amount of PMMA block adsorbed, the fraction of the PMAA-block dissociation and therefore a function of pH.

12.4.3 Adsorption of Coupling Agents

The transferability of attacking forces in reinforced glass-fibre-polymer systems depends on the adhesion strength between the glass fibre and polymer matrix.

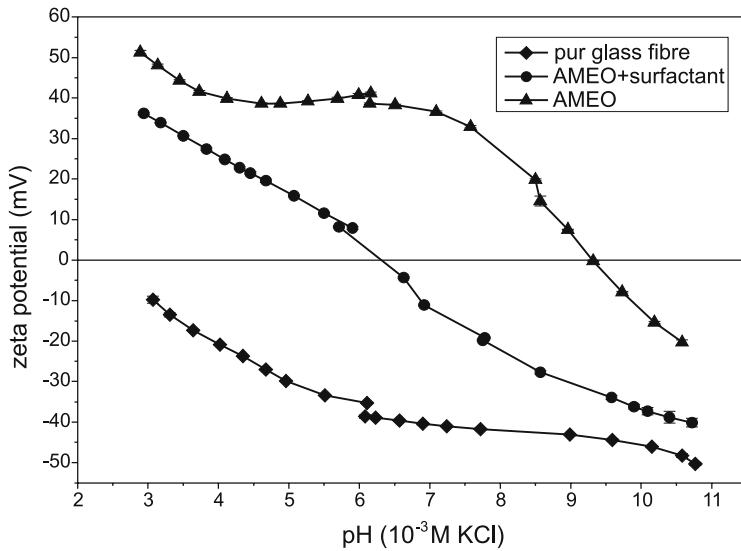


Fig. 12.16 Differently treated glass fibres [55]

High adhesion forces are necessary for optimum mechanical properties. The adhesion force acting between solid bodies is caused by a number of factors [54]. It depends on the geometry of the adhesion contact, the mechanical properties of the two materials and the interface, and, on the other hand, on the forces acting in the interface. In addition to dispersion forces, which are working generally, polar forces can occur like dipole–dipole, acid–base, or electrostatic interactions. In such cases, functional groups are the basis of these forces. Therefore, coupling agents are used to increase acid–basic interaction forces in the interface.

By means of streaming potential measurements (Fig. 12.16) it can be shown that the surface of untreated glass fibres has a low isoelectric point ($\text{IEP} = \text{pH}|_{\zeta=0} < 3.0$) as expected [55]. The chemical nature of the surface is determined by acid functional groups – silanol groups. In comparison, the IEP of γ -aminopropyltriethoxysilan (AMEO) treated glass fibres was measured with $\text{pH} \sim 9.3$. In this case, alkaline amino groups determine the fibre surface. In the case of the fibre treated with a mixture of AMEO and alkyltrimethylammoniumchloride as surfactant the surface properties change in an unexpected way. In this case both amino groups of AMEO and ammonium groups of surfactant are not effective. Competitive adsorption processes prevent the effectiveness of these groups.

The coating of metal surfaces needs modification processes to prepare those surfaces for good adhesion, too. Here, the first step in pre-treatment of metals consists of pickling. The second step is the treatment with an adhesion agent. The first issue for corrosion prevention is the strong interaction force at the boundary layer. In the case of an Al/Mg surface, (Fig. 12.17) dodecyl phosphonic acid was used [40]. The IEP changed from $\text{pH} \sim 8.4$ to $\text{pH} \sim 4.8$. The phosphonic groups dominate the surface properties of the sheet. To describe the building process of

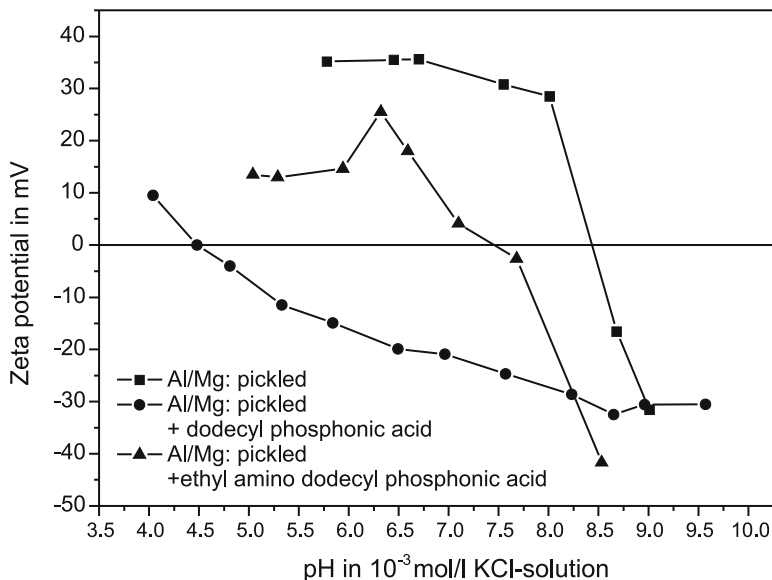


Fig. 12.17 Differently treated Al/Mg sheets [40]

the adhesive layer more clearly, the first oligomer was substituted by ethyl amino dodecyl phosphonic acid. In this case, it was expected to find basic surface properties because of the existence of $-NH-$ groups. The IEP of 7.6 shows this behaviour. In experiments with isocyanates, urea groups were found as evidence of the existence of amino groups at the surface [56].

References

1. A. Dąbrowski, *Adv. Colloid Interface Sci.* 93, 135–224 (2001)
2. G.D. Parfitt, C.H. Rochester (eds.), “Adsorption from Solution at the Solid/Liquid Interface”, Academic Press, London, 1983
3. R.H. Ottawil, C.H. Rochester, A.L. Smith (eds.), “Adsorption from Solution”, Academic Press, London, 1983
4. D.H. Everett, “Basic Principles of Colloid Science”, Royal Society of Chemistry, London, 1988,
5. P.W. Atkins, “Physical Chemistry”, Oxford University Press, Oxford, 2002
6. D.B. Houg, H.M. Rendal, “Adsorption of Ionic Surfactants” in “Adsorption from Solution at the Solid/Liquid Interface” eds. G.D. Parfitt and C.H. Rochester, Academic Press, Inc. London, 1983
7. J.N. Israelachvili, “Intermolecular and Surface Forces” 2nd edn, Academic Press, London, 1992
8. J. Lyklema (ed.), “Fundamentals of Interface and Colloid Science”, vol. 1, Academic Press, London, 1991
9. F. Rouquerol, J. Rouquerol, K. Sing, “Adsorption by Powders and Porous Solids”, Academic Press, London, 1999

10. L.W. Bruch, M.W. Cole, E. Zaremba, "Physical Adsorption, Forces and Phenomena", in "The International Series of Monographs on Chemistry", vol. 33, Clarendon Press, Oxford, 1997
11. M.J. Rosen, "Surfactants and Interfacial Phenomena" 2nd edn, A Wiley-Interscience Publication, New York, 1989
12. D.H. Everett, "Manual of Symbols and Terminology for Physicochemical quantities and Units", Appendix II, Part I, Adopted by the IUPAC Council at Washington DC, USA, 1971, www.iupac.org/reports/2001...of s and t/manual of s and t.html
13. H.-D. Dörfler, "Grenzflächen- und Kolloidchemie", VCH Verlagsgesellschaft mbH, Weinheim, 1994
14. M.J. Schwuger, "Lehrbuch der Grenzflächenchemie", Georg Thieme Verlag, Stuttgart, New York, 1996
15. H.-J. Jacobasch, "Oberflächenchemie faserbildender Polymerer", Akademie-Verlag, Berlin, 1984
16. C.H. Giles, T.H. MacEwan, S.N. Nakhawa, D. Smith, *J. Chem. Soc.* 3973 (1960)
17. C.H. Giles, D. Smith, A. Huitson, *J. Colloid Interface Sci.* 47, 755 (1974)
18. R. Hogg, "Evaluation of a Macroscopic Model for Polymer Adsorption" in "Polymer Adsorption and Dispersion Stability", ACS Symposium Series 240, Washington, 1984
19. E. Killmann, in "Adsorption on Silica Surfaces" E. Papirer (ed.), Surfactant Science Series, vol. 90, Marcel Dekker, Inc. New York, 2000
20. I. Grosse, H.-J. Jacobasch, *Prog. Colloid Polym. Sci.* 101, 135–140 (1996)
21. C.H. Bamford, S.L. Cooper, T. Tsuruta (eds.), "The Vroman Effect", VSP, Zeist, 1992
22. G.J. Fleeer, J. Lyclema, in "Solid/Liquid Interface" G.D. Parfitt and C.H. Rochester (ed.) Academic Press Inc. Ltd., London, 1983
23. R. Simha, H.L. Frisch, F.R. Eirich, *J. Phys. Chem.* 57, 584 (1953)
24. S. Minko, D. Usov, E. Goreschnik, M. Stamm, *Macromol. Rapid Commun.* 22, 206–211 (2001)
25. J.M.H. Scheutjens, G.J. Fleeer, *Macromolecules* 18, 1882 (1995)
26. M.A. Cohen Stuart, G.J. Fleeer, J. Lyclema, W. Norde, J.M.H.M. Scheutjens, *Adv. Colloid Interface Sci.* 34, 477–535 (1991)
27. M. Kosmulski, "Chemical Properties of Material Surfaces", Surfactant Science Series, vol. 102, Marcel Dekker, Inc. New York, 2001
28. I. Grosse, N. Petong, *Tenside Surf. Det.* 39, 164–170 (2002)
29. S. Manne, H.E. Gaub, *Science* 270, 1480–1482 (1995)
30. R.A. Johnson, R. Nagarajan, *Colloid Surf. A* 167, 21–46 (2000)
31. A.W. Adamson, A.P. Gast, "Physical Chemistry of Surfaces" 6th edn, A Wiley-Interscience Publication, New York, 1997
32. E. Papirer, "Adsorption on Silica Surfaces", 1st edn, Surfactant Science Series, vol. 90, Marcel Dekker, Inc., New York, 2000
33. A.W. Neumann, J.K. Spelt, "Applied Surface Thermodynamics", 1st edn, in Surfactant Science Series, vol. 63, Marcel Dekker, Inc., New York, 1996
34. D.J. O'Connor, B.A. Sexton, R.St.C. Smart, "Surface Analysis Methods in Material Science", 1st edn, in Surface Science, vol. 23, Springer-Verlag, Heidelberg, 1992
35. W. Hickie, D. Kamp, W. Knoll, *Nature* 339, 186 (1989)
36. M. Born, "Optik", 3rd edn, Springer-Verlag, Berlin, 1985
37. W. Göpel, C. Ziegler, "Struktur der Materie: Grundlagen, Mikroskopie und Spektroskopie", 1st edn, Teubner Verlag, Stuttgart, 1994
38. R.J. Hunter, "Foundations of Colloid Science" Vols. I+II, 4th edn, Clarendon Press, Oxford, 1992
39. H.-J. Jacobasch, *Prog. Org. Coat.* 17, 115–133 (1989)
40. C. Bellmann, Ch. Klinger, A. Opfermann, F. Böhme, H.-J.P. Adler, *Prog. Org. Coat.* 44, 93–98 (2002)
41. H.-J. Jacobasch, F. Simon, C. Werner, C. Bellmann, Vol. 63, 439–446 (1996)

42. A. Drechsler, N. Petong, C. Bellmann, A. Synytska, P. Busch, M. Stamm, K. Grundke, O. Wunnicke, *The Canadian Journal of Chemical Engineering* 84, 3–9 (2006)
43. J. Lyclema, in: J.W. Goodwin (ed.), “Colloidal Dispersions”, The Royal Society of Chemistry, London, 1981
44. H.-J. Jacobasch, F. Simon, C. Werner, C. Bellmann, Vol. 63, 447–452 (1996)
45. D.H. Napper, “Polymeric Stabilization of Colloidal Dispersions”, Academic Press, London, 1983
46. E.J.W. Verwey, J.T.H.G. Overbeek, “Theory of the Stability of Lyophobic Colloids”, Elsevier Publishing Company Inc., Amsterdam, 1948
47. C. Bellmann, D. Zeidler, *Tenside Surf. Det.* 39, 206–210 (2002)
48. H.-J. Jacobasch, in “Surfactants in Solutions” Vol. 9, ed. K. L. Mittal, New York, Plenum Press, 1989
49. D.W. Fuerstenau, in “The Chemistry of Biosurfaces” ed. M.L. Hair, Marcel Dekker, New York, 1971
50. C. Bellmann, A. Caspari, *Key Eng. Mater.* 314, 19–24 (2006) (in preparation)
51. J. Meier-Haack, M. Müller, *Macromol. Symp.* 188, 91–103 (2002)
52. G. Decher, J.-D. Hong, J. Schmitt, *Thin Solid Films* 831, 210–211 (1992)
53. J. Orth, W.H. Meyer, C. Bellmann, G. Wegner, *Acta Polym.* 48, 490–501 (1997)
54. H.-J. Jacobasch, *Angew. Macromol. Chem.* 128, 47–69 (1984)
55. R. Plonka, E. Mäder, S. Gao, C. Bellmann, V. Dutschk, S. Zhandarov, *Composites: Part A* 35, 1207–1216 (2004)
56. I. Mäge, E. Jähne, A. Henke, H.-J.P. Adler, C. Bram, Ch. Jung, M. Stratmann, *Prog. Org. Coat.* 34, 1–12 (1998)

Chapter 13

Nanostructures in Thin Films from Nanostructured Polymeric Templates: Self-Assembly

Alexander Sydorenko

University of the Sciences in Philadelphia, Department of Chemistry and Biochemistry, Philadelphia, Pennsylvania, 19104, a.sidorenko@usip.edu

Abstract The microphase segregation of copolymers leads to interesting ordered morphologies at nanoscales, which form by a self-assembly process during the preparation procedure. Utilizing thin copolymer films on a solid substrate highly ordered polymeric templates may be formed, which contain nanoscopic cylindrical holes in hexagonal arrangement. The preparation procedure of the ordered nanotemplates is discussed and the filling of the nanoreactors for nanoparticle production is described.

13.1 Introduction

The current trend of modern high-tech industry towards minimization and increase of surface/bulk feature density dictates the search of novel principles and routes. Although photolithography is currently able to achieve feature sizes down towards 100 nm, the associated cost of their manufacturing increases rapidly as the process shifts to shorter wavelengths (X-Ray or electron beam). Therefore, self-assembly by means of a chemical or a physical driving force has attracted considerable interest as an alternative way to build periodic nanostructures with a feature size ranging from a few nm up to sub-micrometres [1, 2, 3]. Nanostructured inorganic and soft materials obtained by means of self-assembly open an avenue to fabricate periodic arrays which are to be explored as templates for further processing.

13.2 Self-Assembly for Nanostructuring

Recently, the formation of arrays of high aspect ratio nanopores during the anodic oxidation of ultra-pure aluminum attracted significant interest as an example of self-assembly in inorganic materials. The occurrence of a periodic pore arrange-

ment in porous anodic alumina was first reported by Masuda in 1995 [4]. The method has been developed by Gösele, of the Max Planck Institute of Microstructure Physics, Halle. Combination of nanoimprint lithography and self-assembly of porous alumina allows the preparation of defect-free porous alumina arrays having a hexagonal pore arrangement [5,6]. Moreover, the alumina membranes with ordered nanopores were used as templates for fabrication of metal nanodots and columns [7, 8].

Another elegant method of the patterning of metal nanoparticles, sequestered within the core of block copolymer micelles deposited onto solid substrates has been pioneered by Spatz and Möller [9]. The proposed approach is rather combination of self-assembly of block copolymer micelles on surface with metal nanoparticle deposition. The idea consists in preparation of ordered monolayer of micelles with the core enriched by metal ions (e.g. AuCl_4^-) embedded in block copolymer core-shell structure. Subsequent reduction of ions to metals followed by plasma etching allows to produce metal nanodots of the desired periodicity, enabling precise control of the lithographically templated nanostructure [10, 11].

13.2.1 Self-Assembly in Block Copolymers

Self-organization in soft materials, particularly in block copolymers, offers a rich variety of nanoscale periodic patterns which are to be used for nanotemplate fabrication. A block copolymer molecule contains two or more polymer chains attached at their ends (Fig. 13.1).

For the simplest classes of block copolymers, AB diblock and ABA triblock copolymers, four morphologies are known to be stable as proved in experiments and theoretically: spherical, cylindrical, lamellae and gyroid (bicontinuous) [12, 13]. ABS triblock copolymers offer much wider range of patterns. The morphology and periodicity of the self-assembled material depend on molecular weight, segment size, and interaction between the blocks described in the terms of Flory-Huggins theory (i. e. immiscibility parameter χ) (Fig. 13.2). In more detail, the theory of dynamics and thermodynamics of self-assembly in block copolymers is described in the reviews by Bates and Fredrickson [14, 15].

BC thin films confined by copolymer-substrate and copolymer-air (or vacuum) interfaces undergo both surface relaxation and surface reconstruction. It is caused by surface phenomena which induce changes in the periodicity and force one of the blocks to occupy an interface [16–21]. In films of practical interest (thickness in the range of several bulk periods) the surface phenomena dominate over the morphology of the films hampering the fabrication of the ordered material with the desired orientation of nanoscopic domains. Therefore, in terms of practical applications of the block copolymer thin films at least three following key problems should be overcome.

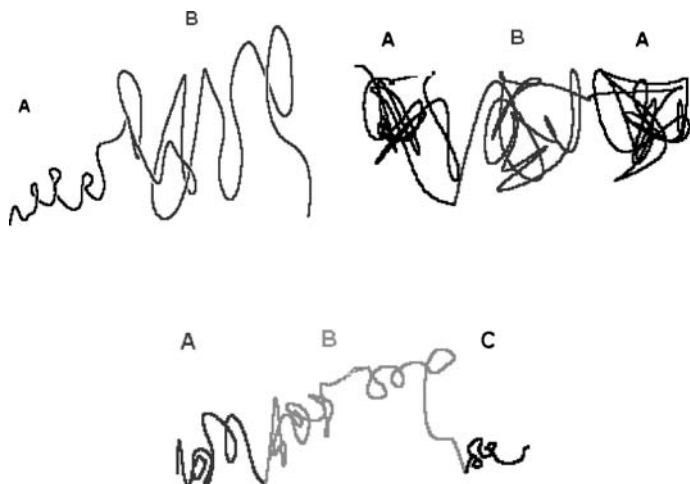


Fig. 13.1 Architecture of AB diblock copolymer, ABA and ABC triblock copolymers

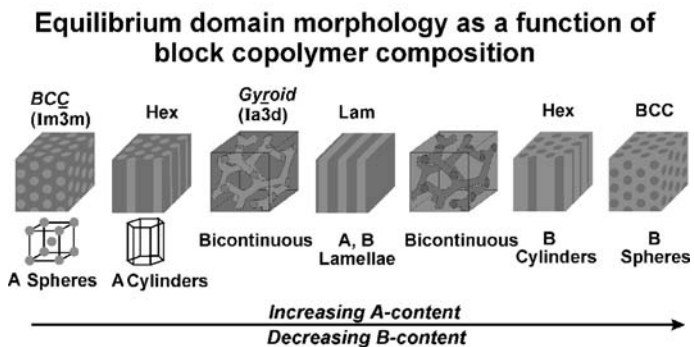
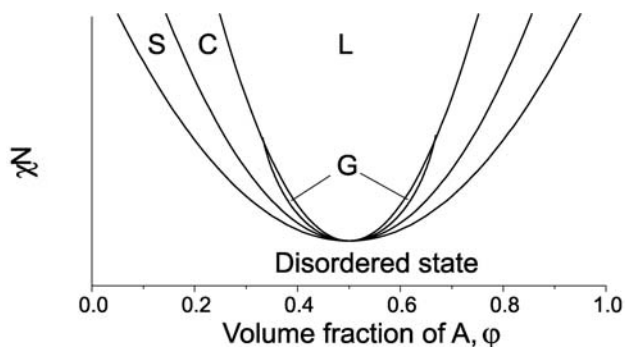


Fig. 13.2 Scheme of morphologies in diblock copolymers as described in [12]

Firstly, thin films of BC are to be well ordered to provide the highest density of the domains and an equal distance between them. The widely used approach to improve the order in BC is annealing at temperature above the glass transition (T_g) [22] resulting in the formation of the thermodynamically stable (or metastable) state, and in the improvement of lateral order. Recently, Krausch and coworkers [23] proposed an elegant alternative method to promote self-assembly into nanometre-scale domains. The procedure consists in controlled swelling of BC thin films in vapor of solvent. Solvent quality and swelling ratio may affect morphology and, particularly, orientation of nanoscopic domains in films of triblock copolymers. Very recent approach was suggested by Kramer and coworkers [24]. They explore the phenomenon of topographical confinement (lithographically patterned Si wafer) to induce a single crystalline order in a single layer of block copolymer spheres.

Secondly, the desired alignment of the domains (the typical example is represented by cylindrical or lamellar domains oriented perpendicular to the substrate surface) is required for practical application. However, the perpendicular orientation is in contradiction with the tendency to the alignment parallel to the confining surface caused by preferential wetting of an interface with one of the blocks [14, 25]. Several approaches have been proposed to overcome this problem. Russell and coworkers [26] showed that annealing in external electric field of a high strength (at least 30 kV/cm) provided the orientation of polymethylmethacrylate (PMMA) cylinders or lamellae of polystyrene-*block*-polymethylmethacrylate (PS-PMMA) thin film along the field lines, in either normal ($C\perp$) or in-plane ($C\parallel$) direction depending on the applied electric field orientation. The effect of external electric field on the BC film structure and on the order–disorder transition temperature was discussed in several publications [27–29]. Another approach proposed by Russell et al. consists in the orientation of BC film by “neutral surface” of solid substrate [30]. Also, many recent reports are dedicated to solvent induced orientation [23, 31–33].

Thirdly, most applications require that the minor component (nanodomains forming block) is eliminated to transform the BC film into a membrane/template. Russell and coworkers [34] proposed UV etching to remove selectively PMMA from the BC film of PS-PMMA. Also, plasma etching was applied for several BC films [35]. An elegant method based on a polymeric supramolecular assembly was proposed by Ikkala and coworkers [36]. They used hydrogen bonding between 4-vinylpyridine monomer units and 3-pentadecyl phenol (PDP) to modify the morphology of poly(styrene-*block*-4-vinylpyridine) (PS-PVP). The investigation of PS-PVP+PDP in the bulk showed that the supramolecular assembling of PVP and PDP changed the BC morphology from spherical to cylindrical [36]. PDP can be easily removed by washing with selective solvent providing nanoscopic channels in the major component matrix [37].

Generally, nanostructure fabrication using block copolymers and associated problems are analysed in detail in the recent nice review by Hamley [38].

13.2.2 Supramolecular Assemblies Based on Block Copolymers

It is a challenging task to develop appropriate materials and technology allowing a simple solution of the three above mentioned problems and fast fabrication of well ordered nanomembranes/nanotemplates from block-copolymer films deposited on solid substrate. Here we focus on a new approach developed in the Group of Nanostructured Materials, Department of Nanostructured Materials, IPF Dresden. The approach is based on the idea to adjust properties of a block-copolymer supramolecular assembly with low molar mass additive. This component helps to solve most of the problems: the appropriate alignment, the crystalline-like order, and the easy transformation of the film into a membrane. It is straightforward that the addition of the third component may strongly modify interactions at the interface and change the surface reconstruction. Taking into account the great number of parameters affecting the morphology in such a system, our search of the third component was based mainly on a qualitative analysis of hydrogen bonding with BC, a capability to form mesophases, and a capability for the selective extraction from the BC matrix. Finally, we have selected the system from PS-PVP and 2-(4'-hydroxybenzeneazo)benzoic acid (HABA) (Fig. 13.3(a)). Depending on the experimental conditions, PS-PVP + HABA supramolecular assembly (SMA) demonstrates microphase separation with hexagonally packed cylinders of either C_{\perp} or C_{\parallel} orientation as shown schematically in Fig. 13.3(b), (c). Moreover, HABA can be easily removed by washing in selective solvent giving the ordered array of nanochannels (Fig. 13.3(d)). Finally, electrodeposition throughout the nanotemplate results in the ordered array of metal dots or nanowires (Fig. 13.3(e)).

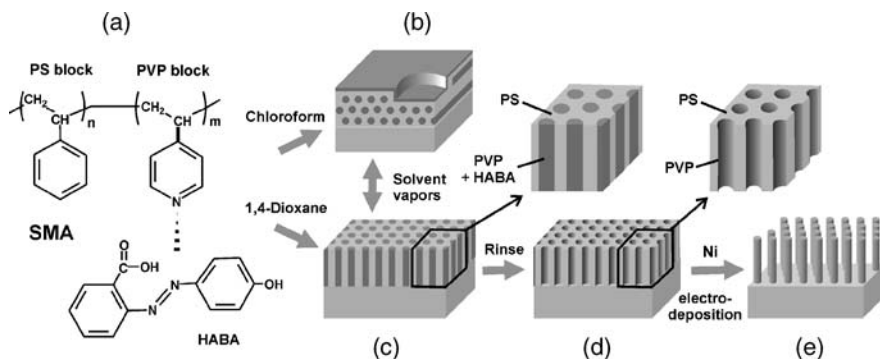


Fig. 13.3 (a–e) Scheme of the nanotemplate fabrication approach based on the BC assembly

13.2.3 Self-Assembly in SMA

SMA polymer films on Si wafers were prepared by dip-coating. In optical microscope the polymer films with the thickness ranging from 20 to 100 nm (ellipsome-

try) are macroscopically and microscopically smooth and show no signs of HABA phase separation, such as crystals or stains. It suggests that HABA molecules are associated with PVP blocks building comb-like polymer chains. The AFM scratch test gives the same film thickness as ellipsometry if the SMA film is modeled as a layer with apparent refractive index $n = 1.63$. Such an elevated value of apparent refractive index as compared to that for PS-PVP (1.59) is attributed to significant fraction of HABA.

FTIR spectroscopy evidences for the formation of hydrogen bonds between HABA and pyridine fragments of PVP detected from the shifts (δ) of PVP characteristic bands sensitive to the formation of hydrogen bonds at 1415 cm^{-1} ($\delta = 5\text{ cm}^{-1}$) and 993 cm^{-1} ($\delta = 8\text{ cm}^{-1}$) as compared with PS-PVP spectra (Fig. 13.4(a)) [39]. This result is very similar to reported elsewhere for hydrogen bonds of PVP with PDP [39, 40]. To improve our understanding for the mechanism of the interaction between PVP blocks and HABA in different media we study interactions in the model system consisted of HABA and pyridine in 1,4-dioxane and chloroform solutions (Figs. 13.4(b), 13.2 and 13.3). As a reference we use the FTIR spectra of HABA in 1,4-dioxane (Fig. 13.4(b), 1). We found very pronounced difference between the spectra in 1,4-dioxane and chloroform. Hydrogen bonding involving carbonyl groups results in appearing of the new band at 1720 cm^{-1} in 1,4-dioxane, while a new band at 1275 cm^{-1} in chloroform indicates the formation of hydrogen bonds with phenolic groups of HABA. Consequently, the spectra give evidence for switching between different mechanisms of hydrogen bond formation in different solvents introduced by the competition with solvent.

An important information for understanding of the SMA film structure was extracted from the analysis of UV-vis spectra. HABA demonstrates the very intensive absorption peak at 382.0 nm (Fig. 13.5(a)). In contrast, the SMA film spectrum shows a blue shift of the main peak (367.4 nm) as compared with the spectra of

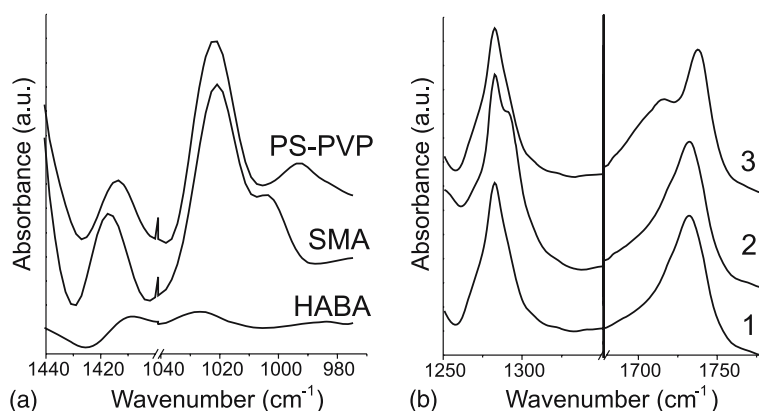
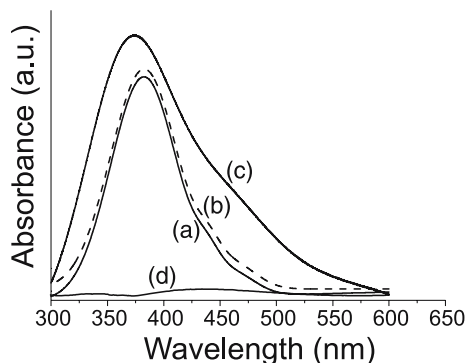


Fig. 13.4 Infrared spectra of (a) PS-PVP, HABA and SMA film, respectively, in the region of pyridine ring bands; (b) a model system HABA + pyridine in 1,4-dioxane (3), chloroform (2) in the regions of phenolic and carbonyl bands compared with HABA without pyridine (1)

Fig. 13.5 UV-vis spectra of (a) HABA $1.8 \times 10^{-3} \text{ g} \times \text{l}^{-1}$ chloroform solution, 10 mm quartz cell, (b) SMA $0.01 \text{ g} \times \text{l}^{-1}$ chloroform solution, 10 mm quartz cell, and (c) SMA 110 nm thick film, (d) the SMA nanotemplate after HABA extraction



HABA or SMA solution (Fig. 13.5(a)–(c)). It is a strong argument for H-aggregation of HABA (parallel face-to-face, according to the molecular exciton model) [41, 42]. This specific structure may play an important role for the morphology of the film.

The PS-PVP copolymer exhibits spherical morphology in bulk when the structure is formed by PVP core surrounded by PS shell [43]. From SAXS experiments we have found that the PS-PVP-HABA equimolecular assembly produces the hexagonal cylindrical bulk structure with the characteristic period of 26 nm.

The detailed investigation of SMA films with AFM shows the dependence of the morphology on the deposition conditions. SMA films deposited from chloroform solution demonstrate the terrace formation (Fig. 13.6(a)). The films are very smooth inside of the terraces with rms roughness of about 0.3 nm for $1 \times 1 \mu\text{m}^2$ lateral scale. In contrast, SMA films deposited from 1,4-dioxane are flat and featureless. The rms roughness is 0.15 nm as measured on $1 \times 1 \mu\text{m}^2$ lateral scale. We did not visualize the fine structure of the materials because of poor contrast between the mechanical behavior of PS and PVP + HABA domains in the film.

It is noteworthy to discuss briefly the strength of the hydrogen bonding between pyridine and HABA. For that, we chose a solvent selectively good for PVP block and HABA, on one hand, and with high polarity, on another, namely methanol. We expected that methanol destroys supramolecular assemblies and removes selectively HABA from SMA leaving cylindrical cavities in the film. We used the absorption peak at 382.0 nm in UV-vis spectra to examine the films after the rinsing procedure. Comparing the band intensities for the polymer film before (Fig. 13.5(c)) and after (Fig. 13.5(d)) the rinsing we may conclude that HABA was completely washed out with methanol from the film. The experiment clearly shows that HABA is assembled by weak bonds.

The AFM scratch test showed no difference in film thickness before and after washing. It gives evidence that almost all HABA is located in PVP domains because the thickness of the PS matrix remains unchanged. Ellipsometric data for the same film thickness were fitted with the apparent refractive index $n = 1.50 \pm 0.01$. Such decrease of n from 1.63 for SMA film (before washing) to 1.5 (after washing) is effected by the formation of porous morphology of the film due to the elimination of HABA. Note, that the obtained n value is much lower than $n = 1.59$

for the PS-PVP reference film which gives additional evidence for the formation of membrane with porous morphology. The pore fraction of the thin polymer films was estimated from the effective refractive index (n , measured with ellipsometry) using the following equation [44]:

$$n^2 = \sum_i v_i n_i^2 \quad (13.1)$$

where n_i and v_i are the refractive indices and volume fractions of the constituent phases of the thin film.

The estimated volume fraction of the pores in the membrane ($n_{\text{PS}} = n_{\text{PVP}} = 1.59$) is in good agreement with the concentration of HABA in the initial mixture (17.8 %).

13.3 Ordering and Orientation in SMA

The rinsing with methanol develops the fine structure of the films clearly observed with AFM. The film deposited from chloroform shows well aligned stripes (Fig. 13.6(b)) which can be assigned as $C \parallel$ cylindrical domains [22].

The film deposited from 1,4-dioxane and washed with methanol demonstrates caves of about 8 nm in diameter which are projection of $C \perp$ domains (channels) with periodicity of about 24 nm (Fig. 13.7(a)). The center–center distance analysis reveals a relatively narrow distribution of spacing between channels with the standard deviation <20 % as visualized by the Gaussian fit (Fig. 13.7(b)) and Fourier-transform image (inset). The center–center distance distribution found for the membranes prepared from the “as deposited” films is comparable with the distribution of an optimized PS-PVP film obtained by the “neutral surface” approach [45]. We observed the same level of order for different film thickness ranging from 20 to 100 nm.

Alignment of cylindrical domains in SMA films can be easily changed with an appropriate solvent. For example, we annealed the 60 nm thick film deposited

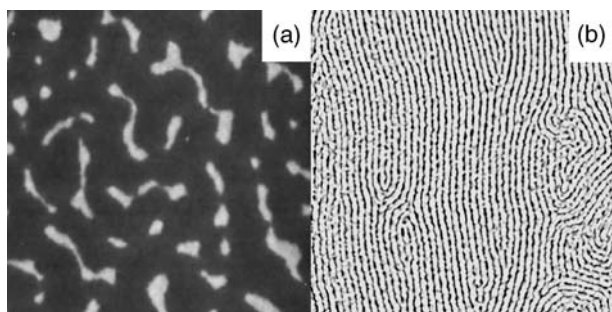


Fig. 13.6 AFM images of SMA films (a) dip-coated from chloroform solution, 40 nm thick, lateral scale $16 \times 16 \mu\text{m}^2$, z scale 30 nm; (b) dip-coated from chloroform solution and washed with methanol, 40 nm thick, lateral scale $1 \times 1 \mu\text{m}^2$, z scale 5 nm

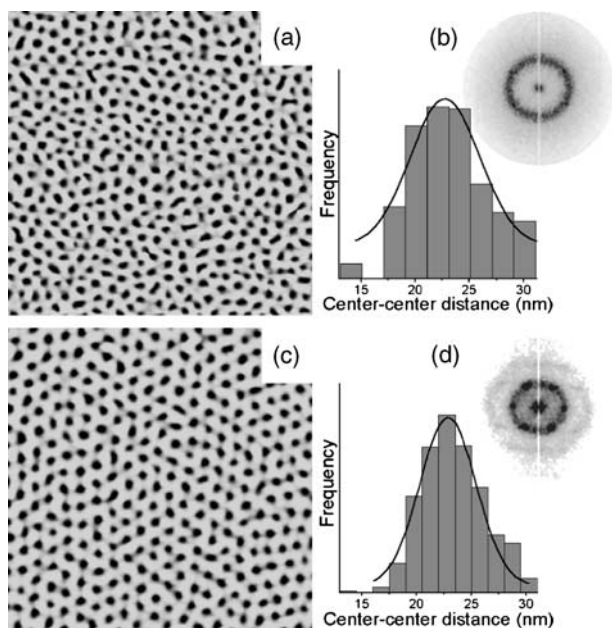


Fig. 13.7 AFM images of SMA films (a) dip-coated from 1,4-dioxane solution, dried and washed with methanol, 40 nm thick, lateral scale $500 \times 500 \text{ nm}^2$, z scale 5 nm; (b) histogram of center–center distances with Gaussian fit and FFT image of (a); (c) SMA after swelling in 1,4-dioxane vapor, dried and washed with methanol, 40 nm thick, lateral scale $500 \times 500 \text{ nm}^2$, z scale 5 nm; (d) histogram of center–center distances with Gaussian fit and FFT image of (c)

from 1,4-dioxane ($C\perp$ pattern, Fig. 13.7(a)) in saturated vapor of chloroform for 30 min at room temperature. Once the sample was removed from the chamber, it dried in about 1 sec. Then we rinsed it with methanol. The film reveals the characteristic $C\parallel$ morphology similar to the morphology obtained directly after deposition from chloroform solution. Conversely, SMA films deposited from chloroform with $C\parallel$ alignment were re-oriented into hexagonal $C\perp$ morphology by annealing in 1,4-dioxane saturated vapor atmosphere for 30 min at room temperature. Moreover, swelling of the SMA film in 1,4-dioxane vapor results in a significant increase of order (Fig. 13.7(c)). The center–center distance distribution is very narrow (standard deviation 9%, Fig. 13.7(d)). Six sharp first order peaks and the presence of higher order reflections are clearly seen on the FFT image (Fig. 13.7(d) inset) demonstrating the almost perfect hexagonal order spreading over area of $0.2\text{--}2 \mu\text{m}^2$. We assume that the well ordered structure is promoted by aggregation of HABA molecules. The re-alignment occurring in SMA is reversible, relatively fast, and can be repeated several times for not rinsed films.

Kinetics of the re-alignment was monitored by analysing morphology of the films as a function of time and swelling degree (evaluated with ellipsometry). We found out that the re-alignment began upon exposure to saturated vapor of solvent if the swelling approached 2.5 times increase of film thickness (in our experiments

this swelling degree was observed in 10 min). Then the completed re-alignment was approached in about 10 min. Very similar kinetics was observed for different solvents.

It is noteworthy, that the same behavior was found for substrates of *different chemical compositions*, for example PS brush, gold, ITO-glass, Ni. Thus, the film morphology is insensitive to the substrate surface nature.

The fast switching between two different alignments of the cylindrical domains and the indifference of alignment to the substrate surface energy evidences for the very strong modification of the SMA film behavior as compared to BC films. Reconstruction of BC films morphology by vapor or thermal annealing was reported in literature [22, 23, 31]. However, this process is typically very slow and usually results in morphologies representing co-existence of different alignments of nanodomains. Perpendicular orientation/reorientation requires combination of thermal annealing with strong electric field and occurs even more slowly [26, 46]. The “neutral surface” approach is limited by film thickness of about one period and requires sufficient time and temperature [45]. In contrast, the SMA films demonstrate ordering in either $C\perp$ or $C\parallel$ orientation *without* influence of additional external stimuli.

The experiments were performed in different solvents and we found that the stability of the $C\perp$ alignment increased with the increased reactivity of the solvent in formation of hydrogen bonds. For example, the $C\parallel$ alignment was found in toluene and chloroform. The SMA film deposited from THF exhibits a co-existence of $C\parallel$ and $C\perp$ structures, while in 1,4-dioxane the $C\perp$ structure is stable.

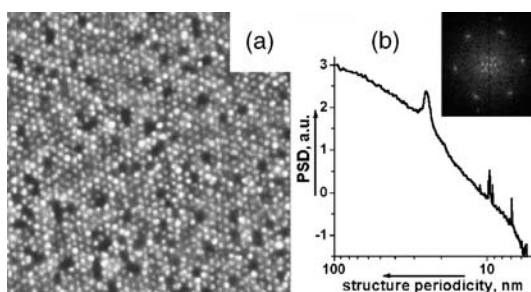
Taking into account the above mentioned behavior and the structure of the SMA film we may speculate that the reversible and dynamic supramolecular aggregation between PVP and HABA via hydrogen bonds may introduce the mechanism of self-adapting of the interface composition. Redistribution of HABA molecules between bulk and interface occurs to approach a minimum interface energy for the particular alignment and environment, making the morphology to be insensitive to the confining surface. Solvent plays a very important role competing with PVP for HABA molecules so that a subtle interplay between HABA-PVP-solvent interface interactions may result in conditions to switch in the mechanism as it proved by the FTIR spectra (Fig. 13.4(b)). This mechanism helps to overcome surface dominant alignment as compared to BC films. The detail investigation of the mechanism requires consideration of many parameters and it is out of the focus of this contribution. The prevalent role of HABA is the subject of our future investigations.

It is noteworthy, that the walls of the channels formed after rinsing with methanol are constituted from the brush of PVP chains. The free space left by HABA molecules can be reversibly occupied by swollen PVP chains upon exposure the membrane to selective solvent or acidic aqueous solution. Thus, the fabricated membranes belong to the class of smart membranes with uniform reactive channels of a narrow distribution in size.

13.4 Nanoreactors for Nanoparticles

The nanomembrane prepared by rinsing in methanol of the SMA film in the $C\perp$ orientation on the gold coated Si substrate was filled with Ni clusters. Nickel was introduced into the cylindrical channels of the membrane via electrodeposition method. Then we washed out the polymer template with THF. The well ordered lattice of Ni dots of 15–20 nm in the diameter, 10 nm in the height with 24 nm in the period was observed with AFM (Fig. 13.8). Taking into account the widening effect of AFM tip, the apparent size of the dots is in good agreement with the nanotemplate channel diameter (8 nm). Few defects (lacunas) appear in the array of Ni dots due to the non uniform electrodeposition kinetics of the metal clusters in nanochannels. Besides the potential application, this experiment gives evidence that the cylindrical channels cross the membrane from the top to the bottom.

Fig. 13.8 Ni dots electro-deposited throughout 45 nm thick PS-PVP nanotemplate, lateral scale $1 \times 1 \mu\text{m}^2$: (a) topography image, z scale 30 nm, (b) power spectrum density, the main peak (24 nm) corresponds to the SMA periodicity. Inset: FFT image of (a) showing perfect hexagonal ordering of Ni dots. Occasional lacunas appear due to inhomogeneity



13.5 Conclusions

Self-assembled polymer materials in the twenty-first century may represent building blocks comparable to those of alloys, plastics, and semiconductors in the twentieth century. Opportunities offered by self-assembled materials are becoming a significant factor in current research directions in the fields of polymer chemistry, physics and materials science. Polymer self-assembled materials, and especially those based on supramolecular block copolymer assemblies open a venue to new technologies of fabrication of nanometre scale arrays with a wide variety of optical, magnetic, electronic properties as well as biological applications.

References

1. Lawrence DS, Jiang T, Levett M (1995) Self-assembling supramolecular complexes. *Chem Rev* 95:2229
2. Whitesides GM, Mathias JP, Seto CT (1991) Molecular self-assembly and nanochemistry – a chemical strategy for the synthesis of nanostructures. *Science* 254:1312
3. Whitesides GM, Boncheva M (2002) Beyond molecules: self-assembly of mesoscopic and macroscopic components. *Proc Natl Acad Sci USA* 99:4769
4. Masuda H, Fukuda K (1995) Ordered metal nanohole arrays made by a two-step replication of honeycomb structures of anodic alumina. *Science* 268:1466
5. Choi J, Nielsch K, Reiche M, Wehrspohn RB, Gösele U (2003) Fabrication of monodomain alumina pore arrays with an interpore distance smaller than the lattice constant of the imprint stamp. *J Vac Sci Technol B* 21:763
6. Masuda H, Yotsuya M, Asano M, Nishio K, Nakao M, Yokoo A, Tamamura T (2001) Pattern of nanometer dimensions based on self-compensation properties of anodic porous alumina. *Appl Phys Lett* 78: 826
7. Nielsch K, Wehrspohn RB, Fischer SF, Kronmüller HJ, Barthel J, Kirschner J, Schweinboeck T, Weiss D, Gösele U (2002) High density hexagonal nickel nanowire arrays with 65 and 100 nm-periods. *MRS Symp Proc* 705:Y9.3.1
8. Sauer G, Brehm G, Schneider S, Nielsch K, Wehrspohn RB, Choi J, Hofmeister H, Gösele U (2002) Highly-ordered monocrystalline silver nanowire arrays. *J Appl Phys* 91:3243
9. Spatz J, Mössmer S, Möller M, Kocher M, Neher D, Wegner G (1998) Controlled mineralization and assembly of hydrolysis-based nanoparticles in organic solvents combining polymer micelles and microwave techniques. *Adv Mater* 10:473
10. Spatz JP, Roescher A, Möller M (1996) Gold nanoparticles in micellar poly(styrene)-b-poly(-ethyleneoxide) films. *Adv Mater* 8:337
11. Spatz JP, Herzog T, Mössmer S, Ziemann P, Möller M (1999) Inorganic-polymer hybrid systems: a tool for nanolithography. *Adv Mater* 11:149
12. Hamley IW (1998) *The Physics of Block Copolymers*. Oxford University Press, Oxford
13. Matsen MW (2001) The standard Gaussian model for block copolymer melts. *J Phys Condens Matter* 14:R21
14. Bates FS, Fredrickson GH (1990) Block copolymer thermodynamics: Theory and experiment. *Annu Rev Phys Chem* 41:525
15. Fredrickson GH, Bates FS (1996) Dynamics of block copolymers: Theory and experiment. *Annu Rev Mater Sci* 26:501
16. Fasolka MJ, Mayes AM (2001) Block copolymer thin films: Physics and applications. *Annu Rev Mater Res* 31:323
17. Green PF, Limary R (2001) Block copolymer thin films: pattern formation and phase behavior. *Adv Coll Interface Sci* 94:53
18. Huinink HP, van Dijk MA, Brokken-Zijp JCM, Sevink GJA (2001) Surface-induced transitions in thin Films of asymmetric diblock copolymers. *Macromolecules* 34:5325
19. Peters RD, Yang XM, Wang Q, de Pablo JJ, Nealey PF (2000) Combining advanced lithographic techniques and self-assembly of thin films of diblock copolymers to produce templates for nanofabrication. *J Vac Sci Technol B* 18(6):3530
20. Rehse N, Knoll A, Magerle R, Krausch G (2003) Surface reconstruction of lamellar ABC triblock copolymer mesostructures. *Macromolecules* 36: 3261
21. Wang Q, Nath SK, Graham MD, Nealey PF, de Pablo JJ (2001) *J Chem Phys* 34:3458
22. Kim H-C, Russell TP (2001) Ordering in thin films of Asymmetric diblock copolymers. *J Polym Sci Part B Polym Phys* 39:663
23. Fukunaga K, Elbs H, Magerle R, Krausch G (2000) Large-scale alignment of ABC block copolymer microdomains via solvent vapor treatment. *Macromolecules* 33:947
24. Segalman RA, Hexemer A, Hayward RC, Kramer EJ (2003) Ordering and melting of block copolymer spherical domains in 2 and 3 dimensions. *Macromolecules* 36:3272

25. Schwark D, Vezie D, Reffner J, Annis B, Thomas E (1992) *J Mater Sci Lett* 11:352
26. Morkved TL, Lu M, Urbas AM, Elrich EE, Jaeger HM, Mansky P, Russell TP (1996) Local control of microdomain orientation in diblock copolymer thin films with electric fields. *Science* 273:931
27. Amundson K, Helfand E, Patel SS, Quann X (1991) Effect of an electric field on block copolymer microstructure. *Macromolecules* 24:6546
28. Amundson K, Helfand E, Quann X, Hudson SD, Smith SD (1994) Alignment of lamellar block copolymer microstructure in an electric field. 2. Mechanisms of alignment. *Macromolecules* 27:6559
29. Gurovich E (1995) Why does electric field align structures in copolymers. *Phys Rev Lett* 74(3):482
30. Huang E, Russell TP, Harrison C, Chaikin PM, Register RA, Hawker CJ, Mays J (1998) Using surface active random copolymers to control the domain orientation in diblock copolymer thin films. *Macromolecules* 31: 7641
31. Elbs H, Drummer C, Abetz V, Krausch G (2002) Thin film morphologies of ABC triblock copolymers prepared from solution. *Macromolecules* 35: 5570
32. Kim G, Libera M (1998) kinetic constraints on the development of surface microstructure in SBS thin films. *Macromolecules* 31:2670
33. Kim G, Libera M (1998) microstructural development in solvent-cast polystyrene-polybutadiene-polystyrene (SBS) triblock copolymer thin films. *Macromolecules* 31:2569
34. Turn-Albrecht T, Steiner R, DeRouchey J, Stafford CM, Huang E, Bal M, Tuominen M, Hawker CJ, Russell TP (2000) Nanoscopic templates from oriented block copolymer films. *Adv Mater* 12:787
35. Park M, Harrison C, Chaikin PM, Register RA, Adamson DH (1997) Block copolymer lithography: periodic arrays of 1011 holes in 1 square centimeter. *Science* 276:1401
36. Ruokolainen J, Mäkinen R, Torkkeli M, Mäkelä T, Serimaa R, ten Birke G, Ikkala O (1998) Switching supramolecular polymeric materials with multiple length scales. *Science* 280:557
37. Mäki-Ontto R, de Moel K, de Odorico W, Ruokolainen J, Stamm M, ten Brinke G, Ikkala O (2001) Hairy tubes: mesoporous materials containing hollow self-organized cylinders with polymer brushes at the walls. *Adv Mater* 13:117
38. Hamley IW (2003) Nanostructure fabrication using block copolymers. *Nanotechnology* 14:R39
39. Lee JY, Painter PC, Coleman MM (1988) Hydrogen bonding in polymer blends. 4. Blends involving polymers containing methacrylic acid and vinylpyridine groups. *Macromolecules* 21:954
40. Ruokolainen J, ten Brinke G, Ikkala O, Torkkeli M, Serimaa R (1996) Mesomorphic structures in flexible polymer-surfactant systems due to hydrogen bonding: poly(4-vinylpyridine)-pentadecylphenol. *Macromolecules* 29:3409
41. Dante S, Advincula R, Frank CW, Stroeve P (1999) Photoisomerization of polyionic layer-by-layer films containing azobenzene. *Langmuir* 15: 193
42. McRae EG, Kasha MJ (1964) The molecular exciton model. In: Augenstein L, Mason R, Rosenberg B (eds) *Physical Processes in Radiation Biology*. Academic, New York, pp 23–42
43. Ruokolainen J, Saariaho M, Ikkala O, ten Brinke G, Thomas EL, Torkkeli M, Serimaa R (1999) Supramolecular route to hierarchical structures: comb-coil diblock copolymers organized with two length scales. *Macromolecules* 32:1152
44. Wedgewood AR, Seferis JC (1984) *Polym Eng Sci* 24:328
45. Guarini KW, Black CT, Yeung SHI (2002) Optimization of diblock copolymer thin film self assembly. *Adv Mater* 14:1290
46. Böker A, Knoll A, Elbs H, Abetz V, Müller AHE, Krausch G (2002) Large scale domain alignment of ABC triblock copolymers from solution using electric fields. *Macromolecules* 35:1319

Chapter 14

Influencing the Interface in Polymer Blends by Compatibilization with Block Copolymers

Doris Pospiech

Leibniz Institute of Polymer Research Dresden, Hohe Str. 6, 01069 Dresden, Germany,
pospiech@ifdd.de

Abstract As discussed in Chaps. 9 and 10 most polymers are incompatible with each other and form phase segregated morphologies with sharp interfaces and poor mechanical properties in binary blends. Based on thermodynamic arguments two routes for blend compatibilization are discussed: (i) the introduction of functional groups and the stimulation of interfacial interactions and reactions between components, or (ii) the addition of block copolymers as compatibilizers. Several examples of the effect of compatibilization of polymer blends are given and discussed with respect to interface, morphology and properties.

14.1 Introduction: Why Block Copolymers and Polymer Blends?

All systems that are thermodynamically demixed or heterogeneous contain a large amount of interfaces between the demixed phases. The nature of these interfaces, i. e., their thickness and mechanical strength, determines mainly the macroscopic properties of the resulting materials, for instance mechanical properties and stability. This is particularly true in all materials containing polymers. Mixtures of polymers (polymer blends) or mixtures of polymers with other organic or inorganic materials are in most cases heterogeneous, or, in other words, thermodynamically immiscible. However, physical mixtures of polymers have high practical relevance because they have often been used to tailor the property profile of polymeric engineering materials.

The basic idea of polymer blends was based on the assumption that a combination of two or more polymers in one material would result in a combination of the advantageous physical properties of the polymers contained, whereas negative properties could be outbalanced or even superimposed by property synergies [1–3]. A significant improvement of properties and the extension of the application fields

of polymers was expected. Moreover, simple mixing of polymers in melt or solution was regarded to be a faster and cheaper way to develop new materials than synthesis of polymers with a new chemical structure [1]. Therefore, the field of polymer blends is increasingly growing with about 10 % growth per year [3].

The development of materials by polymer blending has a very long tradition and was already performed even before the term “polymer” was scientifically defined [2]. Mixtures of polymers have been used:

- To combine high toughness and high stiffness of polymers in one material
- To improve the processability of polymers in the melt by adding an easy-flowing polymer
- To enhance the dimension stability and heat deflection temperature of a polymer by adding a high T_g polymer
- To improve the barrier properties of a polymer by adding a polymer with high crystallinity

Thus, ABS enhances the melt processability of PVC. Addition of ABS has also turned out to be a tool to enhance the toughness and impact behaviour of brittle polymers like polycarbonates. Liquid crystalline polymers (LCP) are used to lower the high melt viscosity of high performance resins like polyethersulfone, as well as to improve the mechanical strength, chemical stability and dimension stability of engineering plastics like polyamides and polyesters [4–6]. Many other examples of commercialized polymer blends can be found which were invented to tailor the property profile of polymeric materials [1, 3].

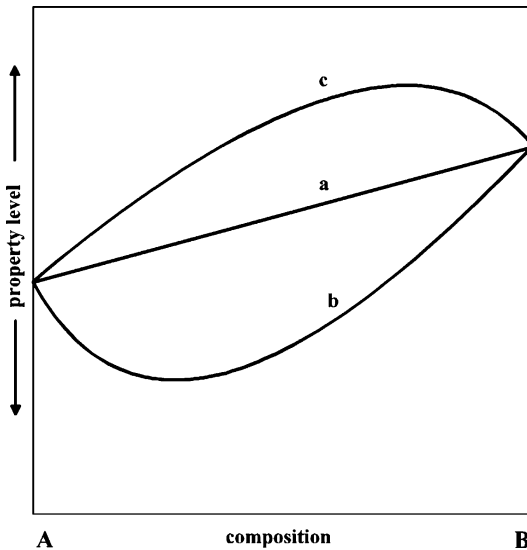


Fig. 14.1 Compositional influences on the properties of polymer blends (a) additivity: miscible polymer blend; (b) immiscible polymer blend; incompatible; (c) synergy; compatible polymer blend

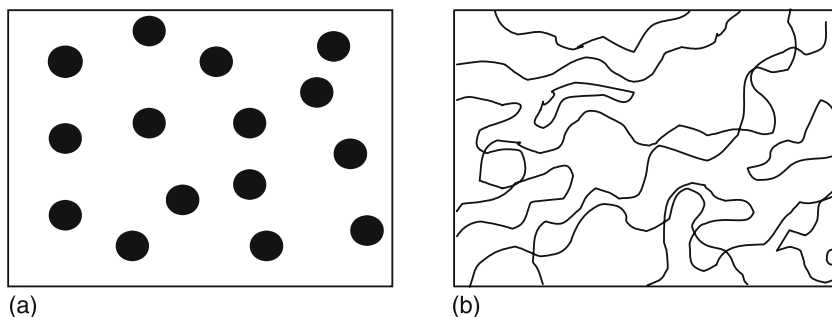


Fig. 14.2 Schematic phase morphologies of immiscible polymer blends consisting of polymers A and B according to Bates [7]: (a) disperse phase morphology; (b) continuous morphology

The properties of polymer blends are however very sensitive to the state of miscibility in the material. The change of a certain property (like E-modulus, tensile strength, glass transition temperature, melt viscosity or others) with the composition of the blend in dependence on the state of miscibility is illustrated in Fig. 14.1.

The desired combination of properties results in the case of additivity (curve a) depending on the concentration of the blend components. A property synergy, i. e., a maximum in the curve as shown in curve (c) can be found very seldom. In most cases of immiscible blends curve (b) is observed: the property of the resulting polymer blend is in each composition below the level of the mixed homopolymers and goes through a minimum. The main reason for this behaviour is the thermodynamic immiscibility of polymers which causes heterogeneous, biphasic mixtures with a large number of interfaces. The interfacial adhesion between immiscible polymers is usually very low and the interface is very thin, typically in the range of 2–3 nm. Moreover, in the demixed system, the polymers are driven to minimize their interface, resulting in typical demixed morphologies, as illustrated in Fig. 14.2.

If the volume fraction of polymer A is lower than that of polymer B, a disperse phase of A within a matrix of B is observed (Fig. 14.2(a) with A as black dots). If the volume fractions of both polymers are roughly equal, a continuous morphology can be found (Fig. 14.2(b)), and if the volume fraction of B is larger than that of A, B forms the disperse phase in the A matrix (Fig. 14.2(a) with B as black dots). The dimensions of the phases depend on the degree of demixing and range between 0.1 up to several hundreds of micrometres. This state is called *macro-phase separation* and is typical for immiscible polymer blends [7]. Upon annealing at higher temperature, the demixed morphology can change further driven by the thermodynamic rule of minimization of surface area and usually further demixing is obtained. Droplets of the disperse phase can coalesce, resulting in an increase of drop radii, and continuous structures usually show spinodal decomposition. Thus, the dimensions of the typical demixing structures raise further, which

can often be observed during melt processing of polymer blends, i. e., by injection moulding [8].

The intention of this chapter is to enlighten *chemical* strategies that have been reported to influence the compatibility of polymer blends positively in the framework of thermodynamic miscibility of polymers. Possibilities to estimate miscibility of polymers will be discussed and recent developments to investigate the interfaces in “real”, non-model polymer blends will be shown. All the other parameters that also affect the morphology and properties of polymer blends, for instance material parameters like melt viscosity or melt rheology in general, as well as influences of melt processing parameters will not be considered here.

14.2 Miscibility of Polymers: Thermodynamic Basics

Flory explained the thermodynamic immiscibility of the most polymers by a simple grid model [9]. By placing the segments of two macromolecules on a grid he could easily demonstrate that the probability that segments of one polymer are completely surrounded by segments of the second polymer is statistically very small, i. e., the free entropy of mixing (ΔS_m) is almost zero. Moreover, the enthalpy of mixing (ΔH_m) is often positive (i. e., mixing is endothermic). Hence, the thermodynamic condition for a molecular mixture:

$$\Delta G_m = \Delta H_m - T\Delta S_m < 0 \quad (14.1)$$

is very seldom fulfilled. The thermodynamic condition of miscibility ($\Delta G_m < 0$) is the same as for low molecular compounds:

$$(\delta^2 \Delta G_{\text{mix}} / \delta^2 \phi_i) T, p > 0. \quad (14.2)$$

ΔG_m can be described in polymers by the Flory–Huggins equation (14.3):

$$\Delta G_m = RTV_c [(\phi_A/N_A) \ln \phi_A + (\phi_B/N_B) \ln \phi_B + \chi_{AB} \phi_A \phi_B] \quad (14.3)$$

where R is the gas constant, T is the temperature in K, V_c is the molar volume of each segment, ϕ_A , ϕ_B are the volume fractions of polymers A and B in the mixture, N_A , N_B are the number of segments in the polymers A and B and χ_{AB} is the Flory–Huggins interaction parameter describing the interactions between A and B segments.

The parameters mainly determining miscibility are the volume fractions ϕ_A and ϕ_B in the mixture (composition), the molar volumes of the polymers A (V_A) and B (V_B), representing the size of the segments on their places, as well the interaction parameter χ_{AB} , reflecting indirectly the chemical structure of the polymers.

Although a large number of efforts has been made [7, 10–17], prediction of the miscibility of polymers remains still very complicated. One possibility is given by regarding the solubility parameters δ of the two polymers blended [12, 13, 17, 18].

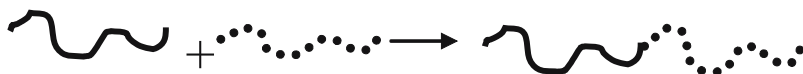


Fig. 14.3 Formation of diblock copolymers by covalent linking of the ends of two polymer chains

The lower the difference between δ_A and δ_B , the lower is the resulting interaction parameter χ_{AB} , and the higher is consequently the probability of an homogeneous system. According to Painter and Coleman [18], in each system a critical difference of solubility parameters $\Delta\delta_c$ exists below which miscibility can be reached. $\Delta\delta_c$ typically ranges between 0.1 (for polymer blends with dispersive interactions) and 3.0 (for polymer blends forming strong H-bonds between the blend partners). This rule is also reflected by (14.4), an estimation to obtain χ_{AB} [16]:

$$\chi_{AB} = (\delta_A - \delta_B)^2 V_c / RT. \quad (14.4)$$

There are a number of deviations from this rule. Also, the seldom case of negative χ_{AB} cannot be described by this equation.

The solubility parameters necessary for solution of (14.4) can either be determined experimentally, for instance by determination of solution viscosities in certain solvents or by swelling measurements [19], and other methods, or calculated by increments, for example with the method proposed by Van Krevelen [16, 20] according to (14.5):

$$\delta = \rho \sum F_i / M_0 \quad (14.5)$$

where ρ is the density, F_i are the group contributions and M_0 is the molecular weight of the polymer repeating unit.

Interaction parameters may be directly determined experimentally by neutron reflectivity measurements using the determination of the thickness of model double layers of polymers, as reported in detail by Stamm and coworkers [21]:

$$1 = (2^a/2) \cdot (\chi/\chi_c - 1) 1/2 / (\chi_c 3/2) \quad (14.6)$$

with a as characteristic segment length, χ as interaction parameter, $\chi_c = 2/N$ as critical interaction parameter.

From (14.6) it becomes obvious that an increase in miscibility of two polymers consequently broadens the interfacial thickness between both, which opens the opportunity to use this principle to enhance miscibility in polymer blends by an “artificial” increase of the interfacial thickness. Thus, immiscible phases are rendered to be “more compatible”. The process of doing so is called (thermodynamically not correct, but often used) “compatibilization”. Compatibilization methods for two immiscible polymers will be discussed more detailed in Sects. 14.3 and 14.4.

Let us first imagine that the two ends of both immiscible polymer chains are linked by only one covalent bond, as shown in Fig. 14.3.

In this case a diblock copolymer of the structure A-B is formed. Although the chemistry of both blocks is not altered compared to the blend, the single covalent bond between the polymers causes the macrophase separation on a micrometre scale to not occur. Only *microphase separation* on a scale related to the length of

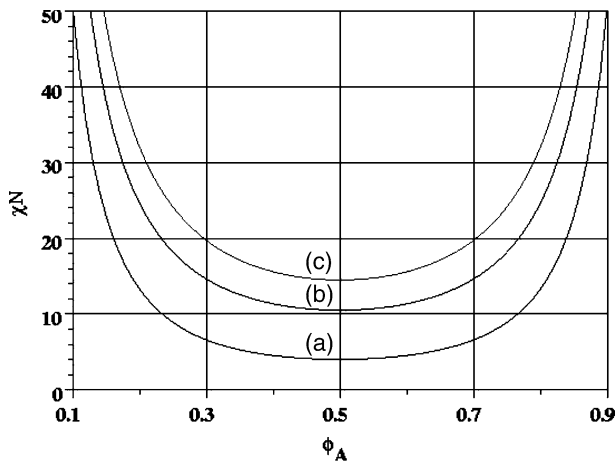


Fig. 14.4 Comparison of phase diagrams of blends (a), diblock copolymers (b) and segmented block copolymers (c)

both homopolymer chains (typically in the nanometre range) can be observed. The typical microphase separation in diblock copolymers results in a number of distinct periodic micro- or better nanostructures that have been already discussed in this book in Chaps. 11 and 13, as well as reported in detail in the literature, see, for example [22–27].

The onset of phase separation in block copolymers requiring as in blends $\Delta G_M < 0$ can be estimated by mean field calculations and is expressed in phase diagrams [22, 23, 28–30]. Figure 14.4 illustrates the large difference between the phase diagram of an immiscible blend and a diblock copolymer with two flexible, monodisperse blocks. As soon as the blocks are connected by chemical bonds, the spinodals are shifted to higher χN , i. e., the homogeneous, non-phase separated region is extended. The higher the number of blocks in the block copolymer, the larger is the region of the homogeneous state. Block copolymers with more complicated structure require larger χ_{AB} values or higher molecular weights of the blocks to obtain microphase separation. This general principle can be used to change the miscibility between two polymers, resulting in an altered physical behavior of the whole blend (which will be discussed in more detail in the next section).

$(A-B)_1$ (b) and segmented block copolymers $(A-B)_n$ with $n=8$ (c), calculated by the mean field method by Friedel et al. [29] according to Benoit et al. [28]

An increasing number of linkages between the two blocks results in the formation of block copolymers with different architecture (Fig. 14.5).

The macroscopic properties of block copolymers are sensitive to the number of blocks of A and B in $(A-B)_n$ architectures. Spontak et al. [31] reported an increase of mechanical parameters like tensile strength and E-modulus in poly(styrene-*b*-isoprene) $_n$ block copolymers with increasing number of n , but comparable total molecular weight. Obviously, the higher intermixing between the phases in $(A-B)_n$ block copolymers and more entanglements enhance the mechanical strength, while

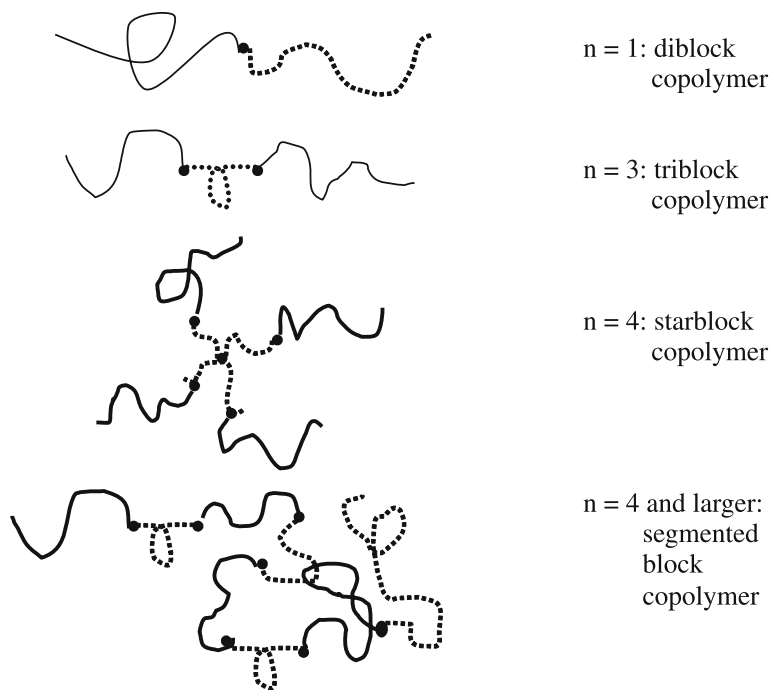


Fig. 14.5 Schematic architecture of block copolymers consisting of two chemically different blocks and different number of linking units (thin line: A-block; dotted line: B-block), according to Bates [22]

sharp interfaces in diblock copolymers act as hyphenation points between the phases upon mechanical stress. The special structure of block copolymers gives rise to special applications that can almost exclusively be achieved with these architectures. Examples are:

- Thermoplastic elastomers [32]
- Thermoplastic materials with high impact strength [1, 32, 33]
- Coatings and films with tunable wetting properties from lattices [34]

Block copolymers often behave as amphiphilic molecules owing to the different chemistry of the linked blocks [25, 26, 34–36]. Therefore, they can act as polymeric emulsifiers [26, 34], which is one of the main reasons for their use as compatibilizers in polymer blends. This topic will be outlined in the next section.

14.3 Compatibilization of Immiscible Polymer Blends: General Options

In Sect. 14.2 we could conclude from the thermodynamics of polymer mixtures that the interfacial thickness between two phases is raised if miscibility is increased. The

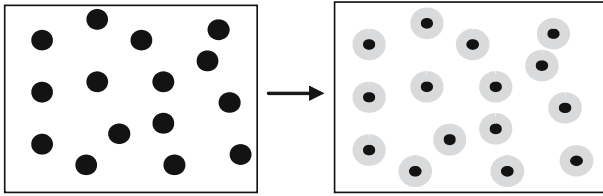


Fig. 14.6 Modification of the interface in immiscible polymer blends (white: polymer matrix A; black: disperse phase B) by compatibilization (gray: interface between disperse phase B and matrix A)

final limit is an interface with infinite thickness in case of the miscible system. Thus, tailoring the interfacial thickness is one of the keypoints of changing the properties of an immiscible polymer blend. The modification of the interface by compatibilization (widening of interface) is schematically shown in Fig. 14.6.

A variety of methods to extend the interfacial thickness between two immiscible polymer phases and to increase the interactions between the phases have already been reported in the last decades and a number of extensive summaries is available in the literature for further reading [1, 37, 38]. The most important methods are summarized below:

1. Introduction of specific interactions between the blend partners, lowering the enthalpic contribution ΔH_M [10]
2. Reactions between the blend partners: in situ formation of block and graft copolymers during blending (reactive blending) [4, 5, 35, 37–39]
3. Adding block or graft copolymers consisting of blocks chemically comparable to the blend components to the immiscible blend, leading to the thermodynamically driven segregation of the block or graft copolymer to the interface between the phases [1, 6, 11, 14, 15, 40, 41]

Besides these main methods, a lot of exotic methods like adding reactive fillers or low molecular reactive compounds to the blend system causing the formation of reactive groups in the phases or cross-linking between the phases [1] are known. In the following, only the above mentioned main methods will be outlined.

14.3.1 Introduction of Specific Interactions

The interaction between two immiscible polymers can be enhanced if the chemistry of the polymers is modified in a way that specific interactions between the two phases develop. According to Painter and Coleman [10] the following interactions can be used to enhance miscibility:

- H-bonds (strong interaction)
- n - Π -complexes between oxygen ion pairs and Π -electrons of aromatic rings

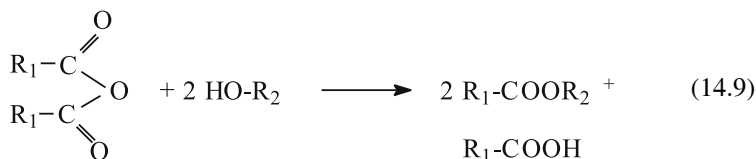
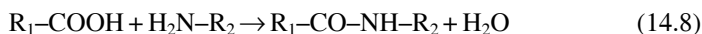
- Ion–dipole interactions [1]
- Ion–ion interactions [1]

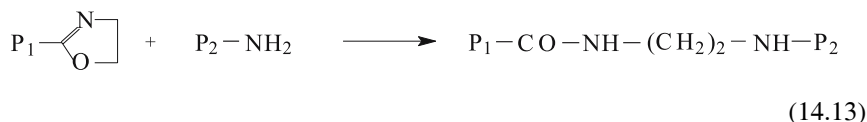
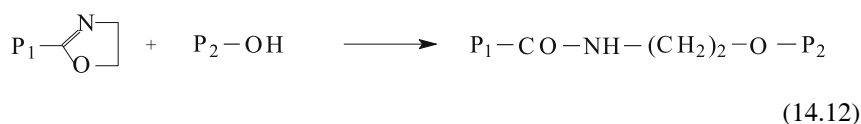
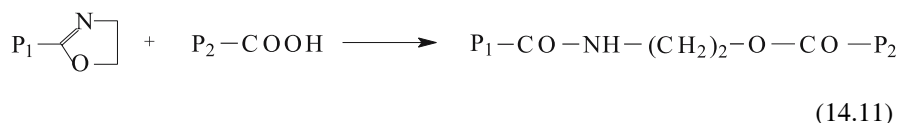
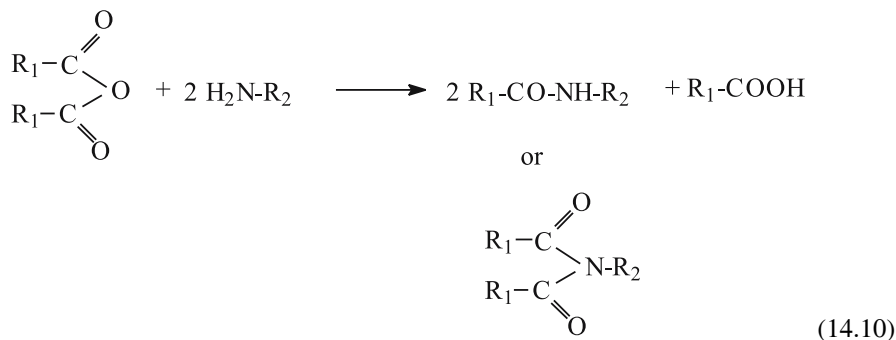
The strength of the intermolecular interaction increases in the order donor–acceptor complexes ~ H-bonding < ion–dipole interaction < ion–ion interaction [1] and determines significantly the change of miscibility. The stronger the specific interaction, the more miscibility increases.

The miscibility of polystyrene with polymers containing ester bonds like PMMA, PEMA SAN PC, PPO, PET and others can be enhanced if OH-groups are incorporated into the polystyrene chain, e. g., by copolymerization with p-hydroxystyrene and other copolymers. As one example the blend of poly(p-hydroxystyrene) and poly(n-alkylmethacrylates) may serve. The strength of the H-bonding between both is higher with poly(n-alkylmethacrylates) with shorter alkyl groups (up to $n=5$), thus, miscibility could be shown to be higher in this case than with longer alkyl substituents [10]. More examples can be found in literature using this method.

14.3.2 Reactions Between the Polymer Phases in the Blend

If this method is considered to be used in enhancing miscibility, only reactions can be selected proceeding relatively fast during the melt blend procedure which might take some minutes in a discontinuous melt mixer (often used on lab scale), but only short time, typically about 60 seconds in a conventional continuous melt mixer like extruders. A summary of the most important, fast reactions for reactive blending is given in (14.7)–(14.13). Further applicable reactions can be found in the review literature [1, 37–39].

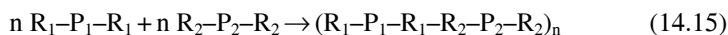
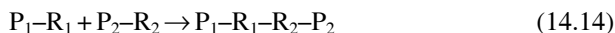




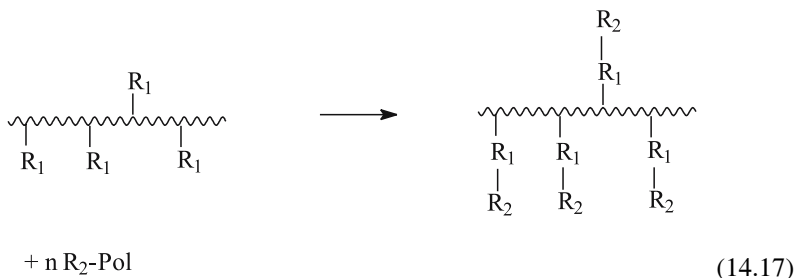
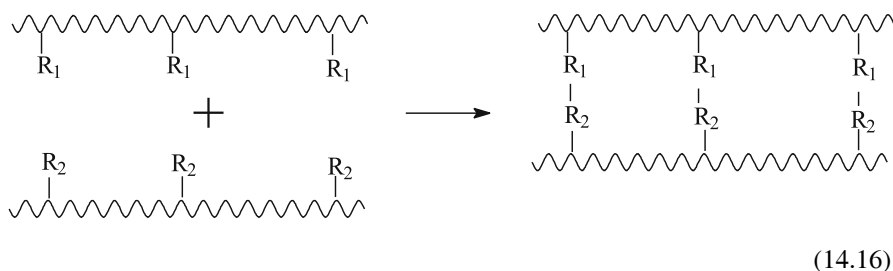
While reactions between carboxylic acids and OH- or amino-groups proceed rather slowly, the reactions between anhydride groups and OH- or amino groups in polymer melts at elevated temperatures are fairly fast and take only some minutes. The reaction of cyclic groups like oxazolines with carboxylic groups takes only about a minute at about 200°C and can very successfully be applied in polymer melts. Practical applications of these reactions will be given in Sect. 14.4.1.

To increase miscibility in a polymer blend, both blend partners have to be completely or partially equipped with functional groups able to undergo reactions with each other, as outlined above. Thus, the two blend polymers can be terminated with one or two end groups (14.14) and (14.15) with adequate reactivity, with reactive substituents along the polymer chain allowing different types of reaction (14.16) and (14.17) or heterolinkages that are already contained in the polymer, as ester or amide groups, might react with those of neighbouring chains (14.18) and (14.19):

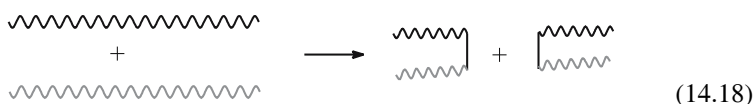
Reactions of two polymers via end groups:



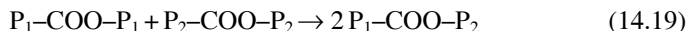
Reactions of two polymers via pendant reactive groups (substituents):



Exchange reactions between two different polymer chains:



which can be, for example, transesterification:



Reactions according to (14.14) result in the formation of diblock copolymers, equation (14.15) leads to segmented (multiblock) copolymers, while reactions (14.16) and (14.17) give graft copolymers. Exchange reactions according to (14.18) and (14.19) finally result in copolymers containing chain segments of the starting homopolymers (blend partners) distributed randomly along the chain, with a certain degree of blockiness as intermediate state. All these reactions have been used in real blend systems, as outlined in Sect. 14.4.1.

It should be noted that the interfacial tensions within such reactive systems are quite complicated and considering the interfacial tension in the starting blend component can only give a first indication. If both polymers are equipped with reactive groups, the situation changes dramatically. Fleischer et al. [42,43] were able to show that introduction of only one amino group into PDMS resulted in a reduction of interfacial tension by 20 % in blends of PDMS with polyisoprene.

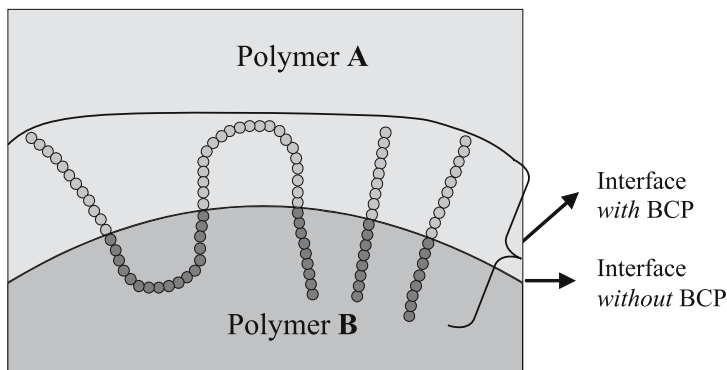


Fig. 14.7 Arrangement of block copolymers at the interface of polymer blends (left: segmented block copolymers; right: diblock copolymers)

14.3.3 Block Copolymers as Compatibilizers

Block or graft copolymers with blocks having a chemical structure comparable to that of the blend components or which are at least thermodynamically miscible with the respective blend components may be added to immiscible polymer blends. The interfacial active block copolymer (BCP) migrates in the melt or upon annealing of the blend above the glass transition temperature to the interface of the two phases and arranges there according to its architecture (Fig. 14.7). In the case of diblock copolymers (right) the A-block is located in the phase of polymer A and the B-block in polymer B. Segmented block copolymers (left) are considered to arrange flat (in a pancake-like structure, according to Noolandi et al [14, 15]) at the interface. From Fig. 14.7 it can easily be concluded that the interface with block copolymer should be widened significantly by the block copolymers, independently of their chain architecture. However, it has been pointed out that diblock copolymers are more efficient than segmented block copolymers and, particularly, random copolymers [11, 14, 15, 41].

Most of the analytical methods for interfaces in polymer blends, such as neutron scattering, X-Ray reflectivity etc. work only for flat, smooth double layer model systems. In contrast, only a few analytical methods that are able to analyse interfaces in real blends have been reported until now. Beside direct methods as transmission electron microscopy, one of the most promising new methods is positron annihilation lifetime spectroscopy allowing the determination of the interphase volume in a real blend [44–47].

From the schematic drawing in Fig. 14.7 it is also obvious that the segments of the block copolymer used for compatibilization need to have a certain minimum number of repeating units, i. e., a certain molecular weight. Otherwise A and B blocks would not be able to entangle far enough into the respective homopolymer phase (for diblock copolymers) or to form loops able to penetrate into the homo-

polymer phases. The minimum or critical segment molecular weight is related to the so-called entanglement molecular weight M_e and should at least exceed M_e . M_e can be regarded as the molecular weight necessary to form coiled, interpenetrated polymer chains [18]. It depends strongly on the basic chemical structure of the repeating units: for polycondensates it was measured to be in the range of 2000 to 6000 g/mol, while polymerization polymers with only C–C linkages in the main chain gave values of at least 15000 g/mol (for instance, for polystyrene).

Beside *extension of the interfacial width*, block copolymers also lower efficiently *the interfacial tension* between two homopolymers which was demonstrated in calculations theoretically by Noolandi [14, 15, 17]. The calculated interfacial energies dropped with increasing molecular weight of the block copolymer segments. Lower interfacial tension supports the dispersion of the minor component and leads to more homogeneous particle size distributions in the blend (emulsifying effect) [35, 36]. Moreover, disperse phases that are surrounded by block copolymer films are more stable upon processing in the melt and after processing, making the macroscopic behavior of the material at all more stable and predictable.

A third effect of adding block copolymers reported is the mechanical reinforcement of the interface resulting in an improved fracture toughness which was proven experimentally for several blend systems [11]. Also here the block molecular weights play an important role: if they are below M_e , the blocks do not stick to the respective homopolymer phases and upon shear stress the interfaces break, resulting in a macroscopic fracture of the material.

Besides segment molecular weights also the concentration of the block copolymer added in the blend is an essential parameter: only the amount necessary to form a thin film around the dispersed particles should be added (typical block copolymer concentrations from 0.5 to 5 % block copolymer in the blend). Otherwise, the block copolymer forms a further separate phase, enhancing the overall heterogeneity of the blend.

Block copolymers as compatibilizers are particularly important in blends containing two immiscible polymers which are not able to undergo reactions with each other, as, for instance, in mixtures of high performance polymers (like poly(ether ether sulfone)s and poly(ether ether ketone)s).

14.4 Compatibilization in Polymer Blends: Examples

14.4.1 *Compatibilization by Using Reactions Between the Polymers*

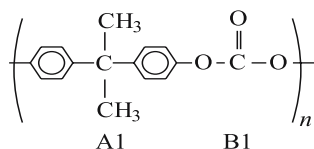
Compatibilization using reactions between the blend partners usually requires the introduction of reactive groups because most of the polymers do originally not have any functional groups incorporated in the polymer chain. With partial or complete substitution of the blend polymers by functionalized ones having a com-

parable main chain, the whole blend system (interaction parameter, interfacial tension and so on) is changed. Only in blends where exchange reactions between linkage groups according to (14.18) and (14.19) can occur the addition of functionalized polymers is not required.

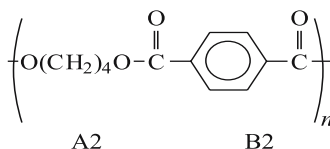
Exchange reactions between different ester groups as well as different ester and amide groups are observed in blends of different polyesters (e.g., PET/PBT; PET/liquid crystalline polyesters (LCP)), of polyesters with polycarbonate (e.g., PET/PC; PBT/PC; LCP/PC), and in blends of polyesters with polyamides (e.g., PET/PA-6), rendering the mixture from an immiscible to a compatibilized blend. Transesterifications or transamidations can only occur in the melt, usually above 200°C, during the melt blending process or in a post-annealing step after processing and shaping. They are catalysed by the same catalysts used for polyester synthesis, and usually it is not necessary to add further catalysts because polyesters still contain the one from synthesis. As melt polycondensation itself, transesterifications are diffusion-controlled and depend on temperature, shear stress, number of interfaces and other parameters [48, 49].

Pompe [50] investigated blends of polycarbonate (PC) and polybutylene terephthalate (PBT) and proved the occurrence of transesterification reactions according to the general equation (14.20):

PC:



PBT:



Segment designation:



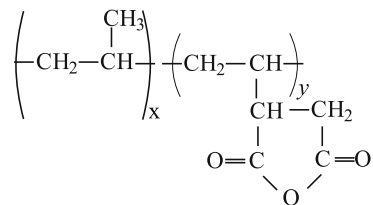
The reaction rate is determined by the concentration of the catalyst and the temperature [49]:

$$k = 3.22 \times 10^{25} (c_{\text{kat}})^{2.5} \exp(-A/RT). \quad (14.21)$$

The resulting products are block copolymers consisting of PC and PBT blocks which are formed at the interface between PC and PBT, acting as compatibilizers in the blend. Transesterification reactions in PC/PBT blends with a 50/50 wt/wt composition may increase the impact strength by up to the 16-fold. Thus, even impact strengths higher than for pure PC may be obtained which can be discussed as synergistic effect of block copolymer formation.

Transesterification reactions play also an important role in blends of liquid crystalline polyesters (LCP) with engineering resins like polyesters and PC. Blending LCPs with other polymers has been performed to obtain a combination of advantageous properties of LCP, like high melt viscosity and excellent mechanical strength, with those of the engineering plastics like PET, PBT or PC, thus yielding well-processable materials with excellent property profile at lower price than for pure LCP. Several investigations (for instance [51]) proved the occurrence

Fig. 14.8 Chemical structure of maleic anhydride grafted polypropylene (PP-g-MA)



of transesterification in LCP blends with PET, PBT or PC by direct (NMR) or indirect (DSC, TEM, SEM, WAXS) methods.

Polyolefines are one of the most important class of polymers characterized by low cost, low density for lightweight applications, superior low-temperature impact strength, good overall mechanical performance and high chemical resistance [52]. Blends of polyolefines, particularly polypropylene (PP) have been developed to combine these properties with those of engineering plastics to improve strength and E-modulus, heat stability and heat deflection temperature, and to extend the application fields. However, polyolefines are highly unpolar owing to their chemical structure and therefore, they are not miscible with other polymers. Blends of polyolefines usually show significant macrophase separation, and consequently the initial property profile is awful. Compatibilization of polyolefine blends by partial or complete functionalization is therefore essential to obtain the desired property level. One of the most common methods of polypropylene functionalization is grafting with unsaturated carboxylic acid anhydrides, carried out either in a continuous process in the melt (as reactive extrusion, or discontinuously in solid state [52]). Polypropylene grafted by maleic anhydride (PP-g-MA) is one of the most important functionalized polyolefines (Fig. 14.8) with an increasing number of applications (for example, as compatibilizer for glass fibre reinforced polyolefines, in wood reinforced polyolefines, as compatibilizer in nanocomposites with layered silicates, as well as starting product for polymer-analogous reactions in order to raise the polarity of PP further, resulting in glueable and paintable polyolefines).

A comparable grafting procedure was applied by Weber and coworkers [4] to prepare maleic anhydride modified polysulfone as reactive compatibilizing agents in PSU blends.

The anhydride and carboxylic groups in PP-g-MA are able to undergo esterification, amide and imide formation [see (14.9) and (14.10)] and can be used for a variety of polymer-analogous reactions with functionalized low molecular and high molecular compounds which is widely applied for compatibilization of polyolefin blends particularly during extrusion [53]. Relevant examples to be mentioned are PP/polyamide blends, PP/LCP blends as well as blends of PE (or PP) with PET, as an important contribution for the recycling of PET waste [49].

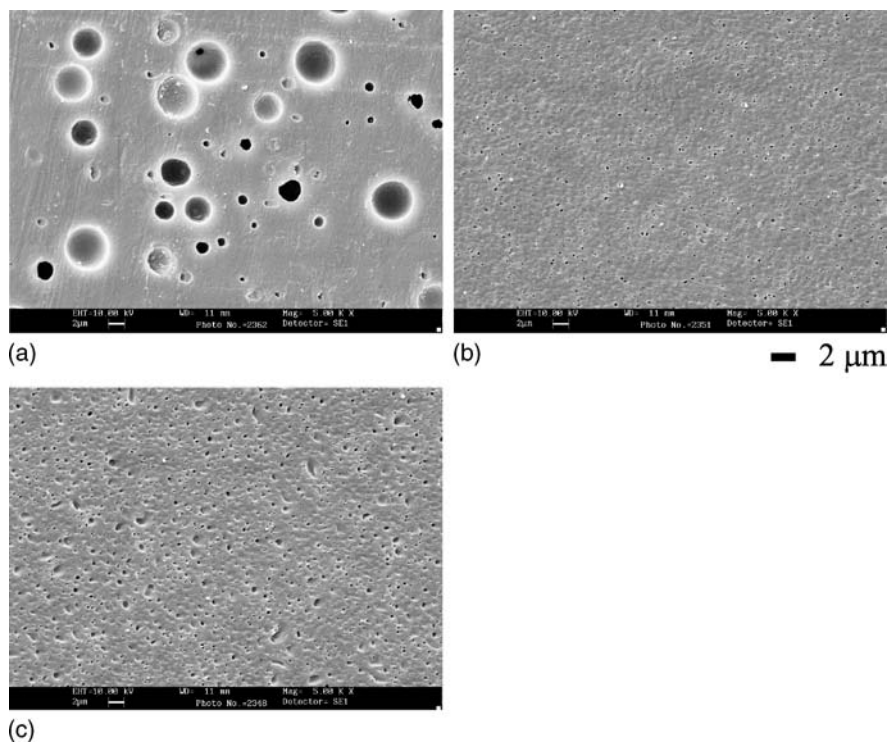


Fig. 14.9 Morphology of PP/PA blends (90/10 wt %), thin cuts of extruded strands, etched with formic acid, SEM micrographs: (a) PP/PA, (b) PP-g-MA/PA, (c) thin cut of an injection molded test bar of etched PP-g-MA/PA (90/10 wt %)

The compatibilization of PP/polystyrene (PS) blends may serve as a second example. Figure 14.10 displays the SEM morphologies of non-reactive blends of PS with oxazoline-end functionalized PP (upper pictures) in comparison to the same blend compositions containing two reactive blend partners (PS-COOH and polypropylene with oxazoline grafts). The COOH end groups of PS obtained by controlled radical polymerization [55] can react in the melt with the oxazoline grafts of PP to give a PP-PS graft copolymer which should again act as compatibilizer in the blend.

Raising concentration of PS in PP-g-Ox/PS leads to a huge increase in particle size of the disperse PS phase. The interface is again very smooth and thin. In contrast, the reaction of -Ox and -COOH in the reactive blend, according to (14.11), results in all compositions in significantly lower particle sizes and, moreover, in diffuse interfaces. The compatibilization reaction was proven by ^1H NMR investigation of the THF insoluble fraction (containing 1.5 wt % PS in a 50/50 blend of PP-Ox/PS-COOH) and by a slight increase of the molecular weight of PP-g-Ox after blend formation, as obtained by SEC. Table 14.1 summarizes the surface tensions of the polymer melts at 200°C obtained by pendant drop analysis.

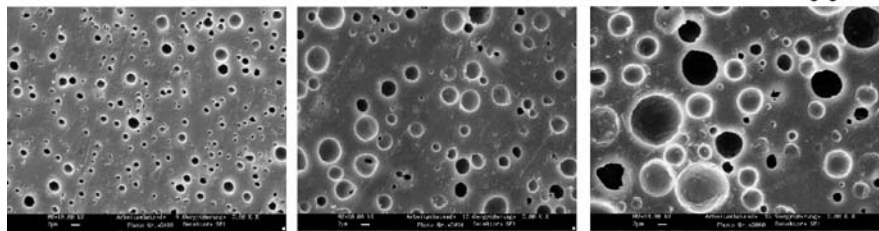
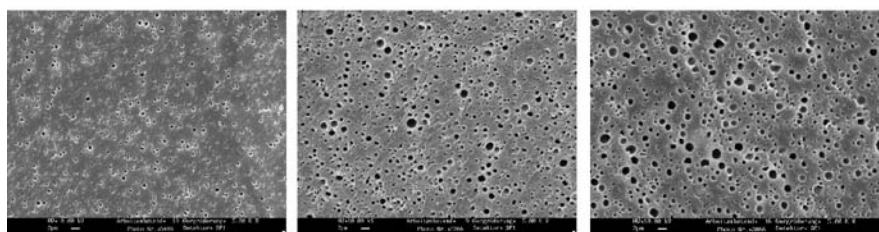
PP-g-Ox/PS20 μm **PP-g-Ox/PS-COOH****90/10****80/20****70/30****wt/wt**

Fig. 14.10 Morphological changes in PP/PS blends with different blend composition without and with reactive groups according to Pionteck [56], upper line: PP-g-OX/PS; lower line: PP-g-Ox/ PS-COOH

Table 14.1 Surface tensions of non-reactive and reactive polypropylene and polystyrene at 200°C obtained by pendant drop analysis [56]

Polymer sample	Surface tension at 200°C (mN/m)
Polypropylene	20.5
PP-g-Ox	19.7
Polystyrene	28.2
PS-COOH	28.0

It has to be noted that the interfacial tensions of the different blends at 200°C also measured by pendant drop analysis were not significantly altered by introduction of reactive groups. Increasing concentration of these reactive groups lead, however, to reduced particle sizes of the blends up to a ratio of 0.5 of $c_{\text{COOH}}/c_{\text{Ox}}$.

14.4.2 Compatibilization with Block Copolymers

Generally, all types of block and graft copolymers can be used for compatibilization of the parent homopolymer blends, as discussed in Sect. 14.3. The block copolymer arrangement at the interface is then determined by the basic polymer

structure, which was schematically shown in Fig. 14.7 for diblock copolymers and segmented block copolymers.

Detailed investigations about the reinforcement of the interface of immiscible polymer blends by *diblock copolymers* were reported by Kramer et al. [11,41]. The authors showed that symmetric diblock copolymers (e.g., with two blocks having comparable molecular weights) resulted in an increase of fracture toughness in blends of PS and polymethylmethacrylate (PMMA), as well as in blends of PS and polyvinylpyridine (PVP). The maximum fracture toughness was reached at a block copolymer concentration of 0.2 BCP chains per nm^2 [11]. From that result it could be concluded that the optimal concentration of block copolymer in the blend relates to a complete coverage of the disperse phase by the BCP. Excess concentrations lead to a drop of mechanical properties. The averaged optimal concentrations are in the range of 1 wt % BCP in the blend [57]. Diblock copolymers consisting of PS and PMMA affect a compatibilization of the parent homopolymer blends, but also act in blends of SAN and PPO although the block copolymer was in that case chemically different from the polymers mixed. With different methods it was proven that the block copolymer in each case was positioned at the interface of the blend partners [57].

The fracture toughness of blend interfaces containing *triblock copolymers* is further enhanced in comparison to the corresponding diblock copolymers, which was demonstrated by Kramer and coworkers [41] for PS/PVP blends, compatibilized by either PS-PVP diblocks or PS-PVP-PS triblocks. TEM revealed a widening and roughening of the interface allowing a better flow of mechanical stresses from the interface to the matrix. This finally increases the mechanical properties. According to that report, triblock copolymers are better suited for compatibilization as diblocks.

Practically, different triblock copolymers, for example SBS (polystyrene/polybutadiene/polystyrene triblock copolymer), SEBS (polystyrene/polyethylene/polybutadiene/polystyrene block), or maleic anhydride grafted SEBS are often used as compatibilizers in polyolefine blends [52]. SEBS is applied as compatibilizer in PE/PS blends [52] which possess an increasing importance for the development of paintable and printable polyolefines [52].

Segmented block copolymers have to be used in polymer blends of polymers which are not able to undergo reactions and where respective diblock copolymers of the blend partners are not available, which is typical for all types of polycondensation and polyaddition polymers. Basically, almost all types of blends of high performance polymers (like polysulfone (PSU), polyether ether ketone (PEEK), polyethersulfone (PES), polyphenylene oxide (PPO) or polyphenylene sulphide (PPS) require compatibilization by block copolymers.

Segmented block copolymers (multiblock copolymers) $(A-B)_n$ that are able to compatibilize immiscible blends of high performance polymers can be prepared by polycondensation type reactions [58–61]. Systematic investigations of blends of these block copolymers with the parent homopolymers showed that the state of mixing depended on the molecular weight of the block copolymer segments. In case of flexible block copolymer segments, the molecular weight has to be at least the

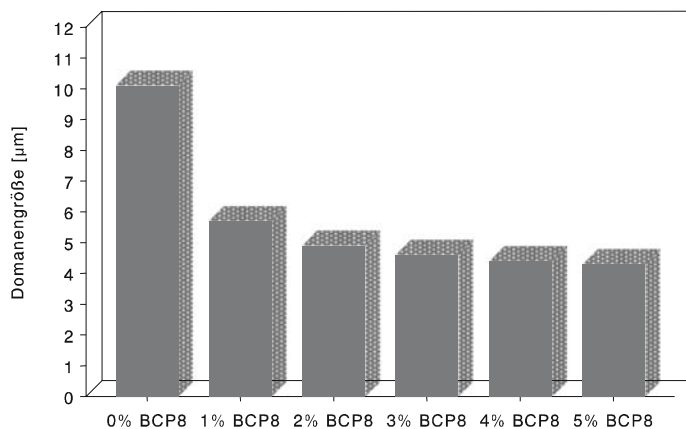
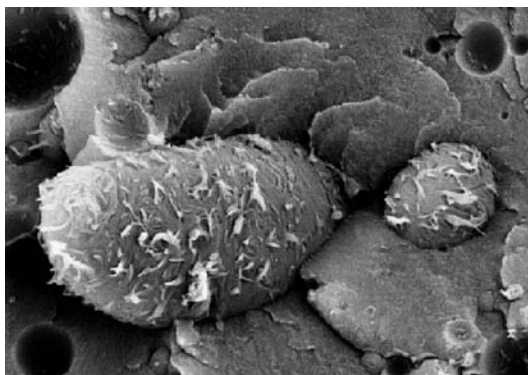


Fig. 14.11 Particle size of PPS/Vectra blends (80/20 wt %) with different contents of corresponding block copolymers added (PPP 3460 g/mol/LCP 6400 g/mol)

Fig. 14.12 Morphology of the interphase of PPS/Vectra blend (80/20 wt %), compatibilized by 5 wt % block copolymer



At the present time, the question of whether the direct addition of block copolymers or in situ formation of block copolymers to a polymer blend is the better choice cannot be answered generally, because both ways seem to have advantages and shortcoming, depending on the special blend system regarded as well as the blend processing parameters.

14.4.3 Conclusions

Summarizing, it can be stated that the miscibility of polymers can be influenced by a variety of methods including chemical reactions and physical methods. Additionally, the proper choice of suitable processing methods and parameters helps to optimize the property profile of the resulting materials and enhances the mechanical properties of polymer blends. The scientific understanding of the interfaces in

immiscible polymer blends is however one of the basic requirements to create materials with optimized properties.

References

1. Koning C, Van Duin M, Pagnoulle C, Jerome R (1998) Strategies for compatibilization of polymer blends. *Prog Polym Sci* 23:707–757
2. Utracki LA (1989) *Polymer Alloys and Blends*. Hanser, New York
3. Utracki LA (1998) *Commercial Polymer Blends*. Chapman and Hall, London, pp 98
4. Charoensirisomboon P, Chiba T, Solomko SI, Inoue T, Weber M (1999) Reactive Blending of Polysulfone with Polyamide: a difference in interfacial behavior between in situ formed block and graft copolymers. *Polymer* 40:6803–6810
5. Charoensirisomboon P, Chiba T, Inoue T, Weber M (2000) In situ formed copolymers as emulsifier and phase-inversion-aid in reactive polysulfone/polyamide blends. *Polymer* 41:5977–5984
6. Pospiech D, Häußler L, Eckstein K, Jehnichen D, Gottwald A, Pötschke P (2000) The influence of segmented block copolymers in immiscible polymer blends. In: *Polymer Blends*. Stamm M (ed), Wiley-VCH, Weinheim (Macromol Symp 149:219–224)
8. Bates FS (1991) Polymer–polymer phase behavior. *Science* 251:898–905
9. Pötschke P, Wallheinke K, Stutz H, Fritsche H (1997) *J Appl Polym Sci* 64:749–762
10. Flory PJ (1953) *Principles of Polymer Chemistry*. Cornell University Press, Ithaca, NY
11. Coleman MM, Painter PC (1990) *Specific Interactions and the Miscibility of Polymer Blends*. Technomic, Basel, Switzerland
12. Creton C, Kramer EJ, Brown HR, Hui C-J (2002) Adhesion and fracture of interfaces between immiscible polymers: from the molecular to the continuum scale. *Adv Polym Sci* 156:53–135
13. Krause S (1972) Polymer compatibility. *J Macromol Sci Revs Macromol Chem* C7(2):251–314
14. Krause S (1978) Polymer–polymer compatibility. In: Paul DR, Newman S (eds) *Polymer Blends*, vol. 1. Academic, London
15. Noolandi J (1992) The influence of multiblock copolymers in immiscible polymer blends. *Macromol Chem Theory Simul* 1:295–296
16. Noolandi J, Shi A-C (1995) Reinforcement of polymer interfaces with random copolymers: an example of interfacial self-stitching? *Phys Rev Lett* 74:2836–2837
17. Van Krevelen DW (1990) *Properties of Polymers, Their Correlation with Chemical Structure; Their Numerical Estimation and Prediction from Additive Group Contributions*. Elsevier, Amsterdam
18. Vilgis TA, Noolandi J (1990) Theory of homopolymer-block copolymer blends. The search for a universal compatibilizer. *Macromolecules* 23:2941–2947
19. Eckstein A, Suhm J, Friedrich C, Maier R-D, Sassmannshausen J, Bochmann M, Mülhaupt R (1998) Determination of plateau moduli and entanglement molecular weights of isotactic, syndiotactic, and atactic polypropylenes synthesized with metallocene catalysts. *Macromolecules* 31:1335–1340
20. Mangaraj D (1963) Cohesive-energy-density of high polymers. *Makromol Chem* 67:84–89
21. Pospiech D, Gottwald A, Jehnichen D, Friedel P, John A, Harnisch C, Voigt D, Khimich G, Bilibin AYu (2002) Determination of interaction parameters of block copolymers containing aromatic polyesters from solubility parameters obtained by solution viscosities. *Colloid Polym Sci* 280:1027–1037

22. Scherble J, Stark B, Stühn B, Kressler J, Budde H, Höring S, Schubert DW, Simon P, Stamm M (1999) Comparison of interfacial width of block copolymers of d8-poly(methyl methacrylate) with various poly(n-alkyl methacrylate)s and the respective homopolymer pairs as measured by neutron reflectivity. *Macromolecules* 32:1859–75
23. Bates FS, Frederickson GH (1990) Block copolymer thermodynamics: theory and experiment. *Annu Rev Phys Chem* 41:525–557
24. Bates FS, Frederickson GH (1999) Block copolymers – designer soft materials. *Physics Today* 2:32–38
25. de Gennes PG (1988) *Scaling Concepts in Polymer Physics*. Cornell University Press, Ithaca, NY
26. Mishra MK (ed) (1994) *Macromolecular Design: Concept and Practice*. In: *Advanced Polymers via Macromolecular Engineering Series*. Polymer Frontiers International, Hopewell Junction, NY
27. Riess G (1985) Block copolymers. In: *Encyclopedia of Polymer Science and Engineering*, 2nd edn. Wiley, New York
28. Schulz M, Bates FS (1996) Morphologies of block copolymers. In: *Physical Properties of Polymers Handbook*, Mark JE (ed). American Institute of Physics, Woodbury, NY
29. Benoit H, Hadziioannou G (1980) Scattering of block copolymers. *Macromolecules* 13:1703–1715
30. Friedel P, John A, Pospiech D, Jehnichen D, Netz RR (2002) Modeling of the phase separation behavior of semiflexible diblock copolymers. *Macromol Theory Simul* 11:785–794
31. Leibler L (1980) The scattering function of block copolymers. *Macromolecules* 13:1602–1610
32. Spontak RJ, Smith SD, Ashray A (1994) Block copolymers in immiscible polymer blends. *Micr Res Techn* 27:412–419
33. Holden G (1987) In: *Thermoplastic Elastomers: A Comprehensive Review*, Legge NR, Holden G, Schroeder HE (eds), chap 13. Hanser, New York
34. McGrath JE (1983) An Introductory Overview of Block Copolymers. *MMI Press Symp Ser* 3:1–16
35. Riess G, Hurtez G (1996) Block copolymers: syntheses, colloidal properties and application possibilities of micelle systems. In: *Solvents and Self-Organization of Polymers*, Webber SE (ed). Kluwer Academic, Amsterdam, p 33
36. Favis BD (1991) Polymer alloys and blends: recent advances. *Can J Chem Eng* 69:619–625
37. Jerome R, Creutz S, Leemans L, Teyssie P (1996) Efficiency of amphiphilic block copolymers as surfactants and dispersion agents. *FATIEPEC Congr* 23:A100–A111
38. Adedej AA, Jamieson AM (1995) Interfacial adhesion in immiscible polymer blends compatibilized with block copolymers. *Compos Interf* 3:51–71
39. Xanthos M (1988) Interfacial agents for multiphase polymer systems: recent advances. *Polym Engin Sci* 28:1392–1399
40. Liu NC, Baker WE (1992) Reactive polymers for blend compatibilization. *Adv Polym Technol* 11:249–262
41. Plochicki AP, Dagli SS, Andrews RD (1990) The interface in binary mixtures of polymers containing corresponding block copolymer: effects of industrial mixing processes and of coalescence. *Polym Eng Sci* 30:741–752
42. Shull K, Kramer EJ, Hadziioannou G, Tang W (1990) Segregation of block copolymers to interfaces between immiscible homopolymers. *Macromolecules* 23:4780–85
43. Fleischer CA, Koberstein JT (1990) The effect of polymer end groups on the compatibility of immiscible polymer blends. *Polym Prepr Am Chem Soc* 31:541–542
44. Fleischer CA, Koberstein JT (1992) Polymer/polymer interfacial modification utilizing polymer end groups. *Polym Mat Sci Engin* 67:94–95
45. Dlubek G, Bondarenko V, Pionteck J, Kilburn D, Pompe G, Taesler C, Redmann F, Petters K, Krause-Rehberg R, Asharaful Alam M (2003) Studies of interdiffusion in polymer blends by PALS. *Rad Phys Chem* 68:369–373

46. Dlubek G, Pionteck J, Bondarenko V, Pompe G, Taesler C, Petters K, Krause-Rehberg R (2002) Positron annihilation lifetime spectroscopy (PALS) for interdiffusion studies in disperse blends of compatible polymers: a quantitative analysis. *Macromolecules* 35:6313–6323
47. Dlubek G, Pompe G, Pionteck J, Janke A, Kilburn D (2003) Differential Scanning Calorimetry (DSC) for interdiffusion studies in PVC/PnBMA blend: A quantitative analysis. *Macromol Chem Phys* 204:1234–1244
48. Dlubek G, Taesler C, Pompe G, Pionteck J, Petters K, Redmann F, Krause-Rehberg R (2002) Interdiffusion in a particle matrix system of two miscible polymers: an investigation by positron annihilation lifetime spectroscopy and differential scanning calorimetry. *J Appl Polym Sci* 84:654–664
49. Berti C, Bonora V, Pilati F (1992) Reactive blending of poly(ethylene terephthalate) and polycarbonate, 1, a reappraisal of the reactions occurring during melt mixing. *Makromol Chem* 193:1665–1677
50. Pilati F, Marianucci E, Berti C (1985) Study of the reactions occurring during melt mixing of poly(ethylene terephthalate) and polycarbonate. *J Appl Polym Sci* 30:1267–1275
51. Pompe G (1997) Influence of transesterification on the thermal properties of PC/PBT blend – miscibility of PC and PBT. *Recent Res Devel Polym Sci* 1:109–147
52. Dutta D, Fruitwala H, Kohli A, Weiss RA (1990) polymer blends containing liquid crystals: a review. *Polym Eng Sci* 30:1005–1018
53. Gahleitner M (2001) Advances in polypropylene. *Progr Polym Sci* 26:895–914
54. Tzoganakis C (1989) Reactive extrusion. *Adv Polym Technol* 9:321–349
55. Majumdar B, Keskkula H, Paul DR (1994) Polymer blends. *J Appl Polym Sci* 54:339–347
56. Malz H (2002) Dissertation, Technical University of Dresden
57. Pötschke P, Zhao H, Schulze U, Kaya A, Malz H (2000) Synthesis of functionlaized polymers and their use in PP/PS blends. In: *Proceedings of the 38th Macromolecular IUPAC Symposium, IUPAC Macro 2000*
58. Auschra C, Stadler R, Vogt-Martin IG (1993) Poly(styrene-*b*-methyl methacrylate) block copolymers as compatibilizing agents in blends of poly(styrene-coacrylonitrile) and poly(2,6-dimethyl,4-phenylene ether): 2. Influence of concentration and molecular weight of symmetric block copolymers. *Polymer* 34:2094–2110
59. Böhme F, Pospiech D, Kappler D, Häußler L (1998) PPS/LCP Block Copolymers as Compatibilizers in High-Performance Polymer Blends. In: *PPS Regional Meeting 98, Toronto, Canada*
60. Kappler D, Böhme F, Pospiech D, Schneller A, Blatter K (1997) Synthese von Copolymeren aus einem Polyarylsulfid und einem aromatischen Polyester sowie deren Verwendung zur Kompatibilisierung von Blends. DE 19742057 (24.9.1997)
61. Pospiech D, Häußler L, Voit BV, Böhme F, Kricheldorf HR (1998) Synthesis of LC multi-block copolymers. In: *Solvent-Free Polymerizations and Processes: Minimization of Conventional Organic Solvents*. Hunt M, Long TE (eds) ACS Symposium Series 713:8–27. American Chemical Society, Washington, D.C.
62. Pospiech D, Häußler L, Eckstein K, Komber H, Voigt D, Jehnichen D, Friedel P, Gottwald A, Kollig W, Kricheldorf HR (2001) Synthesis of high-performance multiblock copolymers by polycondensation reactions in the melt. *High Perform Polym* 13:275–292
63. Pospiech D, Häußler L, Jehnichen D, Kollig W, Eckstein K, Grundke K (2003) Bulk and surface properties of blends with semifluorinated polymers and block copolymers. *Macromol Symp* 198:421–434
64. Jehnichen D, Friedel P, Kummer S, Häußler L, Eckstein K, Pospiech D (1999) Interface characterization of immiscible polymer blends by means of XR and NR investigations. *Mater Sci Forum* 321–324:475–480

Chapter 15

Interfacial Phenomena of Biomaterials

Carsten Werner

Leibniz Institute of Polymer Research Dresden & Max Bergmann Center of Biomaterials
Dresden, Hohe Str. 6, 01069 Dresden, Germany, werner@ipfdd.de

Abstract Since biomaterials are generally used in diagnostic or therapeutic devices with direct contact to the human body, the bio-interfacial interactions are of great interest. Several aspects of surface interactions of biomaterials are discussed, in particular the interaction of polymeric biomaterials with proteins, cells and tissues. To ensure biocompatibility non-specific interactions should be minimized. This may be achieved by particular polymer coatings, but also by implementation of bioactive components or specific surface morphologies and supramolecular biopolymer assemblies.

This chapter provides a simplistic survey of the current opinion about interfacial phenomena of polymeric biomaterials. Emphasis will be put rather on conceptual than on methodological aspects. After introducing the hierarchy of bio-interfacial phenomena, recent trends in the surface modification of polymeric materials will be briefly summarized.

15.1 Introduction

Biomaterials are the substance of devices used for diagnostics and therapy in direct contact with the human body (see Fig. 15.1). Polymeric biomaterials represent a large and most versatile fraction of biomaterials including implant materials such as poly(tetrafluoroethylene) or poly(ethylenterephthalate) applied in cardiovascular surgery, ultra-high molecular weight poly(ethylene) utilized in artificial hip pans, extracorporeal artificial organs such as poly(sulfone)-based hemodialysis membranes or poly(propylene)-oxygenator membranes, degradable suture and cell scaffolds made of poly(lactide) or poly(glycolide) as well as disposables such as poly(amide) catheters or poly(vinyl chloride) blood bags and tubing. The listed examples have in common that polymer bulk materials introduced for non-medical technologies were adapted for medical devices based on their physical properties – strength, elasticity, fatigue resistance, permeability – and by excluding toxicity.

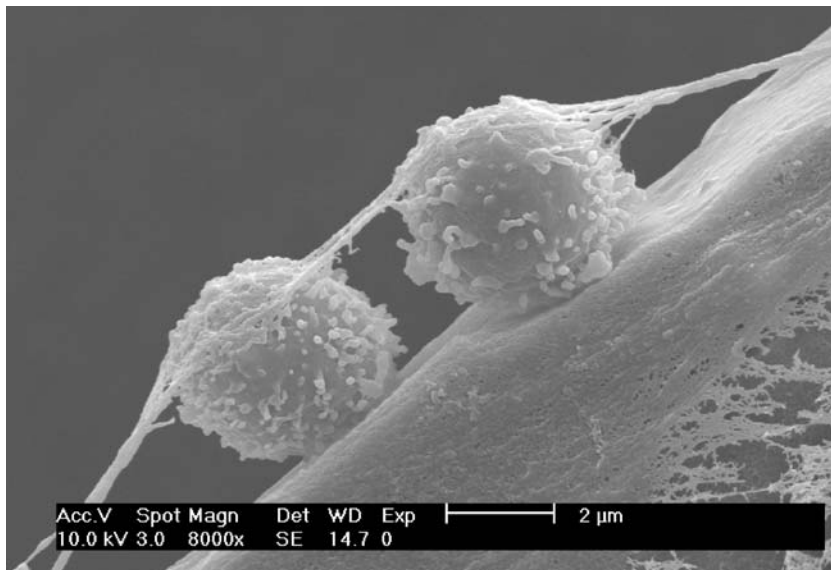


Fig. 15.1 Human hematopoietic stem cells on a fibronectin-coated polymer thin film visualized by scanning electron microscopy

However, depending on the kind of interaction between the biomaterials and the human organism, i.e. depending on the medical device in question, undesired side-effects due to the activation of body-own defence mechanisms may interfere with the success of the applications. This experience provided a major motivation for the formation of a self-contained discipline defined as “biomaterials science”.

As biocompatibility almost exclusively relates to interfacial phenomena biomaterials science is mainly concerned with strategies for the control of bio-interfacial interactions. The need for surface-selective approaches is evident by the fact that composition and characteristics of the bulk material and the surface may differ quite considerably. While this is valid for any type of material and relevant for many applications the performance of biomaterials very often essentially depends on interfaces challenged by a most dynamic and complex adjacent phase, the living organism. It is mainly due to this reason that surface science is – although most sophisticated with numerous non-medical technologies such as microelectronics and catalysis – still in its infancy with respect to biomedical materials.

However, the structural complexity of living matter as it creates difficulties to control interfacial phenomena of biomaterials also contains a wealth of concepts to be applied in the design of advanced biomaterials surfaces: Interfaces within tissues and organs most efficiently realize signal transduction and mass conversion by dedicated assemblies of lipids and biopolymers using the general principles of supramolecular association, minimization of non-specific interaction and modulated specific binding. The rapid evolution of molecular cell biology, developmental biology, structural biology and biochemistry revealing structure-property interrela-

tions of interfaces in multicellular organisms very much stimulates the development of advanced concepts for materials supporting both new and well-established medical technologies. Progress towards this aim depends on the scientific depth and adequacy of research at the boundary of materials/surface science and life sciences.

Despite numerous analogies between surface problems at different types of biomaterials this survey will be restricted to bio-interfacial phenomena of polymers. Polymeric biomaterials are distinguished by the unique structural and functional variety of the materials belonging to this category. Therefore, a most widespread use of polymeric biomaterials is already now found in medical devices of entirely different kinds. However, since advanced synthetic polymers and biopolymers are “variations of a similar theme” the future trends of biomedical engineering requiring a higher quality of biomimetic functionality of materials will rely on dedicated branches of polymer science.

15.2 The Hierarchy of Bio-Interfacial Phenomena

As schematically shown in Fig. 15.2 bio-interfacial phenomena can be categorized according to the level of complexity with respect to both the material and to the adjacent (model) biosystem. The subheadings of this section will roughly follow the horizontal direction in this scheme.

Although there is a general need for biocompatibility there is no “good” or “bad” surface per se – the desired patterns of interfacial processes can be very different depending on the type of medical device: Numerous biomaterials – such as those of intraocular lenses, membranes for blood purification – require low protein adsorption and cell adhesion. However, there are similarly numerous examples of biomaterials depending on strong binding of cells for tissue integration of implants in hard and soft tissues.

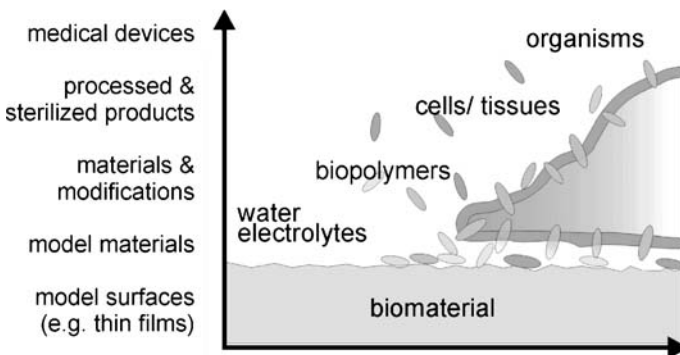


Fig. 15.2 Scale of complexity in bio-interfacial phenomena

15.2.1 Surfaces of Biomaterials in Pre-Application Settings

In view of the relevance of even subtle differences in the surface characteristics of polymeric materials for the interaction with living organism careful analysis of physical and chemical surface parameters is essential both in the development of new or surface-modified biomaterials and in the quality control of the production of medical materials or devices. The measures and methods applied for that purpose are not different from those utilized for the evaluation of materials for non-medical technologies and comprehensively discussed in earlier chapters of this book: Elemental (X-Ray photoelectron spectroscopy) and molecular composition (time-of-flight secondary ion mass spectrometry, surface-sensitive variants of vibrational spectroscopies such as infrared or Raman spectroscopies), structural features (scanning force and electron microscopy, confocal laser scanning microscopy), wetting (contact angle goniometry), electrical charging (electrokinetic measurements, titrations), adsorption/desorption (gas and vapour sorption measurements, for adsorption of macromolecules from solution see below) and adhesion characteristics (surface force apparatus, atomic force microscope) are considered. As the bio-interfacial phenomena very often involve amphiphilic biomolecules capable of interacting with solid surfaces through entirely different mechanisms (see below) surface characterization of biomaterials has to provide an as complete as possible picture of physical and chemical surface parameters which forces to apply a spectrum of analytical methods. A major challenge with many of the above-listed methods concerns the fact that biomaterials are applied in aqueous environments while several powerful analytical tools require air or even vacuum conditions. To address this task cryo-preparations for the conservation of water-swollen interfacial structures in the solid state and special techniques making vacuum-based methods applicable to humid samples – such as the environmental scanning electron microscopy – have been developed. Several excellent books and reviews provide further details on the surface characterization of polymeric biomaterials [1–5].

Surface characteristics of polymeric biomaterials can be significantly altered prior to any contact with the human organism due to deposition of ad-layers, the interfacial accumulation of additives such as plasticizers, or in consequence of degradation, leaching and chemical alterations. The probability of these processes is increased during processing of the materials which often involves heating and contact with solvents or processing aids. Chemical conversions – such as hydrolysis or oxidation – not only occur under processing but even under inappropriate storage conditions. While the above-mentioned factors influence the surface properties of polymeric materials in general sterilization is a procedure almost exclusively applied with medical devices [6]. As sterilization aims at the quantitative extermination of any microbial contaminations associated with the materials it requires rather rigorous treatments such as gamma- or electron beam irradiation, elevated temperature and pressure or cytotoxic chemicals (e.g. ethylene oxide). The conditions of these treatments often cause modifications of both bulk and surface properties of polymeric biomaterials. In turn, intentionally performed

surface modification such as thin film coatings or immobilized biomolecules may be severely affected by inadequate sterilization procedures. Considering the dramatic changes materials may undergo in pre-application settings surface analysis of realistically processed, sterilized and stored polymeric biomaterials urgently deserves more attention.

15.2.2 Biopolymers at Interfaces

Initial steps upon contact of biomaterials with living matter include wetting, swelling and the adsorption of electrolyte ions and low-molecular substances. However, the bio-interface of any material receives significance just by the interaction with biopolymers and namely proteins: Proteins preferentially adsorb at the solid liquid interface, associate there with similar or different proteins, undergo structural changes, become displaced from the interface by similar or different proteins and carry through these processes the message “met a foreign material” into the adjacent human body. Therefore, it is certainly possible to imagine biopolymers as “translators” converting the language of the polymer surface in the tongue of the living organism. While a key aspect of biopolymers in tissues is their interaction with cells (see below) dedicated functions of living matter entirely base on protein–protein cascade reactions triggering – among many essential features of life – important defence mechanisms against injury or foreign invaders: blood coagulation and complement activation. It is through these reactions – and through some cell-based processes similarly activated by proteins at interfaces – that biomaterials induce localized and systemic reactions in the organism which cause clinical responses designated as “bio-incompatibility problems”. Thus, where biocompatibility issues motivate research on biomaterials proteins at interfaces are in the center of interest.

However, the importance of protein adsorption in biomaterials science is faced with the persisting lack of a complete picture of driving forces and mechanisms. Through the last few decades the problem was approached from different sides [7, 8]: While Norde [9] and some others selected small globular model proteins and model surfaces Brash [10] and several others studied protein adsorption and retention out of complex multicomponent solutions such as serum or plasma in contact with “real world biomaterials” including hemodialysis membranes. In between these two “extremes” are numerous studies dealing with isolated large plasma proteins in contact with biomaterials or model surfaces or investigations using complex biofluids in contact with model substrates as done in the now classical work of Vroman [11]. With very few exceptions biopolymer adsorption onto biomaterials has been so far mainly studied *in vitro*.

The choice of analytical tools to study biopolymers at interfaces very much depend on the choice of one of the above-mentioned experimental approaches: While single biopolymer adsorption onto planar model substrates can be conveniently studied with respect to the adsorbed amount by numerous methods for thin

film characterization such as ellipsometry, surface plasmon resonance, amino acid analysis, quartz microbalance, optical waveguide and a similar variety of techniques measuring depletion of solutions can be used for the quantification of biopolymer adsorption onto large surface areas of, for instance, dispersed particles only a few dedicated methods based on micro differential scanning calorimetry, circular dichroism, and infrared spectroscopy provide information about the protein conformation and a similarly limited set of techniques – including atomic force microscopy, total internal reflectance fluorescence or infrared spectroscopy – is adequate to derive information about lateral distribution and orientation of proteins at solid surfaces. For complex, multicomponent protein systems adsorption is usually studied by methods established in biochemical laboratories [12]. A semi-quantitative determination of proteins out of multicomponent mixtures can be achieved by two-dimensional gel electrophoresis combined with immunoblotting techniques. Also, immunosorbent assays for the quantification of single components and immunolabeling techniques using either fluorescence or radioisotope labels are applied both for quantification of proteins at interfaces and for the detection of available subunits. In general, methods to study biopolymers at interfaces are much more elaborated for proteins than for non-proteinaceous biopolymers. For a comprehensive survey of experimental methods to study biopolymers at interfaces see [7, 8]. Very recently, substantial progress was achieved in the use of theoretical methods for the analysis of proteins at interfaces [13].

Experiments with model systems evaluated in the light of surface thermodynamics [7, 9] could clarify that the major subprocesses contributing to protein adsorption are (i) electrostatic interactions between protein and substrate, involving the co-adsorption of small electrolyte ions, (ii) dispersion interactions, (iii) changes in the hydration state of both the solid surface and parts of the protein molecules, and (iv) structural rearrangements in the protein. It is important to consider that these subprocesses may severely affect each other, e.g. efficient hydrophobic interactions may induce changes in the protein structure to expose its hydrophobic interior which is normally hidden in the dissolved state of the protein. In turn, the degree of conformational flexibility of the protein can be substantially altered. Weighing the different contributions for a number of selected systems it was concluded that all proteins adsorb to hydrophobic surfaces, even under electrostatically adverse conditions. For the adsorption onto hydrophilic surfaces the structural stability of the proteins needs to be considered. While “hard” structurally stable proteins adsorb to hydrophilic surfaces only if they are electrostatically attracted structurally labile – “soft” – proteins may gain sufficient degrees of conformational entropy upon adsorption to anchor even on an electrostatically repelling surface. The impact of the different contributions to the protein–substrate interaction may also be substantially influenced by the dynamics of the subprocesses leading to rather different characteristics of adsorbed protein layers at different transport conditions. For instance, the degree of structural changes of a protein at any given surface can substantially increase with decreasing the solution concentration during adsorption since the individual protein may cover a larger sur-

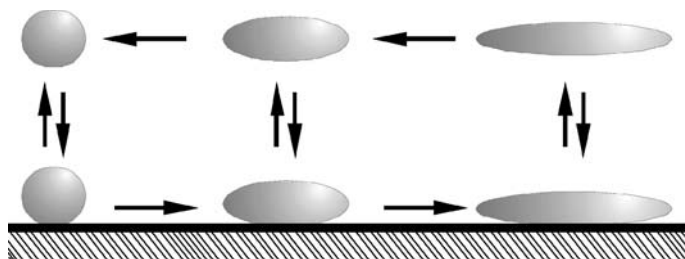


Fig. 15.3 Proteins at solid/liquid interfaces. Schematic representation of the interplay of adsorption, structural change and desorption

face area by unfolding during time if no competing protein occupies the required space (compare Fig. 15.3).

While protein adsorption, desorption and displacement could be mechanistically explained for a number of simple model systems the patterns of biopolymers at interfaces currently remain enigmatic in application-related settings: Biofluids such as blood not only contain hundreds of different protein components to be distinguished in size and structural as well as functional characteristics, they also contain these proteins at very different concentrations. Accordingly, only very few general conclusions were drawn so far concerning biomaterials in contact with multicomponent protein solutions. In view of the transport and concentration conditions smaller proteins present in biofluids at higher concentrations are thought to initially cover materials in these settings first. Subsequent reorganization processes of the protein ad-layers were concluded to depend on the type of interactions of the initially adsorbed and the competing (larger, less abundant) proteins with the substrate. Vroman and some others studied this time- (and also concentration-) dependent displacement series of plasma proteins at model surfaces and established correlations of the interfacial protein–protein exchange with the activation of the kinin system, a cascade reaction initiating blood coagulation [11].

15.2.3 Biomaterials in Contact with Cells and Tissues

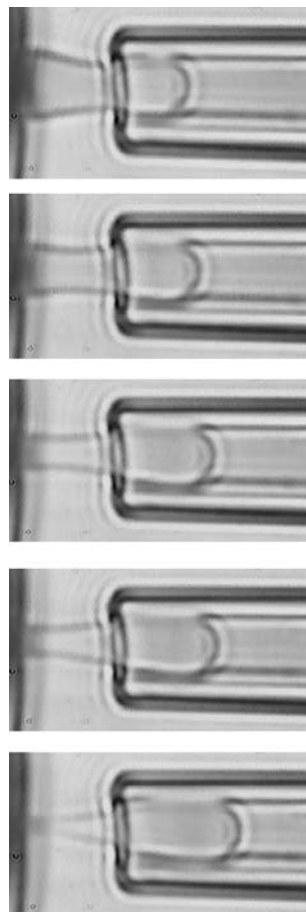
Adsorbed biopolymers represent the forefront of any biosystem brought into contact with a biomaterial and, in turn, significantly trigger the subsequent interaction with cells and tissues. Thus, cell adhesion to solid surfaces is always the result of a certain balance of non-specific forces and specific interactions mediated by biopolymer ad-layers. Attachment and spreading of cells is either a required feature of biomaterials or needs to be suppressed for the desired performance of implant materials. However, throughout the recent years there was more and more evidence that more subtle differences in the status of adherent cells can be induced by the characteristics of solid surfaces and the biopolymers adsorbed on top of them. The cell-own secretion and reorganization of biopolymers was identified to

be a key issue in that context. Surface-associated physical and chemical cues were convincingly shown to even provide control over cell proliferation, differentiation and programmed cell death (apoptosis). Therefore, surface profiles of biomaterials may become powerful instruments to switch the fate of adherent cells and to direct the integration of biomaterials into host tissues. Namely polymer scaffolds for regenerative therapies need to make use of these options. However, a substantially extended understanding of the relevant signals to be generated by the biomaterial's surfaces is required.

Cell-biomaterial interactions are very often studied at standard cell culture conditions using various cell types including fibroblastic, endothelial and neuronal cells or myocytes which may conserve dedicated functional characteristics through the adhesive contact with artificial materials, and also less adhesive cells such as blood progenitor cells. Analytical methods to study shapes and molecular markers of cells and tissues in contact with biomaterials originate from cell biology and from histology and include various types of microscopy such as phase contrast microscopy, confocal – fluorescence – laser scanning microscopy, scanning electron microscopy and transmission electron microscopy as well as flow and image cytometry and molecular biology (DNA hybridization) techniques [14–16]. Many of these tools essentially depend on labelling procedures to visualize or quantify certain molecular constituents which indicate vitality and the regenerative, metabolic or functional status of the analysed cell populations. In addition, dedicated biophysical techniques have been developed to analyze physical aspects of cell adhesion by probing the strength of attachment [17]. For illustration, Fig. 15.4 shows a micropipet-aspiration experiment realizing the stepwise separation of the adhesive contact between a human erythrocyte and a poly(styrene) surface. (For details see [18].)

Theories on cell adhesion onto artificial surfaces were first developed from the classical concept of colloidal interactions emphasizing van der Waals attraction and electrostatic repulsion between the negatively charged cell membranes and the also very often negatively charged solid surfaces. The bridging of the contact zone by biopolymer chains and the osmotic forces arising from the interfacial hydrogel phase were later introduced to improve the relevance of this approach [19]. Also, the mechanics of the deformation of cell membranes were extensively studied in order to explain the formation of adhesive contact between cells and between cells and solid surfaces. Sophisticated models could be developed and verified for certain, carefully chosen experimental settings [20], however, the primarily physicochemical approach is limited by not sufficiently reflecting the crucial role of specific binding between cellular receptors and extracellular biopolymers for the adhesion of cells to biomaterials.

Fig. 15.4 Stepwise separation of an erythrocyte from a polymer substrate upon increase of the suction pressure applied by a glass micropipet (substrate polystyrene, pre-adsorbed anti-Glycophorin C, initial contact diameter $4.2\ \mu\text{m}$, separation dynamics $2\ \text{nN}/\text{min}$, separation energies increasing from upper to lower image: $33, 162, 283, 360, 455 \times 10^{-6}\ \text{Nm}^{-1}$, for further details see [18])



Simultaneously, a wealth of knowledge about the molecular machinery of cell adhesion was collected throughout the last few years. Namely the integrin receptors binding to extracellular matrices of biopolymer assemblies were studied in very much detail. It was shown that binding of integrin receptors to ligands such as fibronectin, collagen or laminin not only provides a most efficient means for cell attachment to biopolymer-coated substrates but generates important intracellular downstream signals determining cellular behaviour and fate [21]. Also, the capability of many cell types to reshape their extracellular matrix by releasing proteolytic enzymes and by secreting and reorganizing matrix biopolymers was extensively studied.

In consequence, the impact of biomaterials on cell adhesion has to be considered with respect to (i) cues for initial contact and (ii) guidance for subsequent cell-own matrix organization. Both preadsorption of various proteins of the extracellular matrix (e. g. collagen, fibronectin, laminin) onto polymeric materials and physicochemical surface modification of solids favouring the adsorption of these

“adhesive” proteins out of serum-containing cell culture media were successfully established as robust methods to trigger cell attachment. However, precise and long term control over cellular states requires the modulation of biomolecular signals going far beyond that. For that purpose, the impact of physical and chemical surface parameters of polymeric biomaterials has to be reconsidered. Pioneering work in that context was done by Ingber and Whitesides [22], showing that the micropattern of adhesive/antiadhesive surface segments on solid surfaces can switch fate-decisions of adherent endothelial cells from apoptosis to proliferation or differentiation. Further studies were also dedicated to the mechanisms of formation of supramolecular structures in cell-secreted matrix [23] and on the impact of the pliability of polymer substrates on the formation of adhesion clusters [24].

In contrast to the above-mentioned work which was entirely based on cell culture *in vitro* biomaterials are also extensively analyzed after implantation. These studies usually characterize the structure of the contact zone between the implant surface and the surrounding tissue. A most remarkable finding of these investigations was that a set of implant materials exposing a wide variety of different surface characteristics – which provoke distinct differences in cell-adhesion under culture conditions *in vitro* – obviously similarly lead to encapsulation via inflammatory reactions *in vivo* [2]. This result sheds light on the fact that surface modification strategies need scrutiny with respect to their relevance for the formation of long term tissue templates.

15.3 Surface Modification of Polymeric Biomaterials

Polymeric materials currently applied in medical devices were selected according to their mechanical properties and several additional features determined by their bulk characteristics. To enhance the biocompatibility of the materials adjustment of the surface characteristics according to the desired interaction with the living organism has to be achieved while keeping the bulk properties required for performance invariant. Developing an entirely new polymer is only the option of choice if indeed the characteristics of the volume phase have to be altered as well. For the vast majority of cases a surface-selective modification of the material provides substantial advantages. Therefore, numerous strategies of surface modification of polymeric biomaterials have been suggested. To categorize these approaches one may distinguish the modification of physical and chemical surface characteristics, the implementation of bioactive elements and the formation of biomimetic supramolecular assemblies. Section 15.3 will follow this distinction.

15.3.1 Minimizing Non-Specific Interactions

A most simple general approach starts from the fact that bio-incompatibility is caused by activation reactions at the surface of the biomaterial which doubtlessly

have to involve the interaction of biomolecules with the surface. Preventing any interaction between the surface and the biopolymers of the biosystem would, therefore, prevent the activation of the reaction mechanisms of the living organism.

Hydrogel coatings, and especially non-ionic gel layers, were found to support this idea. With that concern, poly(ethylene glycol) (PEG)/poly(ethylene oxide) (PEO) is in the center of interest for several years now. It could be shown that both rather short oligo(ethylene oxide) chains and long poly(ethylene oxide) chains end-grafted to various carrier materials can efficiently suppress protein adsorption in vitro [25, 26]. Several methods of immobilization have been established – including self assembly of thin films of EO-containing amphiphils, numerous variants of reactive attachment via functional terminating groups of the PEO, adsorptive binding of PEO-containing block copolymers, low pressure plasma or electron beam treatments of preadsorbed PEO layers [25] and the degree of protein resistance was found to depend on the oligo/poly(ethylene oxide) layer structure which, in turn, is influenced by grafting density and chain length. Tetraglyme structures and star-like PEO structures were concluded to be most efficient in preventing protein adsorption [27]. In order to unravel the mechanism of the protein resistance of surfaces a recent study compared a large number of non-ionic, hydrophilic moieties with respect to protein binding [28]: It could be shown, that several molecular structures exhibiting a low degree of hydrogen-donor act similarly efficient as compared to PEO with respect to protein resistance in vitro. Since the limited stability of PEO against hydrolytic attack interferes with clinical success of PEO-modified surfaces more stable alternatives with comparable protein resistance but higher stability in biofluids are of highest interest.

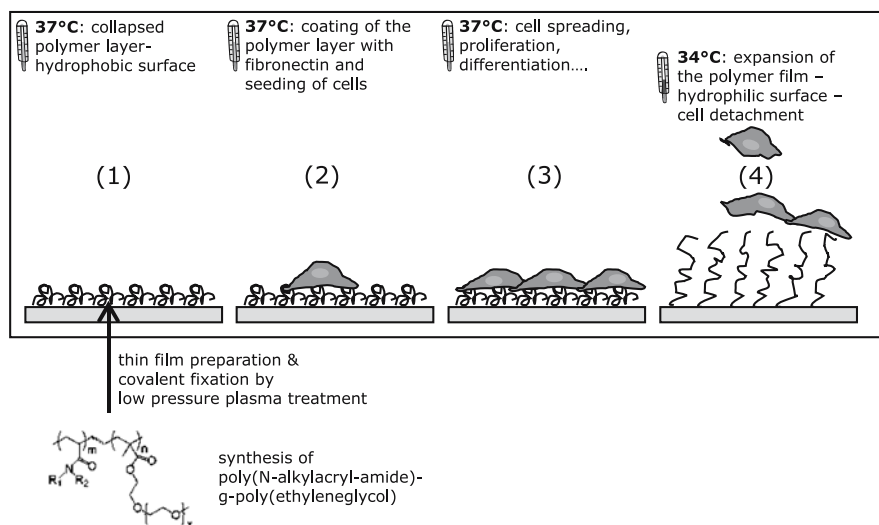


Fig. 15.5 Thermoresponsive copolymers grafted with PEO can be used as thin film cell culture carriers allowing for gentle harvesting of cells without enzymatic treatments or mechanical stress. For details see [29]

A recently suggested example of the PEO-modification of polymer surfaces made use of stimuli-responsive polymers to switch the hydrophilic characteristics of the coated surface (Fig. 15.5 [29]): Surface-bound thin films of poly(N-alkyl-acryl-amide)-g-poly(ethyleneglycol) – immobilized by a plasma-cross-linking technique to a carrier polymer – respond to a slight change of the environmental temperature with a phase transition leading to a rapid exposure of hydrophilic or hydrophobic subcomponents to the outermost surface. Accordingly, the protein binding of these polymers is dramatically changed allowing for the efficient detachment of cell layers grown on the coated surfaces without enzymatic treatments.

Another promising approach to minimize non-specific binding of biomolecules makes use of immobilized biopolymers. While earlier attempts to passivate surfaces by adsorption of proteins were found to be of limited success poly(saccharides) – such as hyaluronic acid or dextrane derivatives – appear to be advantageous since they create the non-adhesive layers within living organism [30]. Poly(saccharide) molecules often carry charged moieties – which was concluded to be less favourable when comparing gel layers of synthetic polymers – and the origin of their protein resistance needs to be unravelled. Although technically less elaborated so far, this approach provides the most valuable option of creating biomimetic anti-adhesive surfaces of biomaterials.

15.3.2 Implementing Bioactive Elements – Modulating Molecular Signals

The identification of biomolecular components providing certain functional features towards living organisms provoked their use in the surface modification of biomaterials. Among the longest-known examples is the immobilization of heparin onto blood contacting surfaces (tubing, membranes) in order to prevent blood coagulation. Another prominent example concerns the immobilization of adhesive proteins, which can mediate cell adhesion by providing ligand structures for integrin receptors of cells.

The type of activity of the immobilized bioactive molecules may require entirely different binding modes: While many molecules can be tightly bound to provide a localized activity towards biomolecules and cells other molecules, such as certain growth factors, need to be released for cellular internalization. In either case immobilization of bioactive molecules has to conserve their desired activity upon immobilization.

A general distinction can be further made between biomolecules -isolated from natural materials or produced by genetic engineering – and synthetic bioactive substances. The used biomolecules are most often rather large and complex structures which may undergo conformational changes at interfaces affecting their functions. In contrast, synthetic bioactive molecules are often tailored for any desired interaction with a molecular target and therefore substantially smaller and robust. This principle has been recently elaborated for the example of benzamidin-

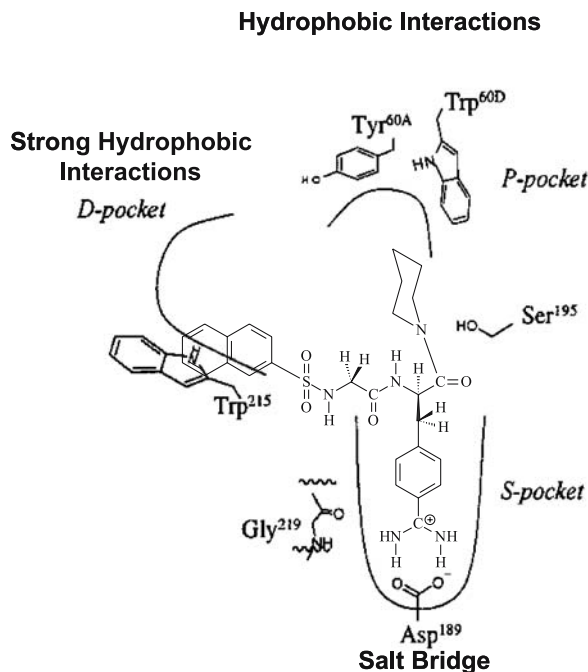


Fig. 15.6 Structure of a synthetic thrombin inhibitor functionalized for covalent attachment to reactive polymer surfaces. The important interactions with the active center of thrombin are schematically shown. For details see [31]

derivatives which mimic the function of hirudin, a thrombin-binding anticoagulant, and can be conveniently immobilized to polymer surfaces (Fig. 15.6 [31]). However, environmental requirements also exist for synthetic bioactive molecules and need to be considered when choosing an immobilization technique.

The binding principles applied for the attachment of bioactive molecules to the surfaces of polymeric biomaterials include physisorption and specific or covalent binding. Adsorption is rather easily attained and can be advantageous where release of the immobilized molecules is required. To facilitate release, adsorption within surface bound hydrogel layers can be applied. The volume phase of the layer acts as a reservoir and the degree of cross-linking of the gel layer can be adjusted to control the dynamics of this process. Covalent binding does usually not allow for a precise control of the orientation of biopolymers at interfaces since the utilized reactions involve several protein side chains simultaneously. A very common approach to realize covalent binding consists of the functionalization of the biomaterial surface with reactive derivatives of carboxylic acids such as active esters or anhydrides to bind lysine side chains of the proteins. However, if this principle interferes with the required activity of the immobilized protein – for instance due to blocking of an active site – an alternative method may be used to link different amino acid side chains. A more advanced method to attach proteins to surfaces consists of the use of protein-*tags* and their surface-bound counterparts

to achieve a highly oriented, reversible binding. (The degree of reversibility can be certainly very different depending on the affinity of the bond.) Examples comprise the binding of proteins by Ni^{2+} controlled complexation of a histidin residue to a N,N'-bis(carboxymethyl)lysine-modified surface, the linkage between leucine-rich peptide sequences attached to both the protein and the surface ("leucine zipper") or the immobilization of antibodies or antibody fragments binding to the target protein structure or to a *tag*-element of this protein. While this approach is very elegant it requires the modification of the protein. Both, covalent and specific binding have to consider the geometric constraints of the activity of the immobilized molecules. Since almost any interaction with dissolved proteins or cell membranes to be realized by the surface-bound molecules requires some distance to the surface of the carrier biomaterial the use of "spacer" molecules in between the surface of the biomaterial and the bioactive molecule is most common now. A key requirement for spacer molecules is hydrophilic behaviour and flexible, chain-like characteristics. The preferred spacer type in numerous recent studies consists of end-functionalized poly(ethylene oxide), other commonly used spacers include poly(acrylic acid) and dextrane sulphate.

The spacer concept for the immobilization of bioactive molecules is also attractive for another important reason: Bioactive molecules not only need to be protected against structural changes during binding – the performance of bioactive coatings also very much depends on the minimization of undesired, non-specific adsorption occurring with the functionalized surface. Thus, the general approach discussed in Sect. 15.3.1 is highly relevant also for the implementation of bioactive molecules into the surfaces of biomaterials and there are many similarities of the spacer structures for binding bioactive molecules with the "bioinert coatings" discussed above.

However, the active molecule linked to the biomaterial through a flexible, hydrophilic polymer chain which is simultaneously preventing protein adsorption just represents one extreme out of a variety of relevant options: The physical and chemical constraints of bioactive molecules at interfaces of polymeric substrates cannot only support or hamper the functional characteristics of the bioactive components, these conditions even allow to switch between different performance profiles which may either be relevant for the control of interfacial phenomena of biomaterials. Therefore, it is certainly justified to consider the kind of immobilization of bioactive molecules to the surfaces of biomaterials as an option to modulate molecular signals towards the adjacent organism. An example (Fig. 15.7 [23, 32]) concerns the anchorage of adsorbed fibronectin to thin films of alternating maleic acid. The choice of the comonomer determines the hydrophilicity and charge density of the copolymer films. In turn, the binding strength of similar amounts of pre-adsorbed fibronectin leads to distinct differences in the reorganization of the protein by endothelial cells grown in contact with these substrates. This difference, however, was found to be essential for the cellular decision to form capillary networks: Only the weakly bound fibronectin layer was reorganized by the cells in the third dimension and supported, by that, the process of angiogenesis which is required for the vascularization of engineered tissues.

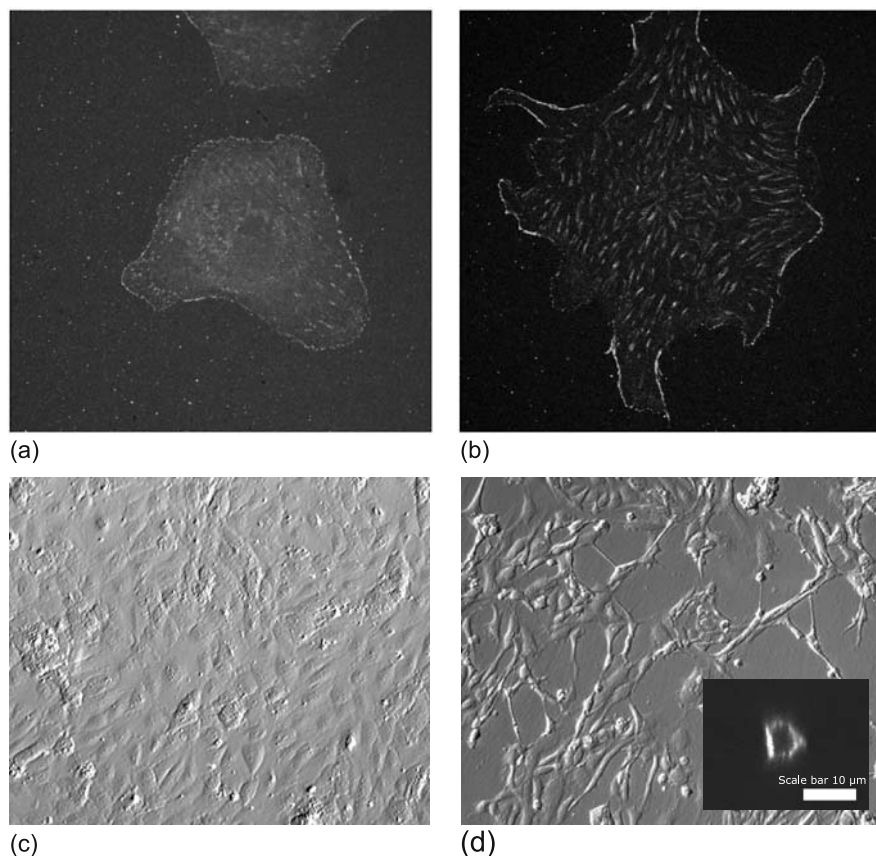


Fig. 15.7 Human endothelial cells grown in contact with fibronectin-precoated maleic acid copolymer films. Strong binding of fibronectin on the more hydrophobic and less anionic poly(octadecene *alt* maleic acid) (**a**, **c**) prevents reorganization of the preadsorbed fibronectin [(**a**) confocal images of a single cell after 50 minutes of contact with the substrate – fibronectin labelled in red, focal adhesions green] and stimulates the formation of a flat, tightly immobilized endothelial cell layer after 5 days (**c**) while weaker binding of fibronectin on the more hydrophilic and more anionic poly(propene *alt* maleic acid) (**b**, **d**) permits extensive reorganization of fibronectin in fibrils (**b**) and supports formation of three-dimensional capillary endothelial networks. (**d**) Insert: cross-sectional view of a single cell. Image sizes: above 90 μm , below (horizontally) 700 μm . For details see [23, 32]

15.3.3 Supramolecular Biopolymer Assemblies Providing Morphogenetic Cues

Reorganization of immobilized biopolymers into supramolecular aggregates – as discussed in the example in the last part of Sect. 14.3.2 – points at interfacial phenomena in the context of a new generation of polymeric biomaterials. Many cur-

rent concepts still rely on a traditional design of implants or artificial organ systems and aim at improved performance and biocompatibility to be achieved through “decoration” of the biomaterial surface by dedicated bioactive molecules. In contrast, polymeric biomaterials in the era of regenerative medicine now have to be bioactive *and* biodegradable. Their most important task is to act as a template for tissue regeneration and to guide cells – either growing in from surrounding tissues or implanted with the polymer scaffold – to form a fully functional regenerated tissue while the scaffold material is gradually replaced.

The structure these biomaterials are referring to is extracellular matrix: Extracellular matrices are tissue-specific biopolymer assemblies providing a three-dimensional viscoelastic milieu rich with biomolecular information and highly dynamic with respect to the interaction with the embedded cells. It is through these matrices that the living organism directs development, homeostasis and regeneration. Therefore, mimicking these matrices is not a new idea in the context of tissue engineering for regenerative therapies [33]. The related approaches make extensive use of biopolymers forming assemblies *in vitro* – such as collagen fibrils and fibrin meshworks – and currently undergo an evolution by first reconstituting limited structural and mechanical aspects, adding more and more advanced variants of growth factor immobilization and now enter the stage of designing synthetic matrices with proteolytic susceptibility, adhesive binding sites and modulated growth factor anchorage to achieve a faithful imitation of the bi-directional interactions between cells and the matrix surrounding them. Progress at this end requires substantial input from different sides: First – and beyond the scope of this survey – the set of degradable polymer materials needs to be enriched with new variants allowing to implement peptide sequences for dedicated binding of growth factors and cellular receptors and sites cleavable by enzymes. Also, the materials need to be adjustable with respect to mechanical properties which can be achieved through the degree of cross-linking. Secondly, the character of the cell adhesion in the matrices needs to be triggered by arranging a certain molecular composition together with an appropriate set of physical parameters (porosity, anchorage of the molecules, pliability). Third, the local distribution and binding of growth factors in the matrices has to be engineered through both modification of the factors and the matrix binding sites. Fourth, the proteolytic sensitivity of the matrices should be fine-tuned with respect to the reorganization rate of any tissue in question.

A few advanced examples demonstrate the feasibility of this approach: Hubbell and coworkers introduced an engineered variant form of VEGF that mimics matrix-binding and cell-mediated release by local cell-associated enzymatic activity in fibrin with the result that the quality of angiogenesis in the matrix was substantially improved [34]. Also, he could demonstrate the utility of integrating two types of protein signals into networks containing a combination of oligopeptides mediating cell adhesion and substrates for cellular-controlled degradation to engineer bone [35]. Mooney and coworkers reported about a single matrix capable of delivering multiple growth factors (VEGF and PDGF) with distinct kinetics which dramatically increased blood vessel maturity [36]. While these examples concern matrices intended for implantation cell carriers for *in vitro* expansion of progenitor

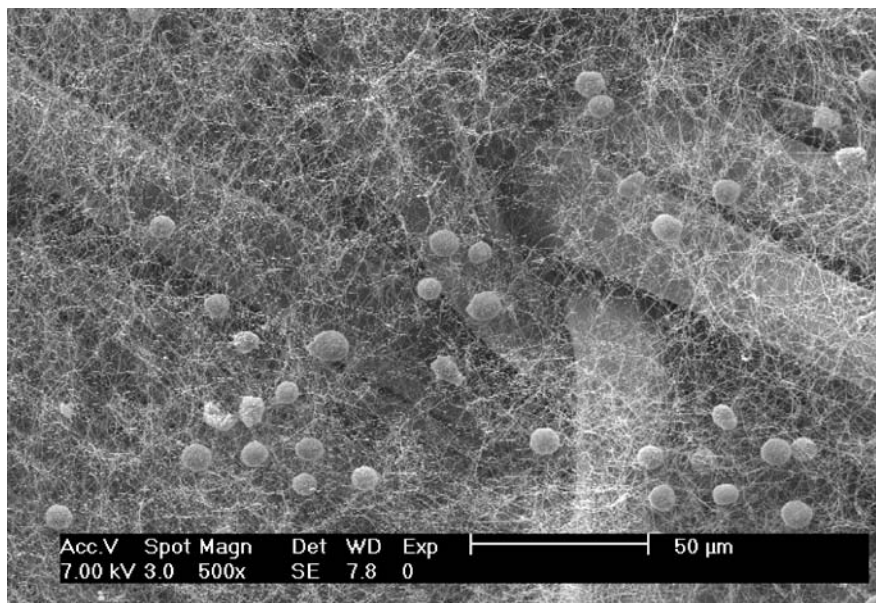


Fig. 15.8 Human hematopoietic stem cells growing in a collagen I based microfibrillar matrix which was reconstituted in a poly(ethyleneterephthalat) fibre structure

cells in bioreactor systems have to fulfil comparable requirements. Figure 15.8 shows human hematopoietic stem cells grown in the presence of SCF, IL3 and FLT3 in a three-dimensional matrix of collagen I fibrils [37]. Such matrices are prepared to mimic molecular and structural characteristics of the stem cell micro-environment of the bone marrow in artificial settings to generate high numbers of early progenitor cells for transplantation.

Developing polymeric biomaterials capable to act as tissue templates has to include substantial contribution from genetic engineering to produce the required protein components. Likewise, supramolecular chemistry has to enter the scenery. However, with these new approaches, the old tasks related to biointerfacial phenomena revive – minimizing non-specific adsorption, controlling competitive adsorption and directing anchorage and conformation of proteins are essential again.

15.4 Conclusion

Biointerfacial phenomena occurring with polymer materials applied for diagnostic or therapeutic purposes often reveal the limits of traditional surface science and provoke interdisciplinary innovation in analytical and preparative approaches. Surface characteristics of materials determine performance in medical devices – such as implants, extracorporeal artificial organs, disposables – as in microelectronic

circuits or catalysts. However, the structural and functional complexity and dynamics of living matter create numerous additional challenges. A key task concerns the biocompatibility of interfaces, i. e. preventing the activation of defence processes of the human organism against foreign invaders. To address this problem, several variants of stealth coatings for materials have been developed to minimize non-specific interactions of biopolymers with materials and to allow for the efficient interfacial presentation of selected bioactive molecules. Despite the impressive evolution of the related strategies for tailoring polymer surfaces clinically successful biocompatible coatings remain to be achieved. This underlines the need for an in-depth understanding of driving forces and mechanisms of the interactions between biomolecules and polymer surfaces. Expanding knowledge in molecular life sciences and the promise of regenerative therapies dramatically aggravate the relevance of the latter task. In the beginning era of engineered tissues bio-artificial matrices consisting of supramolecular associates of biopolymers or their synthetic mimics play a crucial role to guide cellular fate decisions and organization by providing scaffolds and morphogenetic cues. Progress in the rational design of such polymer-based biomimetic tissue templates requires new options for precise functional modulation of bioactive molecules at interfaces of polymer matrices.

Acknowledgements

The author thanks his coworkers at the Leibniz Institute of Polymer Research Dresden & The Max Bergmann Center of Biomaterials Dresden for contributing to the examples given in this chapter. Financial support by Bundesministerium für Bildung, Forschung und Technologie, Berlin, by Sächsisches Staatsministerium für Wissenschaft und Kunst, Dresden, and by Deutsche Forschungsgemeinschaft, Bonn, is gratefully acknowledged.

References

1. Ratner BD, Hoffman AS, Schoen FJ, Lemons JL (eds) (1997) *Biomaterials Science: An Introduction to Materials in Medicine*. Academic, New York
2. Castner DG, Ratner BD (2002) *Biomedical surface science: Foundations to frontiers*. *Surf Sci* 500:28–60
3. Morra M (ed) (2002) *Water in Biomaterials Surface Science*. Wiley, New York
4. Davies J (1997) *Surface Analytical Techniques for Probing Biomaterial Processes*. CRC, Boca Raton, FL
5. Merrett K, Cornelius RM, McClung WG, Unsworth LD, Sheardown H (2002) Surface analysis methods for characterizing polymeric biomaterials. *J Biomater Sci Polym Ed* 13:593–621
6. Rodriguez-Benot A, Santamaria R, Martin-Malo A, Aljama P (2002) Sterilization procedures and biocompatibility. *Contrib Nephrol* 137:138–145

7. Horbett TA, Brash JL (eds) (1995) *Proteins at Interfaces II: fundamentals and applications*, ACS Symposium Series 602. American Chemical Society, Washington, D.C.
8. Malmsten M (ed) (1998) *Biopolymers at Interfaces*. Dekker, New York
9. Norde W, Lyklema J (1991) Why proteins prefer interfaces. *J Biomater Sci Polym Ed* 2:183–202
10. Cornelius RM, Brash JL (1991) Identification of proteins absorbed to hemodialyser membranes from heparinized plasma. *J Biomater Sci Polym Ed* 4:291–304
11. Vroman L (1987) The importance of surfaces in contact phase reactions. *Semin Thromb Hemost* 13:79–85
12. Kellner R, Lottspeich F, Meyer HE (eds) (1999) *Microcharacterization of Proteins*. Wiley, New York
13. Wilson K, Stuart SJ, Garcia A, Latour RA (2004) A molecular modeling study of the effect of surface chemistry on the adsorption of a fibronectin fragment spanning the 7–10th type III repeats. *J Biomed Mater Res* 69:686–98
14. Spector DL, Goldman RD, Leinwand LA (1997) *Cells: A laboratory manual*. Cold Spring Harbor Laboratory, Cold Spring Harbor, NY
15. Matsumoto B, Matsudaira PT, Wilson L (eds) (1993) *Cell biological applications of confocal microscopy*. Academic, New York
16. Shapiro HM (1999) *Practical flow cytometry*. Wiley-Liss, New York
17. Flyvbjerg H, Jülicher F, Ormos P, David F (eds) (2002) *Physics of bio-molecules and cells, Les Houches Session LXXV*. Springer, Berlin Heidelberg New York
18. Werner C (2004) Cell adhesion to polymer substrates characterized by the micropipette aspiration technique. *J Adh* (in press)
19. Curtis ASG, Lackie JM (eds) (1991) *Measuring cell adhesion*. Wiley, New York
20. Orsello CE, Lauffenburger DA, Hammer DA (2001) Molecular properties in cell adhesion: a physical and engineering perspective. *Trends Biotechnol* 19:310–6
21. Cukierman E, Pankov R, Yamada KM (2002) Cell interactions with three-dimensional matrices. *Curr Opin Cell Biol* 14:633–639
22. Dike LE, Chen CS, Mrksich M, Tien J, Whitesides GM, Ingber DE (1999) Geometric control of switching between growth, apoptosis, and differentiation during angiogenesis using micropatterned substrates. *In Vitro Cell Dev Biol Anim* 35:441–448
23. Pompe T, Kobe F, Salchert K, Jørgensen B, Oswald J, Werner C (2003) Fibronectin anchorage to polymer substrates controls the initial phase of endothelial cell adhesion. *J Biomed Mater Res* 67A:647–657
24. Roos WH, Roth A, Konle J, Presting H, Sackmann E, Spatz JP (2003) Freely suspended actin cortex models on arrays of microfabricated pillars. *Chem Phys Chem* 4:872–877
25. Harris JM (ed) (1992) *Poly(ethylene glycol): Chemistry, Biotechnical and Biomedical Applications*. Plenum, New York
26. Halperin A, Leckband DE (2000) From ship hulls to contactlenses: Repression of protein adsorption and the puzzle of PEO. *CR Acad Sci Paris 1 Série IV*:1171–1178
27. Shen M, Martinson L, Wagner MS, Castner DG, Ratner BD, Horbett TA (2002) PEO-like plasma polymerized tetraglyme surface interactions with leukocytes and proteins: in vitro and in vivo studies. *J Biomater Sci Polym Ed* 13:367–390
28. Chapman RG, Ostuni E, Takayama S, Holmlin RE, Yan L, Whitesides GM (2000) Surveying for surfaces that resist the adsorption of proteins. *J Am Chem Soc* 122:8303–4
29. Schmaljohann D, Oswald J, Jørgensen B, Nitschke M, Beyerlein D, Werner C (2003) Thermo-responsive PNiPAAm-g-PEG films for controlled cell detachment. *Biomacromol* 4:1733–1739
30. McLean KM, Johnson G, Chatelier RC, Beumer GJ, Steele JG, Griesser HJ (2000) Method of immobilization of carboxymethyl-dextran affects resistance to tissue and cell colonization. *Colloids Surf B Biointerfaces* 18:221–234
31. Gouzy MF, Sperling C, Salchert K, Streller U, Simon F, Rauwolf C, Böhme F, Voit B, Werner C (2004) In vitro blood compatibility of polymeric biomaterials through covalent immobilization of an amidine derivative. *Biomater* 25:3493 – 3501

32. Pompe T, Markowski M, Werner C (2004) Modulated fibronectin anchorage at polymer substrates controls angiogenesis. *Tissue Eng* (in press)
33. Hubbell JA (2003) Materials as morphogenetic guides in tissue engineering. *Curr Op Biotechnol* 14:551–558
34. Ehrbar M, Djonov VG, Schnell C, Tschanz SA, Martiny-Baron G, Schenk U, Wood J, Burri PH, Hubbell JA, Zisch AH (2004) Cell-demanded liberation of vegf₁₂₁ from fibrin implants induces local and controlled blood vessel growth. *Circ Res* 94:1124–1132
35. Lutolf MP, Weber FE, Schmoeker HG, Schense JC, Kohler T, Muller R, Hubbell JA (2003) Repair of bone defects using synthetic mimetics of collagenous extracellular matrices. *Nat Biotechnol* 21:513–8
36. T.P. Richardson, M.C. Peters, A.B. Ennett, D.J. Mooney (2001) Polymeric system for dual growth factor delivery. *Nat Biotechnol* 19:1029–34
37. Salchert K, Streller U, Pompe T, Herold N, Grimmer M, Werner C (2004) In vitro reconstitution of fibrillar collagen type I assemblies at reactive polymer surfaces. *Biomacromol* (in press)

Index

A

adhesion 2, 13, 150
adsorption 235–247, 249–251, 254–256
 electrostatic interaction 243
 energy 243
 Gibbs energy 243
 hydrophobic interaction 254
 interaction energy 237
 interaction force 243, 249
 isotherm 238, 239, 241
 Langmuir isotherm 236, 239
 surface energy 240, 241
 surface interaction 243
adsorption energy 243, 251
adsorption isotherm 236, 238, 240–242,
 246, 249, 251
adsorption layer 240
adsorption mechanism 237, 251
adsorption process 249
AES 78
AFM 8, 179
AFM-nanotomography 168
alignment 264, 265, 268, 270
 parallel 264
 perpendicular 264
alkoxy-/chloro-silane π -functional 225
alkoxysilane 227
analysis technique 3
angiogenesis 312
anti-wetting 294
array 265, 271
 ordered 265
AR-XPS 75
atomic force microscopy AFM
 8, 181

attenuated total reflexion infrared
 ATR-IR 52
Auger effect 78
auger spectroscopy AS 5, 78
axisymmetric drop shape analysis-profile
 ADSA-P 125

B

beam test double cantilever 148
Benninghoven, Alfred 92, 93
binary brush 219
binding energy 72, 77
binding state 9
bioactive 314
bioactive substance synthetic 310
biocompatibility 299
biodegradable 314
bioinert 312
biomaterials 299
biomaterials polymeric 299
biopolymer 303
blade cutting 139, 152
blend 275, 280, 287, 288, 291, 293
 interface 293
 morphology 290
blending reactive 283
blister test 139, 151
block copolymer 161, 280, 281, 286, 287
 brush 224
block copolymer assembly
 supramolecular 271
block copolymer segmented 293
bond fluctuation model 185, 188, 192
Bragg peak 173
brush 224, 270

brush mixed 229
brush multi-component 220

C

capillary penetration technique 129
capillary wave 185, 189, 190
cell adhesion 301, 305
cellulose 133
channel 264, 268, 270, 271
 cylindrical 271
charging mechanism 119
chemical composition 7, 9, 11, 13, 15
chemical grafting 228
chemical potential 192
chemical shift 72, 81, 82
coarse-grained parameter 184
colloidal probe technique 159
compatibility 278
compatibilization 275, 279, 286, 287, 290,
 291, 293
compatibilizer 286–288
complex modulus 141
composition fluctuation 191
compression shear test CST 148
concentration fluctuation 190
contact angle 4, 7, 103, 109, 111, 197
 advancing 109
 apparent 110
 equilibrium 110
 goniometry 207
 hysteresis 110
 receding 109
 Wenzel 110
 Young 110
continuity equation 192
count rate 74, 77, 95
crack resistance curve 146
crazing 143
critical surface tension 114
CTOD concept 145

D

degree of coverage 85
demixing 277
density functional theory DFT 197
depth profile 93
diblock copolymer 293
diffuse reflexion infrared DRIFT 59
dimple morphology 221
dispersion 290
dispersion interaction 304
DMT 158

domain 262, 264, 267, 268, 270
 cylindrical 264, 267, 268, 271
 spherical 264

E

elastic recoil detection ERD 5
electrical double layer 119, 122
electrokinetic measurements,
 zeta potential 4
electron energy loss spectroscopy
 high-resolution 5
electron spectroscopy, chemical analysis
 7, 72
electrons mean free path 75, 79
electrostatic interaction 304
ellipsometry ELLI 4, 9, 62
emulsifier 281
encapsulation 308
end-functional group 227
end-notched flexure test 148
energy release rate 145
engineering plastic 288
entanglement molecular weight 287
EPD theory 193
equation of state 115, 184, 199
ESCA 72
exchange reaction 288
extracellular matrices 314
extrusion reactive 290

F

fibronectin 312
film pressure 112
film thickness 10
Flory–Huggins parameter 184–186, 188
fluid-like packing 184, 199
fluorescence quenching 6
focused ion beam FIB 4, 5
forward recoil spectroscopy FRD 5
Fourier transform infrared spectroscopy
 FTIR 207
fracture mechanics 144
fracture toughness 144, 156, 293
friction 8
functional group 226
 acidic/basic 124

G

gas bubble adhering 124
GC, inverse 5, 15
geometric mean combining rule 115

Gibbs concept 236, 238
GISANS 35–37, 39
goniometer technique 124
Gouy–Chapman–Stern–Grahame
model 122
graft copolymer 286, 290
grafting 215, 228
to/from 225, 227–229
grafting density 218
grazing incidence infrared GIR 58
grazing incidence X-ray small angle
scattering GISAXS 4, 19, 27,
28, 33, 34, 37, 39

H

hardness 13
heparin 310
Hertz model 156
hydration state 304
hydrogel 309
hydrogen bonding 264–267, 270
hydrophilic/hydrophobic 222

I

immobilization 310
indentation 13
index of refraction 9
information depth 4, 5
infrared attenuated total reflection
ATR-FTIR 4
infrared spectroscopy IR 9
injection molding 290
interaction parameter 279
interdiffusion 171
interface 192, 275
interface fluctuation 189, 190
interface tension 6, 7, 103, 104, 107,
183, 188, 199, 285, 287
interface thickness 279, 282
interface width 10, 15, 165,
168, 184
interfacial region 2
interlaminar strength 147
intermolecular interaction 283
intrinsic width 190
inverse gas chromatography 5, 15
ion technique 15
IR 9
IR dichroism 51
IsGISAXS 26, 37

J

J-integral 146
j–j coupling 77
JKR model 157

L

labelling 82, 83
Laplace equation 107
layer thickness 85
Lennard-Jones potential 194
light quantum theory 71
line tension 111
lithography 15
loss factor 141

M

macrophase separation 277
maleic anhydride 289
mass–charge ratio 92–94
master curve 142
matrix effect 93
mean field calculation 280
mechanical properties 13
micro-hardness 155
micro-indentation MI 4
micropattern 308
microphase separation 279, 280
miscibility 279, 283, 284
mixing 276
molecule ion 93
Monte Carlo simulation 192, 195
morphology 33, 34
mushroom like structure 217

N

nanochannel 265
nanoindentation 154
nanomachining 15
nanostructure 17, 30, 31
nanotemplate 265
nanotomography 179
neutron reflectometry NR 4, 5, 10
neutron scattering 165
nucle 190
nuclear magnetic resonance NMR 6
nuclear reaction analysis NRA 5

O

Onsager coefficient 192, 193
 optical method 47
 optical microscopy OM 4, 12

P

pancake like structure 217
 particle electrophoresis 134
 particle size 290
 peel test 139, 150
 pendent drop 5
 PES 72
 phase diagram 280
 phase segregation 220
 photo-chemical quantum equivalent
 law 71
 photoelectric effect 71, 72
 photoelectron spectrometer 73
 photoelectrons 72
 inelastically scattered 74, 77, 78
 pinned micelle 218, 219
 plasma modification 203
 plasma polymerization 211
 plasma-cross-linking 310
 PMMA 171
 polyampholyte 243
 polyelectrolyte 239, 243, 244, 249, 254
 electrostatic interaction 243
 interaction force 249
 isotherm 243
 polyelectrolyte complex 249
 polyelectrolyte multilayer PEM 55
 polymer 283
 polymer blend 275, 278, 284, 286
 polymer blend immiscible 277, 282
 polymer brush 177, 215
 polymer brush mixed 220
 polymer chain tethered 216
 polymer interface 162
 polymer stimuli-responsive 310
 polymerization “living” free radical 230
 polyolefine 289
 polypeptide
 conformation/orientation 57
 polypropylene graft 289
 polystyrene 161
 polytetrafluoroethylene 130
 positron annihilation lifetime
 spectroscopy 286
 PRISM theory 196
 protein 303
 protein adsorption 56, 301, 303

protein-tag 311
 PS-*b*-PnBMA 174

Q

quality control 302

R

radical polymerization 228
 Raman spectroscopy 61
 Raman spectroscopy resonance
 enhanced 5
 reaction 285
 real space 17, 20, 21, 29
 re-alignment 269
 reciprocal space 17, 20, 21, 23–25, 29,
 30, 32
 reflectivity 167
 reflectometry 162
 regenerative medicine 314
 resolution 3
 ripple morphology 221
 roughness 8, 10
 Rouse model 192
 RSF 79
 Rutherford backscattering RBS 5

S

scanning electron microscopy SEM 4
 scanning force microscopy SFM 4, 6, 8
 scanning near-field optical microscopy
 5, 8
 scanning tunnelling microscopy STM 4, 8
 SCF theory 188–190, 193, 194, 200
 scratch test 153
 secondary ion 92
 secondary ion mass spectrometry
 SIMS 5, 13, 91
 imaging 99, 101
 ion source 93, 99
 lateral resolution 99
 magnetic sector field detector 93
 quadrupole detector 93, 96
 sample (requirement) 95
 time-of-flight detector 93
 ToF-SIMS spectrometer 93
 segregation limit strong 184, 188
 segregation limit weak/strong 187
 self-consistent field (SCF) theory
 184–186
 sensitivity factor relative 79
 sessile drop 124

- shear test double lap 148, 149
 - shear test single lap 148, 149
 - shear yielding 143
 - Siegbahn, Kai 72
 - SIMS 91
 - dynamic 93
 - information depth 93
 - quantitative information 93, 95
 - static 92, 93
 - SIMS spectrum 94
 - fingerprint spectrum 101
 - high-molecular mass fragment 95
 - high-resolution ToF-SIMS 96
 - key peaks 98, 101
 - mass resolution 96
 - molecular mass distribution 97
 - negative 94
 - positive 94, 96
 - ToF-SIMS 95
 - wide-scan 97
 - single chain in mean field 193
 - small angle X-ray scattering SAXS 6
 - solubility parameter 279
 - spacer type 312
 - spinodal decomposition 190, 277
 - sputter process 92
 - sterilization 302
 - stiffness 13
 - streaming potential measurement 135
 - stress intensity factor 144
 - structural rearrangement 304
 - structure 18–23, 25, 28, 30–32, 35–38
 - sub-structure 36
 - supramolecular assembly 264, 265, 267
 - surface 2, 6
 - surface charge 119
 - surface concentration 54
 - surface contamination 79, 85
 - surface force 150
 - surface force apparatus 156
 - surface modification 225
 - surface plasmon resonance SPR 65
 - surface plasmon spectroscopy SP 4, 9
 - surface potential 12
 - surface structured 223
 - surface tension 4, 107, 199
 - component approach 117
 - surfactant 235–237, 239, 244, 245, 247, 250–252, 254, 256
 - adsorption 54, 249
 - adsorption density/force 245
 - adsorption isotherm 244
 - coulomb interaction 245
 - interaction force 245, 250
 - polyelectrolyte complex 241
 - specific interaction 245
 - steric interaction 251
 - surface energy 245
 - switching 222, 224
- T**
- take-off angle 75, 79, 84, 85
 - template 271
 - thickness 9
 - time-of-flight ToF 92, 93, 95
 - topography 8, 12
 - transesterification 288
 - transmission electron microscopy TEM 6, 11
 - transmission infrared 51
 - transmission X-ray microscopy 7
 - transport condition 304
 - triple point 199
- U**
- ultra-hydrophobic state 223
- V**
- vibrational spectroscopy 47
 - viscoelasticity 141
- W**
- weighted-density Ansatz 195
 - Wertheim's perturbation theory 194, 196, 197
 - wettability 113, 184, 223
 - wetting 2, 7, 104
 - complete 106
 - partial 106
 - wetting behaviour 294
 - wetting preferential 264
 - Wilhelmy balance technique 127
- X**
- XPS 4, 71, 210
 - charge compensation 76, 85
 - imaging-XPS 87
 - information depth 74, 75, 84
 - kryo-XPS 86
 - lateral resolution 86, 87
 - sample (requirement) 76
 - small-spot XPS 86
 - XPS angle-resolved 75, 84

XPS spectrum 74
 background 74, 77, 79
 component peak 80
 deconvolution 80, 82
 full width at half maximum 81
 high-resolution spectrum 80
 interpretation 76
 quantification 76, 78
 surface composition 78, 79
 wide-scan spectrum 76
X-ray 10
X-ray photo-electron emission
 microscopy 7
X-ray photoelectron spectroscopy XPS
 4, 72, 207

X-ray reflectometry XR 4, 6
X-ray source 73
 Bremsstrahlung 73

Y

yield 141
Young's equation 197
Young's modulus 13
Young's relation 108

Z

zeta potential 12, 105, 119, 134

ERRATUM

Polymer Surfaces and Interfaces

Characterization, Modification and Applications

Manfred Stamm (Ed.)

ISBN 978-3-540-73864-0

E-ISBN 978-3-540-73865-7

© Springer-Verlag Berlin Heidelberg 2008

Chapter 10: "Plasma Modification of Polymer Surfaces and
Plasma Polymerization"

Mirko Nitschke

The original version of this article unfortunately contained a mistake. The spelling of the author's name (Mirko Nitschke) in chapter 10 was incorrect in the metadata of the eBook.